IAEA-TECDOC-1233

Nuclear fuel behaviour modelling at high burnup and its experimental support

Proceedings of a Technical Committee meeting held in Windermere, United Kingdom, 19–23 June 2000

INTERNATIONAL ATOMIC ENERGY AGENCY IAEA

July 2001

The originating Section of this publication in the IAEA was:

Nuclear Fuel Cycle and Materials Section
International Atomic Energy Agency
Wagramer Strasse 5
P.O. Box 100
A-1400 Vienna, Austria

NUCLEAR FUEL BEHAVIOUR MODELLING AT HIGH BURNUP
AND ITS EXPERIMENTAL SUPPORT

IAEA, VIENNA, 2001
IAEA-TECDOC-1233
ISSN 1011–4289

Printed by the IAEA in Austria
July 2001

FOREWORD

Nuclear energy is competing with the coal, oil and gas industries under the present conditions of privatization and electricity market deregulation. Under these conditions fuel reliability and performance are becoming ever more important for utilities. Fuel that limits operation, causes an early shutdown or cycle interruption is unacceptable. In the six years since the last IAEA meeting on modelling of water reactor fuel performance, the demands on fuel have increased, particularly regarding the requirements for higher burnup and greater operating flexibility. Fuel modelling codes have had to evolve in response to this. New experimental data have emerged from test reactor experiments and examination of lead assemblies at high burnup. The relative importance of the different aspects of modelling has also changed. New materials and designs, including mixed oxide fuel, burnable absorber fuel and other additive fuels, together with corrosion resistant claddings, have become more prominent.

The IAEA, recognizing the importance of good fuel performance modelling for all types of water power reactors, has devoted much attention to this subject. The Technical Committee Meeting on Nuclear Fuel Behaviour Modelling at High Burnup and its Experimental Support is the seventh in a series of IAEA meetings which were held in 1978 and 1980 (Blackpool), 1982 (Preston), 1984 (Windermere), 1988 (Preston) and 1994 (Windermere) upon the recommendation of the International Working Group on Water Reactor Fuel Performance and Technology. All of these meetings were found to be of value in advancing the understanding of fuel behaviour.

The thirty-two papers presented at the meeting covered the status of codes, experimental facilities and the main phenomena affecting the fuel during irradiation, namely: thermal fuel performance, clad corrosion, pellet–cladding interaction (PCI), fission gas release (FGR) and MOX fuel specifics in modelling.

At the invitation of the Government of the United Kingdom and British Nuclear Fuels plc (BNFL), the meeting took place in Windermere, 19–23 June 2000. Sixty-one participants from nineteen countries took part.

The IAEA wishes to thank BNFL for hosting the meeting and, in particular, C. Brown and I. Palmer for chairing and co-ordinating the meeting, respectively, and all the participants for their contributions to this publication. The IAEA officer responsible for this publication was V. Onoufriev of the Division of Nuclear Fuel Cycle and Waste Technology.

EDITORIAL NOTE

This publication has been prepared from the original material as submitted by the authors. The views expressed do not necessarily reflect those of the IAEA, the governments of the nominating Member States or the nominating organizations.

The use of particular designations of countries or territories does not imply any judgement by the publisher, the IAEA, as to the legal status of such countries or territories, of their authorities and institutions or of the delimitation of their boundaries.

The mention of names of specific companies or products (whether or not indicated as registered) does not imply any intention to infringe proprietary rights, nor should it be construed as an endorsement or recommendation on the part of the IAEA.

The authors are responsible for having obtained the necessary permission for the IAEA to reproduce, translate or use material from sources already protected by copyrights.

CONTENTS

DEVELOPMENT OF CODES AND METHODS (Session 5)

HIGH BURNUP FUEL MODELLING (Session 6)

SUMMARY

1. INTRODUCTION

A Technical Committee Meeting on Nuclear Fuel Behaviour Modelling at High Burnup and its Experimental Support was held at Windermere (United Kingdom) from 19–23 June 2000. This was the seventh in the series of fuel modelling meetings dating back to 1978. Sixty-one participants attended the meeting from nineteen countries. A total of thirty-two papers were presented.

Modelling plays an important role in the drive towards improved fuel performance. Reactor operators require both improved fuel cycle economics and greater fuel reliability. This dictates the need for fuel to withstand more demanding duties in terms of burnup, dwell time, and coolant temperature and chemistry, and to exhibit improved failure resistance in both normal operation and under operational transients. Key issues in high burnup fuel modelling include the degradation of fuel conductivity, fission product retention, and fuel behaviour in transients (including fast, reactivity transients). Increasing use of new materials, including advanced cladding alloys and alternative fuel types such as mixed oxide (MOX) fuel and doped fuels, also drives the need for the development of a more mechanistic understanding of fuel behaviour.

Apart the above-mentioned meetings, the following IAEA activities in this direction can be mentioned which create jointly the platform on information exchange and assistance to Member States in fuel modelling:

(a) Assessment of the maturity and prediction capabilities of fuel performance codes, and support for interaction and information exchange between countries with code development and application needs (FUMEX-1 Co-ordinated Research Project — 1993–96 and FUMEX-11 CRP 2002-2006 which is in initiation stage now).

(b) Regional model project RER/4/019 on WWER fuel code licensing (1997-99). In the framework of this project with participation of Eastern European countries the TRANSURANUS code, developed by the EC Institute for Transuranium Elements, was distributed to Eastern European countries in order to model the behaviour of WWER fuel.

(c) The joint OECD/NEA-IAEA International Fuel Performance Experiments (IFPE) database which now includes the data from 381 rods/samples from PWR, BWR, PHWR and WWER fuels. This database was used to validate the modifications to the TRANSURANUS code and to validate national codes.

(d) A series of three international seminars conducted jointly with CEA-Cadarache, France and OECD/NEA on fuel performance modelling (March 1998, September 2000 and 2002).

2. SESSION I: FUEL THERMAL PERFORMANCE

Thermal conductivity values are usually calculated from thermal diffusivity measurements performed using the laser flash technique with measurements done using micro-specimens cut from irradiated fuel. The tendency of thermal conductivity decrease for UO_2 and UO_2-4.5% gadolinia fuels with increasing burnup up to 60 and 50 GWd/t U pellet average, respectively,

was confirmed in paper presented by M Amaya of JNF, Japan. The difference in the thermal conductivity between UO_2 and gadolinia doped fuel becomes insignificant at high burnups. The work also showed that in the case of irradiated samples, preparation techniques could affect the experimental results. Specimen size and shape effects were checked by using unirradiated specimens. Irradiated specimens were taken from flat burnup profile zones of the pellet. Irradiation damage, rather than gadolinia doping, was the dominant influence in reducing the thermal conductivity at high burnups. It was argued that this would explain the small differences observed in this experiment between UO_2 and gadolinia fuel at higher burnups. To check this point, current results will be compared in the future against existing in-pile tests. The same method was applied by T. Shaw of AEA Technology, UK to determine thermal diffusivity of pre-irradiated UO_2 samples oxidized in the laboratory. The results showed inconsistencies with existing data, which implied that the oxidation method has an influence on the results, and further work is deemed necessary. The oxidation technique does not include the steam plus hydrogen mixture atmosphere existing in a failed BWR fuel rod. The existence of hydrogen would inhibit the oxidation reaction.

On-line measurements performed in the Halden Reactor (T. Tverberg of OECD HRP, Norway) addressed the effect of the gas composition and overpressure level on the thermal performance of a re-fabricated high burnup (52–55 MWd/kg UO_2, with a tightly closed gap) PWR fuel rod. The tests showed that under these conditions fuel temperatures are basically determined by the thermal conductivity degradation rather than from the gap conductance even for high internal overpressures. The analytical derivation of the thermal response of a fuel rod during a reactor scram to support the dependences of the time constants typically used to characterize the fuel response was done in EU Institute for Transuranium Elements (A. Schubert). In addition, a comparison of the major time constant calculated using the TRANSURANUS code and those measured in a selected number of experiments carried out in Halden was presented and the results analyzed.

3. SESSION 2: FISSION GAS RELEASE (FGR)

In the session the emphasis was given to fission gas behaviour modeling for high burnup UO_2 fuel and to analysis of new data on FGR and re-evaluation of old data for both, integral release tests and studies focusing on single processes.

A common observation of Marcin Szuta of IAE, Poland is that the radial concentration profile of fission gases correlates with the grain size distribution in a high rated fuel implying their interrelation. Two types of burst fission gas release have been identified: weaker below 700^{o}C and more intensive (depending on burnup) above about 1500^{o}C. Grain re-crystallisation is thought to be the key distinction between these two processes. At the high temperature range, the major contribution of burst release is explained by the purging of the grain of fission products with the help of the recrystallisation process. Assuming a link between grain growth and gas release, the grain growth model of Ainscough was modified by using the Vitanza curve for FGR. A model is then constructed which describes the release kinetics. In the discussion part a question was raised how the amplitude of the burst is seen in the sense of modelling. The answer was that this is done via grain size — the larger the grain the smaller the burst. For the mechanism how the re-crystallisation is accompanied with re-solution it was answered that the re-soluted gas (the chemically bound fission gas) is released due to re-crystallisation process. The lattice of the grain is purged from the immobilised FG products.

At low temperatures, large numbers of very small intra-granular bubbles, typically of around 1 nm diameter, have been revealed by post-irradiation examinations of irradiated UO_2. As a

result, large volumetric swellings — up to 10%, can appear at high temperature reactor transients, in which case these bubbles act as sinks for fission gas atoms and vacancies. Under irradiation, the nucleation and growth of these bubbles comes from the balance between irradiation-induced nucleation, diffusion growth and an irradiation induced re-solution mechanism. This is the conceptual picture of the study reported by R. White of BNFL, UK. It turns out, however, that it is incomplete because in the absence of irradiation the model predicts that the bubble population present from the pre-irradiation would act as the dominant sink for fission gas atoms resulting in large intra-granular swellings and little or no fission gas release. In practice, large fission gas releases are observed from post-irradiation annealed fuel.

In order to deepen into this phenomenon, a series of experiments addressed the issue of fission gas release and swelling in post-irradiation annealed UO_2 originating from advanced gas cooled reactor (AGR) fuel which had been ramp tested in the Halden test reactor. The experimental observations have been carefully analysed, which lead to the following main conclusions: i) there is no evidence of intra-granular bubble loss during post-irradiation anneals and although differences exist from specimen to specimen, these are probably within the experimental scatter. It must be concluded that the grown bubbles are a small sub-population of the large low temperature seed-population. The intra-granular bubble radii and swellings that are observed in out-of-pile anneals tend to be smaller than those observed in-pile; ii) The evidence has been found for lack of thermal re-solution of fission gas atoms from intra-granular bubbles.

An alternative model, leading to two important consequences, has been proposed to explain the slow growth of intra-granular fission gas bubbles. The first is to attenuate the vacancy and fission gas diffusion rates. The second, and probably most important, is to create absorption difficulties at the matrix/bubble interface whereby a certain vacancy gradient is required to initiate absorption of vacancies and gas atoms. This approach could be an explanation for the exponential tails on the distributions and for the fission gas release observed during post-irradiation anneals.

Realistic modelling of FGR at high and very high burnups requires modifications of the existing models. The radial distributions of retained xenon of a high burnup steady state as well as ramped fuel typically show features, release steps that cannot be explained by standard diffusion models solely. Set of EPMA data on irradiated fuel have been analysed by F. Sontheimer of Siemens, and the extraordinary features have been traced down to xenon saturation effects that do not only depend on the burnup but also on local temperature. Fission gas release model of CARO-E has been modified correspondingly. This enables to reproduce the xenon profiles in ramped fuel and in steady state fuel irradiated up to 100 MWd/kg U. The enhanced fission gas release towards high burnups stems, even with falling power histories with lower temperatures, mainly, from the centre of the pellet and to small extent from the rim. The modelling is now in agreement with these observations and well describes the fission gas release enhancement with burnup. A clarification about Figure 6 was given that the fit (solid curve) is based on larger database than the few points plotted.

The database on FGR from AGR fuel was used by W. Ellis of AEA Technology, UK for benchmarking current theories of pre-interlinkage gas release. The following conclusions have been reached: i) a parametric equation describing the pre-interlinkage ("athermal") release was developed. The equation is suitable for standard fuel pins and the data could be predicted with a random error of times/divide 1.2 (1σ); ii) the observed releases are consistent with current theoretical mechanisms of migration of fission gas to free surfaces being primarily controlled by vacancy migration and iii) the diffusion coefficients that have been

derived from analysis of unstable fission gas release in the Halden Reactor test provide a good description of the observed release.

Concluding remarks:

Fission gas phenomena, not only the release to open volumes, but the whole sequence of processes taking place prior to this, need to be modelled in any modern fuel performance code. The presence of gaseous fission products may generate rapid fuel swelling during power transients, and this can cause pellet-clad interaction (PCI) and rod failure. At high burnups, the quantity of released gases could give rise to pressures exceeding the safe limits.

Deficiencies are still encountered in the modelling, and both integral fission gas release tests and studies focusing on single processes such as diffusion, bubble formation, swelling, grain growth and resolution are encouraged to support the modelling. Old tests could be re-evaluated taking advantage of the new knowledge of the high burnup fuel. Fission gas atom diffusion coefficients have been measured/determined over the years, but their magnitudes still have a large scatter. More diffusion data should be provided from the temperatures 400–800^{o}C, which is a typical temperature range for a high burnup fuel under operation.

4. SESSION 3: CLAD MODELLING

Models and modelling of pellet-cladding interaction (PCI), cladding transient behaviour and fission product and coolant impact were the focus of this session. These topics will be in the centre of a new IAEA Co-ordinated Research Project (FUMEX-II) to start in 2002. Previous IAEA CRP (FUMEX-I, 1993–96) concentrated mainly on modelling of fuel thermal characteristics and is still frequently cited, also during this meeting and this session, e.g. the paper on simulation of pellet-cladding thermo mechanical interaction presented by A. Denis of CNEA, Argentina. The paper is a report of a work-in-progress of a 2D finite-element-based fuel rod code. Initial validation efforts using the FUMEX series of experiments look favourable. While the code has good potential, it requires considerable effort to achieve its full potential for fuel behaviour analysis.

New approach to experiments to evaluate stress corrosion cracking (SCC) of Zr-based alloys was presented by O. Fandeur of CEN-Saclay, France. It offers new interesting features relative to conventional SCC tests. Instead of the usual hold time at a single stress level, two-level stress tests, called “discriminating” tests, were performed, in which a higher stress plateau is followed by a lower stress held for a given period of time or until failure. Authors assert that the higher stress in the discriminating tests has no effect on the failure time, despite a hold time of up to one hour. This surprising result is interpreted to mean that SCC failure is independent of the stress history and depends only on the final state of stress at time of failure. The current state of practice of PCI modelling in fuel behaviour codes is to treat the SCC mechanism as a continuous function of stress, temperature and time, which is quantified using the cumulative damage concept to calculate failure time for time-varying stress and temperature. This approach appears to be incompatible with the results, thereby requiring a different method of application of the results to fuel rod modelling. Also, additional tests are needed to evaluate initiation time. Significant finding of this work is that the crack-tip plastic strain field is not important to SCC initiation, because it disagrees with prevailing views in the literature.

The role of computational structure of the code to calculate PCI effects during transients is important. The TOUTATIS code, presented by F. Bentejac of CEN-Saclay, France, has a 3D

finite element computational structure. The TOUTATIS code may be regarded as the ultimate goal. However, the numerics, rather than fuel behavioural modelling, may drive the code's development. For example, the pellet-clad interface is a non-planar sliding-surface problem that is notoriously difficult computationally. Experience indicates that full 2D (r-z and r-θ), together with well-characterized fuel behaviour models and constitutive descriptions provide adequate analysis capabilities. However, certain pellet-cladding interaction effects can only be modelled in three dimensions, such as the enhancement of stress/strain concentration at a radial crack due to pellet hour glassing. Two-dimensional codes can account for this effect only through a multiplier.

An empirical PCI criterion for Siemens fuel to be loaded into Sizewell B was presented by J. Shea of British Energy Generation Ltd, UK. The proposed PCI criterion is, as the title indicates, a statistical correlation model of in-reactor failure data. The correlation was confined to the influence of local power and burnup and sets a threshold power to failure as a function of burnup. This has been used to constrain the chosen core design for Sizewell B Cycle 5. There is no explicit operator action required since the core design ensures the PCI safety case is established for normal operation and frequent faults. The power of the technique is its simplicity and the up-front demonstration of compliance with the PCI design criterion. However, it requires that the vendor always have a substantial database of ramp tests available to utility. A more mechanistic, physically based demonstration of PCI limit compliance is therefore desirable in the longer term. This would require PCI analysis using a predictive fuel behaviour code capable of modelling the complex PCI phenomenon.

The cladding failure model for fuel rods subjected to operational and accident transients presented by Joe Rashid of Annatech, USA combines both the stress and the strain states in an energy-based criterion. It is claimed that the materials capacity to absorb energy before failure is an invariant property of the material. This accords the model a certain level of objectivity with respect to strain-rate dependency and tri-axiality effects, i.e. the model includes these effects implicitly. However, verification of this property using actual data, when such data becomes available, would be highly desirable. The model gives good predictions for both the failures and the successes of the RIA tests. Further testing of the predictive capabilities of the model can be made by applying it to fuel rod tests with improved cladding materials such as M5 and Zirlo. This requires property data for these alloys to be added to the CSED database. Because the model is a continuum based multi-dimensional model, it is fully compatible with its 2D host code FREY/FALCON. However, it is easily adaptable to 1.5D fuel performance codes with hoop and axial stress-strain calculation capabilities.

A systematic approach for development of a PWR cladding corrosion model was presented by M. Quecedo of ENUSA, Spain. The model is an example of combining the attributes of a large database and a good understanding of physical phenomena of importance to the process being modelled. The result is good engineering. The paper identifies the importance of the coolant heat transfer and exploits previously developed heat transfer models to derive several corrosion-enhancement factors. Of these, the hydride-rim enhancement factor emerged as the most important. However, its value saturates at an oxide thickness of 70 microns; i.e. the value of the hydride-rim enhancement factor remains constant for oxide thickness larger than 70 microns. This does not constitute a limitation on the model since the model's database includes oxide thickness greater than 70 microns.

A model for hydrogen pickup for BWR cladding materials was presented by G. Hede of Westinghouse Atom AB, Sweden. The model makes use of rod length measurements to derive an estimate for the average hydrogen concentration in the cladding. Because the

method is non-destructive it offers an inexpensive and convenient procedure for estimating hydrogen contents in spent fuel assemblies that are ready for placement in shipping or storage casks. Such method of estimating hydrogen concentrations may be needed to comply with regulatory requirements for spent fuel storage.

Concluding remarks:

There has not been enough discussion of the need for experimental support of fuel modelling. While this is understandable because of the proprietary nature of experimental data, it is nevertheless important to point out where data are lacking.

Encouraging the use of more physically based mechanistic models in establishing safety criteria is needed.

In discussing model improvements for high burnup effects, the emphasis in the meeting was on fuel behaviour. The cladding seems to be given less attention.

One area of high burnup effects that was not discussed in the meeting is the fuel-clad interface. The occurrence of fuel-clad bonding at high burnup can be important to both PCI/SCC and transient behaviour.

5. SESSION 4: MOX FUEL MODELLING

Although this session was amongst the smallest of this meeting, it delivered important information on MOX fuels.

It is generally recognized, and this was reaffirmed, that fuel performance models developed for UO_2 and based on UO_2 experience are generally applicable to MOX. Only four models need to be adapted to cope with quantifiable differences between MOX and UO_2 fuels: i) radial power and burnup profile; ii) fission product and helium generation; iii) thermal conductivity and iv) fuel creep. Only the two last mentioned characteristics should be affected by the microstructural pattern of the MOX fuel. In this respect, it was fortunate that three papers were dealing with SBR fuel and one with MIMAS fuel, two commercial MOX fuels each with their own microstructural features. No paper in this session touched on fuel creep, but the three other areas of difference between MOX and UO_2 were adequately covered.

For what concerns radial power and burnup profile and fission product and helium generation, the paper presented by R. Weston, G. Rossiter and P. Cook (all-BNFL, UK) indicated how the RADAR model in the ENIGMA code has been improved to cope with deficiencies of the earlier version of the RADAR model. Although the sub-routine of a fuel rod modelling code cannot incorporate the full sophistication of a neutronics code, it was felt necessary to implement: i) a quite extensive number of actinides in the full chain from U-238 to Cm-242 and Pu-238; ii) an explicit modelling of thermal and resonant neutron captures in U-238 and Pu-240 and of fast fissions in U-238; and iii) cross-sections modelled from correlations fitted to predictions from a neutronics code, using a large nuclear data library, for different U-235 and Pu contents and three neutron spectra: a typical spectrum of PWR, a typical average spectrum of BWR and a soft spectrum (Halden reactor). This new version of ENIGMA correctly calculates the quantity of Xe and Kr isotopes in the fuel-clad gap and the radial profiles of burnup and Pu content across the pellets, for 5.5% Pu fuel irradiated in the Beznau

PWR to 36 MWd/kg HM. However the resonance capture of U-238 and Pu-240 needs to be improved to correctly represent the pellet rim region.

Papers on quantification of the homogeneity of BNFL's SBR MOX fuel using compositional X ray mapping, presented by P. Ivison of AEA Technology, UK and co-authored by P. Cook of BNFL, UK, S. Bremier and C. Walker of EU ITU, Germany and the paper on modelling of MOX fuel's thermal conductivity, presented by Byung-Ho Lee and co-authored by Yang-Hyun Koo and Dong-Seong Sohn (KAERI, Republic of Korea) provided the opportunity to schematically define the microstructure of the two commercial types of MOX fuel. Both types present a certain degree of heterogeneity of Pu distribution within the pellet, due to the mechanical blending of PuO_2 and UO_2 powder, specific to MOX fuel fabrication. In most UO_2 fuels indeed enrichment is performed in the gaseous UF_6 phase and the distribution of U-235 is perfectly homogeneous. The 5.5% Pu BNFL SBR (short binderless route) fuel (from the Beznau irradiation) can be characterized as follows: i) 98 vol% of the pellet is an homogeneous mixed oxide with the nominal Pu content and no Pu content gradient in the vicinity of the Pu-rich spots; ii) the Pu content in the Pu spots is typically 21 to 30% with peaks up to 60%; and iii) the size of the Pu spots is typically 8 microns, with peaks up to 20 microns. X ray microanalysis techniques was developed to investigate to what extent the heterogeneity varies with the irradiation of such fuel. As could be expected, results on Beznau fuel show that both the Pu content and the size of the Pu-rich spots were slightly drifting to lower values.

The KAERI paper described MIMAS (Micronized Master Blend) fuel from the FIGARO programme, which is schematically characterized by a spatial variability of the Pu content from 1 to 20% due to the presence of Pu-rich agglomerates in the matrix. The agglomerates, with a Pu content of 20% occupy 6.5 vol% and the matrix 93.5 vol%. The gradient of Pu content from agglomerates into the matrix is one of the distinctive features of MIMAS fuel, differentiating it from OCOM fuel fabricated in the past by Siemens/KWU. The paper characterizes such OCOM fuel as for instance, 34 vol% of the pellet being Pu-rich agglomerates with nominal Pu content of 15% (resulting in a 5.1% Pu MOX fuel), in a pure UO_2 matrix. Questioning whether the discrepancies of fuel conductivity quoted by each MOX fabricator might be due to the heterogeneity of MOX fuel, the thermal conductivity was modeled by applying a different conductivity correlation specific respectively to the matrix and to the Pu-rich agglomerates. It concludes that the reduction of the thermal conductivity of MOX fuel as compared to UO_2 fuel ranges from 10 to 7% (as temperature increases). On the basis of this paper, the conductivity of homogeneous MOX should be the same as UO_2 fuel.

The results of FGR gas flow measurements on UO_2 and SBR MOX fuel at start-of-life, conducted in the Halden reactor, were presented by G. Gates of BNFL, UK. They indicate, on the first rise to power, an initial increase in the surface-to-volume ratio, due to fuel cracking, followed by a decrease in surface-to-volume ratio, due to thermally activated processes. Overall the MOX and UO_2 behaviour are similar, with, however, a slower thermally activated decrease for the MOX fuel.

Concluding remarks:

Altogether, the session indicated that MOX fuel modelling has reached a high degree of development, based on a good understanding of the differences between MOX and UO_2 fuel. This is confirmed by papers describing the improvement of the FPAC code and the state of development of the COPERNIC code, both presented in Session 5. The underlying confidence

and further sophistication are still progressing as additional and confirmatory data are getting into the databases.

There is general agreement on the quantitative trends of the differences between UO_2 and MOX fuels in all the aspects mentioned above. However, there is a need to better define these trends in a quantitative way: i) the radial power and burnup profiles are "flatter" in MOX pellets than in UO_2 pellets. This effect should be evaluated more precisely, mainly at high burnups. Approaches like the RADAR model could breakdown in the pellet rim region. Most importantly, many data come from experiments like the ones conducted in the Halden reactor. These experiments and the Halden reactor may not be fully representation of PWR operation. In particular the radial power and burnup profiles at high burnup could be significantly different from those encountered during PWR operation. It is therefore needed to better refine the radial profiles in the Halden experiments; ii) there is a general agreement that the basic mechanisms for fission gas release are the same for MOX and UO_2 and that there is a slight enhancement of fission gas release in the MOX rod as compared to a UO_2 rod with an identical power history. Part of this enhancement may be understood as coming from the heterogeneous nature of the MOX and from the smaller grain size for MOX. More data are needed to quantify the relative impact of these two effects; iii) there is a slight degradation of the thermal conductivity of the MOX as compared to UO_2. However there is no agreement for the quantitative trend of the degradation. This degradation is described in KAERI paper as a two-phase material with different conductivities in the matrix and the Pu-rich agglomerates. BNFL applies a uniform degradation of 8%. FRAMATOME applies a linear degradation with the Pu content.

6. SESSION 5: DEVELOPMENT OF CODES AND METHODS

Eight papers were presented during this session covering a number of new and improved computer models for predicting high burnup UO_2 and MOX fuel rod behaviour during steady state and transient conditions.

Four fuel rod performance codes were presented:

FPAC: Nuclear Fuel Industry, Ltd, Japan (presented by T. Kikuchi)
COPERNIC: Framatome, France (presented by L.C. Bernard)
SPAN: Reactor Technology and Materials Research Institute of RRC, "Kurchatov Institute", Russian Federation (presented by P. Strizhov)
SPHERE-3: PSI, Switzerland (presented by H. Wallin)

The SPHERE-3 code (paper by H. Wallin of PSI, Switzerland) describes sphere-pac fuel, with emphasis on the specific fuel behaviour such as sintering mechanism, pore migration (fuel re-structuring), and the resulting temperature distribution. A new fission gas model has been developed where the fuel is considered as a collection of spherical fuel grains. Comparisons of SPHERE-3 model predictions with experimental evidence have been so far very successful. The deformation of the cladding during transient was not considered. The fuel concept has interesting features for instance no PCMI in normal operation and a simple dustless fabrication process.

The other three codes fell into the category of standard LWR fuel rod design. Emphasis was given to the burn-up degradation of the thermal conductivity (FPAC), a detailed verification employing a large database (COPERNIC) and on densification using most recent results from specific Halden experiments (SPAN). The SPAN code is a new code with improved models

for densification, swelling, fission gas release and the degradation of thermal conductivity of the fuel. The paper on the COPERNIC code is an excellent example of the detailed verification work routinely done with modern fuel performance code. Whereas the COPERNIC code is well known, some more details of the FPAC code are required to judge its maturity. However, good agreement with experimental evidence has been demonstrated (temperature, fission gas release, cladding creep-down).

The probabilistic approach presented by Siemens is based on performing uncertainty analysis utilizing Monte-Carlo sampling to estimate “with 95% confidence level the expected number of fuel rods exceeding a safety applicable limit, or the 95% percentile of the extreme fuel rod. This approach is similar to that used in the thermal hydraulic/sub channel analysis to evaluate "departure from nucleate boiling" (DNB). The proposed approach was verified and validated based on a simplified test case and the results for fuel rod internal gas pressure of two reload cases were presented. This showed that the statistical approach might provide some flexibility with respect to core reload design.

The Bochvar Research Institute, Moscow, proposed a quasi-random approach (Sobol sequence) instead of the standard Monte-Carlo method to vary rod parameters such as pellet radius, fuel density and cladding dimension on the fuel rod behaviour. The advantage of the proposed method is the substantial reduction in the computation time needed to complete a study.

Both methods are coupled with a best estimate fuel performance code the final goal is to determine the degree of conservatism that is included in a worst-case deterministic analysis.

In the paper by Bibilashvili et al. (presented by F. Sokolov) several example calculations are given employing the well known START-3 code as a best estimate fuel performance code.

The paper of Chan Bock Lee et al. (KAERI, Republic of Korea) on the development of a model describing the thermal conductivity of irradiated fuel was moved from session 1 into session 5. Different correlations for the thermal conductivity are compared and a new correlation is given. This new correlation has been carefully validated. Since gaseous fission products are treated separately, this model allows treating the pores in the rim structure that contain most of the fission product created.

A new constitutive equation to model the cold-worked stress relieved Zircaloy plastic deformation was presented by V.I. Arimescu, Siemens Power Corporation, USA. The goal is to develop a more mechanistic model that describes both primary and secondary creep deformation for a wide range of conditions. The method is based on the “back stress” methodology where the constitutive equation for the back stress describes the competition between hardening and recovery. First results have been presented.

7. SESSION 6: HIGH BURNUP FUEL MODELLING

Modelling of fuel thermal conductivity, FGR and cladding performance supported by PIE results with respect to high burnup operation were the focus of this session.

A high burnup fuel thermal conductivity correlation is developed based on laser flash thermal diffusivity measurements on BWR fuel up to 61 MWd/kg U (M Owaki of NFI Ltd, Japan). The heat-up period is used to derive the irradiation defect influence (unannealed) and the “annealed branch” to derive the influence of the dissolved fission products. Gd and Pu

additions are treated similarly to fission products; comparison to measured data backing this assumption. Rim porosity (starting as low as 30 MWd/kg U) is taken into account by a porosity correction function derived from SEM studies and the rim porosity itself is taken from PIE (up to 75 MWd/kg U), giving rim width and porosity as a function of burnup. The calculated temperatures agree well with Risø-III measurements (up to 50 MWd/kg U). Up to 75 MWd/kg U, the influence of the rim porosity is small in comparison to the effect of the fission products and irradiation defects. Additionally, the influence of the rim on the fission gas release and fuel swelling was found to be small in the burnup region analysed.

Recent developments of the TRANSURANUS code with emphasis on high burnup phenomena were presented by K. Lassmann, EU ITU, Germany. A hyperbolic type phonon term is used for the description of fuel thermal conductivity dependence on burnup and Gd content, giving good explanation to the fuel thermal conductivity data from a wide range of data sources up to 100 MWd/kg U and 19% Gd content. A linear dependence of the local rim porosity on local burnup is used, cut off at a maximum value of 16% at about 155 MWd/kg U. However the data underlying this correlation has a large scatter and it is recommended to increase the experimental efforts for clarification. New radial power density profiles for burnable absorbers (Gd and ZrB_2) are introduced and extensively verified by chemical analysis of isotope distributions.

KOLA-3 low temperature irradiated rods are used to study fission gas release enhancement with burnup. It can either be described by release from the high burnup structure (rim), or by increased athermal diffusion coefficients throughout the pellet. The first hypothesis seems in conflict with measurements of Xe/Kr ratios in other experiments, and it is recommended to increase research efforts to better understand the enhanced fission gas release at high burnup. Additionally, new numerical methods concerning Monte Carlo statistics and treatment of highly non-linear equations are introduced.

Agreement is reached “world-wide” on the degree of fuel thermal conductivity degradation with burnup as can be shown by normalisation of various different fuel thermal conductivity formulations. It seems clear that high burnup fission gas release enhancement comes predominantly from the pellet centre, however the mechanisms are unclear. In this context it was proposed to review Xe diffusion coefficients and also Xe resolution from fission gas bubbles.

Two important aspects of Zircaloy-4 clad behaviour at high burnup, namely clad creep-out and waterside corrosion, were presented by Je-Geon Bang, et al, KAERI, Republic of Korea. Clad creep-out may occur due to rod over pressure at high burnup. Halden measurements show that creep-out is faster than creep-down. By adaptation of the stress exponents, the primary creep rate constant and the secondary creep rate constant, good agreement between measured and calculated creep-out is achieved. The corrosion model development comprised a new assessment of the relevant parameters involved, namely the chemical composition and manufacturing characteristics of the clad, coolant chemistry, hydride formation and fast neutron flux. As examples, validation concerning the influence of Li in the coolant and H_2 clad content were discussed. Good agreement between measurements and modelling was achieved for these parameters. It was commented that Zircaloy is highly anisotropic and that the difference in creep-out versus creep down could be an effect of this anisotropy.

A complete set of investigations of fuel and cladding materials of WWER reactors is presented by V. Kuzmin of RIAR, Russian Federation. Reactor material science and material testing methods of RIAR incorporate methodical software and hardware support of material

science investigations including the validation of products under development, their design, manufacture, testing, metrological certification and application for real measurements, investigating all sets of materials before, under and after irradiation, etc. In particular, results of examinations on cracking, dimensional, structural and density changes of fuel pellets as well as the results of examination of corrosion and mechanical properties of WWER fuel rod cladding have shown that changes of the above-mentioned characteristics are within the permissible limits at burnups up to about 70 MWd/kg U.

The ROFEM code and CAREB code were used to simulate and compare behaviour under the postulated large loss of coolant accident (LOCA) conditions of standard (37-element with natural UO_2) and advanced (43-element with slightly enriched UO_2) CANDU-6 fuels (G. Horhoianu of INR, Romania). ROFEM calculations are performed to estimate steady-state fuel-element conditions at the onset of the accident. Then, after the onset of the accident, the fuel and fuel-sheath behaviour of the outer fuel elements residing in the core pass downstream of the break (i.e. critical core pass) are evaluated by the CAREB code. It has been shown that even at the elevated power of 110% of initial, the centre-line temperature, internal gas pressure and sheath-strain are lower for SEU 43 fuel than those of 37-element fuel. The results indicate that SEU 43 fuelled channel would have an uprating potential of 10% when compared to the 37-element fuelled channel and the consequences of a large break LOCA for the uprated SEU 43 core would be no worse than the consequences after a large break LOCA for a 37-element fuelled core at nominal power.

8. CONCLUSIONS AND RECOMMENDATIONS ON FUTURE WORK

The TCM included separate sessions on the specific topics of fuel thermal performance and fission product retention. On thermal performance, it is apparent that the capability exists to measure conductivity in high burnup fuel either by out-of-pile measurement or by instrumentation of test reactor rods. State-of-the-art modelling codes contain models for the conductivity degradation process, and hence adequate predictions of fuel temperature are achievable. Concerning fission product release, it is clear that many groups around the world are actively investigating the subject, with experimental and modelling programmes being pursued. However, a general consensus on the exact mechanisms of gas release and related gas bubble swelling has yet to emerge, even at medium burnup levels.

Fission gas phenomena, not only the release to open volumes, but the whole sequence of processes taking place prior to this, need to be modelled in any modern fuel performance code. The presence of gaseous fission products may generate rapid fuel swelling during power transients, and this can cause PCI and rod failure. At high burnups, the quantity of released gases could give rise to pressures exceeding the safe limits.

Modelling of PCI effects during transient operation is also an active area of study for many groups. In some situations a purely empirical approach to failure modelling can be justified, while for other applications a more detailed mechanistic approach is required. There was much discussion at the meeting on the relative merits of the two approaches. Another aspect of cladding modelling which featured at the TCM concerned corrosion and hydriding. Although this issue can be the main life-limiting factor on fuel duty, it is apparent that modelling methods, and the experimental measurement techniques that underpin them, are adequate.

A session was included on MOX fuel modelling. Substantial programmes of work, especially by the MOX vendors, appear to be underway to bring the level of understanding

of MOX behaviour up to that for UO_2 fuel. There appears to be a good consensus on how MOX fuel performance differs from UO_2, and on the issues that need to be addressed to achieve higher burnups.

The final sessions of the TCM considered the current status of integrated fuel behaviour codes and the challenges for higher burnup modelling. The meeting provided a valuable forum for a review of the state-of-the-art. Presentations were given on a number of existing codes and others under development, covering PWR, WWER, BWR and CANDU fuel performance. Some specialised methods for specific advanced fuel types were also discussed.

Recommendations on future work in the area of FISSION GAS RELEASE:

Deficiencies are still encountered in the modelling, and both integral fission gas release tests and studies focusing on single processes such as diffusion, bubble formation, swelling, grain growth and resolution are encouraged to support the modelling. Old tests could be re-evaluated taking advantage of the new knowledge of the high burnup fuel. Fission gas atom diffusion coefficients have been measured/determined over the years, but their magnitudes still have a large scatter. More diffusion data should be provided from the temperatures 400-800^{O}C, which is a typical temperature range for a high burnup fuel under operation.

Recommendations on future work in the area of CLAD MODELLING:

There has not been enough discussion of the need for experimental support of fuel modelling. While this is understandable because of the proprietary nature of experimental data, it is nevertheless important to point out where data is lacking.

Encouraging the use of more physically based mechanistic models in establishing safety criteria is needed.

One area of high bumup effects that was not discussed in the meeting is the fuel-clad interface. The occurrence of fuel-clad bonding at high burnup can be important to both PCI/SCC and transient behaviour.

Recommendations on future work in the area of MOX FUEL MODELLING:

There is a general agreement on the quantitative trends of the differences between UO_2 and MOX fuels in all the aspects mentioned above. However, there is a need to better define these trends in a quantitative way:

(i) The radial power and burnup profiles are "flatter" in MOX pellets than in UO_2 pellets. This effect should be evaluated more precisely, mainly at high burnups. Approaches like the RADAR model could breakdown in the pellet rim region. Most importantly, many data come from experiments like the ones conducted in the Halden reactor. These experiments and the Halden reactor may not be fully representative of PWR operation. In particular the radial power and burnup profiles at high bumup could be significantly different from those encountered during PWR operation. It is therefore needed to better refine the radial profiles in the Halden experiments;

(ii) There is a general agreement that the basic mechanisms for fission gas release are the same for MOX and UO_2 and that there is a slight enhancement of fission gas release in the MOX rod as compared to a UO_2 rod with an identical power history. Part of this enhancement may be understood as coming from the heterogeneous nature of the MOX and from the smaller grain size for MOX. More data are needed to quantify the relative impact of these two effects;

(iii) There is a slight degradation of the thermal conductivity of the MOX as compared to UO_2. However, there is no agreement for the quantitative trend of the degradation. The paper by Lee et al. describes this degradation as a two-phase material with different conductivities in the matrix and the Pu-rich agglomerates. The paper by Gates applies a uniform degradation of 8%. The paper by Bernard and Blanpain applies a linear degradation with the Pu content.

FUEL THERMAL PERFORMANCE
(Session 1)

Chairpersons

K. KAMIMURA
Japan

M. QUESEDO
Spain

THERMAL CONDUCTIVITIES OF IRRADIATED UO_2 AND (U, Gd)O_2 PELLETS

M. AMAYA[1], M. HIRAI[1], H. SAKURAI[3], K. ITO[2], M. SASAKI[2],
T. NOMATA[2], K. KAMIMURA[4], R. IWASAKI[4]
[1] Japan Nuclear Fuel Co., Ltd, Ibaraki, Japan
[2] Japan Nuclear Fuel Co., Ltd, Kanagawa, Japan
[3] Nippon Nuclear Fuel Development Co., Ltd, Ibaraki, Japan
[4] Nuclear Power Engineering Corporation, Tokyo, Japan

Abstract.

Thermal diffusivities of UO_2 and (U, Gd)O_2 pellets irradiated in a commercial reactor were measured up to about 2000 K by using a laser flash method. The maximum burnups of the samples were about 60 GWd/t for UO_2 and about 50 GWd/t for (U,Gd)O_2. The samples for thermal diffusivity measurements were disks of 2 mm diameter or squares of 1.5 or 2 mm sides, all 1 mm in thickness. The half-time method was used to calculate the thermal diffusivity from the temperature response curve of a sample. Thermal diffusivities of irradiated pellets decreased compared with those of unirradiated and simulated soluble fission products-doped UO_2 and (U,Gd)O_2 pellets, and the thermal diffusivities of irradiated pellets showed hysteresis phenomena. The measured thermal diffusivities of UO_2 pellets showed good accordance with other reported values for irradiated UO_2 pellets. Thermal diffusivities of irradiated UO_2 pellets began to recover above 750 K and almost completely recovered after annealing above 1400 K. Furthermore, the thermal diffusivities after recovery were close to those of simulated soluble FPs-doped UO_2 pellets, which corresponded with the recovery behaviors of irradiation defects for UO_2 pellets. The thermal diffusivities of (U, Gd)O_2 pellets showed similar recovery behaviors. The thermal conductivities for irradiated UO_2 and (U, Gd)O_2 pellets were evaluated from measured thermal diffusivities, specific heat capacities of unirradiated UO_2 pellets and measured sample densities. The measured thermal conductivities were in fairly good agreement with predictions based on the thermal conductivity expressions already proposed by Amaya and Hirai. The relative thermal conductivities of irradiated UO_2 and (U, Gd)O_2, which were relative to those of unirradiated UO_2 pellets, were evaluated. The difference in relative thermal conductivities between irradiated UO_2 and (U,Gd)O_2 pellets tended to become insignificant with increasing burnups of samples.

1. INTRODUCTION

With increasing burnup of light water reactor (LWR) fuels, it becomes more important to estimate the irradiation behavior of the fuel pellets under high burnup. Thermal conductivity of fuel pellets is one of the most important thermal properties for calculating the fuel temperature during irradiation.

For high burnup fuels, fission products (FPs) accumulate in fuel pellets. The increased crystal lattice strains caused by irradiation-induced point defects and formation of microbubbles are also observed in irradiated UO_2 pellets [1-3]. Thermal conductivity of fuel pellets is affected by these FP impurities and irradiation-induced defects, and it is necessary to evaluate the quantitative changes in the thermal conductivity due to them. It is well known that thermal conductivity of undoped UO_2 pellets decreases with increasing amounts of point defects such as soluble impurities and also with accumulation of defect clusters. Therefore, the thermal conductivity of fuel pellets is expected to degrade with burnup due to the accumulation of FPs and irradiation-induced defects.

The thermal conductivities of stoichiometric UO_2 pellets irradiated in a material test reactor up to about 120 GWd/t (2.8×10^{21} fissions cm^{-3}) have been measured [4-12]. In particular, at temperatures below about 800 K, it was found that the thermal conductivities were degraded in comparison with unirradiated UO_2 and simulated fission products-doped UO_2. After the irradiated samples were annealed at temperatures above 1000 K, the thermal diffusivities and thermal conductivities recovered. However, for (U, Pu)O_2 irradiated up to burnups of 35 GWd/tM in a fast breeder reactor (FBR) [13, 14], the burnup dependence of thermal conductivities and the thermal conductivity recovery were not clearly observed. In addition, there have been few studies on the thermal conductivities of irradiated (U,Gd)O_2 pellets, and the effect of gadolinium on the thermal conductivities of irradiated fuel pellets has not been clarified yet.

The thermal conductivity degradation by soluble FPs has already been formulated [15, 16], but the effects of crystal lattice strain caused by irradiation-induced point defects and of microbubbles were not sufficiently quantified [17-19]. In this study, the thermal diffusivities of UO_2 and (U, Gd)O_2 pellets were measured for base-irradiated samples by using a laser flash method up to 2000 K, and their thermal conductivities were evaluated by using the thermal diffusivities, measured sample densities and specific heat capacities of unirradiated UO_2. The evaluation was carried out to quantify the effects of irradiation-induced defects on thermal conductivities and to explain the thermal conductivity behavior.

2. EXPERIMENTAL

2.1. Sample preparation

Since the fuel pellets irradiated in a commercial reactor generally have many radial cracks (and sometimes circumferential cracks) and high radioactivity, microsamples have advantages of decreasing the crack effects on the thermal diffusivity and of easier sample handling. Therefore, an experimental method for thermal diffusivity measurements was developed previously for small samples [17].

The fuel pellets irradiated in a commercial reactor for 1 to 5 reactor cycles were sliced into disks of about 1mm thickness. From the disks, disk shaped or regular prismatic specimens were micro-sampled at a point between the fuel rim and mid-radius ($0.6 < r/r_0 < 0.9$; r/r_0: relative radius of the pellet) of the slices. Their characteristics are summarized in Table I. Specimens U-1 and U-2 were samples from the top region of a fuel rod. Their irradiated temperatures were evaluated as about 750 K. Specimens U-3–G-4 were samples near the highest power position for fuel rods. Their irradiation temperatures were evaluated as about 1100 K. Specimens G-1–G-4 were obtained from the fuel rods using pellets of doped gadolinia (Gd_2O_3) of 4.5wt% (6.4at%).

For samples U-2 and U-5, thicknesses after the thermal diffusivity measurements were measured and porosity change was estimated. The theoretical densities and porosities of samples were evaluated by considering the mean atomic mass decrease with burnup. Sample porosities were about 4%.

TABLE I. CHARACTERISTICS OF IRRADIATED UO_2 AND (U, GD)O_2 SAMPLES

Sample No.	Burnup (GWd/t)	Gd_2O_3conc. (wt%)	Sample characteristics before experiment			Sample characteristics after experiment		Theoretical Density (g cm^{-3})
			Sample shape*1	Density (g cm^{-3})	Porosity (%)	Density*2 (g cm^{-3})	Porosity*2 (%)	
U-1	8.5	0	1	10.45	4.39	-	-	10.93
U-2	8.5	0	1	10.45	4.39	10.05	8.05	10.93
U-3	39.3	0	2	10.41	3.60	-	-	10.80
U-4	42.7	0	2	10.39	3.68	-	-	10.79
U-5	44.7	0	1	10.28	3.11	9.72	9.88	10.79
U-6	48.8	0	2	10.33	4.04	-	-	10.76
U-7	50.1	0	3	10.32	4.10	-	-	10.76
U-8	53.2	0	3	10.30	4.18	-	-	10.75
U-9	56.0	0	2	10.23	4.74	-	-	10.74
U-10	60.0	0	3	10.26	4.36	-	-	10.73
G-1	43.5	4.5 (6.4at%)	2	10.24	3.67	-	-	10.63
G-2	46.5	4.5 (6.4at%)	2	10.20	3.95	-	-	10.62
G-3	48.8	4.5 (6.4at%)	3	10.19	4.00	-	-	10.61
G-4	50.7	4.5 (6.4at%)	3	10.17	4.14	-	-	10.61

*1: 1: Disk shape specimen of 2mm diameter and 1mm thickness.
2: Regular prismatic (square) specimen of 2mm sides and 1mm thickness.
3: Regular prismatic specimen (square) of 1.5mm sides and 1mm thickness.

*2: Value estimated from thickness change during the experiment

2.2. Thermal diffusivity measurement

Thermal diffusivities of irradiated samples were measured by using a laser flash method. The apparatus for irradiated samples (Type: TC-7000UVH; produced by Sinku-Riko Co., Ltd.) was shielded by iron and lead and modified to allow operation by a remote control system. Schematic diagrams of the apparatus were shown elsewhere [17]. The sample with sample cell was kept in a vacuum of less than 2×10^{-4} Pa during experiments by using turbo-molecular and oil-rotary pumps. The heat source of the laser flash method was a ruby laser with the maximum energy about 6 J. The laser power used was in the range of about 2.5 to 3.8 J cm^{-2}. A tungsten mesh heater was used for heating the sample with sample cell. The sample temperature was monitored by a W-5%Re/W-26%Re thermocouple located near the sample holder. Prior to thermal diffusivity measurements, another thermocouple of Pt/Pt-Rh was inserted at the sample position in order to obtain a calibration curve for the temperature deviation due to radiation effect. Sample temperatures during measurements were calibrated by using the calibration curves.

The thermal energy was induced on one side of the sample by shining a ruby laser beam for about 500 μs and the temperature response of the other side was measured by using an In-Sb infrared sensor. A half-time method (Fourier method) [20] was used to analyze the temperature responses. A logarithmic method (Laplace method) [21] was also used to analyze them in order to check the validity of thermal diffusivities.

The thermal conductivities were evaluated by multiplying the thermal diffusivity by the specific heat capacity and the sample density as follows:

$$\lambda = \alpha C_p \rho, \quad (1)$$

where λ is the thermal conductivity; α, the thermal diffusivity; C_p, the specific heat capacity and ρ, the sample density. The specific heat capacities of irradiated UO_2 and $(U,Gd)O_2$ were assumed to be the same as those of unirradiated undoped UO_2 [22], considering that the difference in the specific heat capacities between undoped UO_2 and simulated soluble FPs-doped UO_2 and $(U,Gd)O_2$ was about 2% even at a simulated burnup of 90 GWd/t [15].

Thermal diffusivity measurements were carried out in the following sequence, based on consideration of prior results of X ray diffraction and TEM observations by other researchers in our laboratory [1-3].

– Run 1 measurement: from room temperature to 1200 K
– Run 2 measurement: from room temperature to 1500 K after Run 1 measurement
– Run 3 measurement: from room temperature to 2000 K after Run 2 measurement.

Some of the high-burnup samples were cracked above 1500 K, and their thermal diffusivities could not be measured above that temperature.

From the thermal diffusivity measurements of unirradiated UO_2 pellets having various sizes, the experimental error of this apparatus was estimated for a micro-specimen to be within ±6% in the temperature region from 400 to 2000 K [17].

3. RESULTS

3.1. Thermal diffusivities of irradiated UO_2 AND $(U,Gd)O_2$ pellets

The examples of the thermal diffusivities for irradiated UO_2 and $(U,Gd)O_2$ pellets are shown in Figs 1 (a)–1 (d). The thermal diffusivities of unirradiated UO_2, $(U,Gd)O_2$ and SIMFUEL (SIMulated high burnup FUEL) pellets [15, 30] are also shown for comparison. The thermal diffusivities of irradiated UO_2 and $(U,Gd)O_2$ pellets decreased with increasing burnup at lower temperature. The hysteresises of thermal diffusivity recoveries were observed after being annealed above 800 K.

3.2. Thermal conductivities of irradiated UO_2 and $(U,Gd)O_2$ pellets

The examples of the thermal conductivities for irradiated UO_2 and $(U,Gd)O_2$ pellets are shown in Figs 2 (a)–2 (d). The thermal conductivities of unirradiated UO_2, $(U,Gd)O_2$ and SIMFUEL pellets [15,30] are also shown for comparison. As shown in these figures, the thermal conductivities of irradiated UO_2 and $(U,Gd)O_2$ samples decreased, compared with those of unirradiated pellets.

Since the thermal conductivity degradation of irradiated UO_2 pellets may be caused by the accumulation of fission products (FPs) and irradiation-induced defects, the measured thermal conductivities of irradiated pellets were compared with the calculated values in the following section.

4. DISCUSSION

4.1. Thermal conductivities of irradiated UO_2 and $(U, Gd)O_2$ pellets

After ceramic materials such as Al_2O_3, SiC and AlN are irradiated, their thermal conductivities decrease and become close to constant values which are independent of temperature [24, 25]. From the discussions using Price's theory [26], it is seen the thermal conductivity decreases due to the irradiation-induced impurities, point defects, dislocations and vacancy/interstitial clusters. This fact indicates that it is necessary to consider the effects of irradiation-induced defects on thermal conductivities as well as those of impurities, in order to analyze the thermal conductivity changes of irradiated UO_2 and $(U,Gd)O_2$ pellets.

The temperature ranges for irradiation-defect recovery and microbubble growth in irradiated UO_2, which are based on Refs. [1-3], are summarized in Fig. 3. The thermal conductivity changes of irradiated UO_2 and $(U,Gd)O_2$ pellets can be classified as the sum of the effects of irradiation-induced point defects, fission products and irradiation-induced microbubbles.

High concentrations of point defects and extended defects coexist in high burnup fuel pellets. According to Klemens' theory [27-29], the phonon thermal conductivity of ceramics is expressed as follows using phonon mean free path:

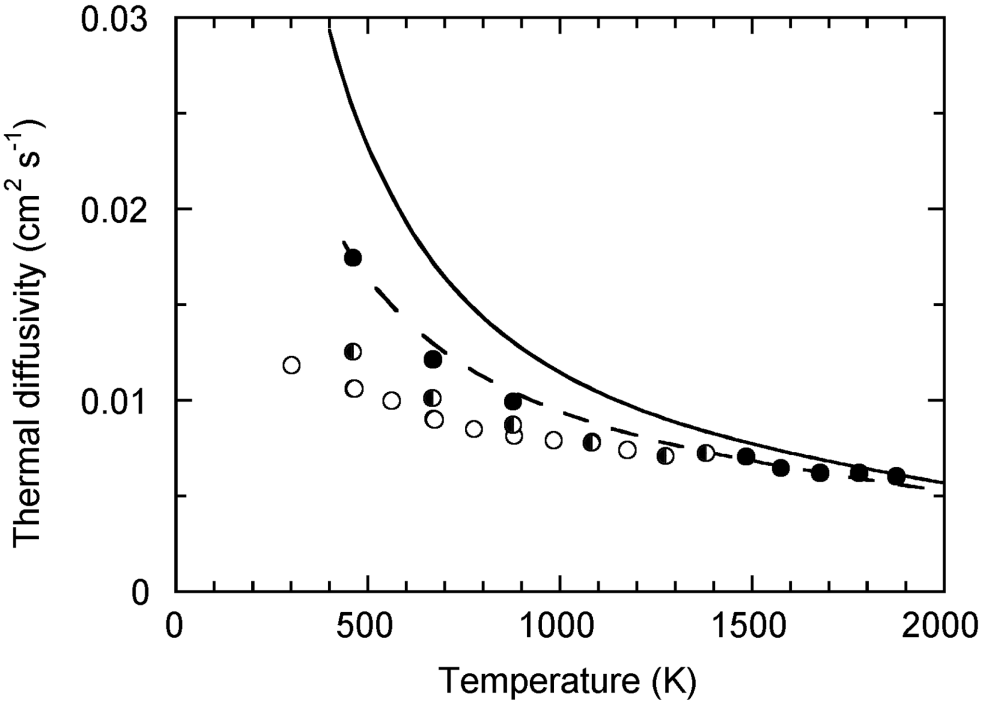

FIG. 1(a) Thermal diffusivities of U-3 sample.
○ , ◐ , ● : measured values, ○ : RUN1, ◐ : RUN 2, ● : RUN 3;
——— : unirradiated UO_2 ;
– – – – – : simulated soluble FPs-doped UO_2 (simulated burnup: 39GWd/t).

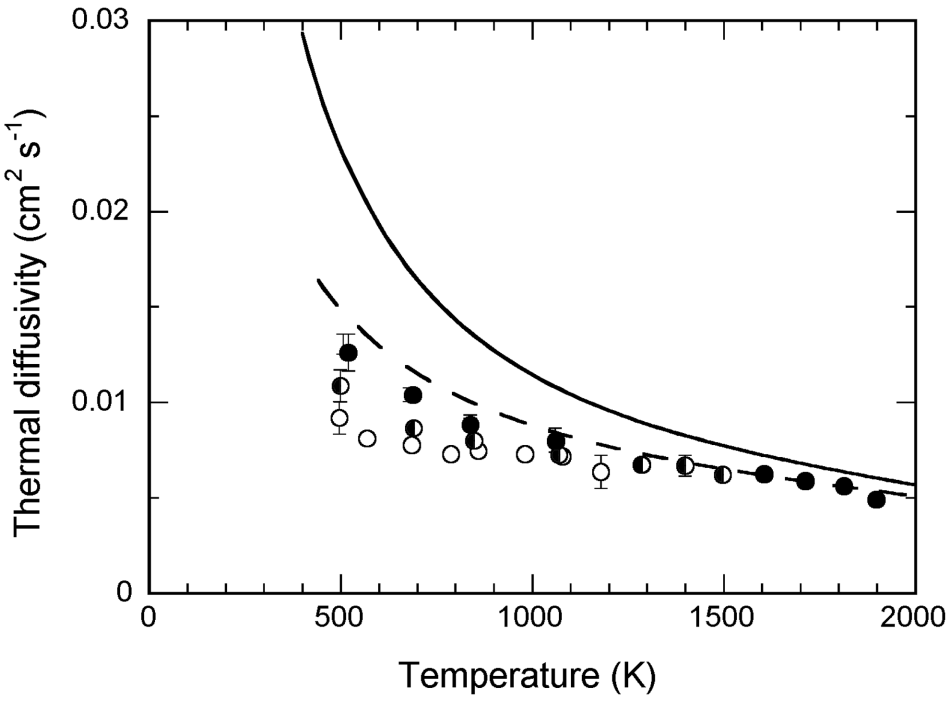

FIG. 1(b) Thermal diffusivities of U-10 sample.
○ , ◐ , ● : measured values, ○ : RUN1, ◐ : RUN 2, ● : RUN 3;
——— : unirradiated UO_2;
– – – – – : simulated soluble FPs-doped UO_2 (simulated burnup: 60GWd/t).

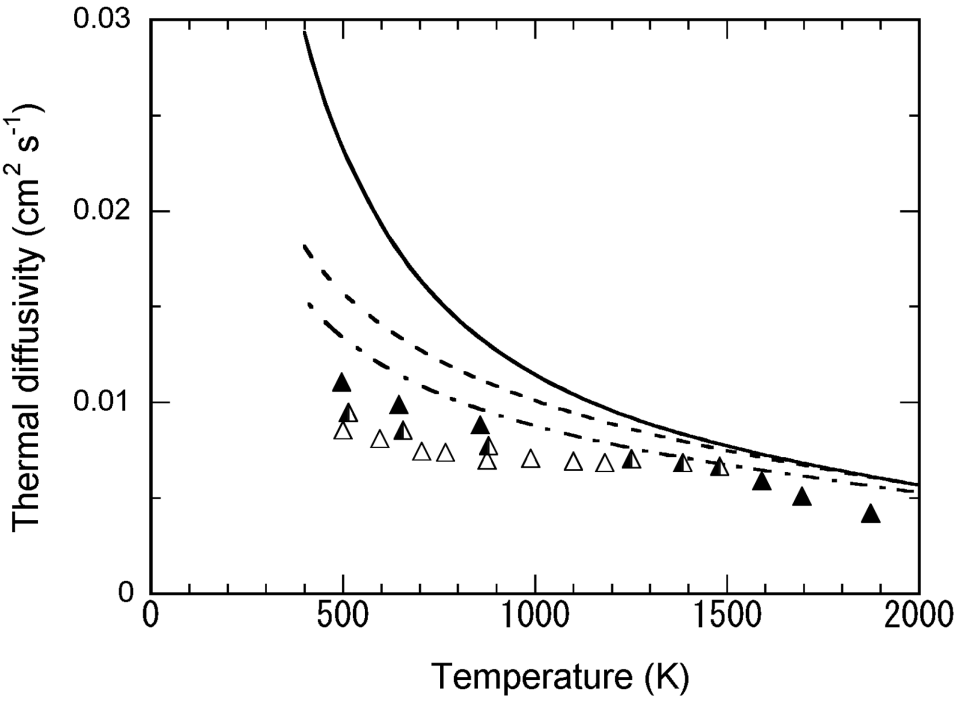

FIG. 1(c) Thermal diffusivities of G-1 sample.
△ , ▲ , ▲ : measured values; △ : RUN 1. ▲ : RUN 2, ▲ : RUN 3;
——— : unirradiated UO_2 ; — — — : unirradiated (U, Gd)O_2 (Gd_2O_3 conc.: 4.5wt%);
— — — : simulated soluble FPs-doped (U, Gd)O_2 (Gd_2O_3 conc.: 4.5wt%, simulated burnup: 44GWd/t).

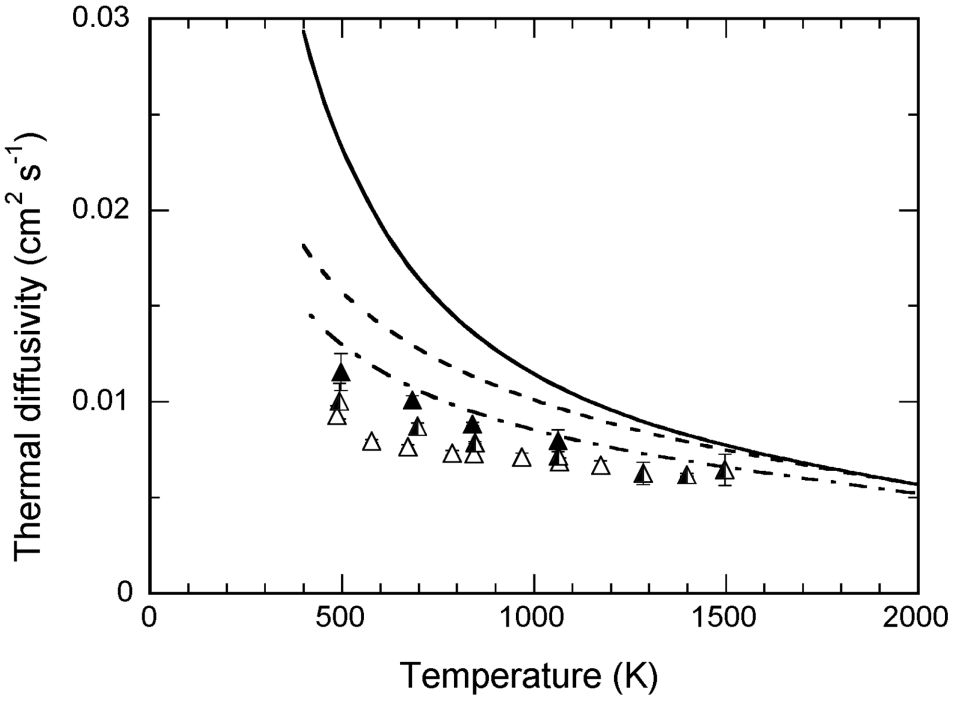

FIG. 1(d) Thermal diffusivities of G-4 sample.
△ , ▲ , ▲ : measured values; △ : RUN 1. ▲ : RUN 2, ▲ : RUN 3;
——— : unirradiated UO_2 ; — — — : unirradiated (U, Gd)O_2 (Gd_2O_3 conc.: 4.5wt%) ;
— — — : simulated soluble FPs-doped (U, Gd)O_2 (Gd_2O_3 conc.: 4.5wt%, simulated burnup: 51GWd/t).

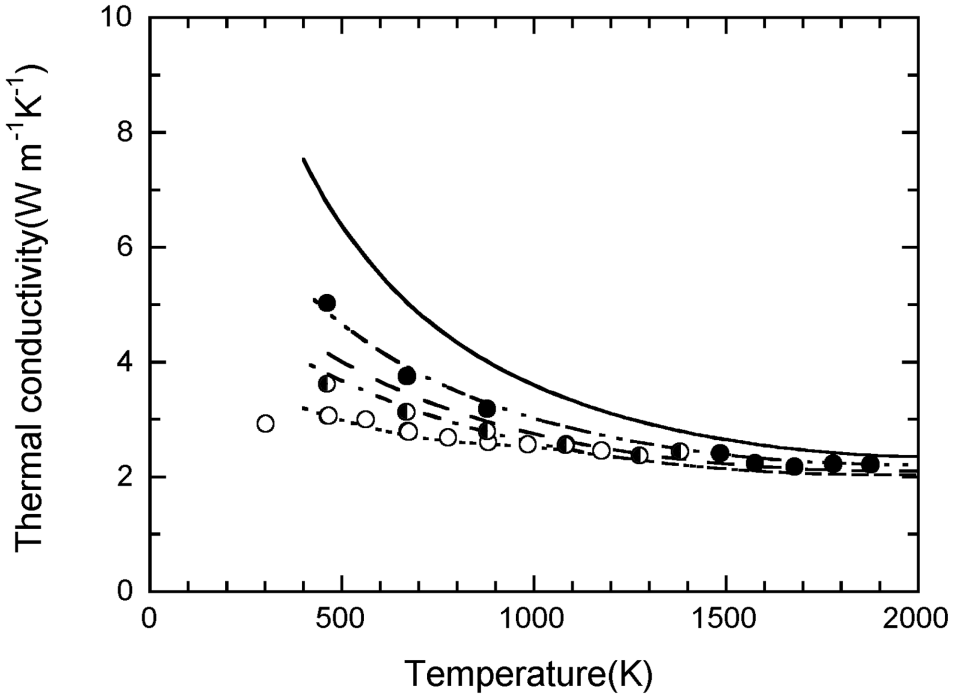

FIG. 2(a) Thermal conductivities of U-3 sample.
○ ,◐ ,● : measured values; ○ : RUN 1, ◐ : RUN 2,● : RUN 3;
·····, —·—·—, - - - - -, —··—··— : calculated values from eq. (4);
·····: before point defect recovery; —·—·—: after point defect recovery; - - - - -: after microbubble growth;
———: unirradiated UO_2 ; —··—··—:simulated soluble FPs-doped UO_2 (simulated burnup: 39GWd/t).

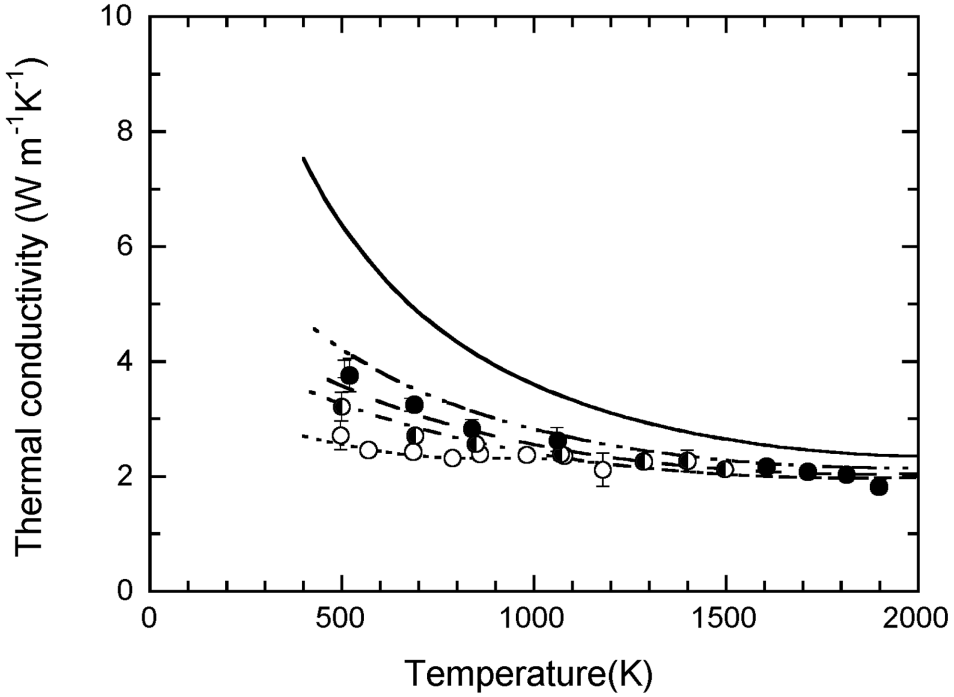

FIG. 2(b) Thermal conductivities of U-10 sample.
○ ,◐ ,● : measured values; ○ : RUN 1, ◐ : RUN 2,● : RUN 3;
·····, —·—·—, - - - - -, —··—··— : calculated values from eq. (4);
·····: before point defect recovery; —·—·—: after point defect recovery; - - - - -: after microbubble growth;
———: unirradiated UO_2 ; —··—··—:simulated soluble FPs-doped UO_2 (simulated burnup: 60GWd/t).

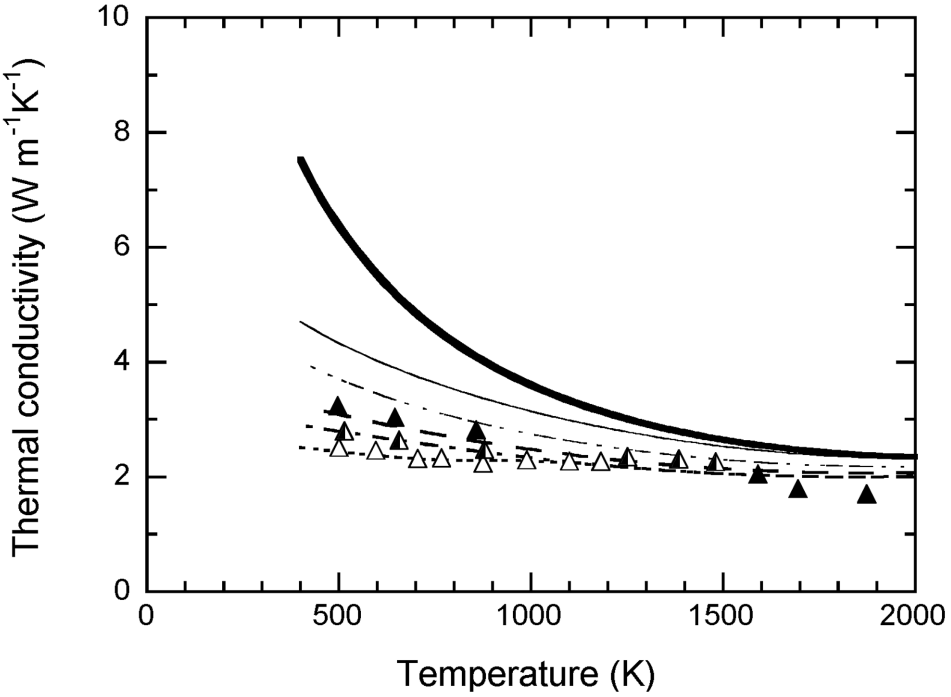

FIG. 2(c) Thermal conductivities of G-1 sample.
△, ◭, ▲: measured values; △: RUN 1, ◭: RUN 2, ▲: RUN 3;
·····, —·—·—, - - - - -, —··—··-: calculated values from eq. (4); ——: unirradiated UO_2;
·····: before point defect recovery; —·—·—: after point defect recovery; - - - - -: after microbubble growth;
——: unirradiated (U,Gd)O_2 (Gd_2O_3 conc. : 4.5wt%);
—··—··-:simulated soluble FPs-doped (U, Gd)O_2 (Gd_2O_3 conc. : 4.5wt%, simulated burnup: 44GWd/t).

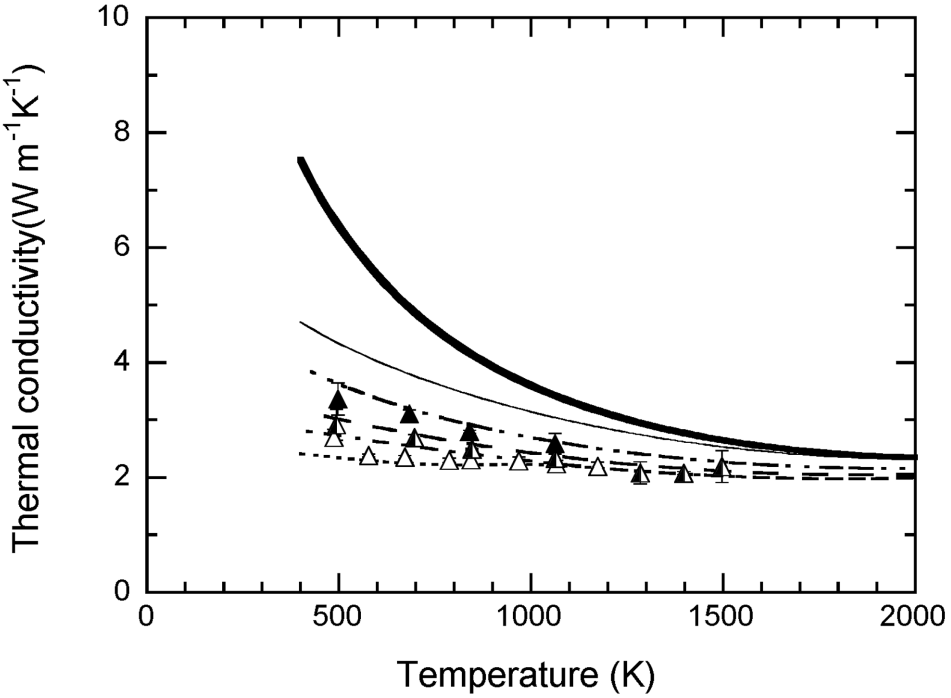

FIG. 2(d) Thermal conductivities of G-4 sample.
△, ◭, ▲: measured values; △: RUN 1, ◭: RUN 2, ▲: RUN 3;
·····, —·—·—, - - - - -, —··—··-: calculated values from eq. (4); ——: unirradiated UO_2;
·····: before point defect recovery; —·—·—: after point defect recovery; - - - - -: after microbubble growth;
——: unirradiated (U,Gd)O_2 (Gd_2O_3 conc. : 4.5wt%);
—··—··-:simulated soluble FPs-doped (U, Gd)O_2 (Gd_2O_3 conc. : 4.5wt%, simulated burnup: 51GWd/t).

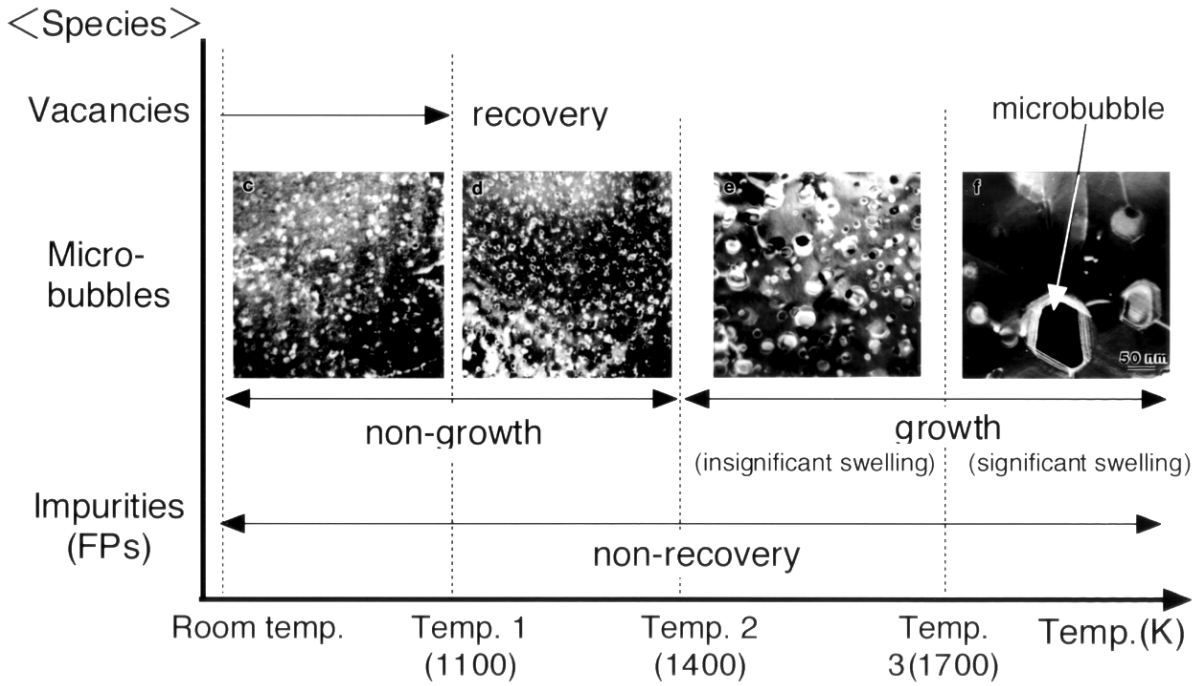

FIG. 3 The temperature range for irradiation-induced defect recovery and microbubble growth based on Refs.[1-3].

$$\lambda = \frac{1}{3}\int_0^{\nu_m} [C(\nu)u(\nu)l(\nu)]\,\mathrm{d}\nu\,, \qquad (2)$$

where $C(\nu)$ is the heat capacity of a material per unit volume; $u(\nu)$, the velocity of a lattice wave; $l(\nu)$, the phonon mean free path; and ν_m, the Debye frequency.The phonon mean free path, $l(\nu)$, changes due to the phonon scattering mechanism and each contribution to the thermal conductivity in high burnup fuel pellets is expressed as follows:

$$(1/l(\nu)) = (1/l_u) + (1/l_p) + (1/l_x), \qquad (3)$$

where l_u is the intrinsic mean free path of phonon scattering due to the Umklapp process; l_p, the mean free path of phonon scattering due to point defects; and l_x, the mean free path of phonon scattering due to extended defects.

Substituting eq.(3) for eq.(2) leads to the following thermal conductivity formula for high burnup fuel pellets after considering the lattice vibration frequency dependence of each phonon scattering process and the other effects on the thermal conductivity except heat conduction by phonons:

$$\lambda_s = \lambda_0\, K\left[\theta_1 \tan^{-1}(1/\theta_1) - \theta_2 \tan^{-1}(1/\theta_2)\right] + CT^3 \qquad (4)$$

where λ_0 is the thermal conductivity of undoped UO_2; K, θ_1 and θ_2, the phonon scattering parameters which express the degrees of phonon scattering by point defects and extended

defects; C, a coefficient which express effects other than thermal conductivity by phonons; and T, the temperature.

Figs 2 (a)–2 (d) compares the values calculated using Eq. (4) with those measured in this study. The measured values agree with the calculated data successfully below 1700 K. Above 1700 K, experimental data are slightly lower than the expected values. This decrease in thermal conductivity can be explained by the porosity change during experiments [17].

4.2. Burnup dependence on the thermal conductivity of irradiated fuel pellet

The measured thermal conductivities were normalized to the values of 96.5%TD (TD: theoretical density) by using the Loeb's equation:

$$\lambda_n = \lambda_m \, (1 - 0.035\varepsilon)/(1 - \varepsilon P), \qquad (5)$$

where λ_n is the thermal conductivity normalized to that of 96.5%TD; λ_m, the measured thermal conductivity; ε, the parameter which express the effect of pore shape on the thermal conductivity of pellets; and P, the porosity evaluated from the sample density. The parameter ε is expressed as follows [30]:

$$\varepsilon = 2.6 - 5 \times 10^{-4} (T(\mathrm{K}) - 273.15). \qquad (6)$$

It was evaluated that the relative thermal conductivities for all irradiated samples of this study to those of unirradiated UO_2 pellets. Fig. 4 ummarizes the relative thermal conductivities of irradiated UO_2 and $(U,Gd)O_2$ pellets at 1273 K, which are nearly the average temperature of the fuel pellets during irradiation. Data obtained by other researchers [12, 31, 32] are also shown for comparison. As shown in Fig. 4 the relative thermal conductivities of irradiated fuel pellets

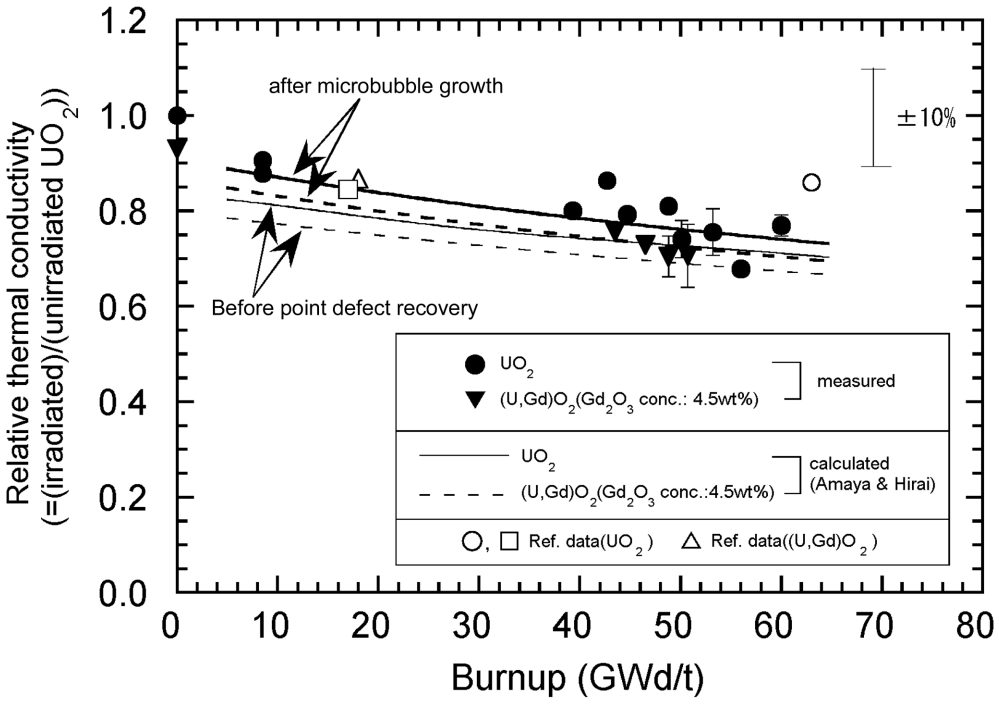

FIG. 4 Burnup dependence of relative thermal conductivity for irradiated fuel pellets at 1273 K.
●, ▼ : measured values; ○, △, □ : from Refs. [12, 31, 32]; ●, ○, □ : UO_2;
▼ :(U, Gd)O_2 (Gd_2O_3 conc. : 4.5wt%); △ :(U, Gd)O_2 (Gd_2O_3 conc. : 6wt%).
——— : calculated by using eq. (4) for UO_2; ----- : calculated by using eq. (4) for (U, Gd)O_2 (Gd_2O_3 conc. : 4.5wt%).

decrease with increasing burnups, but it seems that the relative thermal conductivities gradually saturates. The difference of the relative thermal conductivity between irradiated UO_2 and $(U,Gd)O_2$ pellets tends to become insignificant with increasing burnups. This suggests that the effects of soluble FPs and irradiation-induced defects on the thermal conductivity are larger than those of Gd_2O_3 in high burnup fuel pellets. The values calculated using eq. (4) are in good agreement with the measured data and the data obtained by other researchers.

5. CONCLUSION

Thermal diffusivity was measured from room temperature to 2000 K by a laser flash method for microsamples prepared from UO_2 and $(U,Gd)O_2$ pellets irradiated in a commercial reactor. Their thermal conductivities were evaluated by multiplying the thermal diffusivities by the specific heat capacities of unirradiated UO_2 pellets and sample densities.

Thermal conductivities decreased with increasing burnup at lower temperature, then began to recover above 750 K, and recovered completely above 1400 K, becoming quite similar to the values for SIMFUEL (SIMulated high burnup FUEL). The thermal conductivities of irradiated UO_2 and $(U,Gd)O_2$ pellets were analyzed based on the results of X ray diffraction and TEM observations. The recovery stages of thermal conductivity corresponded with those of the irradiation-induced defects. Good predictions were made using the thermal conductivity expression of Amaya and Hirai, considering the effects of irradiation-induced defects.

ACKNOWLEDGMENT

This study was sponsored by the Ministry of International Trade and Industry (MITI).

REFERENCES

[1] NOGITA, K., UNE, K., J. Nucl. Sci. Technol. 30, 900 (1993).
[2] NOGITA, K., UNE. K., Nucl. Inst. Methods Phys. Res. B91, 301 (1994).
[3] KASHIBE, S., UNE, K., NOGITA, K., J. Nucl. Mater. 206, 22 (1993).
[4] *Thermal Conductivity of Uranium Dioxide*, Technical Report Series No. 59, IAEA, Vienna (1996).
[5] ROSS, A. M., AECL-1096 (CRFD-817) (1960).
[6] DANIEL, J. L., MATOLICH, J. Jr., DEEM, H. W., HW-69945 (1962).
[7] HAWKINGS, R. C., ROBERTSON, J. A. L., AECL-1733 (CRDC-1143) (1963).
[8] CLOUGH, D. J., SAYERS, J. B., AERE-R 4690 (1964).
[9] STORA, J. P., DE SIGOYER, B., DEIMAS, R., DESCHAMPS, P., LAVAND, B. RINGOT, C., CEA-R-2586 (1964).
[10] DANIEL, R. C., COHEN, I., WAPD-246 (1964).
[11] MARCHANDISE, H., EUR-4568f (1970).
[12] NAKAMURA, J., UCHIDA, M., UETSUKA, H., FURUTA, T., IAEA TCM Adv. Pellet Technol. Improv. Perform. High Burnup, No. 3-2, Tokyo, Japan, 28 Oct.- 1 Nov. (1996), IAEA-TECDOC-1036, p.127, August 1998, IAEA, Vienna.

[13] NAMEKAWA, T., MITSUGI, T., TACHIBANA, T., YAMANOUCHI, S., Proc. 35th Conf. Remote Systems Technol. p. 105 (1987).
[14] YAMAMOTO, K., HIROSAWA, T., YOSHIKAWA, K., MOROZUMI, K., NOMURA, S., J. Nucl. Mater. 204, 85 (1993).
[15] ISHIMOTO, S., HIRAI, M., ITO, K., KOREI, Y., J. Nucl. Sci. Technol. 31, 796 (1994).
[16] LUCUTA, P. G., MATZKE, Hj., VERALL, R. A., TASMAN, H. A., J. Nucl. Mater. 188, 198 (1992).
[17] HIRAI, M., AMAYA, M., WAKASHIMA, Y., MATSUURA, T., NOMATA, T., HAYASHI, H., KITAMURA, M., IAEA TCM Adv. Pellet Technol. Improv. Perform. High Burnup, No. 3-3, Tokyo, Japan, 28 Oct.- 1 Nov. (1996), IAEA-TECDOC-1036, p.139, August 1998, IAEA, Vienna.
[18] AMAYA, M., HIRAI, M., WAKASHIMA, Y., KUBO, T., KOGAI, T., HAYASHI, H., KITAMURA, M., Proc. TOPFUEL '97, p.5-236, BNES, June 9-12, 1997, Manchester, UK.
[19] AMAYA, M., HIRAI, M., J. Nucl. Mater. 247, 76 (1997).
[20] AZUMI, T., TAKAHASHI, Y., Rev. Sci. Instrum. 52, 1411 (1981).
[21] TAKAHASHI, Y., YAMAMOTO, I., OHSATO, T., Netsu-Sokutei 15, 103 (1988).
[22] *TREE-NUREG-CR-0497*, HAGRMAN, D. L., REYMAN, G. A. (eds.) (1979).
[23] HIRAI, M., J. Nucl. Mater. 173, 247 (1990).
[24] ROHDE, M., SCHULTZ, B., J. Nucl. Mater. 173, 289 (1990).
[25] CORELLI, J. C., HOOLE, J., LAZZARO, J., LEE, C. W., J. Am. Ceram. Soc. 66, 529 (1983).
[26] PRICE, R. J., J. Nucl. Mater. 46, 268 (1973).
[27] KLEMENS, P. G., Proc. Phys. Soc., A68, 1113 (1955).
[28] KLEMENS, P. G., Phys. Rev. 119, 507 (1960).
[29] KLEMENS, P. G., HURLEY, G. F., CLINARD, Jr. F. W., Proc. 2nd Top. Mtg. Tech. Controlled Nucl. Fusion, Amer. Nucl. Soc., -ERDA-, EPRI, p. 957, Conf-760935 (1976).
[30] BRANDT, R., NEUER, G., J. Non-Equilib. Thermodyn. 1, 3 (1976).
[31] NAKAMURA, J., KAMOSHIDA, K., NAGASHIMA, H., OWADA, I., UETSUKA, H., Proc. 2000 Spring Mtg. Atom. Ener. Soc. Jpn. K40 (2000).
[32] MINATO, K., SHIRATORI, T., SERIZAWA, H., HAYASHI, K., UNE, K., NOGITA, K., HIRAI, M., AMAYA, M., submitted to J. Nucl. Mater.

THERMAL DIFFUSIVITY MEASUREMENTS ON OXIDISED IRRADIATED URANIA FUEL UP TO 900°C

T.L. SHAW, W.E. ELLIS, J.C. CARROL, R.A. GOMME
AEA Technology, Windscale, Seascale, Cumbria, United Kingdom

Abstract

There is a limited amount of available data on the thermal conductivity of oxidised fuel, and none on oxidised irradiated fuel. In this work oxidised samples of irradiated fuel have been prepared and out-of-pile thermal diffusivity measurements have been performed. The usual way to prepare oxidised samples is to anneal at high temperature in a controlled oxygen potential, typically at temperatures ≥ 1200°C in CO/CO_2 atmospheres. However, such conditions are not suitable for irradiated UO_2 because of the restructuring processes that occur above ~900°C and which could confound the thermal diffusivity measurement results. Therefore a low temperature anneal in air at 460°C for 5 minutes was used to oxidise fragments of irradiated UO_2. The results are be reported and compared with oxidation data from different sources and as these cannot be reconciled solely on stoichiometry variation, it is suggested that the method used to produce oxidised samples may be an important contributor. This could explain the difficulty in reconciling Conductivity Integral to Melt data with low temperature measurements. Plans to perform integral oxidation and thermal diffusivity measurements to investigate this phenomenon are being considered.

1. INTRODUCTION

A knowledge of the thermal conductivity of oxidised urania is of key importance to the behaviour of the fuel under accident conditions. However, there is a limited amount of available data on the conductivity of oxidised fuel, the majority of which has been obtained from out-of-pile measurements. Thermal diffusivity measurements on unirradiated UO_2 have been reported by G-oldsmith and Douglas [1] and Lucuta et. al. [2]. Howard and Gulvin [3] have also performed conductivity measurements. Lucuta also reports measurements of the effect of oxidation on SIMFUEL with various levels of simulated burnup. However, no such measurements have been performed on oxidised *irradiated* fuel, and the aim of this work was to prepare oxidised samples of irradiated fuel in order to perform out-of-pile thermal diffusivity measurements.

In section 2 the method of sample preparation is described along with experimental techniques used to characterise the oxidation levels achieved. The thermal diffusivity results are then presented in section 3, and are compared against oxidised fuel data from other sources in section 4. Finally, the conclusions are presented in section 5.

2. PREPARATION OF OXIDISED SAMPLES

2.1. Samples

The irradiated fuel used in this investigation was taken from Rod 1 of IFA-558, which had an assembly average burn-up of 40.4 GWd/tU. Two samples were prepared from an adjacent location to that from which both thermal diffusivity and specific heat samples [4] had previously been taken (about 600mm from the bottom end of the rod). In addition, an unirradiated UO_2 sample was chosen to enable comparison with the irradiated fuel data. The sample chosen was one that had already been characterised during validation trials of the Windscale thermal diffusivity rig.

2.2. Equipment

All three oxidised samples were prepared using a differential scanning calorimeter, primarily due to the ability to define precise temperature programmes. The basic equipment comprises a standard Netzsch DSC-404 high temperature differential scanning calorimeter, and in order to allow measurements on irradiated fuel the operation of the calorimeter has been adapted for remote use inside a shielded cell [4].

Differential Scanning Calorimetry is a method by which the heat input into a sample as compared to a known reference material (typically sapphire) is measured while the sample and reference material are subjected to a controlled temperature programme with constant heating and/or cooling rates. The differential heat flux into both the sample and the reference results in temperature differences, which are measured as a function of temperature and time. The recorded signal is a measure of not only the heat capacity of the sample, but also detects any exothermic or endothermic processes that may occur in the sample.

In normal operation the rig is used to measure the specific heat of samples subjected to a controlled temperature programme, while a gas flow of pure argon is fed through the furnace at modest flow rates of between 50–100 cm^3/minute. In the current application the specific heat has not been measured, but the rig has been used in the following ways:

A temperature programme was implemented to oxidise the fuel by running the rig in static air rather than in flowing argon;

On completion of the oxidation run for the unirradiated UO_2 sample it was re-run in a non-oxidising flowing argon atmosphere to look for the characteristic peak corresponding to the energy of transformation for the phase change between U_4O_{9-y} and UO_{2+x} (see for example reference [5]). The temperature at which this transition occurs allows an estimate of the stoichiometry to be made [6].

2.3. Oxidation in air

The method chosen was low temperature oxidation in air so as to minimise the restructuring effects that occur in irradiated fuel on heating to high temperatures. The same oxidation cycle was used for the irradiated samples as well as for the unirradiated sample. However, there are some important considerations to bear in mind:
Some spalling at the surface due to U_3O_8 formation is possible and to minimise this it was decided to keep the target UO_{2+x} oxidation state relatively low (x = 0.05 to 0.1);
At temperatures below 500°C the samples will not achieve equilibrium stoichiometry, and to maximise the penetration of oxygen into the samples it is better to heat to a high temperature for a short time rather than use a long hold at lower temperature. The temperature programme chosen comprised a five minute hold at the peak temperature, combined with heating and cooling rates of ±40°C/minute up to and down from the peak hold temperature.
The oxidation kinetics of unirradiated and irradiated UO_2 are not expected to be identical. However, subjecting the unirradiated sample to the same oxidation cycle as the irradiated samples should result in comparable, if not the exactly the same, oxidation states.

In order to define an appropriate peak hold temperature reference has been made to some unpublished work on the measured oxidation rate of unirradiated fragments of UO_2 in air (up to 500°C). The temperature variation of the oxidation rate from this work has been used to calculate the excess stoichiometry as a function of peak temperature for the chosen

temperature programme. A peak temperature of 460°C was selected, which corresponded to an estimated value of x ~ 0.075 for a sample mass of 100 mg.

2.4. Oxidation results

On completion of the oxidation cycle for the unirradiated sample it was re-run in a flowing argon atmosphere to estimate the oxidation state attained. The temperature programme comprised a heating ramp at 20°C/minute up to 500°C where it was held for 30 minutes before being ramped down at 20°C/minute. The raw signal data showed no evidence of any oxidation peak. Either the sample had not been oxidised significantly, which would be hard to explain, or the oxygen that had been absorbed had not penetrated very far into the surface. In the latter case heating to a higher temperature with a longer hold should serve to better equilibrate the oxygen distribution through the sample. Consequently the sample was run again in flowing argon, but to a higher *annealing* temperature of 700°C (held for one hour). Again no peak was seen on the up ramp, but on the down ramp from 700°C the characteristic oxidation peak was evident at around 500°C. A further repeat of this cycle confirmed the presence of oxidation peaks on both up and down ramps, showing that the initial isothermal anneal at 700°C is indeed significant.

The oxidation state of the unirradiated sample could not be determined from the measured weight change as the sample was dropped after the oxidation run, resulting in a small amount of material loss. Instead, it was decided to make use of the position of the oxidation peak(s) to determine the oxidation level. An *onset temperature* has been defined as the temperature at which the specific heat curve starts to deviate from the expected UO_2 specific heat values (on a 20°C/minute down ramp). From work on other samples where oxidation had occurred and weight change data were available it was possible to correlate the onset temperature with the de Franco and Gatesoupe[6] intersection temperature for the UO_{2+x}/U_4O_{9-y} phase boundary. On doing this for the unirradiated sample used in the present work an O/M ratio of 2.096 ± 0.05 has been determined.

The 700°C *annealing* cycle in a flowing argon atmosphere was repeated using one of the two irradiated oxidised samples. However, in this case no peaks characteristic of the UO_{2+x} to U_4O_{9-y} phase transformation were seen, which is consistent with the view that U_4O_9 formation is inhibited in irradiated fuel (see reference [5] for example). Thus measurements of weight change have to be made to determine the oxidation state of irradiated samples, and for the two irradiated IFA-558 samples this was done after the thermal diffusivity tests by back reduction in Ar/4% H_2. The temperatures were kept below the peak temperature of 900°C at which thermal diffusivity measurements were performed so as to minimise any overestimation of stoichiometry due to weight loss by fission gas release. The O/M ratios of the 700°C *annealed* and *unannealed* samples have been estimated as 2.11 ± 0.01 and 2.09 ± 0.01 respectively.

3. THERMAL DIFFUSIVITY MEASUREMENTS

3.1. Laser flash apparatus

The basic equipment comprises a standard Netzsch LFA 427 Laser Flash Apparatus adapted for use in a shielded facility [7]. Measurements are performed in vacuum on samples contained within graphite sample holders. The arrangement of the measurement rig differs from that previously used at Windscale, in that the sample holder, furnace, laser optics and

detector are arranged in vertical alignment within the cell, with the controlling electronics outside of the cell.

The technique essentially involves a laser pulse striking the front face of the sample. The temperature response of the rear face is then monitored, from which the thermal diffusivity may be derived. Following the laser flash, heat losses will affect the back surface temperature response, and particularly for materials of low thermal conductivity (e.g. ceramics such as UO_2), this can result in an incorrect determination of the thermal diffusivity, if not appropriately corrected. As irradiated ceramic fuel becomes increasingly cracked with burn-up only small fragments are usually available for measurement. Such small samples do not possess the ideal (~10:1) aspect ratio to allow the "standard" analysis techniques to be used with any degree of confidence, since there are additional routes for heat loss via radial conduction to the outer rim of the sample, and to the sample holder.

Of the "standard" techniques available the Cowan method [8] which assumes that the heat loss is by radiation alone, will be superior to the standard logarithmic technique [9] at high temperatures where radiation heat loss dominates. However, at low temperatures, where radial heat conduction contributes significantly to the total heat loss, the logarithmic method is more suitable, because at short times, the effects of radial heat losses are less important. A unified analysis route [10] has therefore been developed at Windscale to combine the beneficial features of the two "standard" methods, so that it can be applied to both low and high temperature data. This "modified logarithmic method" essentially comprises the logarithmic method, modified to include a heat loss correction term, derived from fits to idealised data over the temperature range of interest.

3.2. Temperature programme

The measurements were all performed at low temperatures (below 1000°C) where both the stoichiometry change and the effects of restructuring (for the irradiated fuel only) should be minimal during the measurement. The basic temperature programme consisted of three cycles, with three measurements being made at each temperature:

Cycle 1: 200°C $\rightarrow$ 500°C $\rightarrow$ 200°C in steps of 100°C

Cycle 2: 200°C $\rightarrow$ 700°C $\rightarrow$ 200°C in steps of 100°C

Cycle 3: 200°C $\rightarrow$ 900°C $\rightarrow$ 200°C in steps of 100°C.

3.3. Unirradiated UO_2 results

This sample had originally been used as part of a validation programme for the LFA-427 and the Windscale heat loss correction method [10]. A set of different sample geometries had been used and the results shown in Figure 1 are those relevant for the present application, where the sample is in the form of a fragment taken from a full disk, with a 2 mm diameter target area for the laser strike. The results shown in Fig. 1 compare very favourably with predictions for unirradiated fuel (assuming a theoretical density of 95%).

A representation of the temperature programme used for the thermal diffusivity testing of the oxidised fuel samples is shown in Fig. 2, and the corresponding results are shown in Fig. 3.

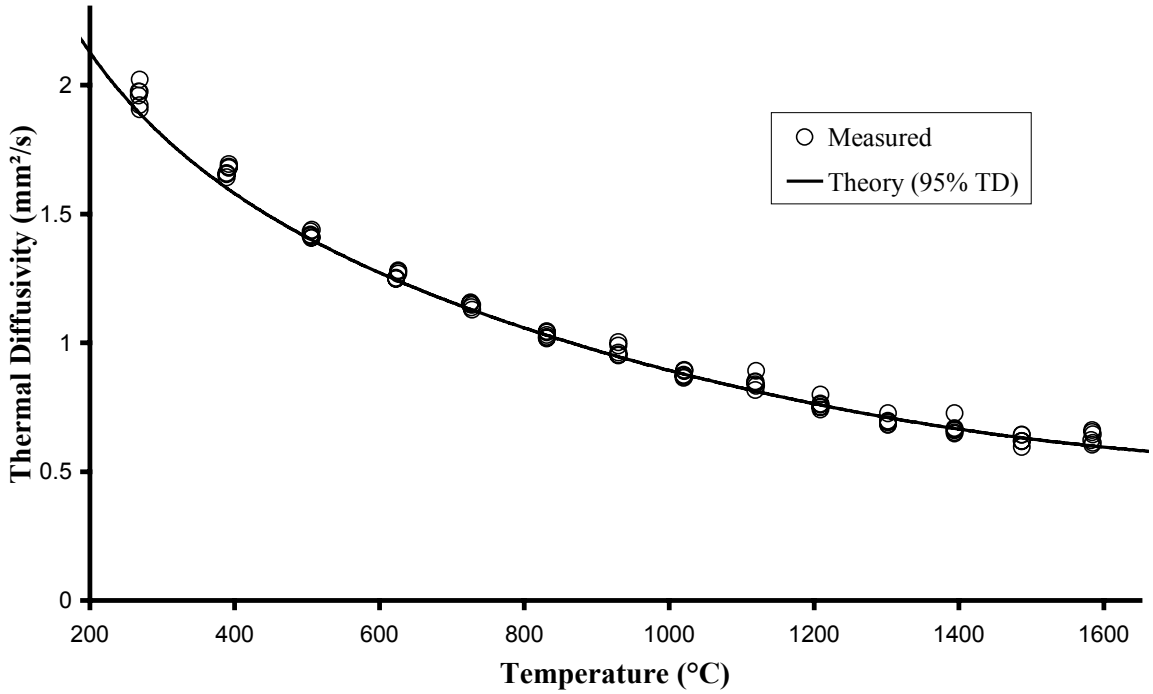

FIG. 1. Results for unirradiated UO_2 sample (unoxidised).

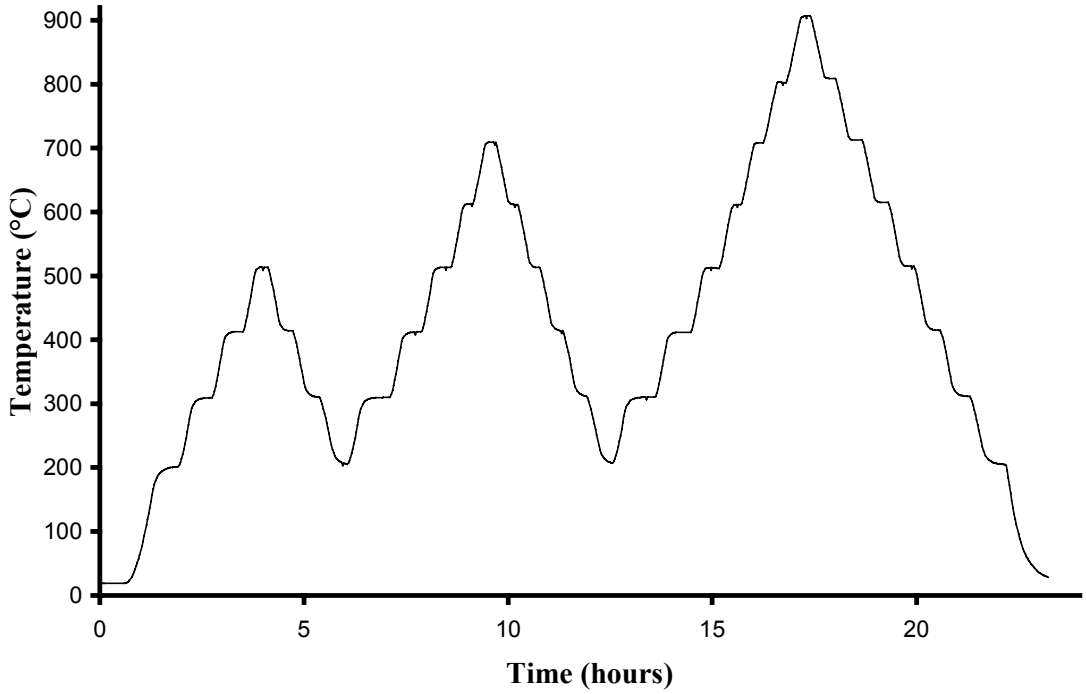

FIG. 2. Temperature programme for thermal diffusivity tests.

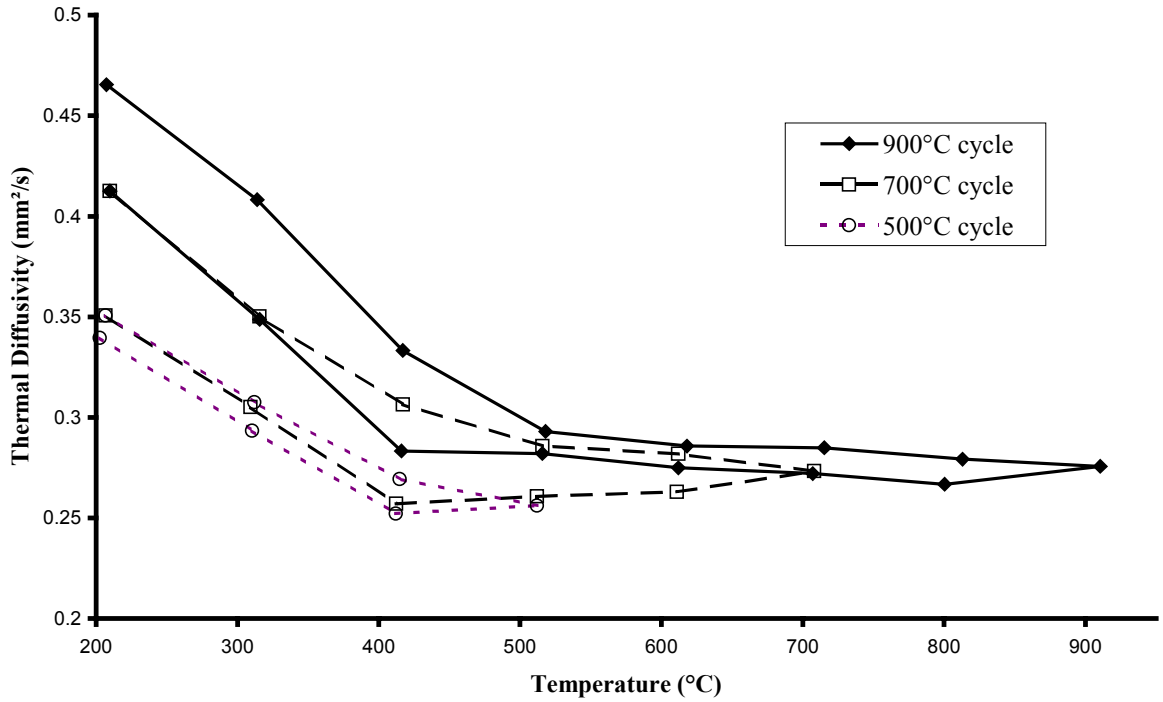

FIG. 3. Results for unirradiated oxidised UO_2 sample.

Above and below the UO_{2+x}/U_4O_{9-y} phase boundary (between 400 and 500°C) there is a marked difference in behaviour. Below the boundary there appears to be a recovery or increase in observed thermal diffusivity on each subsequent cycle to higher temperature. There is also a strong temperature dependence with the thermal diffusivity falling with increasing temperature. Above the phase boundary the measured thermal diffusivity appears to be essentially independent of temperature between 500 and 900°C.

Comparison with the unoxidised results shown in Fig. 1 reveals a significant degradation to have occurred and the oxidised values are much lower (about a factor of two) than expected for fuel oxidised to this stoichiometry. This is discussed further in section 4.

3.4. Irradiated IFA-558 results

For all the IFA-558 samples studied, the nature of the fuel dictated that only small fragments of dimension ~2x2mm could be obtained. Samples were therefore studied using sample holders with 1.5 mm diameter holes. Fig. 2 shows the form of the temperature history used in the thermal diffusivity measurements of all three irradiated IFA-558 samples.

The thermal diffusivity data obtained for the *unannealed* sample are shown in Fig. 4. The data show the temperature cycle to 500°C to have little effect on thermal diffusivity values, with data on the up and down legs of the cycle being almost coincident (apart from a small dip at 400°C on the heating ramp). However, during the second heating cycle the effect of heating to above 500°C is to cause the thermal diffusivity to *increase* with temperature up to 700°C, with a large net recovery (~40%) then being apparent at 200°C compared with the starting value. Heating in the next cycle to 900°C shows a more 'normal' temperature dependence, with a further (smaller) recovery apparent on the return to 200°C. The behaviour over the first

two cycles is attributed to the low temperature at which the oxidation was performed. Subsequent heating to a temperature above the sample preparation temperature appears to have led to a more uniform redistribution of the oxygen, with a significant increase in thermal diffusivity occurring in the temperature range 500–700°C (on the second cycle).

The thermal diffusivity data are shown in Fig. 5 for the sample that had been *annealed* at 700°C prior to the measurements. Qualitatively the data show the expected trends when compared with the data from the *unannealed* sample shown in Fig. 4. The step change seen for the *unannealed* sample on the second cycle is now absent, and the first and second cycle results are virtually identical.

The observation of higher values for the 900°C *annealed* thermal diffusivity (i.e. taken on the cool down from 900°C) for the *unannealed* sample compared with the *annealed* sample is consistent with their respective O/M ratios of 2.09 and 2.11.

A final test was performed in order to investigate the effect of fission gas re-distribution at these temperatures by subjecting an unoxidised IFA-558 sample to the same measurement cycle as was applied to all the oxidised samples. The data are shown in Figure 6, and data are fully consistent with data previously reported for this fuel [4].

It can be seen that a small amount of recovery is obtained on thermal cycling up to temperatures of 900°C, but the main feature is that of a significant degradation in thermal diffusivity of the oxidised fuel compared to the unoxidised values (almost a factor of two). It is interesting to note that in absolute terms the amount of recovery at 200°C achieved in the third cycle (up to 900°C) is comparable for each of the irradiated samples. However, in percentage terms the increases are much more significant for the oxidised samples as the absolute values are so much lower.

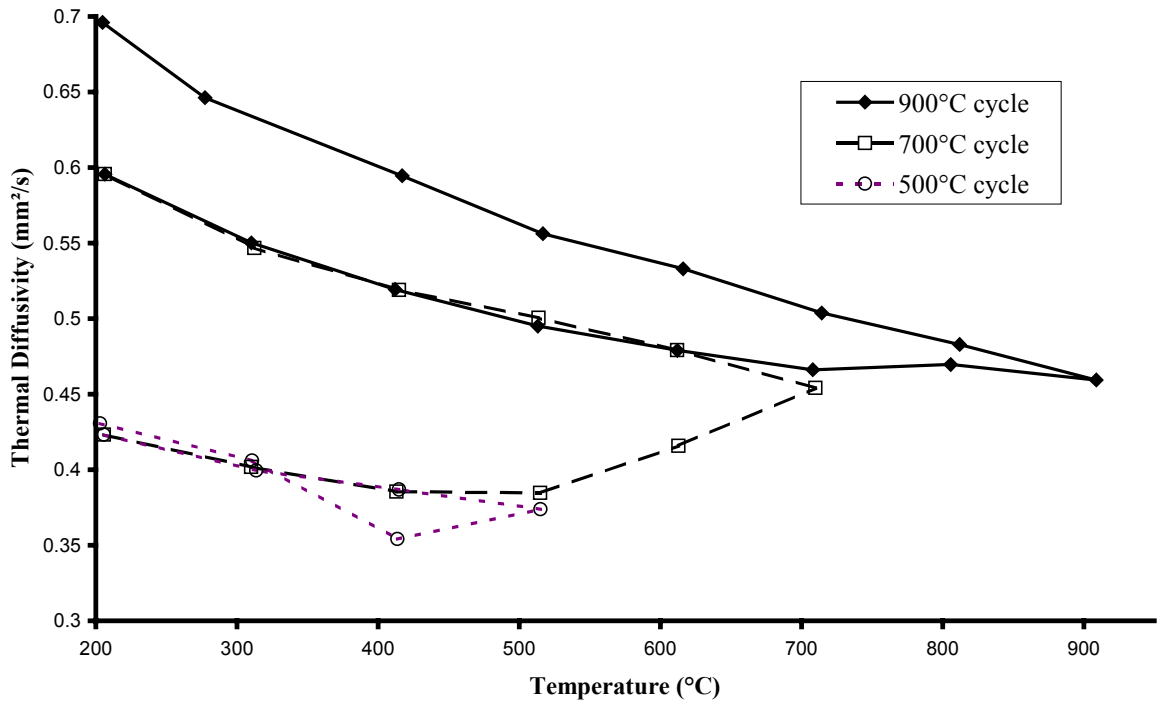

Figure 4. Results for unannealed oxidised IFA-558 sample.

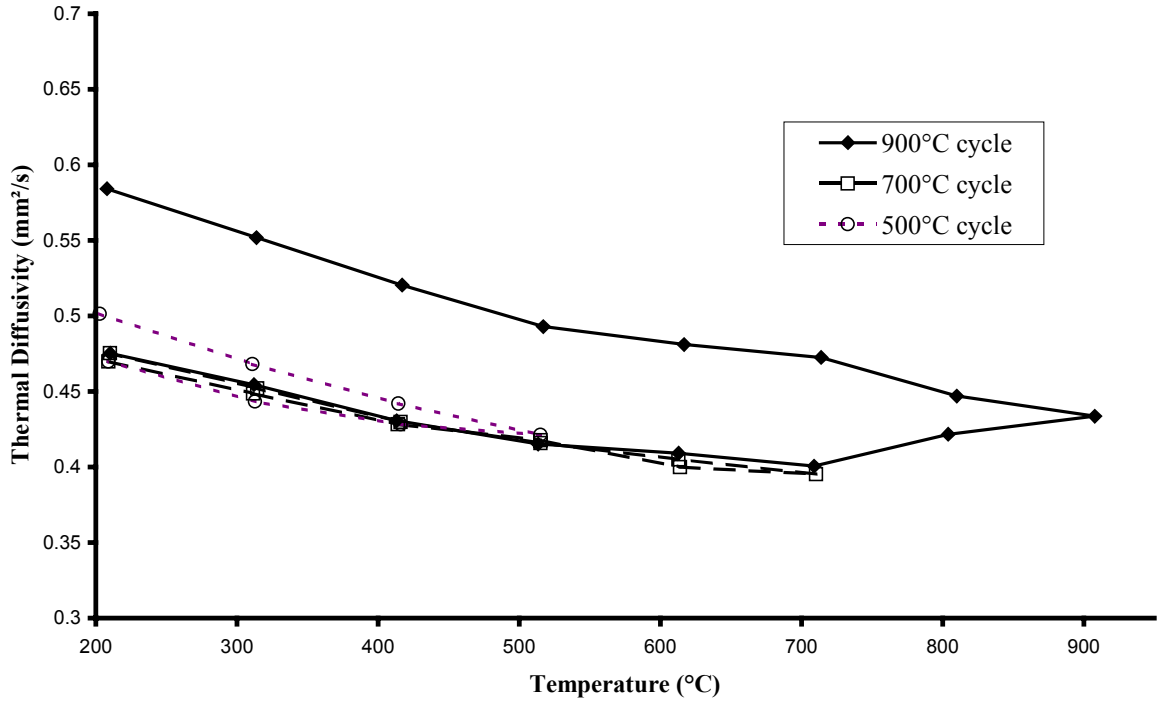

FIG. 5. Results for annealed oxidised IFA-558 sample.

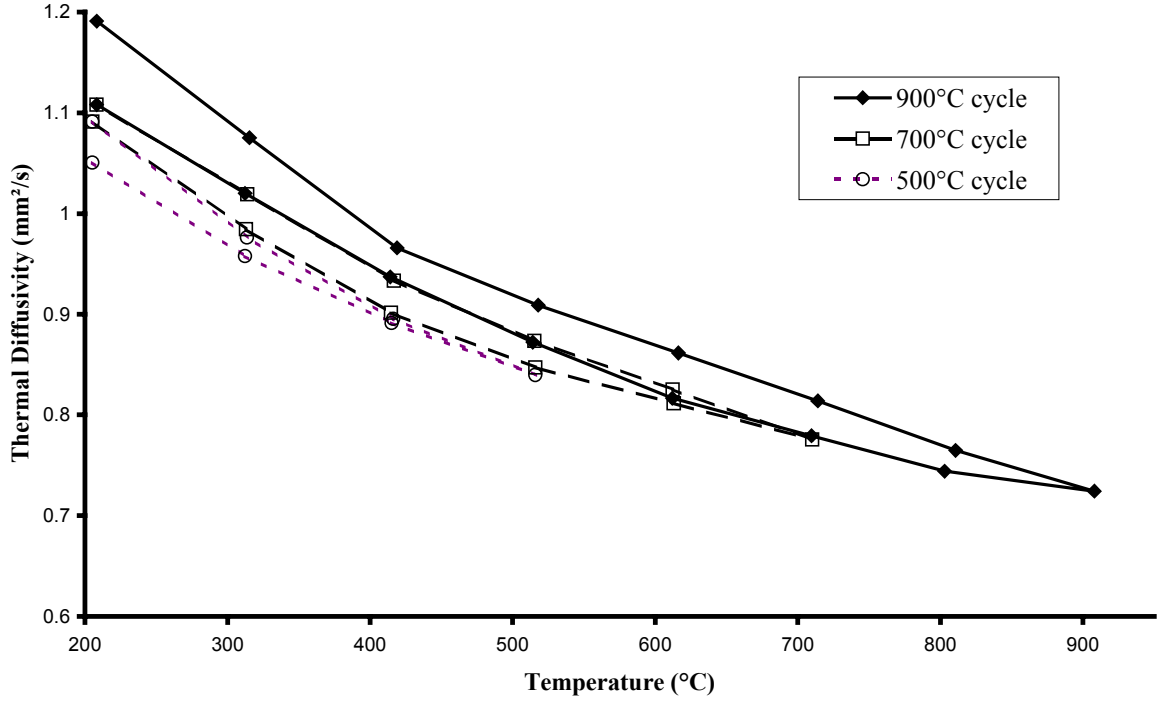

FIG. 6. Results for unoxidised IFA-558 sample.

COMPARISON OF 900°C ANNEALED RESULTS WITH DATA FROM OTHER SOURCES

Thermal diffusivity measurements have been reported on four samples. Three originated from IFA-558 (40 GWd/tU) and comprised one as-irradiated sample and two samples oxidised to O/M ratios of 2.09 and 2.11. A fourth sample of unirradiated UO_2, oxidised to an O/M ratio of 2.096 was also subjected to a similar measurement programme. For all samples a progressive recovery in measured thermal diffusivity was observed by cycling to higher temperatures, with 900°C being the peak temperature attained. A comparison of the 900°C *annealed* results is plotted in Fig. 7. A striking feature of this plot is that the unirradiated fuel diffusivities are lower than the values for both the IFA-558 samples, despite the fact that their O/M ratios are all comparable at around 2.10.

The results in Fig. 7 have been analysed in terms of a standard phonon conductivity model of the form:

$$k = \frac{1}{A + BT} \qquad (1)$$

where T is the absolute temperature (K). Knowing the fuel density and taking the specific heat to be that of unirradiated UO_2 the parameters A and B can easily be determined from linear regression fits. Care has to be exercised for the unirradiated fuel due to the UO_{2+x}/U_4O_{9-y} phase transition that occurs at around 500°C, and as a consequence only data in the range 600–900°C have been included in the fitting procedure for this sample (corresponding to UO_{2+x}).

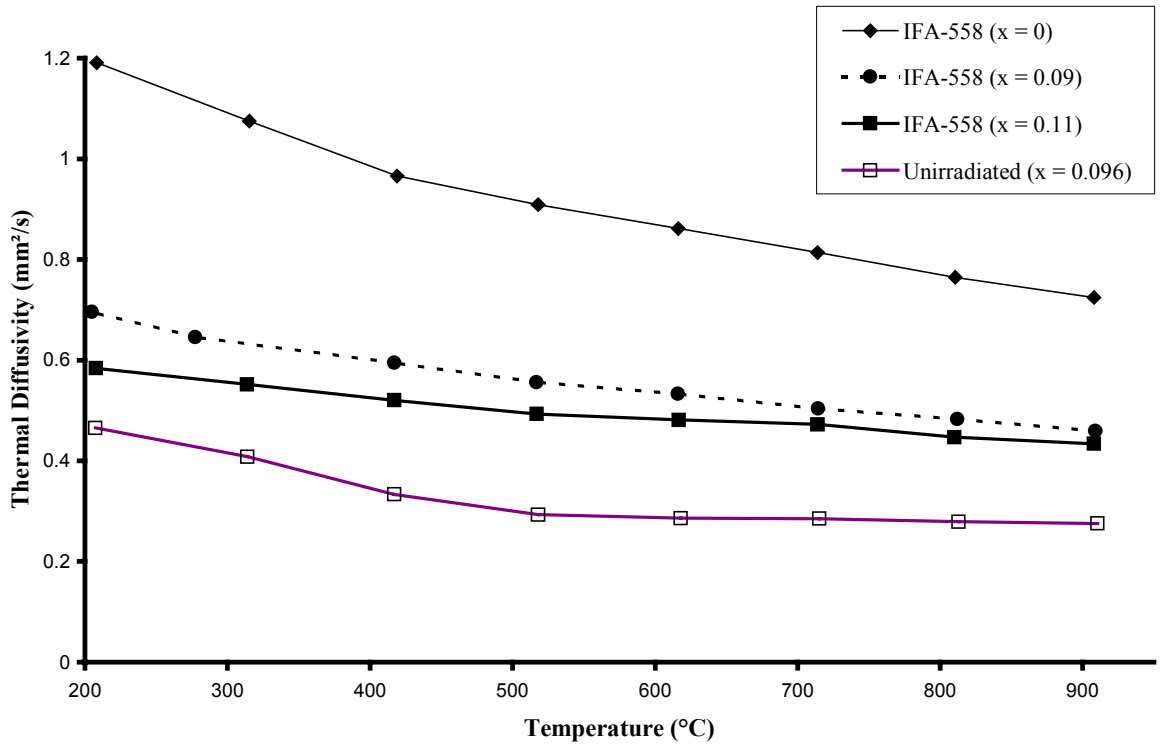

FIG. 7. Comparison of 900°C annealed results.

In Fig. 8 the effect of stoichiometry (represented as the O/M ratio of the material) on A is shown, based on information derived from a variety of sources. This is discussed in detail in reference [11], but the data shown in Fig. 8 can be grouped into three distinct sets:

- the AEAT data points shown correspond to the A values derived from equation (1) for the measurements presented in this paper. These samples were oxidised at low temperature.

- the Goldsmith and Douglas[1], Howard and Gulvin[2] and Lucuta et al.[3] data all refer to out-of-pile measurements made on fuel that had been oxidised at high temperatures (> 1000°C) in a controlled oxygen potential.

- the CIM data refer to values inferred from Conductivity Integral to Melt (CIM) measurements. These are in-pile measurements and provide useful information on the behaviour of the conductivity at very high temperatures. In reference [11] an unpublished compilation of data due to Martin[12] was used, which draws on the work of Marchandise[13], Christensen[14], Ridal[15] and Hawkings[16] was used in the present study. The CIM value is defined as:

$$CIM = \int_{773}^{T_m} K\,dT \qquad (2)$$

where K is the thermal conductivity
T_m is the melt temperature (K)

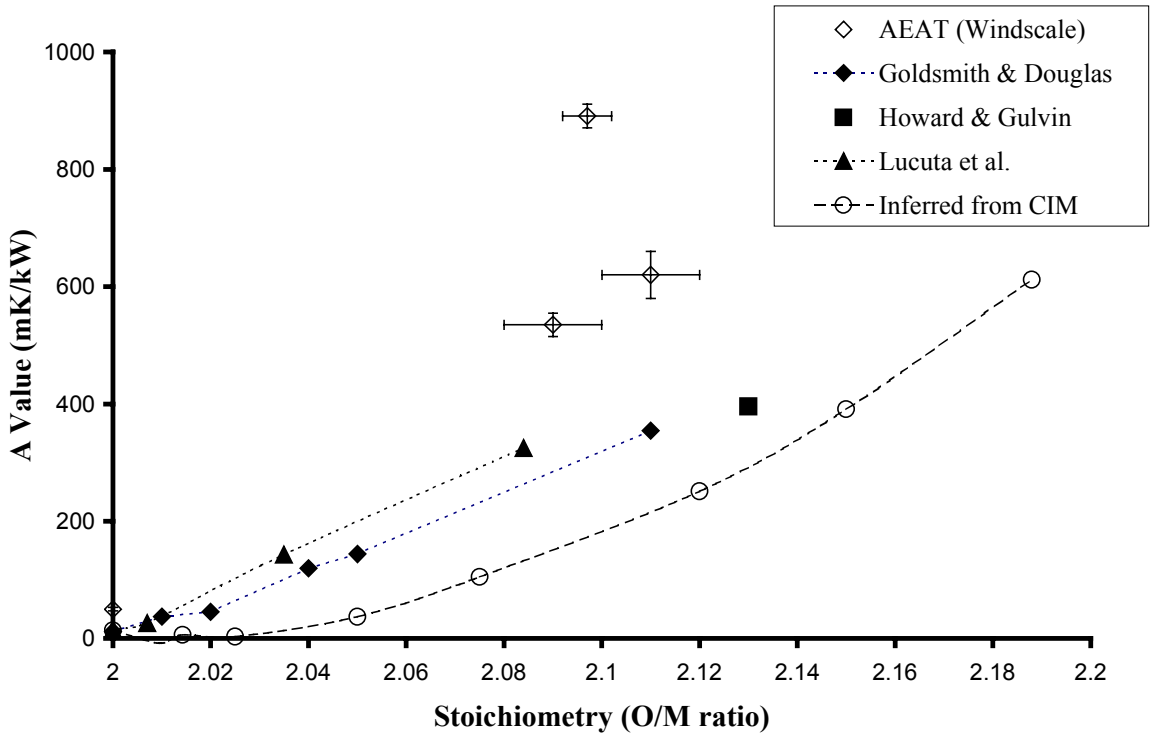

Figure 8. Variation of A with Stoichiometry (O/M ratio).

This question could be addressed by taking the AEAT samples to higher temperatures to determine whether more recovery can be generated. In addition, laser-flash measurements could be performed in situ while the samples are undergoing oxidation at high temperatures. The aim would be to investigate the variation of the thermal properties with the degree of oxidation for samples that are maintained at the temperatures at which the oxidation occurred, and that are not brought down to low temperatures prior to the measurement. The feasibility of performing such measurements is currently being considered.

CONCLUSIONS

Thermal diffusivity measurements have been reported on four samples. Three originated from IFA-558 (40 GWd/tU) and comprised one as-irradiated sample and two samples oxidised to an O/M ratios of 2.09 and 2.11. A fourth sample of unirradiated UO_2, oxidised to an O/M ratio of 2.096, was also studied.

In order to avoid the restructuring processes that occur above ~900°C in irradiated UO_2 a low temperature anneal in air at 460°C for 5 minutes was used to oxidise the fragments of UO_2 used in this work. A Netzsch DSC-404 was used which ensured a high degree of reproducibility in the temperature history between the oxidation runs on the different samples.

The level of oxidation for the unirradiated UO_2 sample was determined by the position of the characteristic peak in the specific heat curve, which corresponds to the UO_{2+x}/U_4O_{9-y} phase transition. This peak was only seen after the sample had been annealed to 700°C, implying that heating to a temperature above the sample preparation temperature leads to a more uniform redistribution of the oxygen. This view is supported by the thermal diffusivity results for the *unannealed* IFA-558 oxidised sample for which a significant increase in thermal diffusivity occurred between 500 and 700°C.

For all three oxidised samples and the unoxidised IFA-558 sample the thermal diffusivity was observed to improve on progressively heating the sample to temperatures higher than previously attained. The unirradiated UO_2 diffusivities were markedly lower than the values for both the IFA-558 samples, despite the fact that their O/M ratios are all comparable at around 2.10.

There was a significant degradation in thermal diffusivity for the oxidised IFA-558 fuel compared to the unoxidised values. The observation of higher values for the 900°C *annealed* thermal diffusivities for one of the two IFA-558 samples is consistent with a lower O/M ratio of 2.09, compared with 2.11 for the other sample.

For out-of-pile experiments markedly different values of A are obtained for oxidised samples manufactured in different ways, implying an effect of the manufacturing process on the effectiveness of the phonon scattering centres in the material. The inconsistencies between the A values inferred from out-of-pile data and in-pile data could also imply that the present approach to the manufacture of samples for laboratory measurements results in materials which are not representative of in-pile conditions. This could be investigated by taking the AEAT manufactured samples to higher temperatures to determine whether more recovery can be generated.

Laser-flash type measurements could also be made while samples are undergoing oxidation at high temperatures, so as to avoid cooling the samples down to low temperatures prior to the measurement. The feasibility of performing such measurements is currently being considered.

REFERENCES

[1] GOLDSHMITH, L.A., DOUGLAS, J.A.M., Measurements of the thermal conductivity of uranium dioxide at 670-1270K, J. Nucl. Mater. **47** (1973) 31-42.

[2] HOWARD, V.C, GULVIN, T.F, UKAEA Report-IG Report 51 (RD/C) (1961).

[3] LUCUTA, P.G., VERALL, R.A., MATZKE, Hj., Thermal conductivity of hyperstoichiometric SIMFUEL, J. Nucl. Mater. **223** (1995) 51-60.

[4] SHAW, T.L., CARROL, J.C., GOMME, R.A., Thermal conductivity determinations for irradiated urania fuel, High Temperatures - High Pressures **30** (1998) 135-140.

[5] MATZKE, Hj., LUCUTA, P.G., VERALL, R.A., HENDERSON, G., Specific heat of UO_2-based SIMFUEL, J. Nucl. Mater. **247** (1997) 121-126.

[6] De FRANCO, M., GATESOUPE, J.P., Plutonium and Other Actinides, North Holland Publishing Co. (1976).

[7] GOMME, R.A., "Thermal properties measurements on irradiated fuel: An overview of capabilities and developments at AEA Technology Windscale", Thermal Performance of High Burn-up LWR Fuel (Proc. CEA-OECD/NEA-IAEA Seminar Cadarache, 1988), OECD, Paris (1988) 31-41.

[8] COWAN, R.D., Pulse method of measuring thermal diffusivity at high temperatures, J. Appl. Phys. **34** (1963) 926-927.

[9] JAMES, H.M., Some extensions of the flash method for measuring thermal diffusivity, J. Appl. Phys. **51** (1980) 4666-4672.

[10] SHAW, T.L., ELLIS, W.E., Heat loss corrections applied to the measurement of thermal diffusivity of small samples by the laser flash technique, High Temperatures - High Pressures **30** (1998) 127-133.

[11] ELLIS, W.E., PORTER, J.D., SHAW, T.L., Effect of oxidation, burnup and poisoning on the thermal conductivity of UO_2: A comparison of data with theory, Light Water Reactor Fuel Performance (Proc. International Topical Mtg Park City, Utah, USA, 2000), ANS (2000) 565.

[12] MARTIN, D.G., UKAEA Internal Document (1990).

[13] MARCHANDISE, H., Commission of the European Communities Report EUR-4568F, 1970.

[14] CHRISTENSEN, J.A., Report BNWL-536 (1967).

[15] RIDAL, A., BAIN, A.S., ROBERTSON, J.A.L., Report CRFD-994 (AECL-1199), Canada (1961).

[16] HAWKINGS, R.C., BAIN, A.S., Report CRDC-1153 (AECL-1790), Canada (1963).

THERMAL BEHAVIOUR OF HIGH BURNUP PWR FUEL UNDER DIFFERENT FILL GAS CONDITIONS

T. TVERBERG
OECD Halden Reactor Project,
Halden, Norway

Abstract

During its more than 40 years of existence, a large number of experiments have been carried out at the Halden Reactor Project focusing on different aspects related to nuclear reactor fuel. During recent years, the fuels testing program has mainly been focusing on aspects related to high burnup, in particular in terms of fuel thermal performance and fission gas release, and often involving re-instrumentation of commercially irradiated fuel. The paper describes such an experiment where a PWR rod, previously irradiated in a commercial reactor to a burnup of ~50 MWd/kgUO_2, was re-instrumented with a fuel central oxide thermocouple and a cladding extensometer together with a high pressure gas flow line, allowing for different fill gas compositions and pressures to be applied. The paper focuses on the thermal behaviour of such LWR rods with emphasis on how different fill gas conditions influence the fuel temperatures and gap conductance. Rod growth rate was also monitored during the irradiation in the Halden reactor.

1. INTRODUCTION

Since most changes which occur in reactor fuel during irradiation are strongly temperature dependent, it is important that modelling codes provide good estimates of fuel temperatures. For this to be achieved, the codes obviously need to be validated through comparison with in-pile measurements. As target burnups in commercial reactors are being extended, more focus is being put on investigating the effects of increased burnup on in-pile performance and on implementing these in modelling codes. The Halden Reactor Project has over the years provided extensive data suitable for use in such code validation purposes; either through instrumentation fresh fuel but also, as has become increasingly important in recent years, re-instrumentation of commercially irradiated fuel.

Several phenomena need to be taken into account when analysing behaviour of high burnup fuel. The fuel-cladding gap closes during irradiation through fuel swelling and cladding creep down. Fission gas released from the fuel can reach the fuel-clad gap and decrease the gap conductance and thus increase fuel temperatures. Furthermore it has been shown, both through out-of-pile laser flash measurements and in-pile temperature measurements, that the thermal conductivity of the fuel degrades considerably with burnup [1, 2]. The instrumentation and areas subject to measurements with respect to thermal behaviour include, of course, above all fuel centre temperature measurements, but also pressure measurements for investigation of fission gas release and (for fresh fuel) fuel densification, fuel stack and clad elongation measurements to assess fuel densification and swelling rates. External gas lines providing the possibility to pressurize fuel rods at different pressure and gas composition provide means for investigating gap conductance and also gas flow measurements for investigation of hydraulic diameter and thus fuel-cladding gap in addition to assessing fission release.

This paper discusses an experiment performed in the Halden Boiling Water Reactor (HBWR) which provided several of the subjects mentioned above. A UO_2 rod, previously irradiated in a PWR reactor was re-instrumented with a fuel centre thermocouple, a cladding elongation

detector and external high- and low-pressure gas lines. During the irradiation in the HBWR, the rod was subject to several gas pressurization steps, using argon, up to as high as 300 bar overpressure while fuel temperature and clad elongation were monitored. The discussion of the data concentrates on the influence of gas composition and pressure on gap conductance and thus thermal behaviour in such a high burnup rod with a tight gap.

2. DESCRIPTION OF THE RIG AND TEST ROD

A schematic of the rig is shown in Fig. 1. The fuel segment used in this test was irradiated for 4 reactor cycles in a commercial PWR reactor. The discharge burnup was 52 MWd/kgUO_2. A simplified power history for the commercial irradiation is shown in Figure 2. During the final cycle of the commercial irradiation, the Linear Heat Rate (LHR) was ca. 20 kW/m.

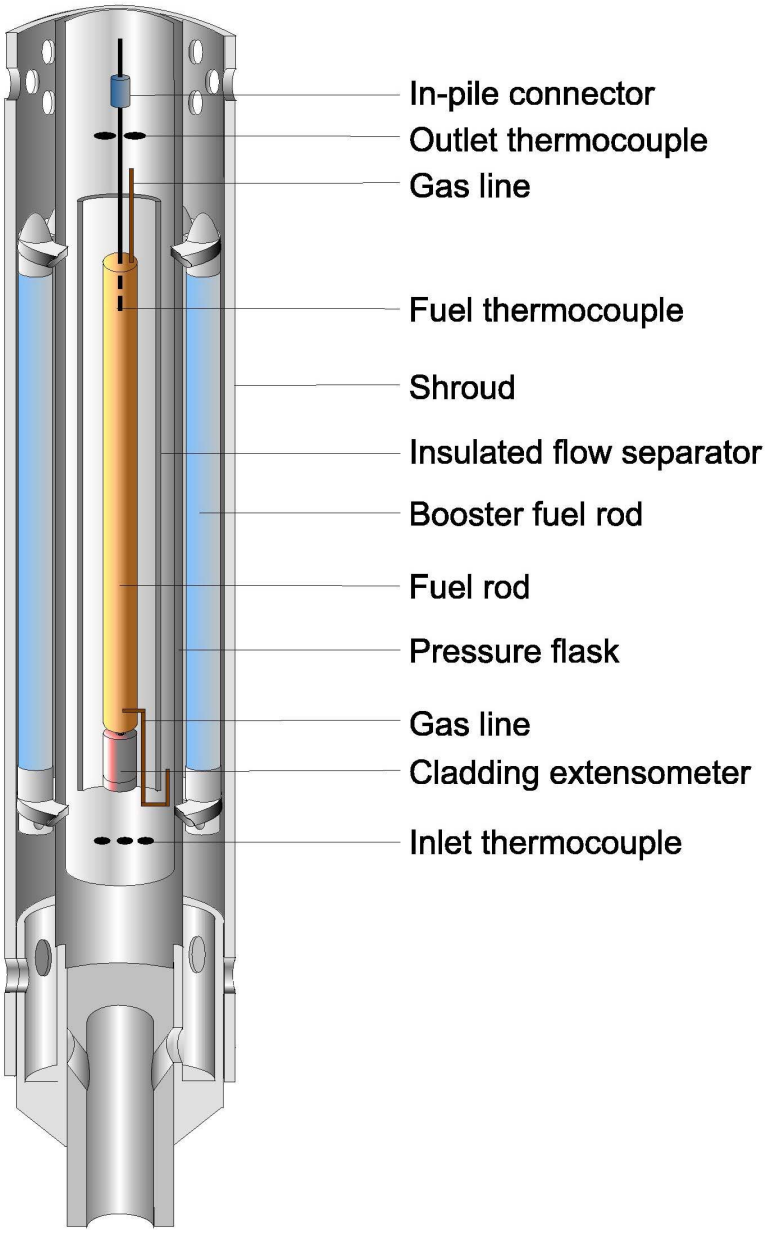

FIG. 1. Schematic of test rig.

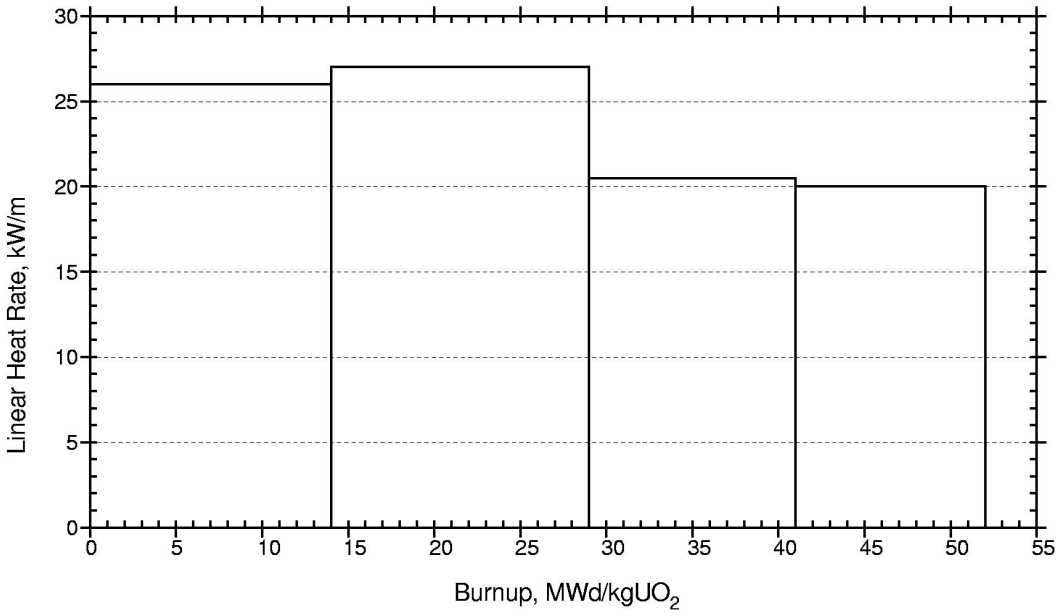

FIG. 2. Base irradiation history.

The testing in the HBWR was performed under simulated PWR conditions; i.e. ~160 bar coolant pressure at 310°C. The rod instrumentation consisted of:

- a fuel centre thermocouple (TF) in the upper end of the rod (ca. 40 mm drilled hole, 2.5 mm diam.)
- a clad extensometer in the lower end
- a high pressure system for pressurisation of the rod with argon
- a low pressure system to perform gas flow measurements for assessing hydraulic diameter. The low pressure system also allows for sweeping out fission gases to a spectrometry system.

In addition to the rod instrumentation, the rig was equipped with vanadium neutron detectors to monitor the axial flux distribution in the rig.

The test rig was situated inside a pressure flask which ensures the high pressure conditions of a PWR (~160 bar). To provide a fast neutron flux more representative of PWRs, the pressure flask was surrounded by 12 booster rods of PWR type with a high enrichment (13% U-235). The main characteristics of the fuel rod is summarized in Table I.

3. IN-PILE PERFORMANCE

3.1 Power history

The rod was irradiated for a total of 4400 full power hours (fph) and the burnup increase during the test was 4.1 MWd/kgUO_2. Fig. 3 shows the average linear heat rate and fuel temperature for the first 2300 fph. The heat rate varies slightly around 15 kW/m throughout this period.

During the irradiation, the pressure was changed in steps of ca. 50 bars by pressurizing with argon. In terms of gas thermal conductivity, Ar corresponds to a Xe/He gas mixture of about 70%/30%. The fuel temperature stays at ca. 700°C during this period. Indicated in the plot is also the peak fuel temperature, which is estimated through calculating the difference between the temperatures of a solid and hollow pellet, the difference being ca. 100°C.

TABLE 1. FUEL ROD FABRICATION DETAILS

Parameter	
Fuel Enriched Length (mm)	422
Fuel Weight (g)	273.5
Initial Density (% of T.D.)	96.1
Initial Enrichment (w/o U^{235})	3.8
Grain Size (□m)	8.5
Initial Fuel - o.d. (mm)	9.12
Fuel - i.d. - for TF (mm)	2.5
Thermocouple Penetration (mm)	~40
Clad Material/Heat Treatment	Zr-4 (partly recrystallised)
Initial Clad - o.d. (mm)	10.75
Initial Clad - i.d. (mm)	9.29
Initial diametral gap (□m)	170.
Fill Gas/Pressure Base Irr. (bar)	He/21.5
Instrumentation	TF1/EC1
Burnup (MWd/kgUO_2)	52.
Oxide layer (μm)	40–60

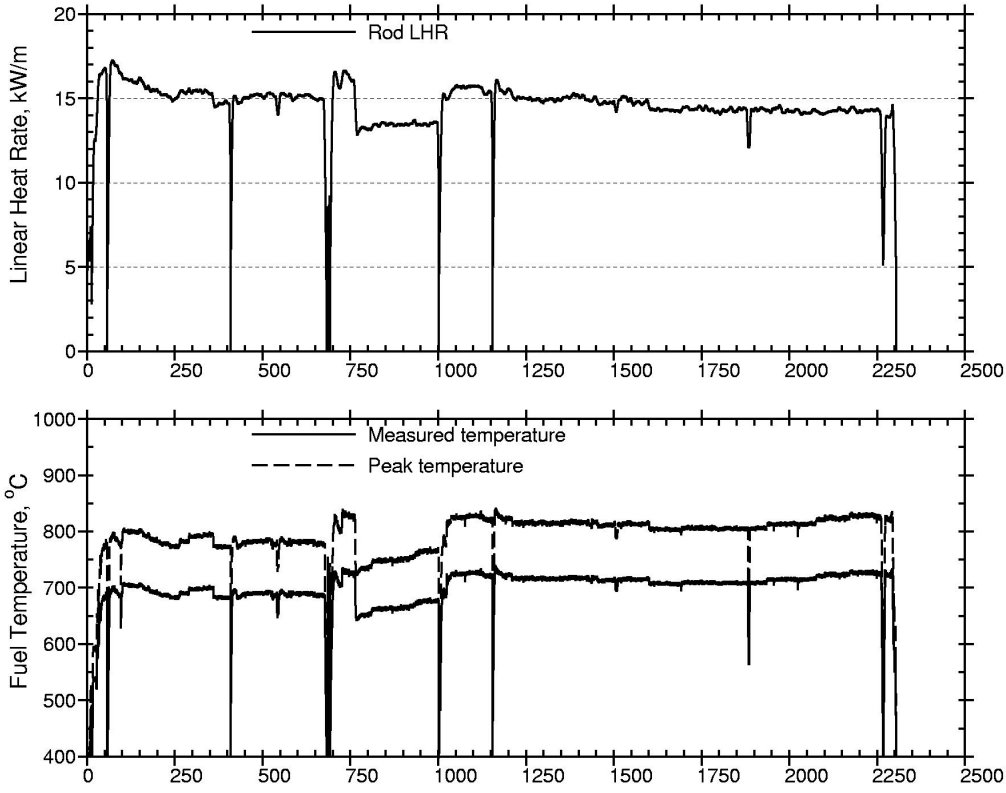

FIG. 3. Average linear heat rate and fuel temperature versus full power hours.

3.2 Clad elongation behaviour

Fig. 4 shows the measured clad elongation and average heat rate for the same period as Fig. 3. The clad elongation follows the rod power fluctuations, indicating that there is pellet-clad contact throughout the period. This can also be seen in Fig. 5, where measured elongation is plotted versus AHR for various power ramps. The dashed lines in the figure are estimated clad free thermal expansion curves. The measured elongation deviates from the clad free thermal expansion at powers 10–15 kW/m indicating that gap closure occurs at this power level.

Elastic deformations can be seen for each step in pressure. Fig. 6 shows a close-up of such a pressure step where the observed elastic deformation induced by the pressure increase is 28 μm. For the other pressurisations that were performed, the elastic deformation was in the same order.

A tendency of permanent increase in elongation in the same range as what could be expected from solid fission product fuel swelling can be seen (the dashed curve included in the plot indicates a swelling rate of 0.7% ΔV/V per 10 MWd/kgU). This is similar to what has been observed for other rods in the same burnup range [3], where clad elongation increase was found to be indicative of fuel swelling.

3.3 Fuel temperature response to pressurisation

Fig. 7 shows the temperature-power relation for two early power ramps. The first ramp shown is from before the first argon pressurization, i.e. helium at low pressure. The second ramp is after ca. 400 fph when the rod was pressurized to +100 bar Ar. The dashed lines in the plot are least square fits to the data. The influence of gas change on the temperature is small, but measurable. At a heat rate of 12 kW/m the observed temperature increase is ca. 20°C.

Fig. 8 shows the same ramps as Fig. 7 together with two additional ramps at rod overpressure +100 and +200 bar respectively. Between the two +100 bar ramps, the temperature increases further (again, ca. 20°C at 12 kW/m), whereas for the +200 bar ramp, the temperature-power relation remains unchanged from the previous +100 bar ramp. In the following sections, possible explanations for the observed temperature behaviour will be discussed.

4. DATA EVALUATION

4.1 Assumptions used in the model

For such high burnups as in the case of this rod, experience has shown that the radial distribution of burnup and porosity will be highly non-uniform. Also the radial power distribution will be very different from the case for fresh fuel. In the calculations used hereafter, the radial power, burnup and porosity have been assessed according to the TUBRNP model [4]. An example of calculated power and burnup distribution is shown in Fig. 9.

It has been shown, both from in-pile and laser flash measurements, that fuel thermal conductivity degrades significantly with burnup. In the calculations, this degradation has been taken into account using the following modified correlation for UO_2 conductivity [5]:

$$\lambda = \frac{1}{0.1148 + 0.0040 \cdot B + 2.475 \cdot 10^{-4} \cdot (1 - 0.00333 \cdot B) \cdot \delta + 0.0132 \cdot e^{0.00188 \cdot T}}$$

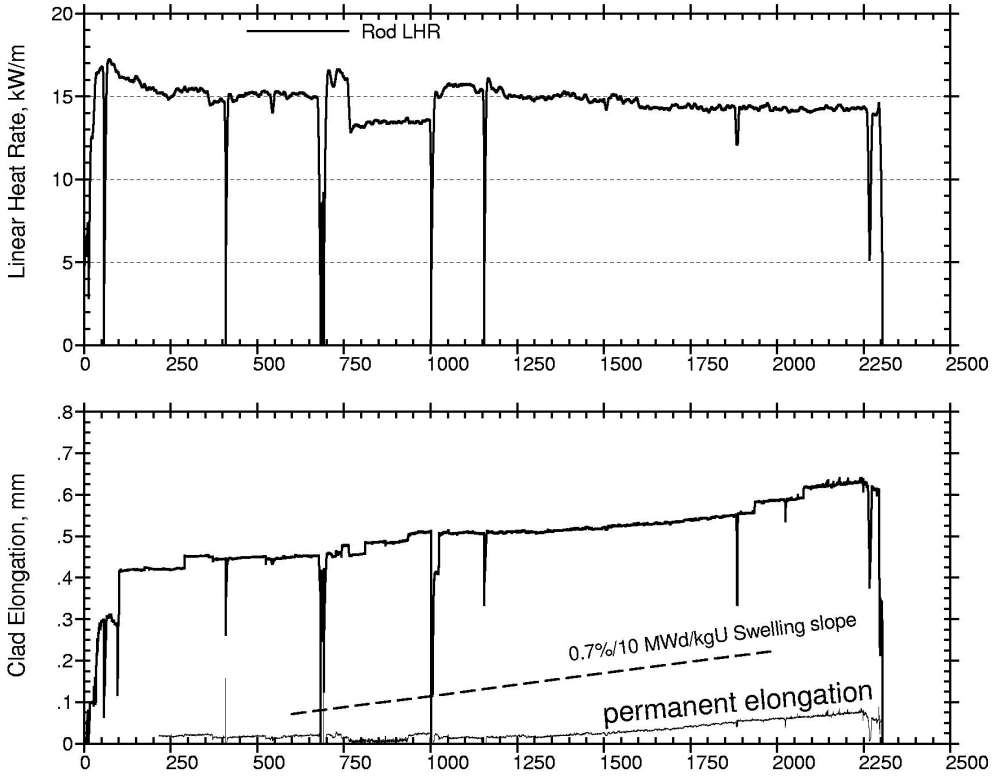

FIG. 4. Clad elongation history.

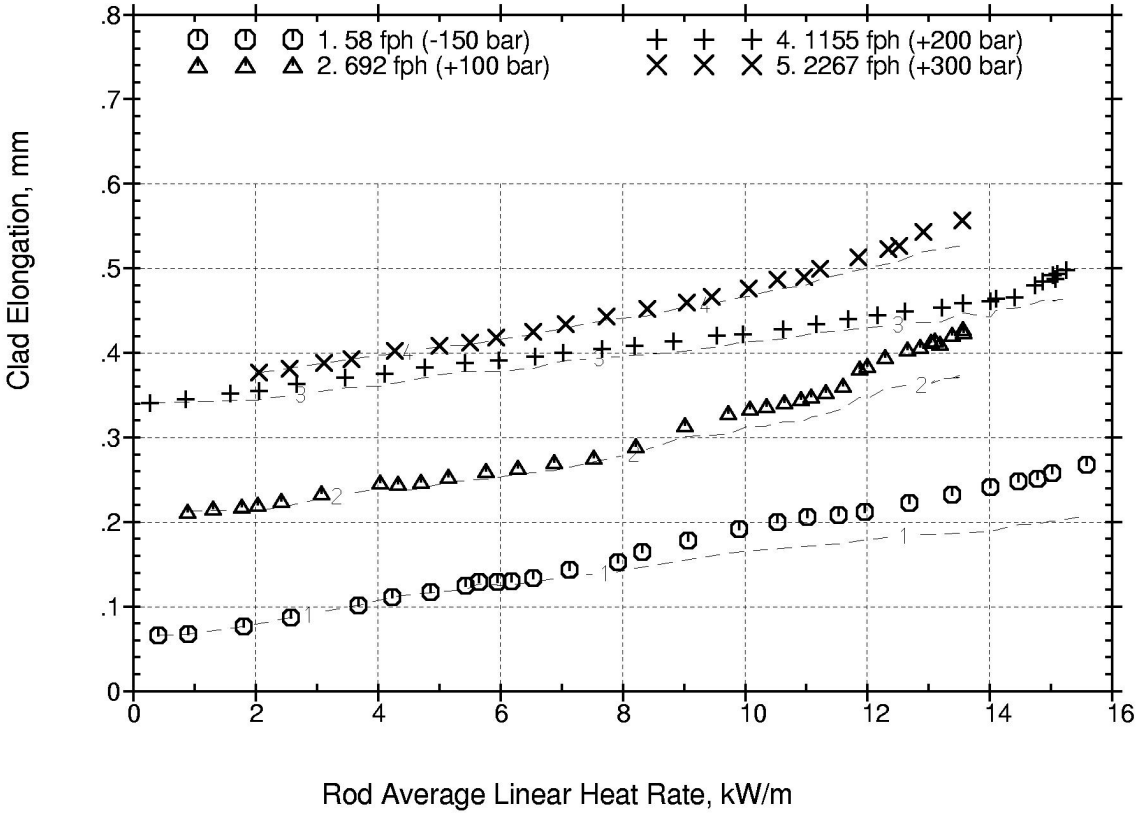

FIG. 5. Clad elongation versus average heat rate for different power ramps. The dashed lines show the estimated free thermal expansion of the cladding.

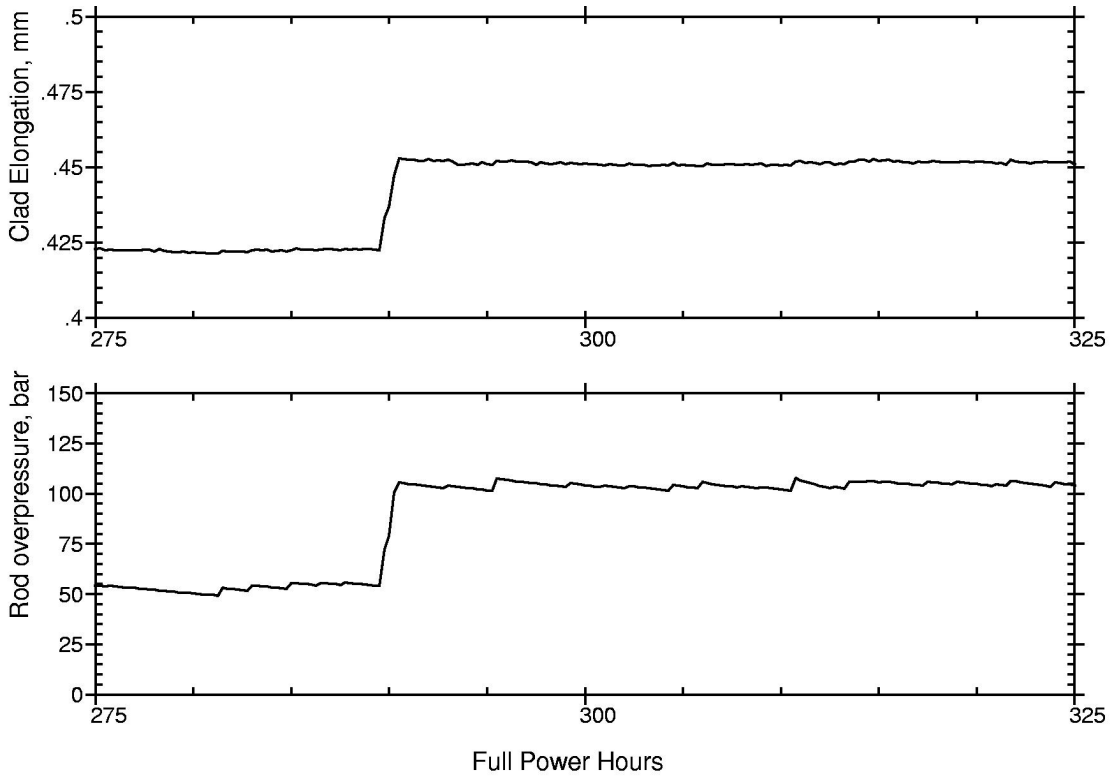

FIG. 6. Close-up of clad elongation response to pressure increase.

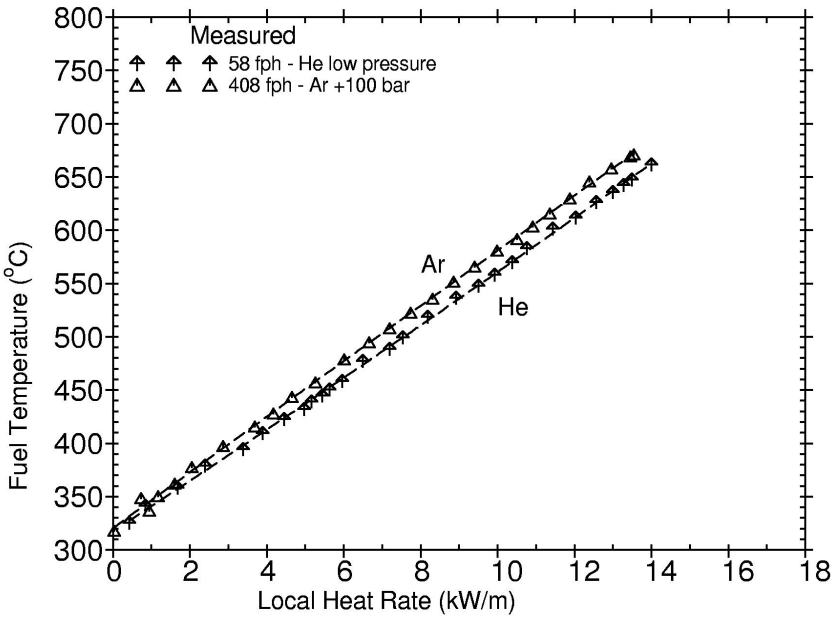

FIG. 7. Power ramps before and after first pressurisation with Ar. Dashed lines are least squares fit to the data. At 12 kW/m the temperature increase after pressurisation is 20°C.

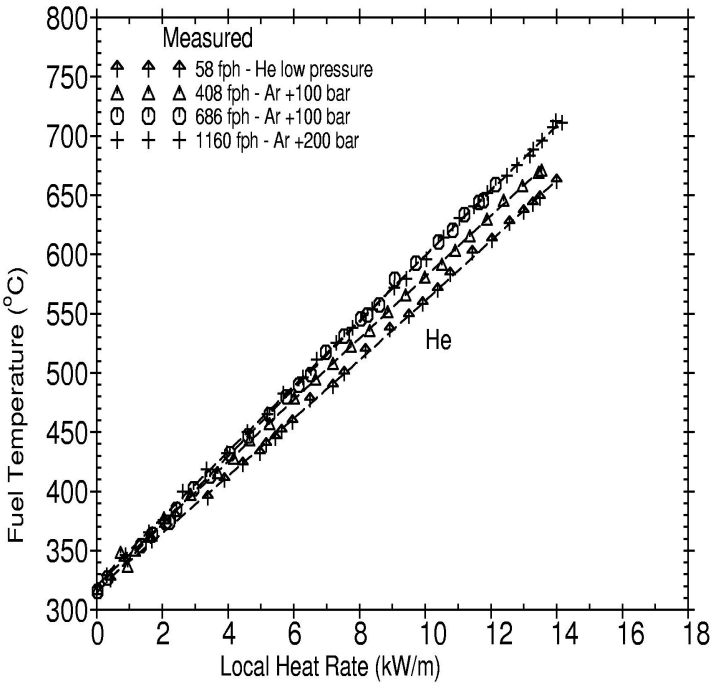

FIG. 8. The power ramps shown in figure 7 and two additional Argon ramps at pressures +100 and +200 bar. Dashed lines are least squares fit to the data.

with burnup B in MWd/kgUO_2, temperature T in °C and δ = min (T,1650). The local burnup is used in the calculations. The correlation above is plotted in Fig. 10 for different burnups. The outer oxide layer of the clad was assessed to be 60 μm (see table) and this value has been used in the calculations.

4.2. Assessment of fuel-clad gap

Several hydraulic diameter measurements were performed in this rod at various power levels. These measurements, summarized in Fig. 11, indicate that a cold diametral gap of 30 μm would be a reasonable value for the start of the test and this was chosen for the calculations. For this cold gap, the calculations estimate gap closure at powers between 12 and 15 kW/m, which is consistent with the observed clad elongation data.

4.3. Temperature calculation

Fig. 12 shows the He-ramp shown in Fig. 7 together with calculations using the assumptions stated above. A reasonably good fit to the data is obtained. Included in the figure are also temperature calculations for fresh fuel (leaving the other parameters unchanged) illustrating the influence of conductivity degradation. This amounts to ca. 100°C at 12 kW/m.

Indicated in Fig. 12 is also the first argon ramp, shown in Fig. 7. When 100% Ar is assumed as fill gas, the temperatures are somewhat overestimated. A possible explanation for this could be that there is still some helium trapped in the fuel rod at the time of the first argon ramp. After the pre-pressurisation and the first ramp (with He at 58 fph), some helium gas could have been trapped inside the rod when the gap is closed at power. Most of this helium was probably released when the internal Ar overpressurisation later on was increased from 50 to 100 bar, but the rest possibly only at the scram and following up-ramp at 408 fph. A calculation for this ramp using a gas mixture of 25% He/75% Ar shown in the figure gives a better fit to the measured data.

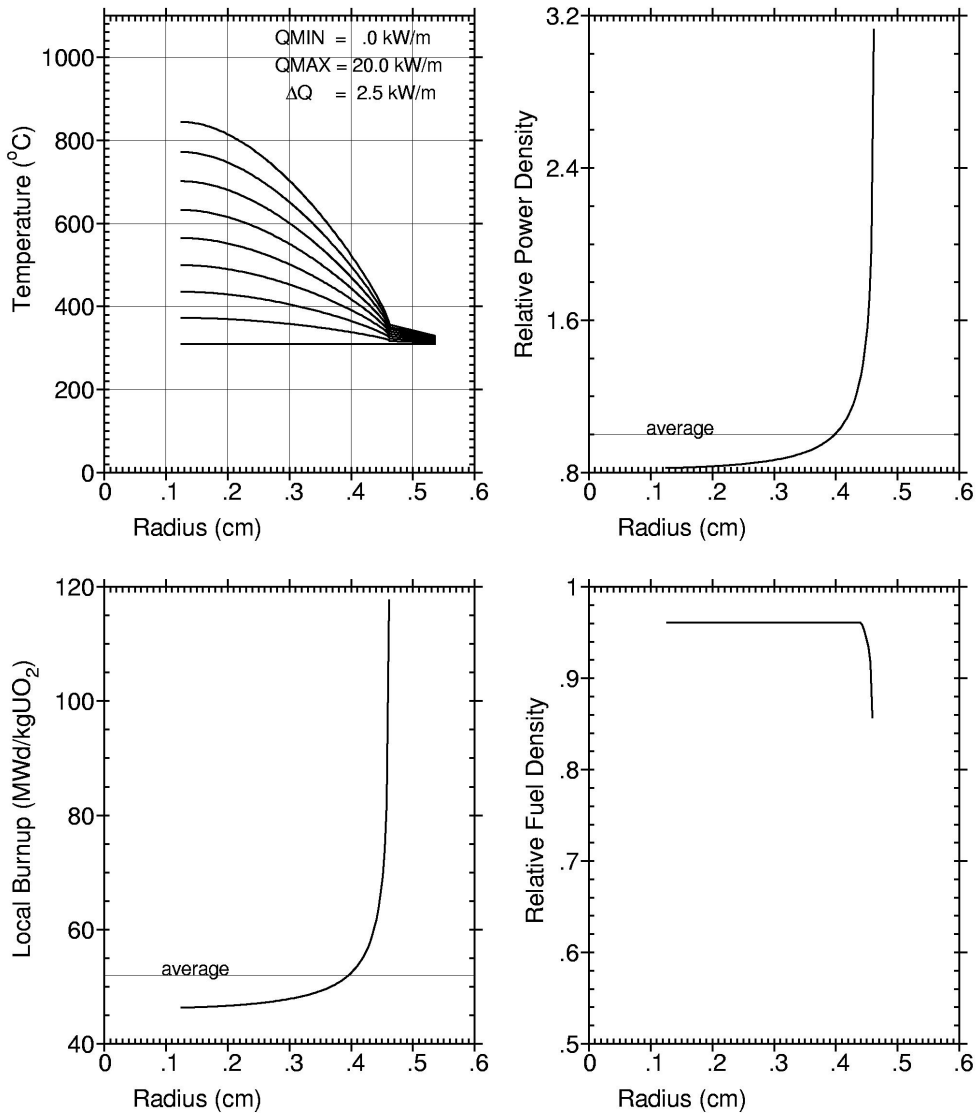

FIG. 9. Radial power and burnup distribution.

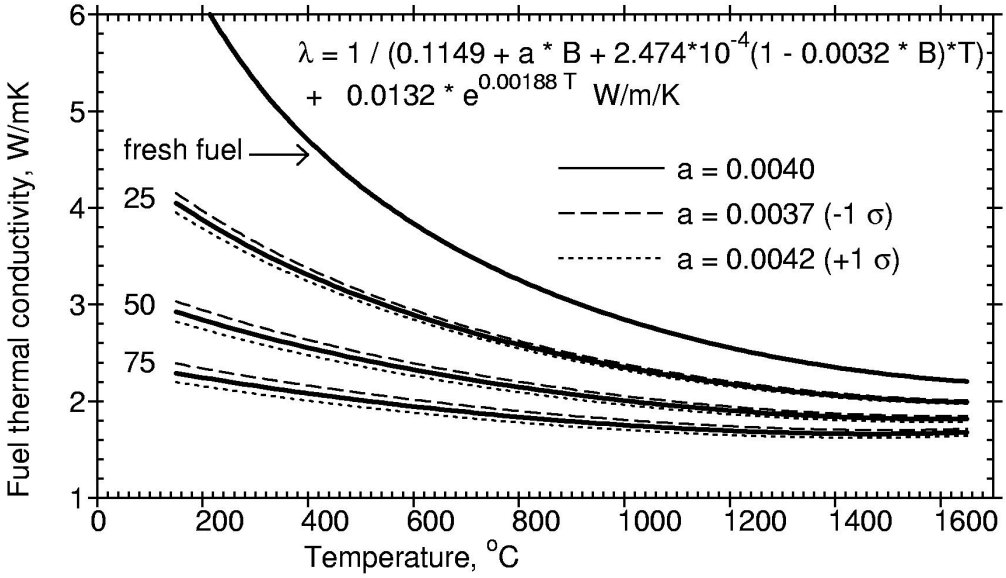

FIG. 10. Fuel thermal conductivity correlation.

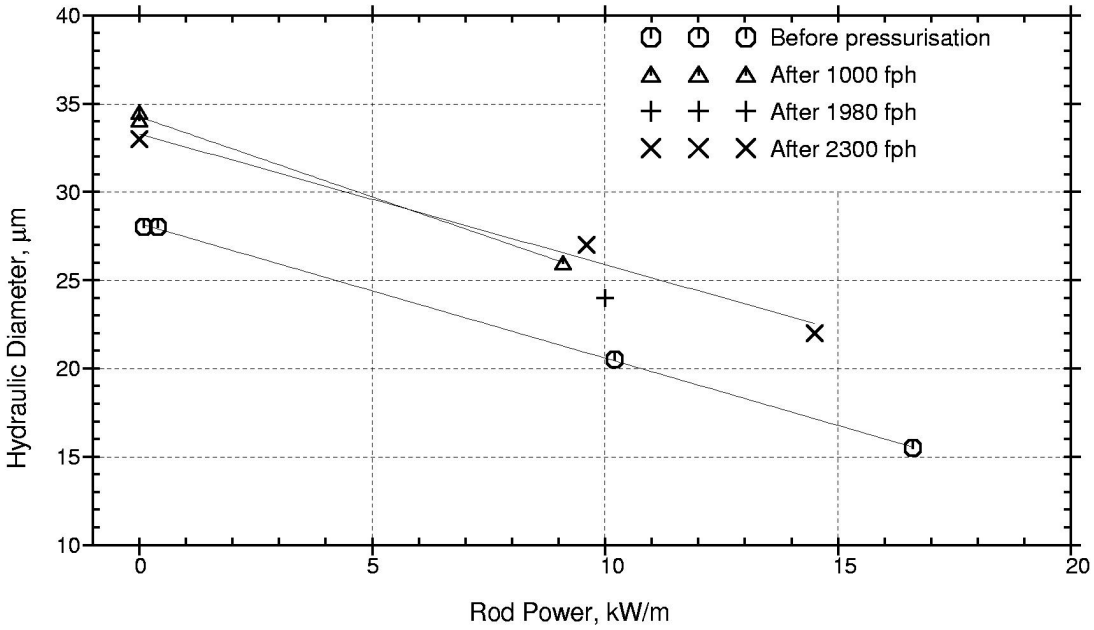

FIG. 11. Hydraulic diameter measurements.

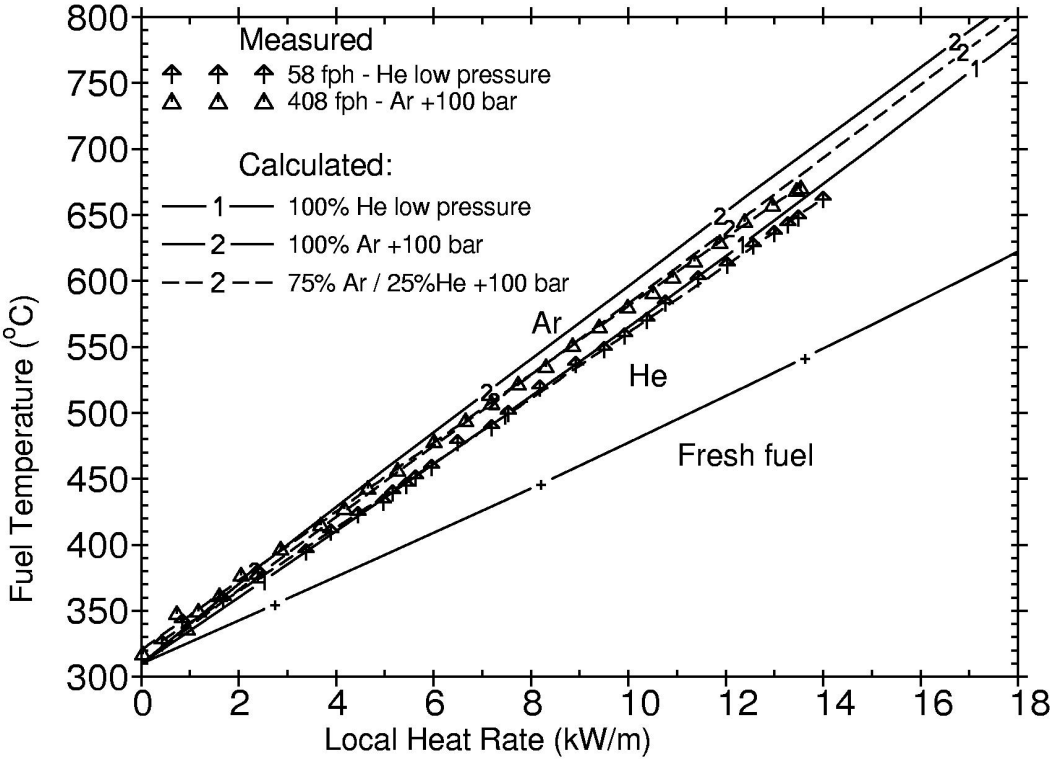

FIG. 12. The ramps in Fig. 7 together with calculations. For the Argon ramp, a gas composition of 25% He and 75% Ar gives a reasonable fit to the data.

Fig. 13 shows calculations for all ramps. Apart from the above mentioned first argon ramp, there is good agreement between measured and calculated temperatures. Note that in all calculations a cold gap of 30 μm is assumed. The elastic deformations observed in the clad elongation measurements correspond to a 2 μm diametral elastic deformation per 50 bar pressure step (see Appendix I), i.e. an 8 μm gap increase for the +200 bar ramp compared with the He ramp at low pressure. Adjusting the gap in the calculations according to the above, gives about 10°C higher temperatures at 12 kW/m. The fact that this temperature increase is not seen in the measured data, may be an indication that fuel bonding is occurring in the rod.

4.4 Scram data

Several reactor scrams were recorded and time constants calculated during the period of irradiation for this rod and are shown in Fig. 14. The calculated fuel time constant is related to the overall conductance in the rod during the transient. Given the small difference in rod burnup between the scrams, progressing conductivity degradation will have only a small influence on the fuel conductivity. It can thus be assumed, that the main changes in fuel time constant are due to differences in gap conductance. Fig. 15 shows the calculated time constant plotted versus argon pressure. While the time constants for different levels of Ar pressure are basically the same, the time constant for the scram performed during He pressurisation is considerably lower.

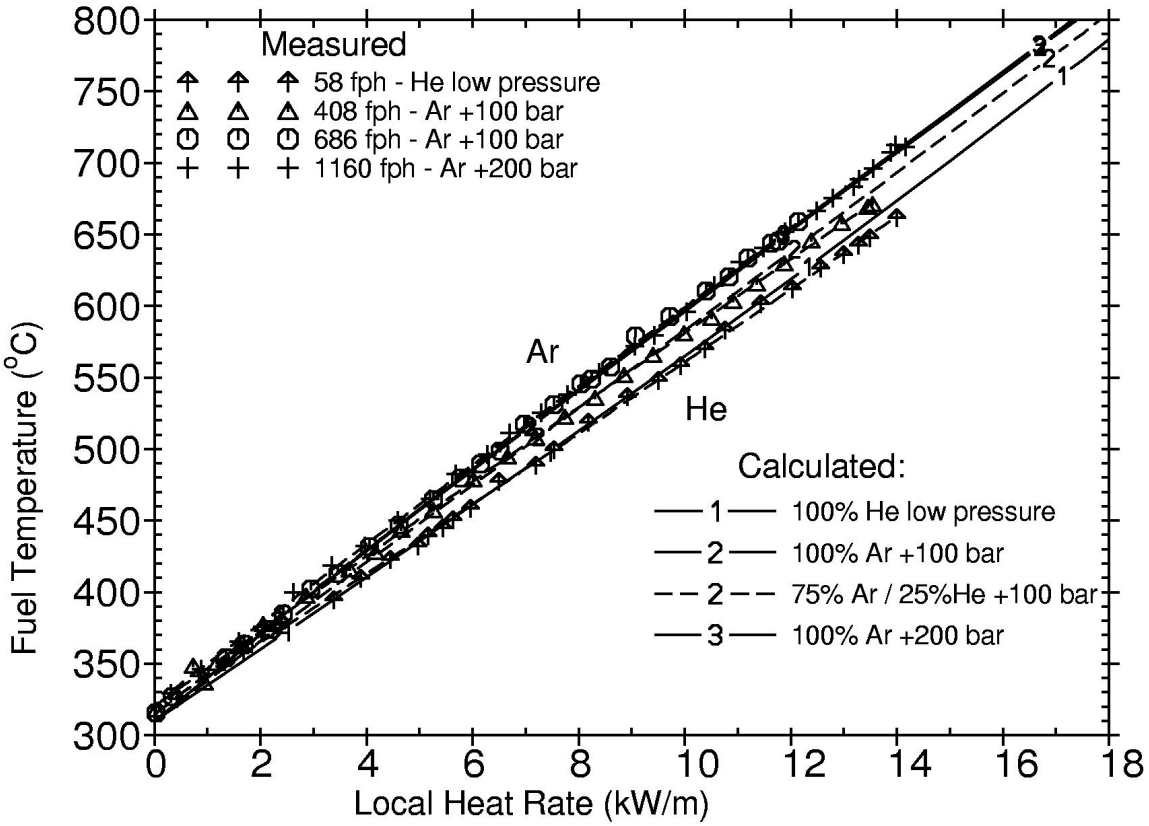

FIG. 13. All ramps in figure 8 together with calculations.

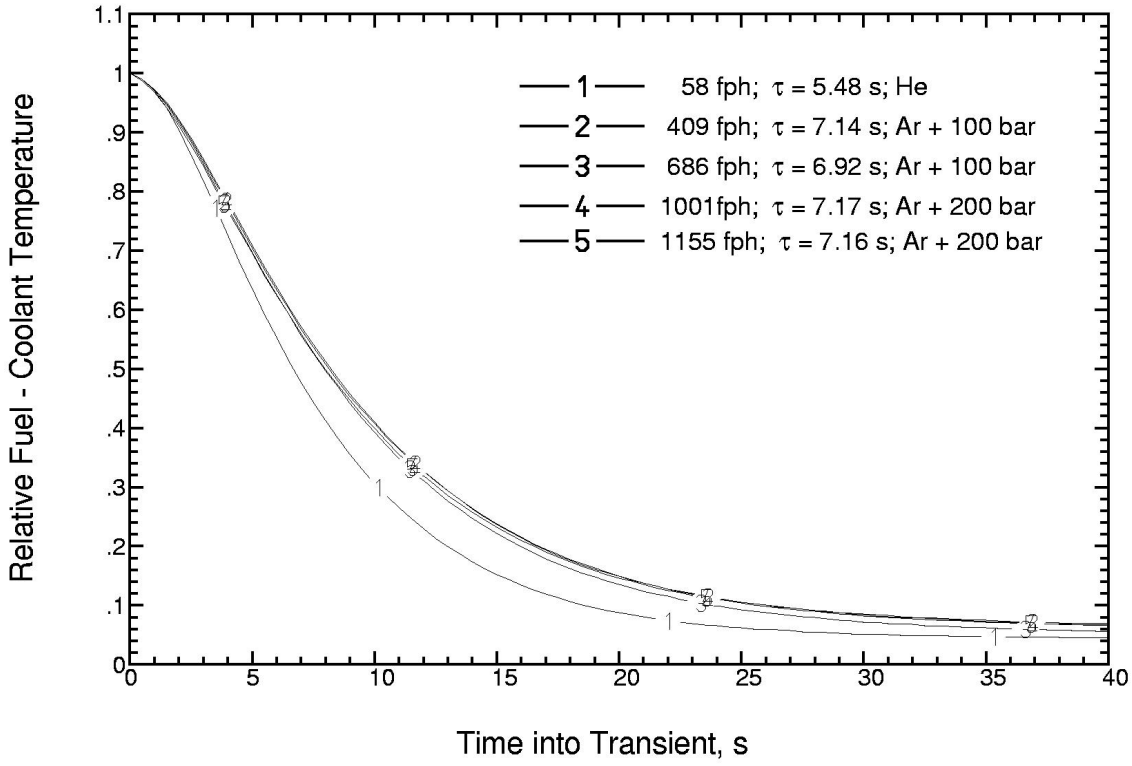

FIG. 14. Fuel temperature response to scram with calculated fuel time constants. The temperatures are normalised to initial differential fuel-coolant temperature.

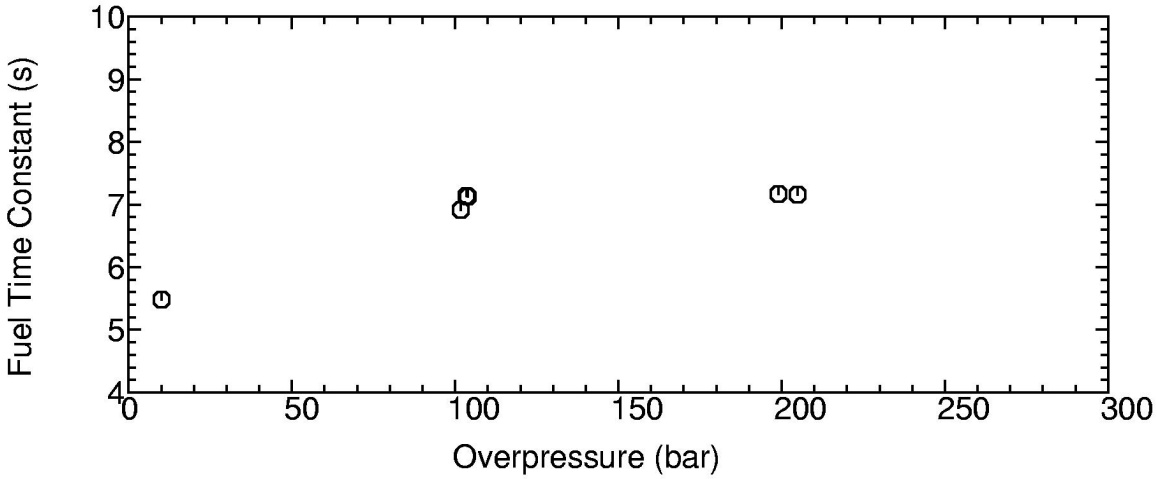

FIG. 15. Calculated fuel time constants.versus argon content.

5. SUMMARY

- Clad elongation data show that there is contact between pellet and cladding throughout the irradiation. The observed permanent clad elongation increase is in the range of fuel swelling.
- Temperatures can be modelled using as-measured gap and gas composition.
- Fuel thermal degradation is the main contributor to temperature increase compared with fresh fuel.
- Change of fuel temperature due to replacing He with Ar as fillgas (equivalent to a Xe/He gas mixture of 70%/30%) are relatively small because of the narrow or closed gap prevailing in high burnup fuel.

REFERENCES

[1] OHIRA, K., ITAGAKI, N.: "Thermal conductivity measurements of high burnup UO_2 pellets and a benchmark calculation of fuel centre temperature", Light Water Reactor Fuel Performance (Proc. Int. Topical Mtg Portland, Oregon, March 1997), ANS (!997) 541.

[2] WIESENACK, W.: "Assessment of UO_2 conductivity degradation based on in-pile temperature data," Light Water Reactor Fuel Performance (Proc. Int. Topical Mtg Portland, Oregon, March 1997), ANS (!997) 507.

[3] TVERBERG, T.: "Studies of PCMI from Cladding Elongation Measurements Performed in the HBWR", Fuel Chemistry and Pellet-Clad Interaction Related to High Burnup Fuel Proc. IAEA TCM Nyköping, Sweden September 1998), in press.

[4] LASSMANN, K., O'CARROLL, C., VAN DE LAAR, J., WALKER, J.T.:" The radial distribution of plutonium in high burnup UO_2 fuels", J. of Nucl. Mat. **208** (1994) 31.

[5] WIESENACK, W., TVERBERG, T.: "Thermal performance of high burnup fuel - in-pile temperature data and analysis", Light Water Reactor Fuel Performance, (Proc. Int. Topical Mtg Park City, Utah, April 2000), ANS (2000) 626.

[6] HAGRMAN, D. L., REYMANN, G. A. (eds.): "MATPRO version 11-A Handbook of Materials Properties for Use in the Analysis of Light Water Reactor Fuel Rod Behaviour", TREE-NUREG-1280, February 1979

Appendix I
CALCULATION OF ELASTIC STRAIN

With the following abbreviations and nomenclature:

$$A = \frac{a^2 p_i - b^2 p_0}{b^2 - a^2} \qquad and \qquad B = \frac{(p_i - p_0)\cdot a^2 b^2}{r^2 (b^2 - a^2)}$$

where:
- a = initial tube inner radius,
- b = initial tube outer radius,
- p_i = internal pressure [MPa],
- p_o = external pressure [MPa],

The radial, circumferential (hoop) and axial stresses for a thick-walled tube are:

$$\sigma_r = A - B \qquad \sigma_c = A + B \qquad \sigma_a = A$$

For a tube under an applied stress, the elastic hoop strain, $\varepsilon_{c(elastic)}$, and the elastic axial strain, $\varepsilon_{a(elastic)}$, are given by:

$$\varepsilon_{c(elastic)} = \frac{1}{E}\left[\sigma_c - \mu(\sigma_r + \sigma_a)\right] \qquad and \qquad \varepsilon_{a(elastic)} = \frac{1}{E}\left[\frac{\sigma_c}{2} - 2\mu\sigma_a\right]$$

where:
- E = Young's modulus [MPa]
- μ = Poisson's ratio

The radial displacement of the cladding inner wall and the cladding length change are:

$$(\Delta D) = D \cdot \varepsilon_{c(elastic)} \quad and \quad (\Delta L)_{elasticc} = L \cdot \varepsilon_{a(elastic)}$$

where L is the cladding length.

In order to simplify these equations, one can assume

$$a \cong b \cong d \quad and \qquad b^2 - a^2 = 2 \cdot d \cdot t$$

where *d* is the average diameter of the cladding and *t* its thickness, and obtain:

$$\frac{(\Delta D)_{elastic}}{D} = \frac{A}{E}\cdot(2-\mu) \quad and \qquad \frac{(\Delta L)_{elastic}}{L} = \frac{A}{E}\cdot(1-2\mu)$$

For a clad temperature of 360°C, μ ~ 0.25 [6]. Thus we obtain the following relation:

$$\frac{(\Delta D)_{elastic}}{D} = 3.5 \cdot \frac{(\Delta L)_{elastic}}{L}$$

Assuming a clad length subjected to overpressure of 450 mm and a cladding inner diameter of 9.29 mm, we obtain a 2μm deformation of the inner clad wall per 50 bar pressure step.

DEPENDENCE OF THE TIME-CONSTANT OF A FUEL ROD ON DIFFERENT DESIGN AND OPERATIONAL PARAMETERS

D. ELENKOV
Institute for Nuclear Research and Nuclear Energy,
Sofia, Bulgaria

K. LASSMANN, A. SCHUBERT, J. van de LAAR
European Commission, Directorate General JRC,
Institute for Transuranium Elements (ITU),
Karlsruhe, Germany

Abstract

The temperature response during a reactor shutdown has been measured for many years in the OECD-Halden Project. It has been shown that the complicated shutdown processes can be characterized by a time constant τ which depends on different fuel design and operational parameters, such as fuel geometry, gap size, fill gas pressure and composition, burnup and linear heat rate. In the paper the concept of a time constant is analyzed and the dependence of the time constant on various parameters is investigated analytically. Measured time constants for different designs and conditions are compared with those derived from calculations of the TRANSURANUS code. Employing standard models results in a systematic underprediction of the time constant, i.e. the heat transfer during shutdown is overestimated.

1. INTRODUCTION

The temperature response of a fuel rod during reactor shutdown has been measured for many years in the OECD-Halden Project [1]. It has been shown that the complicated shutdown processes can be characterized by a time constant τ which depends on different fuel design and operational parameters, such as fuel geometry, gap size, fill gas pressure and composition, and linear heat rate.

In this paper, the time constants of fuel centre temperatures measured in selected experiments are compared with theoretical results obtained from the TRANSURANUS code [2] and analysed as function of burnup. One basic question is whether temperature measurements in reactor shutdown experiments reveal information on the time evolution of thermal properties of a fuel element during irradiation. Further insight is expected from a detailed investigation of the behaviour of the modelled thermal properties within the time frame of the reactor shutdown.

2. ANALYTIC SOLUTIONS

2.1. Basic equations

Analytic solutions derived from Refs. [3, 4] shall be used to get some insight into the problem. We consider the fuel as an infinite solid cylinder with an outer radius r_o surrounded by a stagnant coolant (moderator) at a given temperature ϑ_{cool}. The heat transfer between fuel and coolant is prescribed by a constant (overall) heat transfer coefficient h which includes the heat transfer through the gap h_{gap} (gap conduction), the cladding as well as from the cladding

to the coolant (heat transfer coefficient α). We further assume that the material properties (thermal conductivity λ, density ρ and specific heat at constant pressure c_p) are constant and the power density is a given function of time only ($q'''F(t)$). The general schematic solution can be written as a superposition of an infinite number of Bessel functions of order zero:

$$\vartheta(r,t) = \vartheta_{cool} + \sum_{n=1}^{\infty} (\vartheta_{1n} + \vartheta_{2n}) J_0(r\alpha_n) \tag{1}$$

where under the conditions listed above α_n are the positive roots of

$$\alpha J_1(r_o\,\alpha) + \frac{h}{\lambda} J_0(r_o\,\alpha) = 0 \tag{2}$$

and ϑ_{1n}, ϑ_{2n} arise from the initial temperature distribution at $t = 0$ and from the power source term, respectively:

$$\vartheta_{1n}(r,t) = \beta_n \left(\int_0^{r_0} \vartheta(r, t=0) r J_o(r\,\alpha_n) dr \right) e^{-a\alpha_n^2 t} \tag{3}$$

$$\vartheta_{2n}(r,t) = \left(\frac{r_0}{c\rho} \frac{\beta_n}{\alpha_n} J_1(r_0\,\alpha_n) q''' \int_0^t F(s) e^{a\alpha_n^2 s} ds \right) e^{-a\alpha_n^2 t} \tag{4}$$

Here $a = \dfrac{\lambda}{c_p\,\rho}$ stands for the diffusivity. The terms β_n are derived from the normalization of the Bessel functions:

$$\beta_n = \frac{1}{\int_0^{r_0} r \left[J_0(\alpha_n r) \right]^2 dr} = \frac{2\alpha_n^2}{r_0^2 J_0^2(r_0\,\alpha_n) \left\{ \alpha_n^2 + \left(\dfrac{h}{\lambda} \right)^2 \right\}} \tag{5}$$

For the analysis of a reactor shutdown we start from a steady-state parabolic temperature distribution in the fuel and switch off the reactor power at $t = 0$. Thus the solution includes the terms of ϑ_{1n} only. For the initial conditions

$$\vartheta(r, t=0) = \vartheta_{cool} + \frac{q'''r_o}{2\,h} + \frac{q'''(r_o^2 - r^2)}{4\,\lambda} = \vartheta_{cool} + \vartheta_i - k\,r^2$$

$$q''' = const \qquad for\ t = 0$$

$$q''' = 0 \qquad for\ t > 0$$

we obtain

$$\vartheta_1(r,t) = \sum_{n=1}^{\infty} \frac{\beta_n}{\alpha_n^2} r_o J_o(r\,\alpha_n) \left(\alpha_n J_1(r_o\,\alpha_n)(\vartheta_i - k r_0^2) + 2k r_0\, J_2(r_o\,\alpha_n) \right) e^{-a\alpha_n^2 t} \tag{6}$$

It is interesting to note that the roots α_n of equation (2) depend on r_o, h and λ. In order to study the thermal behaviour of a realistic fuel rod we estimate an overall heat transfer

coefficient h between 3000 $\frac{W}{m^2\ K}$ (large gap) and 9000 $\frac{W}{m^2\ K}$ (small gap). Solving eq. (2) gives

$$\alpha_1 = \frac{1.989815}{r_o}, \alpha_2 = \frac{4.713142}{r_o}, \alpha_3 = \frac{7.617708}{r_o}, \ldots \text{(large gap)}$$

and

FIG. 1. Solution of Eq. (6) for a large gap rod. Shown are the terms for n=1,2, 3 as well as the complete solution.

$$\alpha_1 = \frac{2.250880}{r_o}, \alpha_2 = \frac{5.177253}{r_o}, \alpha_3 = \frac{8.142228}{r_o}, \ldots \text{(small gap).}$$

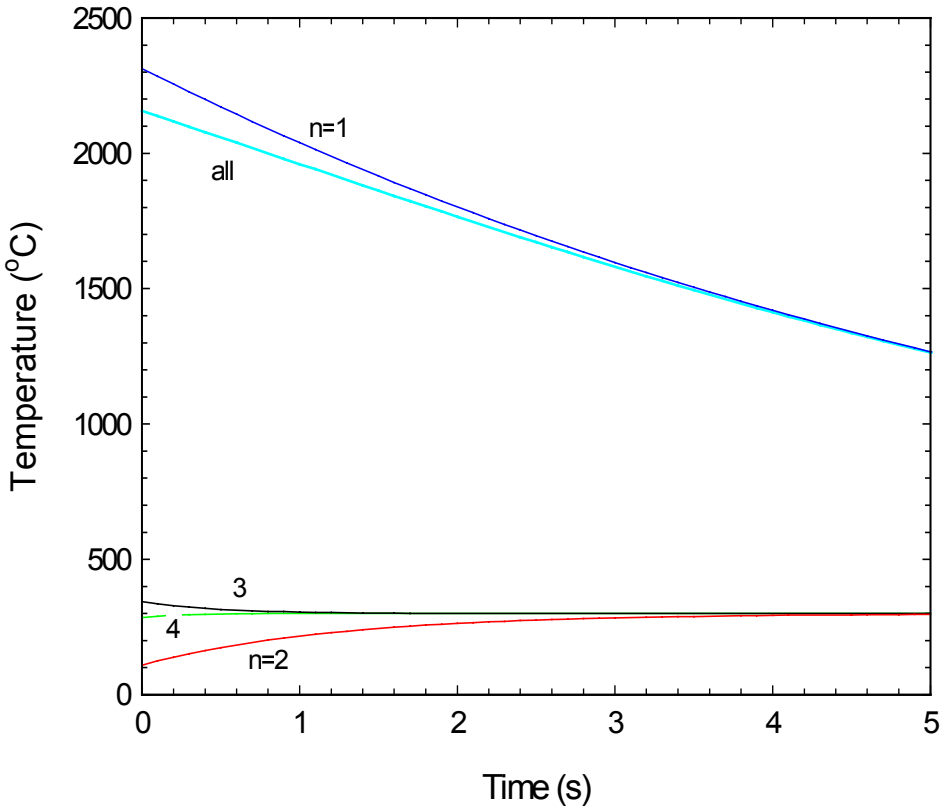

FIG. 1. Solution of Eq. (6) for a large gap rod. Shown are the terms for n = 1,2,3 as well as the complete solution.

If $h \to \infty$ the solution is

$$\vartheta_1(r,t) = \vartheta_{cool} + 4\sum_{n=1}^{\infty} e^{-a\alpha_n^2 t} \frac{J_o(r\,\alpha_n)}{\alpha_n^2\ J_1^2(r_o\,\alpha_n)} k\ J_2(r_o\,\alpha_n) \qquad (7)$$

In this case α_n are the well known positive roots of $J_0(r_o\,\alpha) = 0$ amounting to

$$\alpha_1 = \frac{2.404825}{r_o},\ \alpha_2 = \frac{5.520078}{r_o},\ \alpha_3 = \frac{8.653728}{r_o},\ldots$$

These relations allow to study the problem. Fig. 1 shows that the terms $n > 1$ are only significant during the first 2-3 s of the shut-down transient. Therefore, Eq. (6) can be applied to the fuel centre temperature at $r = 0$ and be simplified to

$$\vartheta(r=0,t) \approx \vartheta_{cool} + a_0\ e^{-\frac{t}{\tau}} \tag{8}$$

where

$$\tau = \frac{c_p\ \rho}{\lambda\ \alpha_1^2} = \frac{1}{a\ \alpha_1^2} \tag{9}$$

may be considered as the time constant of this transient shut-down process. For our "typical" fuel rod we obtain a time constant of 6.8 s for the large gap rod and 5.3 s for the small gap rod.

Eq. (2) can be solved approximately for α_1 :

$$\alpha_1 \approx \frac{2.404825}{r_0}\left(1 - \frac{\lambda}{h\ r_o}\right) \tag{10}$$

which leads to

$$\tau \approx \frac{c_p\ \rho\ r_o^2}{5.8\ \lambda\left(1 - \frac{\lambda}{h\,r_o}\right)^2} \tag{11}$$

If $\frac{\lambda}{hr_o}$ □ 1 (ν1) we may write Eq. (11) as

$$\tau \approx \frac{c_p\ \rho\ r_o\left(r_o + \frac{2\lambda}{h}\right)}{5.8\ \lambda} \tag{12}$$

which is very similar to the solution

$$\tau \approx \frac{c_p\ \rho\ r_o(r_o + \frac{4\lambda}{h})}{8\lambda} \tag{13}$$

given in Ref. [5]. For a lumped parameter model El-Wakil gives [6]:

$$\tau \approx \frac{c_p\ \rho\ r_o}{2\ h} \tag{14}$$

Eq. (8) was used by Slovacek [7]. In his paper the principal dependencies of the time constant τ were evaluated. The important conclusion was that by determining the time constant experimentally from shut-down experiments, many details of the fuel rod such as the degradation of the thermal conductivity and/or the variation of the gap conductance (gap size) with burn-up can be revealed.

We performed similar analyses for a set of WWER fuel configurations. The corresponding results are compiled in annex 1.

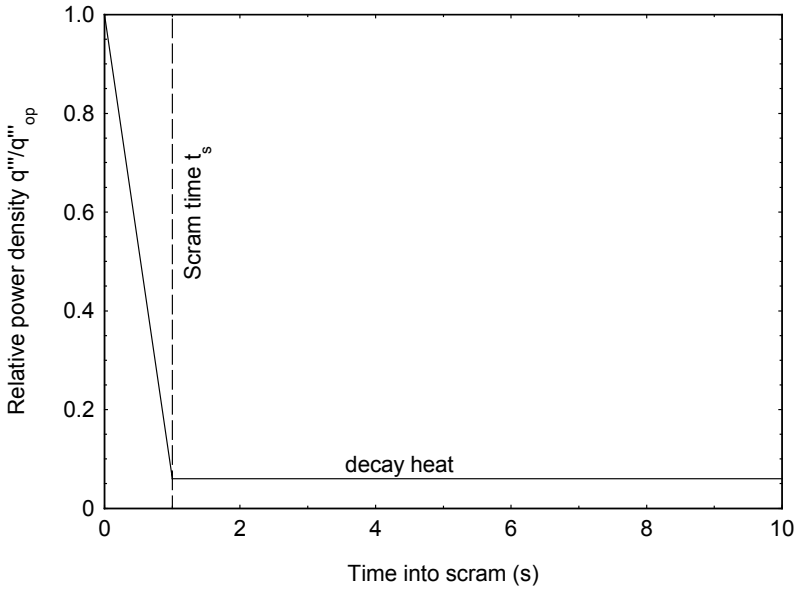

FIG. 2. Simplified power density vs. time evolution

.

When considering a realistic power scram the source term $q'''F(t)$ has to be taken into account leading to non-zero expressions for ϑ_{2n}. We apply a simplified time evolution as illustrated above which can be described by the following equations:

$$F(t) = 1 - bt \qquad for \quad 0 < t \le t_s \qquad where \quad b = \frac{1 - \frac{q'''_d}{q'''_{op}}}{t_s}$$

$$F(t) = 1 - bt_s = \frac{q'''_d}{q'''_{op}} \qquad for \quad t \ge t_s \tag{15}$$

Here q'''_{op} is the operational reactor power density prior to shutdown. The behaviour after the completion of the scram is approximated by a constant power density q'''_d arising from the decay heat.

For $0 < t \le t_s$ the solution can be written as

$$\vartheta_2(r,t) = \frac{q'''_{op}}{\lambda} \sum_{n=1}^{\infty} \left\{ \frac{\beta_n}{\alpha_n^3} r_0 J_1(r_0 \alpha_n) \left[1 - bt + \frac{b}{a\alpha_n^2} - \left(1 + \frac{b}{a\alpha_n^2} \right) e^{-a\alpha_n^2 t} \right] J_o(r\alpha_n) \right\} \tag{16}$$

and for $t \ge t_s$ it becomes

$$\vartheta_2(r,t) = \frac{q'''_{op}}{\lambda} \sum_{n=1}^{\infty} \left\{ \frac{\beta_n}{\alpha_n^3} r_0 J_1(r_0 \alpha_n) \left[1 - bt_s + \left(\frac{b(e^{a\alpha_n^2 t_s} - 1)}{a\alpha_n^2} - 1 \right) e^{-a\alpha_n^2 t} \right] J_o(r\alpha_n) \right\} \tag{17}$$

Hence, in addition to the exponential terms already existing from ϑ_{1n} a constant and a linear term arises, the latter disappearing for $t > t_s$. After summation of ϑ_1 and ϑ_2 the total solution can be expressed as follows:
For $0 < t \le t_s$:

$$\vartheta(r,t) = \frac{q'''_{op}}{\lambda} \sum_{n=1}^{\infty} \left\{ \frac{\beta_n}{\alpha_n^3} r_0 J_1(r_0 \alpha_n) \left[1 - bt + \frac{b}{a\alpha_n^2} \right] J_o(r\alpha_n) \right\} + \sum_{n=1}^{\infty} w_n J_o(r\alpha_n) e^{-a\alpha_n^2 t}$$

with (18)

$$w_n = \frac{\beta_n}{\alpha_n^2} r_0 \left\{ \left(\alpha_n J_1(r_o \alpha_n)(\vartheta_i - kr_0^2) + 2kr_0 J_2(r_o \alpha_n) \right) - \frac{q'''_{op}}{\lambda \alpha_n} J_1(r_0 \alpha_n) \left(1 + \frac{b}{a\alpha_n^2} \right) \right\}$$

For $t \ge t_s$:

$$\vartheta(r,t) = \frac{q'''_{op}}{\lambda} \sum_{n=1}^{\infty} \left\{ \frac{\beta_n}{\alpha_n^3} r_0 J_1(r_0 \alpha_n) \left[1 - bt_s \right] J_o(r\alpha_n) \right\} + \sum_{n=1}^{\infty} w_n J_o(r\alpha_n) e^{-a\alpha_n^2 t}$$

with

$$w_n = \frac{\beta_n}{\alpha_n^2} r_0 \left\{ \begin{array}{l} \left(\alpha_n J_1(r_o \alpha_n)(\vartheta_i - kr_0^2) + 2kr_0 J_2(r_o \alpha_n) \right) + \\ + \frac{q'''_{op}}{\lambda \alpha_n} J_1(r_0 \alpha_n) \left(\frac{b(e^{a\alpha_n^2 t_s} - 1)}{a\alpha_n^2} - 1 \right) \end{array} \right\} \quad (19)$$

Equations (6), (7), (18) and (19) have been used to check the correct numerical treatment of the thermal analysis of the TRANSURANUS code. Excellent agreement has been found in all cases. Two examples are shown in Figs 3 and 4.

2.2. Fitting functions

For later comparison of experimental data to TRANSURANUS calculations we used the same fitting procedure as described in [7], i.e. a sum of a constant and two exponential functions:

$$\vartheta(t) - \vartheta_{cool} = A + B\, e^{-\frac{t}{\tau_1}} + C\, e^{-\frac{t}{\tau_2}} \quad (20)$$

where $\vartheta(t)$ is the fuel centre temperature at time *t* after start of the shutdown and ϑ_{cool} denotes the coolant temperature. Expression (20) includes a total of five free parameters systematically evaluated for all fits: The temperature constant *A*, the amplitudes *B* and *C*, and the times τ_1, τ_2 which are called major and minor time constants, respectively. The parameter *C* and the minor time constant τ_2 summarize the sum of all terms arising from higher roots $\alpha_n (n > 1)$ in eq. (2). This assumption is justified by the rapidly decreasing amplitudes for the higher terms (Fig. 2). The term of the minor time constant also includes the details of the shutdown as given in equation (16) for $0 < t \le t_s$.

In order to confirm these conclusions a set of numerical experiments was performed applying the TRANSURANUS code to the Halden reactor configuration TF-18-562 (cf. chapter 3.1) with a short irradiation time of 2 hours. Under these conditions the influence of the time evolution of the power density during the shutdown on the above mentioned fitting parameters was analysed. The power density q'''_d persisting after completion of the shutdown

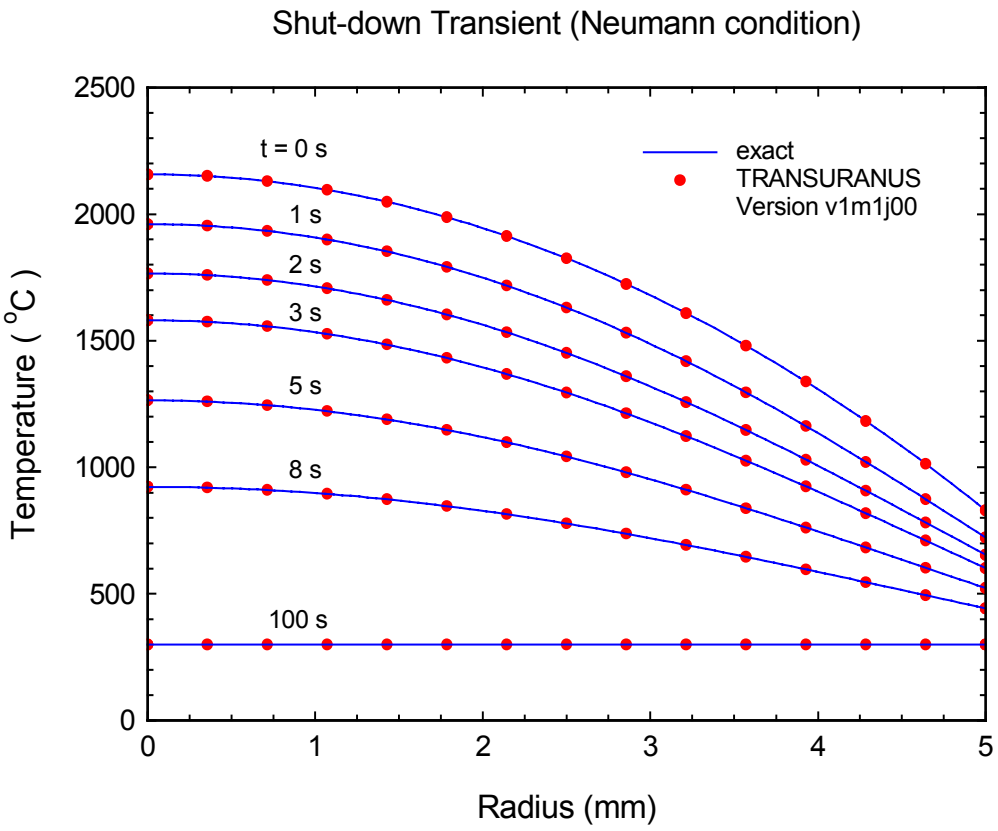

FIG. 3. Radial temperature distribution in the fuel at different times. Compared are the exact solutions (6) and (7) with the numerical result of the TRANSURANUS code.

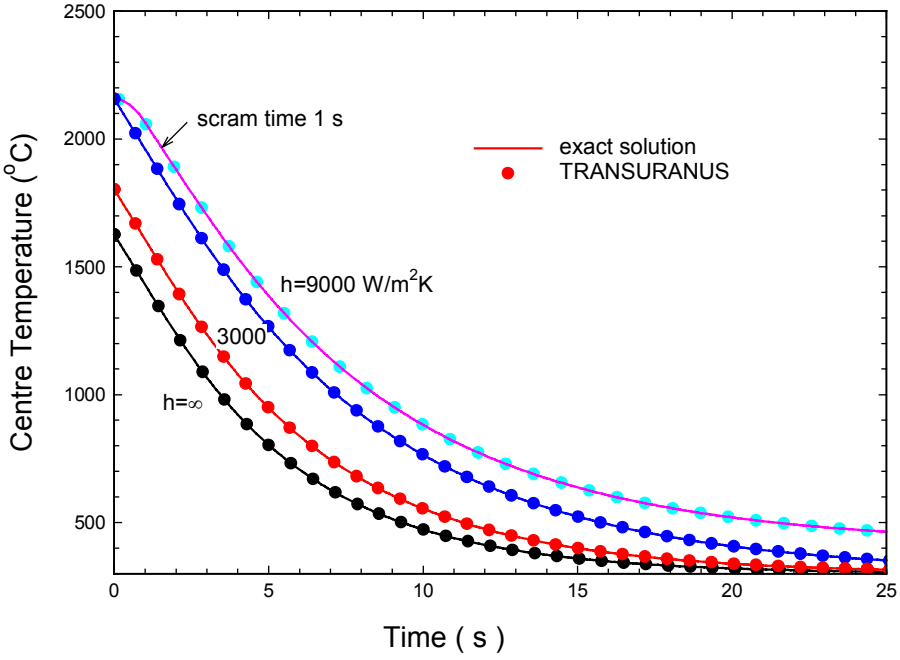

Fig. 4. The centre line temperature of a fuel rod during shutdown. Compared are the exact solutions (6) and (7) with the numerical result of the TRANSURANUS code.

was assumed to be constant within the time interval from 0 to 20 s. Starting from parameters typical for the real experiments ($t_s = 1$ s, $q'''_d / q'''_{op} = 6\%$, cf. (15)) both the level of the decay heat and the scram duration were systematically varied in the TRANSURANUS input. TABLE I shows a selection of the combinations investigated.

TABLE I. ANALYSIS OF THE INFLUENCE OF SHUTDOWN CONDITIONS ON THE RESULTS OF THE TWO-EXPONENTIAL FIT

t_s [s]	q'''_d / q'''_{op} [%]	τ_1 [s]	τ_2 [s]	A [K]	B [K]	C [K]
1	6	3.78 ± 0.03	0.85 ± 0.02	34.7 ± 0.5	669 ± 4	-169 ± 4
1	2	3.76 ± 0.03	0.85 ± 0.02	15.4 ± 0.6	696 ± 4	-177 ± 4
0.1	6	3.85 ± 0.03	0.81 ± 0.04	34.2 ± 0.5	585 ± 4	-82 ± 4
0.1	2	3.80 ± 0.03	0.83 ± 0.04	15.0 ± 0.5	611 ± 4	-89 ± 4

The behaviour of the calculated fuel centre temperature is shown in FIG. 5. Obviously the duration of the scram has significant impact only in the first few seconds whereas the decay heat determines the long-term behaviour represented by the fit parameter A. The analysis confirms that both conditions have insignificantly low influence on the major time constant. As expected from the closed-form solutions the influence of the scram on the minor time constant τ_2 is small, too, and the term of the minor time constant persists although it is not evident from FIG. 5. The clear difference between the curves for $t_s = 1$ s and $t_s = 0.1$ s arises from the different amplitudes of the higher terms of the infinite sum of exponentials.

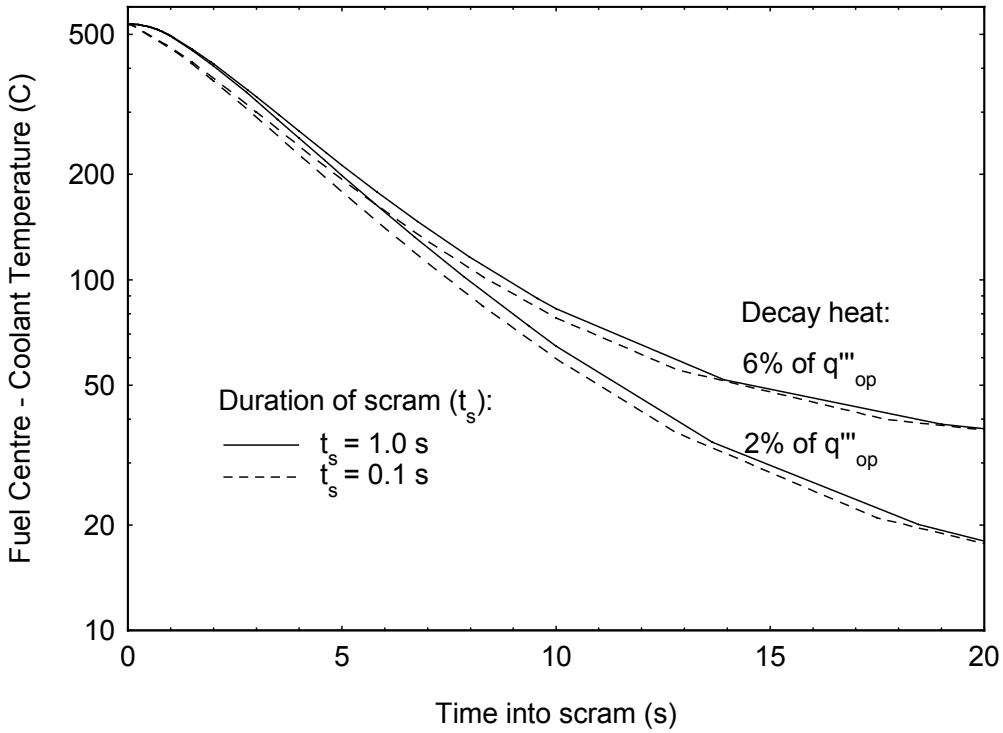

FIG. 5. Time evolution of difference between fuel centre temperature and coolant temperature for two different durations of the scram t_s and two different levels of decay heat (6% and 2% of the mean operational power).

The previous considerations do not yet take into account the impact of the response time of the temperature measurement (thermocouple) affected by heat transfer processes from the fuel to the thermocouple, and leading to a delay of the signal. This can in a first approximation be described by a time transformation making use of the time t' obeying $t' = t - \Delta t$. For any infinite sum of exponential terms we obtain:

$$\sum_{n=1}^{\infty} a_n \, e^{-\frac{t-\Delta t}{\tau_n}} = \sum_{n=1}^{\infty} a'_n \, e^{-\frac{t}{\tau_n}} \qquad (21)$$

$$with \quad a'_n = a_n \, e^{\frac{\Delta t}{\tau_n}}$$

It is evident that this correction does not influence the time constants of the individual terms. However, the strength factors or amplitudes a_n are enhanced and the smaller the individual time constant the higher the impact on the corresponding amplitude. It is interesting to note that a response time of 0.5 s causes an effect on the parameters *B* and *C* comparable to that of the prolongation of the shutdown time from 0.1 s to 1 s.

The impact of the temperature measurement was further analysed by two different approximations describing the heat transfer to the thermocouple. Several calculated centre line temperatures were corrected in this way. Confirming the mathematical considerations above it was found that the effect of the thermocouple is only included in the amplitude of the second exponential. The major time constant τ_1 - as obtained by the fitting - is not affected by the thermocouple correction. Therefore, no corrections for the temperature response were taken into account in all further analyses. For any evaluation of the experimental evidence during a reactor scram the major time constant should be used as basic descriptor.

3. ANALYSIS OF EXPERIMENTAL DATA

3.1. Overview

In order to draw further conclusions from the fuel temperature evolution during and after reactor shutdown a detailed comparison of model calculations with experimental data is required. Our present analysis is based on part of a compilation of shutdown experiments performed at the OECD boiling water research reactor in Halden/Norway [7] where the fuel centre temperatures from a total of 52 scrams (recorded since 1979) had been analysed. For our investigation we selected experiments where only He was used as fill gas and according to [7] the fuel temperature was permanently kept below the Vitanza threshold for fission gas release. TABLE II lists the corresponding available basic fuel design data [8]. These configurations were chosen to allow for an optimum study of the impact of the fuel design although it is impossible to completely separate the influence of the individual parameters.

For discussing a general trend of the available experimental information [7] all major time constants τ_1 related to the experiments listed in TABLE II were compiled as function of burnup. Because – apart from a linear function - the experimental data do not exhibit more complex dependencies on the burnup they were fitted with a straight line and normalized to $\tau_1(bu = 0)$. FIG. 6 shows a clear common trend of all data. It can be compared to the behaviour

TABLE II. BASIC FUEL DESIGN DATA OF EXPERIMENTS USED CALCULATIONS FOR COMPARISON WITH TRANSURANUS

Experiment ID	Fuel outer radius [mm]	Fuel inner radius [mm]	Radial gap size [mm]	Cladding thickness [mm]	He fill gas pressure [MPa]	^{235}U initial enrichment [w/o]	
TF-18-562	5.295	1.02	0.036	0.80	0.1	3.95	
TF-2-552	4.045	0.90	0.065	0.64	1.0	3.5	
TF-2-553.1	5.2265	1.0	0.0995	0.81	0.5	4.45	
TF-2-567	5.22	1.0	0.115	0.79	0.5	4.023	

of the correction factor for the major time constant when assuming constant heat flow from fuel to coolant (cf. eq.(11)):

$$\tau_1^{norm} = \frac{\tau_1(bu)}{\tau_1(bu=0)} = \frac{\lambda_0}{\lambda} \frac{\left(1 - \frac{\lambda_0}{hr_o}\right)^2}{\left(1 - \frac{\lambda}{hr_o}\right)^2} \qquad (22)$$

Here r_o represents the outer fuel radius, h the overall heat transfer coefficient between fuel and coolant and λ the mean thermal conductivity of the fuel. For illustration in FIG. 6 a mean value for $hr_0 = 20\frac{W}{mK}$ is used (corresponding to a value of $h = 4000\frac{W}{m^2K}$ for $r_0 = 5$ mm). The related behaviour is compared to that for assuming infinite heat transfer leading to a simple function of the inverse mean thermal conductivity. The trends are shown for a mean fuel temperature of 900 K (dashed line) or 1000 K (full line) confirming that a realistic uncertainty of the mean fuel temperature has only minor influence on the general behaviour. FIG. shows that the fuel thermal conductivity clearly dominates the overall dependence of the major time constant on the burnup.

3.2. TRANSURANUS analyses

For all fuel designs compiled in TABLE II calculations with the TRANSURANUS code were performed. Standard coolant conditions typical for the OECD Halden reactor were assumed involving a coolant pressure of 3.36 MPa and surface boiling according to the Jens-Lottes relation.

The comparisons between the measured and calculated major time constants τ_1 are given in Fig. 7. Unexpectedly, there is a consistent under-prediction when TRANSURANUS standard models are applied. This directly implies that the heat transfer during shutdown is overestimated.

An attempt has been made to analyse the experimental result with a fictitious heat transfer coefficient between fuel and cladding (also referred to as gap conductance h_{gap}) kept constant over the complete irradiation time and during the shutdown. As illustrated in Fig. 7 a case-dependent constant gap conductance is in principle able to explain the experiment.

Calculations were performed with two different average linear heat rates (15 and 25 kW/m). It is evident that the uncertainty of the local heat rate influences the fictitious value of h_{gap} but can not resolve the differences in the burnup dependencies.

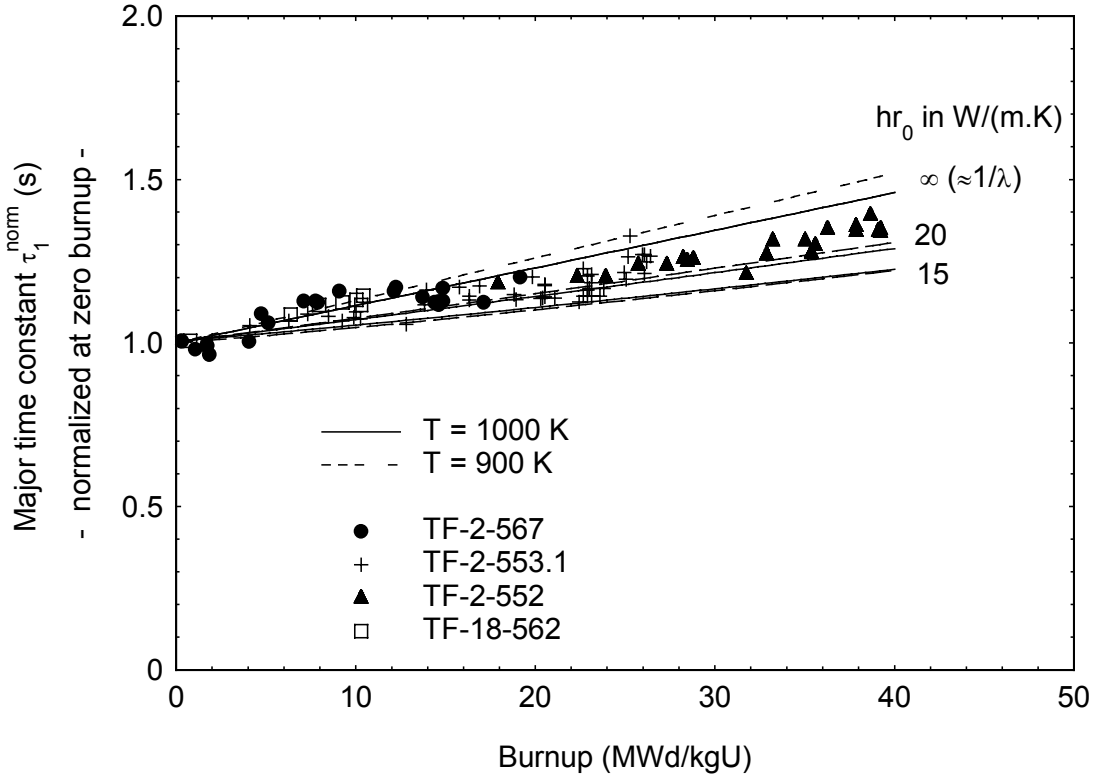

FIG. 6. Dependence of the major scram time constant τ_1 on fuel average burnup, normalized to $\tau_1^{norm} = 1$ for zero burnup. The lines show the expected evolution of τ_1^{norm} following equation (22) for an assumed mean fuel temperature of 900 K (dashed) and 1000 K (full).

Further details of heat transfer coefficients are shown in Fig. 8. It can be seen that the calculated gap conductance lies – especially in the first seconds of the scram – significantly above the fictitious constant value. However, the physics behind this assumption is unclear. A limitation may arise from the theoretical assumption that the fuel fragments are described as an axially symmetric, one-dimensional body which is still considered as one continuum. Another hypothesis is that cracks in the fuel open during shutdown or new cracks are formed deteriorating the thermal transport in the fuel.

A closer look at the experiments shows that the difference between measurement and prediction by standard models gets smaller for larger gap sizes. In the low-burnup region of configuration TF-2-567 the behaviour of the fuel centre temperature can be satisfactorily described. However, further conclusions are possible only if, in addition to the approach of fitting time constants, calculated and measured temperatures will be compared directly.

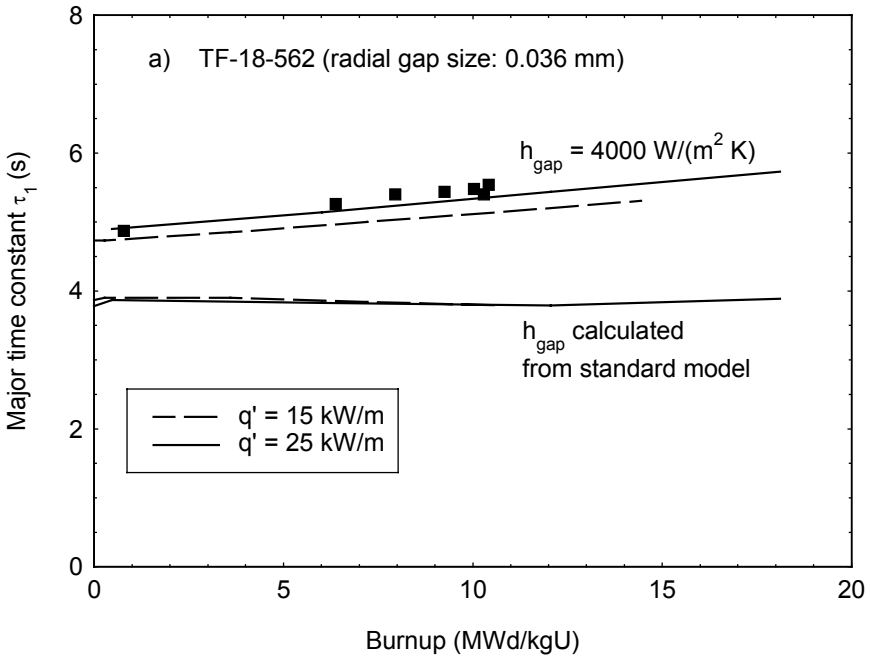
a) TF-18-562 (radial gap size: 0.036 mm)
h_gap = 4000 W/(m^2 K)
h_gap calculated
from standard model
q' = 15 kW/m
q' = 25 kW/m
Major time constant τ_1 (s)
Burnup (MWd/kgU)
0
2
4
6
8
0
5
10
15
20

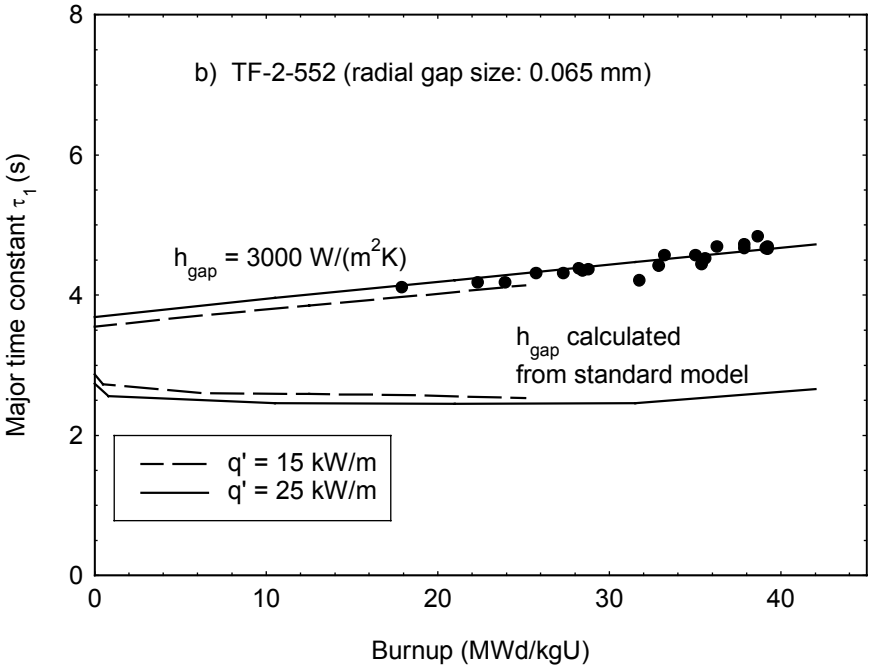
b) TF-2-552 (radial gap size: 0.065 mm)
h_gap = 3000 W/(m^2K)
h_gap calculated
from standard model
q' = 15 kW/m
q' = 25 kW/m
Major time constant τ_1 (s)
Burnup (MWd/kgU)
0
2
4
6
8
0
10
20
30
40

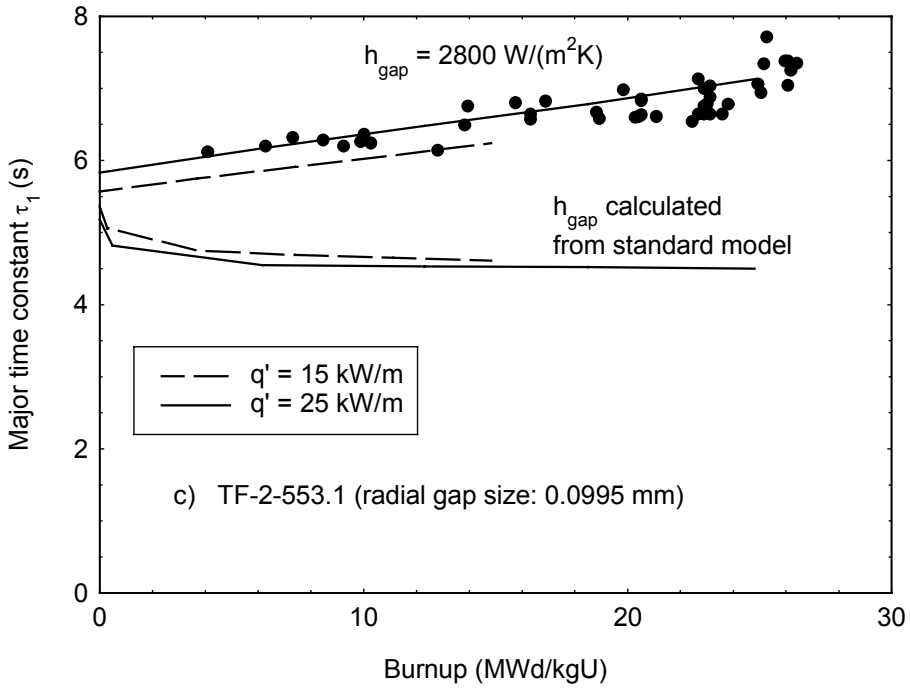

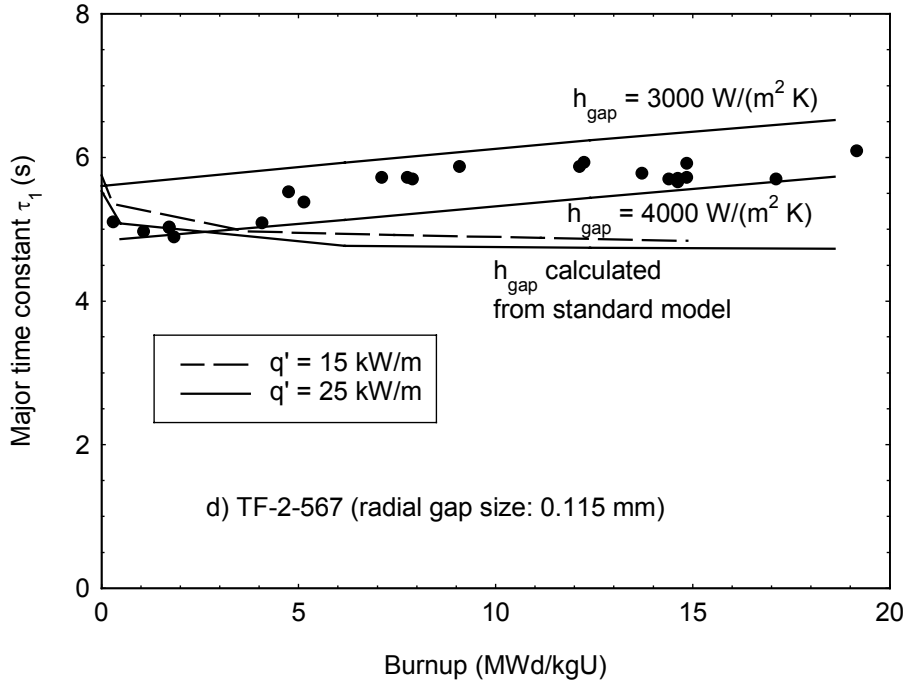

FIG.7(a-d). Burnup dependence of the major time constant from experiments performed at the OECD Halden reactor. Comparison to TRANSURANUS model calculations assuming a gap conductance as constant and as deduced from the GAPCON relocation model. The dashed lines illustrate the qualitative sensitivity to the assumed linear heat rate.

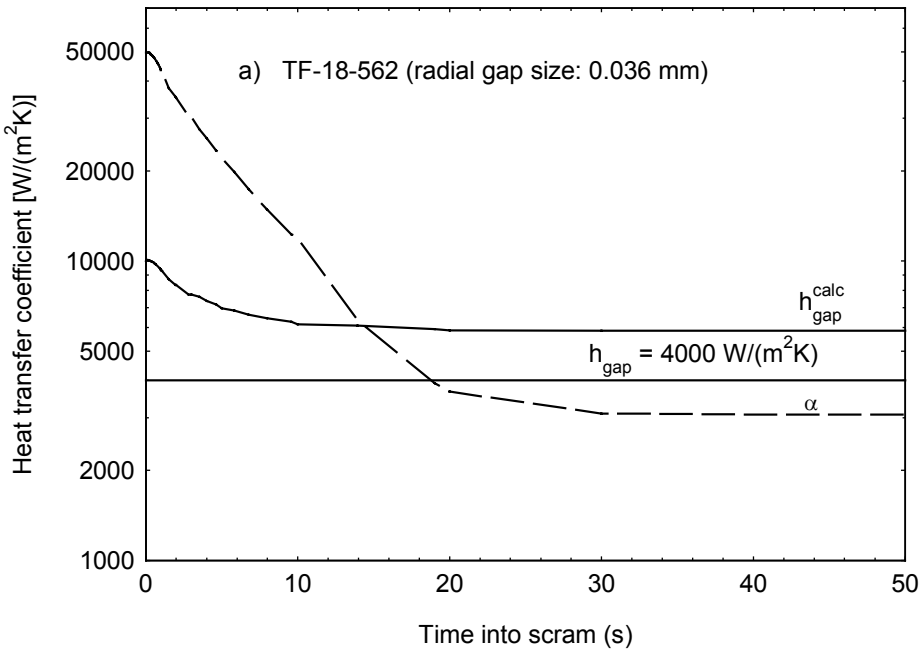
a) TF-18-562 (radial gap size: 0.036 mm)
Heat transfer coefficient [W/(m2K)]
50000
20000
10000
5000
2000
1000
0
10
20
30
40
50
Time into scram (s)
hgapcalc
hgap = 4000 W/(m2K)
α

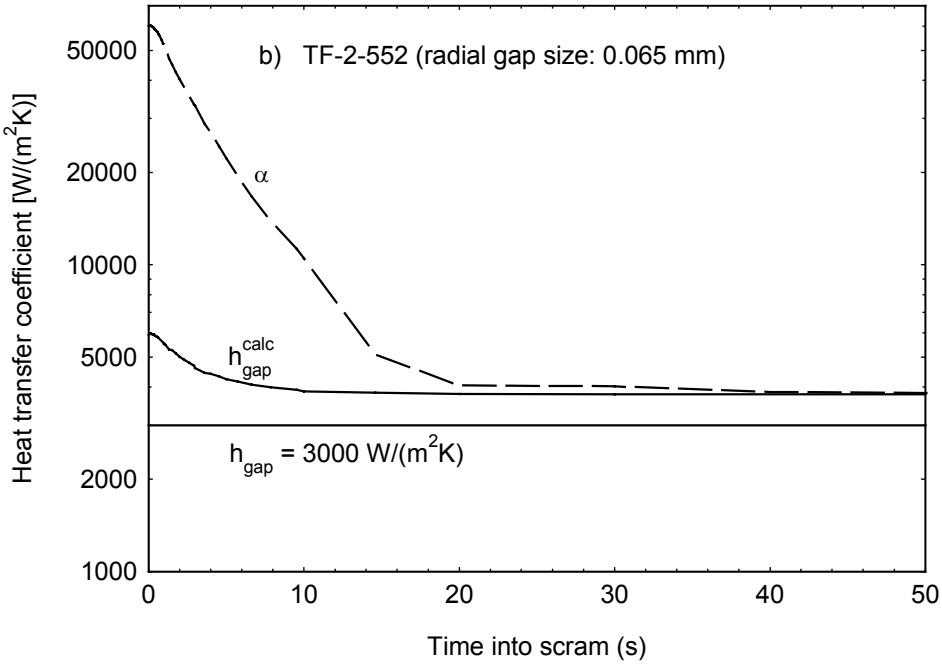
b) TF-2-552 (radial gap size: 0.065 mm)
Heat transfer coefficient [W/(m2K)]
50000
20000
10000
5000
2000
1000
0
10
20
30
40
50
Time into scram (s)
α
hgapcalc
hgap = 3000 W/(m2K)

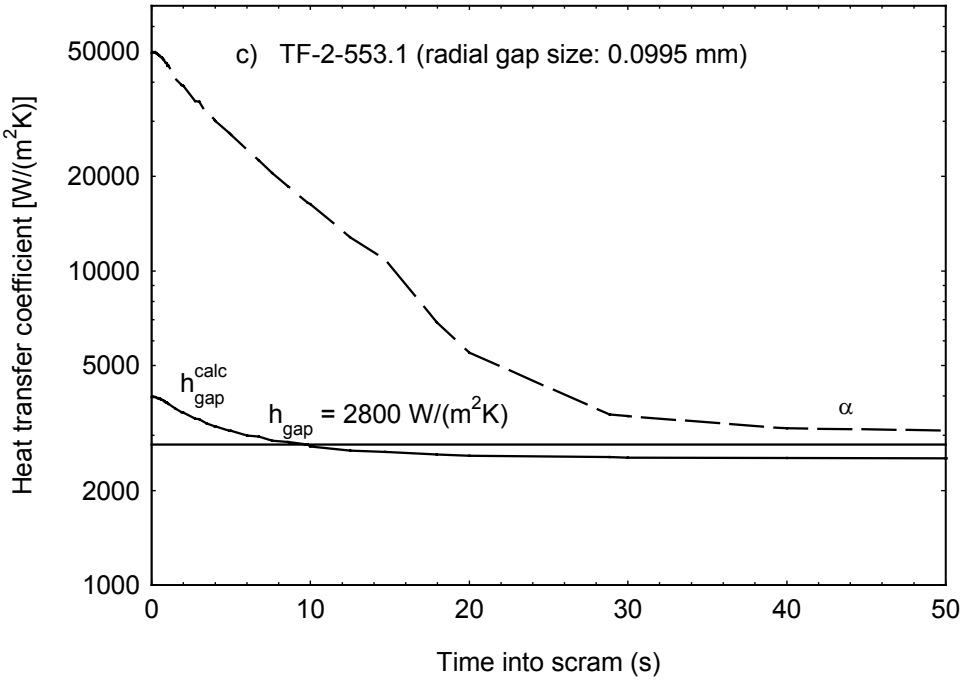

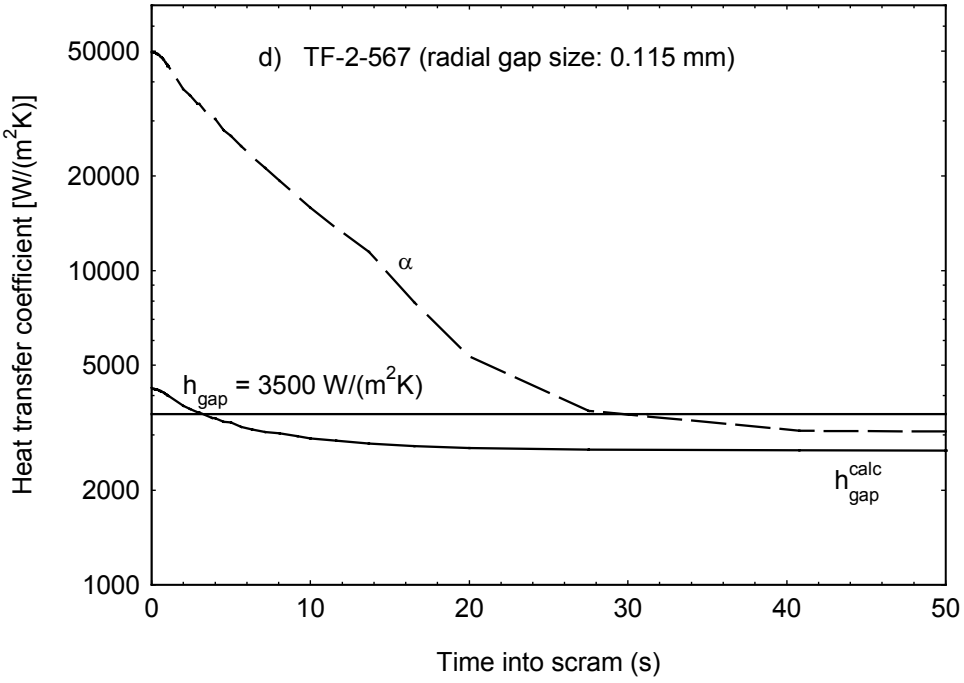

FIG. 8(a-d). Time dependence of main ingredients contributing to the total heat transfer coefficient h in a reactor scram at begin of life: α - heat transfer coefficient between cladding and coolant, h_{gap} – gap conductance.

4. SUMMARY AND CONCLUSIONS

The following conclusions can be drawn:

1. The time evolution of the fuel centre temperature during reactor shutdown can be well approximated by the sum of a constant and two exponential functions, where a major time constant can be deduced from. It can be shown that the exponential term of the minor time constant accounts for the influence of shutdown duration (scram time) and measurement response time. The exponential term containing the major time constant reveals details of the fuel rod, averaged over the scram time.

2. TRANSURANUS calculations are in excellent agreement with closed-form solutions for simplified cases.

3. Experimentally found dependencies of the major time constant on the burnup are basically linear and can, for a given linear heat rate, be reproduced by TRANSURANUS model calculations using a constant heat transfer coefficient between fuel and cladding. Standard models applied within the TRANSURANUS system for calculating the heat transfer lead to a clear under-estimation of the measured major time constants.

4. More detailed direct comparisons between measured and calculated temperatures have to be made in order to resolve the obvious discrepancy between experiment and the predictions obtained with the standard models. These analyses must be based on the detailed rod design and irradiation history.

ACKNOWLEDGEMENT

The authors would like to thank Mrs. M. Georgieva and Mrs. S. Boneva for valuable support in performing the TRANSURANUS calculations.

REFERENCES

[1] W. WIESENACK et al., "Review of Halden Reactor Project high burnup fuel data that can be used in safety analyses", Nucl. Eng. and Design **172** (1997) 83
[2] K. LASSMANN, "TRANSURANUS: a fuel analysis code ready for use ", Journal of Nuclear Materials **188** (1992) 295
[3] I.N. BRONSTEIN, K.A. SEMANDJEJEW, Taschenbuch der Mathematik, BSB Teubner Leipzig 1979, Chap. 3.3.2
[4] H.S. CARSLAW, J.C. JAEGER, Conduction of heat in solids, Oxford University Press 1959, Chap. VII
[5] K. LASSMANN, "Die transiente Version des Rechenprogramms URANUS, Internationale Zeitschrift fur Kernenergie (ATW) **XXII** (1977) 7.
[6] M.M. EL-WAKIL, Nuclear Heat Transport, International Textbook Company (1971).
[7] M. SLOVACEK, Utilisation of transient data for assessment of fuel thermal properties, report HWR-414 (1994).
[8] H. DEVOLD, An updated compilation of test fuel data sheets in the 500 series, report HWR-273 (1990).
[9] V.I. VLADIMIROV, Manual on power reactors operation, Energoizdat, Moscow, USSR (1981).

Annex 1

DEPENDENCE OF THE TIME CONSTANT ON DIFFERENT DESIGN AND OPERATIONAL PARAMETERS OF WWER FUEL

1. CALCULATION OF THE TIME CONSTANT τ

The present section considers the problem of the time constants in the case of WWER – Russian fuel and cladding material, power history, core design and operational conditions for rod 126 of fuel assembly FA-198, irradiated for 4 years at the Kola NPP, Russia. Experimental data for the temperature decrease after a scram are not available, for which reason only the trends of the different dependencies are considered.

After the reactor is shut down, the decay heat has been accounted for only by its $N_{\beta\gamma}$ component (absorption of β- and γ-emission of the fragments and their decay products). According to [9], during the first second after reactor is shut down, $N_{\beta\gamma} = 0.065 N_0$, (i.e. initial value of the decay heat is 6.5% of N_0). N_0 is the power at the steady state before the transient. Then, in the time interval of $1s \le t \le 100\ s$, $N_{\beta\gamma}$ follows the approximation [9]:

$N_{\beta\gamma} = 0.1 N_0 \left[(t+10)^{-0.2} - 0.03 \right]$, t is the time after $t_0 = ttrans$ (transient onset).

This approximation of $N_{\beta\gamma}$ is taken as power history after *ttrans* and TRANSURANUS calculates the fuel central temperature up to t = 100 s. The temperature decreases exponentially, so it is fitted by the expression

$$\vartheta = a + b \exp\left(-t/\tau\right)$$

where a is the coolant temperature ϑ_{cool} and b is: $\vartheta(t=0) - \vartheta_{cool}$. Coolant geometry and mass flow rate have been accounted for.

2. DEPENDENCE OF τ ON GAP SIZE, LINEAR HEAT RATE (LHR), BURNUP, AND OUTER DIAMETER

The gap size S_d has been varied by changing the fuel outer diameter from 7.70 to 7.40 mm. (The external diameter of the FA-198 fuel pellet is 7.56 mm). The internal cladding diameter is 7.755 mm. The linear heat rate (*LHR* or *q'*) is set to a constant of 15 W/mm. The transient starts at 720 s after the beginning of operation when the burnup is still 0 MWd/tU. Strong influence from the gap size was found. The results are shown in Fig. 1-1. In a similar way the dependence of the time constant on the outer fuel diameter was analysed using the following parameters: Initial gap = 0.2 mm, cladding thickness = 0.8 mm; LHR = 15 W/mm, ttrans = 43.2 s. Results are summarized in Fig. 1-2.

To study the dependence of the time constant on the LHR, its value has been set to a constant for different runs. The transient starts again at 720 s after the beginning of operation. As expected, the LHR has a much smaller effect on the time constant, see the results in Fig. 1-3. For investigating the intrinsic dependence on the burnup the following approach was chosen: some random value of the gap at *ttrans* was fixed (preliminary and occasionally chosen) – at 0.02 mm, after which the initial gap was varied. The LHR has been set to a constant of 15 W/mm. Apparently, the fixed gap of 0.02 mm will be reached at different times of the irradiation history (at different burnup). The bigger the initial gap is, the later (at higher burnup) the fixed gap of 0.02 mm will be reached. Then transients were simulated at these different burnups and the result for one and the same slice is shown in Fig. 1-4.

It should be noted that all predictions of TRANSURANUS excellently agree with the theoretical expectations for the dependencies on different parameters as gap, LHR, and burnup. The next step should be a comparison of experimental temperatures with those calculated by TRANSURANUS. This will be possible as soon as Russian experimental transient data become available.

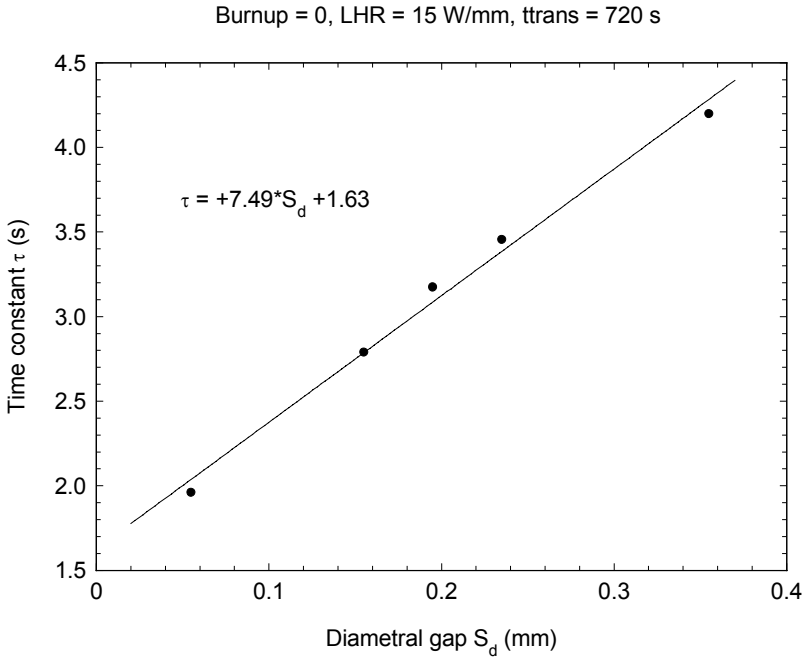

FIG. 1-1. Calculated time constants (ϑ_{cool} = 296^{o}C) as function of gap size.

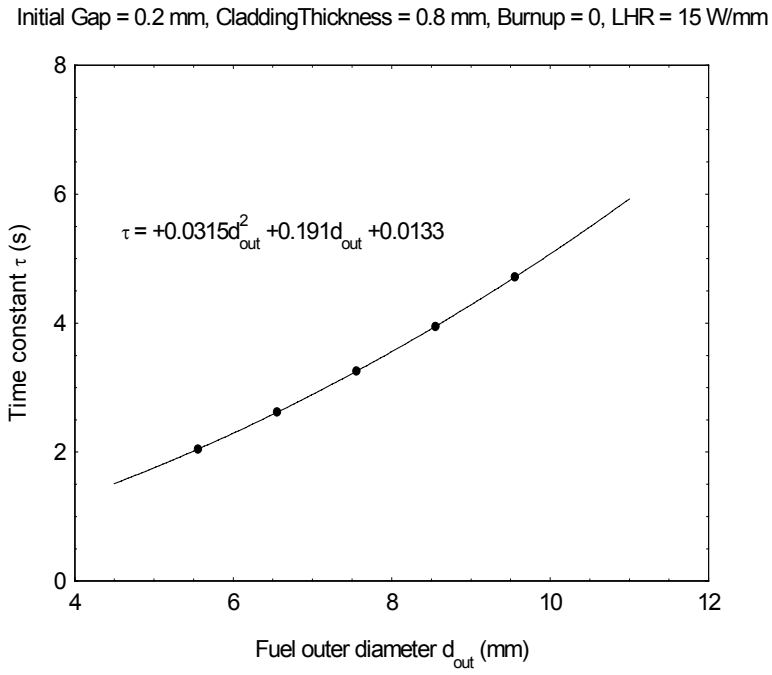

FIG. 1-2. Calculated time constants as function of fuel outer diameter.

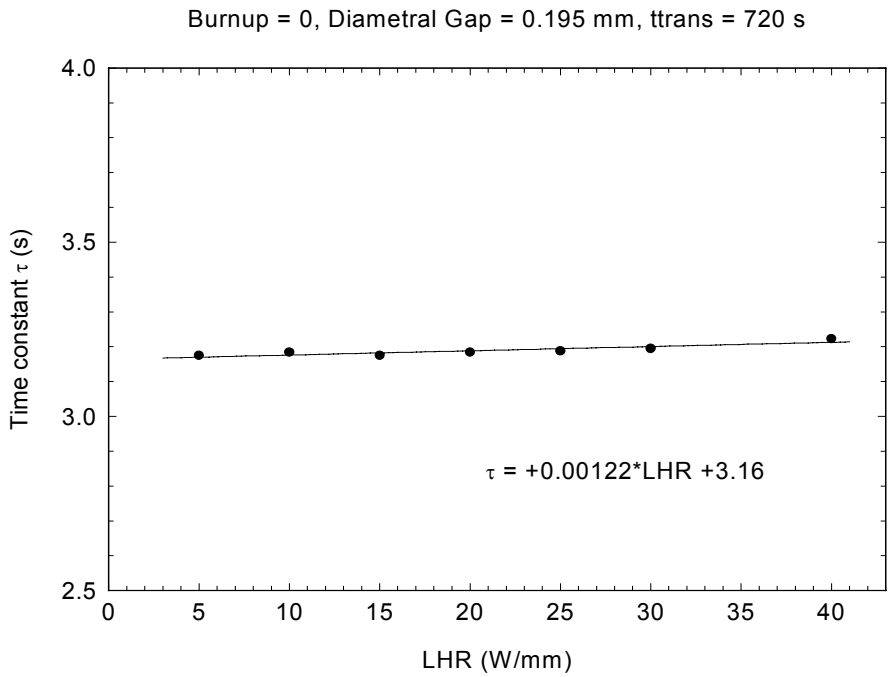

FIG. 1-3. Calculated time constants as function of linear heat rate.

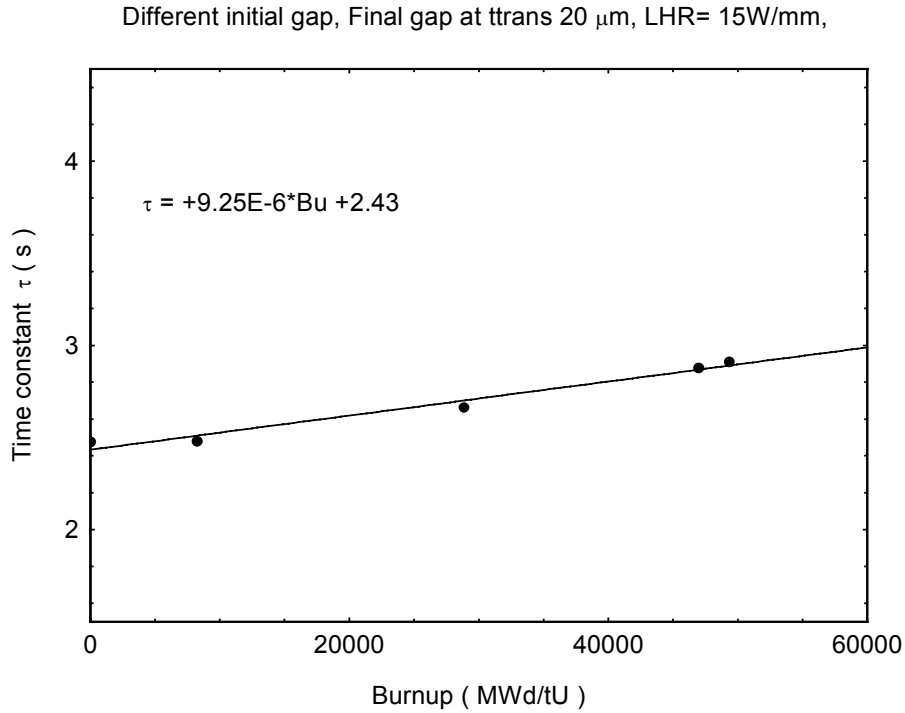

FIG. 1-4. Calculated time constants as function of burnup.

FISSION GAS RELEASE
(Session 2)

Chairpersons

D. ELENKOV
Bulgaria

K. RANTA-PUSKA
Finland

TRANSIENT FISSION GAS RELESE FROM UO_2 FUEL FOR HIGH TEMPERATURE AND HIGH BURNUP

M. SZUTA
Institute of Atomic Energy,
Otwock-Świerk, Poland

Abstract

In the present paper it is assumed that the fission gas release kinetics from an irradiated UO_2 fuel for high temperature is determined by the kinetics of grain growth. A well founded assumption that Vitanza curve describes the change of uranium dioxide re-crystallization temperature and the experimental results referring to the limiting grain size presented in the literature are used to modify the grain growth model. Algorithms of fission gas release due to re-crystallization of uranium dioxide grains are worked out. The defect trap model of fission gas behaviour described in the earlier papers is supplemented with the algorithms. Calculations of fission gas release in function of time, temperature, burn-up and initial grain sizes are obtained. Computation of transient fission gas release in the paper is limited to the case where steady state of irradiation to accumulate a desired burn-up is performed below the temperature of re-crystallization then the subsequent step temperature increase follows. There are considered two kinds of step temperature increase for different burn-up: the final temperature of the step increase is below and above the re-crystallization temperature. Calculations show that bursts of fission gas are predicted in both kinds. The release rate of gas liberated for the final temperature above the re-crystallization temperature is much higher than for final temperature below the re-crystallization temperature. The time required for the burst to subside is longer due to grain growth than due to diffusion of bubbles and knock-out release. The theoretical results explain qualitatively the experimental data but some of them need to be verified since this sort of experimental data are not found in the available literature.

1. INTRODUCTION

It is noticed that the radial distribution of concentration of retained fission gas in the fuel rod is in very close correlation with the radial grain size distribution. It is roughly the mirror reflection. It implies that the grain growth mechanism mainly determines the fission gas release for high temperature.

On the other hand it is noticed that the Vitanza curve is the threshold temperature change of uranium dioxide re-crystallization temperature with burn-up. This is well founded assumption.

Out-of-pile experiments show that during annealing the irradiated UO_2 samples bursts of fission gas release occur [1]. After a small burst release at relatively low temperature, a large burst release appears at high temperature. The critical temperature for high temperature burst release is about 1800^oC for low burnup (about 7 MW•d/kg U) and decreases to about 1500^oC for high burnup (30 MW•d/kg U).

The point defects induced by radiation begin to recover at $450–650^oC$ and are completely almost recovered above 850^oC, while defect clusters of dislocations and small intragrannular bubbles require $1150–1450^oC$ [2].

Thermal recovery of radiation defects and microstructure change in irradiated UO_2 fuel studied by X-ray diffraction and transmission electron microscopy lead to the conclusion that the gas release kinetics from irradiated UO_2 is determined by the kinetics of thermal recovery of the radiation induced defects.

If the point defects, defect clusters of dislocation and small intragranular bubbles are thermally recovered at the temperatures below 1450°C, a natural question concerns the nature of forces which immobilise the noble gases. Hence an additional trapping process of inert gas atoms with the uranium dioxide material is suspected to occur.

The process of strong binding of the fission gas fragments with the irradiation defects is described in the literature as a process of chemical interaction with UO_2 [3]. It is assumed further that the vicinity of the fission fragment trajectory is the place of intensive irradiation induced chemical interaction of the fission gas products with UO_2 [3].

We can further assume that above a limiting value of fission fluency a more intensive process of irradiation induced chemical interaction occurs. Significant part of fission gas products is thus expected to be chemically bound in the matrix of UO_2.

Furthermore, it is expected that the gas can be released only in the process of re-crystallization. The higher burnup the higher amount of gas should be released and the lower re-crystallization temperature should be observed. Out-of-pile experiments [1] support this assumption since the critical temperature of fission gas burst during annealing decreases with burnup.

This that the critical temperature decreases with burn-up suggest that the re-crystallization temperature of UO_2 is changed by the process of chemical interaction. It is clear that during irradiation the grain growth should be observed above the re-crystallization temperature and grain subdivision below the temperature should be observed when saturation of fission damage is obtained. This means further that the re-crystallised region will be adjacent to the subdivided grains region and the appearance of interface between the two regions will be determined by the re-crystallization temperature. It can also be expected that in the re-crystallised grains the defects are swept out. This seems also to be natural that the chemically bound fission gas atoms replacing the uranium atoms in the crystallographic lattice will increase the fission gas product release. So the process of grain growth is the process of purging the contaminated lattice.

This seems also to be natural that the chemically bound fission gas atoms substituting for example a uranium atom in the crystallographic lattice can form weak facets. At certain saturation conditions subdivision of the grains can occur and the increase in fission gas products release may be expected. So it can be stated either re-crystallization or subdivision have to occur in the saturation circumstances.

The fact that the process of grain subdivision for high burnup (70–80 MW•d/kg U) forms an extremely fine structure to a temperature as high as 1100 °C and that the decrease in fission gas concentration in the fuel [4] supports this concept. Also the re-crystallised grain region is found to be adjacent to the subdivided grain region and in the re-crystallised grain region no defects or bubbles are observed [5]. This means that we can treat the re-crystallised volume of uranium dioxide as a fresh fuel where all the processes connected with irradiation start from the beginning. So the process of grain growth is the process of purging the contaminated lattice.

The decrease in critical temperature to about 1100°C for over 1% fractional fission gas release from the fuel and for high burn-up, reported by Vitanza et al. [6] well correlates with the experiments [1] and [4] mentioned above. This that the limiting grain size begins to increase practically at the temperature about 1000–1100°C for high burn-up ⟨40 MW•d/kg U) [7]

supports the concept that the threshold temperature for UO_2 for high burn-up is about 1000°C where above the threshold temperature the re-crystallization takes place and below the threshold temperature the grain subdivision can occur under the condition of irradiation damage saturation.

This also gives evidence for the concept of chemical interaction of the fission gas atoms with the atoms of the fuel. It is assumed in this paper that all retained gas atoms in the lattice are released from the volume of re-crystallised grains.

2. UO_2 GRAIN GROWTH KINETICS

The above assumptions lead to the conclusion that the gas release kinetics from irradiated UO_2 fuel for high temperature is determined by the kinetics of grain growth. It is well known [8] that the irradiation damages introduced by fission events have two opposing effects on grain growth. The large concentration of fission gas atoms in the lattice introduced in fission spikes enhances the transfer of atoms across a boundary, increasing the rate of growth. It means that the higher is the burn-up the quicker is the process of grain growth–the stable state is quicker obtained. Conversely the impurities introduced by fission events inhibit grain growth by limiting the grain size.

Assuming that the Vitanza curve [6] describes the change of uranium dioxide re-crystallization temperature we can say that the grain growth rate depends on the burn-up in the way given by the best fit of the grain size change with the curve [9]. To obtain this we have modified the grain growth model of Ainscough et al. [10], which is generally considered to be the best available one in the open literature. These assumptions enable us to evaluate the change of grain growth in function of fuel burn-up. By help of this assumption we have been able to modify the coefficient $\underline{k}$ which is responsible for the grain growth rate.

According to the experimental data presented by Bagger et al. [7] much smaller values for the limiting grain size must be assumed at higher burn-up than in the Ainscough model. Fig. 1 presents the comparison of limiting grain size in function of temperature for the unirradiated fuel and the irradiated fuel [40 MW•d/kg U). The experimental results show that while decreasing the temperature the limiting grain size for burn-up of 40 MW•d/kg U decreases asymptotically to 5 μm and practically reaches the value at the temperature about 1000 °C.

Extrapolating the limiting grain size curve of irradiated fuel for low temperature we can see that the limiting grain size is not smaller than 5 μm, while for the unirradiated fuel the limiting grain size tends to zero. So, the limiting grain size in function of temperature for burn-up range 0–40 MW•d/kg U is to lie between these two curves. Taking into account these assumptions we finally obtained the modified differential equation of Ainscough of grain growth which describes the grain growth kinetics.

$$\frac{dD}{dt} = k\left(\frac{1}{D} - \frac{1}{D_m}\right) \tag{1}$$

Where:

$$k = 5.27\times10^{7}\exp\left(-\frac{2.67\times10^{5}}{R\left(T+371\left(1-\exp\left(-\frac{B}{2700}\right)+0.041\times B\right)\right)}\right) \quad (2)$$

$$D_m = 2.23\times10^{3}\exp\left(-\frac{7620}{T-520(1-\exp(-\frac{B}{8400}))}\right) + \boldsymbol{5}\,(1-\exp(-\frac{B}{8400}))\,\boldsymbol{)} \quad (3)$$

where

D = grain size (μm),

D_m = limiting grain size (μm),

B = burn-up in MWd/tU

T = fuel temperature (K),
t = time (h).

The equation (3) can be extended for higher burn-up than 40 MW•d/kg U since correlating the limiting grain size with the Vitanza curve we can see that for burn-up equal 40 MW•d/kg U the stable state is reached.

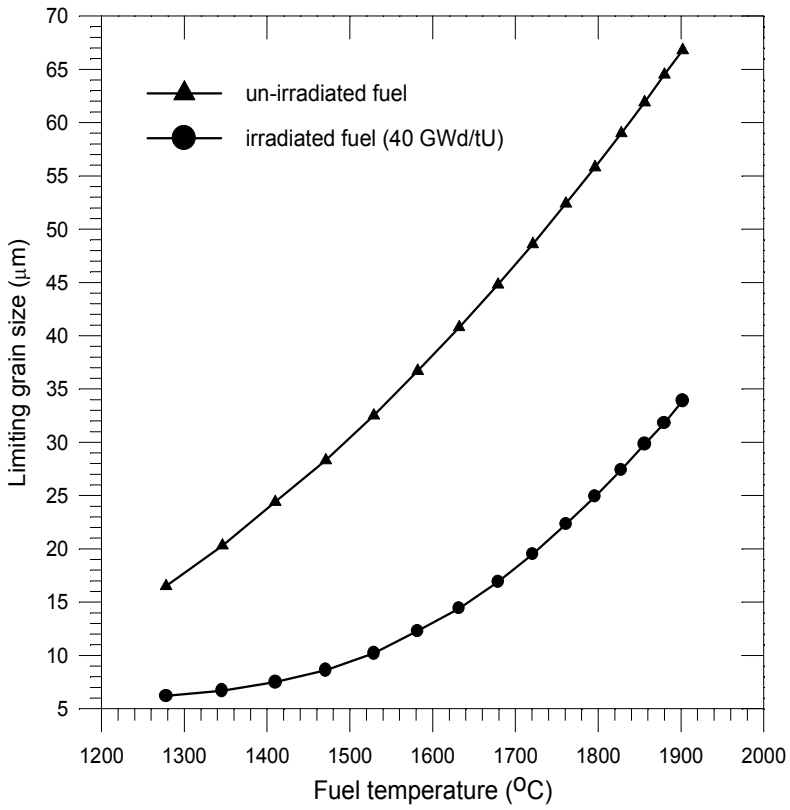

FIG. 1. Limiting grain size in function of fuel temperature for the un-irradiated and the irradiated fuel [7].

3. ALGORITHM OF FISSION GAS RELEASE DUE TO UO_2 GRAIN GROWTH

It is well known that the grain growth in polycrystalline materials is caused by a preferential shrinkage of smaller grains due to their relatively smaller radii of curvature. An average number of grains, (N_0), in a unit volume is of un-irradiated fuel:

$$N_o = \frac{1 - \frac{p}{100}}{\frac{4}{3}\pi\left(\frac{D_o}{2}\right)^3} \tag{4}$$

where p –porosity in%, D_0–initial grain diameter.

At the elevated temperature the number of grains, N, in the unit volume is fixed by the limiting grain size, $D_{m.}$:.

$$N = \frac{1 - \frac{p}{100}}{\frac{4}{3}\pi\left(\frac{D_m}{2}\right)^3} \tag{5}$$

The initial grain size, D_0, is easily measurable while the limiting grain size after the grain growth, $D_{m.}$, is determined by equation (3) at which grain growth ceases.

The release rate of re-soluted gas (chemically bound fission gas in the UO_2 lattice) and trapped in bubbles is to be determined. . Multiplying the rate of volume change of grain by the concentration of re-soluted gas atoms in the matrix, M_r, and trapped gas atoms in the bubbles, M_{tr}, we obtain the release from one grain, R_{go}:

$$R_{go} = \frac{1}{2}\pi(M_r + M_{tr})D^2\frac{dD}{dt} \tag{6}$$

where dD/dt is determined from the Ainscough's modified differential equation (1).

The product of release rate from one grain, R_{go}, and the number of grains, N, at elevated temperature, defined by equation (5) determines the release rate from a unit volume.

The defect trap model presented previously [9, 11, 12, 13 and 14] can be supplemented with the description due to grain growth process, according to the aforementioned assumptions:

$$\frac{dM}{dt} = \beta_i f + \alpha_1 f M_r + g_3 f M_{tr} - \alpha_2 M - g N_{tr} M \tag{7}$$

$$\frac{dM_{tr}}{dt} = g N_{tr} M - g_2 f M_{tr} - g_3 f M_{tr} - \lambda M_{tr} - \frac{1}{2} M_{tr} D^2 \frac{dD}{dt} N \tag{8}$$

$$\frac{dM_r}{dt} = \alpha_2 M - \alpha_1 f M_r - \lambda M_r - \frac{1}{2} M_r D^2 \frac{dD}{dt} N \tag{9}$$

$$R = g_2 f M_{tr}(S \times r) + \frac{1}{2}\pi(M_{tr} + M_r)D^2 \frac{dD}{dt} N \tag{10}$$

Where

$$\left\langle N_{trI}^{D} \right\rangle = \frac{1}{r}\int_0^r N_{trI}^{D} dx \tag{11}$$

$$N_{tr} = N_{tr}^{ko} + \left\langle N_{trI}^{D} \right\rangle \tag{12}$$

$$S = S_0 + S_1\left(1 - \exp\left(-\frac{Bu - B_0}{\tau}\right)\right) \tag{13}$$

$$\frac{dN_{tr}^{ko}}{dt} = g_1 f - (g_2 + g_3) f N_{tr}^{ko} \qquad \text{for} \quad 0 \le x \le r \tag{14}$$

$$\frac{\partial N_{trI}^{D}}{\partial t} = D_b \nabla^2 N_{trI}^{D} - (g_2 + g_3) f N_{trI}^{D} \qquad \text{for} \quad 0 \le x \le r, \tag{15}$$

$$\frac{\partial N_{trII}^{D}}{\partial t} = D_b \nabla^2 N_{trII}^{D} + g_1 f - g_3 f N_{trII}^{D} \qquad \text{for} \quad r \le x < \infty, \tag{16}$$

N_{tr} – concentration of bubbles in the surface layer,
N_{tr}^{ko} - bubbles created in the surface layer,
N_{trI}^{D} – bubbles diffused into the surface layer from the bulk,
N_{trII}^{D} –bubbles in the bulk,
r –fission product range
λ – decay constant of isotope i,
β_i – formation yield of the intermediate gas of isotope i,
f – fission rate,
t – time,
x – distance into the fuel from the sample surface,
r – fission product range,
D_b – diffusion coefficient of bubbles,
Bu – burnup,
M – concentration of intermediate gas atoms,
$M_{.tr}$ – concentration of gas atoms in the bubbles,
$M_{.r}$ – concentration of gas atoms in the matrix,
S – total surface area,
g, g_1, g_2, g_3, α_1, α_2, S_0, S_1, B_0, τ –constants.

It is assumed that the total surface area versus burn-up described by Eq. 13 does not change during the process of grain growth. The coupled Eqs. (7- 16) are solved numerically using the modified Runge-Kutta method and the explicit finite-difference technique; Crank-Nicholson scheme.

4. BURSTS OF FISSION GAS RELEASE

Knowledge of fission gas release mechanisms during transients at high burn-up is very important from the exploitation point of view. The experimental programmes on the subject are mainly concerned with the hot cell examination after irradiation, without information on the detailed kinetics of the phenomena.

In order to contribute to filling this gap, the analysis of fission gas release for temperature transient (which occurs during power transient) is performed and the theoretical results are compared with the few experimental results available in the literature.

Experimental observations show [7, 15, 16 and 17] that during transient tests, bursts release occur of two types. The main difference between this two types of fission gas release is that they refer to the range of about 0.1–1% fractional release for the first type, and to the range of about 1–95% fractional release for the second type.

It is considered that the first type of fission gas release is proportional to the total fuel surface area, but the second type depends on the volume of the sample. Below the re-crystallization temperature, the main contribution to the fission gas release from the UO_2 fuel is from the bubble traps by knock-out process and diffusion of bubbles [11–14]. The knock-out process affects the UO_2 total fuel surface layer to a depth not more than 10 μm–the fission fragment range. The bubble migration is due to the following sequence "kinetic excitation of gas atoms, intermediate gas formation and bubble formation at their new location". Since the same knock-out release mechanism applies to the bubbles created in the thin surface layer and to the bubbles diffused into the layer from the bulk, the combination of temperature independent release process and temperature dependent release process is explained. So, it is sometimes doubtful whether gas release measurements reflect the volume characteristics of the solid or the surface characteristics.

Above the re-crystallization temperature, the main contribution to the fission gas release is due to purging the contaminated lattice from fission gas atoms by the re-crystallization. At the beginning of the re-crystallization process, the surface of the grains is also affected which takes part in forming the total surface area.

5. COMPUTATION RESULTS

Computation of transient fission gas release is limited to the case when the steady state of irradiation to accumulate a desired burn-up is performed below the temperature of re-crystallization and then the subsequent step temperature increase follows. Two kinds of step temperature increase for different burn-ups are considered:

— the final temperature of the step increase is still below the re-crystallization temperature,
— the final temperature after the step increase is above the re-crystallization temperature.

Calculations show that bursts of fission gas are predicted when the temperature is increased in both kinds. The amount of gas liberated for the final temperature above the re-crystallization temperature is much higher than for the final temperature below the re-crystallization temperature. This is clearly seen on FIG. 2. and FIG. 3. These two figures show the theoretical krypton 87 release rate in function of time when fuel temperature is increased from 865°C to 1240°C at constant fission rate of 3.3 10^{12} fission/cm^3·s and fuel burn-up of 40 MW•d/kg U but for two different initial grain size of 5 μm (FIG. 2.) and of 9 μm (FIG. 3.). For the initial grain size of 5 μm (FIG. 2.) the re-crystallization temperature is crossed and that is why the grain growth begins and in consequence the release rate is much higher than for the initial grain size of 9 μm (FIG. 3.) where grain growth does not occur. Duration of the two bursts are different since grain growth kinetics is responsible for the fission gas release rate (FIG. 2.) for the first one and diffusion of bubbles from the bulk to the total surface layer of the fuel is responsible for the second one (FIG. 3.).

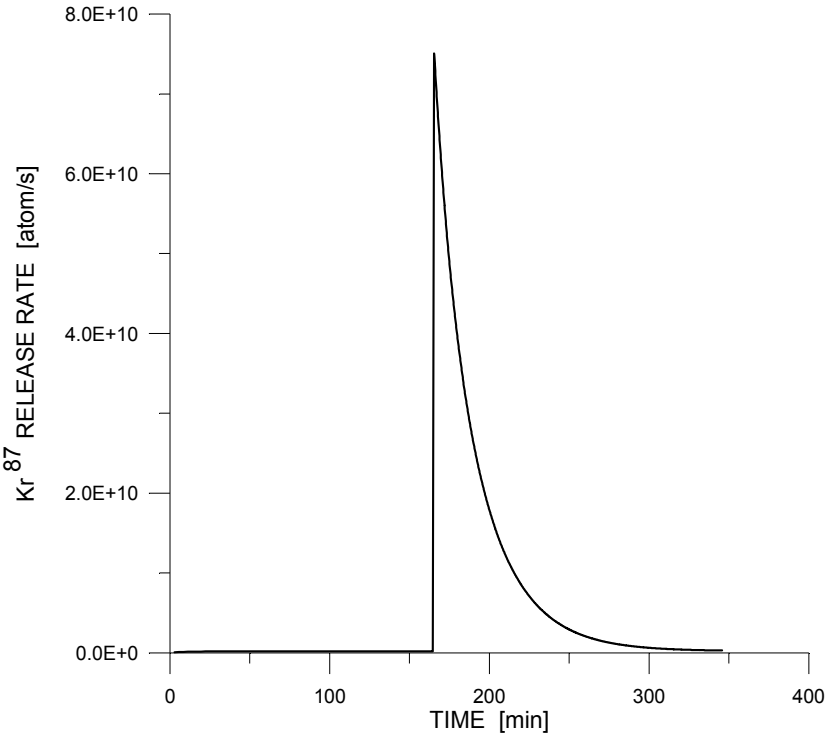

FIG. 2. Theoretical krypton release when fuel temperature is increased from 865 ° C to 1240 ° C at constant fission rate of 3.3 10^{12} fission/cm^3·s, initial grain size of 5 μm and burn-up of 40 MW•d/kg U.

Release rate both before and after the bursts for the stable state are equal because in this time the knock-out release process only exists. Both stable state values of the release bursts are equal. The stabilised release rate after the burst is a little bit higher than before the burst due to the step increase of temperature for both cases.

Duration of these bursts are different. It is far longer when the final temperature crosses the re-crystallization temperature. The duration of this burst is dependent on burn-up. The higher is the burn-up the shorter is the release burst. This is seen in FIG. 4 which presents theoretical krypton burst half decrease duration in function of burn-up at constant fission rate of 3.3 10^{12} fission/cm^3·s, initial grain size of 5 μm and 6 μm when fuel temperature is increased from 865°C to 1240°C. The smaller is the initial grain size the shorter is the duration of release burst.

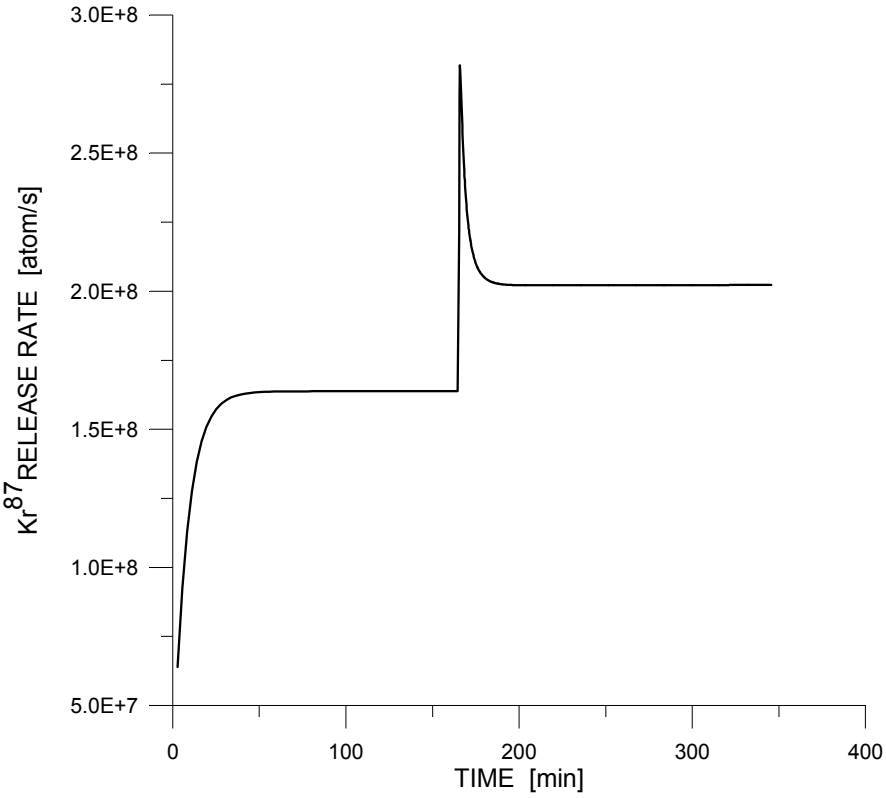

FIG. 3. Theoretical krypton release when fuel temperature is increased from 865 ^{o} C to 1240 ^{o} C at constant fission rate of 3.3 10^{12} fission/cm^3·s, initial grain size of 9 μm and burn-up of 40 MW•d/kg U.

Maximal release rate of the burst generally increases with burn-up except the initial grain size is very close the limiting grain size. In FIG. 5. The curve of maximal release rate for the initial grain of 6 μm starts to decrease when the burn-up reaches the value of 30 MW•d/kg U. For this burn-up the limiting grain size is equal 6.59 μm at the temperature of 1240 ^{o} C. For burn-up of 35.3 MW•d/kg U the limiting grain size becomes about 6.01 μm what is very close the initial grain size and crossing the burn-up of 36 MW•d/kg U the limiting grain size becomes lower than the initial grain size. This means that the grain growth vanishes and the gas release vanishes as well.

The experimental results presented in ref. [15] indicate that an abrupt burst of fission gas was emitted when the single crystal UO_2-specimen temperature was increased. FIG. 6. presents the theoretical krypton release for the same temperature conditions and fission rate as in the experiment carried by R.M. Carroll et al. (FIG. 8. of Ref. [15]). The defect trap model of fission gas release permits a qualitative interpretation of the results. The times required for the burst to increase and subside are of the same about value as in the experiment. The values of release rate before the burst and after the burst are of the same order except the value during the burst. The burst in the experiment is bigger than the burst obtained theoretically. The total surface area in the theoretical calculations for the unit volume of 1 cm^3 is about 135 times bigger than in the experiment of R.M. Carroll et al. [15] than in the experiment. Taking this into consideration we can state that the theoretical krypton isotopes release rate is of the same order as in the experiment for the stable state.

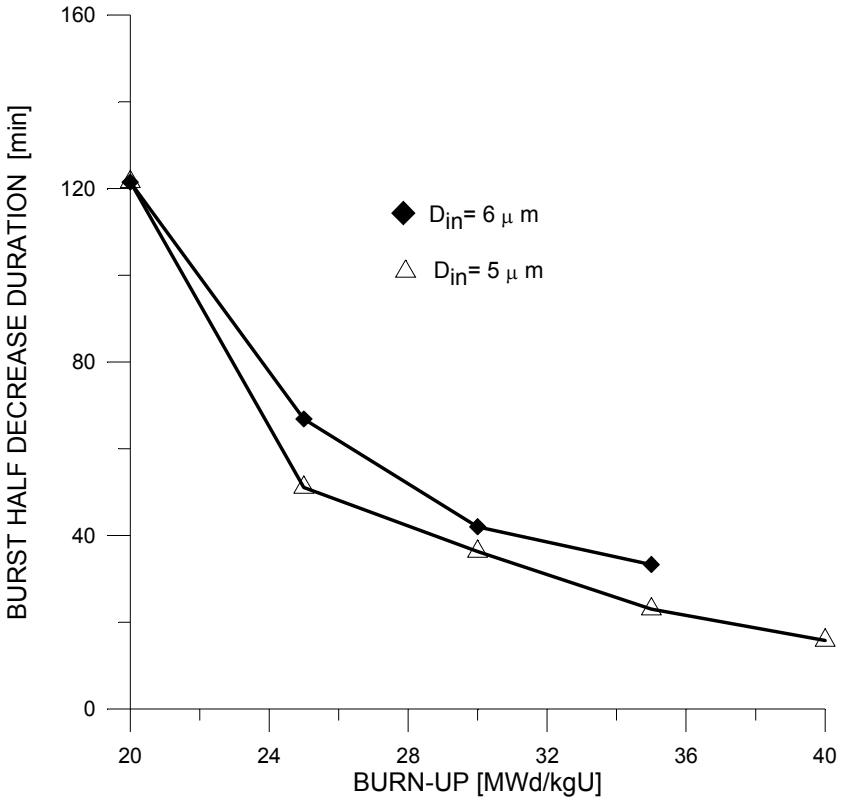

FIG. 4. Theoretical Kr^{87} burst half decrease duration in function of burn-up at constant fission rate of 3.3 10^{12} fission/cm^3·s, initial grain size of 5 μm and 6 μm when fuel temperature is increased from 865 ^{o} C to 1240 ^{o} C

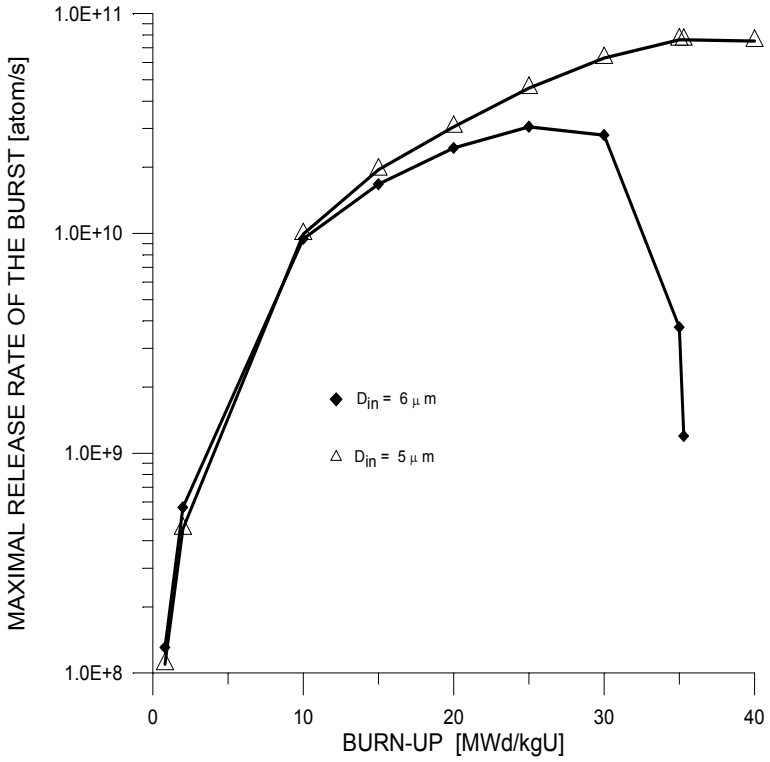

FIG. 5. Theoretical maximal Kr^{87} release rate of the burst in function of burn-up at constant fission rate of 3.3 10^{12} fission/cm^3·s, initial grain size of 5 μm and 6 μm when fuel temperature is increased from 865 ^{o} C to 1240 ^{o} C

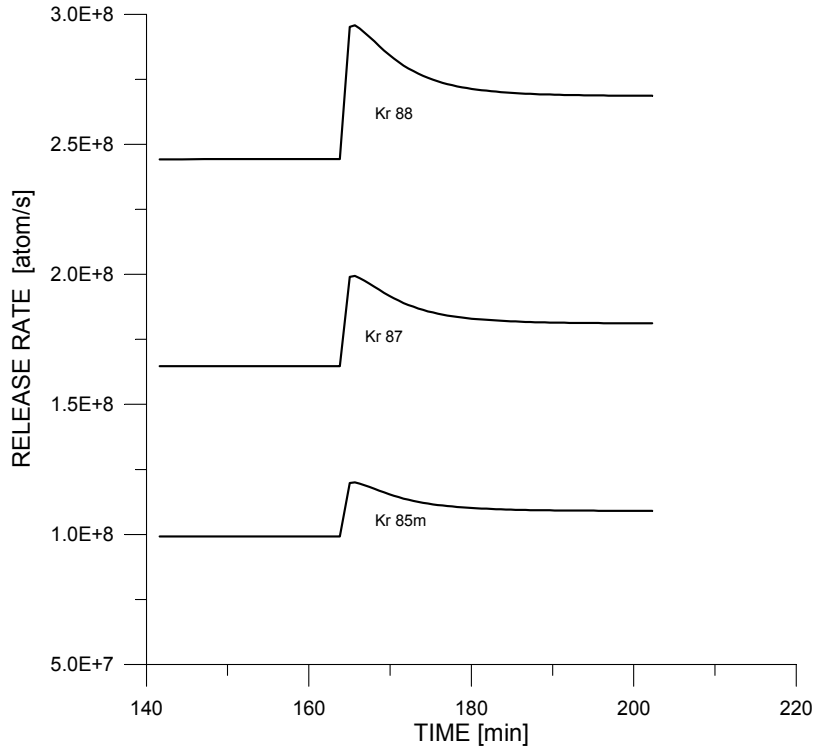

FIG. 6. Theoretical krypton release when fuel temperature is increased from 865 ^{o} C to 1040 ^{o} C at constant fission rate of 3.3 10^{12} fission/cm^{3}·s, initial grain size of 9 μm and burn-up of 35 MW•d/kg U.

Also the experimental results presented in ref. [16] show that an abrupt burst of fission gas was emitted when the UO_2 fuel temperature was increased. So both from single crystal and UO_2 fuel an abrupt burst of fission gas is emitted what means that the same process is responsible for this. Some of the theoretical results explain qualitatively the experimental data but some of them need to be verified since this sort of experimental data are not found in the available literature.

6. CONCLUSIONS

Two opposing effects of enhancement and inhibition of irradiation damage introduced by fission effect on grain growth have a significant impact on fission gas release for high temperature. The large concentration of point defects in the lattice introduced in fission spikes enhances the transfer of atoms across a boundary, increasing the rate of growth. Conversely the impurities introduced by fission events inhibit grain growth by limiting the grain size.

There is no doubt that during the process of grain growth the fission gas products retained in the matrix of uranium dioxide being there immobilised are released. It is natural that the process of grain growth is the process of purging the contaminated lattice. So we can treat the re-crystallised volume of uranium dioxide as a fresh fuel where the processes connected with the radiation start from the beginning.

Supplementation of the defect trap model of fission gas release by the grain growth process let to form complementary model for low, intermediate and high temperatures.

It can be concluded that the additional assumptions made in this model make it possible to give the experimental results described in the literature, regarding fission gas release from UO_2 fuel during high temperature irradiation a satisfactory qualitative interpretation.

The higher is the initial grain size, the higher is the threshold temperature of re-crystallization of the grain. It means, if the limiting grain size for the appointed temperature is equal to the initial grain size, then the re-crystallization does not occur. In consequence, the fission gas release due to re-crystallization also does not occur and the retained gas concentration remains on the level of accumulation.

Calculations show that bursts of fission gas are predicted for the same step function of temperature both when the initial grain size is below and above the limiting grain size. The release rate of gas liberated for the final temperature above the re-crystallization temperature is much higher than for final temperature below the re-crystallization temperature. The time required for the burst to subside is longer due to grain growth than due to diffusion of bubbles and knock-out release.

The model gives theoretical results which need to be verified since this sort of experimental data are not found in the available literature.

REFERENCES

[1] K. Une, S. Kashibe, J. Nucl. Sci. Technol. 27, 2000 (1990).
[2] Y. Nogita, K. Une, J. Nucl. Sci. Technol. 30, 900 (1993).
[3] D.A. McInnes, P. W. Winter, J. Phys. Chem. Solids 49, 143 (1988).
[4] K. Lassman, C. T. Walker, J. Van de Laar, F. Lindstrom, J. Nucl. Mater. 26, 1 (1995).
[5] K. Nogita, K. Une, Nucl. Instrum. Methods Phys. Res. B 91, 301 (1989).
[6] C. Vitanza, E. Kalstod, U. Gracioni, in Proc. Am. Nucl. Soc., Topical Meeting on Light Water Reactors Fuel Performance, American Nuclear Society, Portland (OR) 1978, p. 361.
[7] C. Bagger, M. Mogensen, C.T. Walker, J. Nucl. Mater. 211 (1994) 11.
[8] MacEwan, J. Hayashi, Proceedings of the British Ceramic Society, Vol. 7 (1967) 75.
[9] M. Szuta, M.S. El-Koliel , Acta Physica Polonica A, Vol. 96, No. 1 (1999) 143.
[10] [J. B. Ainscough, B. W. Oldfield, J. O. Ware, J. Nucl. Mater. 49 (1973/74) 117.
[11] M. Szuta, J. Nucl. Mater. 58 (1975) 278.
[12] M. Szuta, J. Nucl. Mater. 97 (1981) 149.
[13] M. Szuta, J. Nucl. Mater. 130 (1985) 434.
[14] M. Szuta, J. Nucl. Mater. 210 (1994) 178.
[15] R. M. Carroll, O. Sisman, Nucl. Sci. Eng. 21, 147–158 (1965).
[16] J. E. Harbottle, J. A. Turnbull, A BNL Review and Analysis of CEA and EdF Data on Defective PWR Fuel, Central Electricity Generating Board, TPRD/0803/R86, EdFWG P(86)32, June 1986.
[17] Hj. Matzke, H. Blank, M. Conquerelle, K. Lassmann, I. L. F. Ray, C. Ronchi, C.T. Walker, J. Nucl. Mater. 166 (1989) 165.

THE GROWTH OF INTRA-GRANULAR BUBBLES IN POST-IRRADIATION ANNEALED UO_2 FUEL

R.J. WHITE

MOX Research and Technology,
BNFL, Sellafield, Seascale,
Cumbria, United Kingdom

Abstract

Post-irradiation examinations of low temperature irradiated UO_2 reveal large numbers of very small intra-granular bubbles, typically of around 1 nm diameter. During high temperature reactor transients these bubbles act as sinks for fission gas atoms and vacancies and can give rise to large volumetric swellings, sometimes of the order of 10%. Under irradiation conditions, the nucleation and growth of these bubbles is determined by a balance between irradiation-induced nucleation, diffusional growth and an irradiation induced re-solution mechanism. This conceptual picture is, however, incomplete because in the absence of irradiation the model predicts that the bubble population present from the pre-irradiation would act as the dominant sink for fission gas atoms resulting in large intra-granular swellings and little or no fission gas release. In practice, large fission gas releases are observed from post-irradiation annealed fuel. A recent series of experiments addressed the issue of fission gas release and swelling in post-irradiation annealed UO_2 originating from Advanced Gas Cooled Reactor (AGR) fuel which had been ramp tested in the Halden Test reactor. Specimens of fuel were subjected to transient heating at ramp rates of 0.5°C/s and 20°C/s to target temperatures between 1600°C and 1900°C. The release of fission gas was monitored during the tests. Subsequently, the fuel was subjected to post-irradiation examination involving detailed Scanning Electron Microscopy (SEM) analysis. Bubble-size distributions were obtained from seventeen specimens, which entailed the measurement of nearly 26 000 intra-granular bubbles. The analysis reveals that the bubble densities remain approximately invariant during the anneals and the bubble-size distributions exhibit long exponential tails in which the largest bubbles are present in concentrations of 10^4 or 10^5 lower than the concentrations of the average sized bubbles. Detailed modelling of the bubble growth process indicates that these distributions are inconsistent with the presence of *thermal re-solution* of fission gas atoms from heavily over-pressurised bubbles. Further analysis suggests that under out-of-pile conditions the bubble growth is severely restricted by vacancy starvation effects. A model is presented to account for the observed behaviour.

1. INTRODUCTION

The fission gases, xenon and krypton, are produced in abundance during the thermal fissioning of ^{235}U, ^{239}Pu and ^{241}Pu and can present difficulties in fuel management whether retained in the matrix or released to the pin free volume. The problems associated with release involve the dilution of the helium fill gas leading to poorer heat transfer between fuel and cladding. This, in turn, gives rise to higher fuel temperatures and escalating gas release. At high burn-ups the quantity of gas could give rise to potential rod over-pressurisation with respect to the coolant. Alternatively, retained gases provide the possibility of rapid swelling during power transients and this can cause pellet-clad interaction (PCI) which can lead to rod failure.

Two principal modes of fission gas swelling are of interest, namely, intra-granular swelling where spherical bubbles occur within the grains and inter-granular swelling caused by gas which has migrated to the grain boundaries. Because of the short diffusion distances involved, intra-granular swelling provides the possibility of the extremely rapid development of large volumetric swellings in excess of ten percent.

Transmission Electron Microscope studies [1] of irradiated UO_2 reveal large populations - typically 10^{24} m^{-3} - of nano-metre sized intra-granular bubbles. Following the observation that large numbers of these bubbles appear to lie in straight-line tracks, Turnbull [2] has suggested that the bubbles are nucleated in the wake of energetic fission fragments. Furthermore, the fact that the populations appear independent of burn-up led to the suggestion [2] that they were also destroyed by impact by other fission fragments. At low temperatures these bubbles exhibit little growth but brief excursions to high temperatures [3] reveal that a sub-population of the bubbles grow to radii in excess of 100 nm and give rise to large volumetric swellings.

Consideration of the potential sink strength of these bubbles suggested that in the absence of irradiation, and hence, the irradiation induced re-solution process, the fission gas release would be minimal as the gas migrated to the predominant internal sinks rather than the grain boundaries. These suppositions were confounded by the observation of large gas releases during the thermal annealing of pre-irradiated fuel [4]. The subsequent proposal that thermal re-solution of fission gas occurred from the heavily over-pressurised intra-granular bubbles [5] provided a mechanism to avoid the total precipitation of gas into bubbles but the model was not widely supported because of the low inherent solubility of xenon and krypton in UO_2.

Recently, a series of tests has been performed under the auspices of the IMC[1] to address specifically the issue of thermal re-solution of fission gas from intra-granular bubbles.

2. THE IMC POST-IRRADIATION ANNEALING PROGRAMME

As part of a detailed study of fuel swelling, Nuclear Electric[2] performed a number of ramp tests on pre-irradiated AGR fuel in the Halden Reactor [6]. Samples of this fuel were subjected to detailed PIE including Scanning Electron Microscopy [3]. The SEM revealed the presence of large intra-granular swellings in fuel ramped to temperatures in excess of 1600°C. The concentrations of intra-granular bubbles were typically three to five orders of magnitude lower than those of the small bubbles present in the low temperature irradiations, i.e. typically 10^{18} to 10^{20} m^{-3}.

As a means of addressing the issues of bubble nucleation densities and thermal re-solution, it was decided to use unramped samples of the AGR fuel[3] as part of a post-irradiation annealing experiment. The fuel was transported to AEA Technology at Harwell for thermal annealing in the transient heating furnace [6] before being returned to the Shielded Electron Optics Suite at Magnox Electric's Berkeley Facility for a detailed SEM examination [7]. The test matrix is shown in Table I below and was designed to provide similar temperature ramps to those experienced in the in-pile tests but in the absence of irradiation.

Seventeen of the twenty specimens exhibited intra-granular swellings and these are shown as shaded areas in the table above. Of the others, the lowest temperature of the low burn-up, slow ramp rate tests may have had small intra-granular bubbles but these were too small to be revealed by the SEM. The remaining two tests were performed at 1900°C and the measured gas release in these was in excess of 90% indicating possible oxygen ingress into the furnace and no bubbles were observed.

---

[1] The IMC is the Industrial Management Committee of the United Kingdom Health and Safety Executive and directs research funded by British Energy and BNFL.

[2] Now British Energy Generation Ltd.

[3] The ramping of the fuel in Halden involved the moving of the fuel from behind a neutron absorbing shield. Parts of the fuel rods were never exposed to high powers and these are referred to as the unramped parts.

TABLE I. TEST MATRIX FOR POST-IRRADIATION EXAMINATION ANNEALS

Burn-Up (MWd/kgU)	Ramp Rate (°C/s)	Hold Time (minutes at top temperature)			
		1600°C	1700°C	1800°C	1900°C
9.8	0.5 (slow)	0	0	0	0
20.8	0.5 (slow)	0	0	0	0
20.8	25.0 (fast)	2	2	2	2
20.8	25.0 (fast)	20	20	20	20
20.8	25.0 (fast)	60	60	60	60

The SEM study of the seventeen useable specimens involved the measurement of approximately 26000 bubbles and bubble size distributions were obtained by use of a bubble population de-convolution procedure [9] to correct for sectioning.

3. EXPERIMENTAL OBSERVATIONS

The total bubble concentrations measured in the fast ramp specimens are shown in Figure 1 for both in-pile and out-of-pile tests.

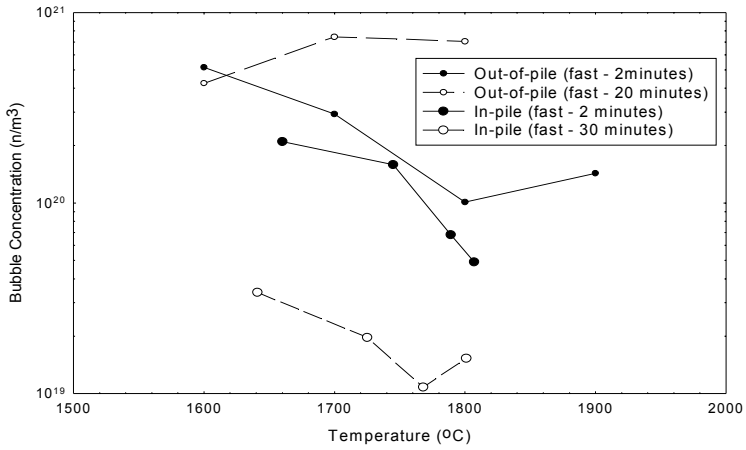

FIG. 1. Bubble concentrations for fast ramps in and out-of-pile. Note that considerable in-pile bubble loss occurs at each temperature between the 2 and 30 minute holds while none occurs out-of-pile.

The key feature in Figure 1 is the reduction in bubble numbers between the 2 minute and 30 minute anneal for the in-pile test confirming the presence of irradiation induced re-solution. If thermal re-solution were operating in the out-of-pile tests there might be expected to be a reduction in bubble concentration in these data also but, if anything, there is a slight increase, particularly at higher temperatures. This increase is possibly a result of more bubbles becoming visible during the growth in the longer anneal rather than additional bubble nucleation.

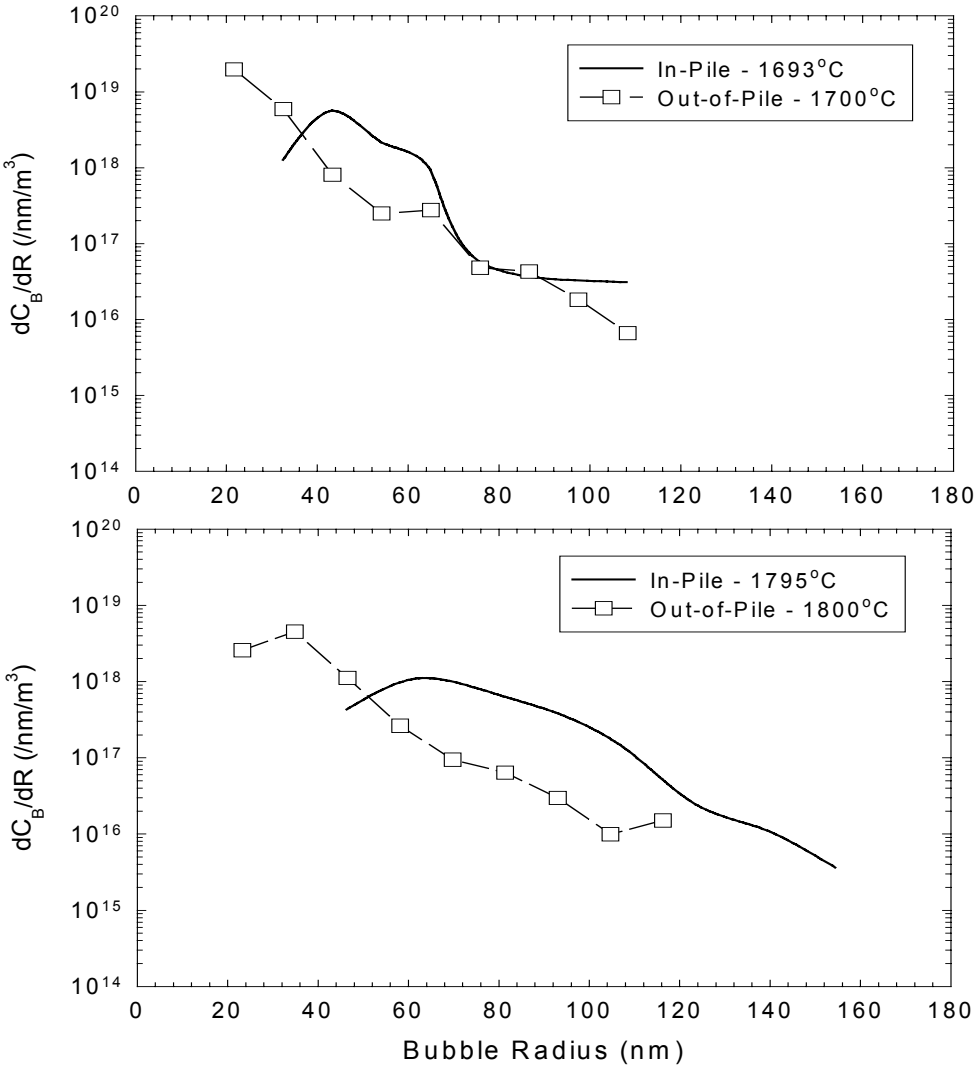

FIG. 2. The bubble size distributions for in and out-of-pile anneals.

Comparisons of the bubble size distributions for two two-minute hold fast ramp specimens are shown in Figure 2.

The lower temperature anneals show similarities between in-pile and out-of-pile behaviour but the higher temperature data reveal striking differences. In both of the out-of-pile anneals, the distributions are of an exponential nature with no well-defined maximum whereas the in-pile data show bell-like features. There is a distinct absence of bubble growth between the 1700°C and 1800°C out-of-pile anneals in contrast to the in-pile data.

The intra-granular volumetric swelling for fast ramps followed by short and extended holds at the target temperature are shown in Figure 3.

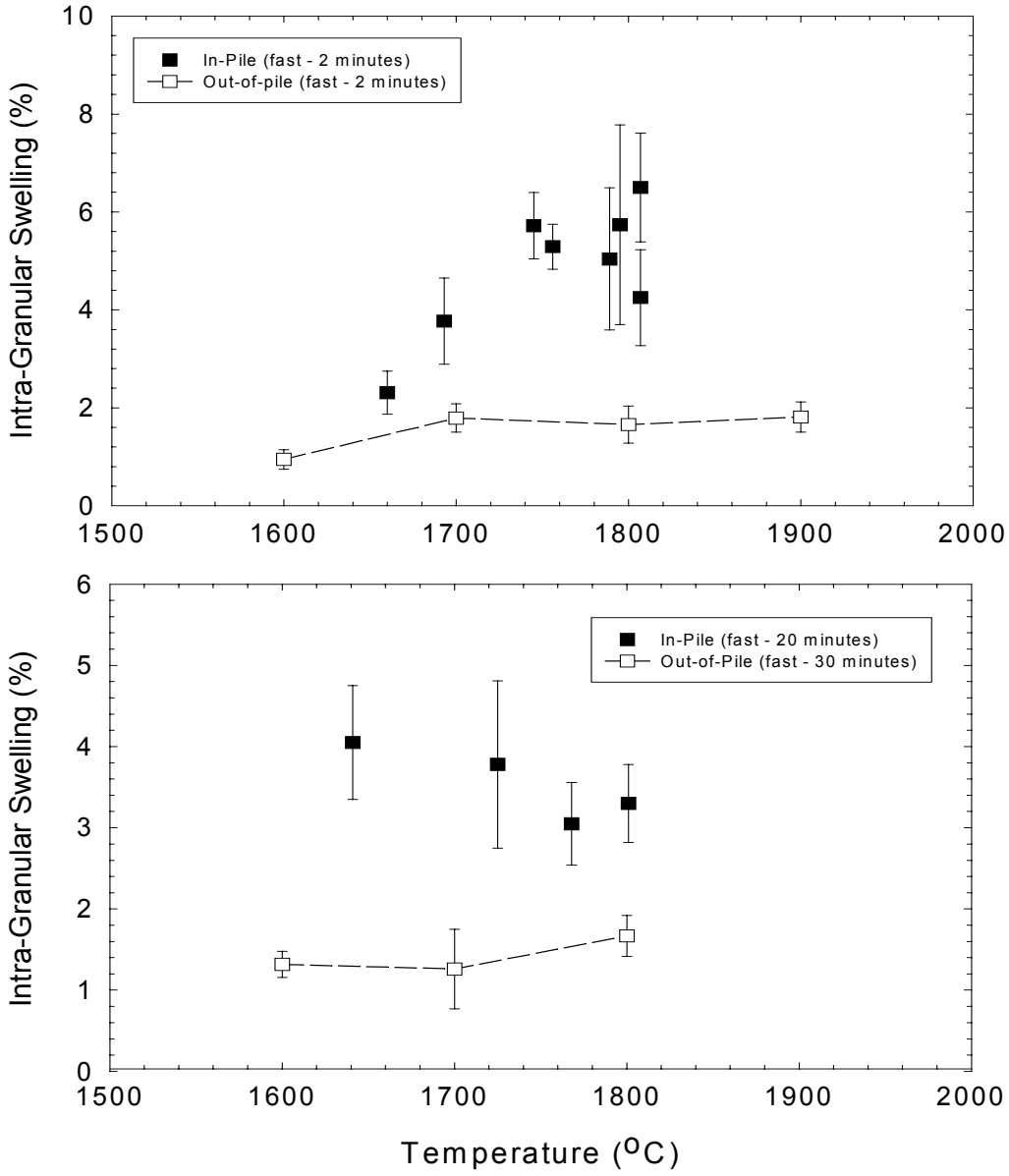

FIG. 3. The temperature dependence of intra-granular swelling during fast ramps out-of-pile.

For the two-minute hold the in-pile data show an increase in swelling with increasing top temperature while the out-of-pile data are approximately independent of temperature. Since the diffusion rates are considerably higher at 1900°C than at 1700°C it is difficult to see why additional growth has not occurred. The in-pile cases with a thirty-minute hold show a slight reduction in swelling with temperature and this may be associated with irradiation induced re-solution but the out-of-pile anneals exhibit little growth over this additional annealing period. The overall behaviour of the out-of-pile annealed data may be summarised, as follows; there is little or no evidence of bubble loss during annealing. Virtually all of the specimens have total bubble numbers around $(3.6 \pm 2.0)\cdot 10^{20}$ m^{-3}, a variation which is within the experimental scatter and is indicative of conserved bubble numbers rather than evidence of a bubble loss mechanism. There appears to be a marked reluctance for bubble growth in out-of-pile anneals compared to similar in-pile anneals despite the presence of irradiation induced re-solution.

4. BUBBLE GROWTH KINETICS

4.1 Diffusion control and thermal resolution

The diffusive flow of fission gas atoms to alternative sinks in the medium is given by

$$\frac{dC_g}{dt} = -k_g^2 D_f C_g \quad (1)$$

where C_g is the concentration of gas in the matrix, D_f is the fission gas diffusivity and k_g^2 is the 'strength' of the relevant sink. The total sink strength for all bubbles is $4\pi RC_B$ [11] where R is the bubble radius and C_B is the bubble concentration while that for the grain boundaries is π^2/a^2 [12] where 'a' is the grain radius. Using the average concentration measured above and an initial bubble radius of 1 nm, the bubble sink strength is equal to $4 \cdot 10^{12}$ m^{-2} while that of 5 μm radius grains is $4 \cdot 10^{11}$, a factor of 10 smaller. On this basis, the intra-granular bubbles always present a more favourable sink for gas atoms than the grain boundaries so if Equation 1 is correct there should be no observable gas release from annealed fuel. In practice, fractional releases as high as 80% are not uncommon.

The concept of thermal re-solution [5] was introduced as a means of ensuring that the matrix gas concentration could not drop to zero, that is, some gas would always remain in solution. The mechanism plays a role in the coarsening of second phase precipitates in alloys [13] and the rate of thermal re-solution usually depends on the curvature of the bubble/matrix or precipitate/matrix interface. In this way, Equation 1 would be modified to

$$\frac{dC_g}{dt} = -4\pi RC_B D_f \left(C_g - C_R\right) \quad \textit{where}$$
$$C_R = C_0 e^{\frac{2\gamma\Omega}{kTR}} \quad (2)$$

The actual form of the solubility, C_R would depend on the equation of state of the contents of the precipitate or bubble and the form given above is typical of that of a second phase precipitate particle. The consequence of this modified growth law is that the concentration adjacent to a bubble of small radius is much greater than that adjacent to one of large radius so the solute/gas tends to migrate from the small bubbles to the large ones. In this way, large bubbles will grow at the expense of small ones and there will be a gradual reduction in bubble numbers as the small bubbles shrink and disappear. The process is generally referred to as *Coarsening* or *Ostwald Ripening*. Since material/solute/gas is always being emitted from the smaller particles/bubbles and diffusing to the larger ones, there will always be gas in transit available for release so thermal re-solution provides a convenient mechanism to avoid the consequence of total gas absorption.

Another consequence of thermal re-solution is that the distribution of bubbles soon attains an equilibrium normalised shape and although the average size will grow, the normalised distribution remains static [14]. Furthermore, for a purely diffusion controlled mechanism, there is a maximum normalised bubble size beyond which growth becomes unstable. This is typically one and a half times the radius of the average sized bubble/particle. This distribution is shown in Figure 4 along with the measured distribution from a typical post-irradiation annealed sample. The measured distributions with long exponential tails are totally at variance with the predictions of thermal re-solution so it is hard to justify the use of the model in the growth of fission gas bubbles.

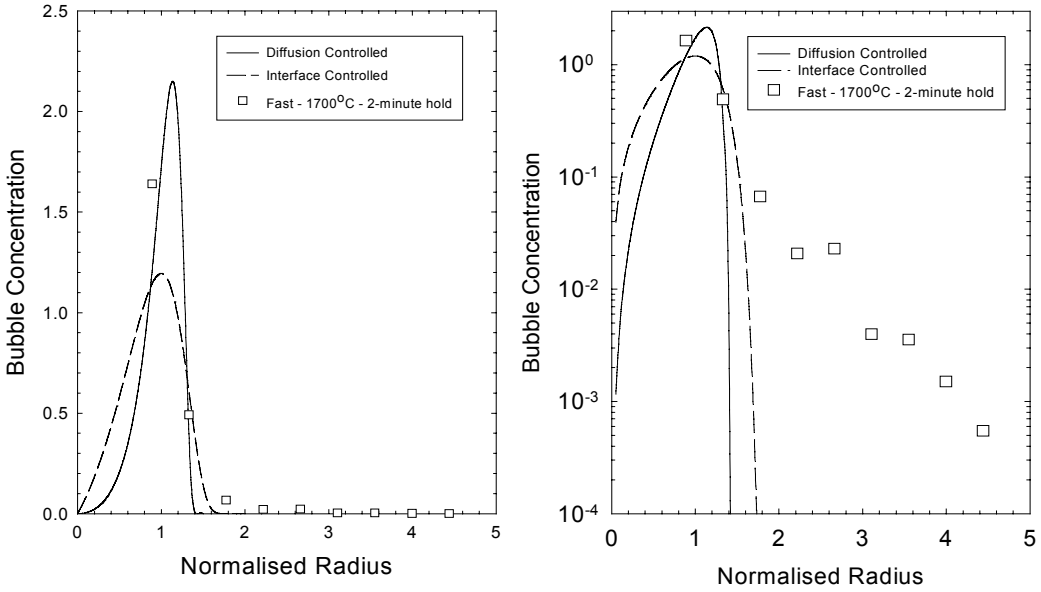

FIG. 4. Comparison of the measured bubble size distributions from out-of-pile anneals with those expected from systems exhibiting thermal re-solution. The trace on the right uses the same data but the bubble concentration is plotted logarithmically to emphasise the experimental tails.

4.2 Selective inhibited growth

The consequence of all diffusion-based models is that the bubble-size distribution rapidly becomes front-loaded. This arises because the bubble sink-strength is linearly dependent on the bubble radius so the larger bubbles attract more gas atoms and in the limit all the bubbles end up the same size and the distribution is a delta-function. The introduction of thermal re-solution works on the smaller bubble sizes and tends to give rise to the exponential rise to the mean shown in the left-hand trace of Figure 4. The measured distributions exhibit long exponential tails at the large bubble sizes and these cannot be explained using standard diffusion theory.

Conceptually, the exponential tails could be explained by invoking an interface control mechanism on bubble growth. Diffusion theory predicts that gas will migrate from regions of high concentration (strictly - chemical potential) to regions of low concentration. An interface control mechanism would limit the absorption rate of gas at the bubble interface until certain conditions were met. What these conditions are can only be guessed at but a number of proposals have been made in the context of other growth processes. For example, Bullough & Perrin [15] considered the example of vacancy absorption in void growth in fast reactor cladding materials. This could only occur at certain points on the void surface where *growth-ledges* existed. This may be what is happening in intra-granular bubble growth but an argument against this is that it would also be expected to operate under irradiation conditions and the growth process there appears to be easily explained by standard diffusion theory approaches as long as irradiation induced re-solution is also considered [3].

An alternative approach could be based on the vacancy supply situation in out-of-pile tests. The situation in-pile is such that the presence of fission fragments ensures an adequate supply

of vacancies[4] [16] whereas out-of-pile tests require a ready supply of thermally activated vacancies to ensure bubble growth. The model proposed here is based on the following assumptions:

(i) Intra-granular bubbles act as sinks for fission gas atoms and vacancies.

(ii) The bubbles are over-pressurised and act preferentially as vacancy sinks rather than vacancy sources.

(iii) The over-pressure in the bubble is balanced by a stress field in the atomic layers outside the bubble. This stress field can be relaxed by the presence of vacancies and intensified by the presence of over-sized fission gas atoms. It therefore acts to attract vacancies and to repel gas atoms.

(iv) There is a dislocation network in the fuel that can act as a vacancy sink or a vacancy source. The equilibrium vacancy concentration is controlled by the balance of absorption and emission by gas bubbles and dislocations.

(v) The probability, p_i, of a particular bubble absorbing vacancies and gas atoms depends on the flux of vacancies to the bubble interface.

(vi) This probability is manifested as a *selective growth* mechanism whereby p_i of the bubbles grow while the remainder, in seemingly identical environments, remain static.

A bubble of radius R_i consists of n_g^i gas atoms and n_v^i vacancies. The volume occupied by a gas atom is referred to as the Van der Waal's volume, b, while that of a vacancy is Ω.

Therefore

$$V_i = \frac{4\pi R_i^3}{3} = n_g^i b + n_v^i \Omega \tag{3}$$

The increase in the number of gas atoms in an individual bubble of radius, R_i, is equal to

$$\frac{dn_g^i}{dt} = 4\pi D_f R_i C_g \tag{4}$$

while the absorption rate of vacancies is given by

$$\frac{dn_v^i}{dt} = \frac{4\pi R_i D_v C_v^{equ}}{kT} \cdot \left(P_i - \frac{2\gamma}{R_i} - \frac{4\pi \overline{R} C_B}{k_v^2} \cdot \left(\frac{\overline{PR}}{\overline{R}} - \frac{2\gamma}{\overline{R}} \right) \right) \tag{5}$$

under conditions where k_v^2 is the total vacancy sink-strength is given by

$$k_v^2 = 4\pi \overline{R} C_B + Z_v \rho_d \tag{6}$$

and $Z_v\rho_d$ is the sink-strength of the dislocation density, ρ_d. P_i is the pressure in the i'th bubble and the 'barred' parameters are averages over the population.

Under extreme vacancy starvation conditions, there are no under-pressurised bubbles so the entire bubble population acts as a vacancy sink thereby precluding *Ostwald Ripening*. As a result, all bubbles are over-pressurised to the same degree and Equation 5 reduces to

[4] This isn't strictly true because bubble growth still occurs at such a rate that the bubbles are over-pressurised but growth does occur whereas growth appears inhibited out-of-pile.

$$\frac{dn_v^i}{dt} = \frac{4\pi R_i D_v C_v^{equ} \Omega}{kT}\left\{\frac{Z_v \rho_d}{k_v^2}\right\}\cdot\left\{P_i - \frac{2\gamma}{R_i}\right\} \quad (7)$$

It is straightforward to demonstrate that the vacancy flow to cavities in a vacancy-rich medium is given by

$$\frac{dn_v^i}{dt} = \frac{4\pi R_i D_v C_v^{equ} \Omega}{kT}\cdot\left\{P_i - \frac{2\gamma}{R_i}\right\} \quad (8)$$

so, comparison of Equations 7 and 8 reveals that the effect of extreme vacancy-starvation is to reduce the vacancy diffusivity by the factor $Z_v\rho_d/k_v^2$. Since fission gas atoms migrate by a vacancy mechanism it is reasonable to suppose that the fission gas diffusion coefficient is also attenuated by the same factor.

It is proposed that the absorption probability is given by the vacancy gradient at the bubble surface since it is this gradient which drives vacancies into the interfacial region. It might be supposed that it is the vacancy concentration at the surface, which determines the absorption probability, but this is determined by the thermodynamic stability of the bubble. In addition, the probability will be decreased as the bubble over-pressure increases since this will lead to increased stresses at the interface which tends to exclude over-sized xenon atoms. Solution of the vacancy diffusion equation in the vicinity of the bubble under vacancy-starved conditions results in an absorption probability of

$$p_i = \frac{Z_v \rho_d}{k_v^2}\cdot\frac{R_c}{R_i} \quad (9)$$

where R_c is a constant of proportionality.

Figure 5 shows typical predictions for a post-irradiation anneal fast ramped to 1600°C and held for 20 minutes compared with the experimental data from the actual test. The right-hand trace shows the calculated over-pressure for the bubbles and demonstrates the validity of the assumptions leading to Equation 7.

4.3 Simplified growth model

The model described in §4.2 is too complicated and time-consuming to be used as a sub-model in a fuel modelling code with present hardware limitations. Instead, the validation of the assumption that the over-pressure is independent of bubble radius means that bubble growth can be modelled by assuming only a single bubble population of radius equal to the average radius. In this case, the absorption probability is re-interpreted as meaning that all of the bubbles absorb a fraction, p, of the incident diffusive flux of gas atoms and vacancies rather than p of them absorbing all and 1-p absorbing none. This distinction is important when considering a population of different size bubbles but irrelevant for the delta-function distribution considered here.

The critical component in the *Selective Inhibited Growth* model is the dislocation density and its relative magnitude compared to the bubble sink-strength. When $Z_v\rho_d$ is much less than

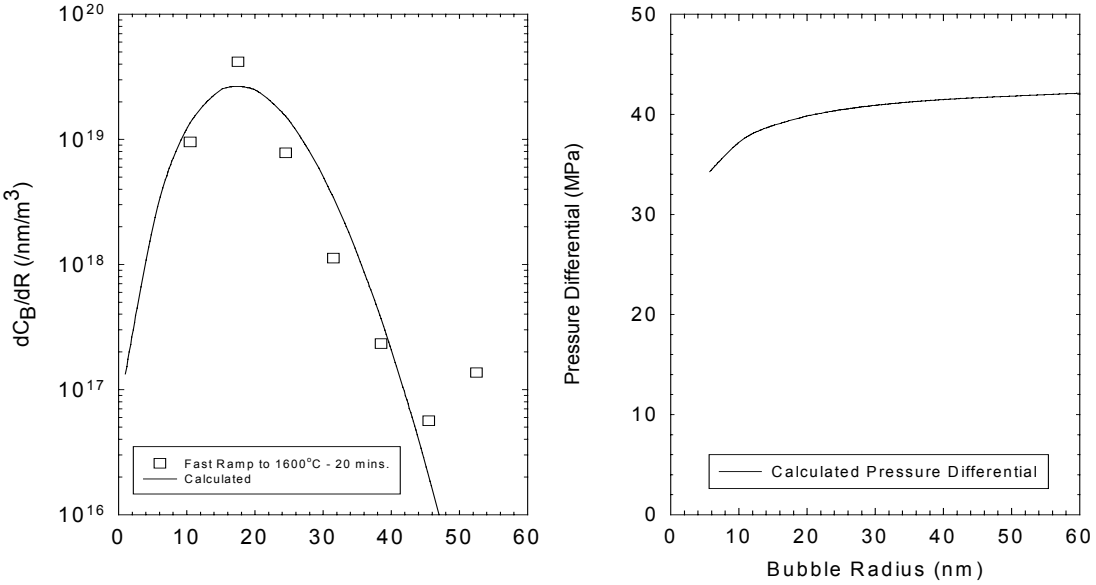

FIG. 5. Comparison of the measured bubble-size distribution of intra-granular bubbles in post-irradiation annealed fuel with predictions based on the selective inhibited growth model. The right-hand trace shows the calculated over-pressure in the bubbles.

$4\pi RC_B$, vacancy starvation will occur and bubble growth will be inhibited. In §4.1, the bubble sink-strength for a population of $3.5{\cdot}10^{20}$ m^{-3} one nanometre bubbles was calculated as $4{\cdot}10^{12}$ m^{-2} while typical measured dislocation densities in irradiated UO_2 vary from 1–$4.5{\cdot}10^{13}$ m^{-2} [17]. On this basis, the bubble growth is likely to proceed normally until a radius of around 10 nm is achieved and then vacancy starvation effects are likely to be manifested. This is in accord with the bubble size distributions which exhibit the start of the exponential tail at radii in excess of 10–15 nm - see Figures 2 and 5, for example. The predictions of the simplified model are given for two values of dislocation density in Table II below and demonstrate the sensitivity of this parameter on the swelling rates.

Note also that the swelling calculations were all performed with a single bubble concentration of $3.5{\cdot}10^{20}$ m^{-3} for all tests despite the differences in measured values. In most cases the predictions bracket the experimental measurements and there is a tendency for the larger dislocation densities to provide a better fit. The exceptions here are for the high temperature cases, particularly the longer hold cases and this may be evidence that the dislocation density in the fuel following irradiation is starting to anneal. Additional support for this is discussed below.

4.4 Fission gas release during annealing

Two particular cases are of interest here. The first concerns a ramp from 1000°C at 1°C/s to a top temperature of 1900°C followed by a rapid quench. In this case, the entire anneal was complete in under 25 minutes. The predictions of the gas release model[5] using the simplified bubble growth model are shown in Figure 6 using three separate values of the dislocation density. In this case the release was small and the predictions are equally good regardless of choice of dislocation density.

[5] The gas release model incorporates a treatment of inter-granular bubble growth and grain face venting so the total release to the boundaries is much greater than the release shown here.

TABLE II. COMPARISON OF PREDICTED AND MEASURED SWELLINGS

Case	Temp. (°C)	Radius (nm)	C_B ($x10^{20}$ m^{-3})	ΔV/V (%)		
		Measured Values			$\rho_d = 1 \cdot 10^{13}$	$\rho_d = 4.5 \cdot 10^{13}$
K2	1700	21.8 ± 3.3	0.74	0.32 ± 0.13	0.12	0.53
K3	1800	17.1 ± 3.0	2.57	0.54 ± 0.24	0.25	1.13
K4	1900	17.1 ± 1.3	5.47	1.15 ± 0.20	0.45	2.06
K5	1600	13.1 ± 1.7	3.47	0.33 ± 0.09	0.09	0.39
K6	1700	15.8 ± 1.4	4.76	0.78 ± 0.26	0.20	0.88
K7	1800	23.1 ± 3.9	3.67	1.89 ± 0.88	0.38	1.73
K8	1900	25.4 ± 8.0	3.14	2.15 ± 0.73	0.67	3.10
K9	1600	16.4 ± 1.4	5.15	0.95 ± 0.20	0.07	0.26
K10	1700	24.4 ± 2.8	2.93	1.79 ± 0.29	0.13	0.56
K11	1800	33.9 ± 4.7	1.01	1.66 ± 0.38	0.24	1.08
K12	1900	31.2 ± 3.0	1.43	1.81 ± 0.31	0.39	1.77
K13	1600	19.5 ± 2.5	4.25	1.32 ± 0.16	0.31	1.41
K14	1700	15.9 ± 1.4	7.44	1.26 ± 0.49	0.58	2.69
K15	1800	17.8 ± 1.4	7.05	1.67 ± 0.25	1.01	4.65
K17	1600	23.4 ± 4.0	2.10	1.12 ± 0.50	0.62	2.88
K18	1700	24.1 ± 5.7	2.66	1.56 ± 0.64	1.14	5.19
K19	1800	129 ± 32	0.024	2.14 ± 1.05	1.89	8.31

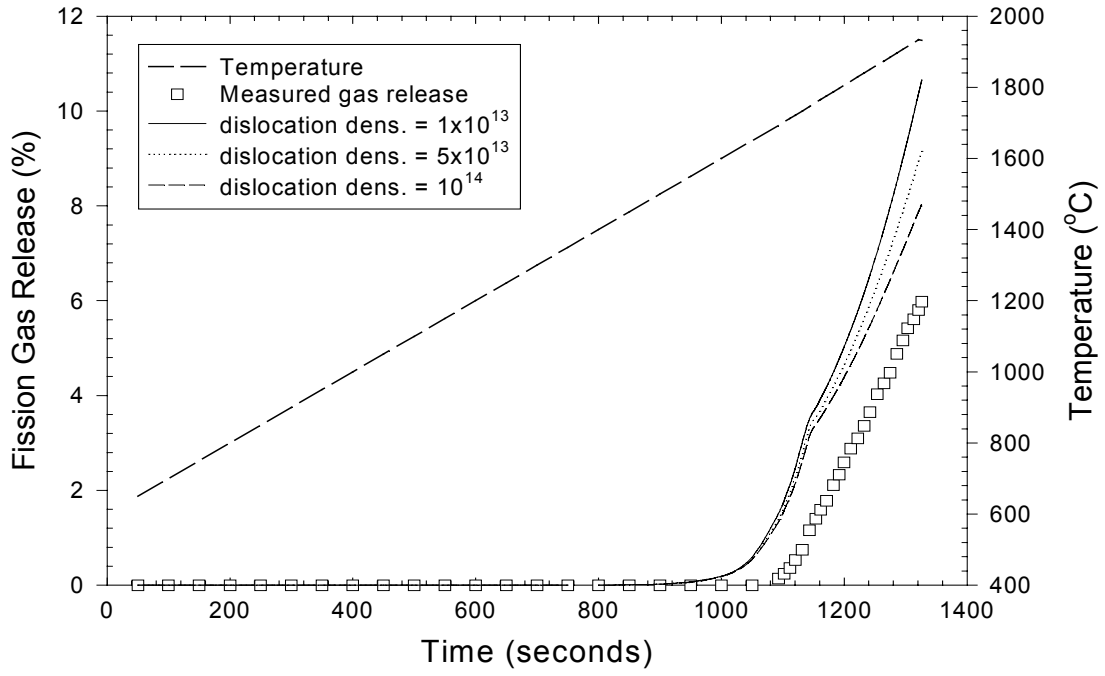

FIG. 6. Comparison of the measured fission gas release during a post-irradiation anneal with predictions for different dislocation densities.

In contrast, Figure 7 (see next page) shows the case of a much slower ramp at 0.2°C/s to 1650°C followed by a 30 hour hold at the top temperature. In this case the measured release exceeds 40% but predictions with a dislocation density of $3 \cdot 10^{13}$ m^{-2} saturate at about 20% because most of the gas has been trapped by the bubbles. Consideration of the alternative calculations suggests that it is possible that the dislocation density started at this high value and gradually annealed to a final value of around or slightly less than 10^{13} m^{-2} where the inhibition of bubble growth permits the gas release to rise to higher values.

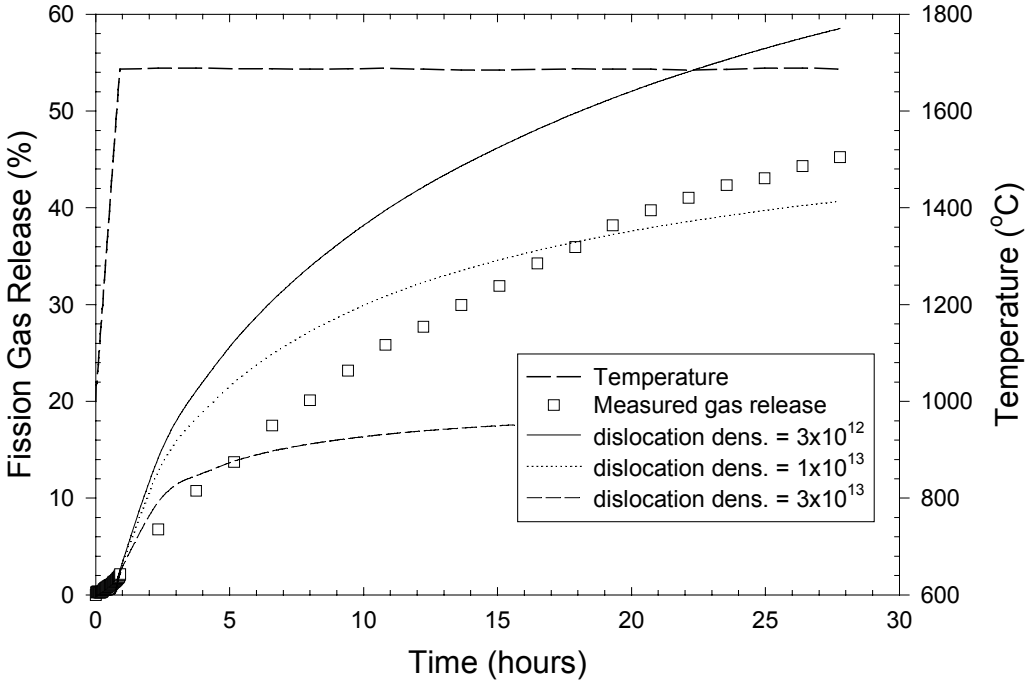

FIG. 7. Comparison of the measured fission gas release from a post-irradiation anneal held at 1700°C for thirty hours with predictions based on three different values of dislocation density. The continued increase in the release may be a result of the annealing of the dislocation density during the extended anneal.

5. CONCLUSIONS

The issue of intra-granular bubble growth in post-irradiation annealed fuel has presented an obstacle to the understanding of fission gas release for many years. Recent experiments conducted under the auspices of the IMC - see footnote in §1 - in which pre-irradiated fuel has been subjected to out-of-pile thermal annealing followed by detailed SEM of the intra-granular bubbles[6] have provided sufficient information to assist in the understanding of the growth phenomenon. The following conclusions have been drawn:

[6] Note that a full study of the inter-granular pores was also made in which over 9400 pores on 84 grain boundaries were measured and catalogued according to morphology. These data will be published at a later date.

(i) There is no evidence of intra-granular bubble loss during post-irradiation anneals and although differences exist from specimen to specimen, these are probably within the experimental scatter. The concentration of grown bubbles is around $3.5 \cdot 10^{20}$ m^{-3} which is much smaller than the concentration of nanometre sized bubbles present in low temperature irradiated fuel. It must be concluded that the grown bubbles are a small sub-population of the large low temperature seed-population.

(ii) The intra-granular bubble radii and swellings that are observed in out-of-pile anneals tend to be smaller than those observed in-pile.

(iii) The intra-granular bubble size distributions exhibit long exponential tails in which the largest bubbles are present in concentrations of four or five orders of magnitude lower than the average radius bubbles. These distributions are significantly different from those expected from a thermal re-solution mechanism. This, in conjunction with the invariance of the bubble populations during anneals is taken as evidence for lack of thermal re-solution of fission gas atoms from intra-granular bubbles.

An alternative model has been proposed to explain the slow growth of intra-granular fission gas bubbles. A detailed balance of the sources and sinks for vacancies in the fuel indicates that for most of the period of growth the intra-granular bubbles are starved of vacancies. This has two important consequences. The first is to attenuate the vacancy and fission gas diffusion rates. The second, and probably most important, is to create absorption difficulties at the matrix/bubble interface whereby a certain vacancy gradient is required to initiate absorption of vacancies and gas atoms. This mechanism operates as a selective absorption probability and, out of a large population of bubbles, a proportion may absorb gas and vacancies while the remainder may be unable to do so. This mechanism offers an explanation for the exponential tails on the distributions and for the fission gas release observed during post-irradiation anneals. The controlling parameter in this model is the dislocation density present at the end of irradiation period and the growth and release kinetics may change as this thermally anneals.

REFERENCES

[1] CORNELL, R. M., "The Growth of Fission Gas Bubbles in Irradiated Uranium Dioxide", Phil. Mag., **19** (1969) 539.

[2] TURNBULL, J. A., "The Distribution of Intra-Granular Fission Gas Bubbles in UO_2 during Irradiation.", Journal of Nuclear Materials **38** (1971) 203.

[3] BAKER, C., CORCORAN, R., DONALDSON, A. T. & WHITE, R. J., "An Investigation of Intra-Granular Fission Gas Distributions in CAGR Fuel Following Power Ramps in the Halden Reactor.", Presented at the Enlarged Halden Programme Meeting, Loen, May 1996.

[4] KILLEEN, J. C. & BAKER, C., "Fission gas release during post-irradiation annealing of UO_2 up to 1750 ^oC", Light Water Reactor Fuel Performance (Proc. ANS Topical Mtg Orlando, Florida, April 1985), vol 2, ANS (1985) 4-69.

[5] COLEMAN, P. E., ELTON, P. T. & MACINNES, D. A., "A Mechanism for Fission Gas Release from High Temperature Fuel.", UKAEA, Safety and Reliability Directorate, Report SRD R 335, April 1985.

[6] WISE, C. & TEMPEST, P. A., "Experiments on Pellet-Clad Interaction in Advanced Gas Cooled Reactor Fuel in the Halden BWR Facility.", HPR 345/25, Presented at the Enlarged Halden Programme Group Meeting, Bolkesjρ, Norway, November 1994.

[7] COPELAND, P. S. & PUNNI, J. S., "Fission Gas Release from Annealed Halden/AGR Fuel", Report AEAT-4052 Issue 1, August 1998.
[8] SPELLWARD, P., CORCORAN, R., STOOK, K. & STUMP, J., "Scanning Electron Microscopy of Annealed Halden AGR Fuel performed under IMC contract BB/G/40712 (FC/AGR/5038)", Report M/TE/EXT/REP/0107/99, Issue 1, April 1999.
[9] WHITE, R. J., CHUTER, J., GILMOUR, T. C., LIDDINGTON, M. J., MOWLES, S., STOOK, K. & STUMP, J. M., "Swelling Measurements on AGR Fuel Ramped in the Halden Reactor", Nuclear Electric Report EPD/AGR/REP/0050/96, August 1996.
[10] TURNBULL, J. A., WHITE, R. J. & WISE, C., "The diffusion coefficient for fission gas atoms in uranium dioxide", Water Reactor Fuel Element Modelling in Steady state, Transient and Accident Conditions (Proc IAEA TCM Preston, 1988), IAEA, Vienna, IWGFPT/32, (1989) 174.
[11] HAM, F. S., "The Theory of Diffusion-Limited Precipitation.", J. Phys. Chem. Solids. **6** (1958) 335.
[12] DAMASK, A. C. & DIENES, G. J., "Point Defects in Metals.", Gordon and Breach, New York, 1963.
[13] GREENWOOD, G. W., "Particle Coarsening.," Proceedings of a Conference on the Mechanisms of Phase Transformations in Crystalline Solids. Manchester. Institute of Metals, London, 1968.
[14] LIFSHITZ, I. M. & SLYOZOV, V. V., J. Phys. Chem. Solids, **19** (1961) 35.
[15] BULLOUGH, R. & PERRIN, R. C., "Growth, Stability and Interactions of Voids and Gas Bubbles in Solids", Radiation Damage in Reactor Materials, June 2-6, 1969, Volume 2, 233-251.
[16] TURNBULL, J. A., FRISKNEY, C. A., FINDLA, J. R., JOHNSON, .F A. & WALTER, A. J., "The Diffusion Coefficients of Gaseous and Volatile Species During the Irradiation of Uranium Dioxide.", Journal of Nuclear Materials. **107** (1984) 168.
[17] BAKER, C., CORCORAN, R., STOOK, K., STUMP, J. & CALLEN, V. M., "A Transmission Electron Microscope Investigation of the Effect of Power Ramps on the Precipitation of Fission Gas Bubbles in Irradiated AGR Fuel", Magnox Electric Report TE/EXT/REP/0013/96, May 1996.

PUZZLING FEATURES OF EPMA RADIAL FISSION GAS RELEASE PROFILES: THE KEY TO REALISTIC MODELLING OF FISSION GAS RELEASE UP TO ULTRA HIGH BURNUP OF 100 MWD/kg M WITH CARO-E

F. SONTHEIMER, H. LANDSKRON
Siemens AG, Unternehmensbereich KWU,
Erlangen, Germany

Abstract

Radial matrix fission gas release (FGR) profiles of UO_2 fuel measured by electron probe micro analysis usually have the shape of a bowler hat: High release in the fuel central part, low release in the rim and a continuous transition zone in between; this holds for both steady state irradiated fuel and ramped fuel. Good fission gas release models based mainly on diffusional processes are capable of describing such radial FGR profiles with the shape of a bowler. Occasionally, the bowler becomes battered: The formerly smooth transition zone between rim and center has pronounced steps and the height and width of the bowler increase (continued FGR in central part) despite decreasing temperatures at high burnup. Additionally, the rim of the bowler swings up at high burnup due to the rim effect which transports gas from the matrix to the rim bubbles. Standard diffusional FGR models are unable to describe "battered bowlers" and especially the steps in the transition zone, which also show up in the etched cross-sections of the fuel as dark double rings or even multiple rings instead of the usual single dark ring, still await theoretical explanation. For the rim, it is meanwhile well known, that saturation processes are responsible for the redistribution of the fission gas from the matrix to the rim bubbles; empirical models as for example published by Lassmann from ITU/Karlsruhe do a good job in this regard. In this paper, it is shown that saturation processes are also responsible for the steps in the transition zone sometimes seen in radial matrix fission gas release profiles of both steady state irradiated and ramped UO_2 fuel rods. Also the steadily increasing height and width of the bowler at high burnups of steady state irradiated rods, where temperatures fell so low that diffusional fission gas release in the central parts of the fuel stopped long before end of irradiation, is due to such saturation processes. These saturation processes are modeled with a concept based on Lassmann's ideas for description of the fuel rim processes using in addition measurements of fission gas saturation concentrations in UO_2 fuel published some time ago by Zimmermann (also from the former Karlsruhe nuclear fuel research center KfK, now FZK), which indicate that the saturation burnup (also called threshold burnup) and the saturation concentration in the fuel matrix decrease with increasing temperature. This new generalized model for athermal FGR by saturation processes in combination with the former diffusion model is used in the new version of CARO-E. It excellently describes even details of various "battered bowlers" type radial FGR profiles of both steady state irradiated rods with very high burnup and of ramped UO_2 fuel rods. Application to total FGR of 100 normal long UO_2 and MOX fuel rods from PWRs with burnup in the range of 44 to 100 MWd/kg M (rod average, 22 rods well above 60 MWd/kg U) gives excellent agreement of calculations and measurements and precisely describes the FGR enhancement with burnup.

1. INTRODUCTION

Ever since Siemens has performed integral fission gas release measurements, extensive microstructural investigations on the fuel, including determination of radial profiles of fission gas retention in the fuel pellets have been performed to improve the understanding and ultimately the modeling of fission gas release (FGR) processes.

One method of determining radial FGR profiles, often used on Siemens fuel, is electron probe micro analysis (EPMA), which can measure the xenon concentration in the fuel matrix in

single fuel grains. Such EPMA profiles exist both for ramped fuel of pre-irradiated fuel segments and for steady state irradiated fuel from power reactors.

These EPMA profiles sometimes exhibit puzzling features. Pertinent examples investigated in this paper comprise four ramped segments from the Studsvik Super-Ramp program (pre-irradiated at KWO for 3 and 4 cycles) and three normal long rods steady state irradiated up to 102 MWd/kg U (local pellet burnup) at KKGg.

The ramped segments show double dark rings in the etched fuel cross-section (normally, only single rings are observed), sharp release steps in the EPMA radial FGR profiles (coinciding with the double rings) and a sharp release step at the very edge of the fuel pellet in the 4-cycle rods.

The high burnup KKGg rods indicate slight steps in the EPMA profiles correlated with indications of multiple dark rings in the cross-sections, very strong release in the cold pellet shoulder and – particularly – strong release between cold rim and fuel center despite fuel temperatures far too low to account for this high matrix release by diffusional processes.

New FGR mechanisms have to be added to the standard diffusion theory to be able to describe the new features of the radial FGR profiles. It will be shown that generalized fission gas saturation effects in the fuel matrix are suited to model these new features. Moreover, these model extensions lay the basis for accurate description of FGR enhancement at high burnup up to very high burnup near 100 MWd/kg U.

This paper is based on a similar paper presented already at the Enlarged Halden Program Group Meeting in Norway, Loen, May 1999 [1]. The work is successfully extended to still higher burnup and the model of FGR by generalized saturation is described in more detail.

2. EXPERIMENTAL

2.1. Fabrication and pre-irradiation

Some relevant data for the four KWO segments and the three KKGg long UO_2 rods are given in the Table 1. Dxyz is the KWO rod number (engraved), while PKx/y is the rod designation at the Studsvik Super Ramp (SR) Project, ‘P’ standing for ‘pressurized’ and ‘K’ for ‘KWU’.

The main pre-irradiation data and ramp test data for the four segments are given in the Table II [8] and the irradiation history of the long KKGg rods is given in Table III [9].

Some important aspects of the power histories are to be pointed out.

- The axial power profile is rather flat for most part of the fuel rods; the fuel sections investigated have been taken in this region.
- The pre-irradiation power of the segments in KWO is sufficiently low to ensure negligible FGR before the ramps (<1%).
- Beyond the 3rd KKGg cycle, the calculated maximum fuel center-line temperatures in the long rods are well below 1000 °C, ensuring small FGR by diffusion later on (the calculated fuel temperatures are regarded reliable, as commented below). In cycles 8 and 9 with 140 W/cm, where FGR is still enhanced considerably, the fuel center-line temperatures are even below 900 °C and FGR by diffusion is negligible.

TABLE I. DATA FOR THE FOUR KWO SEGMENTS AND THE THREE KKGg LONG UO_2 RODS

Fuel Pin	KWO-segments D455, D453 (PK1/1&3)	KWO-segments D171, D169 (PK2/1&3)	Long KKGg rods AC01, 2301,12C3
Pellet density (%TD)	94.53	94.34	95.3,95.1,94.8
Grain size (μm)	6.0		7.0,6.5,9.1
Enrichment (%U^{235})	3.2		3.8,3.8,3.5
Stoichiometry (O/U)	2.00	5.5	2.00
Pellet diameter (mm)	9.11	3.2	9.11
Diametrical gap (μm)	200	145	190
Column length (mm)	311,310	317.4,319.0	3400
Fill gas He (bar)	22.5	22.5	22.5
Clad material	Zry	Zry	Zr alloy

TABLE II. THE MAIN PRE-IRRADIATION DATA AND RAMP TEST DATA FOR THE FOUR SEGMENTS [8]

Base irradiation at KWO						Ramp test (Studsvik SR)		
Fuel pin	Average cycle power (W/cm) cycle 1	cycle 2	cycle 3	cycle 4	Burnup (MWd/kg U)	Ramp rate (W/cm/min)	Power (W/cm)	Hold time (hrs)
D455	255	213	214	-	34	90	415	12
D453	254	217	207	-	34	85	475	12
D171	209	248	216	192	44	85	410	12
D169	207	245	218	185	44	85	490	12

TABLE III. IRRADIATION HISTORY OF THE LONG KKGG RODS [9]

KKGg-cycle	Cycle average LHGR (W/cm)	Cumulative aver. Burnup (MWd/kg U)
1	270-340	15-19
2	260-290	29-37
3	210-230	41-48
4	180-200	51-59
5	170-180	60-67
6	160-170	71-72
7	150-160	78-82
8	140	90
9	140	98

2.2. Measurements

All the fuel rods under discussion were punctured and cut after irradiation and the radial FGR profiles determined by EPMA. The EPMA radial profiles will be discussed below in comparison with the modeling. Results of the integral FGR measurements, the rim effect and the on-set radii for FGR (steps) as determined from the fuel sections cut are given in Table 4.

EPMA was carried out at the Transuranium Institute (ITU) at Karlsruhe. Radial xenon concentration profiles were obtained by point analysis at intervals of 50 to 150 μm. The local amount of retained xenon was determined from the average of six measurements at each location. The six measurements, all placed to avoid pores and cracks, were up to 50 μm apart.

The EPMA procedure gives the concentration of xenon dissolved in the fuel lattice, mainly. Practically no xenon contained in intergranular bubbles contributes to the measured xenon concentrations because the analysis is made away from the grain boundaries.

TABLE IV. RESULTS OF THE INTEGRAL FGR MEASUREMENTS, THE RIM EFFECT AND THE ON-SET RADII FOR FGR (STEPS)

Fuel pin	Pellet burnup (MWd/kg U)	Ramp power (W/cm)	Integral FGR (%)	Rim width (□m)	FGR steps 1/2/3 (relative radius)
D455	34	415	9	-	0.42/0.75
D453	34	475	22	-	0.55/0.82
D171	44	410	28	≈ 50	0.60/0.78
D169	44	490	45	≈ 50	0.70/0.85
AC01	69	-	9.2	≈ 200	≈0.50/0.65*)
2301	85	-	11.6	≈ 500	≈0.50/0.65/0.85*)
12C3	102	-	23	≈ 1150	no clear steps

*) only weakly indicated.

A distinct rim effect with a relatively broad restructured fuel shoulder is evident in the KKGg rods. The ramped segments with a burnup of 44 MWd/kg U show the beginning of a rim effect; no rim effect is seen in the ramped segments with 34 MWd/kg U burnup.

Figs. 1 and 2 show typical examples of etched fuel sections for the ramped segments and the KKGg rods, respectively. The double dark ring ("tube" in the longitudinal section) for the ramped rods and the multiple rings for the KKGg rod can be clearly seen. Earlier work has shown, that the multiple rings "grow" with burnup /2/, additional rings also being generated in the "cold" irradiation phases of the rods (later than cycle 3).

The second ring in the ramped rods (larger ring, see indications in Fig.1) is an effect of the power ramps, because almost no FGR occurred before during pre-irradiation. The distance between the outer ring and the inner ring corresponds to the extension of the FGR steps seen in the EPMA profiles. It is bigger for the lower burnup rod in agreement with the FGR profiles shown below (see Figs.7 to 10). It will become clear below, that the larger dark ring in the ramped fuel is also clearly outside the "diffusional region" in these rods, in an area, which did not release significant amounts of fission gas by diffusion.

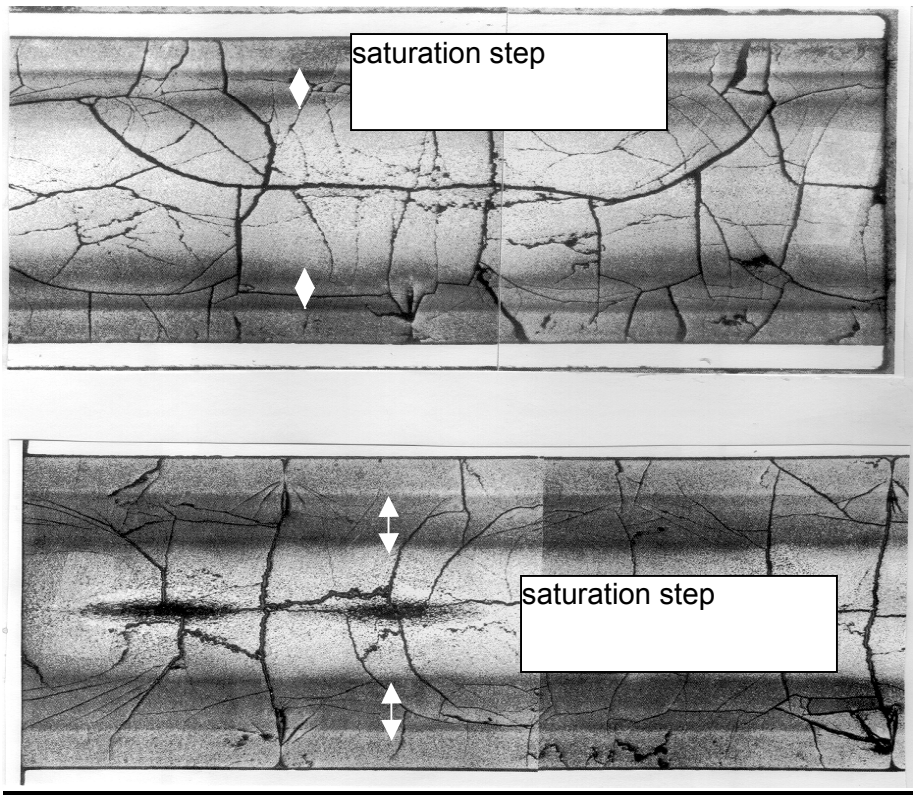

FIG. 1. Sections of rods rods PK1/2 (bottom, 34 MWd/kg U) ramped to 440 W/cm and PK2/2 (top, 44MWd/kg U) ramped to 460 W/cm. The rods are sister segments to PK1/1&3 and PK2/1&3 analysed in the paper.

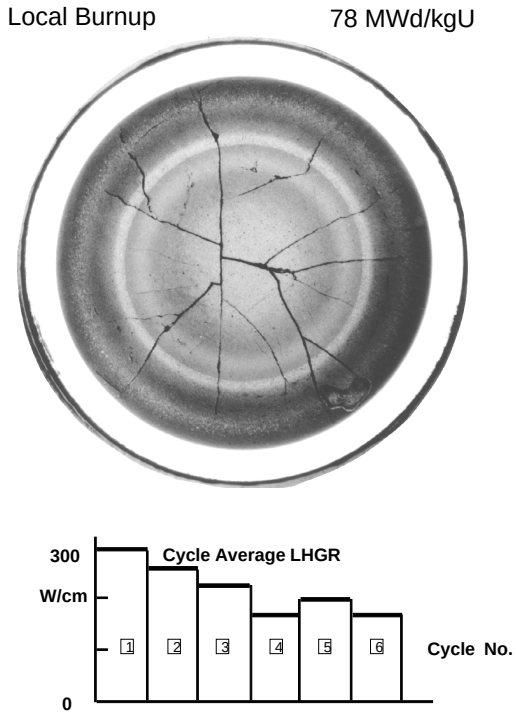

FIG. 2. Typical cross-section of a KKGg rod irradiated to 78 MWd/kg U.

3. WHAT POINTS TO SATURATION EFFECTS?

The key idea in the search for a common explanation of the puzzling features in the ramped fuel and the steady state irradiated fuel is that "there is distinct FGR seen in regions of the fuel, which are too cold for relevant diffusional contributions to FGR, both at steady state irradiation and at ramps".

This is absolutely clear and meanwhile well known for the fuel pellet rim, where temperatures are well below 500 to 700°C throughout irradiation and many measurements have shown that beyond a certain local pellet edge burnup (65–70 MWd/kg U), the matrix concentration of the retained fission gas is asymptotically lowered down to an equilibrium concentration value around 0.25 weight per cent. Meanwhile an empirical model exists /3/, which describes the concentration as a function of local pellet edge burnup very well. A comparison of measurements and the model is shown in Fig.3.

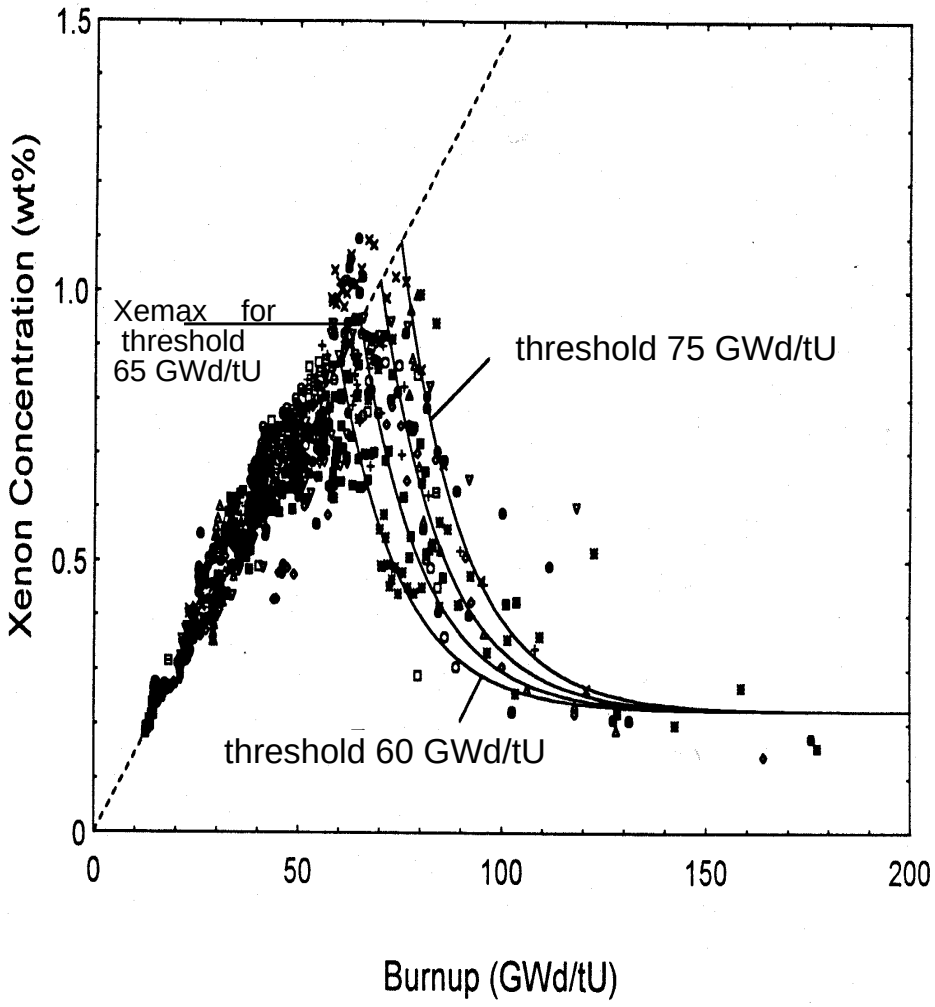

Fig. 3: Xenon concentration measured at ITU in the fuel pellet rim. Solid curves: Lassmann model [3].

Measurements on MOX fuel have clearly shown, that an analogous saturation effect is also operable in higher enriched MOX fuel particles [4], which reach very high burnup already early in irradiation (due to the high enrichment with fissionable plutonium). MOX particles at positions throughout the pellet cross-section reach a constant xenon concentration near 0.25 w/o (!) – not only at the cold pellet edge – but also in the hotter central fuel parts, and the saturation concentration seems to decrease somewhat with fuel temperature towards fuel center.

Early extensive measurements of Zimmermann on isothermally irradiated fuel [5] clearly show that there generally exists a temperature dependent equilibrium concentration for xenon in UO_2 fuel for burnups above about 30 MWd/kg U. Some of these results are shown in Fig. 4. It is recognized, that these equilibrium concentrations are in the same order of magnitude range as the saturation concentration seen in high burnup fuel rim and MOX particles. Below, the temperature dependent equilibrium concentrations of Zimmermann will be used in the Lassmann formulation as temperature dependent asymptotic equilibrium Xe concentrations (high burnup level in the right side of Fig.3 becomes temperature dependent).

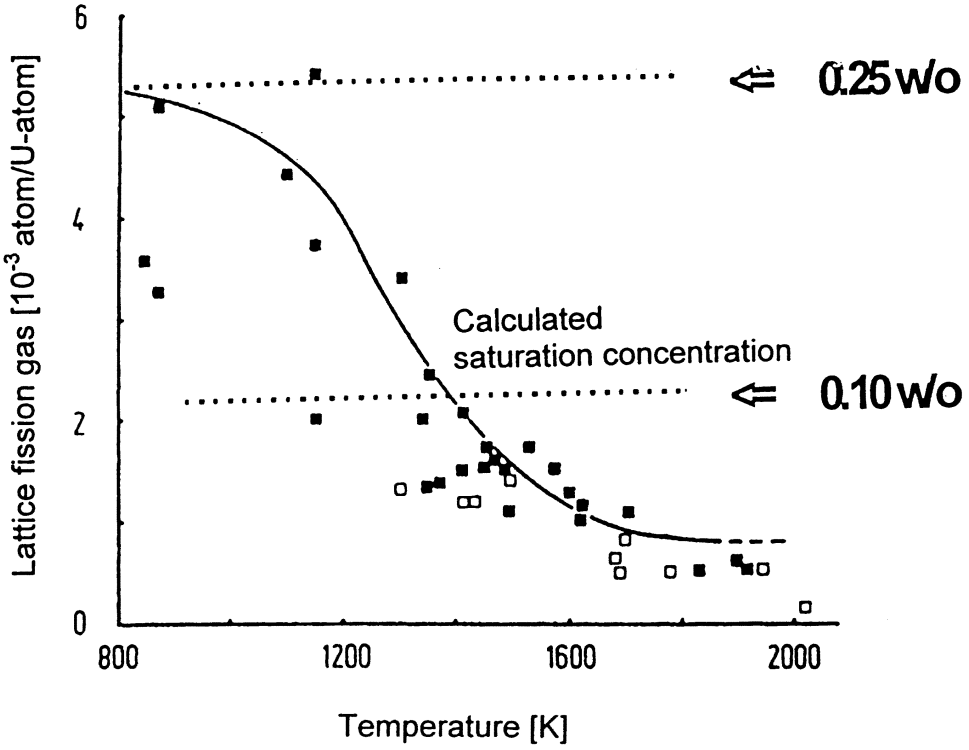

FIG. 4. Concentration of lattice fission gases in UO_2 calculated for burnup higher than 30 MWd/kg U [5]:

- ❑ *without fuel-cladding contact,*
- ■ *with fuel-cladding contact.*

Could a saturation effect also be responsible for the continuing FGR from cold central parts of high burnup fuel and for release steps in ramped fuel outside the "diffusional region"? Clearly, saturation concepts are not generally compatible with diffusion theory, except for the very specific situation of equal rates of fission gas generation and diffusional release at specific temperatures and powers. This makes a new modeling concept, where saturation effects are combined with diffusion theory worthwhile, as demonstrated next.

4. ANALYSIS

4.1. CARO-E high burnup features

An advanced version of the present Siemens fuel rod analysis and design code CARO-E is used for the FGR profile analysis. As FGR profiles of fuel up to a local pellet burnup of 102 MWd/kg U are regarded, it is important to have the relevant known high burnup features modeled in the code and be sure to calculate realistic radial fuel temperature and burnup profiles. A realistic FGR model concerning the hitherto well-known thermal (diffusional) and athermal release processes is also required.

4.1.1. Fuel thermal conductivity (ftc) degradation with burnup

A new ftc correlation for UO_2, $(U,Gd)O_2$ and MOX fuel is implemented in CARO-E, which is based on the relaxation-time theory of Klemens [6,7,10]. The correlation is chosen because of its validity in a wide range of defect concentrations as for instance encountered in fuel with a wide range of burnup, gadolinia additions and Pu content. The phonon term in this new ftc correlation has an arctan form, which for low defect concentrations (e.g. low burnup) is identical with the classical hyperbolic term. For high defect concentrations, this term saturates, reducing the progression of the ftc degradation at e.g. high burnup.

The new ftc correlation has been fitted to fuel temperature measurements in a wide range of burnup and gadolinia additions. Many of these measurements have been performed at Halden.

4.1.2. High burnup rim porosity

A burnup dependent porosity correlation is used in CARO-E, which is fitted to own measurements of the rim porosity of Siemens fuel from power reactors [10]. At very high burnups, the rim porosity increases to about 20% at the pellet edge and has a relevant influence on fuel temperature. In the pellet central parts, where thermal processes are active, no rim porosity exists.

Fig. 5 shows the separated effects of ftc degradation with burnup and the rim porosity, respectively, on the fuel center-line temperature calculated with CARO-E at a linear power of 250 W/cm. While the temperature increase due to ftc degradation with burnup is operative over the entire burnup range (the asymptotic behavior reflects the ftc degradation saturation at high defect concentrations), the rim porosity effect is relevant above about 50 MWd/kg U only.

4.1.3. New radial power profiles

Correct radial profiles of power and burnup are prerequisite to reliable calculations of radial dependencies of ftc and porosity profiles in order to get realistic radial temperature distributions. The burnup profile also directly determines the fission gas generated.

The new power profiles were generated with a modern neutronic Siemens code using a one-dimensional collision-probability method with burnup. The results were validated against

various measurements of radial fission product distributions. Especially the strongly enhanced burnup at the pellet edge due to U238 conversion to fissionable Pu is well described [11].

4.1.4. A mechanistic FGR model

The mechanistic FGR model in CARO-E is based on the concept that FGR occurs in two steps. In the first step fission gas diffuses from the grain matrix to the grain boundaries (Booth model). Fission gas is stored at the grain boundaries and is released from there to the void volume of the fuel rod in a second step. Parallel to this thermally activated basic process, also the release processes due to grain growth and athermal release mechanisms are described. The FGR model in CARO-E is well validated concerning the dependence on fuel temperature and micro structure. A major improvement of the burnup dependence is achieved by introducing saturation effects into the model, as described in the next chapter.

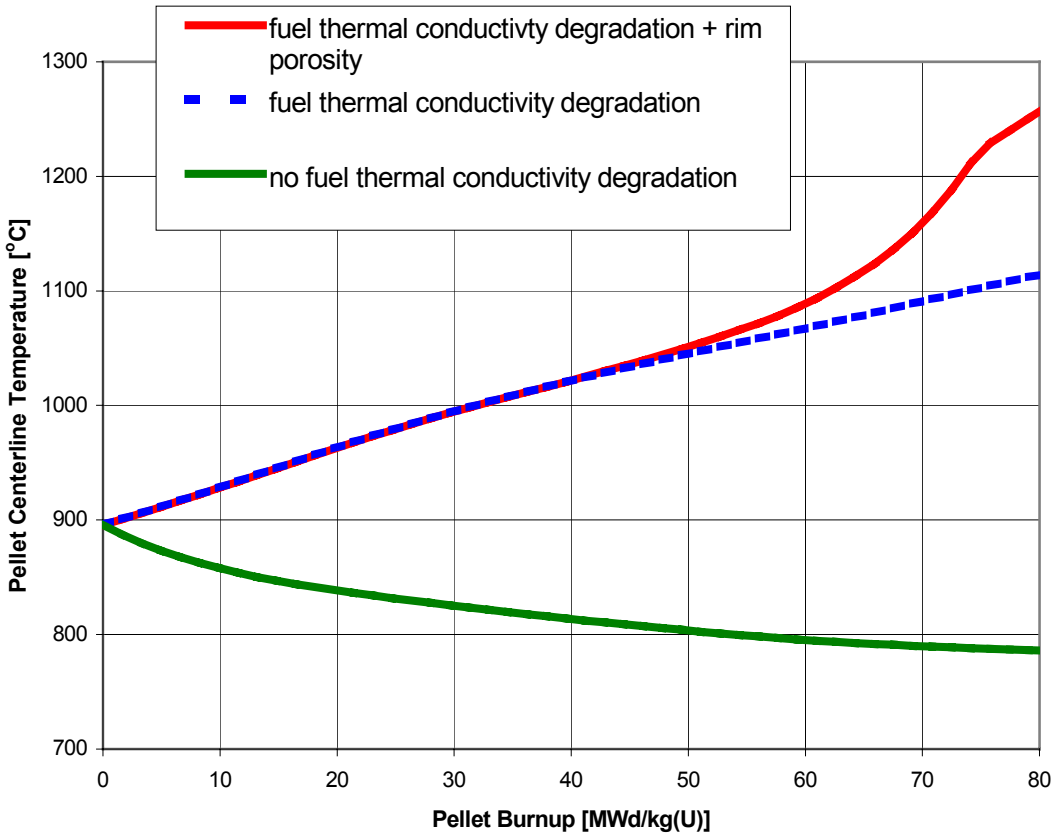

Fig. 5. Fuel center-line temperature for a PWR rod (18 × 18) as a function of burnup with and without fuel thermal conductivity degradation and rim porosity effect for a linear power of 250 W/cm.

4.2. Extension of the CARO-E FGR model

4.2.1. Gas release from the matrix

The basis for this extension is the rim model already mentioned above [3]. That model assumes a xenon loss term from the fuel matrix to pores, which is proportional to the xenon (Xe) concentration,

$$\frac{dXe(BU)}{dBU} = -a \cdot Xe(BU) + cr_{Xe}$$

where cr_{Xe} is the Xe creation rate (constant Xe creation per unit burnup) and a is a fitting constant. An integration over burnup gives the matrix concentration as a function of burnup ("Lassmann formula"):

$$Xe(BU) = cr_{Xe} \cdot \left[\frac{1}{a} + \left(BU_0 - \frac{1}{a} \right) \cdot \exp(-a \cdot (BU - BU_0)) \right] \quad for \quad BU > BU_0$$

and

$$Xe(BU) = cr_{Xe} \cdot BU \quad for \quad BU \le BU_0$$

At a threshold burnup BU_0 the fuel matrix concentration of Xe reaches its maximum possible value and for higher burnups the Xe concentration continuously goes down to an equilibrium value $Xe_{BU\to\infty} = cr_{Xe} / a$ (Fig.3). In the original Lassmann rim model, BU_0 is a constant (set to 68 MWd/kg U in CARO-E) as well as $Xe_{BU\to\infty}$ (0.25 weight per cent).

On the basis of what was said in chapter 3 concerning general effects of saturation of the fuel matrix with fission gases, the above model, originally devised for the cold fuel rim only, is now extended to all parts of the fuel by replacing the original constants BU_0 and $Xe_{BU\to\infty}$ by temperature functions $BU_0(T)$ and $Xe_{BU\to\infty}(T)$; T = local fuel temperature.

The temperature function $Xe_{BU\to\infty}(T)$ is taken from the measurements of equilibrium concentrations (Fig. 4) given by Zimmermann [5]. In CARO-E, a rough envelope of these measurements is used, taking 0.25 w/o below 1200 K, 0.1 w/o above 1750 K and a linear function in-between.

Zimmermann's measurements already indicate, that the threshold burnup $BU_0(T)$ can be as low as 30 MWd/kg U. The complete temperature function is determined from the EPMA radial FGR profiles introduced in chapter 2 above (see also Figs 7 to 13 in the next chapter), as follows:

The marked features of the ramped rods' FGR profiles PK1/1&3 and PK2/1&3 are the release steps in the relative radius range 0.4 to 0.8. If they are interpreted as saturation effects then the step on-set points directly deliver 4 points on the $BU_0(T)$ curve (one point for each rod).
Within a relatively small temperature interval, the saturation concentration then goes down when we reach the plateau of the steps, indicating the existence of a minimum value of $BU_0(T)$; thereby the difference between 100% release and the plateau corresponds to the Xe saturation concentration Xe(BU) using the minimum value of $BU_0(T)$ in the Lassmann formula above (the saturation concentration Xe(BU) at a specific temperature and burnup is not to be confused with the equilibrium saturation concentration $Xe_{BU\to\infty}(T)$!). We will soon see, that this minimum value is very consistently in the range of 29 to 33 MWd/kg U. This minimum value directly explains that the plateaus are more than twice as high for the 44 MWd/kg U rods PK2/1&3 compared to the 34 MWd/kg U rods PK1/1&3, by simply inserting the local radial burnup and the minimum value into Lassmann's formula above

(taking into account the temperature dependence of the equilibrium saturation concentration, which, however, has only a small influence).

Also the FGR profiles of the steady-state irradiated KKGg rods AC01, 2301 and 12C3 can be used to gain points for the $BU_0(T)$ curve, due to the fact that the profiles in the central pellet parts strongly evolve due to the saturation effects in the burnup region covered (69 to 102 MWd/kg U). The edge at radius 0.6 in AC01 (bottom in Figs 11-12) gives the temperature, where the threshold burnup starts to decrease below 68 MWd/kg U and the local burnup and temperature in the pellet centers yield further points for $BU_0(T)$ (insert EOL burnup and temperature at specific radial position into Lassmann's formula).

Fig. 5 shows the results together with the function $BU_0(T)$ used in CARO-E (exponential between 975 K and 1257 K). The points gained from the measured FGR profiles are surprisingly consistent, with only little scatter in view of the very different conditions met in the power ramps compared to the completely different steady-state long-term irradiation in KKGg up to ultra high burnup.

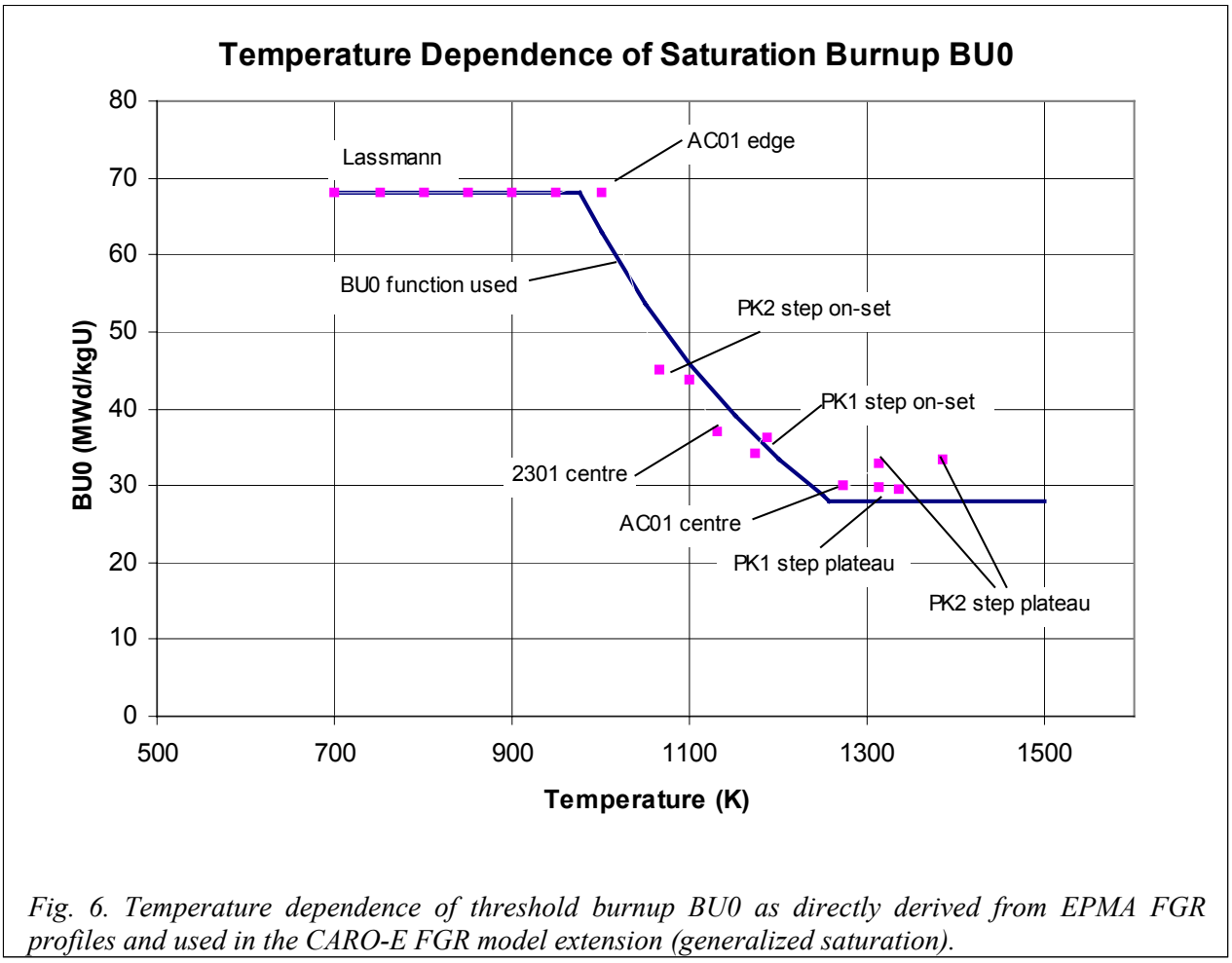

Fig. 6. Temperature dependence of threshold burnup BU0 as directly derived from EPMA FGR profiles and used in the CARO-E FGR model extension (generalized saturation).

Extending the Lassmann formula in CARO-E by the use of $BU_0(T)$ and $Xe_{BU\to\infty}(T)$ as derived above in combination with the Booth model gives an excellent prediction of the measured FGR profiles and the FGR burnup enhancement, as will be shown below. A model which can reduce seemingly different effects found in very different situations to one phenomenon gains credibility. That is why the generalized saturation effects we claim to see in fuel irradiated both in transient and stationary conditions are most likely real and believed to be adequately described by the Lassmann formalism with temperature dependent threshold burnup $BU_0(T)$ and equilibrium saturation Xe concentration $Xe_{BU\to\infty}(T)$.

4.2.2. Gas release paths after generalized saturation of the matrix

The fission gas released by generalized saturation effects from the fuel matrix follows various paths, depending on the fuel structure and temperature at a specific radial pellet position.

In the **cold fuel rim** it is mainly stored in largely isolated rim bubbles (rim porosity). In CARO-E, in accordance with most literature data, 80% of the gas released from the matrix by saturation are kept in the rim bubbles and only 20% are released to grain boundaries which can eventually be depleted to the rod void volume.

In the **hotter restructured central fuel pellet parts**, the "saturation gas" from the matrix is partly directly swept to grain boundaries and intergranular porosity (partly interlinked), which had been formed previously by thermal diffusion processes, and partly also to new rim-like, partly isolated bubbles. PIE at different burnups was used to assess the relative fractions of gas going to new rim-like bubbles and "old" intergranular porosity/grain boundaries, respectively. In CARO-E, the relative fractions of matrix saturation gas going to rim-like bubbles and to grain boundaries/intergranular porosity is governed by an exponential function of burnup.

The saturation gas reaching the grain boundaries and the intergranular porosity is treated exactly like the gas released by diffusional processes: the release to the void volume is depending on interlinkage and local temperature. That is why – in contrast to the saturation effect in the cold pellet rim – the saturation effect in the central parts of the fuel pellet considerably contributes, or even mainly determines the FGR enhancement with burnup.

5. COMPARISON OF CALCULATED AND MEASURED RADIAL FGR PROFILES

5.1.1. Profiles of ramped rods PK1/1 and PK1/3 with 34 MWd/kg U

As summarized in the table above, the segments had been pre-irradiated to 34 MWd/kg U in KWO and then been ramped for 12 hours to 415 W/cm and 475 W/cm respectively in the R2 Studsvik in the frame of the Super Ramp Project.

The EPMA radial FGR profiles measured are compared to the calculated profiles in Fig. 7 and Fig. 8. The striking feature in both cases is the sharp release step at a large relative radius (outer dark ring in the etched cross-sections, see Fig.1 bottom), which marks nearly the same temperature in the steep temperature gradient in both segments. The step stretches from radius 0.75 to 0.42 with a plateau at ≈22 % in PK1/1 (low ramp power) and from 0.82 to 0.55 with a plateau at ≈25 % in PK1/3 (high ramp power).

The on-sets and the height of the steps (plateaus) deliver a set of 4 points for the temperature function of the threshold burnup $BU_0(T)$ used in the extended CARO-E FGR model, as explained above (Fig.5).

Without the saturation effect extension of the FGR model, only the "body" of the profiles is well described by the calculation (dashed lines, old CARO-E FGR model). This body, which makes up most of the release, is obviously the diffusional part of the FGR profile; the release steps are clearly outside this diffusional range. Both the body and the saturation steps are rather well described by the extended FGR model despite a slight bias concerning on-set and depth of the release steps (continuous lines).

It should also be noted, that no matrix release is calculated at the pellet edge by the extended FGR model, in agreement with the observations (not yet any rim effect in the cold rim at a pellet burnup of 34 MWd/kg U).

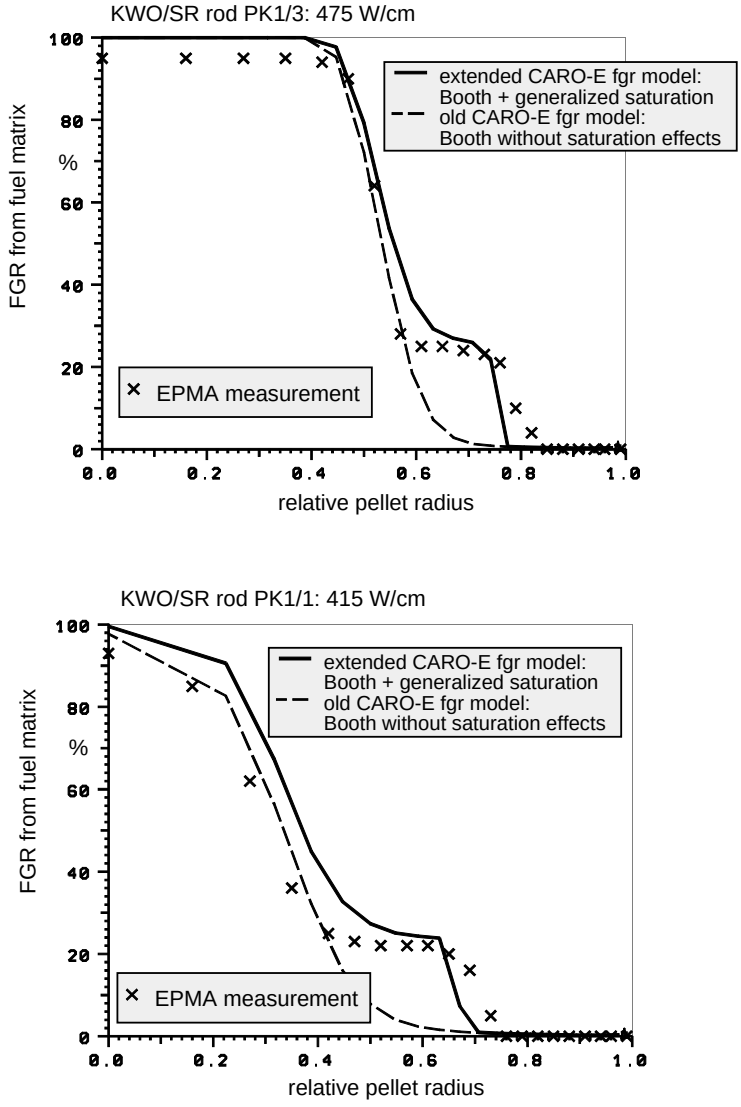

FIGs 7 and 8. Pellet radial Xe release profiles (matrix) calculated with CARO-E for two ramped rods with a burnup of 34 MWd/kg U in comparison to measurements.

5.2.Profiles of ramped rods PK2/1 and PK2/3 with 44 MWd/kg U

These segments with a similar design as the previous segments had been pre-irradiated to 44 MWd/kg U in KWO and then been ramped for 12 hours to 410 W/cm and 490 W/cm respectively in the SR Project.

The EPMA radial FGR profiles measured are compared to the calculated profiles in Fig. 9 and Fig. 10. Again the release step is evident in both segments (outer dark ring in the etched cross-sections, see Fig. 1 top), although quite different in height and extent. Also the on-set has moved further out (lower temperature) compared to the lower burnup segments above, as would be expected from higher burnup/earlier saturation. The step stretches from radius 0.78 to 0.60 with a plateau at ≈52 % in PK2/1 (low ramp power) and from 0.85 to 0.70 with a plateau at ≈54 % in PK2/3 (high ramp power).

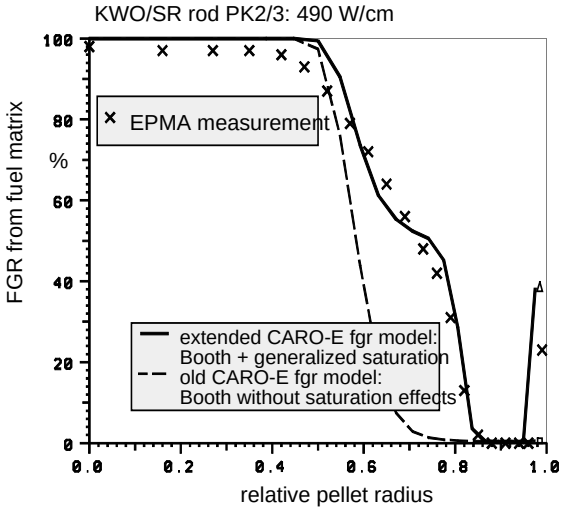

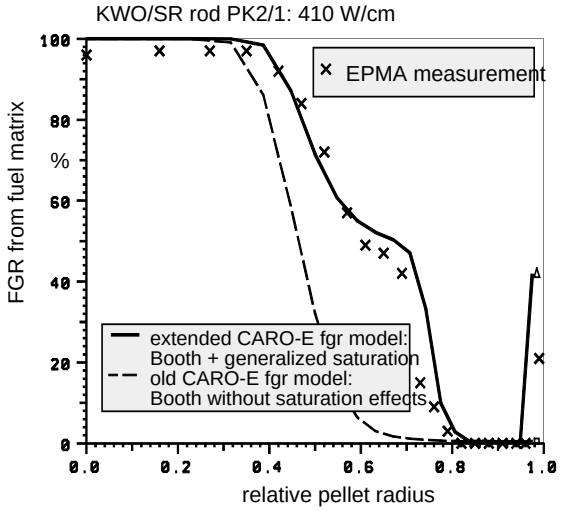

FIGs 9 and 10. Pellet radial Xe release profiles (matrix) calculated with CARO-E for two ramped KWO rods with a burnup of 44 MWd/kg U in comparison to measurements.

The on-sets (lying again at similar temperatures for both segments) and the height of the steps (plateaus) deliver another set of 4 points for the temperature function of the threshold burnup $BU_0(T)$ used in the extended CARO-E FGR model, as explained above (Fig. 6). It should again be pointed out, that the higher plateaus of the PK2 rods are a consequence of the higher burnup of 44 MWd/kg U versus 34 MWd/kg U for the PK1 rods, giving a larger distance to the minimum threshold burnup $BU_0(1257K)$ = 28 MWd/kg U used in CARO-E and hence a lower Xe saturation concentration Xe(BU) in the plateau.

Again, only the extended FGR model is able to describe the measured profiles. The different on-set, height and extent of the saturation steps in the higher burnup segments are rather well described. The difference between the "purely diffusional" and the extended model (dashed lines versus continuous lines) is however much bigger than for the lower burnup segments. This is a consequence of the second part of the generalized saturation effect, namely the decrease of the equilibrium saturation concentration $Xe_{BU\to\infty}(T)$ with temperature.

Starting Xe depletion is observed in the 44 MWd/kg U segments at the pellet edge, indicating the on-set of the rim effect in the cold rim at this burnup, which is also described by our extended FGR model.

5.2.1. Profiles of steady state irradiated KKGg rods AC01, 2301 and 12C3

These normal long rods had been irradiated in KKGg to burnups reaching locally 69 MWd/kg U (AC01), 85 MWd/kg U (2301) and 102 MWd/kg U (12C3). The PIE on these rods has been discussed earlier [2, 9].

The measured and calculated EPMA radial FGR profiles are shown in Figs 11-13. Great differences to the PK segments are obvious:

— The matrix release in the fuel rim is much stronger, and from 69 to 102 MWd/kg U the rim release still evolves strongly, eventually merging with the release from the central pellet parts to an overall pellet release between 80% and 90%.

— Only a rather small fraction of the overall matrix release is due to diffusion processes (compare area below dashed line to area below continuous line).

— While the profile of rod AC01 still bears some resemblance with the PK profiles (central depletion, cold shoulder without release and rim), the profile of rod 2301 is characterized by a strong release all over the pellet cross-section, and even more so in rod 12C3 with a nearly uniform high release between 80% and 90%.

— Release steps in the center are hard to discern; indications are only seen in rod AC01 (especially in the center).

In view of the large differences of these profiles to those from the ramped rods, the totally different history of profile formation ("instantaneous" formation during the PK ramps versus formation in years of irradiation in AC01, 2301 and 12C3) and the dramatic evolution of the steady state profiles in a burnup interval of only 16 MWd/kg U (from AC01 to 2301) and still

further in a burnup interval of 17 MWd/kg U (from 2301 to 12C3), the agreement between measurements and calculation is excellent. Except for the weakly indicated steps in AC01, all important profile features listed above, are described by the extended FGR model, while diffusion theory alone is completely unable to explain the features observed (continuous lines versus dashed lines).

The small diffusional contribution to the overall release from the matrix might look like a calculation error, either due to too low calculated fuel temperatures or too low fission gas diffusion coefficients, or both. However, the good agreement between the calculated and measured diffusional contribution to the overall release in a wide temperature range is well verified by the large over-all data base of CARO-E and does not allow such a conclusion.

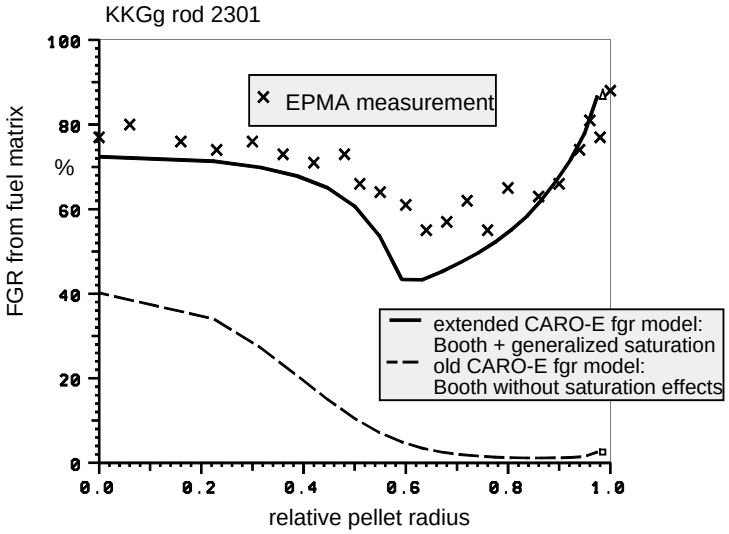

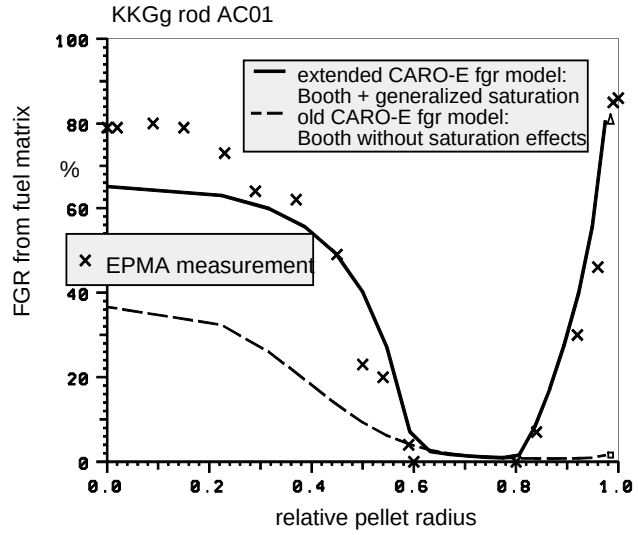

FIGs. 11 and 12. Pellet radial Xe release profiles (matrix) calculated with CARO-E for two KKGg rods with burnups of 69 MWd/kg U (AC01, bottom) and 85 MWd/kg U (2301, top) in comparison to measurements.

As for the PK profiles, the high variability of the steady state profiles helps in fixing the temperature functions $BU_0(T)$ and $Xe_{BU\to\infty}(T)$ (of course, identical functions are used for the ramped and the steady state irradiated rods!). While in the cold rim region, good agreement between calculation and measurement is reached for BU_0 = 68 MWd/kg U and an equilibrium Xe concentration of 0.25 weight per cent, the strong difference between the diffusional release and the measured release in the fuel central parts dictates decreasing equilibrium Xe concentrations and decreasing threshold burnups beyond a certain temperature, as described above and shown in Figs .4 and 6 (use of the measured Xe concentrations, radial local burnups, temperatures and the Lassmann formula).

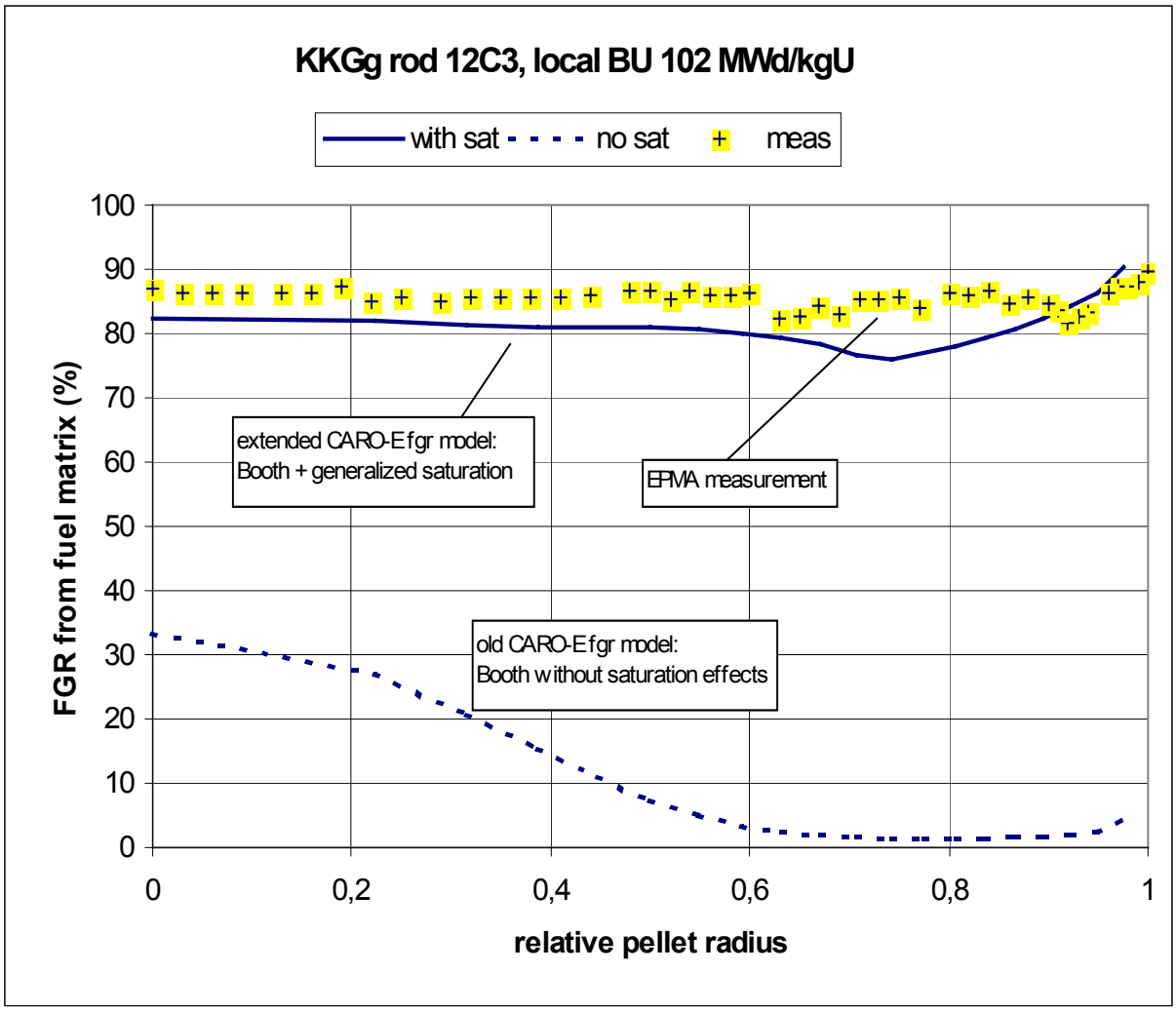

FIG. 13. Pellet radial Xe release profile (matrix) calculated with CARO-E for the KKGg rod 12C3 with the highest available burnup of 102 MWd/kg U (pellet) in comparison to the EPMA measurement

.

6. CALCULATION OF KWU HIGH BURNUP PWR FGR DATABASE

At present, the KWU data base comprises 316 rods with 100 PWR fuel rods in the high burnup range 44 to 98 MWd/kg U (rod average burnup), 22 rods thereof above 60 MWd/kg U and several rods in the range 70 to 98 MWd/kg U. Most of the rods are from various power reactors (normal long rods) with various designs, but also ramp tested fuel is included. Moreover, also some MOX fuel rods are in this high burnup range.

The comparison of the measured and calculated FGR to the fuel rod void volumes is shown in Fig. 14. This plot contains also the rods with radial FGR profiles discussed above. The agreement between calculation and measurements is very satisfactory. It is worth pointing out that also the long PWR power reactor rods with a burnup of near 90 and 98 MWd/kg U and a high steady state release above 20% (accentuated in the plot) are well calculated. This means that the new extended FGR model describes the burnup enhancement of the FGR very well, which is visualized in Fig. 15, where measured and calculated FGR values of the steady-state irradiated rods are plotted linearly against the rod average burnup.

7. CONCLUSIONS

Successful calculation of puzzling features in radial matrix FGR profiles of ramped and steady state irradiated fuel with medium and very high burnup was achieved by the introduction of generalized saturation mechanisms into the former diffusional FGR model in CARO-E. The saturation mechanisms can be very accurately modeled using an extension of the formalism originally devised for the cold fuel pellet rim by Lassmann [3].

Saturation effects can play a role already at relatively low burnup near 30 MWd/kg U, provided the fuel temperatures are high enough. For short enough hold times at ramp power, these effects can become visible as steps in radial FGR profiles of ramped fuel; normally however, the major release fraction due to power ramps still stems from diffusional processes.

In steady state irradiated fuel, steps in radial FGR profiles may also be indicative of saturation processes. A clearer hint to saturation processes comes from FGR enhancement with burnup despite falling powers and temperatures too low to produce enough FGR by diffusional processes.

From the on-set and the height of the steps seen in ramped fuel FGR profiles and the depth and width of the FGR profiles of the steady-state high burnup rods, the temperature dependence of the threshold burnup $BU_0(T)$ can be derived very consistently: An exponential drop of $BU_0(T)$ from 68 MWd/kg U to 28 MWd/kg U in the temperature interval of 975 to 1257 K, as used in CARO-E, is a good approximation.

The temperature dependence of the equilibrium Xe saturation concentration $Xe_{BU\to\infty}(T)$ can be taken directly from measurements of equilibrium concentrations at isothermal irradiation made long ago by Zimmermann [5]. An envelope of these measurements, as taken for CARO-E, gives a linear decrease of the equilibrium saturation concentration between 1200 K and 1750 K. This means, that its influence on FGR is at higher temperatures compared to the influence of the threshold burnup BU0.

As already found in previous work, the FGR enhancement, which occurs even for falling power histories with low fuel temperatures over much of the irradiation history, mainly stems from central parts of the fuel pellets and – if at all – only to a small extent from the restructured pellet rim [2]. Our modeling is in agreement with these observations: In the cold rim 80% of the matrix release by saturation is contained in the rim porosity, whereas the saturation processes working also in the hotter part of the fuel pellet are coupled to the rod void volumes, mainly by pre-formed intergranular bubble interlinkage. The latter processes

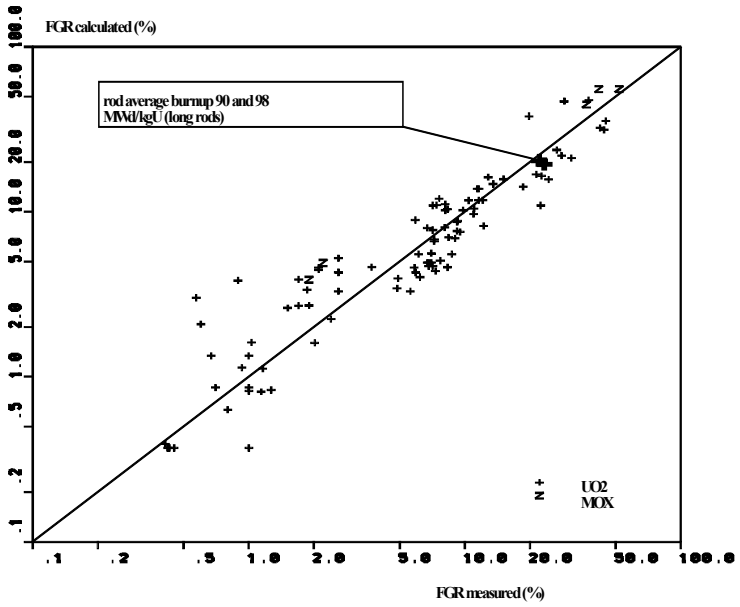

FIG. 14. Calculated versus measured FGR to rod void volume for burnups between 44 and 98 MWd/kg U (100 rods).

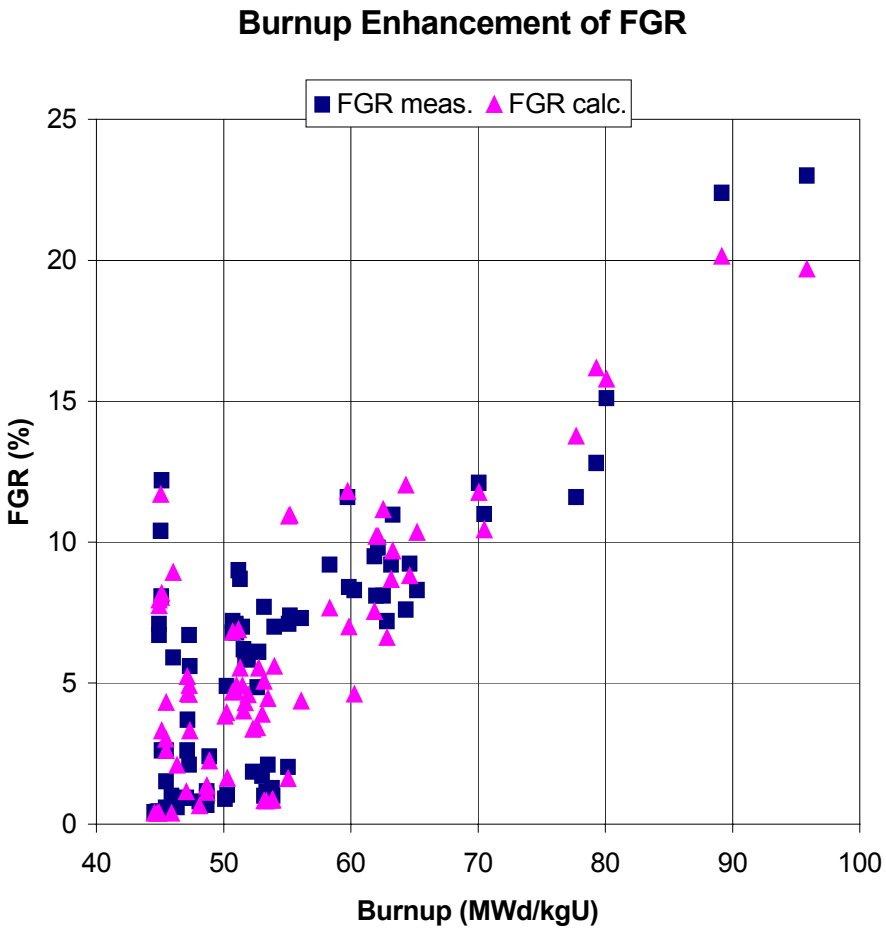

FIG. 15. FGR burnup enhancement above 44 MWd/kg U: Measurements (steady-state irradiation) and calculations with CARO-E with extended FGR model (generalized saturation).

are thus indispensable for a realistic description of the FGR enhancement with burnup; they are the key high burnup features in the new FGR model of CARO-E.

A realistic description of the high burnup FGR enhancement with CARO-E containing the new extended FGR model is proved by successful application of the code to a large data base with high average rod burnup up to 98 MWd/kg U (102 MWd/kg U pellet burnup). This provides a sound basis for the mechanical design of high burnup and very high burnup fuel rods concerning rod inner pressure.

REFERENCES

[1] SONTHEIMER, F., LANDSKRON, H., "Puzzling features of EPMA radial fission gas release profiles: The key to realistic modeling of fission gas release up to ultra high burnup", EHPGM in Loen, Norway, May 1999.

[2] MANZEL, R., COQUERELLE, M., "Fission gas release and pellet structure at extended burnup", LWR Fuel Performance (Proc. Int. Topical Mtg Portland, March1997), ANS (1997) 463.

[3] LASSMANN, K., et al, "Modeling of the high burnup UO_2 structure in LWR fuel", Journal of Nuclear Materials **226** (1995) 1-8.

[4] WALKER, C.T., et al, "Effect of inhomogeneity on the level of fission gas and caesium release from OCOM MOX fuel during irradiation", Journal of Nuclear Materials **228** (1996) 8-17.

[5] ZIMMERMANN, H., KFK Rep. 2467 (June 1977).

[6] SONTHEIMER, F., LANDSKRON, H., BILLAUX, M.R., "A fuel thermal conductivity correlation based on the latest experimental results", Thermal Performance of High Burn-Up LWR Fuel (Proc. CEA-NEA/OECD-IAEa Int. Seminar Cadarache, France 3-6 March 1998), OECD/NEA (1998) 119.

[7] LANDSKRON, H., SONTHEIMER, F., BILLAUX, M.R., "A uniform fuel thermal conductivity correlation for UO_2 and gadolinia fuel - comparison with Halden data for thermal conductivity and other experimental results", EHPGM Lillehammer, March 1998.

[8] Final Report of the Super-Ramp Project, Seved Djurle, STUDSVIK-STSR-33, Dec. 1984

[9] MANZEL, R., WALKER, C.T., "High burnup fuel microstructure and its effect on fuel rod performance", LWR Fuel Performance (Proc. Int. Topical Mtg Park City, Utah, 2000, ANS (2000) 604.

[10] M.R.BILLAUX, V.I.ARIMESCU, F.SONTHEIMER AND H.LANDSKRON, "Fuel and cladding properties at high burnup", ", LWR Fuel Performance (Proc. Int. Topical Mtg Park City, Utah, 2000), ANS (2000).

[11] F.DUSCH, "Improved power profile model for calculating burnup-dependent radial power distributions in light and heavy water reactor fuel pins", Annual meeting of German Nuclear Society (JTK) May 2000, Germany, Bonn (in press).

AN ASSESSMENT OF THE PRIMARY MECHANISMS CONTROLLING THE PRE-INTERLINKAGE RELEASE OF STABLE FISSION GAS USING AN AGR DATABASE

W.E. ELLIS
AEA Technology,
Windscale, United Kingdom

Abstract

Since 1981 measurements have been made at Windscale of the stable fission gas release from Commercial Advanced Gas-Cooled Reactor pins. In all, to date, over 900 measurements have been made on fuel irradiated in the Hunterston B and Hinkley Point B reactors, the vast majority exhibiting only pre-interlinkage release. The pins, which consist of hollow pelleted uranium dioxide fuel clad in stainless steel, have been irradiated with a wide range of cladding temperatures, fuel ratings and burn-ups and the observed releases are shown to be extremely well correlated with these primary irradiation parameters. The database has therefore proved an almost ideal basis for benchmarking current theories of pre-interlinkage gas release. The primary mechanism of release is shown to be diffusion to free surfaces and analysis allows inferences to be drawn as to the diffusion processes occurring and the dimensions of the free surfaces involved in release.

1. INTRODUCTION

The release of fission gas from fuel plays a critical role in pin performance. Initially poisoning of the clad-fuel gap enhances fuel temperatures and ultimately high release can result in pin over-pressure and failure. Since February 1981, AEA Technology Windscale have been monitoring the release of fission gases (Krypton, Xenon and Helium) from Commercial Advanced Gas-Cooled Reactor (CAGR) fuel pins. The measurements are primarily on pins from fuel irradiated in Reactors 3 and 4 at Hunterston and Hinkley Point. Currently the database consists of over 900 measurements on a variety of pin types. This paper considers the behaviour of 503 pins with well-characterised histories for which pre-interlinkage gas release was observed.

The process of release, through diffusion of gases to free surfaces and fuel grain boundaries, is both rating and temperature sensitive. The CAGR stringer design with eight elements each with three rings of pins provides data covering a wide range of time-averaged conditions with cladding temperatures (410ºC to 740ºC) and ratings (6kW/m to 23kW/m). The data also encompassed dwell times from 450 days to 1670 days. Thus the database is sufficiently large and comprehensive to validate the assumed release mechanism.

2. PRIMARY MECHANISM OF PRE-INTERLINKAGE RELEASE

The primary mode of release in the pre-interlinkage state is presumed to be by the diffusion of fission gas atoms to the fuel pellet free surfaces, the outer cylindrical surface, the bore, the two end surfaces and to the fuel cracks which form at power. For a simple homogeneous material operating at constant temperature and rating, the fractional rate of release is given by the standard Booth type relationship[1]:-

$$F = \frac{4S\sqrt{Dt}}{3V\sqrt{\pi}} \qquad (1)$$

where t is the dwell time
S/V is the free surface area to fuel volume with a currently recommended value of 2500m^{-1} for CAGR pellets. This is considered further below.
and D is the effective diffusion coefficient defined by the equation:-

$$D = (D1 + D2 + D3)Fs^2 \qquad (2)$$

where D1 is the Intrinsic Fission Gas Atom Coefficient
D2 is the Irradiation Enhanced Vacancy Coefficient
D3 is the Irradiation Enhanced Athermal Coefficient
and Fs is the fraction of Fission Gas Atoms in the UO_2 matrix

The diffusion coefficient depends on both fuel rating and fuel temperature. The fuel temperature is, in turn, primarily related to fuel rating and clad surface temperature. Therefore, with the release mechanism described above, the observed fractional release should be precisely described by a function of clad temperature and rating and should increase with the square root of time. This is tested below.

3. DATA USED

3.1. Pin types

CAGR pins consist of UO_2 fuel clad in 20/25/Nb stainless steel, which is weak in reactor. The fuel is therefore not subject to significant temperature enhancement through fuel clad gap. The pins are 15mm OD and approximately one metre long. Two designs of fuel pellet appear in the database, the first, initial charge fuel, has a central bore diameter of 5.08mm while the replacement fuel has a central bore of 6.35 mm. The UO_2 was manufactured to different specifications. Pre-1979 the fuel had a density of 10650kg/m^3 with a mean linear intercept grain size of typically 6 μm and Post-1979 the fuel density was increased to 10760kg/m^3 with a mean linear intercept grain size of 12 μm.

As all the initial charge fuel was produced before 1979, the database contains three distinct fuel types. Type A produced pre-1979 with 5.08 mm bore, Type B produced pre-1979 with 6.35 mm bore and Type C produced post-1979 with 6.35 mm bore.

3.2. Pin irradiation history data

The four parameters used in this analysis are:

a) at-power dwell time in the reactor (days)
b) irradiation-averaged mean pin rating (W/g U)
c) irradiation-averaged mean pin cladding temperature (ºC)
d) irradiation-averaged mean pin centre temperature (ºC)
(n. b. mean pin burn-up is item "a" multiplied by item "b")

In fact, there are in effect only three independent variables as, for UO_2 fuel with a given pin geometry, centre temperature is a function of rating, cladding temperature and dwell time. For the data analysed here, the only geometrical difference is bore size and this will be taken into account in the analysis. Porosity differences are small and have a marginal effect on fuel

temperature. The fuel centre temperatures used here are calculated using an algorithm based on the predictions of the ENIGMA[2] fuel modelling code.

4. DETERMINATION OF A PARAMETRIC CORRELATION

The analysis was performed using a multivariable non-linear fitting program. The selected data was fitted to a number of different functions of the dependent variables described above. Examining the regressions in detail, it became clear that fractional fission gas release varied almost precisely with the square root of dwell time. In order to check that this feature did not arise from auto-correlation within the database, a sub-set of the database was identified which contained a wide range of dwell times but had similar ratings and temperatures. When this smaller database was analysed the dwell time index was confirmed to be in the range 0.50 to 0.58 depending on the functional form used to describe rating/temperature effects.

From all the selected data a correlation was obtained based on the parameters obtained directly from fuel performance assessment, namely dwell time, rating and cladding temperature. Equation 1 below was found to give a very good description of the data with a residual variability of times/divide1.2 (1σ).

$$F = \exp(0.2035Rat - 0.0688Bore - 0.015Bore*Rat - 9.987 + 0.04543Tc)\sqrt{t} + 6.087x10^{-7}Rat*t \quad (3)$$

where F is the fractional fission gas release (%)
t is the dwell time (days)
Rat is the mean fuel rating (W/g U)
Tc is the cladding temperature (ºC)
Bore is the bore diameter (mm).

Figure 1 shows a comparison of observed release versus release calculated by equation 1 above along with the 3σ range values. The small residual scatter was unexpected, as it was believed that the variability in fuel cracking patterns would lead to more disparate levels of release. Clearly the database provides an excellent benchmark of release models.

The second term in equation 3 (proportional to t) is much smaller than the first term (proportional to √t), confirming the analysis above. The term is only significant at about the 2.2σ level and could well be a feature of the analysis route chosen rather than an indication that an additional release mechanism is occurring.

5. COMPARISON WITH THEORY

5.1. The diffusion coefficient

D1, D2 and D3 were quantified in the seminal work of Turnbull[3], although more recently Turnbull[4] has recommended that original values of D2 and D3 should each be increased by a factor four. With these revisions the recommended equations are:

D1 = $7.6 \times 10^{-10}\exp(-35000/T)$ m^2/s
D2 = $3.04 \times 10^{-16}R^{½}\exp(-13800/T)$ m^2/s
D3 = $2.35 \times 10^{-22}R$ m^2/s

where T is the fuel temperature(K)
and R is the rating in W/gU.

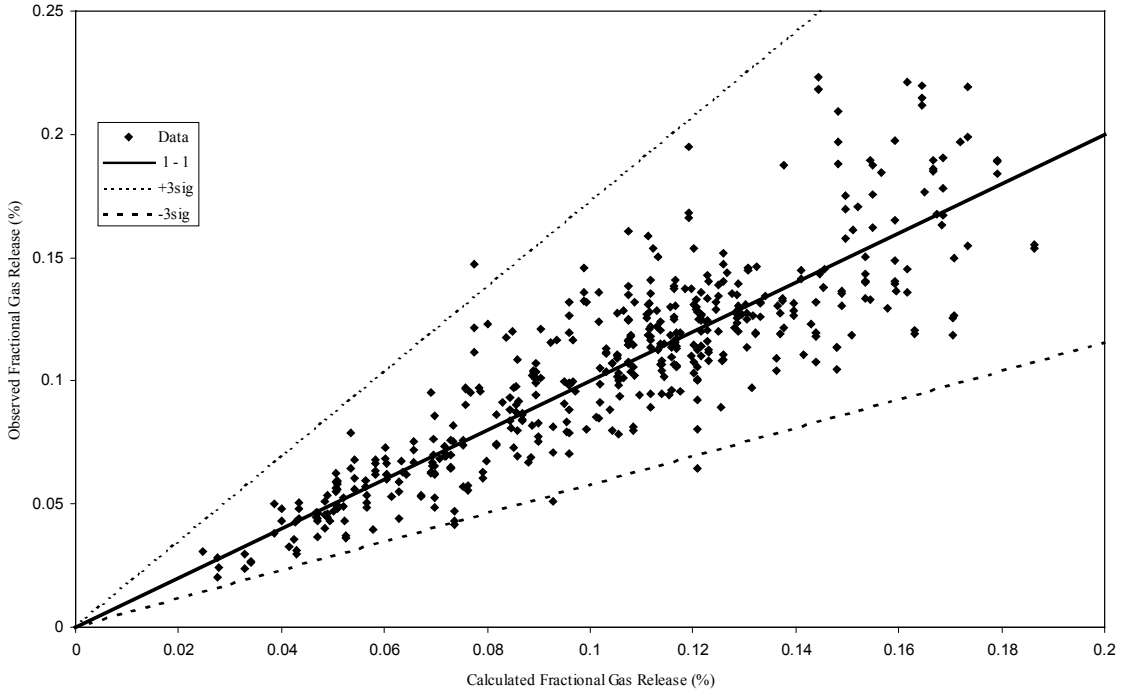

FIG. 1. Comparison of Observed Fission Gas Release with Value Calculated using Parametric Equation 3.

Thus for release from a fuel pellet within which ratings and temperatures vary, the local release proportional to the square root of the diffusion coefficient must be integrated over the full pellet. The correct method of allowing for the effect of rating and temperature variations during irradiation is to sum the local releases with time using the "effective time" principle. Such a procedure is not possible with this database. In the calculations performed here, the average diffusion coefficients are calculated from time-averaged ratings and temperatures. Checks on the validity of this procedure using sample irradiation histories have shown the procedure to be reasonable so long as the fuel follows its normal fuel cycle trajectory of reducing rating with time. The method is not applicable where fuel has been up-rated close to discharge.

5.2. The surface area

As Belle[5] states, the amount of release by diffusion can be seen to depend not only on the diffusion rate but also on the smallest dimension to a free surface. In a completely dense smooth body, the estimation of free surface area can be made from dimensional measurements (i.e. from estimation of the dimensions mentioned in Section 2.1). However, in fuels of technological interest, residual porosity will remain in the fuel in the form either of closed porosity (i.e. not communicating to a free surface), or of open porosity. This open porosity will thus enhance the surface area of the fuel. Belle analyses surface areas measured by gas adsorption using the BET technique[6,7] and recommends that surface to volume ratios be calculated simply from the measured porosity.

Belle's recommendation has been applied to CAGR fuel using recommended methods[8] for calculating irradiation induced porosity sintering. This yields for pre-79 fuel an initial S/V of $4500m^{-1}$ reducing to $660m^{-1}$ when fully densified. For post-79 fuel the initial S/V is $1600m^{-1}$ reducing to $1000m^{-1}$ on densification. These values are a factor 2 to 4 smaller than are needed to

predict the absolute levels of release observed in CAGR fuel. Also such a large variation between fuel types was not observed in the preliminary analysis of these data.

The preliminary analysis also revealed the data to exhibit a stronger rating dependence than would be expected from changes in the diffusion coefficient alone. This was interpreted to result from the fuel cracking. Thus, in order to estimate the surface to volume ratio of fuel, both effects due to cracking and due to porosity and its sintering must be considered separately. On this basis, S/V can be described by the following equation:-

$$S/V = SG.Ro \qquad (4)$$

where SG is the geometrical surface to volume ratio of cracked pellets
and Ro is the enhancement effect of porosity (Roughness factor)

A precise calculation of SG is not possible as no model yet exists for the prediction of radial and circumferential crack patterns in irradiated fuel. SLEUTH[9] calculates the number of radial cracks from the temperature drop across the fuel pellet. This calculation approximates to the assumption that the number of radial fuel cracks is proportional to the linear fuel rating. Though significant cracking pattern variability is observed in practice, available evidence suggests that this approximation is reasonable. SG may therefore be obtained from the expressions of the form:

$$SG = S1 + S2.Rp \qquad (5)$$

where S1 and S2 are factors calculated from the pellet geometry
and Rp is the peak-in-time rating governing the number of radial fuel cracks.

Detailed analysis revealed that if S1 and S2 were calculated directly from the pellet geometry and the number of cracks predicted by the SLEUTH algorithm, then the predicted variation in SG with rating was sufficient to account for the enhanced rating variation detected in the data by the parametric analysis. This is shown later in Section 5.6.

5.3. Matrix gas

Baker[10] has investigated the partitioning of fission gas between intragranular bubbles and the fuel matrix. Over the temperature range of interest here the values of Fs are close to unity and the effect can be ignored.

5.4. The roughness factor

In the light of problems revealed applying Belle's recommendation, the BET data of references [6] and [7] (both due to Aronson) have been re-analysed in terms of roughness factor and the results shown in Figure 2. It is evident that the data form three populations. Aronson's original data[6] follows the steep Belle recommendation, suitably normalised to allow for the geometric surface, while in Aronson's later data[7] the roughness factor varies more slowly with porosity but there is a significant effect of grinding on roughness at low porosity.

Clearly the observed variation in roughness factor makes it difficult to choose an appropriate variation at this point. The database was therefore analysed to determine a roughness factor for comparison with Aronson's results. This is described below.

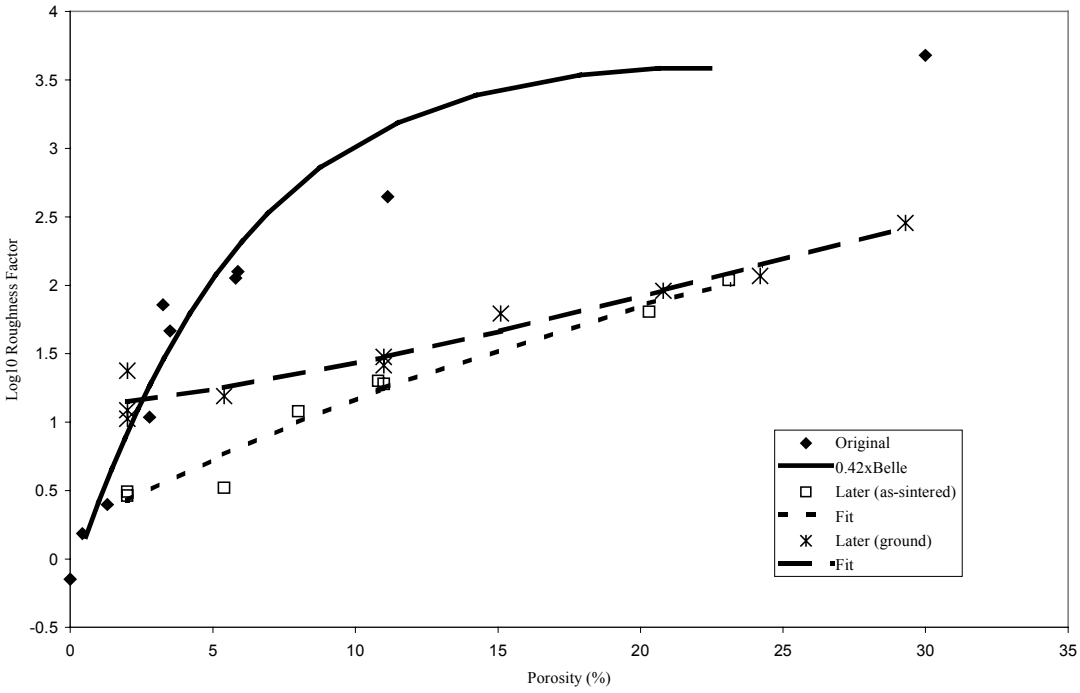

FIG. 2. Comparison of Aronson's Measured Roughness Factors with Belles' Algorithm.

5.5. Estimation of roughness factor and diffusion coefficient

A roughness factor was calculated for each item in the database by using equations 1,2,4 (with Ro set to unity) and 5 to predict the fractional gas release. The observed release divided by prediction gives an estimate of the true roughness factor. Multivariate regression analysis of the roughness factor against rating, temperature, etc. ensures that all parametric variations are accounted for in the analysis.

It became apparent early in the analysis that the recommended value of D3 was too large by a factor of about nine to fit the data and the equation was amended to be:

$$D3 = 2.65 \times 10^{-23} R \qquad m^2/s$$

With this revision, the roughness factors shown in Figure 3 were obtained plotted against mean fuel temperature. The results, plotted separately for each fuel type, show roughness factors typically of order 2.3 with a scatter comparable with a residual variability of times/divide 1.2 (1σ) obtained in the preliminary parametric analysis. Returning to Figure 2 this value is directly consistent with the later as-sintered values of Aronson.

Because of the large scatter, it is not evident from Figure 3 what residual systematic variation exists in the data. The picture becomes clearer in Figures 4A and 4B were the roughness factors have been sorted by temperature and running averages calculated over twenty data points. This reduces the scatter by a factor 4.5 giving an estimated variability of times/divide 1.04 (1σ).

It is clear from Figures 4A and 4B that the roughness factors determined from the release data exhibit some residual temperature variation. If the Belle relationship is used to calculate the roughness factor then a temperature dependence of the appropriate magnitude is predicted for pre-79 fuel but not for post-79 fuel. This suggests that the diffusion coefficients may be actually less temperature sensitive than the modified Turnbull formula predicts. This confirms the

results of White et. al.[11] whose analysis of unstable fission product release from experiments in the Halden reactor resulted in the following recommended functions for D2 and D3:-

$$D2 = 1.49 \times 10^{-17} R^{½} \exp(-10600/T) \quad m^2/s$$
$$D3 = 7.67 \times 10^{-22} R \exp(-2785/T) \quad m^2/s$$

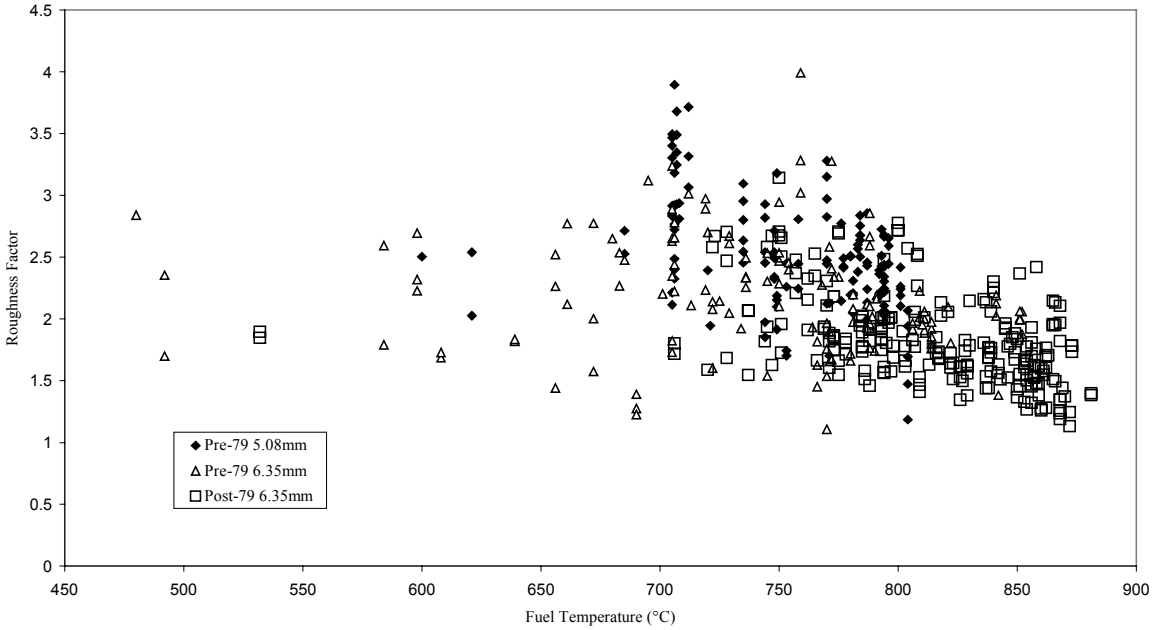

FIG. 3. Roughness Factor Variation Calculated from Measured Release.

When the roughness factor analysis is reworked using these recommendations, the results of Figures 4C and 4D are obtained. Here the temperature variation has been removed and the roughness variation is close to the predictions of the Aronson as-sintered data. Thus Aronson's as-sintered roughness factor taken with the revised diffusion coefficient gives a much-improved description of the CAGR stable gas release database.

The equation that adequately describes the roughness factor for Aronson's as-sintered results is:

$$Ro = \exp(0.494894 + 0.250613p - 0.0031097p^2) \quad (6)$$

where p is the percentage porosity.

For comparison with previous recommendations, the White et. al. recommendations can be reformulated into the standard thermal and athermal terms and the following formulae arise:

$$D2 = 1.24 \times 10^{-18} R^{½} \exp(-7750/T) \quad m^2/s$$
$$D3 = 1.00 \times 10^{-23} R \quad m^2/s$$

These equations provide an equally accurate description of the database and with this formalism the activation temperature of D2 has the value 7750 ± 600 K, only 56% of the original Turnbull recommendation. The D3 value is a factor six lower than Turnbull's original recommendation, confirming the initial analysis here.

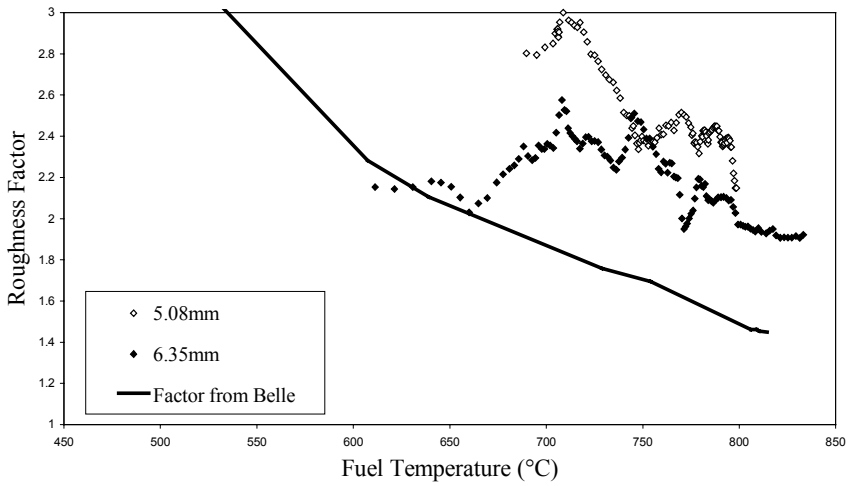

FIG 4A. Pre-79 Factors using Modified Turnbull model.

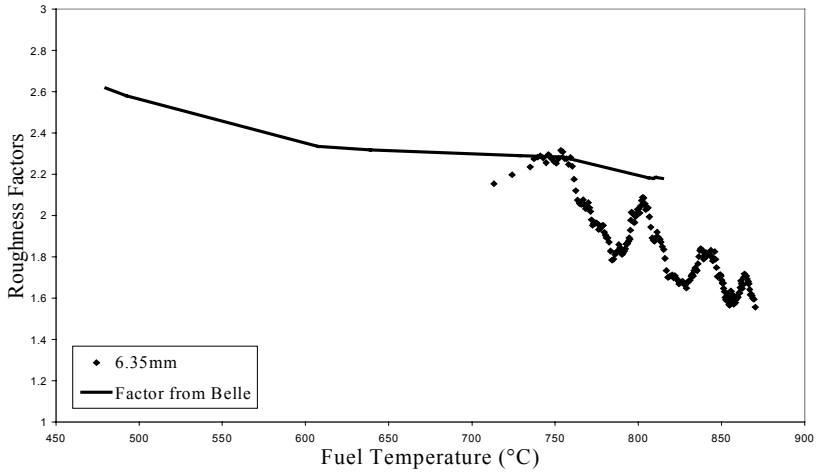

FIG. 4B. Post-79 Factors Using Modified Turnbull model.

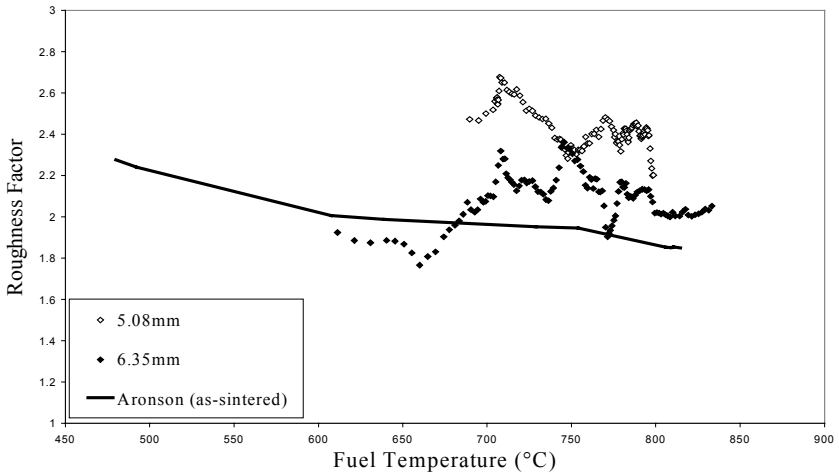

FIG. 4C. Pre-79 Factors using White et. al.

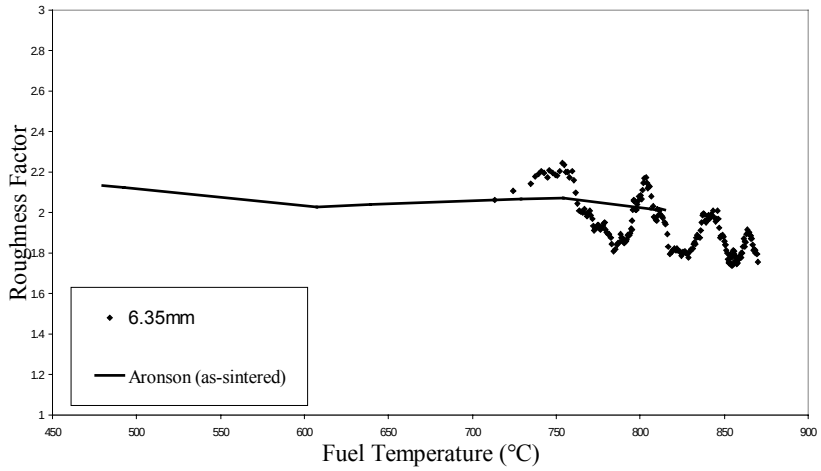

FIG. 4D. Post-79 Factors using White et. al.

Figure 5 shows the magnitudes of the diffusion coefficients obtained from the various formulations, described above. The values have been determined over the range of temperature applicable to the release data using a fuel rating of 16 W/gU. Except for the original Turnbull formulation, all values agree at the highest temperature. As would be expected the reformulation of the White et. al. function is in good agreement with the original over most of the temperature range.

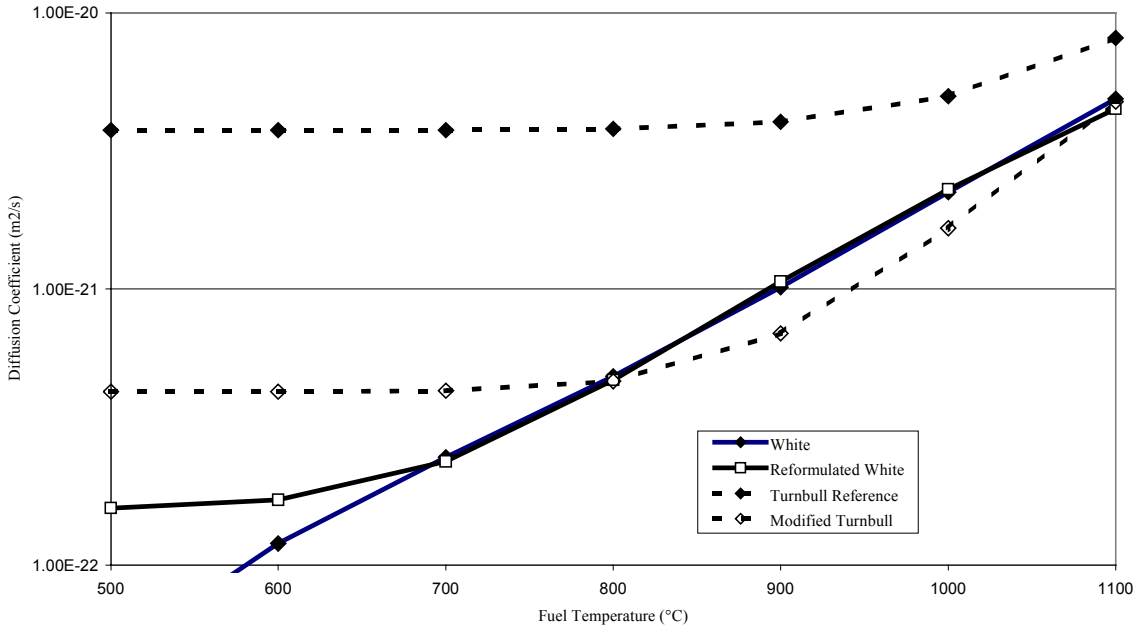

FIG. 5. Comparison of Various Estimates of Diffusion Coefficient at 16W/g U.

One systematic residual cannot be accounted for in the present analysis. It is clear from Figures 4A and 4C that for the Pre-79 fuel the 5.08mm bore fuel has a roughness factor some 15% higher than the equivalent 6.35mm bore fuel even though geometric effects have been accounted for. It is considered that this may be consequence of the difference in fuel cycle

between initial charge (5.08 mm bore) fuel and feed (6.25mm bore) fuel but may be a consequence of slightly different cracking patterns.

5.6. The effect of cracking on the geometric surface

As mentioned in Section 5.2, the effect of cracking on the geometrical surface to volume ratio (SG) can be accounted for by the expected radial cracking pattern using equation 5. In Figure 6, the roughness factors have been calculated using the White et. al. diffusion coefficients both with and without the cracking correction of equation 5. The data shown are here running averages over 20 consecutive rating values for all 3 types of fuel taken together. Without correction the roughness factors vary by a factor of approximately 1.7 over the range of rating and this systematic is removed by the correction for radial cracking.

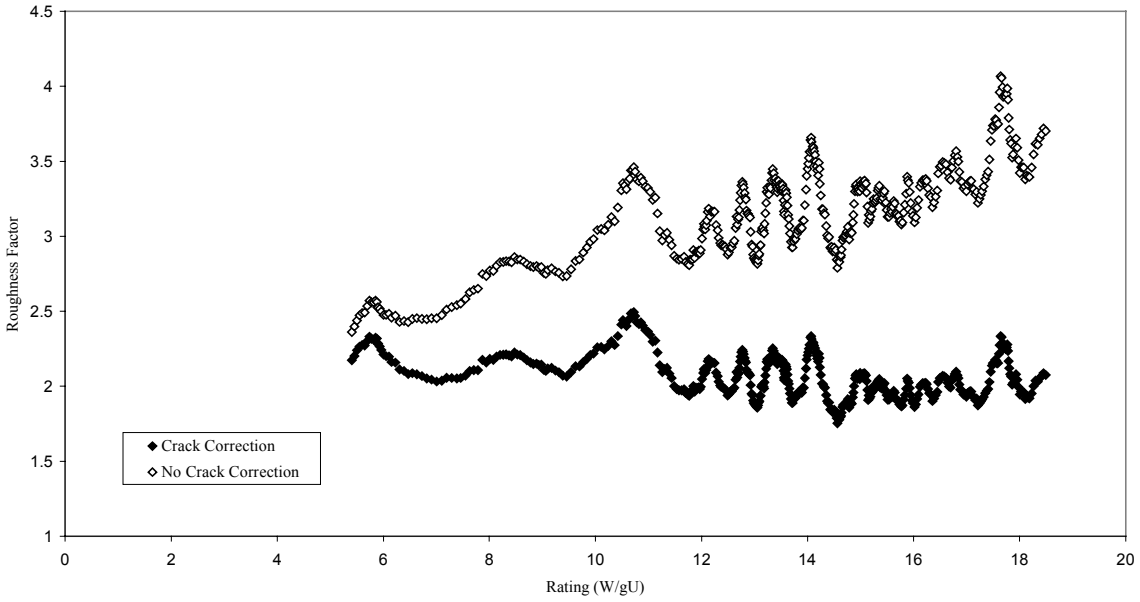

FIG. 6. Roughness Factors Calculated with and without Allowance for Fuel Cracking.

6. DISCUSSION

It is evident from the above analysis that with a suitable fuel densification model both the Belle algorithm and the Aronson data predict similar levels of roughness and therefore will predict adequately the overall levels of fission gas release. As the Belle form is more porosity sensitive the details of the densification model are more important for predictions in this case.

The temperature sensitivity of predicted roughness factor, noted above, is related to the densification model. If the White et. al. diffusion coefficients are used then the fission gas data shows roughness to be remarkably insensitive to temperature, indicating that the Aronson roughness is the more appropriate for the calculation of stable gas release.
Although the above prescription provides a suitable method for calculation pre-interlinkage gas release with some accuracy, there still remains one problem. If the Aronson data was used in estimating surface to volume ratios for the unstable release data used by White et. al., the diffusion coefficient so determined would be markedly changed, removing the agreement achieved above. For a resolution of this problem one must turn to an effect reported by White[12]. He notes that if the unstable fission gas release data is analysed in detail, then the

release rate does not follow exactly the expected $\lambda^{-½}$ relationship and attributes this to a change in the effective roughness of the surface with the lifetime of the species. He suggests for short-lived species the surface behaves in a fractal manner. Species with the shortest "range" (i.e. have the shortest lifetime and are from the coolest parts of the fuel) are released from closest to the surface and therefore are more affected by the roughness of the surface. They thus exhibit the largest surface to volume ratio. It is not clear how such an approach could be extrapolated to stable isotopes but the magnitude and direction of this effect is consistent with the discrepancy found here.

The BET method measures surface areas on the molecular level and therefore on the basis of fractal theory should be most consistent with the release for shortest-lived fission products, exhibiting the greatest degree of roughness. For the release of stable isotopes, the surface will effectively appear much smoother and exhibit a lower roughness factor.

Aronson's as-sintered data are, of course, BET measurements but made on what effectively is a smooth surfaced material. Cracked pellets must, to some extent, have a rough finish but this will not be evident in the gas release because of the smoothing effect mentioned above. Overall therefore, the agreement with Aronson's as-sintered data may be somewhat fortuitous. But the change in roughness factor arises from a recognised physical phenomenon.

The differences between the Aronson data sets does raise questions as to the correct value to be attached to the free surface when interpreting unstable release experiments and thus calls into question the absolute accuracy of the diffusion coefficients currently being recommended.

7. CONCLUSIONS

1. Analysis of the Windscale fission gas release database of some 503 CAGR pins primarily from the Hunterston and Hinkley Point reactors has led to the development of a parametric equation describing the pre-interlinkage ("athermal") release. The equation is suitable for standard fuel pins with grain sizes in the nominal range 6 μm to 12 μm and with weak 20/25/Nb cladding. The data are well predicted with a random error of times/divide 1.2 (1σ).

2. Detailed analysis of the data shows that the observed releases are consistent with current theoretical mechanisms with migration of fission gas to free surfaces being primarily controlled by vacancy migration.

3. The diffusion coefficients derived from analysis of unstable fission gas release in the Halden Reactor provide a good description of the observed release. The equations, in terms of the fuel temperature(T) and rating(R) are:-

$$D2 = 1.49 \times 10^{-17} R^{½} \exp(-10600/T) \quad m^2/s$$
$$D3 = 7.67 \times 10^{-22} R \exp(-2785/T) \quad m^2/s$$

4. The free surface depends on the fuel cracking behaviour, which increases the free surface area, and on the degree of surface porosity, which enhances the overall roughness of the surface.

5. A simple algorithm based on the development of radial fuel cracks adequately describes the observed effects of cracking on release.

6. The BET data of Aronson on as-sintered fuel best describes the roughness effects. Analysis of these data yields a porosity (p) dependent roughness factor given by the equation:-

$$Ro = \exp(0.494894 + 0.250613p - 0.0031097p^2)$$

7. Differences between Aronson's measurements on different fuel surface types gives some uncertainty on the absolute accuracy of current diffusion coefficient recommendations

ACKNOWLEDGEMENTS

The author acknowledges Scottish Nuclear Limited and the Health and Safety Executive for their support in the performance of this work.

REFERENCES

[1] CARSLAW H S and JAEGER J C. "Conduction of heat in solids." Oxford University Press. 1959.
[2] KILGOUR W J. "The ENIGMA Fuel Performance Code, Version 5.8g 1993." Commercial Document, Nuclear Electric plc.
[3] TURNBULL J A, FRISKNEY C A, FINDLAY F R, JOHNSON F A and WALTER A J. "The diffusion coefficient of gaseous and volatile species during the irradiation of UO_2." J. Nucl. Mater. 107, 168, 1982.
[4] TURNBULL J A. "Report to the IAEA Technical Committee Meeting on Water Reactor Fuel Element Modelling at High Burnup and Experimental Support." Windermere, England 19-23 September 1994.
[5] BELLE J. "Uranium Dioxide: Properties and Nuclear Applications." USAEC. 1961.
[6] EICHENBERG J D, FRANK P W, KISIEL T J, LUSTMAN B and VOGEL K H. "Effects of Irradiation on Bulk Uranium Dioxide. Fuel Elements Conference Paris." TID-7546. pp 616-717. Mar 1958
[7] ARONSON S, CLAYTON J C, RULLI J and PADDEN T R. "Surface Areas of Sintered UO_2 Compacts." Bettis Technical Review, WAPD-BT-19, 83-92, June 1960.
[8] UKAEA Internal Document. 1981.
[9] BEATHAM N, HUGHES H, ELLIS W E AND SHAW T L. "Modelling of pellet-cladding interaction in thermal reactor fuel pins using the SLEUTH computer code." Nucl. Energy, 29, No. 2, 115-122. April 1990.
[10] BAKER C. Journal of Nucl. Mater. 66 , 283, 1977
[11] WHITE R J, TEMPEST P A and WOOD P. "An evaluation of diffusion coefficient data obtained from the start-up ramp of IFA 563 and comparison with data from the gas flow rigs IFA 504 and IFA 558." Paper presented at the Enlarged Halden Programme Group Meeting, Storefjell Hotel, Gol, 7-12 March 1993.
[12] WHITE R J. The fractal nature of the surface of uranium dioxide: A resolution of the short-lived/stable gas release dichotomy. Paper presented at the Enlarged Halden Programme Group Meeting, Lillehammer, Norway, 15-20 March 1998.

CLAD MODELLING
(Session 3)

Chairpersons

S. LANSIART
France

J. RASHID
United States of America

SIMULATION OF PELLET-CLADDING THERMOMECHANICAL INTERACTION AND FISSION GAS RELEASE

A. DENIS, A. SOBA
Departamento Combustibles Nucleares,
Comisión Nacional de Energía Atómica,
Buenos Aires, Argentina

Abstract

This paper summarizes the present status of a computer code that describes some of the main phenomena occurring in a nuclear fuel element throughout its life. Temperature distribution, thermal expansion, elastic and plastic strains, creep, mechanical interaction between pellet and cladding, fission gas release, swelling and densification are modelized. The code assumes an axi-symmetric rod and hence, cylindrical finite elements are employed for the discretization. Due to the temperature dependence of the thermal conductivity, the heat conduction problem is non-linear. Thermal expansion gives origin to elastic or plastic strains, which adequately describe the bamboo effect. Plasticity renders the stress–strain problem non linear. The fission gas inventory is calculated by means of a diffusion model, which assumes spherical grains and uses a finite element scheme. In order to reduce the calculation time, the rod is divided into five cylindrical rings where the temperature is averaged. In each ring the gas diffusion problem is solved in one grain and the results are then extended to the whole ring. The pressure, increased by the released gas, interacts with the stress field. Densification and swelling due to solid and gaseous fission products are also considered. Experiments, particularly those of the FUMEX series, are simulated with this code. A good agreement is obtained for the fuel center line temperature, the inside rod pressure and the fractional gas release.

1. INTRODUCTION

Among the numerous phenomena that take place during operation of a fuel element, thermomecanical interaction between pellet and cladding and fission gas release have historically deserved special attention. These phenomena are interconnected and mutually dependent. On the one hand, due to the low thermal conductivity of the fuel material, a quite steep temperature gradient appears in the pellet. The high temperatures developed within the pellet, especially at its center, give rise to thermal expansion. The strain produced in the pellet may be either of the elastic or plastic types. For sufficiently long periods, creep may also have a significant effect. As a consequence, the initially cylindrical pellet surface distorts, bending outwards, the top and bottom faces being displaced further than the central belt [1]. The dimensional changes in the fuel rod provoked by thermal expansion may induce pellet-cladding interaction (PCI) and the consequent plastic cladding strain [2]. To simulate this problem the thermal–elastic–plastic coupled equations have to be solved. On the other hand, fission products accumulate within the pellet. Among them, the gaseous products, namely Xe and Kr, represent about 30%. Their almost complete insolubility in the UO_2 matrix is responsible for the formation of bubbles, either intra and intergranular. They decrease the thermal conductivity of the fuel, and consequently its temperature increases. An important fraction of the gas generated accumulates in the intergranular bubbles, until they saturate and release the gas in excess to the plenum and the gap. In this manner, it contributes to increase the internal pressure in the fuel element, modifies the gap thickness and affects the thermal conductance of the gap.

The code presented here solves first the heat diffusion equation and gives the temperature distribution in the pellet, the gap and the cladding. To this end, a finite element scheme in

cylindrical coordinates is used. Its solution is the input to the stress-strain problem. For simplicity, the system is divided into five cylindrical rings, according to the temperature range. In each ring the gas diffusion problem is solved in an ideal, spherical grain.

2. THE MODELIZATION

2.1 The thermal problem

Since the system is assumed to have axial symmetry, cylindrical coordinates are employed. The temperature depends on r and z only. If T represents the temperature, Q is the volumetric heat generation rate, $\kappa = \kappa(T)$ is the thermal conductivity and assuming steady-state heat transfer conditions, the temperature distribution in each material is obtained by solving the differential equation:

$$\kappa\left(\frac{1}{r}\frac{\partial}{\partial r}(r\frac{\partial T}{\partial r})+\frac{\partial^2 T}{\partial z}\right)+Q=0$$

with the boundary conditions: T = constant at the cladding external radius (Dirichlet condition) and $\nabla T = 0$ (Neumann condition) at the remaining portion of the system boundary. These together with the power history, represent the input data.

Application of the finite element method involves definition of a mesh, which in this case is chosen of triangular elements, definition of the corresponding shape functions and approximation of the continuous unknown function T by a linear combination of the shape functions. A system of linear equations is finally obtained one equation for each unknown nodal value.

For the thermal conductivity of UO_2 the following expression was used [1]:

$$\kappa(T)=\frac{1}{0.034944+2.2430\times10^{-4}T}+\frac{6.157\times10^{9}}{T^2}\exp\left[-\frac{1.41\times1.6\times10^{-19}}{kT}\right]$$

with T in K and κ in $W\,m^{-1}K^{-1}$. The temperature dependence of κ is responsible for the non–linearity of the thermal problem and hence the temperature is calculated by an iterative procedure. The solution of the heat transfer problem becomes the input to the stress analysis. The same discretization is used to solve both.

2.2. The stress-strain analysis

2.2.1. Elasticity and plasticity

The Hill´s theory of plasticity together with the flux rules of Levy Prandtl-von Mises provide the following relation for the plastic strain [3]

$$\Delta\varepsilon^p_{rr}=\frac{\Delta\varepsilon_p}{2\sigma_e}(2\sigma_{rr}-\sigma_{zz}) \quad ; \quad \Delta\varepsilon^p_{zz}=\frac{\Delta\varepsilon_p}{2\sigma_e}(2\sigma_{zz}-\sigma_{rr}) \quad ; \quad \Delta\varepsilon^p_{rz}=\frac{3\Delta\varepsilon_p}{2\sigma_e}\sigma_{rz}$$

The equivalent stress,

$$\sigma_e = (\sigma_{rr}^2 + \sigma_{zz}^2 - \sigma_{rr}\sigma_{zz} + 3\sigma_{rz}^2)^{1/2}$$

and the equivalent strain, $\Delta\varepsilon_p$, are related by an experimental curve characteristic of each material, where the segment corresponding to small stresses and strains is linear and represents the elastic range. For large strains this relation is non-linear and hence an iterative procedure is necessary for the calculations.

2.2.2. Creep

The creep analysis is carried out by means of the flux rules of Levy Prandtl-von Mises and the Norton law [4]

$$\dot{\varepsilon} = K\sigma^m$$

where K and m depend on the material. The values $K = 10^{-6}\text{MPa}^{-3}\text{d}^{-1}$ and m=3 [5] were used in the present work.

2.2.3. The constitutive equations

Given the axial symmetry of the system, neither the geometry nor the surface loading depend on the angular coordinate. The displacements, strains and stresses are functions of r and z only. Let us represent with u and w the displacements in the r and z direction, respectively. The strain-displacement relations are [6]:

$$e_{rr} = \frac{\partial u}{\partial r}\ ;\ e_{\theta\theta} = \frac{u}{r}\ ;\ e_{zz} = \frac{\partial w}{\partial z}\ ;\ e_{rz} = \frac{\partial u}{\partial z} + \frac{\partial w}{\partial r}\ ;\ e_{r\theta} = 0\ ;\ e_{z\theta} = 0$$

The column vector $\{e\}$ contains the four non-zero components of the strain:

$$\{e\}^T = [e_{rr} \quad e_{\theta\theta} \quad e_{zz} \quad e_{rz}]$$

It has four contributions: thermal $\{\varepsilon_{th}\}$, elastic $\{\varepsilon\}$, plastic $\{\varepsilon_p\}$ and creep $\{\varepsilon_c\}$

$$\{e\} = \{\varepsilon_{th}\} + \{\varepsilon\} + \{\varepsilon_p\} + \{\varepsilon_c\}$$

where the first two are expressed as:

$$\{\varepsilon_{th}\}^T = [\alpha\Delta T \quad \alpha\Delta T \quad \alpha\Delta T \quad 0] \text{ and } \{\varepsilon\}^T = [\varepsilon_{rr} \quad \varepsilon_{\theta\theta} \quad \varepsilon_{zz} \quad \varepsilon_{rz}]$$

and α is the thermal expansion constant. The components of the elastic strain are related with the stress by the Hooke law

$$\{\sigma\} = [D]\{\varepsilon\}$$

where the components of the stress vector are:

$$\{\sigma\}^T = [\sigma_{rr} \quad \sigma_{\theta\theta} \quad \sigma_{zz} \quad \sigma_{rz}]$$

and [*D*] is the material matrix, which components are determined with the Young´s modulus and the Poisson´s ratio.

The plastic term is obtained by a recursive procedure in which the values of stress and strain are fitted to the uniaxial curve corresponding to the material involved. In the case of the present study, in the temperature range involved, only the Zry exhibits a significant plastic deformation.

When the finite element method is applied, the unknown displacements *u* and *w* are written in terms of the element nodal values and the shape functions. The above differential equations are thus transformed to linear equations, which are formally similar to those for the thermal problem.

The physical constants employed in the present calculations [7] are listed in Table I.

TABLE I. ELASTIC AND THERMAL CONSTANTS USED IN THE CODE

Young's modulus *E* (Pa)	UO_2: $2.065\text{x}10^{11}$ $(1+1.091\text{x}10^{-4}\ T)$ Zry: $1.236\text{x}10^{11} - 6.221\text{x}10^{7}\ T$
Poisson's ratio μ	UO_2: 0.316 Zry: 0.32
Thermal expansion α (K^{-1})	UO_2: $(-4.972\text{x}10^{-4} + 7.107\text{x}10^{-6}\ T + 2.583\text{x}10^{-9}\ T^2)/\Delta T$ Zry: $(-2.07\text{x}10^{-3} + 6.72\text{x}10^{-6}\ T)/\Delta T$
Thermal conductivity κ ($W\ m^{-1}K^{-1}$)	UO_2: $\left[\frac{4.04\times10^3}{464+T} + 1.216\text{x}10^{-2}\exp(1.867\text{x}10^{-3}T)\right]$ Zry: $7.51 + 2.09\text{x}10^{-2}\ T - 1.45\text{x}10^{-5}\ T^2 + 7.67\text{x}10^{-9}\ T^{-3}$ He: $0.3366\ T^{0.668}$

Temperatures T in K.

2.3 The fission gas release problem

The fission gas model, which was already outlined in some previous works [7, 8], is based on the following hypotheses:

- ☆ The UO_2 fuel is considered as a collection of spherical grains where, due to continuous irradiation, noble gas atoms are produced by fission of the U atoms.
- ☆ Due to the virtually complete insolubility of these gases in the UO_2 matrix, they either precipitate within the grains forming bubbles of a few nanometers (intragranular bubbles) or are released to the grain boundaries forming intergranular, lenticular bubbles, with sizes of some microns.
- ☆ Diffusion is the rate-controlling step.
- ☆ Intragranular bubbles are considered immobile and acting as traps for the diffusing gas.
- ☆ Irradiation can cause destruction of both types of bubbles.

- ☆ The gas atoms contained in the destroyed intragranular bubbles return to the diffusion process. Due to kinetic reasons, a dynamical solubility, much higher than that predicted by the equilibrium diagram is established.
- ☆ Destruction of intergranular bubbles acts as an additional source of gas atoms that affect mainly the region of the grain adjacent to the grain boundary.
- ☆ The amount of gas stored in the grain boundary bubbles grows up to a saturation value. Then, these bubbles interconnect and the gas in excess is released to the plenum and to the gap between fuel and cladding.
- ☆ The grains grow due to the high temperature of the fuel, especially near its center. The grain boundary traps the gas, either free or in bubbles, in the swept volume.

The rate of gas release is calculated by means of the diffusion equation in spherical coordinates, with sources and traps:

$$\frac{\partial c}{\partial t} = D\left(\frac{\partial^2 c}{\partial r^2} + \frac{2}{r}\frac{\partial c}{\partial r}\right) - gc + bm + \beta$$

together with the balance equation for trapped atoms:

$$\frac{\partial m}{\partial t} = gc - bm$$

where c and m are the concentrations of free and trapped gas atoms (at/m^3), ß is the gas generation rate (at/m^{3}s), g and b are the probabilities of capture and release by traps (at/s) and D is the diffusion coefficient of the single gas atoms in the UO_2 matrix. Assuming stationary trapping conditions: $gc–bm=0$ and defining the total gas concentration of gas in the grain $\psi=c+m$ and the effective diffusion coefficient $D'=Db/(b+g)$, the equivalent equation

$$\frac{\partial \psi}{\partial t} = D'\left(\frac{\partial^2 \psi}{\partial r^2} + \frac{2}{r}\frac{\partial \psi}{\partial r}\right) + \beta$$

is obtained, with the boundary conditions: $\psi(r=a)=0$, i.e., the grain boundary at $r=a$ acts as a perfect sink, and $\partial\psi/\partial r=0$ at $r=0$ due to spherical symmetry.

The diffusion coefficient D was given by Turnbull et al.[9]; the bubbles' size and concentration, and the trapping parameters, g and b, are due to White et al. [10]; the equiaxed grain growth rate is that used by Ito et al.[2].

The saturation concentration of the grain boundary, N_S, is calculated assuming that the gas in the intergranular bubbles obeys the ideal gas law, that the gas pressure, the external stress and the surface tension are in equilibrium and that bubbles interconnection occurs when a given fraction, f_S, of the grain boundary area is covered. The value $f_S=0.5$ is usually assigned. However, it seems appropriate to assume that bubbles interconncetion occurs as a percolation process. To this end, let us consider the grain boundary area divided into regular triangles and let us put circles, of radius equal to half the triangle side, in some of the crossing lines that form the triangles. The elementary theory predicts that the percolation threshold occurs when half of the sites are occupied [14]. This corresponds to a fraction of covered area $f_S = \pi\sqrt{3}/12 = 0.453$.

The function representing the gas production rate, $\beta(r)$, was already given in. It contains the uniform gas generation rate due to irradiation, obtained from the fission rate, F (fissions/m^{3}s), times the gas production yield, y, and the contribution due to resolution of intergranular bubbles, which is proportional to the occupation of the grain boundary, N. Its expression is:

$$\beta = \begin{cases} yF & \text{for } 0 \le r \le a-2\lambda \\ yF+h(r) & \text{for } a-2\lambda < r \le a \end{cases}$$

where λ represents the penetration depth of the redissolved atoms and the function $h(r)$ is such that

$$\int_{a-2\lambda}^{a} h(r) 4\pi r^2 dr = 4\pi a^2 b' \frac{N}{2}$$

where N indicates the number of gas atoms per unit area of the grain boundary.

An appropriate choice for $h(r)$ is a Gauss function. For simplicity, a triangular approximation was used [16]. The proportionality constant b'(1/s) represents the probability of resolution of the intergranular bubbles and is one of the parameters of the model.

Before saturation, the gas content per unit area of the grain boundary, N_k, at the time t_k is obtained from a balance equation that includes the gas contained in the grain volume at t_{k-1}

$$C_{k-1} = 4\pi \int_0^{a_{k-1}} r^2 \psi_{k-1} dr ,$$

the gas contained in the grain boundary at t_{k-1}

$$4\pi a_{k-1}^2 \frac{N_{k-1}}{2} ,$$

the amount of gas generated by fission during Δt_k

$$\frac{4}{3}\pi a_k^3 \, y \, F_k \, \Delta t_k ,$$

the amount of gas incorporated to the grain and grain boundary by sweeping of the grain boundary

$$\left(C_{k-1} + 4\pi a_{k-1}^2 \frac{N_{k-1}}{2} \right) \left(\frac{a_k^3 - a_{k-1}^3}{a_{k-1}^3} \right)$$

and the gas contained in the grain volume at t_k (C_k). The balance equation is

$$\left(C_{k-1} + 4\pi a_{k-1}^2 \frac{N_{k-1}}{2} \right) \left(\frac{a_k^3}{a_{k-1}^3} \right) + \frac{4}{3}\pi a_k^3 \, y \, F_k \, \Delta t_k = C_k + 4\pi a_k^2 \frac{N_k}{2}$$

which, with the initial conditions (t=0, k=0) C_0=0 and N_0=0 yields N_k at every instant t_k. Before saturation N_k represents the gas content of the grain boundary. After saturation the grain boundary content is set equal to N_S and the difference $N_k - N_S$ times the grain boundary area gives the number of gas atoms released to the free volume. This number is determined by

$$R_k = max\left(\frac{4\pi a_k^2}{2}(N_k - N_S), R_{k-1}\right)$$

which prevents the decrease of R_k when the temperature decreases.

2.4. Swelling

The contribution to swelling of intragranular and intergranular gas bubbles and of fission products dissolved in the lattice is considered. In the first case, if a concentration C_B of intragranular bubbles is created and if they are assumed to have the same radius R_B, the swelling they produce is

$$\left.\frac{\Delta V}{V}\right|_{\text{int.bub.}} = \frac{(4/3)\pi R_B^3 C_B}{1-(4/3)\pi R_B^3 C_B} \approx (4/3)\pi R_B^3 C_B$$

The concentration C_B is initially zero and grows up to an stationary value, provided that the irradiation conditions are kept constant. This implies that the swelling due to this type of bubbles reaches a saturation value.

To determine the swelling due to intergranular bubbles, we assume that the gas in a bubble obeys the ideal gas law and that the gas pressure balances the external pressure, P_{ext}, and the stress due to surface tension $2\gamma/r_f$, where r_f indicates the radius of curvature of the bubble's faces. The swelling produced when a surface concentration N of gas atoms is established in the boundary of a grain of radius a is

$$\left.\frac{\Delta V}{V}\right|_{\text{g.b.bub}} = \frac{3kTN}{2a(2\gamma / r_f + P_{ext})}$$

Given that the concentraion N reaches a saturation value, the swelling due to intergranular bubbles also saturates. On the contrary, the volume increase due to fission products, either solid or gaseous, dissolved in the lattice, either in interstitial or substitutional sites, although smaller than that due to gas bubbles, maintains a steady growth. As a rough estimate, we assume that the swelling due to fission products in the lattice is described by the empirical relation

$$\left.\frac{\Delta V}{V}\right|_{\text{l.f.p.}} = 0.0032\,\text{Bup[at\%]}$$

2.5. Densification

In the simple densification model used in the present work the porous solid is represented by an assembly of spherical grains which contain a density of spherical pores of equal radius

uniformly distributed in the solid. The pores are assumed to be small compared to the grain size and small compared to the interpore spacing. The fission fragments, passing near a pore, provoke the emission of vacancies to the lattice, which then diffuse to the grain boundary. This process is similar to the resolution of gas bubbles but given that the pores size is considerably larger than that of the bubbles, it is unlikely that a pore can be completely converted to vacancies by a single resolution event. Resolution is rather considered to reduce the size of the pores. However, due to the similarity of both processes we can assume that the probability that a vacancy in a pore will be ejected into the lattice takes a value similar to the rate of bubbles resolution, *b*. With all these assumptions we obtain the time dependence of porosity [17]

$$P = P_0 e^{-bt}$$

where P_0 represents the initial porosity. From here, the fractional volume change due to densification results

$$\left.\frac{\Delta V}{V}\right|_{\text{dens.}} = -\frac{P_0(1-e^{-bt})}{1-P_0 e^{-bt}} \approx -P_0(1-e^{-bt})$$

which is similar to the expression used in Refs. [18].

The total fractional volume change due to swelling and densification is obtained as the sum of these four contributions. This gives origin to an extra strain term

$$\varepsilon_{s.d.} = \frac{1}{3}\left[\left.\frac{\Delta V}{V}\right|_{\text{int.bub.}} + \left.\frac{\Delta V}{V}\right|_{\text{g.b.bub.}} + \left.\frac{\Delta V}{V}\right|_{\text{l.f.p.}} + \left.\frac{\Delta V}{V}\right|_{\text{dens.}}\right]$$

which is added to the thermal, elastic, plastic and creep contributions.

3. RESULTS AND DISCUSSION

With the code just described the six FUMEX experiments were simulated. The real power histories were conveniently simplified to save calculation time. Figures 1-6 show the input data and the results obtained with the code for the central line temperature, the internal rod pressure and the fractional release. The comparison between some results of our calculations and the coresponding data presented in the final report of the FUMEX experiment [19] are summarized in Table II.

The values shown in Table II reveal that the results obtained with our code fit quite well to the experimental results and in all the cases, except the final ramp of experiment 6S, fall within the range of values obtained with the other codes. As it was expected, the fitting is better in the cases of constant or nearly constant power.

The calculation time required to simulate these experiments, with power histories simplified to about 50 power steps, was about 10 minutes in a personal computer with a 330 MHz, Pentium II processor.

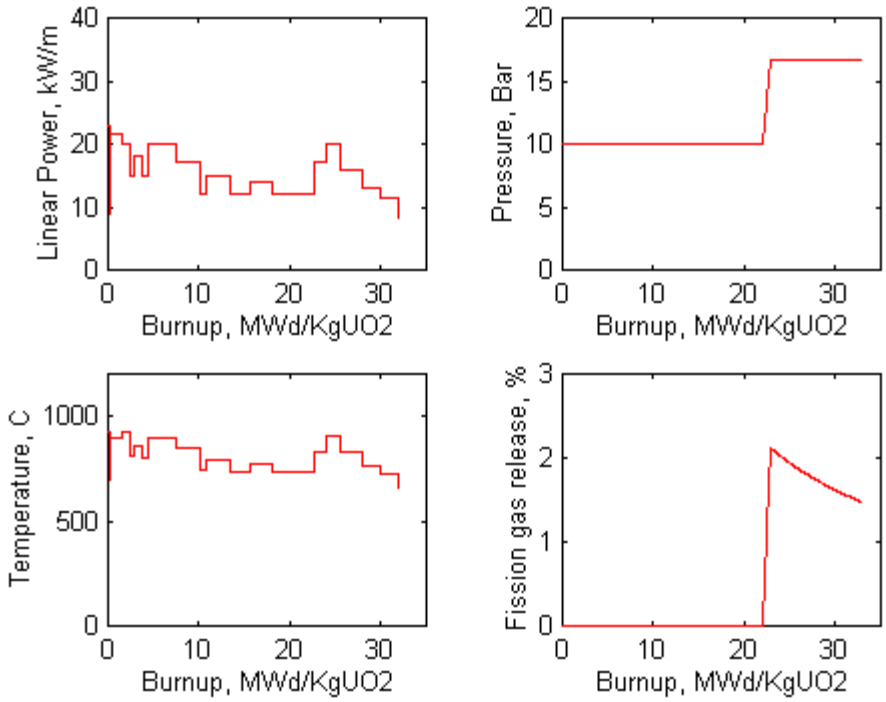

FIG.1. Simplified power history and calculation results corresponding to FUMEX 1.

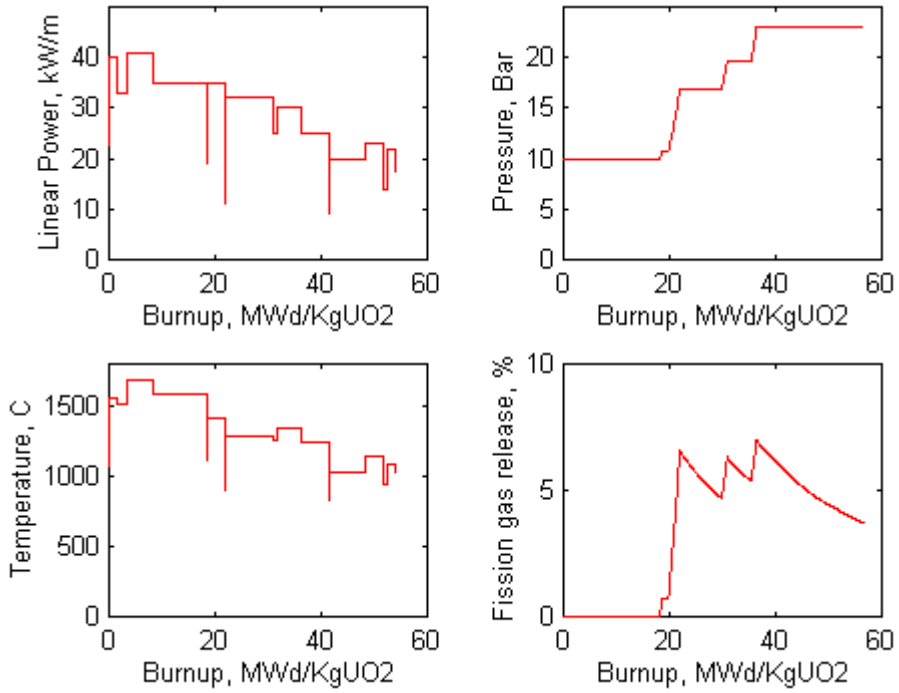

FIG.2. Simplified power history and calculation results corresponding to FUMEX 2.

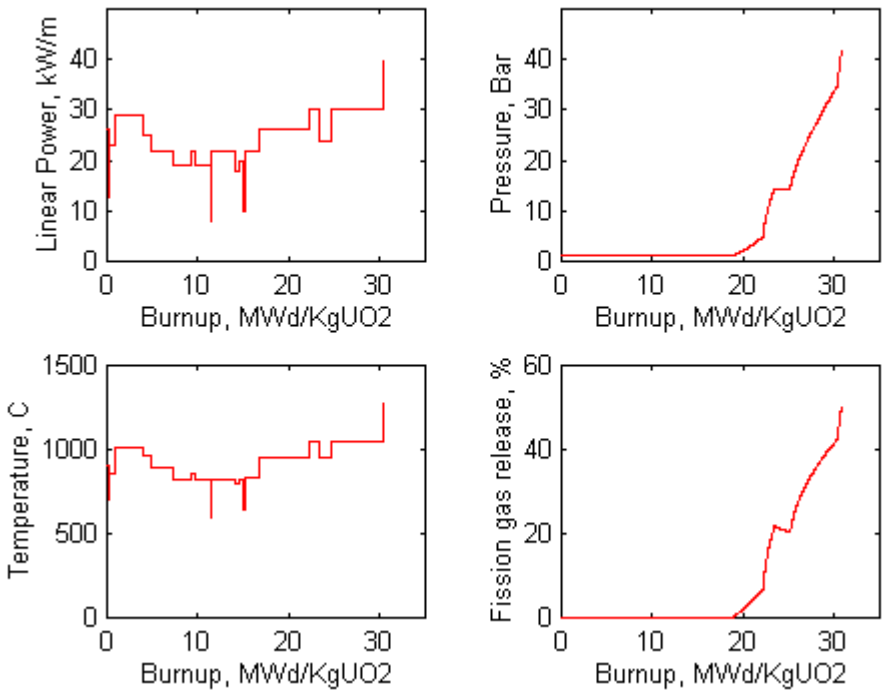

FIG.3. Simplified power history and calculation results corresponding to FUMEX 3 rod 2

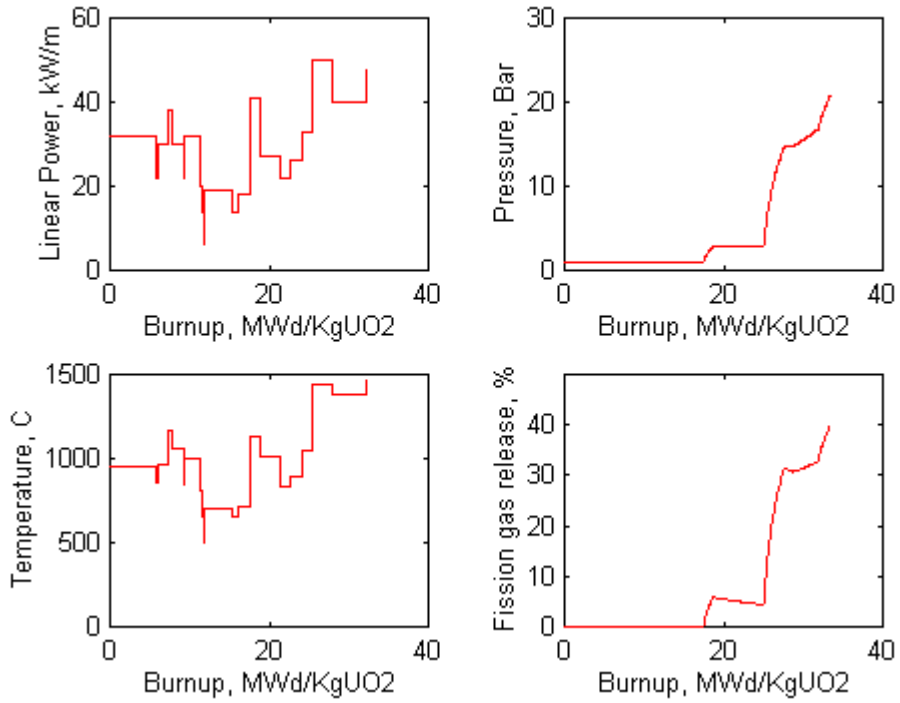

FIG.4. Simplified power history and calculation results corresponding to FUMEX 4 rod B.

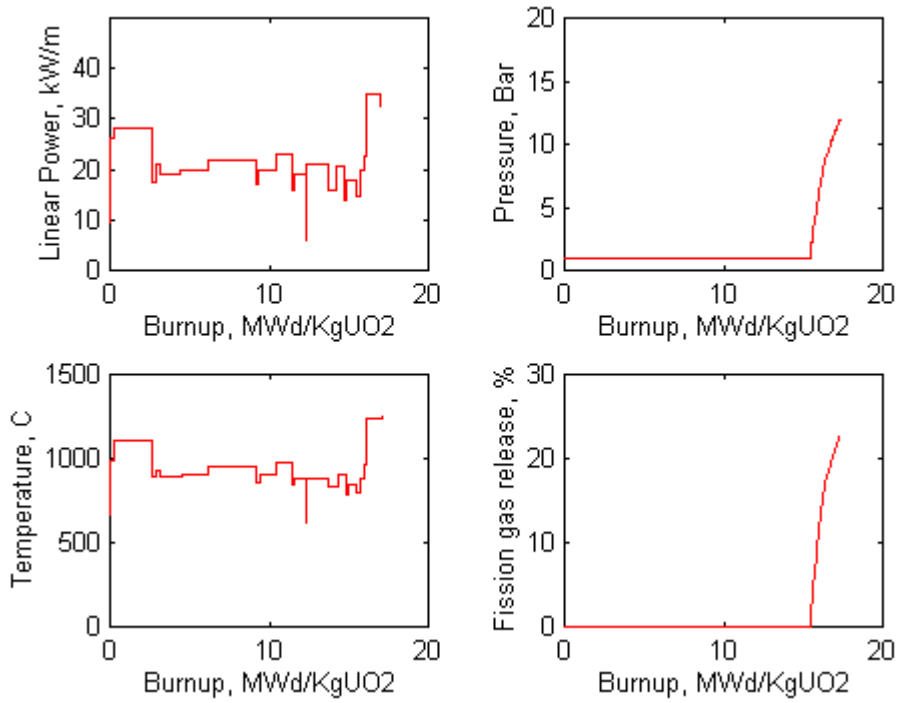

FIG.5. Simplified power history and calculation results corresponding to FUMEX 5.

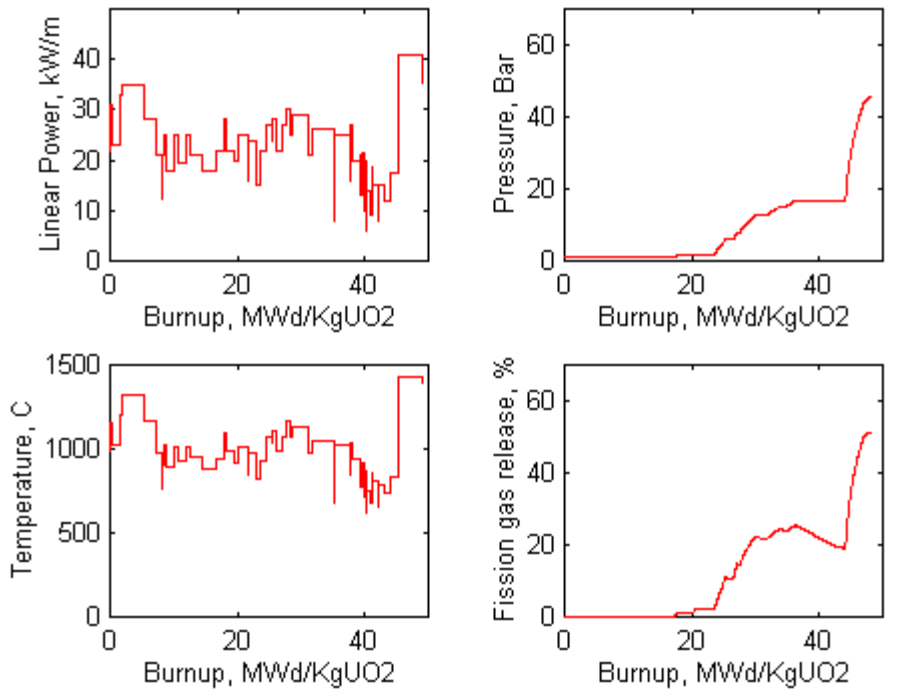

FIG.6. Simplified power history and calculation results corresponding to FUMEX 6F.

TABLE II. COMPARISON BETWEEN DATA OF THE FUMEX EXPERIMENT AND THE PRESENT CALCULATIONS

		experimental	other codes	this code
FUMEX 1	central temperature at 20MWd/kgUO2, °C	740	508–800	734
	FGR at EOL, %	1.8	0.05–2.18	1.47
FUMEX 2	central temp. at 5MWd/kgUO2 and 40kW/m, °C		1210–1820	1584
	FGR at EOL, %	3	1.2–28.8	3.69
	internal rod pressure at power and EOL, bar	20.3	20.1–50	22.9
FUMEX 3 rod 2	central temp. before power ramp, °C	1040	865–1365	1042
	FGR before power ramp, %		0.6–44	42.3
	FGR after power ramp, %		5.3–50.5	50.4
FUMEX 4 rod A	central temp. at start–up and 30 kW/m, °C	1020	876–1398	1067
	central temp. during power ramp, °C	1125	792–1533	1161
	central temp. at EOL, °C	1225	1035–2246	1610
	FRG before power ramp, %		0.3–10.6	7
	FGR during power ramp, %		0.7–26.1	7.1
	FGR at EOL, %		15.4–53.8	38.6
FUMEX 4 rod B	central temp. at start–up, °C	1065	953–1522	957
	central temp. at the top of the ramp, °C	1260	1200–1593	1445
	central temp. at EOL, °C	1290	1213–2203	1482
	FGR at EOL, %		27.5–50	40.3
	pressure at hot standby after power ramp, bar	23.9	3–45.3	19.9
FUMEX 5	FGR before period of high power, %	0	0–43.1	0
	FGR at EOL, %	5.8	1–21.7	2.3
	pressure at start–up, bar	2.3	2.7–66.6	1
	pressure at EOL, bar	9.4	3.9–82.6	12.1
FUMEX 6	FGR at end of base irradiation, %	16.4	7–20.2	19.1
	pressure at end of base irradiation, bar		7.6–79.5	15.7
FUMEX 6F	FGR at EOL, %	45	8.9–38.2	51.2
	pressure at EOL, bar	84.6	40.4–102	44.9
FUMEX 6S	FGR at EOL, %	50	14–50.4	80.6
	pressure at EOL, bar	92.3	40.4–106.7	69.1

5. CONCLUSIONS

Although the results shown above are quite acceptable, the code requires further improvement. For instance, a gas mixing model needs to be included. The code doesn't contain an adequate treatment of the power ramps, which are averaged. The description in the axial direction has to be modified in order to simulate rod elongation. It is expected that these modifications will improve the performance of the code.

ACKNOWLEDGEMENTS

The authors wish to acknowledge Ing. L. Álvarez and Lic. A. Marino for the provision of the data with which the calculations were performed.

REFERENCES

[1] MATHEWS, J.R., The quantitative description of deformation and stress in cylindrical fast reactor fuel pins, in Advances in Nuclear Science and Technology, Vol.6 (1972), Academic Press.

[2] CAILLOT, L., LINET, B., LEMAIGNAN, C., Pellet clad interaction in PWR fuel. Analytical irradiation experiment and finite element modelling, (Proc. SMIRT 12, Stuttgart, Germany, 1993)

[3] DELETE, G., CHARLES, M., "Thermal conductivity of fully dense unirradiated UO_2: a new formulation from experimental results between 100°C and 2500°C and associated fundamental properties", Water Reactor Fuel Element Modelling at High Burnup and its Experimental Support, IAEA–TECDOC–957, IAEA (1997) 203–216.

[4] TIMOSHENKO, S., Theory of elasticity, McGraw Hill, 1951.

[5] PENNY, MARRIOT, Design for creep, McGraw Hill, 1971.

[6] HARRIAGUE, S., COROLI, G., SAVINO, E., BACO, a computer code for simulating a reactor fuel rod performance, Nucl. Eng. and Design 56 (1980) 91–103.

[7] SEGERLIND, L.J., Applied finite element analysis, 2nd Ed., Wiley (1984).

[8] Handbook of materials properties for use in the analysis of light water reactor fuel behavior, MATPRO version 11, NUREG/CR-0497, TREE–1280 (1979).

[9] DENIS, A., PIOTRKOWSKI, R., Simulation of isothermal fission gas release, J. of Nucl. Mater. 229 (1996) 149–154.

[10] DENIS, A., PIOTRKOWSKI, R., A fission gas release model, Water Reactor Fuel Element Modeling at High Burnup and Experimental Support, IAEA-TECDOC-957, IAEA (1997) 455–465.

[11] TURNBULL, J.A., WHITE, R., WISE, C., The diffusion coefficient of Fission Gas Atoms in UO_2, IAEA TC 659/3.5 (1987) 174–181.

[12] WHITE, R., TUCKER, M., A new fission gas release model, J. of Nucl. Mater. 118 (1983) 1–38.

[13] ITO, K.,IWASAKI, R:,IWANO, Y., Finite element model for analysis of fission gas release from UO_2 fuel, J. of Nucl. Sci. and Technol. 22 (2) (1985) 129–138.

[14] NAKAJIMA, T., A comparison between fission gas release data and FEMAXI–IV code calculations, Nucl. Eng. And Design 101 (1987) 267–279.

[15] STAUFFER, D., Introduction to percolation theory, Taylor & Francis, London ans Philadelphia, 1985.

[16] MALDOVÁN, M., DENIS, A., PIOTRKOWSKI, R., Simulation of isothermal fission gas release. An analytical solution, Nucl. Eng. and Design 187 (1999) 327–337.

[17] OLANDER, D., Fundamental aspects of nuclear reactor fuel elements, Technical Information Center, USDOE, 1976.

[18] FRANKLIN, D., ROBERTS, J., LI, C., Low temperature swelling and densification properties of LWR fuels, J. of Nucl. Mater. 125 (1984) 96–103.

[19] MARINO, A., SAVINO, E., HARRIAGUE, S., BACO code version 2.20: a thermomechanical description of a nuclear fuel rod, J.Nucl. Mater. 229 (1996) 155–168.

[20] INTERNATIONAL ATOMIC ENERGY AGENCY, Fuel Modeling at extended burnup, IAEA–TECDOC–998.

MODELLING OF STRESS CORROSION CRACKING IN ZIRCONIUM ALLOYS

O. FANDEUR[1,2], L. ROUILLON[1], P. PILVIN[2], P. JACQUES[3], V. REBEYROLLE[4]

[1] CEA, Centre de Saclay, Gif-sur-Yvette, France
[2] École Centrale Paris, Châtenay-Malabry, France
[3] EDF Septen, Villeurbanne, France
[4] FRAMATOME, Lyon, France

Abstract

During normal and incidental operating conditions, PWR power plants must comply with the first safety requirement, which is to ensure that the cladding wall is sound. Indeed some severe power transients potentially induce Stress Corrosion Cracking (SCC) of the zirconium alloy clad, due to strong Pellet Cladding Interaction (PCI). Since, at present, the prevention of this risk has some consequences on the French reactors manoeuvrability, a better understanding and forecast of the clad damage related to SCC/PCI is needed. With this aim, power ramp tests are performed in experimental reactors to assess the fuel rod behaviour and evaluate PCI failure risks. To study in detail SCC mechanisms, additional laboratory experiments are carried out on non-irradiated and irradiated cladding tubes. Numerical simulations of these tests have been developed aiming, on the one hand, to evaluate mechanical state variables and, on the other hand, to study consistent mechanical parameters for describing stress corrosion clad failure. The main result of this simulation is the determination of the validity ranges of the stress intensity factor, which is frequently used to model SCC. This parameter appears to be valid only at the onset of crack growth, when crack length remains short. In addition, the role of plastic strain rate and plastic strain as controlling parameters of the SCC process has been analysed in detail using the above mechanical description of the crack tip mechanical fields. Finally the numerical determination of the first-order parameter(s) in the crack propagation rate law is completed by the development of laboratory tests focused on these parameters. These tests aim to support experimentally the results of the FE simulation.

1. INTRODUCTION

During normal and incidental operating conditions, PWR power plants must comply with the first safety requirement, which is to ensure that the cladding wall is sound. Indeed some severe power transients potentially induce Stress Corrosion Cracking (SCC) of the zirconium alloy clad, due to strong Pellet Cladding Interaction (PCI) [1]. Since, at present, the prevention of this risk has some consequences on the French reactors manoeuvrability, a better understanding and forecast of the clad damage related to SCC/PCI is needed.

With this aim, power ramp tests are performed in experimental reactors to assess the fuel rod behaviour and evaluate PCI failure risks. However these tests give a global answer whereas a detailed analysis of stress corrosion cracks would be needed. Moreover, Finite Element (FE) simulations of fuel rod behaviour during a power transient show that an accurate evaluation of the clad mechanical state depends on the modelling of phenomena involved in PCI. Thus, to study in details SCC mechanisms, additional laboratory experiments are realised on non-irradiated and irradiated cladding tubes; these internal pressurisation tests are performed with well-defined geometry and boundary conditions.

Numerical simulation of these tests has been developed aiming, on the one hand, to evaluate mechanical state variables and, on the other hand, to study consistent mechanical parameters for describing stress corrosion clad failure. The development of new laboratory tests helps to

validate experimentally the results of these FE simulations and to determine the first-order mechanical parameters in the crack growth law.

2. MATERIAL DESCRIPTION

The material investigated in this study is a Stress-Relieved (SR) low-tin content Zircaloy-4, which is commonly used for fuel claddings in Pressurised Water Reactor (PWR). Its chemical composition in weight percent, in agreement with the ASTM B 350.90 specification, is given in Table I.

Table I. WEIGHT COMPOSITION OF SR ZIRCALOY-4

Alloying elements (%)				
Sn 1.30	Fe 0.22	Cr 0.12	O 0.130	Zr balance

The cladding tube geometry is defined by a 9.5-mm outside diameter and a 0.57-mm thickness. The irradiated specimens were cut from fuel rods which have been irradiated during one or two operating cycles in a French PWR. Table II summarises the three studied Zircaloy-4 batches.

Table II. INVESTIGATED MATERIALS

Batch reference	Fluence (neutrons/m^2)	Burnup (GWd/t U)
A	0	0
B	$1.7\ 10^{25}$	10.0
C	$4.3\ 10^{25}$	23.1

Due to its fabrication processing, SR Zircaloy-4 exhibits a pronounced crystallographic texture, as shown on Figure 1. This texture does not seem to be significantly modified by irradiation [2]. The microstructure of the stress-relieved metallurgical state is characterised by elongated grains along the rolling direction, which corresponds to the axial direction of cladding tubes. The grain size is 20 µm long in the rolling direction and 2 µm wide in the transverse direction.

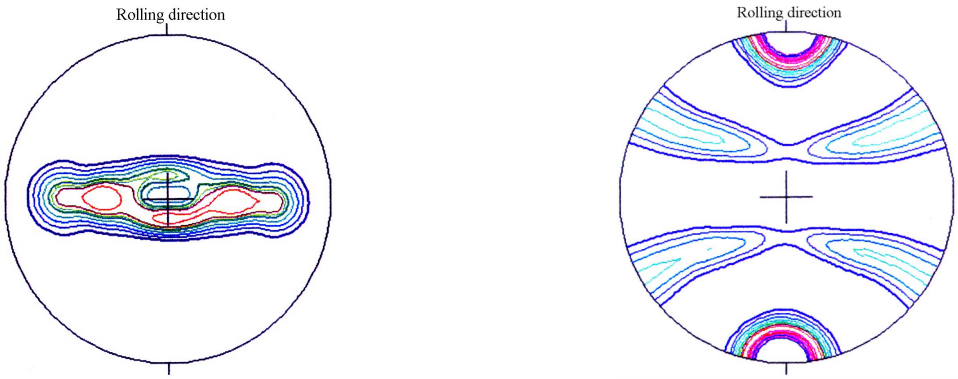

FIG. 1. Cladding tube pole figures (a) (0002) basal plane, (b) $(10\bar{1}\,0)$ prismatic plane [2].

The texture and the hexagonal close-packed lattice imply a strong mechanical anisotropy. Assuming that the anisotropic axis and the texture axis are the same, Zircaloy-4 tubes have an orthotropic behaviour whose directions correspond respectively to the radial, hoop, and axial directions. In spite of a pronounced anisotropy, the elastic behaviour can be considered isotropic and the elastic parameters (Young modulus E and Poisson coefficient ν) are only temperature dependant and not burnup dependant.

3. EXPERIMENTAL PROCEDURE

All the tests performed are internal pressurisation tests, because of commercial product geometry (thin-walled tube) and availability, especially for irradiated material. The working temperature is 623 K (350°C). The inert gas is high purity helium and the aggressive environment is gaseous iodine created by introducing bisublimated iodine (in general 75 mg) inside the tube.

The principal stages of a test are the following:

(i) Sample preparation: metrology, Gyrolock^{TM} seal system, steel end-plugs.
(ii) Iodine preparation: weighting, putting into a Zirconium melting pot.
(iii) Setting up the sample tube into the pressurisation test installation with the iodine carrier inside. To avoid iodine pollution by room air, stages (ii) and (iii) have to be done in about five minutes.
(iv) After air evacuation (primary vacuum), specimens are pressurised up to 5 bars to detect eventual leaks and then heated to the temperature test (iodine crystals vaporise). This step lasts one hour.
(v) Tube pressurisation with a constant pressure-loading rate of 2 bar.s^{-1}.
(vi) Sample examination: metrology, SEM examinations…

Temperature and internal pressure are continuously recorded during each test.

The sample tubes whose length is 135 mm are closed during the test. Hydrostatic end effect must be taken into account and, on the inner tube surface, the hoop, axial and radial stresses are respectively equal to:

$$\sigma_{\theta\theta} = p\frac{R_e^2 + R_i^2}{R_e^2 - R_i^2},\ \sigma_{zz} = p\frac{R_i^2}{R_e^2 - R_i^2} \text{ and } \sigma_{rr} = -p\ ,$$

where p is the internal pressure, R_e and R_i are the outside and inside radius respectively.

Two different types of tests can be achieved (see Figure 2):

(1) The *"conventional"* test, frequently used [1, 3, 4]. The hoop stress (pressure) is increased to the test stress $\sigma_{\theta\theta M}$ and maintained until clad failure.
(2) The *"discriminating"* test. The hoop stress is increased to an *"high"* stress $\sigma_{\theta\theta H}$ and kept constant during a predetermined duration T_S, which can be called *"dwell time"*, then the hoop stress is decreased to a *"low"* stress $\sigma_{\theta\theta L}$ and kept constant with time up to failure.

All the pressure transients are done with a constant pressure rate of 2 bar.s^{-1}.

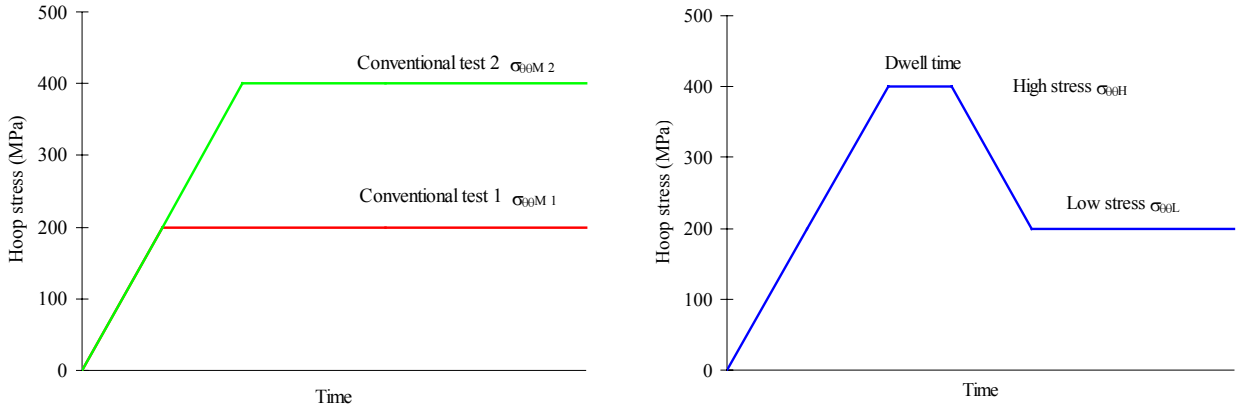

FIG. 2. Description of the different internal pressurisation tests: (left) "conventional" test, (right) "discriminating" test.

4. EXPERIMENTAL RESULTS

4.1. "Conventional" test results on irradiated ZIRCALOY-4

Tables III and IV gather the results of "conventional" tests performed on both irradiated materials (batches B and C). In order to evaluate SCC susceptibility with irradiation, a normalised hoop stress $\|\sigma_{\theta\theta}\|$ has been defined. It corresponds to the ratio between the test hoop stress $\sigma_{\theta\theta M}$ and the hoop conventional yield stress $\sigma_{\theta\theta 0.2\%}$ determined elsewhere. The evolution of $\|\sigma_{\theta\theta}\|$ versus time to failure is reported on Figure 3.

Table III. INTERNAL PRESSURE TESTS ON IRRADIATED ZIRCALOY-4 (BATCH B)

Ref. test	Atmosphere	Hoop stress $\sigma_{\theta\theta M}$ (MPa)	Time to failure (h)	
B_1	Helium	688	0.32	Burst
B_2	Helium	628	5.16	Burst
B_3	Helium	503	78.52	Burst
B_4 / B_5	Iodine	506 / 507	0.49 / 0.46	SCC-burst
B_6 / B_7	Iodine	403 / 403	0.72 / 0.66	SCC-burst
B_8 / B_9	Iodine	202 / 202	1.03 / 1.74	SCC pinhole
B_10 / B_11	Iodine	162 / 162	1.45 / 2.79	SCC pinhole
B_12	Iodine	143	6.05	SCC pinhole

Table IV. INTERNAL PRESSURE TESTS ON IRRADIATED ZIRCALOY-4 (BATCH C)

Ref. test	Atmosphere	Hoop stress $\sigma_{\theta\theta M}$ (MPa)	Time to failure (h)	
C_1	Helium	506	73.90	Burst
C_2	Iodine	506	0.60	SCC-burst
C_3	Iodine	402	0.84	SCC-burst
C_4 / C_5 / C_6	Iodine	207 / 206 / 207	0.55 / 0.96 / 1.75	SCC pinhole
C_7 / C_8	Iodine	167 / 168	1.46 / 3.95	SCC pinhole
C_9	Iodine	143	2.98	SCC pinhole

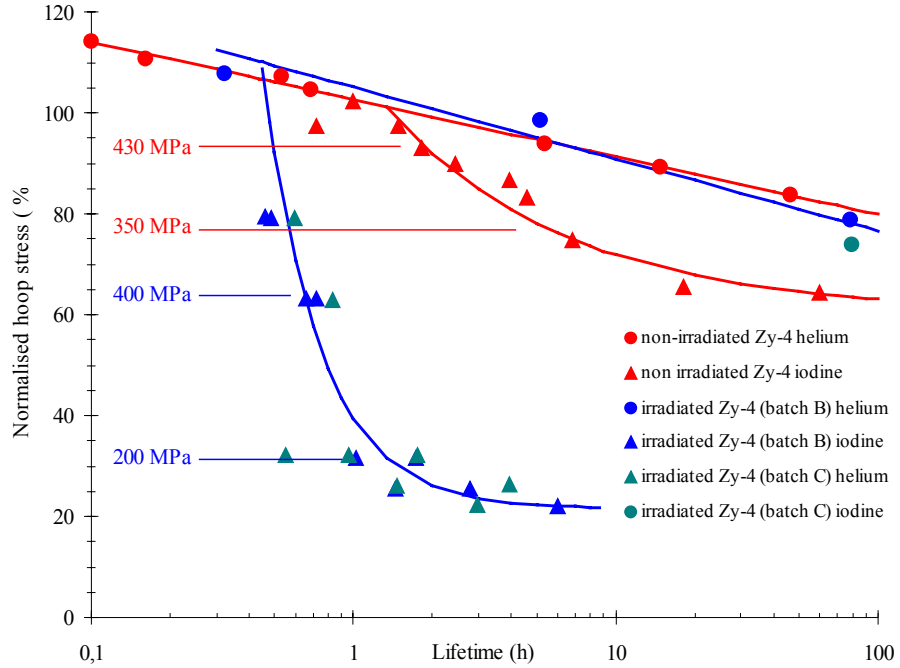

FIG. 3. Normalised hoop stress versus time to failure evolution. Burnup effect on SCC susceptibility.

It is shown that irradiation has an important effect on SCC susceptibility. In particular, time to failure reduction upon irradiation occurs at low stress levels. Moreover no susceptibility change is notable when burnup increases from 10 to 23 GWd/t U.

4.2. "Discriminating" test results on irradiated ZIRCALOY-4

"Discriminating" test validation

During a "discriminating" test, decreasing pressure implies partial internal gas evacuation and a loss of iodine with the pressurisation installation used. To simulate this loss, "conventional" tests have been conducted at a low stress level ($\sigma_{\theta\theta M}$ = 350 MPa) on non-irradiated material with various initial iodine concentrations. The results of the validation tests are reported on Table V.

Table V. INFLUENCE OF INITIAL IODINE CONCENTRATION ON SCC SUSCEPTIBILITY OF NON-IRRADIATED MATERIAL (BATCH A)

Initial iodine concentration (mg)	Time to failure (h)	Average hoop plastic strain	Number of tests performed
30	4.6 ± 0.5	0.34 ± 0.03 %	5
75	3.9 ± 1.6	0.31 ± 0.05 %	4
120	3.7 ± 0.7	0.34 ± 0.05 %	4

It is shown that the initial iodine concentration has almost no influence on the time to failure and on the hoop plastic strain measured after testing. It is therefore assumed that iodine loss following pressure decrease will not explain eventual differences between times to failure in "discriminating" tests and those measured in "conventional" tests.

"Discriminating" test results

The conditions for the "discriminating" tests are the following:

(i) Initial iodine concentration of 75 mg.

(ii) The "high" and "low" stresses are $\sigma_{\theta\theta H}$ = 430 MPa and $\sigma_{\theta\theta L}$ = 350 MPa.

(iii) Various "dwell time" T_S equal to 0, 20 and 60 minutes have been tested.

The experimental results are gathered on Table VI.

Table VI. "DISCRIMINATE" TEST RESULTS. INFLUENCE OF "DWELL TIME".COMPARISON WITH "CONVENTIONAL" TESTS

Test ref.	Hoop stress $\sigma_{\theta\theta M}$ (MPa)	Time to failure (h)	Average hoop Plastic strain	Intergranular crack depth (µm)	Number of tests performed
"Conventional" tests (using as reference)					
A_Cl_1	350	3.9 ± 1.6	0.33 ± 0,05 %	60	5
A_Cl_2	430	1.8	1.1 %	Non measured	1

Test ref.	"Dwell time" T_S (h)	Time to failure (h)	Average hoop Plastic strain	Intergranular crack depth (µm)	Number of tests performed
"Discriminate" tests ($\sigma_{\theta\theta H}$ = 430 MPa, $\sigma_{\theta\theta L}$ = 350 MPa)					
A_D_1	0	4.5 ± 0.3	0.38 ± 0.03 %	130 (*)	2
A_D_2	0.33	4.3 ± 0.2	0.55 ± 0.05 %	150 (*)	2
A_D_3	1	3.9 ± 0.1	0.77 %	150-200 (*)	2

(*) Important oxidation of fracture surfaces.

An important oxidation of fracture surfaces makes difficult the observation and measurement of intergranular crack growth. (An example can be shown on Figure 4). By observing other SCC sites inside the tube, it can be deduced that oxidation follows clad failure.

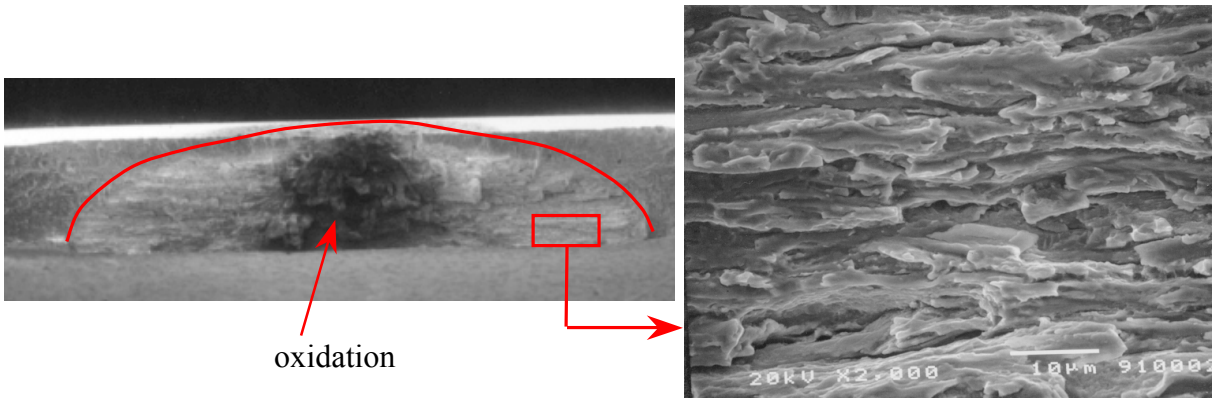

(a) (b)

FIG. 4. "Discriminating" test with a 20-minute "dwell time" (SEM observations): (a) fracture surface with important oxidation, (b) intergranular propagation domain.

In "discriminating" tests, times to failure are close to each other. In contrast with "conventional" test results, overload pressure ("high" stress during "dwell time") has no influence on clad lifetime. Hoop plastic strain increases when "dwell time" increases and

appears not to be a controlling parameter of SCC clad failure. Conversely intergranular crack size increases with "dwell time" increments. In this case, it wonders whether the identical lifetimes are the results of compensating opposite effects: faster crack propagation during "dwell time" at "high" stress than in "conventional" tests and these longer cracks propagate slower at "low" stress than in "conventional" tests conducting to identical times to failure.

5. FINITE ELEMENT SIMULATIONS

To access to local information which can not be obtained during experiments, especially on clad geometry, finite element simulations have been carried out. The finite element ABAQUS^{TM} code has been used.

5.1. Modelling assumptions

The following assumptions are used in the finite element simulations:

(1) Only one crack is propagating. The tube and the SCC crack are supposed to be axially infinite. This is supported by the view that measured ratios between crack length and depth are about 10 to 1. 2D calculations can then be computed. Figure 5 shows respectively the boundary conditions of this 2D model (a) and the mesh (3033 nodes and 2752 linear elements used in calculations (b).
(2) The generalised plane strains case has been used to take into account hydrostatic end effect and stress triaxiality at the crack tip vicinity.
(3) An ElastoViscoPlastic (EVP) constitutive law has been identified on non-irradiated Zircaloy-4 and on irradiated Zircaloy-4 (batch C). More detailed can be found in [5].
(4) As for the test, the temperature is held constant during the computations (350°C).

5.2. Validity range of the stress intensity factor

It is commonly accepted that transgranular crack velocity v_{TG} is linked to stress intensity factor K_I [1, 3, 4]. In particular, transgranular cracking appears when the threshold intensity factor $K_{I\,SCC}$ is reached at the crack tip. Considering the laboratory and reactor conditions (high temperature, Zircaloy-4 creep…), it is worth determining the validity ranges of this linear elastic fracture mechanics approach.

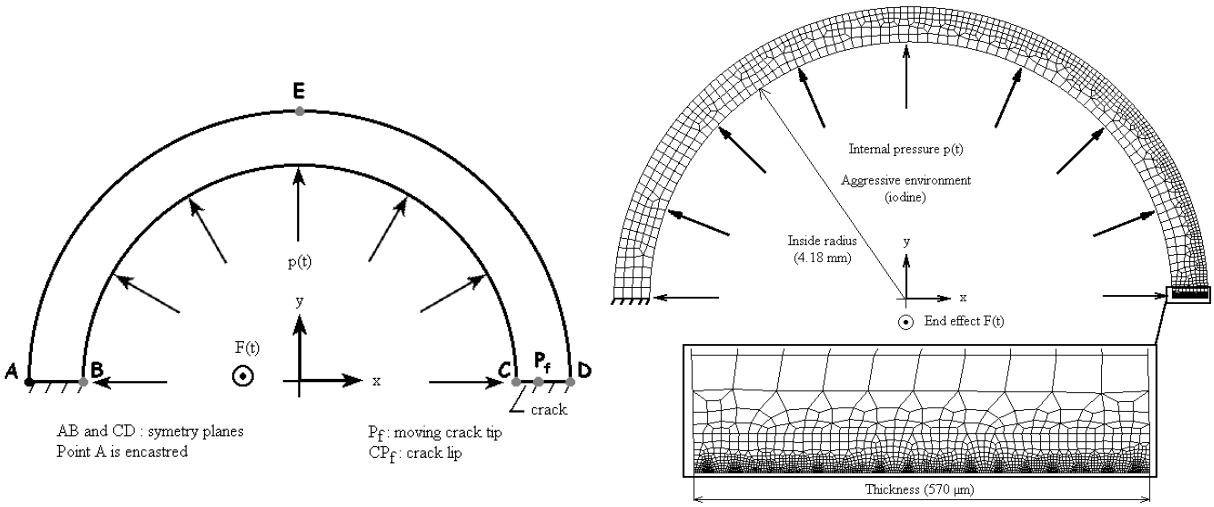

FIG. 5. (a) 2D model boundary condition, (b) 2D mesh used for simulations.

To achieve this study, "conventional" internal pressurisation tests have been simulated where an incipient crack pre-exists at the inner surface of the tube. Figure 6 shows the evolution of the pressure loading and the crack propagation law modelled. The pre-existing crack depth is noted a_{ini}. The internal pressure p is increased to the test level p_M at a constant pressure loading rate δp. The crack initiates when the internal pressure p is equal to p_{SCC}; the threshold stress intensity factor $K_{I\,SCC}$ is reached. The propagation rate v_{TG} is constant in agreement with measured average velocity values.

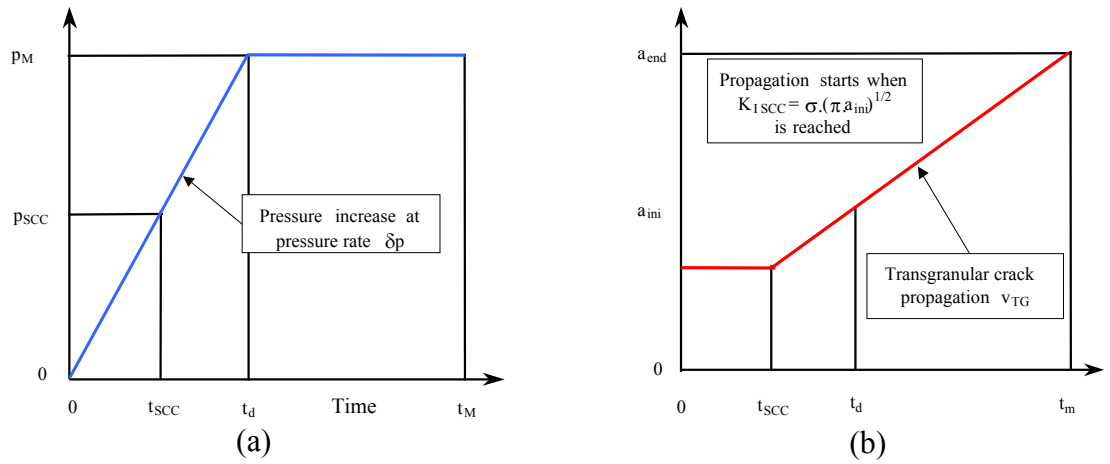

FIG. 6. Loading definition: (a) internal pressure evolution, (b) transgranular crack propagation law.

The comparison between stress fields at the crack tip vicinity calculated respectively with an elastic behaviour and an elastoviscoplastic mechanical behaviour allows to determine the crack depth a_f over which the use of K_I is no longer valid.

The criterion used is the following:

$$\left| \frac{\sigma_{\theta\theta\ \text{Elastic calculation}}(r) - \sigma_{\theta\theta\ \text{Viscoplastic calculation}}(r)}{\sigma_{\theta\theta\ \text{Elastic calculation}}(r)} \right| \leq 0{,}05 \text{ for } r > r_y \,,$$

where r is the distance to crack tip and r_y is the plastic zone size (given by the Irwin's formula for instance). The introduction of the r_y value allows to eliminate numerical problems near the crack tip in finite elements calculations.

Figure 7 shows the hoop stress distribution along the ligament for different crack depths in elastic and EVP calculations. In this example, the crack depth a_f can be estimated at 175 µm.

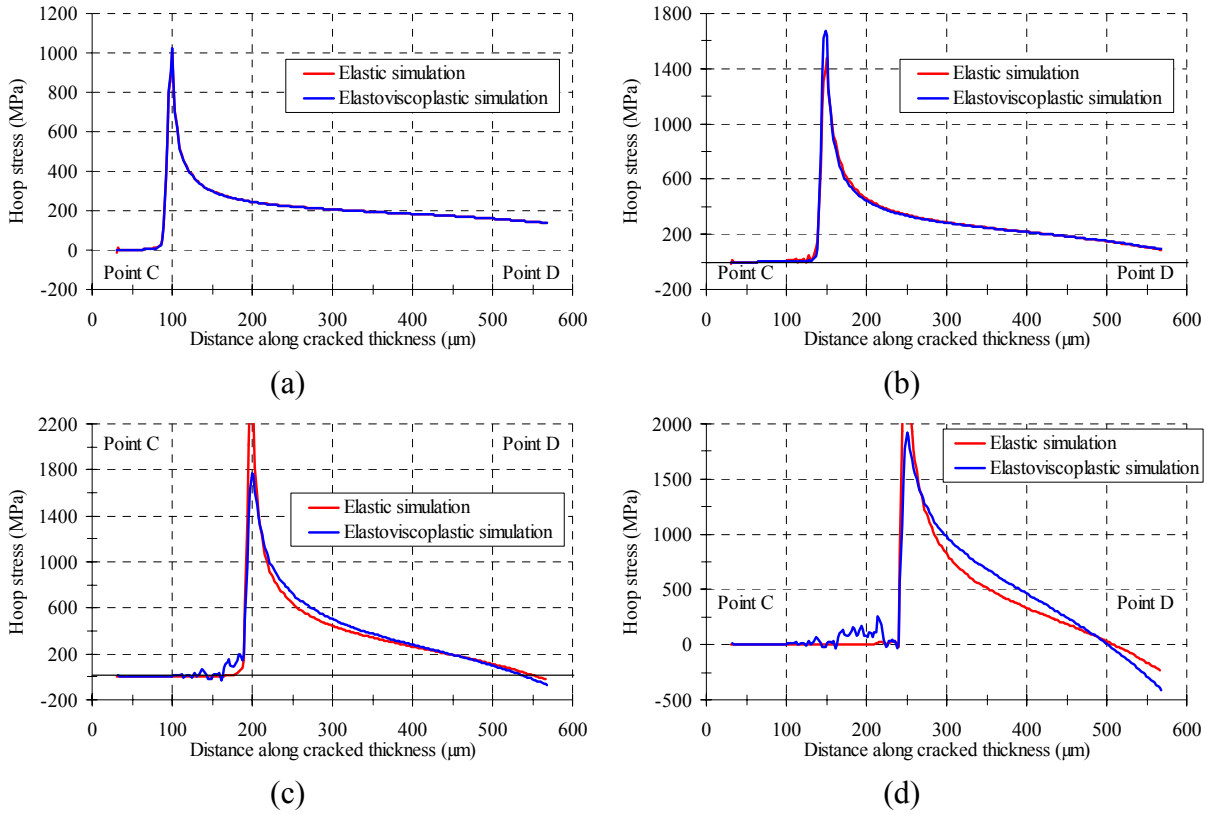

FIG. 7. Hoop stress evolutions during an internal pressurisation test on a batch C tube (a_{ini} = 30 µm, $\sigma_{\theta\theta M}$ = 300 MPa, v_{TG} = 2 µm.s^{-1}) when crack depth is equal to (a) 100 µm, (b) 150 µm, (c) 200 µm, (d) 250 µm. Numerical results.

Table VII summarises the results obtained from "conventional" test calculations with various loading conditions for irradiated cladding material (equivalent to batch C). A pressure rate δp of 13 bar.s^{-1} corresponds to the hoop stress rate calculated during a power transient in a PWR. In particular the K_I validity surface can be drawn as seen on Figure 8.

Table VII. NUMERICAL RESULTS SYNTHESIS: K_I VALIDITY RANGE FOR IRRADIATED ZIRCALOY-4 (BATCH C)

Hoop stress $\sigma_{\theta\theta M}$ (MPa)	Pressure p_M (bar)	Pressure loading rate δp (bar.s^{-1})	Average transgranular crack velocity v_{TG} (µm.s^{-1})	Crack depth a_f "validity boundary" (µm)
200	250	2 2	1 2	$175 < a_f <$ **200** $200 < a_f <$ **225**
300	380	2 2 13	1 2 2	$125 < a_f < 150$ $150 < a_f <$ **175** **100** $< a_f < 125$
400	510	2 13	1 2	$100 < a_f <$ **125** **80** $< a_f < 100$

The main result of these simulations is the determination of the validity ranges of the stress intensity factor K_I which is frequently used to model SCC. This parameter appears not to be valid during the whole crack propagation, but only at the beginning, when crack lengths

remain short. Moreover, the validity range of this factor appears to be independent upon the used viscoplastic behaviour (anisotropic or isotropic), whilst it is affected by the values of pressure loading rates and average crack velocities.

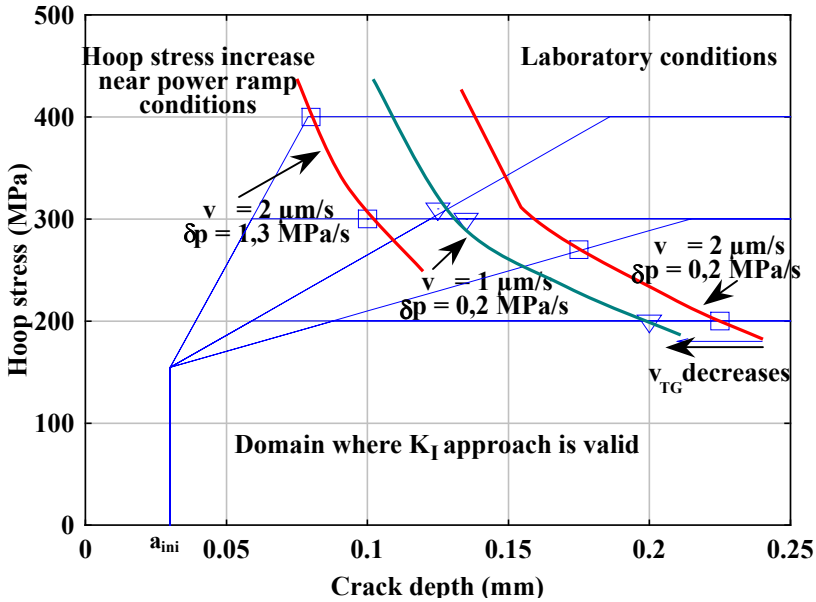

FIG. 8. K_I validity range graph. Irradiated Zircaloy-4 (batch D).

5.3. "Discriminating" internal pressure test simulations

Numerical simulation of "discriminating" tests has been developed aiming, on the one hand, to evaluate mechanical state variables and, on the other hand, to study consistent mechanical parameters for describing stress corrosion clad failure.

The cladding tube is supposed to be initially sound. The crack propagation law is described on Figure 9. Both intergranular and transgranular propagations have been modelled. The average crack velocities are constant and respectively equal to $v_{IG} = 0.01\ \mu m.s^{-1}$ and $v_{TG} = 1\ \mu m.s^{-1}$. These values are compatible with experimental values and published data (see [1] for example). Assuming equal velocities, whatever the simulated test is, helps to study consistent mechanical parameters, because their evolutions are only the consequence of different loadings.

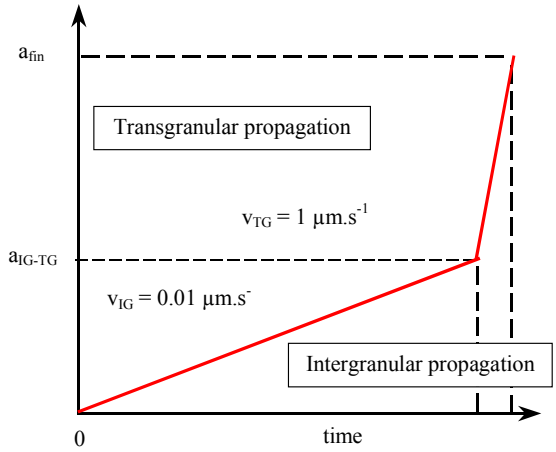

FIG. 9. Crack propagation law in "discriminating" test simulation.

Computations allow to study mechanical parameter evolution at the crack tip during SCC propagation. Comparison between hoop plastic strain, hoop stress and hoop plastic strain during “conventional” test ($\sigma_{\theta\theta M}$ =350 MPa) and “discriminating” tests ($\sigma_{\theta\theta H}$ =430 MPa, $\sigma_{\theta\theta L}$ =350 MPa) with respectively 0 and 20 minute "dwell time". These three calculations correspond respectively to the test A_Cl_1, A_D_1 and A_D_2 (see paragraph 4). Figures 10 to 12 show the evolution of these three parameters at the crack tip during the first 5000 seconds that corresponds to a crack propagation from 0 to 50 µm.

When considering the experimental clad failure times obtained and the modelling assumptions used, crack tip plastic strain cannot be linked to crack propagation rate although plastic strain is found to be the controlling parameter of SCC initiation [6-8]. Conversely, the role of stress and plastic strain rate contributions as controlling parameters is evidenced in agreement with [9, 10]. However the role of each parameter cannot be extracted. Besides, loading path effects in “discriminating” test on non-irradiated material are less important than expected in “discriminating” tests on irradiated Zircaloy-4 smooth clad (Figure 13).

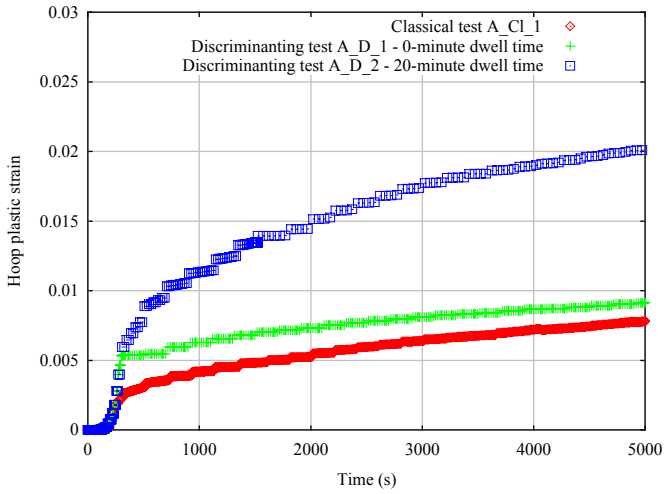

FIG. 10. Crack tip hoop plastic strain evolution versus time during propagation.

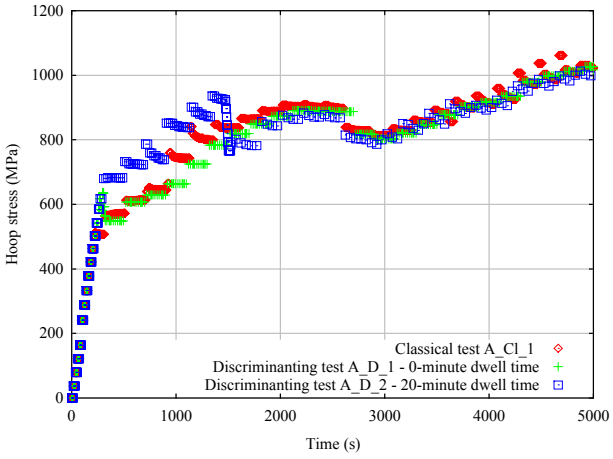

FIG. 11. Crack tip hoop stress evolution versus timeduring propagation.

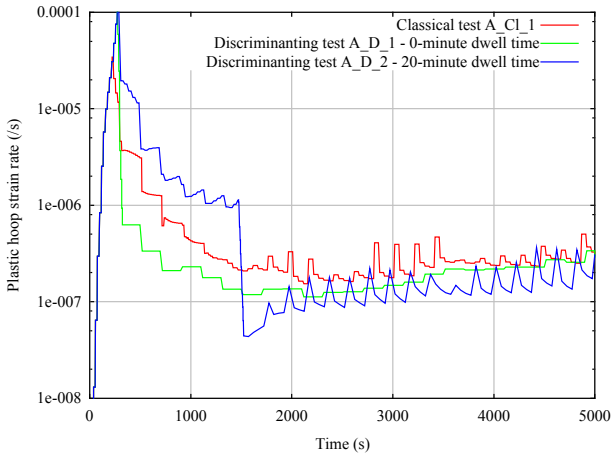

FIG. 12. Crack tip hoop plastic strain rate evolution versus time during propagation.

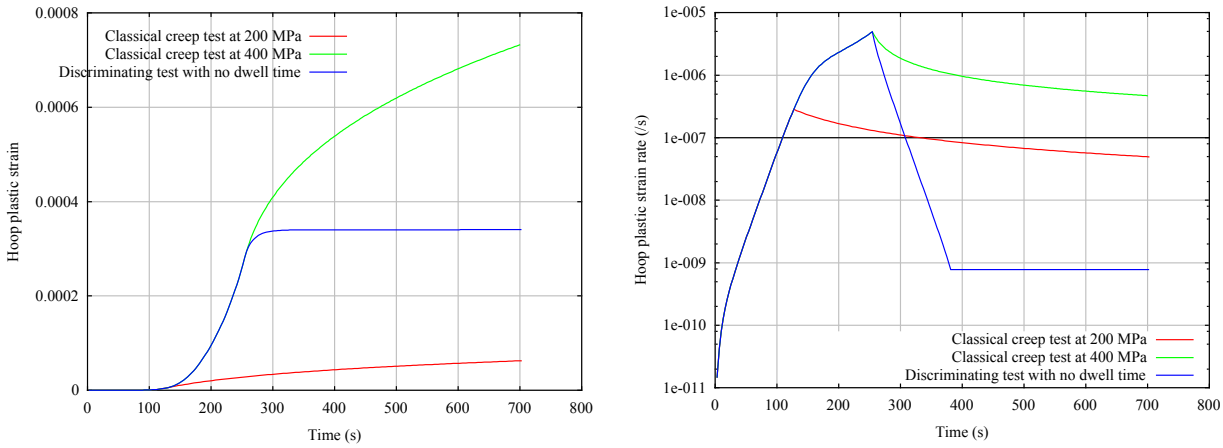

FIG. 13. Simulation of "discriminating" test on irradiated smooth clad (equivalent to batch C). Evolutions versus time of (left) hoop plastic strain and (right) hoop plastic strain rate. Comparison with simulations of "conventional" creep tests.

6. CONCLUSION

New laboratory tests and their associated finite element analyses have been performed in order to determinate the relation between mechanical parameter(s) and SCC propagation.

The main result of these simulations is the determination of the validity ranges of the stress intensity factor. This parameter appears to be valid only at the onset of crack growth, when crack length remains short.

In the literature, plastic strain is pointed out as the controlling parameter of SCC initiation in zirconium alloys. However this assumption seems to be incompatible with the experimental results and the calculations presented here. In contrast this study shows that plastic strain rate appears to play a key role on crack propagation.

Considering that initiation and intergranular propagation lasts about 80 % of the time to failure, a better knowledge of the crack growth law, in particular during the "dwell time", is necessary to improve the finite element modelling. This modelling can then be used to design new experimental tests, especially on irradiated cladding tube, and discriminate between the resistance to SCC of Zirconium alloys to be expected under PCI conditions.

REFERENCES

[1] B. COX, "Pellet-Clad Interaction (PCI) Failures of Zirconium Alloys – A Review", Journal of Nuclear Materials 172, pp. 249-292, 1990.
[2] J.L. BÉCHADE, Private communication, 1999.
[3] L. LUNDE and K. VIDEM, "The Influence of Testing Conditions and Irradiation on the Stress Corrosion Cracking Susceptibility of Zircaloy", Journal of Nuclear Materials 94, pp. 210-218, 1980.
[4] YU.K. BIBILASHVILI, YU.N. DOLGOV, B.I. NESTEROV, and V.V. NOVIKOV, "Propagation of Stress Corrosion Cracks in Zr-1% Nb Claddings", Journal of Nuclear Materials 224, pp. 307-310, 1995.
[5] O. FANDEUR, R. LIMON, P. PILVIN, and C. PRIOUL, to be published, 2000.

[6] P. JACQUES, "Contribution à l'étude de l'amorçage des fissures de corrosion sous contrainte dans le zirconium et le Zircaloy-4", Ph.D., Institut National Polytechnique de Grenoble, 1994.
[7] E. STEINBERG, M. PEEHS, and H. STEHLE, "Development of the Crack Pattern During Stress Corrosion in Zircaloy-Tubes", Journal of Nuclear Materials 118, pp. 286-293, 1983
[8] YU.K. BIBILASHVILI, YU.N., DOLGOV, V.V. NOVIKOV, and A.G. GLAZKOV, "The Initiation of Cracks in Cladding Tubes of Zr-1 % Nb Alloy Under Stress Corrosion Cracking Conditions", Atomic Energy 80, pp. 242-247, 1996.
[9] M. PEEHS, H. STEHLE, and E. STEINBERG, "Out-of-pile Testing of Iodine Stress Corrosion Cracking in Zircaloy Tubing in Relation to the Pellet-Cladding Interaction Phenomenon", Zirconium in Nuclear Industry (Fourth Conference), ASTM STP 681, pp. 229-243, 1979.
[10] S.B. GORYACHEV, A.R. GRITSUK, P.F. PRASOLOV, M.G. SNEGIREV, V.E. SHESTAK, V.V. NOVIKOV, and YU.K. BIBILASHVILI, "Iodine Induced SCC of Zr Alloys at Constant Strain Rate", Journal of Nuclear Materials 199, pp. 50-60, 1992.

THE DEVELOPMENT OF AN EMPIRICAL PCI CRITERION FOR SIEMENS FUEL TO BE LOADED INTO SIZEWELL B

J.H. SHEA
Nuclear Technology Branch, British Energy,
Gloucester, United Kingdom

Abstract

Siemens fuel will be loaded into the core of Sizewell B Power Station. Many Siemens fuel ramp tests have been conducted in test reactors and power reactors. The database has been applied to develop a rod power PCI criterion to describe the failure behaviour of the fuel. Account has been taken of previous experience in this area with the previous vendor's fuel. Qualitative differences are noted between the two PCI databases which indicate different failure probability models are required. The new criterion is discussed in detail. The experience gained has provided guidance for possible relaxation of the criteria while also maintaining safety at the required statistical level.

1. INTRODUCTION

In September 2000 it is intended to load Siemens PCA-2a clad fuel into the Sizewell B cycle 5 core. Amongst the issues requiring to be addressed to aid the planning of this task has been the establishment of a description of the Pellet Clad Interaction (PCI) characteristics of Siemens fuel in normal operation and frequent faults.

A database of almost 200 ramp tests from Studsvik and Petten, and several tests in the operating power reactors at Biblis and Obrigheim were made available by Siemens to aid British Energy in its task. This database has been described in an open literature overview [1].

This paper describes the development of the PCI performance constraint to which Siemens fuel is subject. This has the form of an empirical expression which has been used to assess the suitability of core designs for Sizewell B cycle 5. The expression bears a strong resemblance to that used previously in Sizewell B but has nevertheless some distinctive features.

The determination of the best estimate PCI failure criterion for Siemens fuel was the primary objective of the analysis, where 'best estimate' implies that relation which describes the 50% failure likelihood locus of the entire database. Safety constraints in Sizewell B are however based on the so-called 95/95% criterion line which is that locus below which the likelihood of failure is less than 5% at the 95% confidence level. The safety threshold is based on this latter locus.

2 PREVIOUS PRACTICE WITH PCI

The fuel loaded into Sizewell B prior to cycle 5 has been from a single vendor. The vendor made available a database of ramp results which were used to examine the propensity to PCI failure in this particular fuel [2]. The following features of the database were noted:

(1) The best estimate criterion is a threshold power to failure which decreases weakly with burnup.

(2) The most satisfactory failure probability model for the fuel was a normal distribution based on the end of ramp power with a standard deviation, σ_f, expressed as a fraction of the best estimate transient uprate to failure, ΔP.

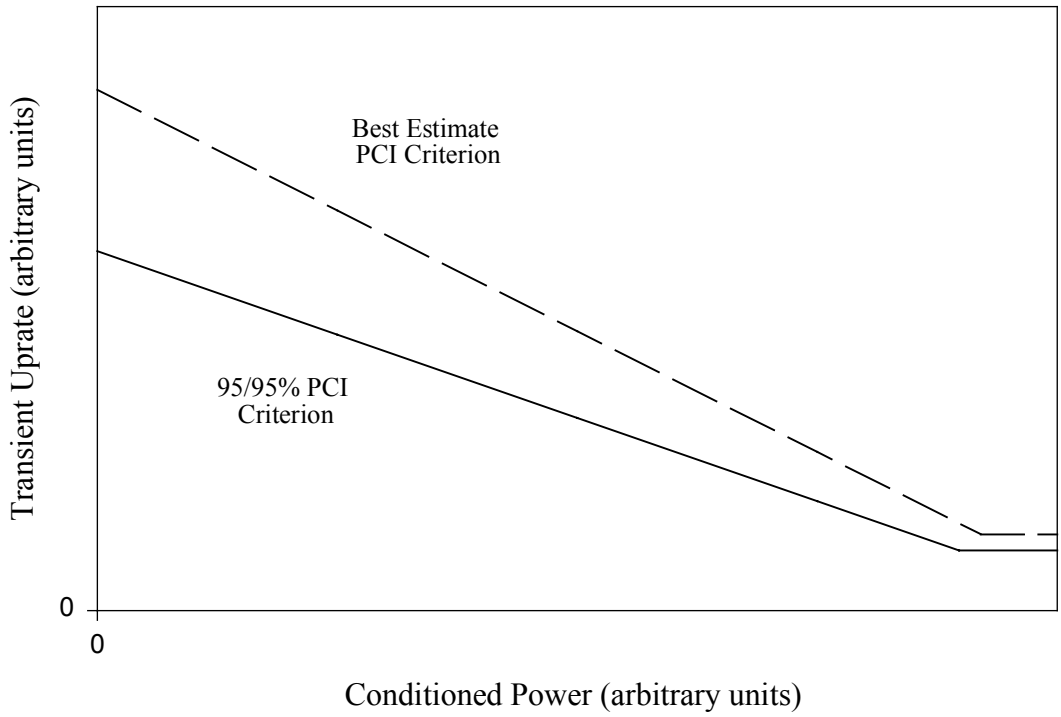

FIG. 1. Comparison of best estimate criterion with 95/95% criterion (equation 2) currently used at Sizewell B.

This conclusion is a consequence of a statistical analysis which uses the failure probability model to maximise the likelihood that the failure rods failed and the survivor rods survived by variation of the model parameters. The model parameters were respectively the best estimate or mean power to failure, the fractional standard deviation σf and the linear coefficient of burnup dependence.

The 95/95% criterion is derived from the best estimate threshold power to failure by reducing it by the number of standard deviations to achieve the required bound.

$$P_{95/95} = P_{be} - K_N \sigma \qquad (1)$$

The 95/95% factor for N data items, K_N, is derived from standard Owens Factor tables [3].This expression thus accounts for the intrinsic failure probability distribution and the finite size of the database. Additionally:

$$P_{be} = [\ P_c + \Delta P\ ]_{be}$$

….where P_c is the conditioned power prior to transient.

Since, for the particular fuel under discussion, the standard deviation is proportional to the transient uprate, ΔP, it follows that:-

$$P_{95/95} = P_{be} - K_N \sigma_f \Delta P_{be}$$

…or alternatively:-

$$P_{95/95} = P_{be} - K_N \sigma_f (P_{be} - P_c) \qquad (2)$$

…from which it follows that a further observation may be made in addition to the two noted above:

(3) The resultant 95/95% criterion is a function of the prior-to-transient conditioned power.

This latter statement has had an important effect on the analysis of the database and on the derivation of the PCI criterion. It has required the prior-to-transient powers P_c to be determined with particular care by using the fuel performance code ENIGMA [4]. For each of the items in the frequent fault database a detailed clad temperature and rating history has had to be constructed to enable the ENIGMA calculations to be performed. The conditioned power prior to the ramp has been defined as either 1) the specified start of transient power if the power has prevailed sufficiently long for the clad hoop stress to be unchanging with time, or 2) the power into the transient at which the clad hoop stress is 50 MPa, whichever is appropriate to the circumstances. The ENIGMA calculations have enabled the database to be transformed from one consisting of values of start of ramp power, transient uprate and burnup to one consisting of conditioned power, P_c, uprate (that is, P_{final}-P_c) and burnup. This transformed dataset is the one from which the currently used PCI criterion for Sizewell B is derived.

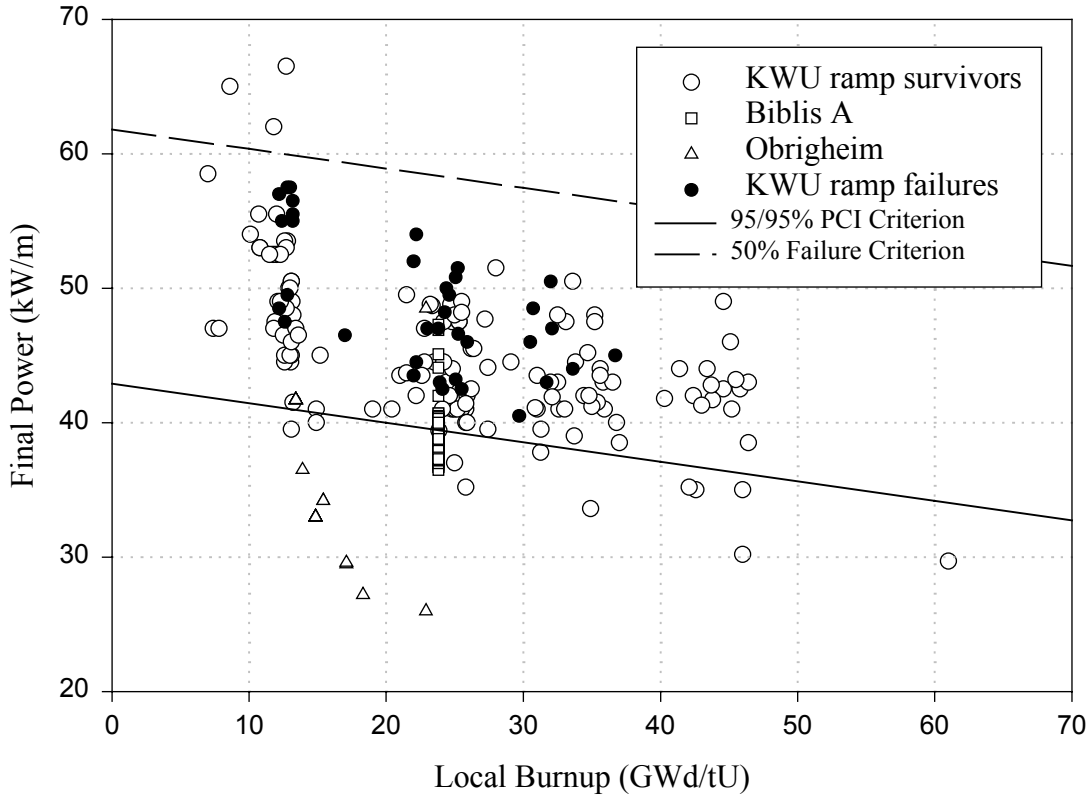

FIG. 2. Siemens final power database versus local burnup.

The final outcome of the analysis described in this section is a best estimate PCI failure criterion having a slope of –1 on a plot of uprate against conditioned power, but with a

95/95% criterion on the same plot having a slope of $-K_N$ which is in practice of order –0.7. Figure 1 depicts these two criteria in arbitrary power units.

3. FUTURE PRACTICE WITH PCI

The previous methodology for the development of a PCI criterion for Sizewell B has been described in some detail to allow the qualitative distinctions between the two types of fuel to be outlined.

The entire Siemens fuel database is depicted in figure 2: the plot shows the final power for each ramped rod or rodlet as a function of the burnup. The black symbols indicate failure and it is notable that there are still many survivors even at the highest final powers. In total about 20% of the test reactor ramps resulted in rod failure. None of the power reactor ramps showed failure. This was intended since these ramps were performed with the intention of demonstrating the existence of a threshold inferred from the test reactor data [1]. It appears from the plot that the incidence of failure decreases at high burnups approaching 40 GWd/tU and beyond.

3.1. Preliminary analysis of the Siemens fuel database

The previous methodology was pursued with the Siemens database. Of the ramp tests performed in test reactors, 48 were determined to have history data suitable for use with the ENIGMA code. The version of the code used was one specially produced for the purpose of assessing the performance of Siemens fuel, ENIGMA 5.10 [4]. The preliminary analysis proceeded with the 48 item subset transformed in the manner described in the previous section so that the dataset ultimately consisted of 48 triplets of respectively conditioned power, uprate to the final power and burnup.

Analysis of this limited dataset initially proceeded with the failure probability model described above. However, the results of the maximum likelihood analysis were quite clear: the fractional standard deviation normal distribution model did not give a reasonable description of the data.

Another, simpler hypothesis was studied. The normal error distribution was retained but the standard deviation was held constant, without any fractional dependence on the magnitude of the uprate. This model was very satisfactory and gave a convincing description of the ramp test results.

This observation has a significant effect on the interpretation of the database, since the confirmation of the effectiveness of a constant standard deviation implies that the 95/95% criterion is a threshold power to failure at the lower 95/95% bound independent of the value of the conditioned power. This means that equation (1) above is sufficient to describe the PCI failure behaviour of the fuel at any statistical confidence level, without the additional complexity of equation (2), so that the 95/95% bound is parallel to the best estimate criterion unlike the situation of Figure 1.

Furthermore, the lack of conditioned power dependence of the power to failure in the criterion implies that the detailed histories for the ENIGMA code are not necessary. This is because for Siemens fuel the conditioned power prior to the ramp need not be determined. Hence the entire database of 182 test reactor ramp results can be included in the statistical optimisation

without additional calculations to determine the conditioned powers. This is the major conclusion from the present stage of analysis.

3.2. The analysis of the complete Siemens fuel test reactor database

The next stage of analysis was to use the final powers and the burnups of each of the 182 test ramps to perform a statistical optimisation with a normal distribution failure probability model, taking advantage of the increased database (from 48 items to 182) to allow definition of a less onerous 95/95% PCI criterion because of the improved precision in the statistics.

However, the database contains much more information than 182 test reactor ramps since, for example, the Biblis A power reactor tests were performed by ramping entire assemblies in relative isolation from the rest of the reactor. It follows that the database supports the adoption of a different failure probability model having a much reduced probability of failure at low powers. Indeed, one showing a threshold effect in PCI vulnerability is indicated. The currently assumed normal distribution does not have this property.

Another acceptable form for the failure probability model is the so-called uniform distribution. This naturally contains a threshold as demonstrated below:

$P_{fail} = 0$ if $P_{final} < P_{be} - W/2$

$P_{fail} = 1$ if $P_{final} > P_{be} + W/2$

$P_{fail} = (P_{final} - P_{be})/W + 0.5$ otherwise

…where W is the total width of the distribution, and [$P_{be} - W/2$] is the assessed threshold power.

The benefit of this failure model in comparison with a more complex one also demonstrating a threshold is that it is entirely sufficient for the purpose and its properties are well understood. It is effectively indistinguishable from the formerly used normal distribution for a broad range ($\sim \pm 1\sigma$) about the mean or best estimate. The distribution full width W can be related to the standard deviation of an equivalent normal distribution by $W = 0.289\sigma$.

The 95/95% factor, K_{182} , applied to the distribution width is readily determined by a Monte Carlo procedure [5] and the final 95/95% PCI criterion for Siemens fuel can be stated as:

$$P_{95/95} = 42.89 - 0.145\ B \qquad (3)$$

…where the local power units are kW/m and the local burnup units are GWd/t U.

Figure 2 shows the 95/95% power to failure criterion, equation (3) for Siemens fuel, expressed as a function of burnup to allow comparison with the Siemens fuel database. The best estimate criterion is also illustrated to demonstrate the way it partitions of the database into failures and survivors, and it is clear the database does not actually encompass the 50% failure likelihood level where numbers of failures and survivors are comparable. This is because the dynamic range of the tests has not reached the best estimate threshold power to failure, although the tests are fully representative of faults to be expected in Sizewell B.

In practice the PCI criterion has usually been defined in terms of the allowable uprate, $\Delta P_{95/95}$, from the current local power level, P_c. Also, the allowable uprate at high conditioned powers is constrained to be small but constant.

$$\Delta P_{95/95} = \text{MAX}(42.89 - P_c - 0.145\ B,\ 4.96) \qquad (4)$$

The uprate criterion of equation (4) is plotted in a total power form against conditioned power in figure 3, superposed on to the database. The test values of ΔP, the uprate, have been corrected by the burnup term, 0.145B, so that only one criterion locus need be plotted, namely $42.89 - P_c$. The conservative nature of the criterion is evident since failures are predominantly above the criterion line.

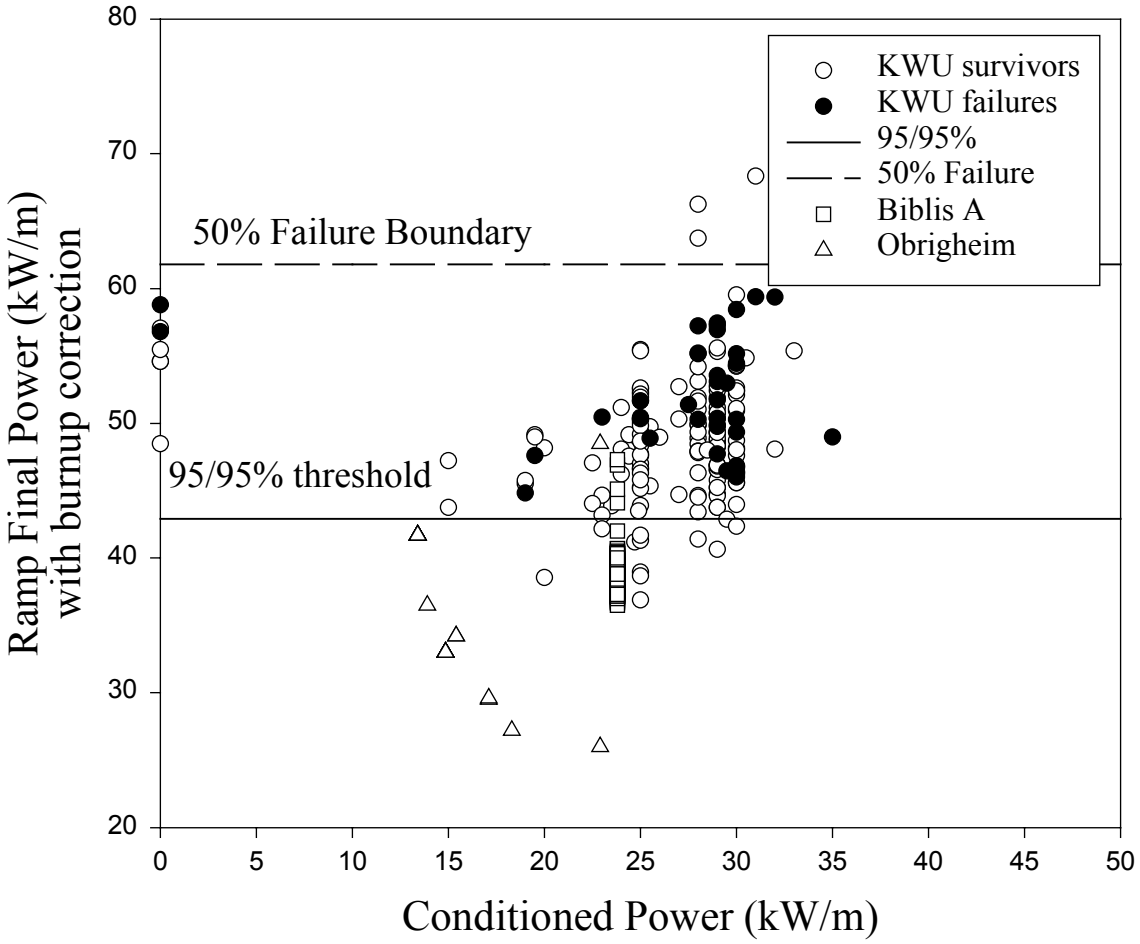

FIG. 3. Siemens Fuel Database with PCI Criteria.

3.3. Further developments

Several additional developments are possible with the analysis already presented and this section will briefly allude to them and indicate the potential benefits.

The possibility of combining the databases for the fuel currently in Sizewell B and the Siemens fuel intended for loading in the imminent cycle 5 is not realistic since the failure probability models required for the respective database analyses have proved to be quite

different. One requires a fractional standard deviation and the other a constant standard deviation. However, the clear evidence of a threshold effect in the Siemens database might reasonably be regarded as a generic feature of LWR fuels. If this is the case, the presently assumed normal distribution with fractional deviation might profitably be replaced by a uniform distribution with fractional width, since the present vendor's fuel will remain in Sizewell B for several cycles and it could provide a relaxation for that fuel.

The calculations described above have been exclusively concerned with the analysis of the 182 item test reactor ramp database. The additional Biblis A and Obrigheim test data has hitherto only been employed to justify the adoption of a failure probability model based upon a uniform distribution, because of its qualitative similarity to the normal model but with a threshold property. The extra datasets are available and it has become clear that the introduction of these explicitly into the database will be to somewhat increase the margin to the criterion boundary by an amount of order 1 kW/m. It is likely we will pursue this relaxation in the criterion for future cycles in Sizewell B beyond cycle 5.

The database shown in figure 2 in comparison with the criterion appears to indicate that the linear decrease in the allowable final power with burnup is too conservative at burnups in excess of about 40 GWd/tU. Above 37 GWd/tU only survivors are observed despite the ramps being of comparable severity to those at lower burnups. It is thus inferred that there is a reduced PCI vulnerability at high burnups. This also appears to be a feature of the fuel currently loaded into Sizewell B. There is also additional recent evidence from the Japanese advanced fuel development programme [6]. These observations could be exploited by introducing a slightly more complex burnup dependence having the familiar linear decrease at low burnups and diminishing in effect at higher burnups. This possibility is presently being evaluated and could provide a further relaxation for the criterion.

The uniform distribution failure model is the simplest one with the required properties but other distributions are possible, notably that due to Weibull. This distribution is useful in situations where failure ensues once a boundary is exceeded. It is a more complex distribution form and its application would require a revision of the methodology described above to derive a suitable 95/95% bound. In practice, the application of this model is unlikely to provide any significant benefits in margin to failure. It will introduce an undesired complexity into the analysis and this is counter to the objective of an explicit and clear demonstration of safety. Hence investigating alternative failure probability models with this distribution is not currently favoured.

The Siemens fuel database is limited to local burnups less than ~45 GWd/t U and it is intended to operate the fuel in Sizewell B to local burnups up to 55 GWd/t U. This is achieved by using a standard extrapolation methodology which has been described in detail elsewhere [7]. The methodology is based on the ENIGMA code which is used to define the criterion of equation (4) in terms of clad threshold hoop stresses to failure. An extrapolation has been developed to allow equation (4) to be extended for application over the entire range of Sizewell B burnups.

4. DISCUSSION AND CONCLUSIONS

This paper has described the development of an empirical power threshold PCI criterion for Siemens fuel. It has been based on a methodology used for the PCI criterion constraining fuel currently loaded into the British Energy Sizewell B power station. The methodology has had to be adapted to account for the different properties of the Siemens fuel and in particular has

required the adoption of a different failure probability model having a constant standard deviation. This has allowed the analysis to be simplified by removing the requirement for a fuel performance code determination of the conditioned powers relating to each test in the database.

The database has also provided strong evidence for a threshold power for the onset of vulnerability to PCI failure and this has justified using a failure model function which embodies this effect. This has allowed the 95/95% bound of the best estimate criterion to be less constraining than if the model were to be based on the previously used normal distribution, which has an extended 'tail'.

The fuel to be loaded into Sizewell B is to be contained in Siemens PCA-2a clad which is represented by several tests in the database. These tests have shown that the PCA-2a clad is typified by the entire database and so is well represented by the PCI criterion presented in this paper.

The utility of the criterion has been tested in earnest during the cycle core design process. The core design is optimised against many key core parameters and is then subject to a rigorous study of the various frequent fault transients with the outcomes compared with the PCI criterion. The criterion has enabled confidence in the Sizewell B cycle 5 design to be established by demonstrating a satisfactory margin between the worst case transient final power and the final power limit of the criterion.

The database has not yet been exploited fully and it is clear the present criterion is actually more conservative than is implied by the designation 95/95% because there is more margin to be gained from an extended analysis.

REFERENCES

[1] GAERTNER, M., FISHER, G "Survey of the Power Ramp Performance Testing of KWU's PWR UO2 Fuel", Journal of Nuclear Materials 149 (1987) 29-40

[2] CHESTNUTT, M. M., "Development of a Pellet Clad Interaction Failure Criterion for PWR Fuel of the Standard W Design for use in Safety Analysis", BE report SXB-IP-096146, February 1992.

[3] OWEN, D. B., "Factors for One Sided Tolerance limits and for variables sampling plans", Sandia Corporation Monograph, SCR-607, March 1963

[4] BROHAN, P., SHEA, J. H. and TEMPEST, P. A., "The ENIGMA Fuel Performance Code Description: Version 5.10", BE report EPD/GEN/REP/0304/98 March 1998

[5] SHEA, J. H., "Specification of a Sizewell B Siemens Clad PCI Criterion" BE report SZB/TNR/109 June 1998

[6] GOTO, K., MATSUMOTO, S., MURATA, T., MIYASHITA, T., ANADA, H., ABE, H., "Update on the Development of Japanese Advanced PWR Fuels", Light Water Reactor Fuel Performance (Proc. Int. Topical Mtg Park City, Utah, April 10-13, 2000), ANS (2000) 457.

[7] CLARKE, A. P., TEMPEST, P. A., SHEA, J. H., "A PWR PCI Failure Criterion to Burnups of 60 GWd/tU Using the ENIGMA Code", High Burnup Fuel Specially Oriented to Fuel Chemistry and Pellet Clad Interaction (Proc. IAEA TCM Nykoeping, Sweden, 7-11 September 1998), IAEA, Vienna (in press).

FUEL ROD MODELLING DURING TRANSIENTS: THE TOUTATIS CODE

F. BENTEJAC[1], S. BOURREAU[1], J. BROCHARD[1],
N. HOURDEQUIN[1], S. LANSIART[2]

[1] CEA Centre de Saclay, Gif-sur-Yvette, France
[2] CEA Centre de Cadarache, Saint-Paul-lez-Durances, France

Abstract

The TOUTATIS code is devoted to the PCI local phenoma simulation, in correlation with the METEOR code for the global behaviour of the fuel rod. More specifically, TOUTATIS objective is to evaluate the mechanical constraints on the cladding during a power transient thus predicting its behaviour in term of stress corrosion cracking. Based upon the finite element computation code CASTEM 2000, TOUTATIS is a set of modules written in a macro language. The aim of this paper is to present both code modules.

- The axysimetric bi-dimensionnal module, modeling a unique block pellet.
- The tri dimensionnal module modeling a radially fragmented pellet.

Having showed the boundary conditions and the algorithms used, the application will be illustrated by:

- A short presentation of the bidimensionnal axisymetric modeling performances as well as its limits.
- The enhancement due to the tri dimensionnal modeling will be displayed by sensitivity studies to the geometry, in this case the pellet height/diameter ratio.
- Finally, we will show up the easiness of the development inherent to the CASTEM 2000 system by depicting the process of a modeling enhancement by adding the possibility of an axial (horizontal) fissuration of the pellet.

As a conclusion, the future improvements planned for the code are depicted.

1. INTRODUCTION

Cladding being the first barrier against the risk of radioactive products dissemination, its integrity is of critical importance for safety. One of the identified risks taken into account is the SCC rupture risk. This risk is induced, on the one hand by the mechanical interaction between the pellet, dilated thermally and/or by swelling, and the cladding, and on the other hand by corrosive fission products such as iodine. This risk is an especially sensitive issue during a class 2 incidental operation, characterised by an important power transient.

An ambitious project is therefore to bring comprehensive and remedies elements to PCMI situations. The TOUTATIS code [1], developed at CEA/DRN, is part of software tools set used in the course of this project in conjunction with the METEOR code [2] for the rod global behaviour simulation and with experimental programs. Its goal is to reproduce the phenomena involved in a PCMI situation and to give a qualitative evaluation of the relative importance of system parameters.

2. DESCRIPTION OF THE SYSTEM TO BE MODELLED

The goal to achieve is the modelling, as precise as possible of a fuel rod section and of the various phenomena that occur within. Physically, the system can be represented on a local scale, by a cylindrical pellet of h length (possibly dished and/or grooved), and by the

corresponding section of cladding -a hollow cylinder. Phenomena involved in the pellet cladding system are complex [3]; however, they can be classified by their nature:

i. Physical phenomena

- At early stage of irradiation, the fuel is subjected to a densification phenomenon due to the UO2 sintering. To this mechanism is superseded a swelling induced by the crystalline UO2 irradiation damage.

- Moreover, during rod irradiation, neutronal reactions induce fission products creation; the main part of those products stay trapped in the fuel, another part is released in the pellet cladding gap, thus elevating the rod pressure. Furthermore, the fission products dissolved in the fuel pellet cause its noticeable swelling during thermal transient.

ii. Thermal phenomena

- The important power source released by the neutron fission, as well as the UO2 low thermal conductivity, induce an important thermal gradient, particularly in the fuel; resulting thermal dilatations, significantly more important in the centre part of the pellet, cause the pellet to adopt a "hourglassing" shape. The associated stresses lead to a pellet fragmentation at an early stage of the rod life.

iii. Mechanical phenomena in steady state operation

- The purely mechanical part of the system load is restricted to the pressure involved : coolant pressure on the cladding outside, and rod inner pressure on the pellet and the inner side of the cladding. The differential pressure associated to the neutron flux induces the cladding creep towards the centre of the system, thus resulting in the pellet cladding gap reduction. This reduction, accelerated by the fuel swelling, leads to a total filling of the gap : there is then Pellet Cladding Mechanical Interaction (PCMI).

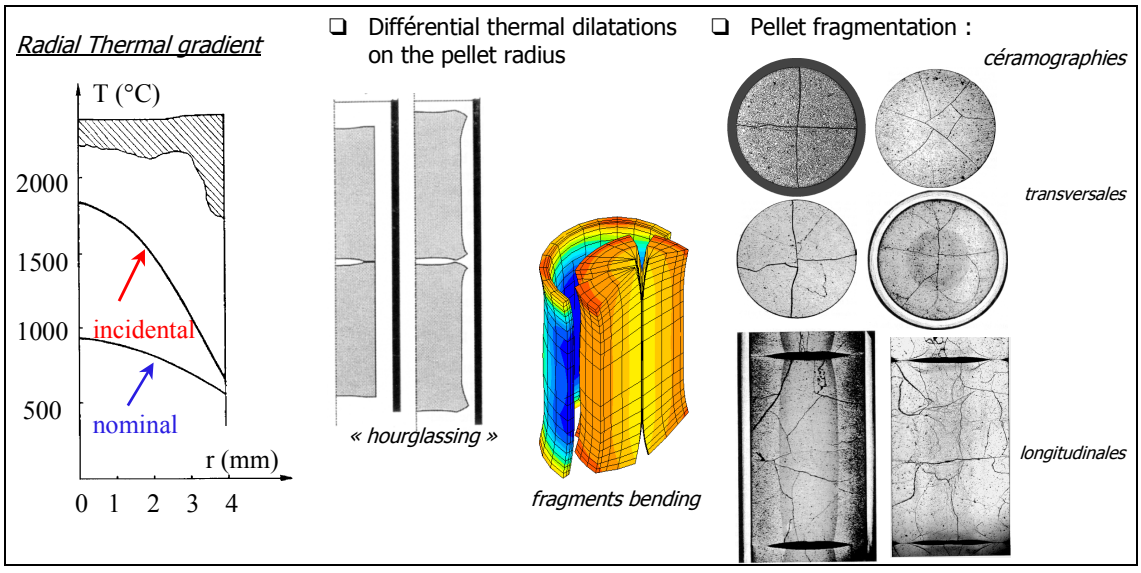

FIG. 1. Physical phenomena in the fuel rod.

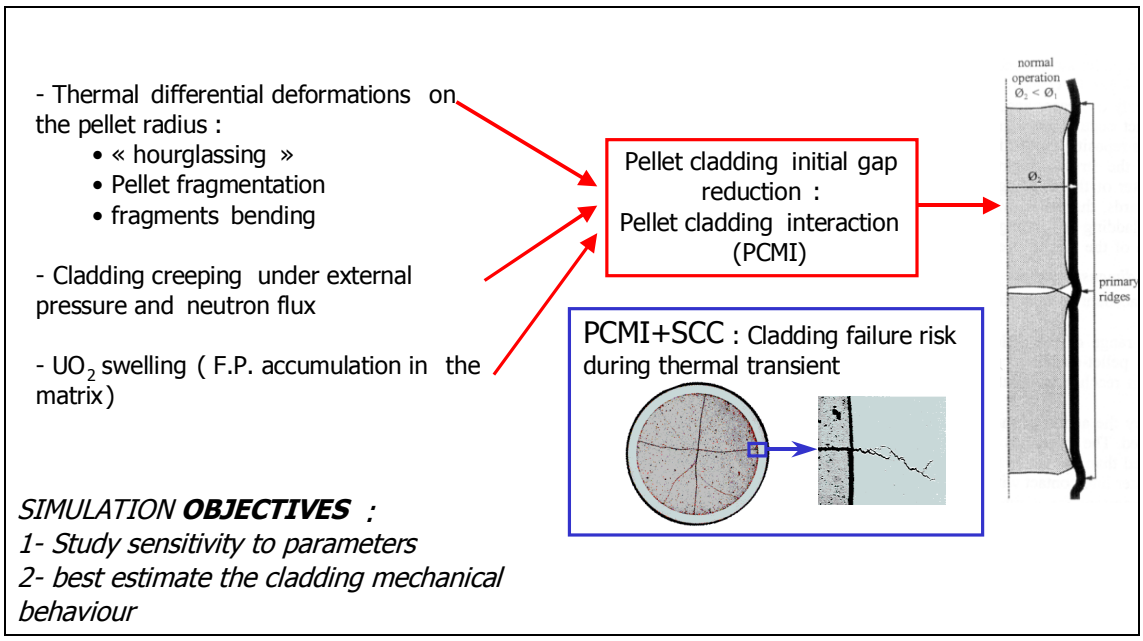

FIG. 2. Thermomechanical phenomena occurring during irradiation.

3. SOFTWARE DESCRIPTION

The objectives worked towards by the TOUTATIS code development are to understand and to model the various mechanisms linked to PCMI in order to best estimate the resulting rod failure. To achieve this goal, the software tool takes into account phenomena detailed below. Various elements of the TOUTATIS model are also detailed.

3.1 System spatial modelling

The pattern adopted in TOUTATIS reproduces the local behaviour of the system. It is depicted by a section of the fuel pile, most often half of a pellet, and its corresponding cladding section.

TOUTATIS refers to a set of two modules, the first one being devoted to an axisymmetrical two-dimensional model, while the second one is based on a three-dimensional model.

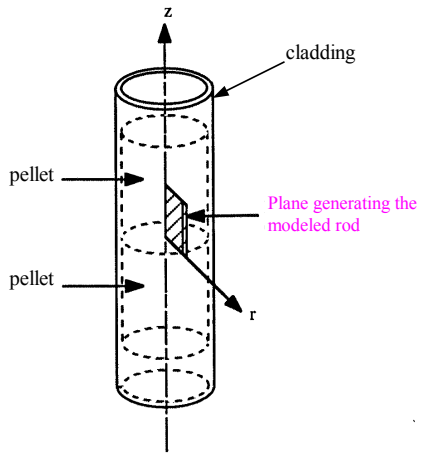

FIG. 3. The modelled rod is generated by rotation and symmetries of the simulated plane.

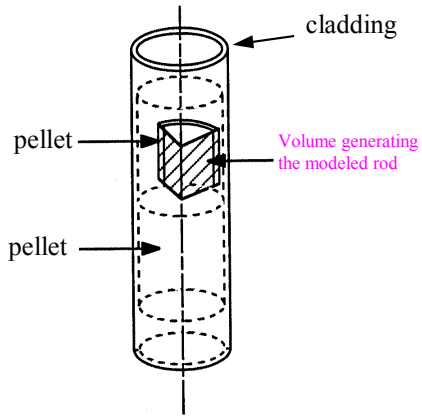

FIG. 4. The modelled rod is generated by symmetry of the simulated volume with respect to its symmetry planes.

The **2D** module is based on an axisymmetrical representation of half a pellet and models the hourglassing pellet shape involved by the quasi parabolic temperature distribution in the fuel.

This model reproduces the primary ridge formation on the cladding at inter pellet level, due to the PCI. However, it underestimates the ridge amplitude.

To reduce this insufficiency, taking into account the radial pellet fragmentation is necessary.
The **3D** model represents, contrary to the **2D** one, both radial and circumferential oxide fragmentation and reproduces, for instance, the fragment spacing created by the bulging of contact surfaces. User can chose the number of fragments of his model.

The modelled volume (hatched) is a part (here one eighth) of the a pellet volume and the corresponding section of cladding. By symmetries, this volume can be considered as representative of the whole rod.

3.2 Main modelled mechanisms

In addition to thermal dilatation and elastic/plastic deformations, the modelled mechanisms are mainly:

i. *densification* and *solid swelling* of the oxide;
ii. *creep* as the effect of various system loadings (mechanical, thermal, contact forces) ;
iii. *mechanical contacts* between pellet and cladding as well as between pellet fragments
iv. Gaseous swelling and other fission products induced phenomena can be taken into account by a link with the METEOR software.

3.3 General principles

TOUTATIS allows power ramp simulations (reactor start or stop), after or not steady state operation. Those situations represent respectively incidental and normal operations of the reactor.

The software computes slow transients depicted as a succession of permanent states or “periods”. The notion of period corresponds to a time lapse during which temperature variation can be neglected so it may be considered as constant. As a result, temperature is computed once for the whole “period”.

It is to be noticed that instantaneous plastic deformations and creep deformations can not be computed simultaneously with the code present version. As a result, each permanent state is divided into two successive “periods” at the same power level (consequently their thermal states are very close): a short plasticity period, and a period corresponding to creep (Fig. 6).
The soft algorithm can be summed up (Fig. 5):

The algorithm is composed of three nested loops. The inner loop called **thermal convergence loop** calculates the system thermal state at the beginning of the current period. The interdependence between mechanical (geometry, contact pressure) and thermal parameters (heat exchange laws in the gap), makes it necessary to adopt an iterative scheme to compute a coherent thermomechanical state.

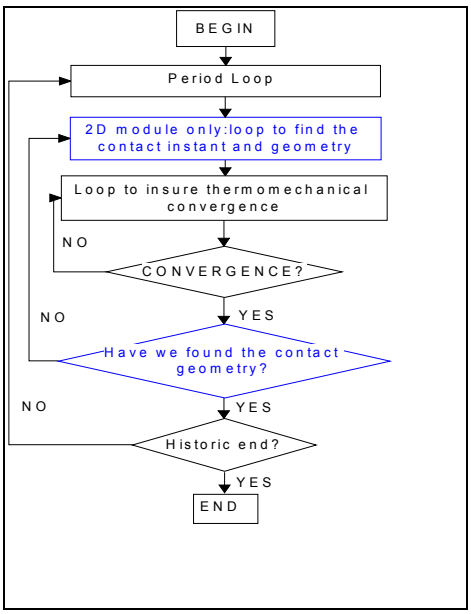

FIG. 5. Algorithm

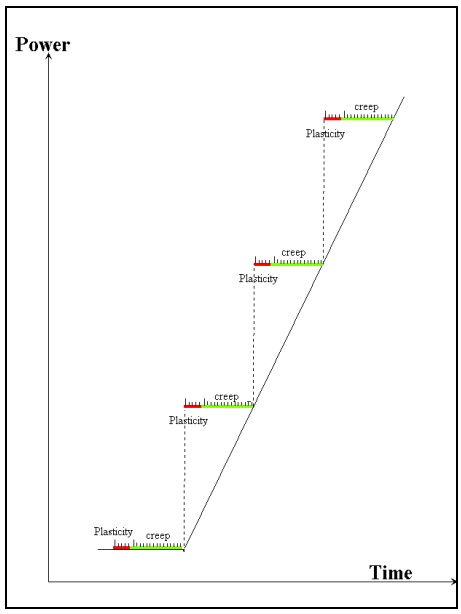

FIG. 6. Computing scheme.

Therefore, there are successive calculations of the steady thermal solution, for the first period instant, then mechanical calculation of the system geometry, the new thermal solution corresponding to the geometry just calculated…, until there is convergence. When convergence is reached, this thermal state is considered as established and valid to the end of the period; it is therefore possible to carry out the computation of the mechanical state to the end of the period with the temperature previously determined.

To be schematic, thermomechanical computations are done as follows:

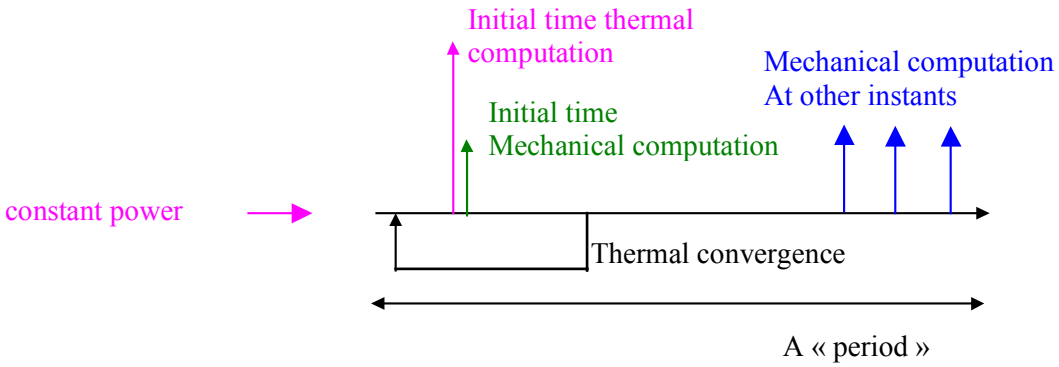

FIG. 7. Computation of a "period".

3.4. Boundary conditions

The symmetries are used at their best to reduce the model spatial dimension : pellets are supposed to be symmetric with regard to their mid level plane, the cladding being a hollow cylinder whose length is infinite in respect to the section modelled (Fig. 8). It can be noticed that those conditions don't allow an axial power variation to be taken into account on the pellet height, and there is no edge effect modelled at the top or the bottom of the fuel pile up.

The 2D axisymmetric model simulates the PCMI by a non-interpenetrating condition between pellet and cladding meshes. Furthermore, a punctual hooking between pellet and cladding at the first contact points can be added (Fig. 9).

The three-dimensional module models an angular sector of the system. It is thus assumed that the radial cracks are evenly disposed. The module simulates PCMI by a single non interpenetrating condition between pellet and cladding meshes, which means it supposes there is sliding at the pellet cladding interface.

To improve the model prediction, it is possible to add an axial hooking between pellet and cladding to impose a binding of their axial deformations after the first contact. However, at the present stage, the stress concentration in front of the pellet crack isn't represented since rubbing at the pellet-cladding interface isn't modelled. A plane 2D model is in progress to analyse this point.

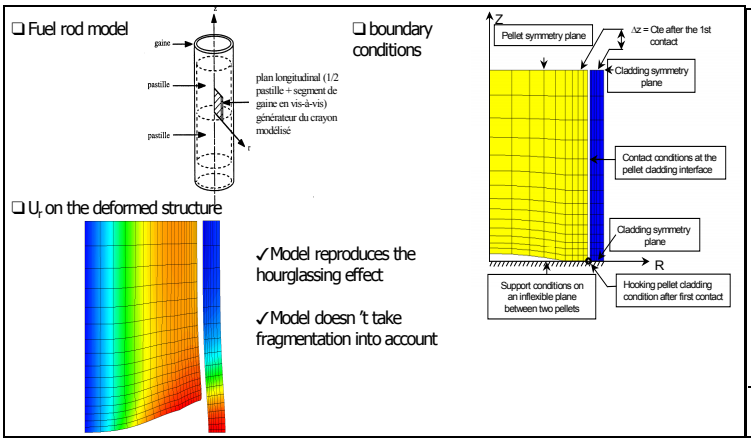

FIG. 8. Bidimensional model.

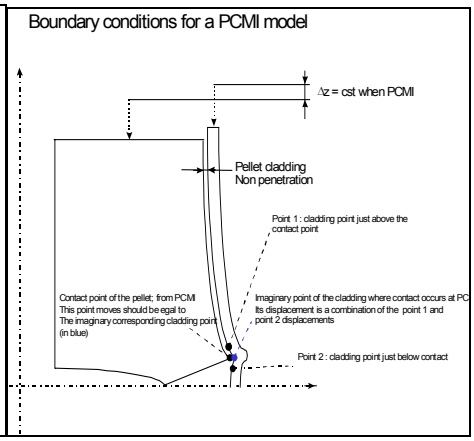

FIG. 9. PCMI modelling.

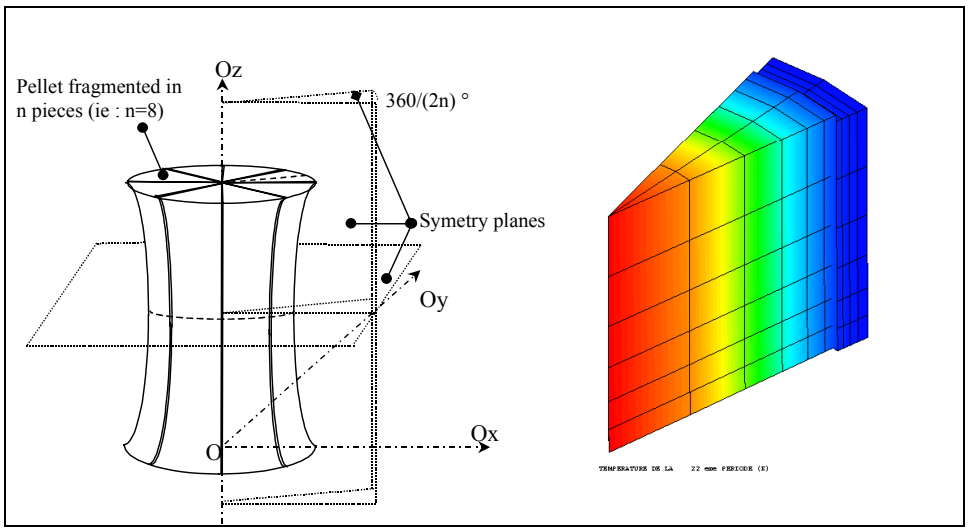

FIG. 10. 3D model.

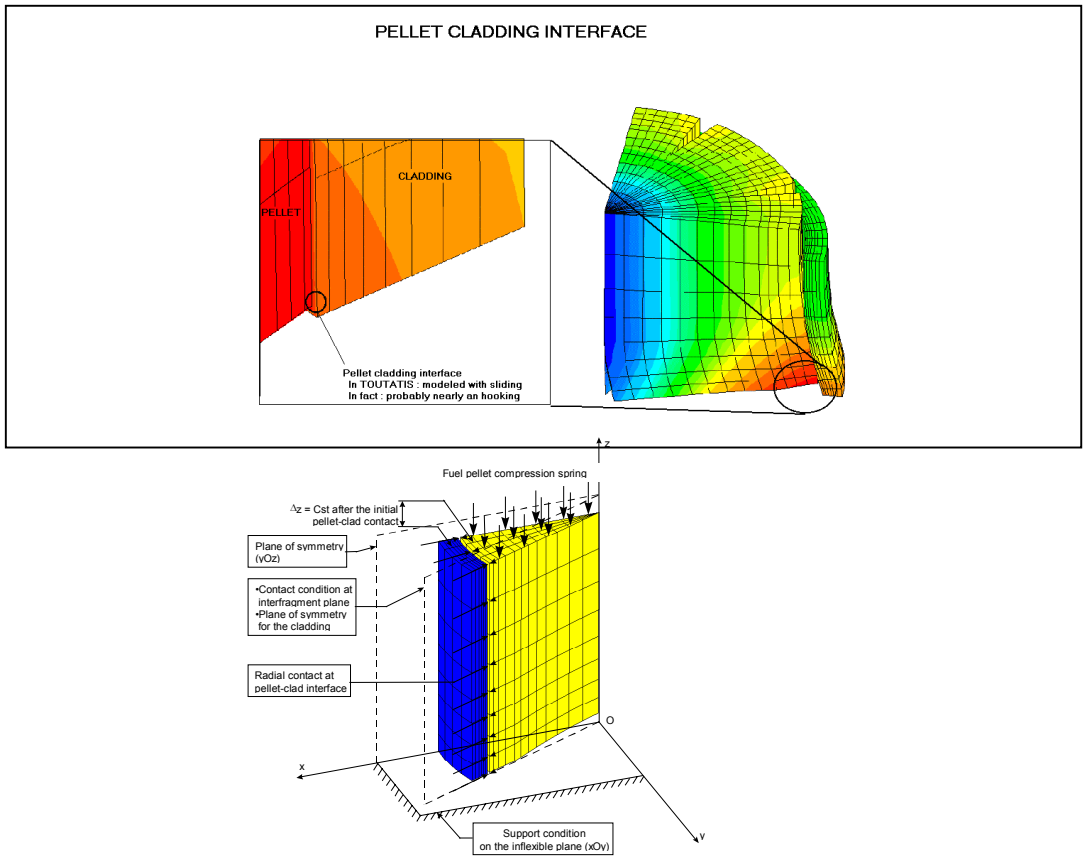

FIG. 11. 3D module boundary conditions.

4. TOUTATIS APPLICATION : POWER RAMPS

One of the issues undertaken by CEA is to understand and predict the fuel rod thermomechanical behaviour, specially under incidental situation. To achieve this, the TOUTATIS code is used in conjunction with experimental irradiation programs made on both fresh and irradiated material. The software gives estimation of factors such as stresses during power ramp, experimentally unmeasurable. In return, measurable factors give an opportunity to study the software liability and the model lacks.

Actually, experiments have two stages: possible irradiation in a power reactor during one or more cycles, followed by non-destructive examinations, then a power transient “power ramp” reproducing incidental reactor environment.

A forecast simulation, usually between the two stages, or before the experiment when dealing with a fresh material, is used for intermediate geometric comparison and to decide the power ramp characteristics.

Finally, the fuel rod undergoes non-destructive, then destructive examination, which show the mechanical system state. TOUTATIS is then used to understand and analyse the results ; simulation computes the cladding stress, an important factor for the SCC. The teaching collected is then used to estimate and improve software liability.

This point, although a major TOUTATIS application, has already been exposed [4, 5], both with 2D and 3D models. It is interesting to remind the main conclusions about the 2D model:

i. It displays “hourglass” shape of the pellet, allowing the formation of primary ridges at inter pellet level.
ii. Undervaluing pellet flexibility, it tends to overestimate primary ridges height.
iii. It does not reproduce mid-pellet secondary ridges.

Those inherent weaknesses make it necessary to apply a three dimensional modelling for some tasks.

5. 3D MODEL APPLICATION

The second main scope of TOUTATIS application is the simulation of idealised cases in order to study the sensitivity to parameters. The principles of those surveys is to simulate an idealised irradiation historic, and to point out the effect of a parameter modification, be it geometric (initial pellet-cladding gap, chamfer…) or physical (creep law), on the SCC-important factors. The research aims at determining the effect of the H/D geometric ratio on the cladding stresses during PCMI.

In order to achieve this survey, three geometries (Fig. 12) will be considered. As 3D modelling will be used, all of the three systems will have radially fragmented pellets; furthermore, one of them will include transversally fragmented pellet, whereas the two others (referred as “undamaged” or “unfragmented”), will include transversally unfragmented pellet.

TOUTATIS will be used to simulate those systems undergoing an incidental power transient, as described at the paragraph 4, after a 2 cycles irradiation at nominal power (Fig. 13). The goal is to study differences induced, in term of cladding stresses, by the modification of the pellet geometry. Furthermore, it will be interesting do determine whether a shorter pellet has a different behaviour than a transversally fragmented longer pellet.

As the aim is to compute the SCC characteristic elements, it is of primary importance to study stresses at the “critical point” (Fig. 14), point of the cladding inner surface, at inter-pellet level, in front of the pellet crack. Other factors, such as deformations, upon which comparison with experiments can be based, will be considered.

This simulation being a sensitivity study, it can not be compared to experimental results. However, it is possible to use classical, average profilometries to compare it. We have two factors of comparison for the system including the longest pellet:

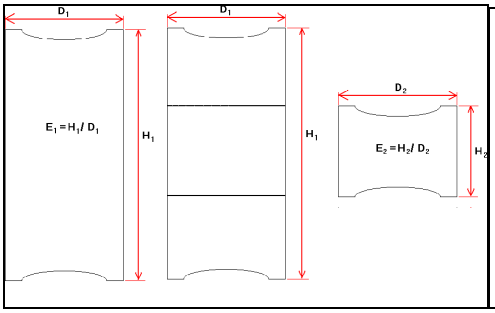

FIG. 12. Three geometries.

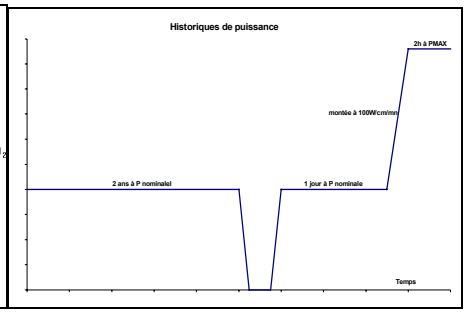

FIG. 13. Power history.

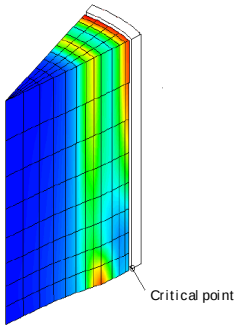

FIG. 14. “Critical point”.

i. After 2 cycles of irradiation at nominal power, a primary ridge should be noticed on the cladding deformation, but the secondary ridge phenomenon should be minimal, if at all perceptible.
ii. After the power ramp, a secondary ridge should have appeared.

The TOUTATIS calculated geometry (Fig. 15) after the 2 cycle irradiation (before power ramp) for the two longest pellet systems shows a noticeable over-deformation at its mid-pellet level. This fact, usual with a TOUTATIS simulation, seems to be a simulation of the "secondary ridge" which could have slightly appeared before power ramp. However, in the case of the system including an unfragmented pellet, this phenomenon is suprising by its amplitude which doesn't correspond to experiment constatations.

The system configuration analysis shows that this over deformation at mid pellet level is due to a remaining PCI after return to null power that can be explained by the reversion of the hourglassing bending effect. Furthermore, results show that, in the simulation, such a situation clearly depends on the pellet geometry, as there is no such constatation for the system with the shortest pellet.

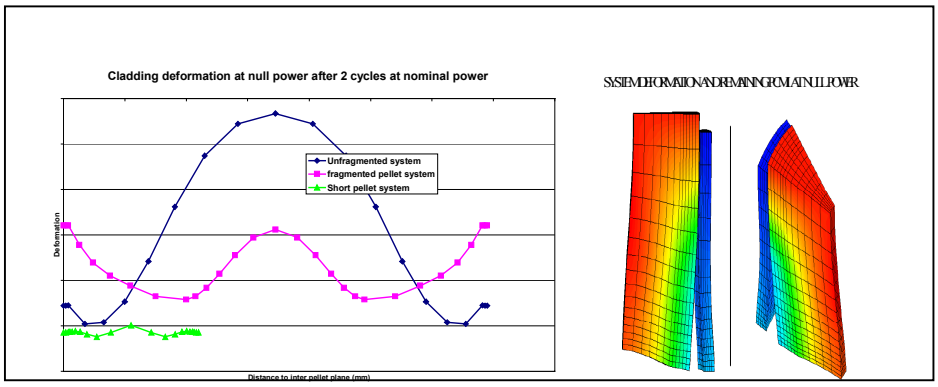

FIG. 15. "Barrel" shaped pellet deformation after 2 cycles irradiation.

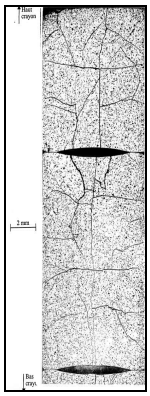

FIG. 16. Structure.

The deformation of the system including fragmented pellet clearly shows a significant reduction of the mid pellet overdeformation for the fragmented pellet although there is still a slight PCMI effect at this location. The computed deformations thus present a more plausible shape.

More interesting, we see that, even with a fragmented pellet, there is one primary ridge, located at the dishing level. This can be explained by the fact that, in the simulation, every pellet fragment is subject to the hourglassing effect before the first pellet cladding interaction but, after contact, hourglassing effect tends to reduce on every fragment except for the dished one (figure 17).

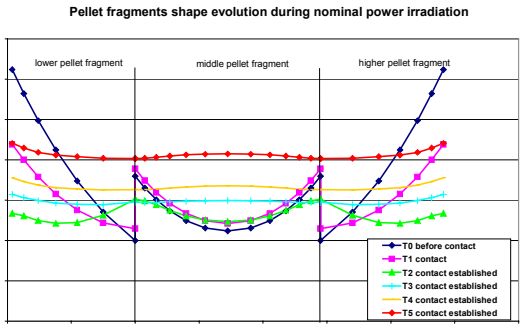

FIG. 17. Pellet fragments shape evolution.

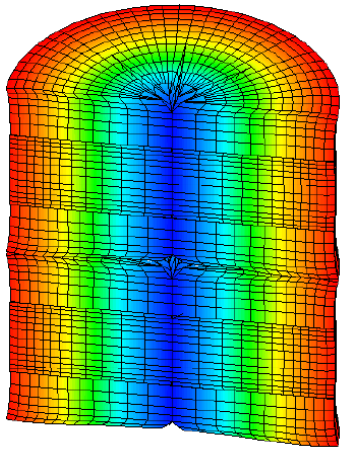

FIG. 18. "Barrel" shape.

It seems that the axial binding condition imposed between pellet and cladding after their first contact is of critical importance in this process, creating in conjunction with the fuel swelling an axial load to the pellet. The hourglassing effect is due to the fact that the internal part of the pellet, by far the hottest, tends to axially expand more than the external part ; this axial expansion is eased by the dishing presence which allows free expansion, but is restrained elsewhere as the axial load created by contact between pellet fragments tend to inverse hourglassing effect and to create a "barrel" shape (Fig. 18).

As mentioned above, in, power ramp situation, there is an important reduction of the cladding deformation for the short pellet based system. This seems logical, since the hourglassing effect, which involves cladding radial displacements at inter pellet level, is linked to the pellet height. As a result, the stress analysis shows a stress reduction (Fig. 19).

At the opposite, one major finding of this survey is that differences on the simulation calculated profilometries at null power for a fragmented pellet do not imply significant differences on the major SCC parameter which is stress in power ramp. Figure 19 shows that there is almost no difference of stress evolution during power ramp between a system including an undamaged pellet and a system including an axially fragmented pellet, the shortest -undamaged- pellet involving lower stresses. A pellet, even fragmented, tends to behave as a whole element because of the boundary conditions.

Finally, at power peak, the central –undished- fragment, compressed by contacts, tends to warp outside, thus creating a "secondary ridge" that remains after power ramp (Fig. 20).

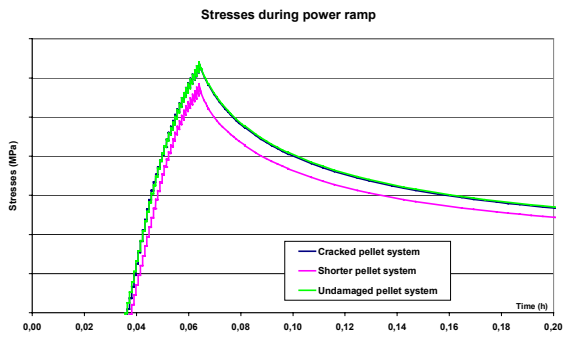

Fig. 19. Stress evolution during power ramp.

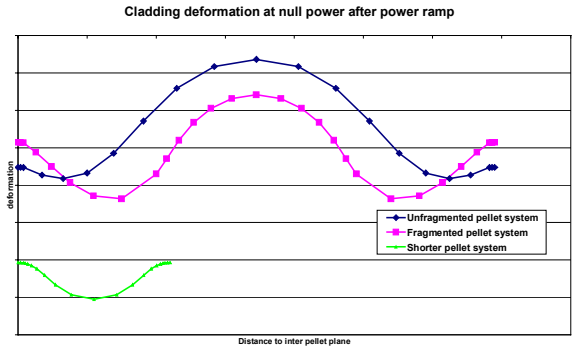

Fig. 20. "Secondary ridge".

Shorter pellet tends to have effect both on the deformations and on the cladding stresses, because of a reduction of the hourglassing effect.

Axial fragmentation modelling improves verisimilitude of the deformation results. Furthermore, it tends to show the lack of primary ridge at non dished levels. However, it does not seem to have any significant effect on the primary SCC parameters, since axial loads tend to make the fragmented system in irradiation to behave closer to an unfragmented one than to a set of smaller ones (Figs 21 and 22).

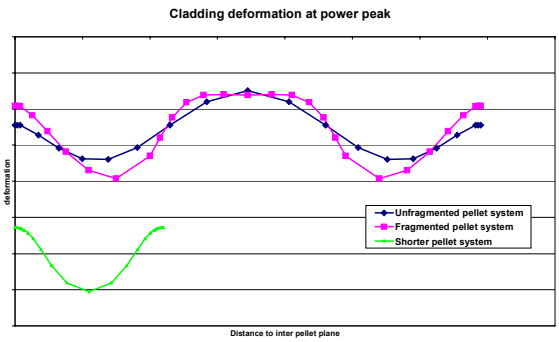

Fig. 21. Clad deformation at power peak.

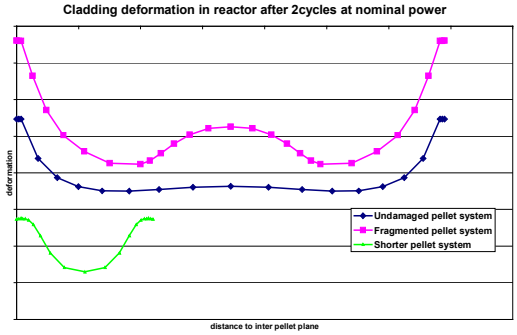

Fig. 22. Cladding deformation at P_{nom}.

6. CONCLUSION

In the framework of the CEA/DRN project for understanding and modelling the PCMI mechanisms during power ramps, software tools are developed. Among them, TOUTATIS code is devoted to model the local thermal mechanical effects at the pellet scale. In this objective, it is based on the general finite element computer code CASTEM 2000, and refined meshes are used. In its present version, two modules are available : 3D and 2D axisymetric models, the former taking into account pellet fragmentation. Regarding the mechanical conditions at the pellet-cladding interface, sliding or fixed boundaries are added after the first contact. The modelling of the rubbing effect is in progress.

Sensitivity study to the pellet geometry has been performed. Calculations show that lowest stresses are obtained when a short pellet is considered. In addition with the radial pellet fragmentation, a development has been recently made to model the axial fragmentation. This development contributes to obtain a better evaluation of the cladding ridges due to the PCMI effect.

REFERENCES

[1] BROCHARD J., BENTEJAC F., HOURDEQUIN N., "Non-linear finite element studies of the pellet cladding Mechanical Interface in a PWR fuel", Structural Mechanics In Reactor Technology (Proc. Int. Conf. Lyon 1997), SFEN (1997).

[2] STRUZIK C., MELIS J.C., FEDERICI E., "Fuel modelling at extended burnup: Comparison between METEOR 1/TRANSURANUS calculationa and examinations on fuel rods irradiated up to 60 GWd/t U", Light Water Reactor Performance (Proc. Int. Topical Mtg West Palm Beach, Fl April 17-21 1994), ANS (1994) 188.

[3] BAILLY H., MENESSIER D., PRUNIER C.,TEC & DOC (eds), “The NUCLEAR FUEL of PRESSURIZED WATER REACTORS and FAST REACTORS: DESIGN and BEHAVIOUR”, Lavoisier Publishing, 11, rue Lavoisier-F-75384 Paris cedex 08 (1999).

[4] BOURREAU S., BROCHARD J, BENTEJAC F., COUFFIN P., VERDEAU C., LANSIART S., CAYET N., GRANDJEAN M.-C., MERMAZ F., BLANPAIN P., “Ramp testing of PWR fuel and multidimensional finite element modelling of PCMI”, Light Water Reactor Fuel Performance (Proc. Int. Topical Mtg Park City, April 10-13 2000), ANS, (2000).

[5] BOURREAU S. LANSIART S., COUFFIN P., VERDEAU C., DECROIX G.M., GRANDJEAN M.-C., HUGOT H., MERMAZ F., VAN SCHEL E., “Influence of hold period on the fuel rod behaviour during a power ramp”, Fuel Chemistry and Pellet-clad Interaction related -to High Burnup Fuel (Proc. IAEA TCM Nykoping, Sweden, September 7-11 1998) IAEA, Vienna, (in press).

A CLADDING FAILURE MODEL FOR FUEL RODS SUBJECTED TO OPERATIONAL AND ACCIDENT TRANSIENTS

J.Y.R. RASHID, R.O. MONTGOMERY, W.F. LYON,
ANATECH Corp., San Diego, California

R. YANG
EPRI, Palo Alto, California

United States of America

Abstract

Concerns about high burnup effects on cladding integrity during operational and accident transients have been invoked by licensing authorities in the United States of America, Europe and Japan as potentially limiting for burnup extension. Transient experiments recently conducted in France and Japan to simulate reactivity initiation accidents (RIAs) in light water reactors have shown that high burnup fuel rods can fail at enthalpy levels well below the current licensing limits. Analytical research conducted by EPRI during the last few years, in support of the RIA tests evaluation, has led to the development of a cladding failure model for reactor transients, including RIA and power oscillation events in boiling water reactors known as ATWS (anticipated transient without scram). The model is incorporated in EPRI's fuel behavior code FALCON, which is the modern version of the FREY code that was presented in previous IAEA fuel behavior meeting. The most distinguishing feature of the model is that it computes the mechanical energy locally at material points in the cladding as function of time during the transient event, from which the failure location and failure time are predicted. The database for the model consists of stress-strain data obtained from mechanical property tests for cladding tubes as function of fast fluence, temperature, hydrogen concentration and material type. From this data, the material's capacity, or resistance to failure, is formulated as the total (elastic+plastic) mechanical energy per unit volume that can be absorbed by the cladding before it can fail, and is termed the critical strain energy density (CSED). The FALCON code calculates the strain energy density (SED) that a transient event can deliver to the cladding through PCMI and internal pressure loading, which is then compared to the CSED for failure determination. Clearly, the complete stress and strain states enter into the calculation of the SED, and therefore, all three true-stress and true-strain components are required to be calculated by the fuel behavior code, which places great demands on the modeling capabilities of the code. The FALCON/CSED methodology has been applied to the recent RIA tests conducted in France and Japan, and the results will be discussed in the paper. The theoretical structure of the model and the database used to quantify the CSED correlation will be described and discussed.

1. INTRODUCTION

Zircaloy cladding, as the first barrier against fission product release from a fuel rod, has been the object of considerable research to characterize its failure properties. Much of this work has been safety related to establish licensing limits for operational transients and accident conditions. The failure mechanisms considered for those events are generally high-temperature ballooning and rupture. The cladding failure mechanisms that are traditionally considered in fuel behavior modeling under normal operations include stress corrosion cracking (SCC) by pellet-cladding interaction (PCI). Well established models for these mechanisms have been developed for use in fuel behavior analysis [1]. High temperature failure caused by post-departure from nucleate boiling (DNB) is not normally considered in fuel rod analyses due to the complexities of high temperature oxidation, phase transformation, and quench fracture.

At burnup levels beyond 40 GWd/t U, a change in the active cladding failure mechanism may occur due to a reduction in cladding ductility and an increase in pellet-cladding mechanical interaction (PCMI) forces. This change in the failure response of fuel cladding was first observed in reactivity initiated accident (RIA) simulation tests in which cladding failure occurred under rapid power ramp conditions at strain levels well below expectations [2,3]. These observations are further supported by mechanical property tests on cladding irradiated to >60 GWd/tU that show decreases in Zircaloy cladding ductility caused by fast neutron damage and hydrogen absorption [4].

A first approach to develop an integrity model for high burnup cladding could be to use a simple strain to failure (ductility limit). This strain to failure model would be derived directly from mechanical property tests and can be a function of temperature, hydrogen content, strain rate etc. Unfortunately, there are two main weaknesses with a strain to failure approach. First, strain to failure data depends strongly on the type of mechanical property tests used to obtain the data. These tests do not generally simulate the strain and stress-state under PCMI loading conditions. Second, the strain to failure is not path independent, and it depends on the rate of loading and the multi-axial condition of the imposed stresses. A preferred approach might be to utilize the strain energy density concept. The strain energy density (SED) concept states that the material's ability to absorb energy before failure is an invariant property. The strain energy density that is released at failure is a material limit and is termed the critical strain energy density (CSED). The CSED depends on the material state defined by temperature, fast fluence, and hydrogen content. The SED represents the accumulation of the total mechanical energy during mechanical loading of the cladding by PCMI or pressure forces.

This paper summarizes the theoretical development of the SED/CSED cladding failure model, the development of the CSED for Zircaloy cladding as a function of temperature and irradiation, and demonstrates the application of the model using transient RIA test results.

2. THEORETICAL BASIS OF THE SED MODEL

The derivation of the SED model is fashioned after the well-known path independent J-integral approach developed by Rice in the sixties [5] for the analysis of strain concentration by notches and cracks, which revolutionized the field of Fracture Mechanics. A brief review of the J-integral development is first presented, followed by an analysis restricting the derivation to conditions unique to fuel cladding.

2.1. Review of path-independent J-integral

Consider a homogeneous body subjected to a two-dimensional deformation field, containing a defect or a crack that can be represented by a notch of the type shown in Fig. 1. Define the strain energy density **U:**

$$U = \int \sigma_{ij} \, d\varepsilon_{ij} \tag{1}$$

where σ_{ij} and ε_{ij} are the stresses and the strains respectively. The J-integral is defined by

$$J = \oint_{\Gamma} U dy - \oint_{\Gamma} F \bullet \frac{\partial u}{\partial x} \, ds \tag{2}$$

In eq. 2, the integration is performed over the curve surrounding the notch tip. **F** is the traction vector such that it is positive in the direction of the outward normal along Γ, i.e. $f_i = \sigma_{ij} n_j$, **u** is the displacement vector, and ds is an element of arc length along Γ. The integral in eq. 2 is path independent; i.e. the value of **J** does not change if another contour enclosing the notch is chosen; proof of path dependence of the J-integral is given by Rice in his classic paper [5].

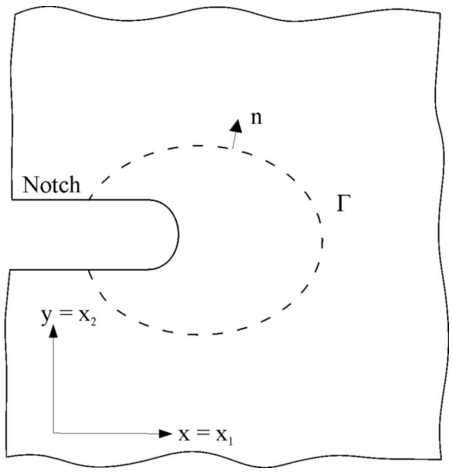

FIG. 1. Flat surface notch in two-dimensional deformation field.

2.2. Application to fuel rod analysis

During the course of irradiation, damage accumulation by two sources, fast-neutron fluence and hydrogen absorption, decreases the ability of the cladding to withstand mechanical loading by PCMI or pressure forces. The damage accumulation by fast-neutron fluence occurs rapidly following the start of irradiation and reaches saturation within a short time (<1 year). The effects of fast fluence are observed as an increase in the yield strength of Zircaloy and a decrease in the material ductility. The damage caused by hydrogen absorption is proportional to the Zircaloy corrosion process and requires long residence times and high duty. The damage caused by the presence of hydrogen in high burnup cladding is of two types. Circumferentially oriented platelets of hydrides distributed in the cladding in a radially varying concentration gradient. In some cases, the hydrides are driven towards the cladding outer region, under the effects of temperature and stress gradients, forming a continuous hydride outer rim beneath the corrosion layer [3]. The average hydrogen concentration in this hydride rim can exceed 2000 ppm, with a gradient that varies from almost pure hydride (16000 ppm) at the hydride/oxide interface to one or two hundred ppm in the interior. The second type of damage is the formation of hydride lenses as a result of oxide spallation [2].

The geometric effects of a coherent corrosion layer and the presence of hydrides (as distributed platelets or as denser outer rim) on the cladding performance is equivalent to a thickness reduction. Hydride lenses, on the other hand, are localized discontinuities, which under certain conditions can penetrate to almost mid wall. They have the effect of a notch, causing strain concentration in the surrounding zircaloy material. Such hydride concentration can be characterized as a notch-type discontinuity, which lends itself quite naturally to the application of the J-integral.

To that end we consider the geometric representations of a typical OD defect as shown in Fig. 2. The choice of a discrete notch-type form of damage is mainly to facilitate the mathematical derivations, but the exact form of the damage is not particularly important. We wish to estimate the value of *J* without analyzing the cracked body.

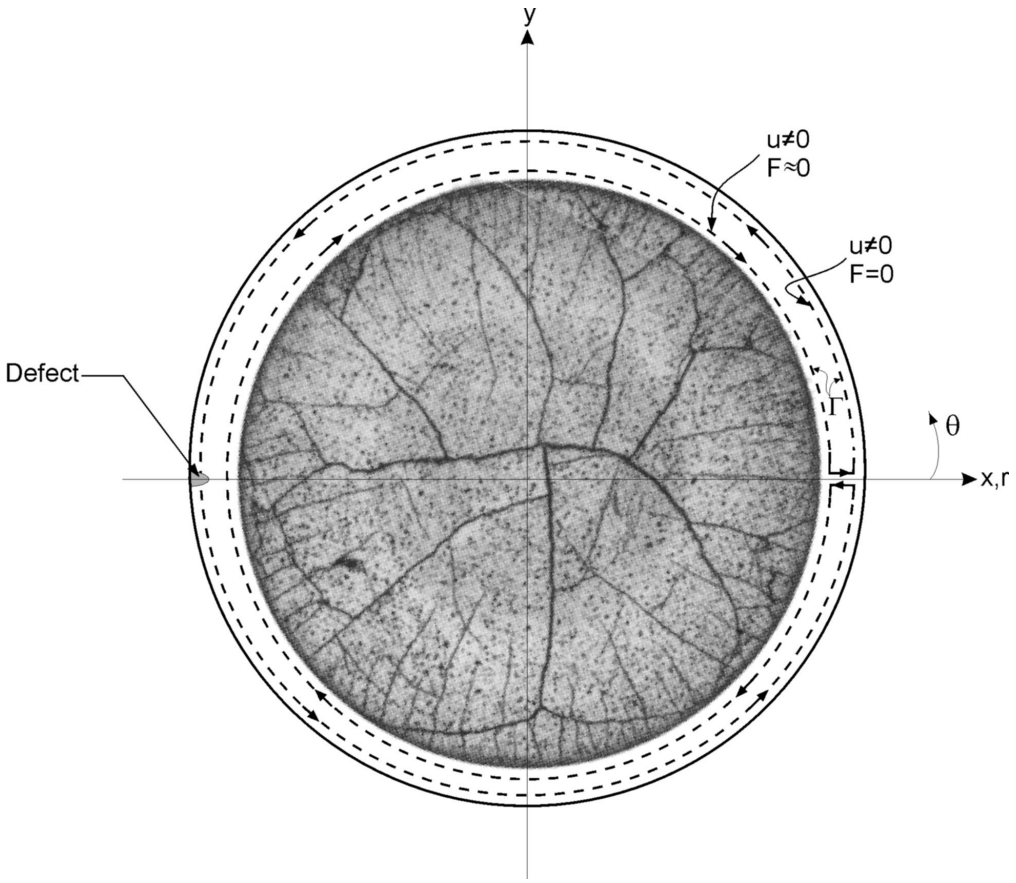

FIG. 2. Cross-section of fuel rod with contour line surrounding defect tip.

Figure 2 is a cross-section of a fuel rod with a notch-type cladding defect. Owing to the path independence of the J-integral, we are free to take the contour shown by the dashed line in Fig. 2. Now,

$$F = 0 \quad \text{at} \quad r = r_0$$
$$F \approx 0 \quad \text{at} \quad r = r_i$$
$$F^+ = F^- \quad \text{at} \quad \theta = 0$$

Therefore, the traction term in eq. 2 drops out, and J becomes, using Green's theorem,

$$J = \oint_{\Gamma} U dy = \int_{A} \frac{\partial U}{\partial x} \, dxdy \tag{3}$$

Working in polar coordinates for convenience, we have:

$$J = \int_{r_i}^{r_o} \int_{0}^{2\pi} \left(\cos\theta \frac{\partial U}{\partial r} - \frac{1}{r} \sin\theta \frac{\partial U}{\partial \theta} \right) r d\theta dr \tag{4}$$

Integrating eq. 4 by parts, and simplifying terms, we obtain:

$$J = \int_{0}^{2\pi} \cos\theta \left(r_o U(r_o, \theta) - r_i U(r_i, \theta) \right) d\theta \tag{5}$$

Near the crack, *U(r,θ)* varies, as shown in the figure below,

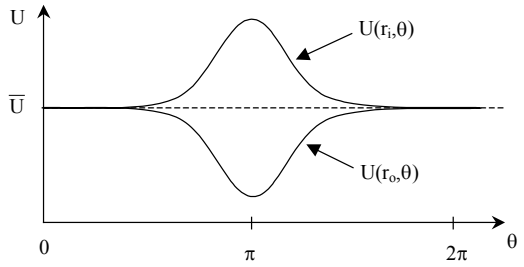

where $\overline{U}$ is the strain energy density in the uncracked body. The presence of the crack will cause U to differ from $\overline{U}$ by the quantity $f(\theta)$. $f(\theta)$ would depend on the depth of the crack, as illustrated in the following figure.

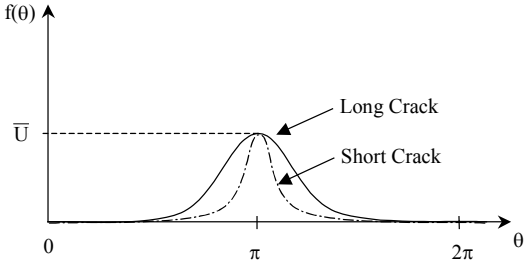

$$U(r_i,\theta) = \overline{U} + f(\theta) \quad , \quad U(r_0,\theta) = \overline{U} - f(\theta) \tag{6}$$

Substituting eq. 6 into eq. 5, we obtain:

$$J = -\int_0^{2\pi} (r_i + r_o)\, f \cos\theta d\theta \tag{7}$$

Now, it remains to estimate a value for *f*. It should be equal to $\overline{U}$ at $\theta = \pi$, and *zero* away from $\theta = \pi$. A simple estimate for *f* would be a triangular shape with values,

$$f = \frac{\overline{U}}{\varphi}(\theta - \pi + \varphi) \quad \text{for} \quad \pi - \varphi < \theta < \pi, \quad \text{and} \quad f = 0 \quad \text{for} \quad \theta < \pi - \varphi \tag{8}$$

This is illustrated in the figure below.

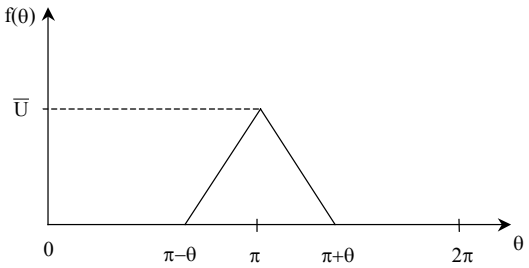

The integral in eq. 7 becomes:

$$J = -2\left(r_i + r_o\right) \int_{\pi-\varphi}^{\pi} \frac{\overline{U}}{\varphi} \left(\theta - \pi + \varphi\right) \cos\theta d\theta = 2\left(r_i + r_o\right) \overline{U} \frac{1 + \cos\left(\pi - \varphi\right)}{\varphi} \tag{9}$$

The parameter φ depends on the crack length and has a maximum value in the range $0 < \varphi < \pi$. A maximum value of $\varphi = 0.742\pi$ is obtained using Newton iteration. Substituting this value in eq. 9 and carrying out the integration gives the following upper bound on *J*:

$$J = 1.45\left(r_i + r_o\right) \overline{U} \tag{10}$$

Equation 10 states :

> *Failure of a cladding with a flaw or a defect can be predicted by calculating the strain energy density in the material without modeling the flaw or performing fracture analysis.*

From eq. 10 we note that, at the time of failure initiation, *J* becomes J_C (the fracture toughness), and correspondingly $\overline{U}$ becomes $\overline{U}_c$, which we designate as the critical strain energy density (CSED). Using the definition in eq.1, this can be can be written as,

$$\overline{U}_c = \int_0^{\varepsilon_f} \sigma_{ij}\, d\varepsilon_{ij} \tag{11}$$

where ε_f is the material failure strain, which is the total elongation in a uniaxial test; in multi-dimensional tests, ε_f becomes a function of the biaxial or triaxial stress ratios. Having thusly established equivalence between CSED and J_C, we can henceforth concentrate on the development of the CSED as a failure model for cladding material. Equation 11 states that the CSED is quantified from stress-strain data obtained from material property tests. The functional dependence of CSED on damage mechanisms, such as hydride lenses, hydride rim, spalled oxide, ID or OD cracks, etc. is reflected in the material property data for irradiated cladding with representative corrosion and hydride conditions to those encountered in high burnup fuel rods.

The first application of the CSED model is in the analysis of the RIA tests recently conducted in France and Japan [2,3]. The analyses were carried out using the transient fuel behavior code FALCON [6,7,8]. The code calculates the strain energy density $\overline{U}$ (SED) at each Gauss (integration) point in the finite element grid as function of time. By comparing the calculated SED to the material failure limit in the CSED model, the failure times can be predicted. As will be discussed later in this paper, the quality of the predictions indicates that the CSED/FALCON methodology can be reliably used to evaluate burnup extensions beyond presently approved limits.

3. CSED DATABASE

3.1. Mechanical property tests

The critical strain energy density (CSED) is developed from material property tests as a function of material conditions, including temperature, fast fluence, outer surface corrosion,

hydrogen concentration, and hydride morphology. In general, three types of mechanical property tests are used: uniaxial tube tension tests, uniaxial ring tension tests, and biaxial tube burst tests. Uniaxial tube tension tests consist of tube samples approximately 125 mm long, with a central gauge section of ~50 mm. These specimens are tested at strain rates of ~10^{-4}/sec in most cases. Uniaxial ring tension tests consist of a thin ring sample (2.5–7 mm wide) with or without a machined gauge section (~3 mm long × 1.5 mm wide). These specimens are tested with special inserts to provide loading in the hoop direction. For uniaxial tube tension and ring tension samples from fuel rods, the pellet material is removed by drilling and chemical etching. Biaxial tube burst tests are performed on 200 mm long tube samples using some type of hydraulic fluid to pressurize the sample. The pellet material is either completely or partially removed prior to testing. Closed-end burst tests are performed in most cases. The measured quantities from these tests include yield stress, ultimate tensile stress, uniform elongation and total elongation.

The database of mechanical property tests on irradiated cladding material used to develop the CSED relations contains a variety of cladding designs, irradiation conditions, oxide thickness levels, and testing conditions (temperature and strain rate). These tests were conducted as part of fuel performance monitoring programs sponsored by EPRI and the US Department of Energy (DOE) to evaluate intermediate and high burnup fuel behavior [9,10,11]. A summary of the important characteristics of the database is shown in Table I. The test samples were obtained from fuel rods that had achieved average burnup levels between 25 GWd/t U and 63.5 GWd/t U. A few samples extracted from high burnup rods exhibited oxide spallation and localized hydrides.

TABLE I. CHARACTERISTICS OF MECHANICAL PROPERTY TESTS

	Biaxial Tube Burst Test	Uniaxial Ring Tension Test	Uniaxial Tube Tension Test
Temperature Range (°C)	315	50–400	40–400
Oxide Layer Thickness (μm)	30–110	14–120	24–102
Hydrogen Content (ppm)	160–730	40–800	110–675
Fast Fluence (n/m^2)	0.1–1 × 10^{26}	0.4–1.2 ×10^{26}	0.1–1.2 × 10^{26}
Strain Rate (sec^{-1})	7 × 10^{-5}	7 × 10^{-5}	7.1 × 10^{-5}

The CSED (U_c) is obtained by calculating the contribution from each deformation regime (elastic and plastic) separately and adding them together to obtain the total CSED. The material parameters used in the calculation of the CSED are depicted in Fig. 3, which shows a schematic of the stress-strain curve for Zircaloy.

The elastic strain energy component ($\varepsilon \le \varepsilon_e$) is derived from Hooke's Law and is given by:

$$U_e = \frac{\sigma_y^2}{2E} \tag{12}$$

where σ_y is the yield stress and E is Young's Modulus.

The calculation of the CSED in the plastic regime is based on the assumption that the material true stress-true strain curve can be represented by the following relationship from MATPRO [12]:

$$\sigma = K\varepsilon^n \left(\frac{\dot{\varepsilon}}{\dot{\varepsilon}_o}\right)^m \quad \text{for} \quad \varepsilon_e < \varepsilon < \varepsilon_e + \varepsilon_{te} \tag{13}$$

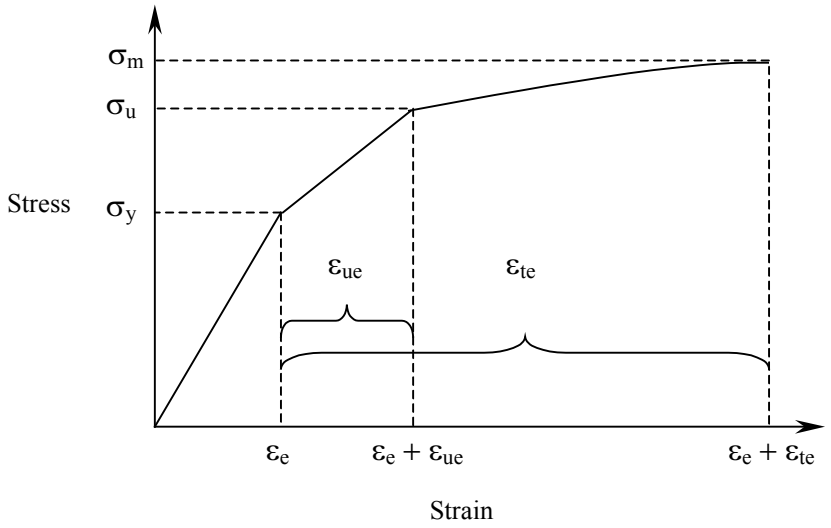

FIG. 3. Schematic of the stress-strain curve illustrating CSED calculations.

where σ is the true stress; ε is the true strain; $\dot{\varepsilon}$ is the strain rate; and K, n, and m are material constants obtained from MATPRO.

The total strain energy in the plastic regime ($\varepsilon > \varepsilon_e$) can be obtained by integrating eq. 13 between the elastic limit (ε_e) and the total elongation as shown in eq. 14.

$$U_p = \int_{\varepsilon_e}^{\varepsilon_e+\varepsilon_{te}} K\varepsilon^n \left(\frac{\dot{\varepsilon}}{\dot{\varepsilon}_o}\right)^m d\varepsilon \tag{14}$$

This expression can be simplified by evaluating eq. 13 at the elastic limit, which yields:

$$K\left(\frac{\dot{\varepsilon}}{\dot{\varepsilon}_o}\right)^m = \sigma_y^{1-n} E^n \tag{15}$$

Substituting eq. 15 into eq. 14, integrating and evaluating the result at the integration limits gives the plastic strain energy component as:

$$U_p = \frac{\sigma_y^{1-n} E^n}{n+1} \left[(\varepsilon_e + \varepsilon_{te})^{n+1} - \varepsilon_e^{n+1} \right] \tag{16}$$

The total CSED is simply the sum of the elastic and plastic strain energy components, i.e.

$$U_c = U_e + U_p \tag{17}$$

3.2. Correction factors

There are three important effects that must be considered before using the data from mechanical property tests to establish a CSED relation for irradiated Zircaloy cladding. These are: material anisotropy, multiaxial stress-state, and strain rate effects.

Anisotropy: Irradiated Zircaloy exhibits significant reduction in anisotropy because of irradiation damage. Existing mechanical property data, obtained for temperatures below the level required to anneal irradiation damage, demonstrate that irradiated Zircaloy cladding exhibits isotropic or near-isotropic behavior [13]. The effect of cladding anisotropy need be considered only when combining irradiated and un-irradiated data.

Multiaxial stress-state: PCMI-induced stresses are generally biaxial, a condition that needs to be accounted for in the CSED Model. To that end, the total elongation values obtained from the uniaxial ring tension and axial tube tension tests were adjusted to account for biaxiality effects on ductility. The total elongation values from the uniaxial tests were reduced using correction factors developed by Koss and Andersson that are a function of hydrogen content and stress ratio [14,15].

Strain rate effects: The rapid PCMI loading caused by RIA transients suggests that strain rate effects should be considered in the CSED development. High strain rates can reduce the ductility; however, the limited experimental data on irradiated Zircaloy above 288ºC show little effect of strain rate in the range observed in RIA tests.

3.3. CSED correlation

The CSED Correlation was determined from the results of the mechanical property tests as a function of temperature, fast fluence, and the hydrogen concentration, or alternatively the oxide thickness. For high burnup Zircaloy cladding, hydride content and distribution can have an important impact on the mechanical response. Hydrogen pickup from outer surface corrosion is the primary source of hydrogen in Zircaloy cladding. Consequently, the hydride content is generally proportional to the oxide layer thickness. In developing a CSED Correlation for high burnup Zircaloy, the ratio of the sample oxide thickness to cladding thickness was used as the correlation parameter. By using this parameter to correlate the CSED results, it is possible to compare results for different initial cladding types, e.g. 14 × 14 vs. 17 × 17. The CSED values from the mechanical property tests listed in Table-I are shown in Fig. 4 for temperatures above 280°C and in Fig. 5 for temperatures below 150°C, along with least-squares best-fit curves. The data above 280°C were divided into two data sets that represent different material conditions: one for samples without oxide spallation and one for samples with oxide spallation. Separate least-square curves were developed for each data set. The results are shown in Fig. 4, which shows significant differences in the CSED values between the samples with spalled oxide layers and those with non-spalled oxide layers.

3.4. Application to reactivity initiated accidents (RIA)

The CSED/SED cladding-integrity model described in this paper was applied to recent RIA experiments [16] performed on intermediate and high burnup fuel by IPSN in France using the sodium reactor CABRI [2], and by JAERI in Japan using the room-temperature NSRR [3]. Fuel rod analyses of the CABRI REP Na tests and the NSRR tests have been performed using the transient fuel behavior code FALCON [7, 8]. The code calculates the SED (U) from the calculated stresses and strains as function of time according to the following equation,

$$U(t) = \int_0^t \left[\sum \sigma_i \cdot \Delta\varepsilon_i,\ i = r,\theta,z \right] dt \qquad (18)$$

The results for the CABRI REP Na tests (T > 280°C) are shown in Fig. 6. The results for the NSRR tests (T < 150°C) are shown in Fig. 7. Also shown for comparison in each figure are the appropriate best-fit CSED curves from Fig. 4 and Fig. 5.

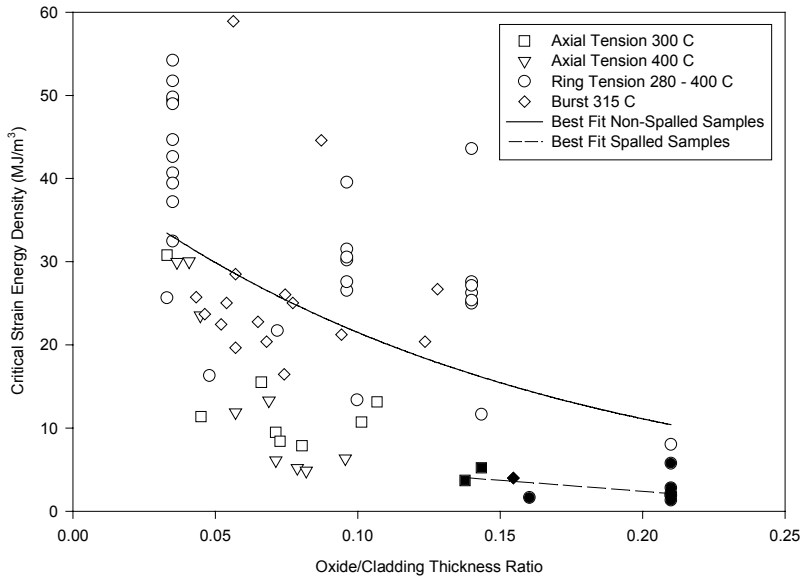

FIG. 4. CSED values from mechanical property tests for temperatures above 280°C. Separate best-fit curves are shown for non-spalled and spalled data.

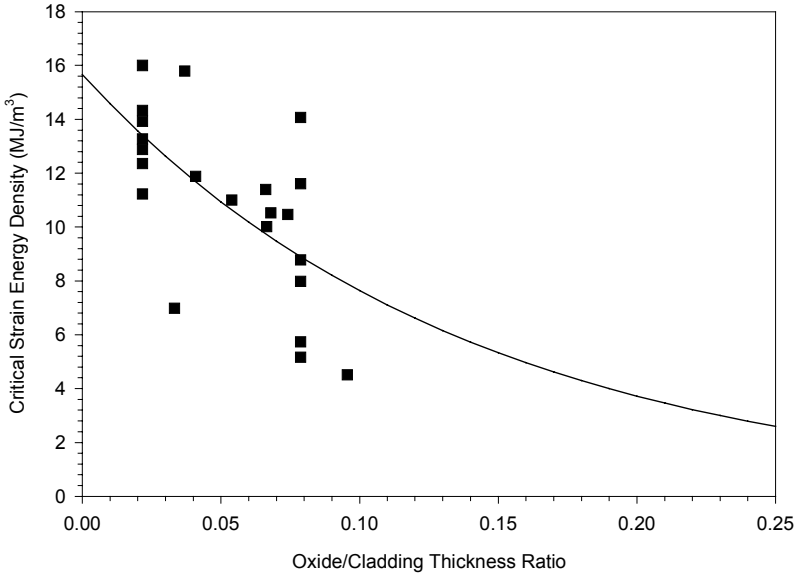

FIG. 5. Critical strain energy density values from mechanical property tests at temperatures below 150°C. Best-fit curve of the data is shown for comparison.

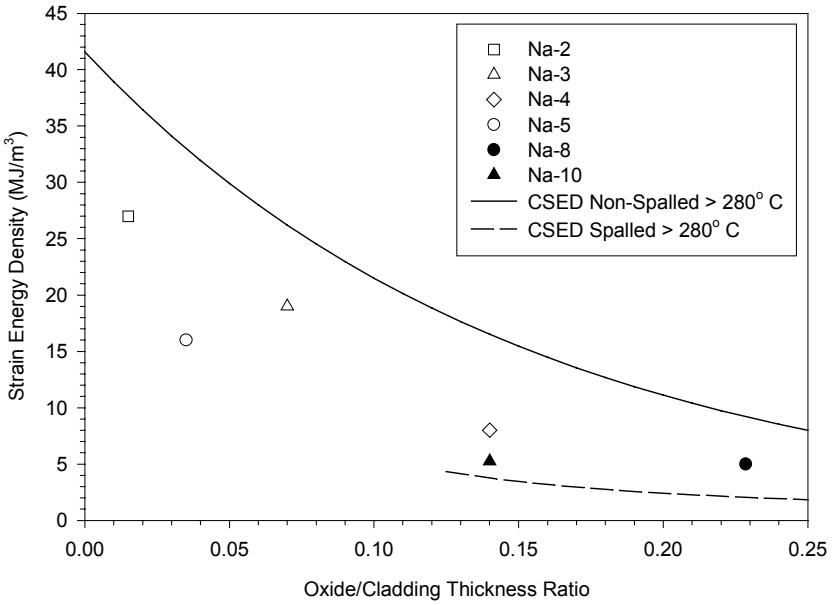

FIG. 6. SED calculated by FALCON for the CABRI REP Na Tests on UO_2 test rods. CSED curve is shown for comparison.

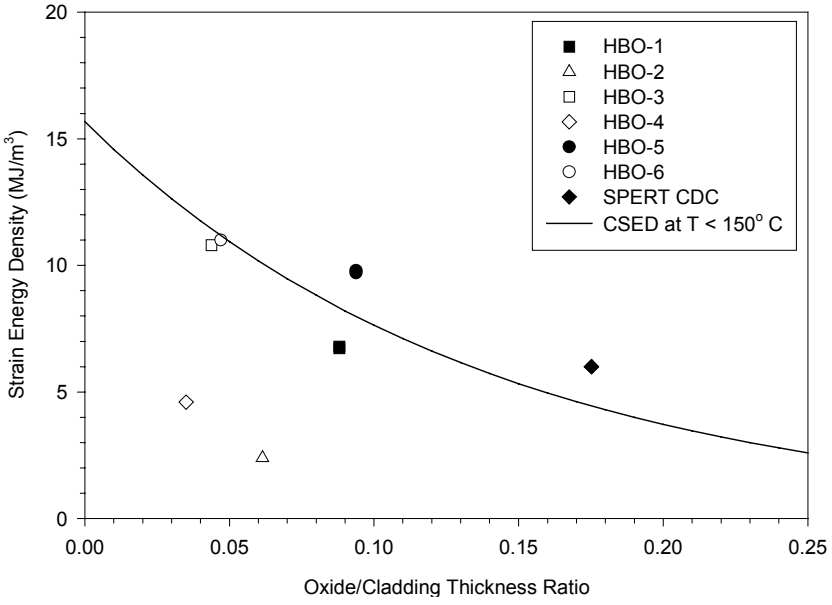

FIG. 7. SED calculated by FALCON for selected NSRR test rods. CSED curve is shown for comparison.

The SED values for the CABRI REP Na tests with rods containing non-spalled oxide lie below the CSED curve for non-spalled cladding, indicating no failure. However, the two tests with rods containing spalled oxide layers (REP Na-8 and Na-10) fall on or above the CSED curve for spalled cladding, indicating possible failure. Post-test examinations found that both of these tests experienced cladding failure during the power pulse [17].

Similarly in Fig. 7, the SED results for the NSRR tests that did not fail fall below the CSED curve for low temperature conditions. Tests that experienced failure or contained micro-cracks in the outer region of the cladding fall near or above the CSED curve. Based on these results, the coupled CSED/FALCON methodology seems to be successful in predicting the tests outcome.

4. CONCLUSIONS

A cladding failure model applicable to PCMI conditions under operational and accident transients has been developed for irradiated Zircaloy cladding based on the strain energy density (SED) concept. The SED approach is derived from the J-integral method used in fracture mechanics evaluations and can allow for the treatment of damaged material without explicitly modeling local defects or performing fracture mechanics analysis. A critical strain energy density (CSED), which defines the material limit for mechanical loading, was developed as a function of temperature, fast fluence, and hydrogen content from mechanical property tests conducted on irradiated Zircaloy cladding. An important aspect of this approach is the fact that the mechanical property data used to derive the CSED includes material that contains incipient hydride and irradiation damage similar to that present in irradiated cladding. When coupled with the fuel behavior program FALCON, the SED methodology has been shown to predict the occurrence of cladding failure under PCMI loading conditions for RIA simulation tests performed on irradiated test rods. The versatility of the proposed cladding failure model allows for analytical evaluation of high burnup fuel performance under operational and accident transients. The coupled FALCON/SED methodology can facilitate the establishment of licensing criteria for higher burnup operation.

REFERENCES

[1] RASHID, Y.R., ZANGARI, A.J., LIN, C.L., "Modeling of PCI Under Steady State and Transient Operating Conditions," Water Reactor Fuel Element Computer Modeling in Steady State, Transient and Accident Conditons (Proc IAEA Technical Committee Meeting Preston, UK, September 18-22, 1988), IAEA-IWGFPT/32 (1989) 91-101.

[2] PAPIN, J., et al., "French Studies on High-Burnup Fuel Transient Behavior Under RIA Conditions," Nuclear Safety, Vol. 37, No. 4, Nuclear Regulatory Commission, Bethesda, Maryland, October 21-23, 1996, pp. 289-327.

[3] FUKETA, T., et al., "NSRR/RIA Experiments with High-Burnup PWR Fuels," Nuclear Safety, Vol. 37, No. 4, Nuclear Regulatory Commission, Bethesda, Maryland, October 21-23, 1996, pp. 328-342.

[4] GARDE, A.M., SMITH, G.P., PIREK, R.C., "Effects of Hydride Precipitate Localization and Neutron Fluence on the Ductility of Irradiated Zircaloy-4," Zirconium in the Nuclear Industry: Eleventh International Symposium, ASTM STP 1295, pp. 407-430.

[5] RICE, J.R., "A Path Independent Integral and the Approximate Analysis of Strain Concentration by Notches and Cracks," Journal of Applied Mechanics, Transactions ASME, 35, June 1968.
[6] MONTGOMERY, R.O., et al., "Assessment of RIA-Simulation Experiments on Intermediate and High Burnup Test Rods," Nuclear Safety, Vol. 37, No. 4, Nuclear Regulatory Commission, Bethesda, Maryland, October 21-23, 1996, pp. 372-387.
[7] MONTGOMERY, R.O., et. al., "FALCON Fuel Analysis and Licensing Code, Vol. 2, User's Manual," ANA-97-0230, ANATECH Corp., San Diego, California, December 1997.
[8] RASHID, Y.R., MONTGOMERY, R.O., ZANGARI, A.J., "FREY-01: Fuel Rod Evaluation System, Volume 1: Theoretical and Numerical Bases, " EPRI NP-3277-V1R3, August 1994.
[9] SMITH, G.P., et al., "Hot Cell Examination of Extended Burnup Fuel from Calvert Cliffs-1," Vol. 2, EPRI TR-103302-V2, Electric Power Research Institute, Palo Alto, California, July 1994.
[10] SMITH, G.P., et al., "The Evaluation and Demonstration of Methods for Improved Nuclear Fuel Utilization," Final Report, DOE/ET/34013-15, UC-523, CEND-432, ABB Combustion Engineering, Windsor, Connecticut, August 1994.
[11] NEWMAN, L.W., "The Hot Cell Examination of Oconee 1 Fuel Rods after Five Cycles of Irradiation," DOE/ET/34212-50, BAW-1874, Babcock & Wilcox, Lynchburg, Virginia, October 1986.
[12] HAGRMAN, D.T., "MATPRO – A Library of Materials Properties for Light Water Reactor Accident Analysis," SCDAP/RELAP5/MOD/3.1 Code Manual, Vol. 4, NUREG/CR-6150, EGG-2720, June 1995.
[13] MURTY, K.L., MAHMOOD, S.T., "Effects of Recrystallization and Neutron Irradiation on Creep Anisotropy of Zircaloy Cladding," Zirconium in the Nuclear Industry: Ninth International Symposium, ASTM STP 1132, American Society for Testing and Materials, Philadelphia, Pennsylvania, 1991, pp. 198-217.
[14] FAN and KOSS, Metall. Trans., 16A, 1985, p. 675.
[15] ANDERSSON, T., WILSON, A., "Ductility of Zircaloy Canning Tubes in Relation to Stress Ratio in Biaxial Testing," Zirconium in the Nuclear Industry: Fourth International Conference, ASTM STP 681, American Society for Testing and Materials, Philadelphia, Pennsylvania, 1978, pp. 60-71.
[16] YANG, R.L., MONTGOMERY, R.O., WAECKEL, N., RASHID, Y.R., "Industry Strategy and Assessment of Existing RIA Data," Proceedings of the International Topical Meeting on Light Water Reactor Fuel Performance, Park City, Utah, April 10-13, 2000, pp. 383-401.
[17] SCHMITZ, F., PAPIN, J., "REP-Na 10, Another RIA Test with a Spalled High Burnup Rod and a with Pulse Width of 30 ms," Proceedings of the 26th WRSIM, Vol. 3, Nuclear Regulatory Commission, Bethesda, Maryland, October 26-28, 1998, pp. 243-254.

A SYSTEMATIC APPROACH FOR DEVELOPMENT OF A PWR CLADDING CORROSION MODEL

M. QUECEDO, J.J. SERNA
ENUSA, Madrid, Spain

R.A. WEINER, P.J. KERSTING
KW Consulting, Inc., Pittsburgh, Pennsylvania, United States of America

Abstract

A new model for the in-reactor corrosion of Improved (low-tin) Zircaloy-4 cladding irradiated in commercial pressurized water reactors (PWRs) is described. The model is based on an extensive database of PWR fuel cladding corrosion data from fuel irradiated in commercial reactors, with a range of fuel duty and coolant chemistry control strategies which bracket current PWR fuel management practices. The fuel thermal duty with these current fuel management practices is characterized by a significant amount of sub-cooled nucleate boiling (SNB) during the fuel's residence in-core, and the cladding corrosion model is very sensitive to the coolant heat transfer models used to calculate the coolant temperature at the oxide surface. The systematic approach to developing the new corrosion model therefore began with a review and evaluation of several alternative models for the forced convection and SNB coolant heat transfer. The heat transfer literature is not sufficient to determine which of these heat transfer models is most appropriate for PWR fuel rod operating conditions, and the selection of the coolant heat transfer model used in the new cladding corrosion model has been coupled with a statistical analysis of the in-reactor corrosion enhancement factors and their impact on obtaining the best fit to the cladding corrosion data. The in-reactor corrosion enhancement factors considered in this statistical analysis are based on a review of the current literature for PWR cladding corrosion phenomenology and models. Fuel operating condition factors which this literature review indicated could have a significant effect on the cladding corrosion performance were also evaluated in detail in developing the corrosion model. An iterative least squares fitting procedure was used to obtain the model coefficients and select the coolant heat transfer models and in-reactor corrosion enhancement factors. This statistical procedure was completed with an exhaustive analysis of the model residuals with respect to the data, as a function of a large number of independent variables, such as rod burnup, average local power, lithium exposure, axial elevation, etc. to evaluate whether there were any remaining systematic biases in the fit to the corrosion data. This systematic approach determined that the coolant heat transfer models should be revised from the standard Dittus-Boelter forced convection and Thom SNB heat transfer models, and that the significant in-reactor corrosion enhancement factors are related to the formation of a hydride rim at the cladding outer diameter, the coolant lithium concentration, and the fast neutron fluence.

1. INTRODUCTION

Current pressurized water reactor (PWR) fuel management uses low leakage loading patterns, high peaking factors and increased end-of-life (EOL) fuel burnups to maximize the economic return on the utility investment in the fuel. These world-wide trends in PWR fuel management lead to more severe thermal duty for the fuel, with higher cladding temperatures and extended periods of operation under sub-cooled nucleate boiling (SNB) conditions. These more aggressive steady-state thermal conditions present a significant challenge to the waterside corrosion performance of PWR fuel cladding. This paper presents a new PWR Zircaloy-4 cladding corrosion model that has been jointly developed by ENUSA and KW Consulting, Inc. based on an extensive database for Improved (low tin) Zircaloy-4 cladding operating under current PWR fuel management practices.

In-reactor Zircaloy corrosion is a thermally activated process, with in-reactor enhancement of the thermal corrosion rates, and an accurate prediction of the coolant temperature at the oxide surface is a critical component of any corrosion model. The need to accurately predict the coolant-cladding interface temperature becomes more critical with the more aggressive thermal duty experienced by the lead PWR fuel rods with current PWR fuel management practices, and could therefore lead to a revision of the coolant heat transfer models used in the corrosion model calculations. Most of the previous efforts to improve the modeling of PWR cladding corrosion have focused on the modeling of the cladding corrosion mechanisms themselves, and relatively little attention has been paid to how the coolant thermal models affect the ability to predict the cladding corrosion behavior. The first section of this paper therefore presents the results of a detailed review of several coolant heat transfer models applicable to PWR conditions. Evaluation of these heat transfer models showed that the differences between them have a significant impact on how well the corrosion model fits the in-reactor data.

The corrosion model development itself, described in the second section of the paper, was based on an evaluation of many of the in-reactor corrosion enhancement factors proposed in the literature, and used a least squares fitting procedure to determine which of these made a significant contribution to improving the fit of the model to the in-reactor data. The model development determined that the significant in-reactor corrosion enhancement factors are related to the formation of a hydride rim at the cladding surface, the cladding exposure to lithium used to control the coolant pH, and the fast neutron fluence.

2. COOLANT HEAT TRANSFER MODELS

As indicated in the Introduction, PWR fuel is now irradiated in a more severe thermal environment than in the past, and the standard heat transfer models, used by the industry for decades, may not be accurate enough for these new thermal conditions. As the initial step in determining the most appropriate coolant thermal models to be used in developing the new cladding corrosion model, a literature survey was done to review the basic research on coolant heat transfer. The primary sources for this literature review were the basic reference monographs on the subject of heat transfer [1] and PWR thermal analysis [2], and the coolant heat transfer models used in the RELAP5 thermal safety analysis code [3]. The original technical literature was consulted where it was necessary to obtain more detailed information than is available in these review monographs.

Bulk coolant temperatures are calculated using an effective closed single channel model, modified by using a mixing factor to account for mixing between heated and unheated channels in the PWR fuel assembly, such that the enthalpy rise in the channel is given by

$$H(z,T(z)) = FMIX \int_0^z \frac{4q''(z')}{GD_e} dz'$$

where:

H = enthalpy

FMIX = mixing factor

T(z) = bulk coolant temperature at the elevation z

q” = heat flux

G = coolant mass flow rate

D_e = hydraulic diameter

The value of the mixing factor used in the effective closed single channel model has been benchmarked against a detailed multi-channel model. Since the purpose of the corrosion model is to calculate the cladding corrosion of individual fuel rods, the additional complexity of using the multi-channel model for calculating the bulk coolant temperatures does not add significant value to the overall model.

The significant coolant heat transfer models for the corrosion model development are those related to the temperature rise through the coolant film layer at the oxide surface. There are two regimes of interest: forced convection heat transfer, with sub-cooled conditions at the oxide surface, and sub-cooled nucleate boiling heat transfer, where the coolant temperature at the oxide surface is greater than the saturation temperature.

The standard model for forced convection heat transfer with turbulent flow in smooth tubes is the Dittus-Boelter model [4], where the temperature rise at the coolant-cladding interface is

$$\Delta T_{film} = \frac{q''}{h_{film}}$$

and the heat conductance h_{film} is given by

$$h_{film} = 0.023 Re^{0.8} Pr^{0.4} \frac{k_l}{D_e}$$

where:

Re = Reynold's number

Pr = Prandtl number

k_l = bulk coolant thermal conductivity

The Dittus-Boelter heat conductance constant, 0.023, has been obtained by fitting to data obtained from single tube heat transfer measurements. Modifications of the original Dittus-Boelter model, involving small adjustments to this constant to give a better fit to the measured in-reactor corrosion data, have been used in some of the PWR cladding corrosion models in the literature [5].

However, heat transfer measurements on rod bundles showed that the pitch-to-rod diameter ratio has a significant effect on the forced convection heat transfer, and a number of forced convection heat transfer models have been developed which have an explicit dependence on the pitch-to-rod diameter ratio. The most significant of these modifications of the Dittus-Boelter model in the literature are those due to Weisman [6]:

$$h_{film} = (0.042\frac{s}{d} - 0.024)Re^{0.8}Pr^{0.4}\frac{k_l}{D_e}$$

and Inayatov [7]

$$h_{film} = 0.023Re^{0.8}Pr^{0.4}\Psi_t\Psi_s\frac{k_l}{D_e}$$

$$\Psi_t = (T_l / T_s)^{1/2}$$

$$\Psi_s = s / d$$

where:

s = rod-to-rod pitch

d = rod diameter

T_l = bulk coolant absolute temperature

T_s = cladding surface absolute temperature

The pitch-to-rod diameter ratio effects in the Weisman and Inayatov models increase the forced convection heat transfer coefficient by 30–50% for typical PWR fuel assembly geometries. A comparison between these different forced convection heat transfer models for a typical current PWR lead rod power, 25 kW/m, is shown in Figure 1. The increased forced convection heat transfer with the Weisman or Inayatov models is a significant effect, reducing the oxide surface temperature by as much as 10°C from the value obtained using Dittus-Boelter forced convection heat transfer for this lead rod. An additional significant consequence of the Wesisman or Inayatov models is that the reduced oxide surface temperature under forced convection conditions will raise the axial elevation for the onset of SNB, by as much as 15% for this typical lead rod case, compared with the elevation for the onset of SNB predicted using the Dittus-Boelter forced convection heat transfer model.

There is a much wider range of models for the heat transfer under SNB conditions, ranging from the early models of Jens and Lottes [8], Thom et. al. [9] and Chen [10] to more recent models developed by Bjorge, Hall and Rohsenow [11] (BHR) and Gungor and Winterton [12] (GW). The Jens-Lottes or Thom models are the SNB heat transfer models are the ones usually used in PWR cladding corrosion heat transfer calculations.

Current PWR fuel management, even with the most aggressive low leakage loading patterns and peaking factors, does not lead to fully developed SNB, and when SNB occurs there is still a significant contribution to the heat transfer from forced convection mechanisms as well as SNB mechanisms. Thus a critical concern for the SNB heat transfer model to be used in the PWR cladding corrosion model is that it combine both SNB and forced convection heat transfer in the transition regime to fully developed sub-cooled nucleate boiling heat transfer. This is an explicit feature of the Chen, BHR and GW SNB heat transfer models, but it is not explicitly included in the Jens-Lottes or Thom models. However, the Jens-Lottes and Thom models implicitly include the effects of the forced convection heat transfer in this transition regime, since much of the data used in developing these two models is in the transition regime where the component of heat transfer due to forced convection is as important as the component due to SNB heat transfer.

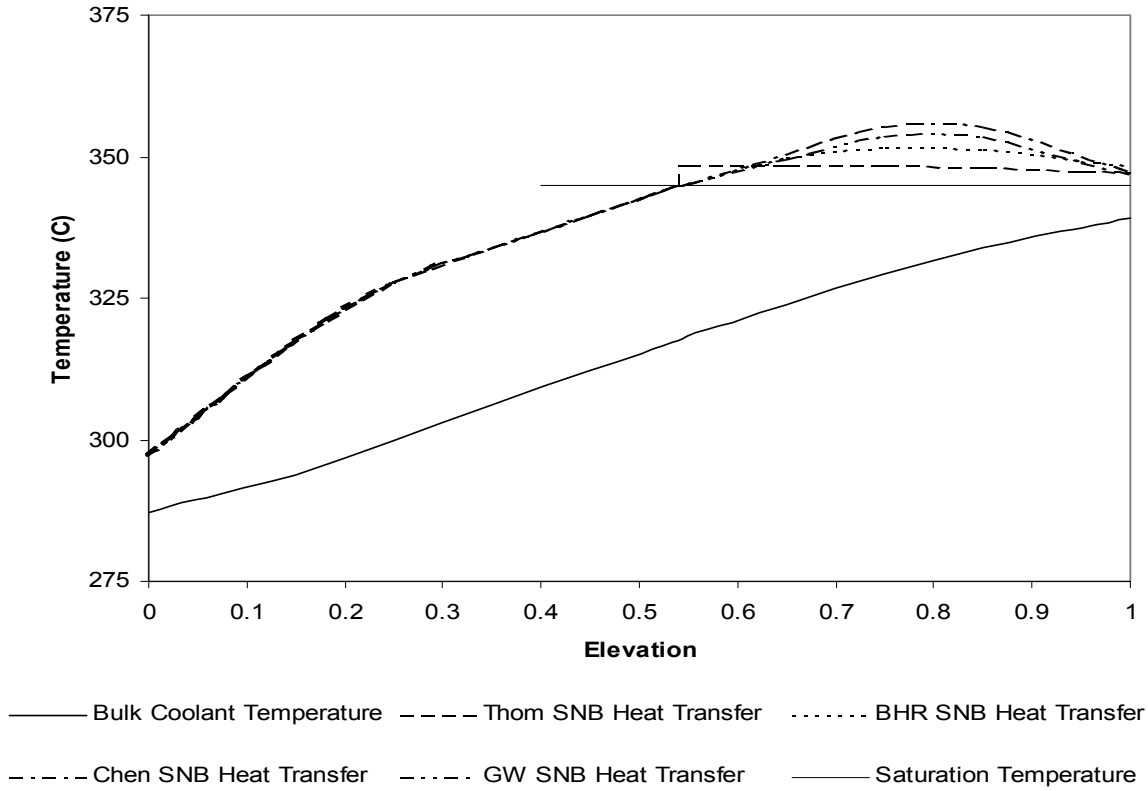

FIG 1. Oxide surface temperature predictions with different forced convection heat transfer models.

The Chen and GW models account for the transition regime by using a parallel heat transfer formalism in which the heat flux q" is given by

$$q'' = h_{FC}(T_{surf} - T_{bulk}) + h_{boil}(T_{surf} - T_{sat})$$

where

h_{FC} = forced convection heat conductance

T_{surf} = oxide (or crud) surface temperature

T_{bulk} = bulk coolant temperature

h_{boil} = fully developed SNB heat conductance

T_{sat} = saturation temperature

The BHR model uses a similar parallel heat transfer formalism, but it combines the forced convection and SNB heat transfer in a root-mean-square convolution, rather than linearly. Because the Chen, GW and BHR models explicitly account for the transition from forced convection to fully developed SNB heat transfer, these models are applicable to a wider range of SNB heat transfer conditions than the Jens-Lottes or Thom models.

A significant consequence of failing to include forced convection in the transition regime is that the Jens-Lottes and Thom models may greatly exaggerate the SNB heat transfer under PWR conditions, even for the lead rods, which results in predictions of significantly lower temperatures at the oxide surface compared with the SNB heat transfer models which properly

model the transition regime. This is illustrated in Figure 2, which compares the oxide surface temperature predictions obtained using the Dittus-Boelter forced convection model and the Thom SNB model with those obtained using Dittus-Boelter forced convection and the BHW, Chen and GW models for a typical PWR lead rod. There are again significant differences, nearly as much as 10°C, between the oxide surface temperatures predicted with the different SNB heat transfer models.

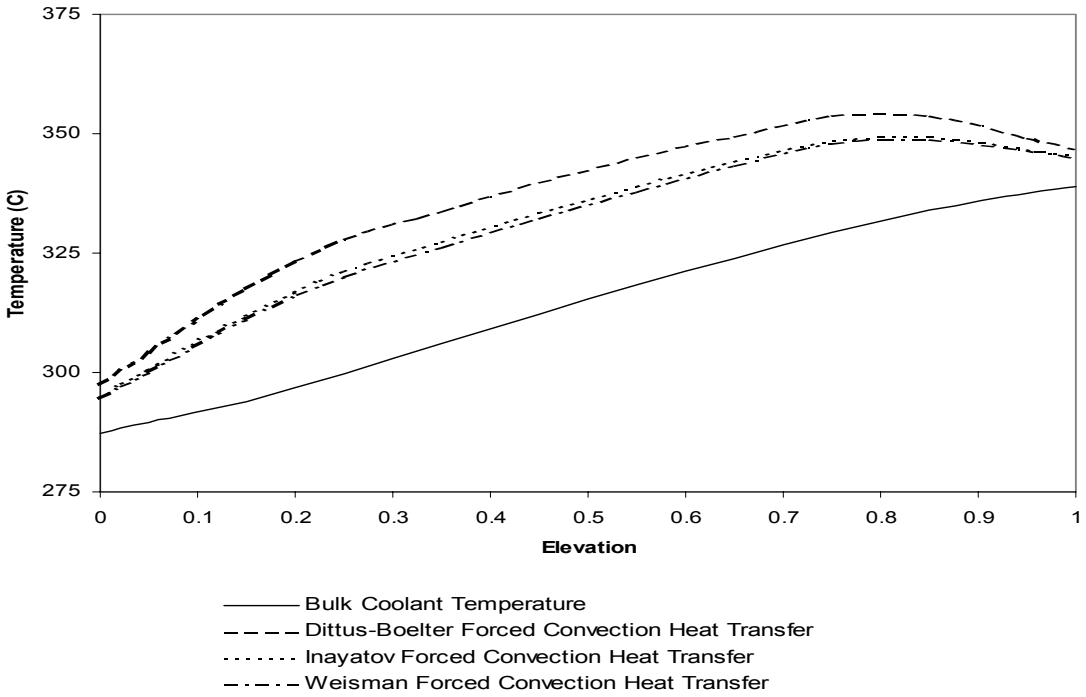

FIG. 2. Oxide surface temperature predictions with the Dittus-Boelter forced convection and SNB heat transfer models.

An Arrhenius form is used for the out-of-reactor thermal component of the Zircaloy corrosion rate,

$$\frac{dw_{th}}{dt} = \exp(C - Q/RT)$$

where

w = oxide weight gain

T = metal-oxide interface temperature

Literature values for the activation energy Q range between 25 000 [13] and 32 000 cal/mole[14]. For the typical PWR lead rod oxide surface temperatures shown in Figures 1 and 2, a 10°C difference in the oxide surface temperature corresponds to a 40–50% difference in the thermal corrosion rate due to the differences in the coolant heat transfer models. This is a large effect, and these comparisons make it clear that the selection of the coolant heat transfer model will have a significant impact on the PWR cladding corrosion model.

This review and evaluation shows that the selection of the coolant heat transfer model can have a large effect on the metal-oxide interface temperature and hence on the ability to consistently describe the in-reactor PWR cladding corrosion behavior. However, there has been no previous systematic assessment of the coolant heat transfer models used in the PWR cladding corrosion models for the severe thermal operating conditions encountered in current PWR fuel management. The focus of attention in the development of these models has been on the mechanisms for the in-reactor cladding corrosion enhancement. As described below, the procedure used here to develop the new PWR cladding corrosion model has included a systematic evaluation of the heat transfer models as well as the in-reactor corrosion enhancement mechanisms. Though this introduces an additional level of complication to the process of fitting the corrosion model to the cladding corrosion data, the benefits of having a more accurate description of one of the fundamental parameters affecting the in-reactor cladding corrosion behavior, the temperature at the metal-oxide interface, are more than sufficient justification for the additional effort required to implement this systematic approach.

3. IN-REACTOR CORROSION ENHANCEMENT FACTORS

The nuclear power industry has devoted considerable effort to fundamental studies in order to understand the mechanisms which cause the in-reactor corrosion enhancement. A number of in-reactor experiments, such as the Halden IFA-593 test [15], have been conducted, and there have been several dedicated meetings and workshops [16, 17]. In addition, there have been a number of detailed review reports on the current status of the understanding of in-reactor cladding corrosion [18, 19].

Among the mechanisms which have received attention in the recent literature are:

- hydride redistribution and enhanced corrosion rates with increased hydrogen concentrations in the metal [20, 21, 22], including hydride redistribution driven by stress gradients [23];
- dissolution in the base metal of the precipitates which stabilize phases in the oxide which, then, is more susceptible to increased corrosion [24];
- a boron buffering effect due to competition between lithium enhancement of the diffusion of oxidizing species through the oxide layer with boron inhibition of the diffusion [25]; and
- precipitates in the oxide layer which impede the growth of circumferential cracks in the oxide and produce a pattern of small isolated cracks which impede the diffusion of oxidizing species to the oxide-metal interface [26].

Though these studies of the fundamental mechanisms responsible for in-reactor corrosion enhancement provide valuable insight into the variables which should be considered in developing a practical corrosion model for use in PWR fuel rod design, these fundamental studies are not readily adaptable to parameterization of the mechanisms. Recent corrosion models reported in the literature [27, 28] give more usable guidance for how to express the in-reactor corrosion enhancement on temperature, fast flux, cladding condition, coolant chemistry, etc. The EPRI model [27] uses thermal feedback, thermally driven radial redistribution of the hydrides in the metal which leads to the formation of a dense hydride rim in the cladding at the metal-oxide interface; cladding precipitate size distributions and in-

reactor precipitate dissolution, lithium hydroxide exposure, and radiation effects on the oxide film, as the important contributors to the in-reactor corrosion rate enhancement. In contrast to the mechanistic and phenomenological bases for the EPRI model corrosion enhancement factors, Reference [28] relies on empirical and statistical analyses to identify the significant factors which give the in-reactor corrosion enhancement. In most cases the empirical enhancement factors in this model account for the same phenomena as the more mechanistic enhancement factors in the EPRI model, but Reference [28] includes a strong enhancement factor proportional to the mass evaporation rate, i.e. an explicit enhancement due to the occurrence of SNB.

4. CORROSION MODEL DEVELOPMENT

Parameterization of the enhancement factors in the new corrosion model is similar to that used in [28], with the exception that the [28] oxide thickness enhancement factor is replaced by a simple parameterization of the Reference [27] model for hydride redistribution and the corrosion rate enhancement due to the formation of the hydride rim. Five in-reactor corrosion enhancement factors have been evaluated in developing the model:

- a fluence enhancement factor proportional to the fast fluence;
- a flux enhancement factor proportional to the fast flux;
- a lithium enhancement factor proportional to the coolant lithium concentration;
- a hydride rim enhancement factor which is a function of the oxide thickness, with a threshold at an oxide thickness of approximately 15 μm and saturation at an oxide thickness of approximately 70 μm; and
- a boiling duty enhancement factor proportional to the product of the lithium concentration and the difference between the oxide surface temperature and the saturation temperature.

Boron buffering effects were evaluated in preliminary studies [29] by considering the dependence of the cladding corrosion on boron concentration, combinations of the boron and lithium concentrations, or the local pH of the coolant, calculated at either the coolant bulk temperature or the coolant temperature at the oxide surface. These preliminary studies indicated that accounting for boron buffering would not improve the fit to the corrosion data, and therefore enhancement factors that explicitly depend on the boron concentration in the coolant have not been included in the final model.

The fluence and flux enhancement factors are simple parameterizations to account for the mechanistic processes of precipitate dissolution within the base metal and precipitate formation within the oxide layer. The lithium enhancement factor is based on the known sensitivity of the Zircaloy corrosion rate to the coolant lithium concentration established in out-of-reactor tests. The boiling duty enhancement factor has been included due to the significant contribution it made to the Reference [28] in-reactor PWR cladding corrosion enhancement. A simple linear dependence on the fluence, flux, lithium concentration, etc. is used to parameterize the enhancement factors in terms of constants, which were determined by statistical fitting of the model to the cladding corrosion data. These simple parameterizations of the mechanistic in-reactor corrosion enhancement processes are sufficient to give good agreement with the data, given the large degree of scatter in the in-

reactor cladding corrosion data, without requiring complicated calculations of the time and exposure dependence of the enhancement factors.

The corrosion model development also evaluated several other model modifications to determine whether it would be possible to improve the agreement between the model and the data. These include:

- modifications to the mixing factors in the bulk coolant temperature model;
- modifications to the oxide thickness dependence of the hydride enhancement factor;
- modifications to the oxide thermal conductivity model to account for possible changes in the conductivity under SNB conditions, or due to delamination of thick oxide layers; and
- alternative models for the out-of-reactor thermal corrosion rate, using activation energies which span the range reported in the literature.

None of these modifications gave any significant improvement in the fit to the data, and therefore have not been included in the final model.

The model has been calibrated and validated using 2430 cladding corrosion data points from more than 600 rods irradiated in 9 commercial reactors. Oxide thicknesses in this database are as high as 130 μm, with fuel residence times to 37 000 hours and rod burnups to 50 GWD/MTU. Though there is a great deal of scatter in this database, use of such a large database to evaluate the candidate cladding corrosion models ensures that the distinctions between the models obtained in this evaluation will be applicable over a wide range of PWR operating conditions. However, with such a large database and such a large degree of scatter, careful analysis is required so that significant differences between the candidate models can be discerned amidst the scatter.

The procedure used to evaluate and compare the candidate models was:

- select a coolant heat transfer model, i.e. a combination of a forced convection heat transfer model and an SNB heat transfer model;
- use an iterative least squares fitting procedure to determine which of the in-reactor corrosion enhancement factors made a significant contribution to fitting the cladding corrosion data. The corrosion predictions for each datapoint are highly non-linear functions of the model constants, and the least squares fit was found by a searching procedure, with a convergence criterion that the least squares solution minimize the residual sum of squares of the predicted minus the measured oxide thickness values to an accuracy of one part in 10^3; and
- compare the predicted minus measured oxide thickness residuals as a function of axial elevation, measured oxide thickness, etc. for each of the resulting best fit models to determine whether there are any significant differences due to the choice of the heat transfer model.

Using this procedure, it was determined [29] that the Inayatov forced convection heat transfer model, combined with either the BHR, Chen or GW SNB heat transfer model, gave the best fits to the cladding corrosion data.

5. RESULTS

The iterative least squares fitting procedure determined that the lithium and hydride enhancement factors give the most significant contributions to fitting the data. The fluence enhancement factor gave a significantly smaller contribution to minimizing the residual sum of squares, but it has been retained because it made a significant improvement to the behavior of the residuals as a function of axial position. The flux and boiling enhancement factors make a negligible contribution to minimizing the sum of squares, with the best fit values giving no more than a 3% enhancement of the corrosion rate for any of the datapoints at any time in life. This is a negligible effect relative to the overall scatter of the PWR cladding corrosion data. The difference between the new corrosion model and the Reference [28] model, i.e. the statistical insensitivity of the new model to an explicit enhancement factor related to the SNB duty, is a consequence of the coolant heat transfer model used in the new corrosion model. This gives significantly higher temperatures under SNB conditions than the SNB heat transfer model used in Reference [28], and with this perspective it can be seen that the Reference [28] boiling enhancement factor is needed to compensate for an underprediction of the thermal corrosion rates under SNB conditions obtained when the Dittus-Boelter forced convection and Thom SNB heat transfer models are used.

The final functional form of the new PWR cladding corrosion model is

$$\frac{dw}{dt} = F_{matl} F_{flu} F_{hyd} F_{Li} \frac{dw_{th}}{dt}$$

where

F_{matl} = material corrosion rate multiplier

F_{flu} = fluence enhancement factor

F_{hyd} = hydride rim enhancement factor

F_{Li} = lithium enhancement factor

The predictions of this model for the most limiting datapoints are quite sensitive to the model constants. After determining the statistical best fit, a final adjustment was made to the constants to improve the fit to the most limiting datapoints in the database. This adjustment had a negligible effect on the residual sum of squares, increasing it by less than 2%, but gives a significant improvement in the model's capability to extrapolate to the most limiting operating conditions for PWR fuel. Figure 3 shows a comparison between the final new PWR cladding corrosion model predictions and the measured oxide thickness data.

A statistical analysis of the residuals has been done to determine if there are any significant biases in the new model. This analysis considered whether there was any statistical significance to the functional dependence of the measured – predicted oxide thickness residuals for more than 40 independent variables which characterize the conditions of the PWR fuel rod operation in the cladding corrosion database. Included in the variables considered in this residual analysis are the axial elevation, residence time, local burnup, local fast fluence and average fast flux, lithium exposure, average bulk coolant and metal-oxide interface temperatures, average and maximum temperature rise above the saturation temperature, total time operating under SNB conditions, average boron exposure, cumulative

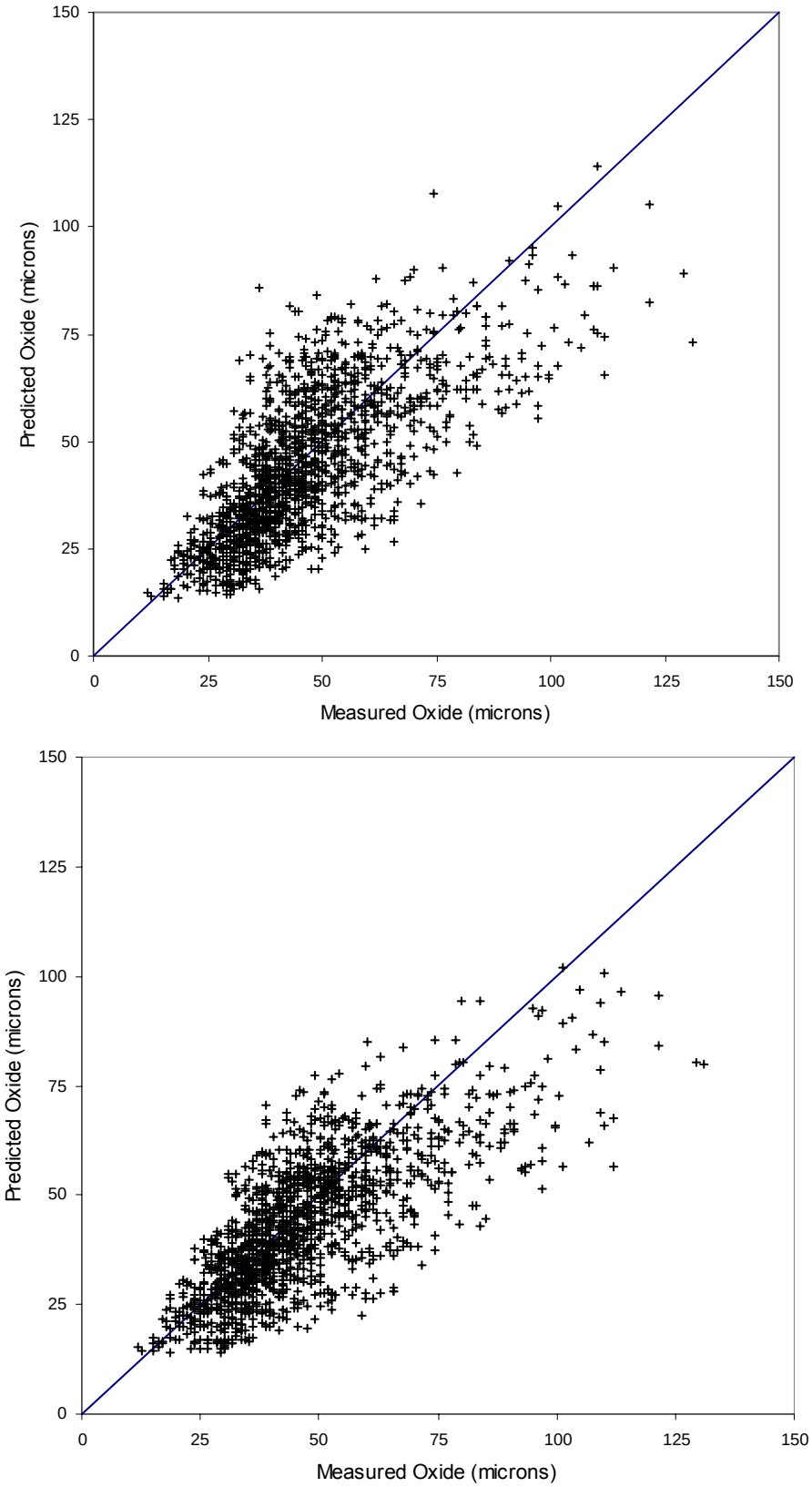

FIGs. 3 and 4. Comparison of new PWR cladding corrosion model predicted oxide thickness values vs. measured oxide thickness data (top); Comparison of predicted oxide thickness values vs. measured ones using the fit based on Dittus-Boetler and Thom models (bottom).

boron exposure, combinations of the boron and lithium exposure, and average local pH calculated at either the bulk coolant temperature or the oxide surface temperature. The maximum R^2 value for any of these residual evaluations is 0.05, which convincingly shows that there are no significant biases in the new corrosion model with respect to any relevant PWR fuel operating condition.

An evaluation of the impact of the revised heat transfer models has been done by applying the model development statistical procedure using the Dittus-Boelter forced convection and Thom SNB heat transfer models to determine the oxide surface temperatures. Not surprisingly, in this case a significant contribution is obtained from the boiling enhancement factor, which gives as much as a 45% increase in the in-reactor corrosion rate with the best fit value. The fit obtained with the Dittus-Boelter and Thom heat transfer models is compared with the measured oxide thickness data in Figure 4. This fit is not as good as that obtained with the revised heat transfer models, though due to the large amount of scatter in the measured oxide data this is not readily apparent in a direct comparison of Figures 3 and 4.

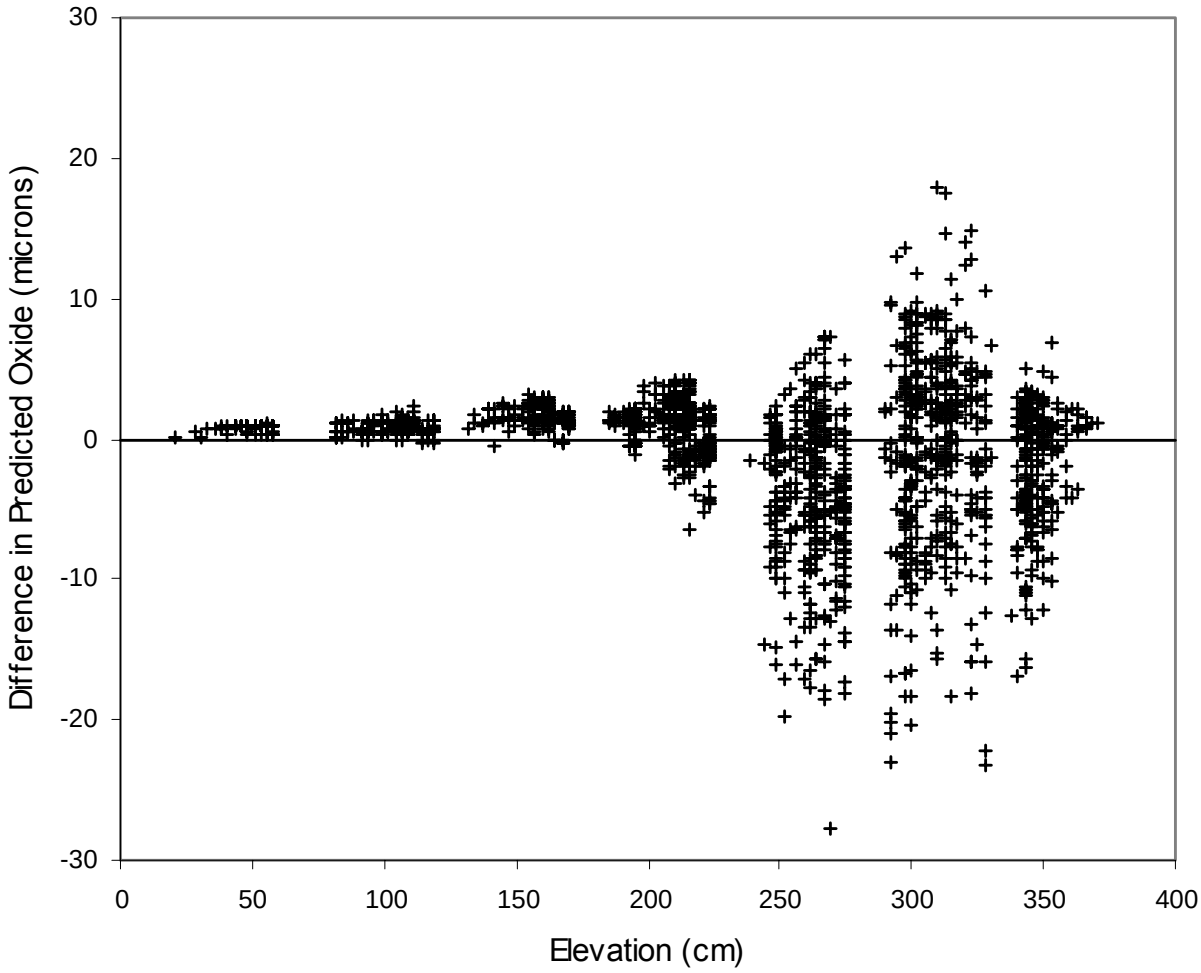

FIG 5. Difference in oxide thickness predictions between the new PWR cladding corrosion model and the fit based on Dittus-Boelter and Thom heat transfer, vs. axial elevation.

The differences between the two fits are more clearly seen by plotting the differences between the predictions of each of the fits as a function of axial position. The predictions of the new PWR corrosion model, with the revised heat transfer models, minus the prediction of the fit using the Dittus-Boelter and Thom heat transfer models, for each point in the PWR cladding corrosion database, are shown in Figure 5. The Figure shows that there are relatively small differences, less than 5 μm, between the predictions of the two fits from the bottom of the rod to the middle of span 4, at about the 200 cm elevation. From the middle of span 4 through span 5, and in span 7, the fit based on the Dittus-Boelter and Thom heat transfer models tends to predict higher oxide thicknesses, by up to 20 μm. However, in span 6, from approximately the 290 cm to 330 cm elevation, the new PWR cladding corrosion model and the equivalent corrosion model based on the Dittus-Boelter and Thom heat transfer models predict the same oxide thickness on the average, though there is a great deal of scatter.

The reason for this difference is that the Dittus-Boelter and Thom heat transfer models are predicting a significant amount of SNB from the middle of span 4 through span 5, and in span 7, and hence a significant additional enhancement of the in-reactor corrosion rate for these data due to the explicit boiling enhancement factor in this fit. Both sets of heat transfer models predict a significant amount of SNB for the data obtained in span 6. In span 7 the revised heat transfer models predict significantly less SNB than in span 6, while the Dittus-Boelter and Thom heat transfer models give nearly as much SNB as in span 6, as can be seen from Figure 2. Because a significant amount of the in-reactor corrosion enhancement in the fit based on the Dittus-Boelter and Thom heat transfer models is due the boiling enhancement factor, this fit must predict excessive in-reactor corrosion enhancement in spans 4, 5 and 7 to be able to give a good fit to the limiting data in span 6. The revised heat transfer models used in the new PWR cladding corrosion model, on the other hand, predict larger temperature differences between span 6 and spans 4, 5 and 7, and is therefore able to give a better overall fit to the data in spans 4 through 7 because it relies only on thermal feedback to give the higher in-reactor corrosion rates needed to fit the data in span 6.

These effects due to the differences in the heat transfer models significantly affect the reliability of the extrapolation of the cladding corrosion models from the PWR cladding corrosion database to the most limiting PWR fuel operating conditions that determine the commercial PWR fuel rod design operating limits. The improved calculation of the oxide surface temperatures with the revised heat transfer models used in the new PWR cladding corrosion model significantly increase the confidence in these extrapolations that are necessary in the commercial fuel design process.

6. SUMMARY

A new PWR cladding corrosion model has been developed and calibrated to an extensive database of commercial PWR Improved Zircaloy-4 cladding corrosion data, obtained under operating conditions typical of current PWR fuel management strategies. Significant improvement in the ability to fit the data has been obtained by revising the coolant heat transfer models used to calculate the coolant temperature at the oxide surface. The model uses simple parameterizations of the in-reactor corrosion enhancement factors which give good agreement with the data, considering the large amount of scatter in the cladding's in-reactor corrosion performance. The in-reactor corrosion enhancement factors which make a significant contribution to fitting the data depend on the fast flux, the lithium concentration,

and hydride redistribution and formation of a dense hydride layer at the cladding's outer surface. A statistical analysis of the residuals shows that the model has no significant biases with respect to many of the parameters which characterize a PWR fuel rod's operating environment.

REFERENCES

[1] W.M. ROSHENOW, Boiling, Chapter 12 of W.M. Rohsenow, J.P. Hartnett and E.N. Ganic, Eds., Handbook of Heat Transfer Fundamentals, 2nd Ed., Mc-graw-Hill, 1985.

[2] L.S. TONG and J. WEISMAN, Thermal Analysis of Pressurized Water Reactors, 3rd Ed., ANS, 1996.

[3] RELAP5/MOD3 Code Manual, Volume IV, Models and Correlations, NUREG/CR-5535, June 1995.

[4] F.W. DITTUS and L.M.K. BOELTER, University of California, Berkeley, Publ. Eng. **2**, 433 (1930).

[5] F. GARZAROLLI, et. al., "Waterside Corrosion of Zircaloy Fuel Rods," Report EPRI NP-2789, December 1982.

[6] J. WEISMAN, Nucl. Sci. Eng. **6**, 79 (1959).

[7] A. Ya. INAYATOV, Heat Transfer-Soviet Research **7** (No. 3), 84 (1975).

[8] W.H. JENS and P.A. LOTTES, U.S. AEC Rep. ANL-4627, 1951.

[9] J.R.S. THOM, W.M. WALKER, T.A. FALLON and G.F.S. REISING, Symposium on Boiling Heat Transfer in Steam-Generating Units and Heat Exchangers, Proc. Inst. Mech Eng. **180**, Part 3C, 226 (1965).

[10] J.C. CHEN, Ind. Eng. Chem., Proc. Des. Dev. **5**, 322 (1966).

[11] R.W. BJORGE, G.R. HALL and W.M. ROHSENOW, Int. J. Heat Mass Transfer **25**, 753 (1982).

[12] K.E. GUNGOR and R.H.S. WINTERTON, Int. J. Heat Mass Transfer **29**, 351 (1986) .

[13] P. BILLOT, P. BESLU, A. GIORDANO and J. THOMAZET, Zirconium in the Nuclear Industry, Eighth International Symposium, ASTM STP 1023, L.F.P. Van Swam and C.M. Eucken (Eds.), ASTM (1989).

[14] S.G. MacDONALD, G.P. SABOL and K.D. SHEPPARD, Zirconium in the Nuclear Industry, Sixth International Symposium, ASTM STP 824, D.G. Franklin and R.B. Adamson (Eds.), ASTM, (1984).

[15] M.A. McGRATH and D. DEUBLE, The PWR Corrosion Test IFA-593.2-4 Irradiation Data, Observation and Modeling Aspects, Report HWR-533, Halden, Norway (1998).

[16] INTERNATIONAL ATOMIC ENERGY AGENCY, Fundamental Aspects of Corrosion on Zirconium Base Alloys in Water Reactor Environments (Proc. TCM Portland, Oregon, 1989), IAEA, Vienna IWGFPT/34 (1990).

[17] Summary of Workshop Meeting on Zircaloy Corrosion and Hydriding, HWR-367, Halden, Norway (1993).

[18] M. LIMBÄCK, Comparison of Models for Zircaloy Cladding Corrosion in PWRs, Report HWR-468, Holden, Norway (1996).

[19] INTERNATIONAL ATOMIC ENERGY AGENCY, Waterside Corrosion of Zirconium Alloys in Nuclear Power Plants, IAEA-TECDOC-996, January 1998.

[20] T. KIDO, K. KANASUGI, M. SUGANO, K. KOMATSU, J. Nucl Mater. **248**, 281 (1997).

[21] M. BLAT, D. NOEL, “Detrimental role hydrogen on the corrosion rate of Zirconium alloys”, Zirconium in the Nuclear Industry (Proc. Eleventh International Symposium Garmisch-Partenkirchen, Germany, Sept 1995), ASTM STP 1295, E.R. Bradley and G. P. Sabol, (Eds.), ASTM (1996) 319.
[22] M. BLAT, J. BOURGOIN, “Corrosion behaviour of Zircaloy 4 cladding material: Evaluation of the hydriding effect”, Light Water Reactor Fuel Performance (Proc Int. Topical Mtg Portland, Oregon, 1997), ANS (1997) 250.
[23] Y.S. KIM, J.S. NOH, S.C. KWON, I.C. KUK, J. Nucl Mater. **223**, 163 (1995).
[24] F. LEFEBVRE, C. LEMAIGNAN, J. Nucl Mater. **248**, 268 (1997).
[25] J.H. HAN and K.S. RHEEM, J. Nucl Mater. **217**, 197 (1994).
[26] B. Hutchinson and B. Lehtinen, J. Nucl Mater. **217**, 243 (1994).
[27] B. CHENG, P.M. GILMORE, .H. KLEPFER, “PWR Zircaloy fuel cladding corrosion performance, mechanisms, and modelling”, Zirconium in the Nuclear Industry (Proc. Eleventh International Symposium Garmisch-Partenkirchen, Germany, Sept 1995), ASTM STP 1295, E.R. Bradley and G. P. Sabol, (Eds.), ASTM (1996) 137.
[28] R.A. WEINER, W.J. LEECH, G.P. SABOL, M. QUECEDO GUTIERREZ, “The effects of coolant chemistry control and fuel management strategies on fuel cladding corrosion” TopFuel ’97 (Proc. Int. Conf. Manchester, UK, 1997),BNES (1997) 5.41.
[29] M. QUECEDO, J.J. SERNA, R.A. WEINER, P.J. KERSTING, Proceedings, Enlarged HPG Meeting, HPR-351, 1999.

A MODEL FOR HYDROGEN PICKUP FOR BWR CLADDING MATERIALS

G. HEDE, U. KAISER
Westinghouse Atom AB,
Västerås, Sweden

Abstract

It has been observed that rod elongation is driven by the hydrogen pickup but not by corrosion as such. Based on this a non-destructive method to determine clad hydrogen concentration has been developed. The method is based on the observation that there are three different mechanisms behind the rod growth; the effect of neutron irradiation on the Zircaloy microstructure, the volume increase of the cladding as an effect of hydride precipitation and axial pellet-cladding-mechanical-interaction (PCMI). The derived correlation is based on the experience of older cladding materials, inspected at hot-cell laboratories, that obtained high hydrogen levels (above 500 ppm) at lower burnup (assembly burnup below 50 MWd/kgU). Now this experience can be applied, by interpolation, on more modern cladding materials with a burnup beyond 50 MWd/kgU by analysis of the rod growth database of the respective cladding materials. Hence, the method enables an interpolation rather than an extrapolation of present day hydrogen pickup database, which improves the reliability and accuracy. Further, one can get a good estimate of the hydrogen pickup during an ongoing outage based on a non-destructive method. Finally, rod growth measurements are normally performed for a large population of rods, hence giving a good statistics compared to examination of a few rods at a hot cell.

1 INTRODUCTION

Several plants are at present aiming at significantly higher burnup than the present day end-of-life burnup. The development of new cladding materials is one key issue in this strive since one possible burnup limiting factor is the cladding hydrogen pickup. This means that fuel needs to be examined, before reaching its projected end-of-life burnup, in order to verify its good hydrogen pickup performance. Earlier, several modelling attempts have been made at correlating the hydrogen pickup to the clad corrosion via the "hydrogen pickup fraction". However, these attempts have not fully succeeded for BWR cladding materials and it is rather costly to perform large series of cladding corrosion measurements. Further, the pickup fraction (and its possible burnup dependence) still needs to be verified for each new cladding material and coolant chemistry. Hence, a non-destructive method for determination of the clad hydrogen content is desired.

2 BACKGROUND OBSERVATIONS

The Westinghouse Atom databases regarding cladding corrosion and fuel rod growth are very similar, indicating that one of these two phenomena affects the other. This similarity is best described by the data obtained from the reactor at which the largest fuel rod growth values have been obtained. In Figure 1 all the cladding corrosion data, for the earlier LK2 cladding material, from one Swedish BWR are depicted while the corresponding fuel rod growth data are depicted in Figure 2.

When plotting the fuel rod growth as a function of the average oxide thickness for rods with both properties measured, a clear correlation emerges, see Figure 3. Here only data obtained for fuel operated for five cycles are included. The mechanism that emerges is that with corrosion follows hydrogen pickup, which in turn gives a volume increase of the cladding tube. This volume increase is easiest studied via an increased fuel rod growth. This can be seen in extreme

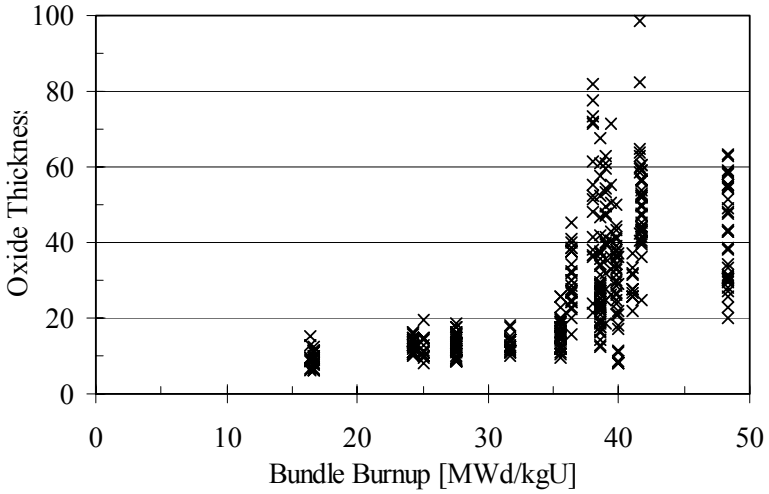

FIG. 1. Cladding corrosion vs. assembly burnup for LK2 in reactor A.

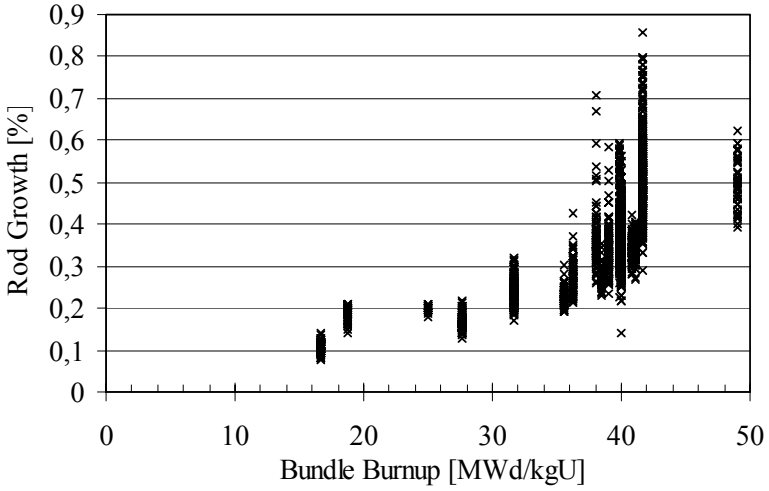

FIG. 2. Fuel rod growth vs. assembly burnup for LK2 in reactor A.

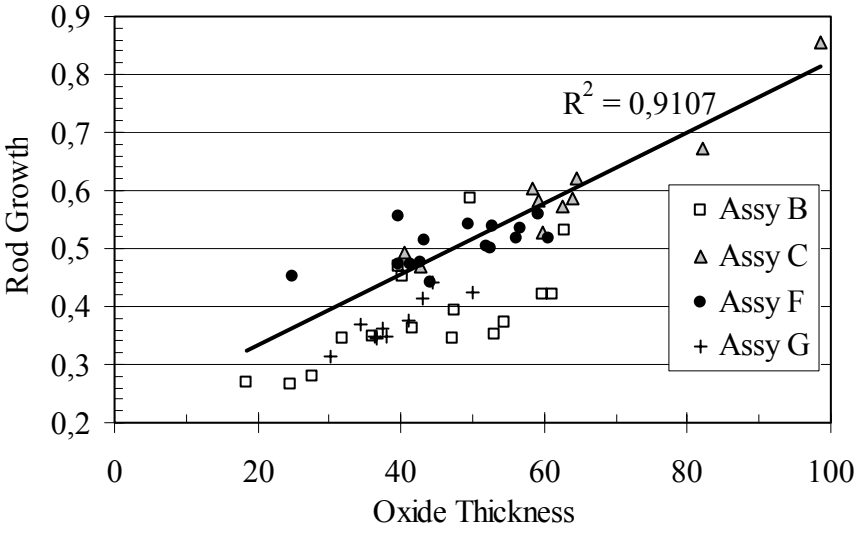

FIG. 3. Fuel rod growth vs. average oxide thickness for fuel irradiated for five cycles in reactor A Linear regression for data from assembly C.

for some failed fuel rods that have picked up hydrogen both from the inner as well as the outer surface and hence have grown significantly more than neighbouring rods.

Here it should be noted that all data presented in the present work are obtained for cladding materials no more used in reload quantities (unless stated as modern) by Westinghouse Atom. Hence, the data do not represent typical present day rod performance. However, since these older cladding materials had poorer resistance against corrosion, it had larger rod growth at "intermediate" burnups (around 40 MWd/kgU) than more modern cladding materials have at significantly higher burnups. This enables an interpolation of the hydrogen pickup experience at the intermediate burnup on rod growth data obtained for significantly higher burnup.

3 ESTIMATED AVERAGE HYDROGEN CONCENTRATION

3.1 General

There are three main causes of the rod growth; the effect of neutron irradiation on the Zircaloy microstructure, the volume increase of the cladding as an effect of hydride precipitation and axial pellet-cladding-mechanical-interaction (PCMI):

$$\varepsilon_g = \varepsilon_i + K_H \times C_H + \varepsilon_{PCMI} \quad (1)$$

where

ε_g	total rod growth, [%]
ε_i	rod growth due to the effect of neutron irradiation on the Zircaloy microstructure, [%]
K_H	constant
C_H	Hydrogen content [ppm]
ε_{PCMI}	rod growth due to the effect of pellet-cladding-mechanical-interaction (PCMI), [%].

Since the clad hydrogen concentration is the parameter of interest, equation (1) is transformed to yield:

$$C_H = (\varepsilon_g - \varepsilon_i - \varepsilon_{PCMI})/ K_H \quad (2)$$

3.2 Rod growth due to the effect of neutron irradiation on Zircaloy microstructure

The precise growth mechanism due to the effect of neutron irradiation on Zircaloy microstructure is not exactly known, but a clear correlation of growth to microstructure evolution exists, e.g. see Ref. [1]. At a low fluence, less than 2×10^{25} n/m^2, growth rate is high but retard with increasing fluence and saturates at a constant growth rate. For fully recrystallized material, the growth rate reaches a second transition where upon it increases and becomes nearly linear with the fluence above about 6×10^{25} n/m^2. A correlation for irradiation induced rod growth is depicted as a function of assembly burnup in Figure 4 together with the rod growth database obtained for LK2 in reactor A (maximum rod growth) and for the modern LK3 cladding in reactor B, where LK3 has reached its highest burnup.

Notice that the effect of a possible second threshold in irradiation growth, resulting in an increase in growth rate is not taken into account here. However, for the present study, the second transition can be disregarded since it will result in a conservative approximation of the clad hydrogen content.

3.3 Pellet-cladding mechanical interaction (PCMI)

When the pellet-cladding gap closes and there is contact between the pellet and the cladding further fuel pellet swelling may force the fuel rod to grow in the axial direction. The closure of the pellet-cladding gap occurs late in life and the PCMI related growth should be small. If the axial PCMI needs to be studied it can be calculated by any fuel rod behaviour code. Since the present study includes an approximation of the rod growth at a higher burnup than what is yet registered for this type of fuel it is possible that PCMI will influence the rod growth at the considered burnup. However, due to the uncertainty of the influence of PCMI on rod growth this influence is disregarded in the present analysis.

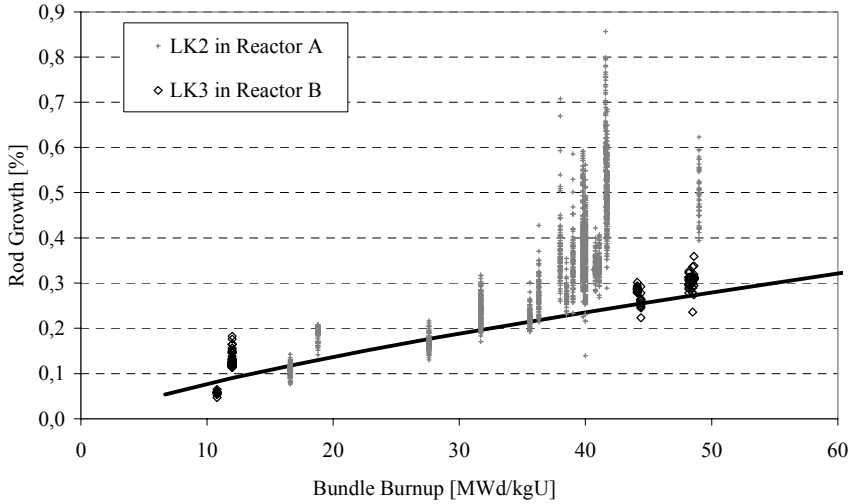

FIG. 4. Rod growth due to the effect of neutron irradiation on the Zircaloy microstructure compared with measured rod growth data.

3.4 Rod growth due to hydriding – theoretical treatment

When performing cladding hydrogen concentration measurements at hot cell by SEM, one translates the measured area fraction of the Zirconium-hydrides (ZrH) into a hydrogen concentration by the formula

$$C_H = C_{ZrH} \frac{\rho_{ZrH} F}{\rho_{Zry} - (\rho_{Zry} - \rho_{ZrH}) F} \qquad (3)$$

where

C_H clad hydrogen concentration
C_{ZrH} hydrogen concentration in the Zirconium-hydrides = 17570 ppm
F area fraction of ZrH in a cross section of the studied clad specimen
ρ_{Zry} density of Zircaloy = 6.54 g/cm^3
ρ_{ZrH} density of ZrH = 5.65 g/cm^3

Under the assumption that the volume increase is isotropic (which probably is not exactly true) we have that the rod growth [%] due to the hydrogen uptake can be estimated as:

$$\varepsilon_H = F\left(1-\frac{\rho_{ZrH}}{\rho_{Zry}}\right)\Big/2 \qquad (4)$$

where $1-\frac{\rho_{ZrH}}{\rho_{Zry}}$ represents the area fraction of the Zirconium-hydrides that are taken up by the hydrogen. By combining equations (3) and (4) we get that $\varepsilon_H \approx 4.5\times10^{-4}\times C_H$, i.e. the constant K_H in equation (1) equals 4.5×10^{-5} (%/ppm H).

3.5 Rod growth due to hydriding – experimental results

Since the cladding is not isotropic, the above correlation of the hydrogen content and increased rod growth can only be viewed as a rather rough estimate. Measurements of clad hydrogen contents have been performed at the Paul Scherrer Institute (PSI) and in Studsvik. There are slight differences between the measuring methods used at Studsvik and at PSI. At PSI the position of the measurements are decided without earlier scanning of the hydrogen distribution in the cladding, while at Studsvik the measurements are made at the axial location where the maximum hydrogen contents are expected based upon neutron radiography examinations. The PSI measurements will thus be used here since they are considered to be more representative for the average hydrogen content values.

Clad hydrogen concentration data from PSI and Studsvik are depicted in figure 5 as a function of the measured rod growth. The considered growth values include growth caused by irradiation, possible axial PCMI and hydride precipitation. In figure 6 the irradiation-induced growth (as given in Figure 4) is excluded and a correlation for the rod growth resulting from hydride precipitation is given. Here it can be noted that the correlation achieved from the PSI data is rather close (within 15%) of the theoretical formula derived above.

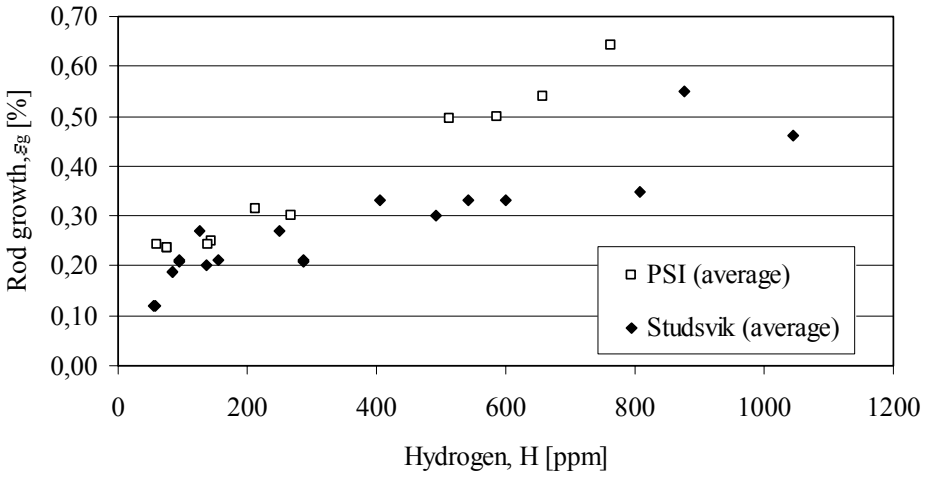

FIG. 5. Total rod growth versus clad hydrogen concentration.

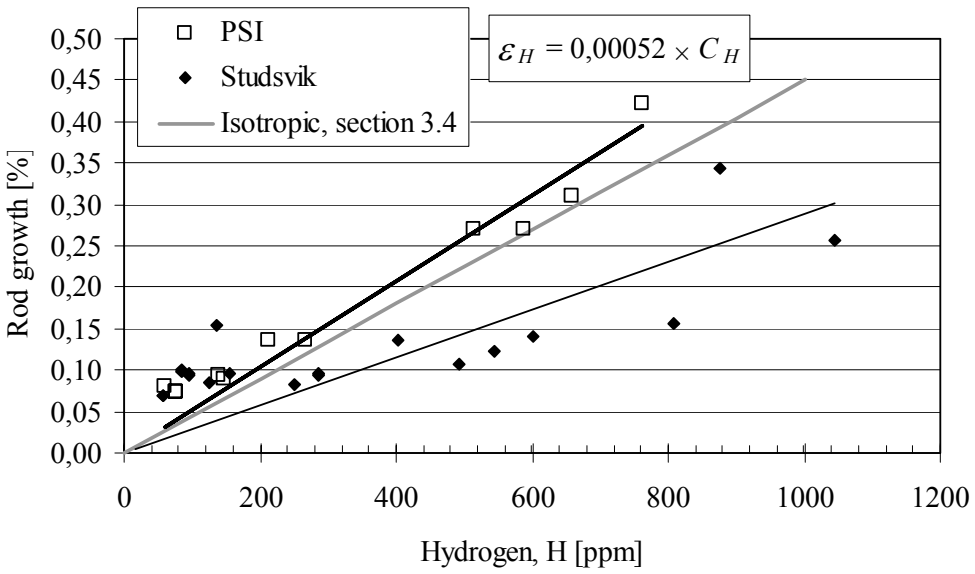

FIG. 6. Rod growth due to the clad hydrogen uptake, the depicted rod growth is the total rod growth minus the irradiation induced rod growth.

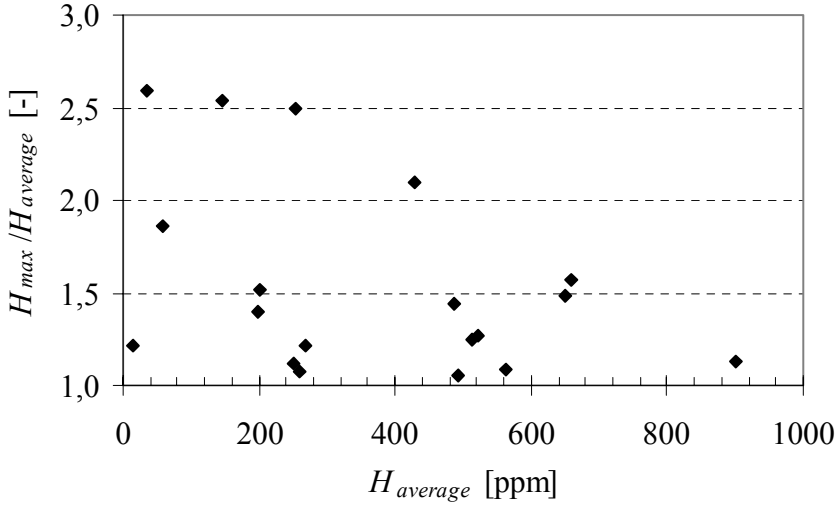

FIG. 7. The $H_{max}/H_{average}$ quotient for LK1, LK2 and LK2-liner cladding at different average hydrogen

4 MAXIMUM VERSUS AVERAGE HYDROGEN CONCENTRATION

The above analysis of the PSI data gives a model for determining the rod average hydrogen content. When verifying the mechanical integrity of fuel rods the maximum local hydrogen concentration is of greater interest. A correlation between the maximum and average cladding hydrogen concentration ($H_{max}/H_{average}$) is received by studying measurements of the cladding hydrogen concentration. According to figure 7, that depicts the quotient $H_{max}/H_{average}$, the maximum ratio is 2.5. Here all representative rods are included for which more than one

hydrogen concentration measurement was performed. The average is here taken as the average of all data bur the maximum value, i.e. if there was only two measurements from a rod the quotient actually equals H_{max}/H_{min}. These large variations of the hydrogen concentration within a rod are caused by

(i) there are axial variations in the oxide thickness due to axial variations in the rod power,
(ii) the hydrogen migrates in the cladding from hotter regions to colder, e.g. to pellet-pellet interfaces.

The quotient $H_{max}/H_{average}$ shows a tendency to decrease with increasing average hydrogen concentration. However, additional measurements are needed to draw a definite conclusion regarding the validity of this observation.

5 VERIFICATION OF MODEL ON MODERN CLADDING MATERIALS

When applying the above model on the rod growth database for the Westinghouse Atom present-day standard cladding LK3, we obtain upper bound models regarding hydrogen uptake in accordance with Figure 8. The models are here compared with all hydrogen uptake data yet documented for LK3. Here only one measurement is performed per rod. As can be seen the average model covers the data, indicating that it is still valid. This model will be further verified as new hydrogen uptake measurements (in hot cell) will be performed. However, the rod growth database (hundreds of data points) gives a firm prediction of the hydrogen content well beyond (in terms of burnup) the database presented in Figure 8. The accuracy of the predictions at extreme burnup will also be improved when further rod growth measurements are performed. Thus, even though there are only three hydrogen uptake measurements for the LK3 cladding, the predictions are still based on hundreds of measurements.

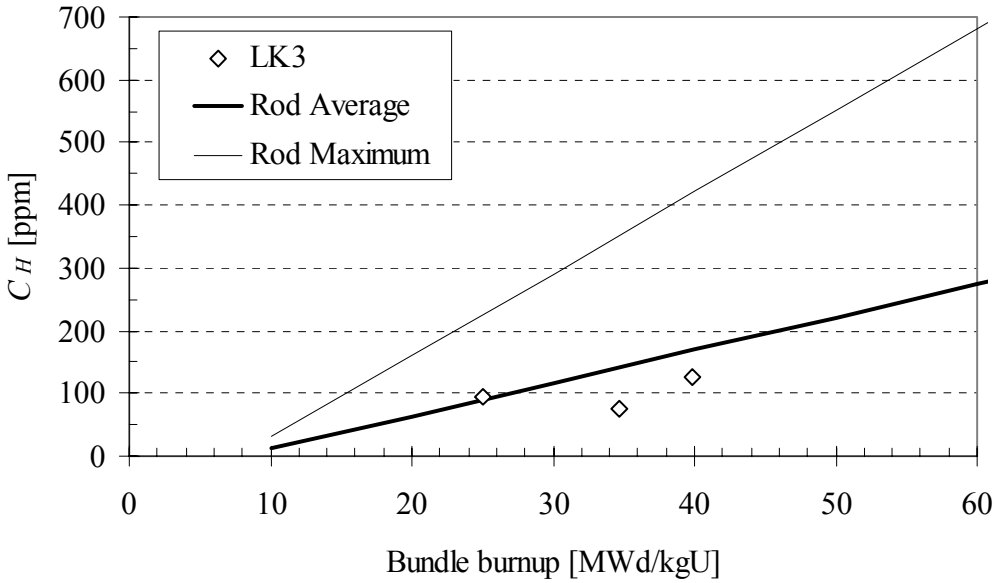

FIG. 8. Calculated hydrogen concentration in LK3 type of cladding depicted along with measured data these cladding types (only one measurement per rod).

6 CONCLUSIONS

A model for non-destructive measurements of the clad hydrogen concentration has been presented. It enables an interpolation of the hydrogen pickup experience at an intermediate burnup (for older, less corrosion resistant materials) on rod growth data obtained for significantly higher burnup (on modern materials). Hence, the methodology adds statistics to the expensive and time consuming hot-cell examinations. Finally, it should be noticed that the above method enables judgement regarding cladding corrosion and hydrogen uptake by visual examination of the differential fuel rod growth within one assembly.

REFERENCES

[1] RONALD B. ADAMSON, “Effects of Neutron Irradiation on Microstructure and Properties of Zircaloy”, Zirconium in the Nuclear Industry; Twelfth International Symposium, ASTM STP 1354, (2000) 15-31.

MOX FUEL MODELLING
(Session 4)

Chairpersons

H. BAIRIOT
Belgium

L.C. BERNARD
France

ISOTOPIC MODELLING USING THE ENIGMA-B FUEL PERFORMANCE CODE

G.D. ROSSITER*, P.M.A. COOK, R. WESTON
MOX Research and Technology,
BNFL, Sellafield, Seascale,
United Kingdom

Abstract

A number of experimental programmes by BNFL and other MOX fabricators have now shown that the in-pile performance of MOX fuel is generally similar to that of conventional UO_2 fuel. Models based on UO_2 fuel experience form a good basis for a description of MOX fuel behaviour. However, an area where the performance of MOX fuel is sufficiently different from that of UO_2 to warrant model changes is in the radial power and burnup profile. The differences in radial power and burnup profile arise from the presence of significant concentrations of plutonium in MOX fuel, at beginning of life, and their subsequent evolution with burnup. Amongst other effects, plutonium has a greater neutron absorption cross-section than uranium. This paper focuses on the development of a new model for the radial power and burnup profile within a UO_2 or MOX fuel rod, in which the underlying fissile isotope concentration distributions are tracked during irradiation. The new model has been incorporated into the ENIGMA-B fuel performance code and has been extended to track the isotopic concentrations of the fission gases, xenon and krypton. The calculated distributions have been validated against results from rod puncture measurements and electron probe micro-analysis (EPMA) linescans, performed during the M501 post irradiation examination (PIE) programme. The predicted gas inventory of the fuel/clad gap is compared with the isotopic composition measured during rod puncture and the measured radial distributions of burnup (from neodymium measurements) and plutonium in the fuel are compared with the calculated distributions. It is shown that there is good agreement between the code predictions and the measurements.

1. INTRODUCTION

BNFL has undertaken a comprehensive programme of work in order to support the development and qualification of its short binderless route (SBR) MOX product [1]. The programme includes characterisation of as-fabricated fuel, test reactor irradiations, post irradiation examination (PIE) of commercially irradiated fuel and fuel modelling.

Modelling work is primarily carried out using the ENIGMA-B fuel rod performance code. The ENIGMA code was initially developed by BNFL and British Energy, to perform fuel safety analyses in support of the Sizewell-B PWR. Since 1991, BNFL has independently developed the ENIGMA-B version of the code as a versatile tool, to model the in-pile behaviour of UO_2, UO_2-Gd, UO_2-Nb and MOX fuels. This version of the code has been used to support fuel licensing in Finland, Switzerland and the UK. Current model developments are mainly focused on MOX fuel [2].

Experimental programmes performed by MOX fuel fabricators, including BNFL, have shown that, in general, the in-pile behaviour of MOX fuel is similar to that of conventional UO_2 fuel [3,4,5,6,7]. These programmes have also shown that fuel performance models based on UO_2 experience provide a sound basis for predicting the irradiation behaviour of MOX.

* Currently address: OECD Halden Reactor Project, PO Box 173, N-1751 Halden, Norway.

However, there are at least four areas where the performance of MOX fuel is sufficiently different from that of UO_2 to warrant model changes. These are:

- radial power and burnup profile
- fission product and helium generation
- thermal conductivity
- fuel creep.

This paper concentrates on modelling the radial power and burnup profile in MOX fuel, which is one area where UO_2 models must be modified to accurately describe the performance of MOX fuel. ENIGMA-B models the radial power and burnup profile using the RADAR (Rating Depression Analysis Routine) model [8]. RADAR has been modified to track the creation and depletion of plutonium and other actinide isotopes during irradiation. An underlying assumption has been made that the plutonium distribution in the fuel has a high degree of homogeneity. The model has been further extended to predict the isotopic composition of the fission gases, xenon and krypton.

The predictions of the new RADAR model are compared with EPMA (electron probe micro-analysis) linescans for the elements, neodymium and plutonium, taken as part of the M501 PIE programme [3, 4]. The predictions of the fuel/clad gap gas inventory are also compared with results from rod puncture tests [3, 4].

2. BACKGROUND TO RADAR MODEL CHANGES

As a result of fission and neutron absorption, the isotopic content of the fuel constantly changes during irradiation. The fission cross section is different for each of the primary fissile isotopes in thermal reactors, ^{235}U, ^{239}Pu and ^{241}Pu, in particular for the resonances in the epi-thermal energy range. The neutron absorption cross-section, the flux and the isotopic concentration determine the extent to which absorption occurs. All the minor actinide nuclei, such as curium, are generated in this way. The presence of fertile species in the fuel, such as ^{238}U and ^{240}Pu, allows the creation of new fissile nuclei to partially replace those consumed during earlier fission events. It is therefore necessary to track the isotopic content of fissile and fertile species within the fuel, to be able to accurately predict the local fission rate within the fuel.

From the number of fissions in the fissile isotopes, the known isotopic yields can then be used to determine the concentration of fission products in the fuel. The yields for the lower mass fission products, such as krypton, are significantly different in uranium and plutonium fissions, so calculating the inventory of certain key fission products provides useful additional fuel performance information. It also means that the amount of experimental data that can be used to validate models of the radial power, burnup and fissile isotope distributions used in fuel performance codes is increased.

3. ENIGMA-B MODELLING

3.1. Earlier RADAR models

Many fuel performance phenomena, including fission gas release and densification, are strongly temperature dependent. An accurate prediction of the intra-pellet radial power distribution and its evolution with burnup, together with the fuel thermal conductivity, is therefore essential in any good fuel performance code. The fuel thermal conductivity modelling in ENIGMA-B is described in [9, 10] and shows good agreement with experiment.

The RADAR model is implemented to calculate the intra-pellet radial power distribution for both UO_2 and MOX fuel. The fuel pellet is divided into a number of radial annuli for the calculations.

In earlier versions of the model simplified calculations of the depletion of the ^{235}U, ^{239}Pu and ^{241}Pu isotopes were performed, using one-group fission and neutron capture cross-sections tuned to match predictions from the WIMS-E neutronics code [11] for a typical PWR reactor environment. The thermal neutron fluxes, in each of the annuli, used in evaluating the depletions were calculated by solving an idealised form of the neutron diffusion equation, based on an approximate inverse diffusion length in each annulus. The start-of-life ^{239}Pu and ^{241}Pu contents were combined into an "effective plutonium content," loosely intended to represent the fissile plutonium content, which was depleted as ^{239}Pu. Plutonium is generated by the capture of both thermal and epithermal neutrons. Both of these mechanisms were modelled. The total amount of ^{239}Pu generated by resonant capture in ^{238}U was calculated from nuclear physics parameters and the radial distribution of the captured material was

$$f(r) = C\left(1 + 3\exp\left(-9.7\sqrt{r_0 - r}\right)\right) \tag{3.1}$$

defined by an empirical function $f(r)$ of the form [8], where r_O is the pellet outer radius and C is a constant, whose value is determined from normalisation considerations.

The radial power distributions determined in this way were satisfactory for MOX fuel at low burnups and with low plutonium contents. However, recent studies have shown some deficiency at higher burnups and/or high plutonium contents, in particular in the soft spectrum of the Halden Boiling Water Reactor (HBWR). Hence, an improved version of the RADAR model has been developed.

3.2. Current RADAR model

The improved RADAR model is significantly more sophisticated than the earlier versions. The key modifications are as follows:

(a) the heavy metal isotope tracking has been expanded to include a more extensive number of actinides. A simplified schematic is illustrated in Figure 1,
(b) thermal and resonant neutron capture in both ^{238}U and ^{240}Pu and fast fission in ^{238}U are modelled explicitly. The radial distributions of the material undergoing resonant capture are described by Equation (3.1), for both ^{238}U and ^{240}Pu, following the approach in [12],
(c) reactor type and ^{235}U or plutonium enrichment dependent fission and neutron capture cross-sections are modelled for each of the heavy metal isotopes,
(d) the use of reactor type and ^{235}U or plutonium enrichment dependent transport cross-sections for the heavy metal isotopes and for oxygen in the calculation of inverse diffusion lengths,
(e) the cross-sections modelled are obtained from correlations fitted to predictions from the CASMO-4 [13,14] nuclear physics code, using the 70 group ENDF-B nuclear data library.

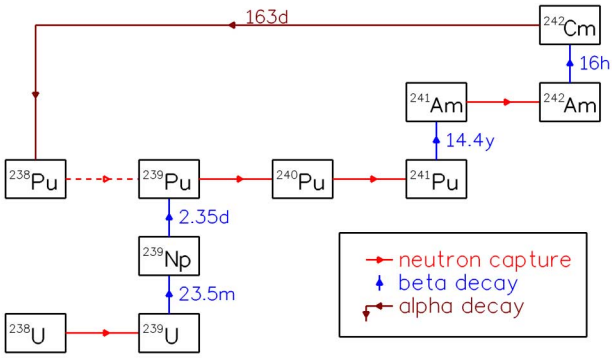

FIG. 1. Simplified schematic of heavy metal isotope modelling.

The reactor types, which can be modelled, include commercial PWRs and BWRs and the Halden reactor. The modelling of the americium and ^{242}Cm isotopes allows accurate calculations of helium generation due to α-decay to be performed, which has been described previously [2]. The calculations performed by RADAR are necessarily highly simplified when compared to those performed by neutronics codes. The applicability of the modelling was therefore assessed by comparing the isotopic number density and radial power profile predictions of the improved RADAR model with those of CASMO. Excellent agreement was observed. The results for MOX fuel of 5 wt% plutonium in a typical PWR environment and with a standard plutonium vector are illustrated in Figure 2.

3.3. Fission gas generation model

A new fission gas generation model has been integrated with the existing fission gas release model, to complement the improved RADAR model. The generation model calculates the through-life radial distributions of each of the krypton and xenon isotopes ^{83}Kr to ^{86}Kr and ^{131}Xe to ^{136}Xe, plus the important precursors ^{131}I and ^{132}Te, in each of the fuel annuli. Generation, neutron capture and decay are computed based on the power history, the distribution of fission events of each of the fissile species (as calculated by RADAR) and the fission gas isotopic distributions. The new model allows a more accurate calculation of the net fission gas generation rate, which takes account of the different krypton and xenon isotopic yields of the various fissile isotopes. In addition, the new generation model allows the isotopic composition of the fission gas in the fuel-clad gap to be evaluated, as the decay and neutron capture in the gap is also modelled.

4. VALIDATION

All the validation data shown in this paper has been taken from the M501 PIE programme. M501 was one of the first four assemblies of SBR MOX fuel to be fabricated in MDF[1] for a commercial reactor. The assemblies were irradiated for three cycles in NOK's Beznau-1 PWR to an average burnup of 33 GWd/tHM. After discharge, seven rods were withdrawn and sent for PIE at ITU (Trans-Uranium Institute, Karlsruhe). Results from this programme have already been published in the open literature [3,4]. Experimental data from the four high enrichment rods are used in this paper.

[1] MDF, MOX Demonstration Facility, Sellafield, UK.

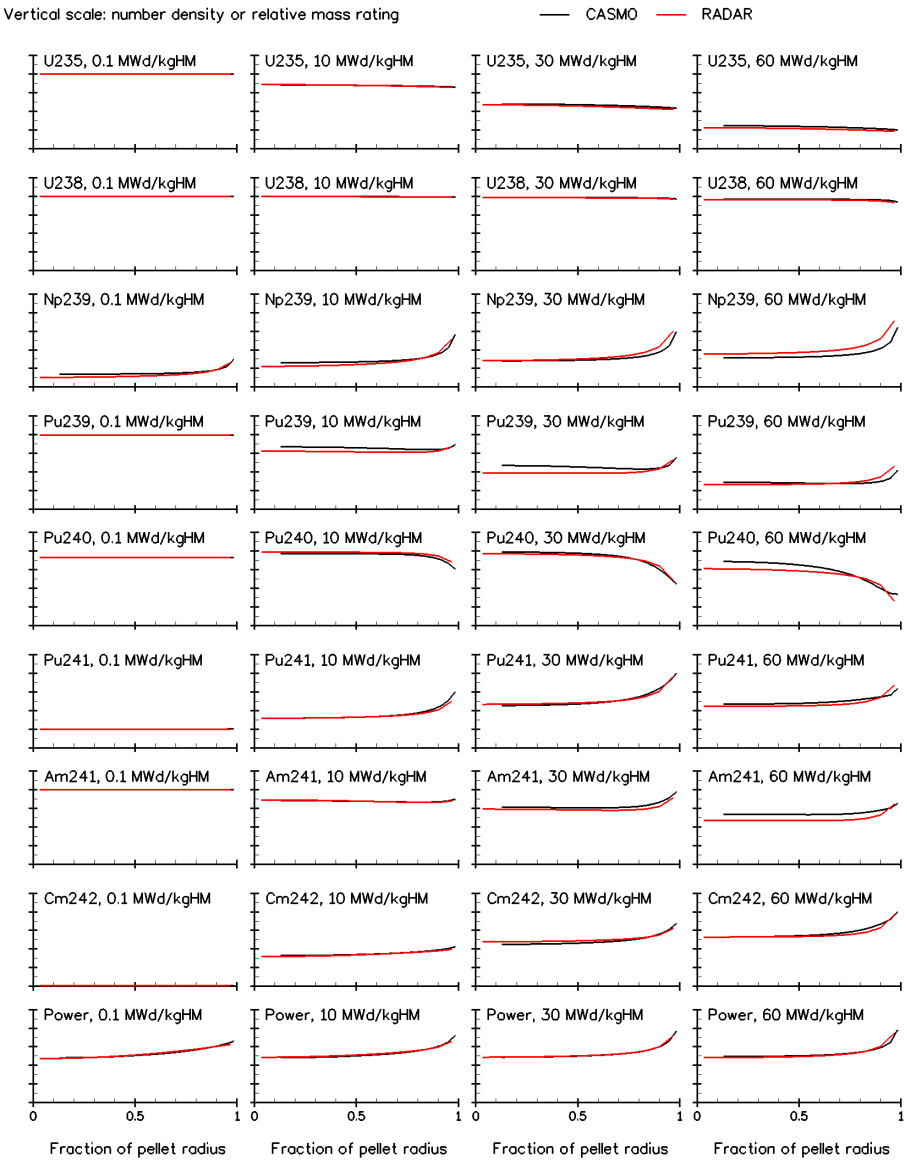

FIG. 2. RADAR and CASMO predictions for typical PWR MOX fuel.

Table 1 shows the initial plutonium content of the rods and the average burnup calculated by the physics codes CASMO-4/Simulate-3 [11]. Figure 3 shows the rod power histories and Figure 4 shows the arrangement of rods in the assembly.

Table I. HIGH ENRICHMENT M501 RODS

Rod	4	5	6	7
Pu_{total} Enrichment (Pu/U + Pu)	5.54	5.54	5.54	5.54
Rod Burnup (Gd/tHM)	33.9	33.7	32.7	35.6

Two different types of data have been used for validation of the new RADAR model. Results from mass spectrometer measurements of the fission gas inventory following rod puncture are compared with ENIGMA-B's prediction for the isotopic content of the fuel/clad gap at the end of life. The predictions for radial plutonium and burnup profiles are compared with results from EPMA linescans.

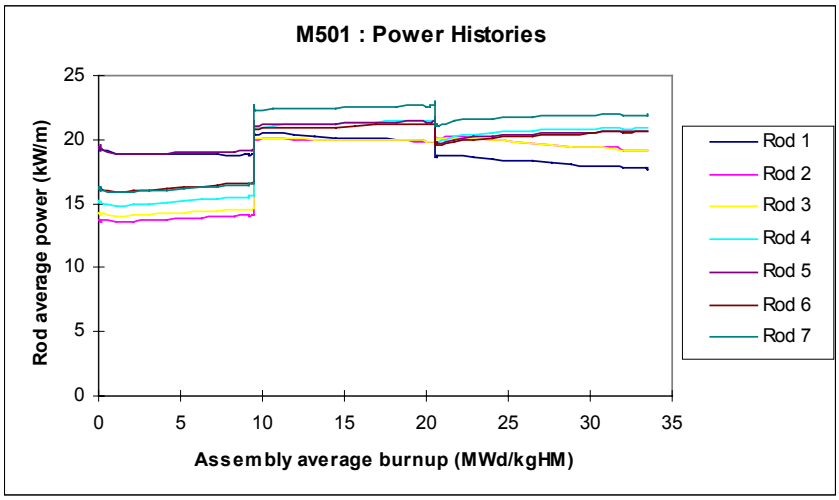

FIG. 3. M501 power histories for all PIE rods.

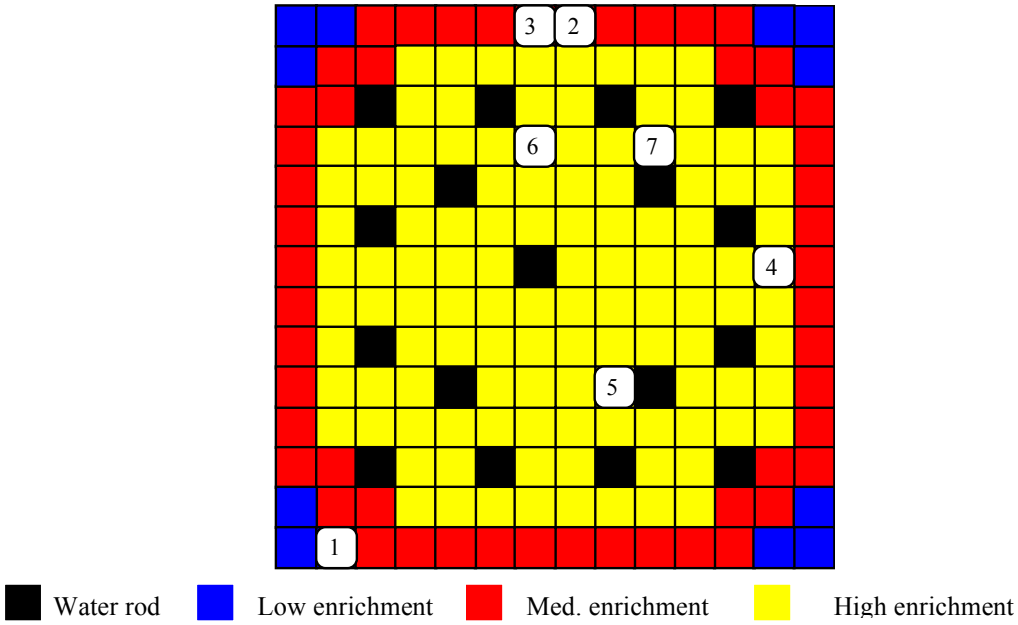

FIG. 4. Assembly M501, showing positions of the PIE rods.

4.1. Isotopic fission gas inventory

The isotopic composition of the fission gases was measured for all of the M501 rods. Figure 5 shows the comparison of the code's predictions of the isotopic content of the gas in the fuel-clad gap with the PIE measurements, for the four high enrichment rods.

Figure 5 shows good agreement between the modelled and experimental results. The gas volume is least well predicted for ^{131}Xe. The over-prediction is due to an under-prediction of the amount of the isotope undergoing neutron capture to ^{132}Xe. The results for rods 4, 5 and 6

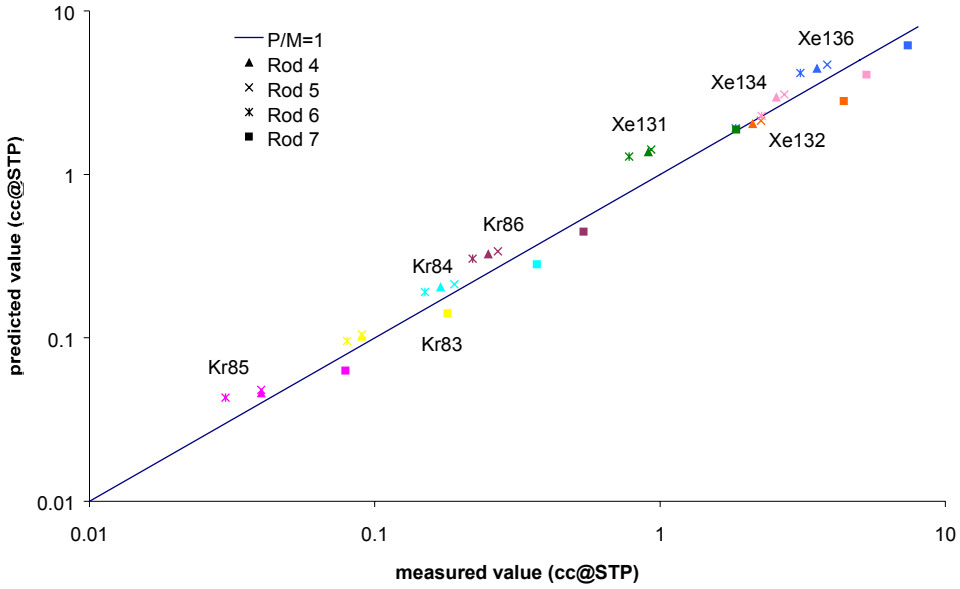

FIG. 5. Predicted versus measured volumes for fission gas isotopes.

lie very close to the P/M = 1 line. There is a slight under-prediction in general for rod 7, which has the highest burnup and for which the centre temperature in a section of the rod just exceeded the Vitanza threshold for fission gas release [15] at the end of its third cycle of irradiation [4].

4.2. EPMA radial linescans

EPMA radial linescans for plutonium and neodymium were performed on two samples from a M501 high enrichment rod. Table 2 lists the samples examined by EPMA and their locations relative to the bottom end cap. For each sample, measurements were performed at 45 points across the fuel radius. The measurements correspond to the amounts of plutonium and neodymium in the fuel matrix.

Table II. EPMA SAMPLES

Sample	Rod	Initial Pu / U+Pu (%)	Rod Burnup (GWd/tHM)	Location (cm)
A	7	5.54	35.6	60
B	7	5.54	35.6	259

4.2.1. Radial burnup profile

The local burnup is determined by measurements of the neodymium concentration [16]. The total amount of neodymium present in the sample is increased by decay of ^{144}Ce and therefore the cooling period between discharge and measurement is taken into account. The fission yield used to derive the burnups below has been calculated using the FISPIN fission product inventory code [17] and has taken neutron absorption and radioactive decay into account. Figures 6 and 7 compare the local burnup profile calculated by ENIGMA-B with the burnup profile inferred from EPMA neodymium measurements. The pellet was divided into 70 radial annuli for the ENIGMA-B calculation.

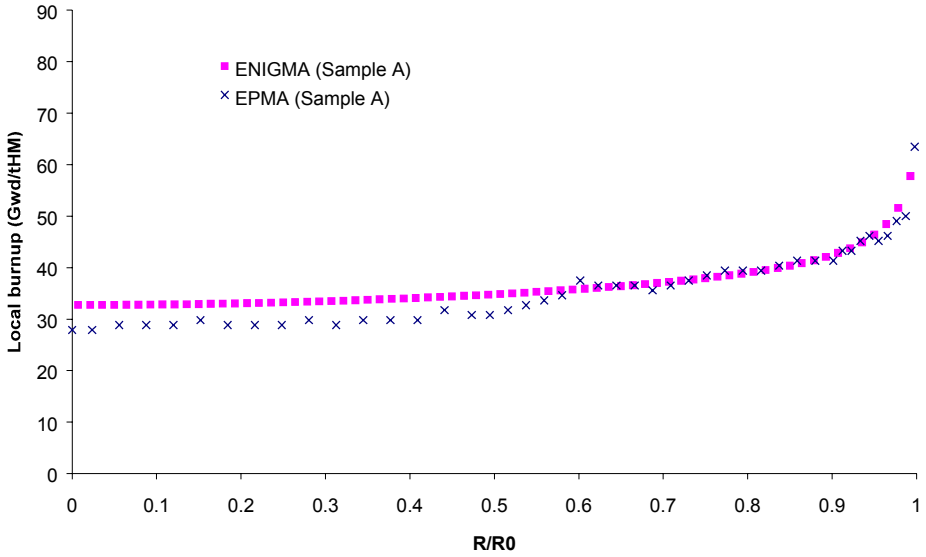

FIG. 6. Local burnup profile for sample A.

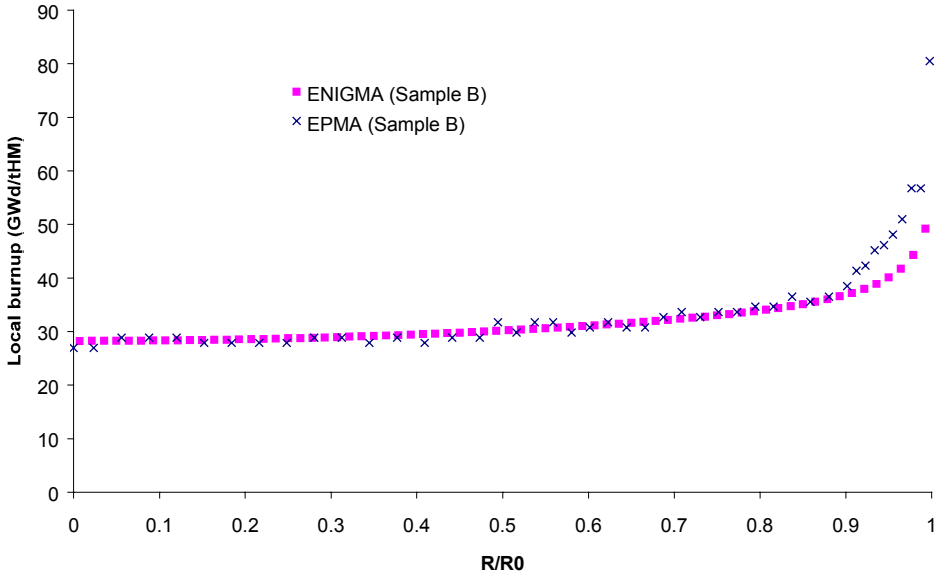

FIG. 7. Local burnup profile for sample B.

In general, there is good agreement between the calculated and experimental data for both samples.

4.2.2. Radial plutonium profile

Figures 8 and 9 compare the prediction of the radial plutonium profile with the EPMA measurements of the plutonium distribution at end of life. The total initial plutonium content is also plotted.

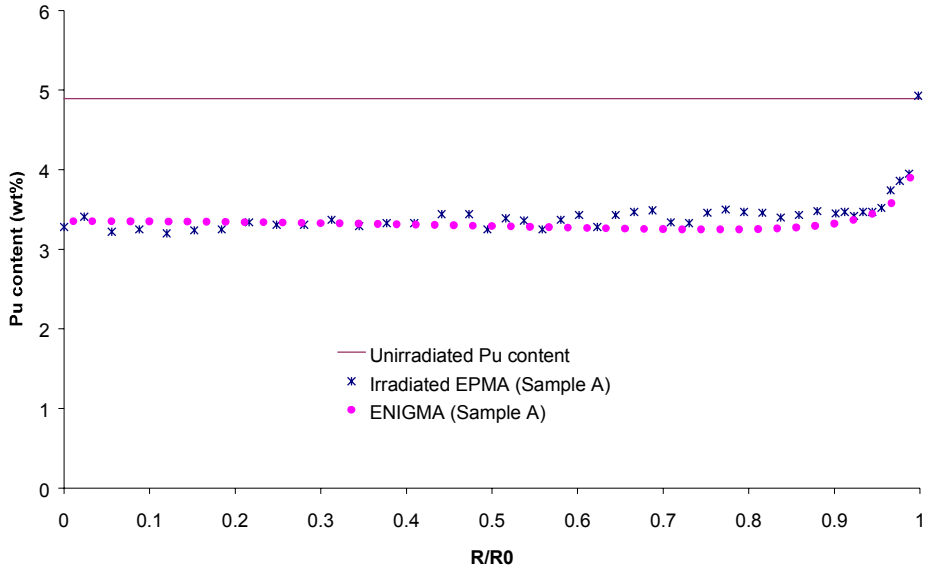

FIG. 8. Radial plutonium distribution for sample A.

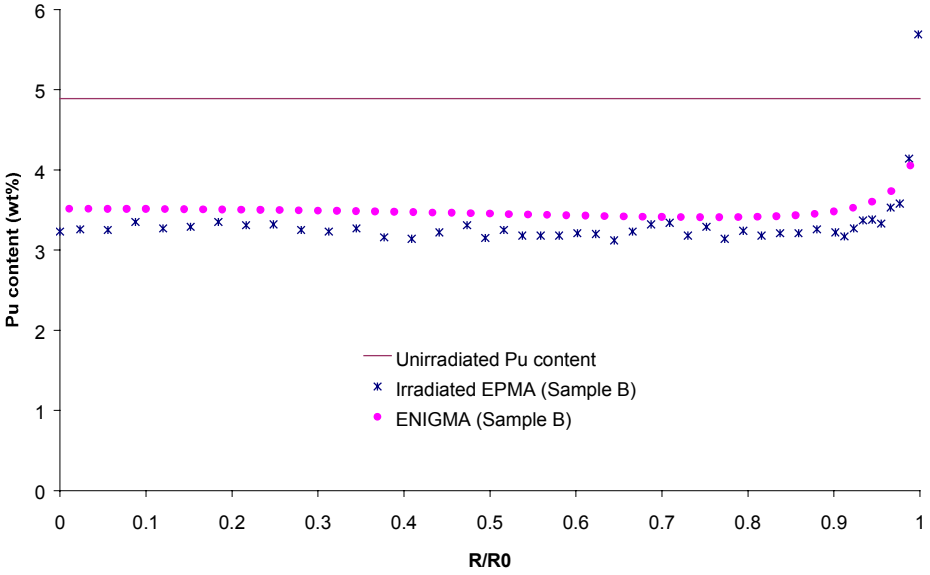

FIG. 9. Radial plutonium distribution for sample B.

In general, there is good agreement between the modelled and experimental data for both samples, though there is a slight over-prediction of the plutonium content for Sample B (Fig. 9). It should be noted that the decay and capture of ^{238}Pu and ^{242}Pu are not tracked in the new RADAR model. Thus the predicted plutonium content, which is plotted, is ^{239}Pu + ^{240}Pu +^{241}Pu. However, the initial percentages of ^{238}Pu and ^{242}Pu are 0.013 wt% and 0.065 wt% respectively, so the above is a good approximation to the total plutonium content.

The predicted radial plutonium distributions, for the isotopes ^{239}Pu, ^{240}Pu and ^{241}Pu, are illustrated in Fig. 10. They show the expected form of the radial distribution of each of these plutonium isotopes. There is an increase in the concentration of ^{239}Pu and ^{241}Pu, and a decrease in the concentration of ^{240}Pu, at the edge of the pellet, due to resonant capture in ^{238}U and ^{240}Pu.

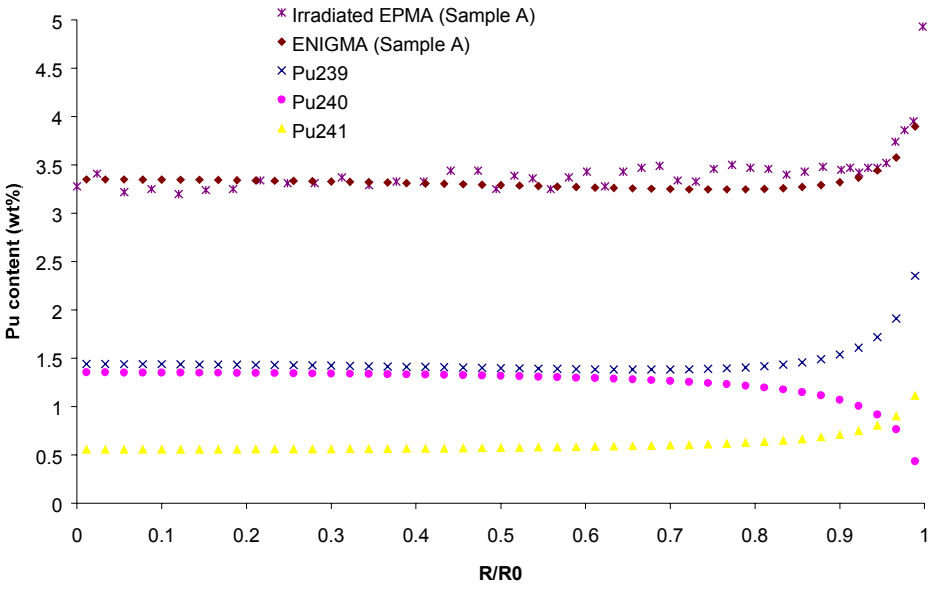

FIG. 10. Radial distribution of plutonium isotopes for sample A.

In Figures 6, 7, 8 and 9, it can be seen that there is some discrepancy between the measured and predicted radial distribution of burnup and plutonium at the pellet rim. This is due to the use of Equation (3.1) in the model to determine the radial distributions of both ^{238}U and ^{240}Pu undergoing resonant capture. Previous work [18] has indicated that this equation is not fully optimised against available EPMA data. This appears to be confirmed by the comparisons of measurements and predictions described in this paper. Hence, further development of the RADAR model is anticipated in the area of pellet rim modelling, using EPMA and SIMS data, when available, to obtain an optimised function.

5. CONCLUSIONS

This paper presented a new version of the RADAR model for predicting the radial power and burnup profile during irradiation, based on the tracking of the underlying fissile isotope distributions and their evolution with burnup. The new model has been incorporated into the ENIGMA-B fuel performance code, together with calculations of the fission gas generation isotopics.

The ENIGMA-B code predictions were compared with experimental data from the M501 programme. In general, the measurements and predictions of the radial profiles of burnup and plutonium distribution were in good agreement. The model also predicted well the xenon and krypton isotopic content of the fission gases in the fuel-clad gap.

The new RADAR model employs the same function, as earlier versions of RADAR, for radially distributing the ^{238}U (and ^{240}Pu) undergoing resonant capture. Thus, little improvement was expected in the modelling of the rim region of the fuel. It is predicted that there will be future development of the RADAR model, using experimental data, to optimise the function used by RADAR, and so improve ENIGMA-B's performance in the rim region.

REFERENCES

[1] BROWN C, COOK P, EDWARDS J, FISHER S, GATES G, PALMER I & WHITE R, "Performance of BNFL MOX Fuel for the Next Decade," TopFuel99, Avignon, September 1999.

[2] PALMER I, ROSSITER G, & WHITE R, "Development and Validation of the ENIGMA Code for MOX Fuel Performance Modelling," IAEA MOX Fuels Symposium, Vienna, May 1999 IAEA-SM-358/20.

[3] COOK P, PALMER I, STRATTON R & WALKER C, "PIE of BNFL's First Commercially Irradiated SBR MOX Fuel," IAEA MOX Fuels Symposium, Vienna, May 1999 IAEA-SM-358/16.

[4] COOK P, STRATTON R & WALKER C, "PIE of BNFL MOX Fuel," ANS International Topical Meeting on LWR Fuel Performance, 9-13th April 2000, Park City Utah USA.

[5] BLANPAIN P, THIBAULT X & TROTABAS M, "MOX Fuel Experience in French Power Plants," International Topical Meeting on LWR Fuel Performance, West Palm Beach USA, April 1994.

[6] GOLL W, FUCHS H, MANZEL R & SCHLEMMER F, "Irradiation Behaviour of UO_2/PuO_2 Fuel in Light Water Reactors," 1993, Nuclear Technology 102 pp.29.

[7] LIPPENS M, MALDAGUE T, BASSELIER J, BOULANGER D & MERTENS L, "Highlights on R&D Work Related to the Achievement of High Burnup with MOX Fuel in Commercial Reactors," IAEA MOX Fuels Symposium, Vienna, May 1999 IAEA-SM-358/15.

[8] PALMER I, HESKETH K & JACKSON P, "A Model for Predicting the Radial Power Profile in a Fuel Pin," IAEA Fuel Modelling Meeting, Preston, March 1982.

[9] GATES G, COOK P, DEKLERK P, MORRIS P & PALMER I, "Thermal Performance Modelling with the ENIGMA Code," OECD/IAEA Meeting in Cadarache, March 1998.

[10] ROSSITER G, "Modelling of MOX Fuel Performance Using the ENIGMA Code," from "Minutes of the Workshop on Fabrication, Performance and Modelling of MOX Fuel, Halden 28-29 September 1999," HWR-623, November 1999.

[11] ASKEW J R & ROTH M J, "WIMS-E: A Scheme for Neutronics Calculations," AEEW-R1315, January 1982.

[12] O'CARROLL C, VAN DE LAAR J, WALKER C T, OTT C & RESTANI R, "Validation of the TUBRNP Model With The Radial Distribution of Plutonium in MOX Fuel Measured by SIMS and EPMA," IAEA Technical Committee Meeting on Water Reactor Fuel Element Modelling at High Burnup and Experimental Support, Windermere, England, 19-23 September 1994.

[13] KNOTT D & EDENIUS M, "The Two-Dimensional Transport Solution Within CASMO-4," Trans. Am. Nucl. Soc., Vol. 68, pp. 457, June 1993.

[14] EDENIUS M, KNOTT D & SMITH K, "CASMO-SIMULATE on MOX Fuel," International Conference on the Physics of Nuclear Science and Technology, Long Island, October 1998.

[15] VITANZA C, KOLSTAD E & GRAZIANI V, ANS Topical Meeting on LWR Fuel Performance, Portland, Oregon, USA, May 1979.

[16] WALKER C, GOLL W & MATSUMURA T, “Effect of Inhomogeneity on the Level of Fission Gas and Caesium Release from OCOM MOX Fuel During Irradiation,” Journal of Nuclear Materials 228 (1996), pp. 8-17.

[17] BURSTALL R F, “FISPIN - A computer code for nuclide inventory calculations,” ND-R-328(R), (October 1979).

[18] LASSMANN K, O’CARROLL C, VAN DE LAAR J & WALKER C T, “Radial Distribution of Pu in High Burnup UO_2 Fuels,” Journal of Nuclear Materials 208 (1994) 223-231.

QUANTIFICATION OF THE HOMOGENEITY OF BNFL SBR MOX FUEL USING COMPOSITIONAL X RAY MAPPING

P.K. IVISON[1], P.M.A. COOK[2], S. BREMIER[3], C.T. WALKER[3]

[1] AEA Technology, Windscale, Seascale, Cumbria, United Kingdom
[2] BNFL, Sellafield, Seascale, Cumbria, United Kingdom
[3] European Commission, Institute for Transuranium Elements, Karlsruhe, Germany

Abstract

The distribution of plutonium on a microstructural scale in mixed oxide (MOX) fuel is an important parameter for both operation and subsequent reprocessing. This paper describes the development and application of X ray microanalysis techniques to produce plutonium concentration 'maps', enabling the quantitative comparison of the plutonium distribution before and after irradiation. The measurements show that SBR MOX is primarily a homogeneous mixture of UO_2 and PuO_2. Quantitative analysis shows that the area fraction and size distribution of plutonium rich regions remains largely unchanged following irradiation. The work demonstrates that the techniques are a useful and efficient way of characterising both unirradiated and irradiated fuel.

1. INTRODUCTION

BNFL commenced fabrication of LWR MOX fuel in the early 1990's using a new fabrication process, the Short Binderless Route (SBR). The SBR Process mechanically blends PuO_2 and UO_2 in an Attritor mill to form a MOX powder with the desired final enrichment. This MOX powder is conditioned in a Spheroidiser then pressed into pellets. The pellets are sintered in a reducing atmosphere, then ground to produce a product ready for loading into standard fuel rods.

A key quality characteristic of MOX fuels is the plutonium homogeneity, the degree to which plutonium, containing fissile isotopes, is evenly dispersed throughout the pellet. Plutonium inhomogeneities within MOX fuel result in local burnup concentrations and have also been linked with enhanced fission gas release [1]. For rods of moderate burnup, the local value within the agglomerates can be as high as 200 MWd/kgHM, leading to accumulations of fission products such as Xe and Cs [1-3].

Many fuel performance phenomena are functions of burnup and modellers are now starting to incorporate the local burnup enhancements in MOX fuel into performance models [4]. To successfully achieve this aim a detailed description of the fuel microstructure and its evolution with irradiation is required.

To fully characterise the plutonium distribution of SBR MOX fuel, BNFL has collaborated with AEA Technology and the Institute for Transuranium Elements. New quantitative analysis methods based on Electron Probe Microanalysis (EPMA) and image analysis have been developed. These methods have been applied to as-fabricated fuel to determine the degree of mixing achieved by the fabrication process [5]. They have also been used to examine the effects of irradiation on the Pu distribution in SBR MOX [2]. This paper collects the work together to provide a comprehensive description of the Pu distribution in SBR MOX fuel.

Samples of irradiated 'M5' SBR MOX fuel have been taken from rods belonging to the M501 PIE programme [2]. M501 was one of the first four assemblies of SBR MOX to be fabricated

in MDF and then irradiated in Beznau-1 for 3 cycles between 1994–1997, to an assembly average burnup of 33 MWd/kgHM. After discharge, 7 rods were extracted and sent for PIE. Detailed X ray mapping has been performed on ceramography samples taken from a rod with an average burnup of 35.6 MWd/kgHM. This fuel was then compared to 'archive' as-fabricated M5 fuel pellets.

2. EXPERIMENTAL PROCEDURES

2.1. Electron probe microanalysis

The methods developed for plutonium mapping were based on conventional EPMA techniques. The feature common to all EPMA measurements is the use of a focused electron beam to generate a characteristic X ray signal from the sample region of interest. This can then be analysed using a variety of detection methods. The energy spectrum of the generated X rays enables the constituents of the analysis region to be determined. The intensity of the signal enables the quantity of those constituents to be measured. The typical spatial resolution of the technique is in the order of one micron. This allows the electron beam to be used to obtain single 'point' analyses on a sample surface, or to be scanned over a larger area to obtain an 'average' analysis for a region.

Quantification techniques for plutonium distribution in fuel were developed using two distinct detection methods: energy dispersive X ray (EDX) analysis and wavelength dispersive X ray (WDX) analysis. Both techniques have particular advantages and are described in more detail in the following sections.

2.2. Energy dispersive X ray analysis

This technique was applied to unirradiated fuel pellets. The relatively wide availability and ease of use of modern EDX systems means that this method could be developed as a semi-routine characterisation method for unirradiated fuel. A wide variety of fuel batches have now been characterised using this method [5]. It is not generally suitable for irradiated fuel due to its sensitivity to the much higher sample activities involved.

Fuel was prepared for analysis by embedding in a resin mount and cutting to produce a longitudinal section through the pellet. The exposed face was polished to provide a high quality surface suitable for analysis.

Measurements were performed using a JEOL JXA-8600 EPMA, equipped with an Oxford Instruments 'Link' Si(Li) detector and 'eXL' analysis system. Quantification was based on the measurement of plutonium 'L' series X ray lines using a 30 kV accelerating voltage and comparing the measured intensity to that of a 'standard' plutonium profile. Concentration maps were constructed by obtaining analyses over a grid of 256 × 256 pixels, covering an area of approximately 1mm^2. The nominal dwell time per pixel was 500ms.

2.3. Wavelength dispersive X ray analysis

This technique was applied to fuel following irradiation. The relative complexity of the technique compared to EDX analysis makes it less suitable for routine analysis. However, it is less sensitive to sample activity, which makes it ideal for post irradiation examination of fuel.

Transverse sections of irradiated fuel rod were prepared for analysis by mounting in resin and polishing to provide a high quality surface for analysis.

Measurements were performed using a shielded CAMECA MS46 instrument. Quantification was based on the measurement of plutonium 'M' series lines using a 20kV accelerating voltage and 100nA beam current. Two types of concentration maps were collected. Large area maps were obtained by collecting a matrix of smaller (250 × 250 μm) maps, each consisting of a grid of 256 × 256 pixels. These individual maps were collected at a magnification of approximately ×400, with a dwell time per pixel of 40ms. The maps were then aligned to produce a composite large area map using proprietary image processing software. Higher resolution maps of specific features were obtained over a grid of 512 × 512 pixels, at a magnification of ×2000 and a dwell-time per pixel of 50 ms.

3. RESULTS

3.1. Plutonium concentration maps

The results of the EDX measurements are in the form of grey-scale images, where the value of each image pixel represents the plutonium concentration at that point. To aid interpretation of the plutonium distribution these were processed using Synoptics 'AnalySIS' software to divide the image into a series of concentration 'bands', each of which can be represented by a different colour. An example of this is given in Fig. 1. This clearly shows that the majority of the fuel matrix is homogeneous and falls within the lowest concentration band. High plutonium concentration regions are visible as discrete, coloured, spots distributed throughout the matrix. Because the map is composed of a grid of individual quantitative analyses it is possible to extract a composition profile across an individual high concentration region. An example of this is shown in Fig. 2. This demonstrates the discrete nature of these regions. The concentration profile is very sharp, with little evidence of diffusion into the surrounding matrix.

The 'point to point' scatter observed in the profile is 'counting noise' due to the relatively short analysis time per point. Noise is also observed in the maps as very small (1-2 pixel) regions. This could be improved by using longer counting times but would make the overall collection time for each map impractical. This 'noise' does not impair the ability to detect and analyse the larger high concentration regions of interest.

The results of WDX measurements on the irradiated fuel also give results as grey-scale images. These were again colour-coded to represent plutonium concentration bands. An example of a composite large area map is given in Fig. 3. This represents the region of the fuel between 0.75 and 0.5 of the pellet radius. It clearly illustrates the distribution of small, high plutonium content, regions spread throughout a predominantly homogeneous matrix. A higher resolution map of an individual high plutonium content region is shown in Fig. 4. This shows the plutonium distribution surrounding a single large pore. It again demonstrates the discrete nature of such regions following irradiation. Figure 5 is an absorbed electron image illustrating the microstructure associated with this region.

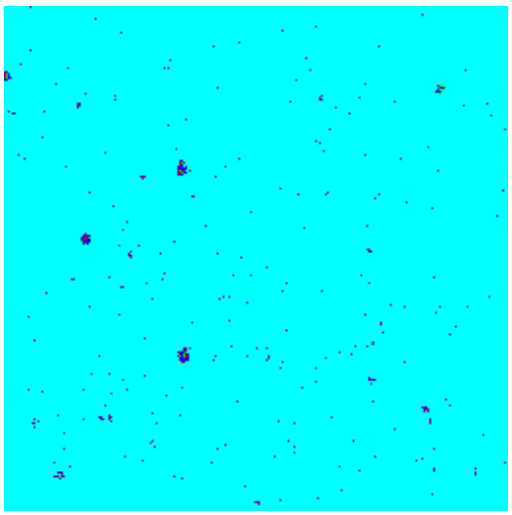

FIG. 1. EDX map showing plutonium distribution in unirradiated M5 fuel.

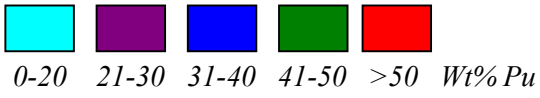

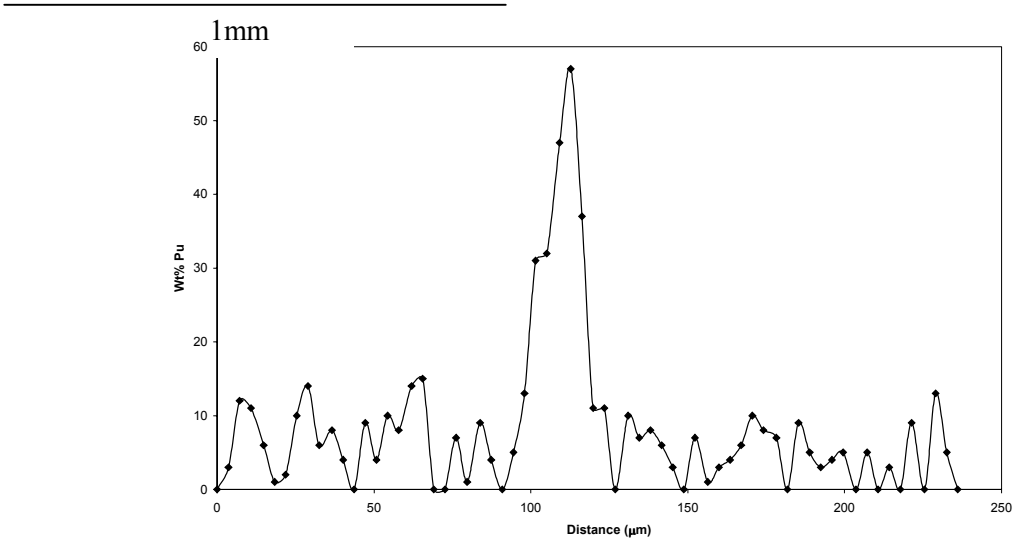

FIG. 2. Plutonium profile across a high concentration region in unirradiated M5 fuel.

3.2. Volume fraction of high plutonium content regions

The key advantage of EPMA mapping techniques is the ability to extract quantitative information regarding plutonium distribution within the fuel. This enables an objective comparison between different fuel batches or, as in this case, before and after irradiation.

Image analysis routines were used to process the maps in order to measure the area fraction associated with each coloured concentration band. This is equivalent [6] to the volume fraction for the pellet.

A programme of work on unirradiated fuel [5] has established that less than 2vol% of the pellet has a plutonium concentration greater than 20wt%. This is illustrated by the histogram in Fig. 6, for the unirradiated M5 fuel. This shows the volume fraction as a function of plutonium concentration for maps obtained at the rim, mid-radius and centre of a pellet section. The histogram also illustrates that there is no change in the shape of the distribution across the pellet radius.

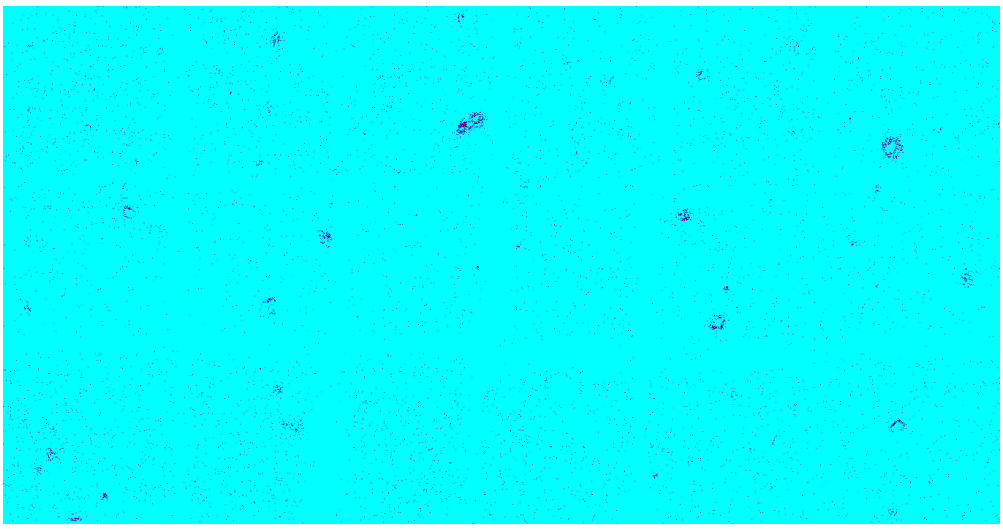

0.75r – 0.5r (1.3mm)

FIG. 3. Large area WDX map showing plutonium distribution in irradiated M5 fuel.

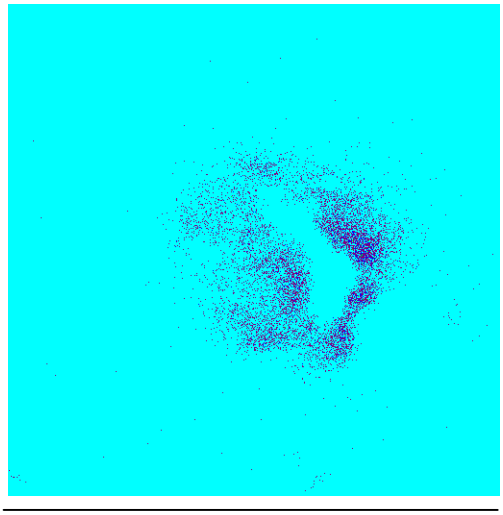

50μm

FIG. 4. *High resolution WDX map showing plutonium distribution for an individual high concentration region in irradiated fuel.*

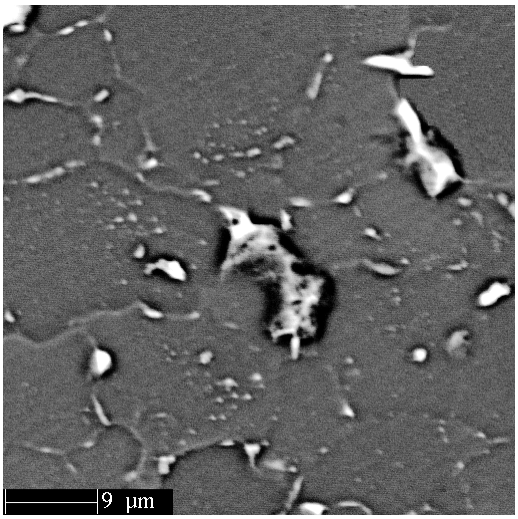

FIG. 5. *Absorbed electron image showing microstructure associated with high concentration region in FIG. 4.*

Figure 7 shows a volume fraction histogram comparing the results from the unirradiated fuel to those following irradiation. The results in both cases were combined from a number of maps obtained across the pellet radius. This shows that irradiation has had little effect on the volume fraction occupied by regions containing >20wt% plutonium.

3.3. Size distribution of high plutonium content regions

Image analysis routines were also used to obtain quantitative information on the size distribution of high plutonium content regions. The areas of all regions having plutonium content greater than 20wt% were measured.

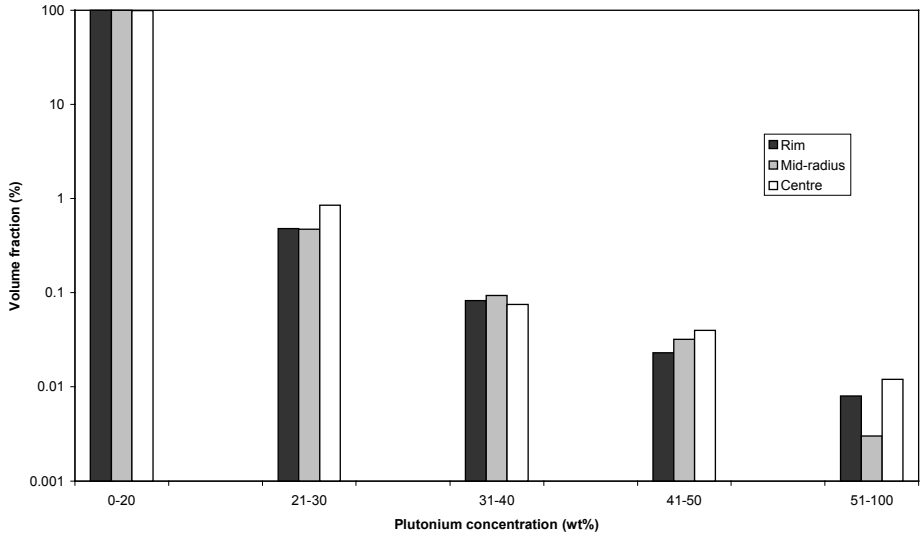

FIG. 6. Radial variation of plutonium volume fraction for unirradiated M5 fuel.

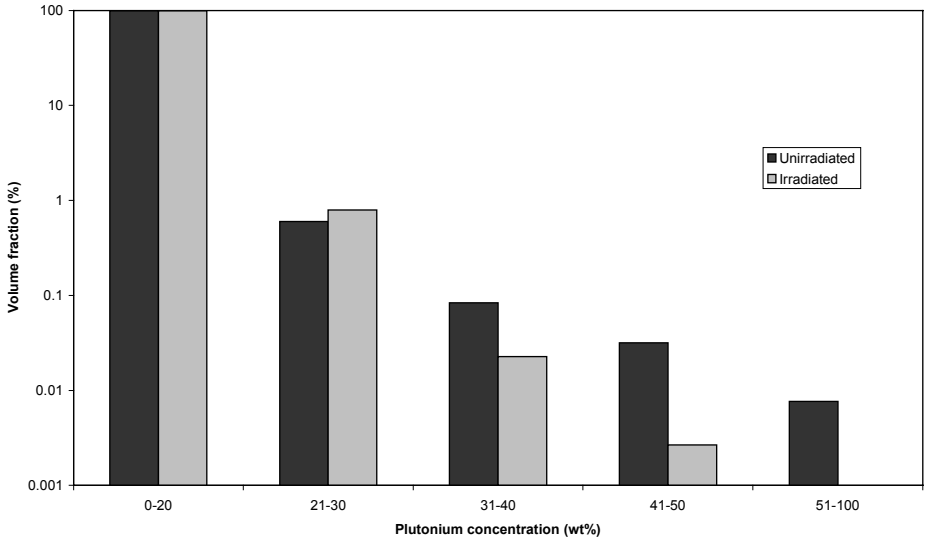

FIG. 7. Comparison of plutonium volume fraction before and after irradiation.

Figure 8 is a size distribution histogram for unirradiated fuel. This compares results from maps obtained at the rim, mid-radius and centre of a pellet section. There is little significant difference in the shapes of these distributions.

Figure 9 compares size distributions before and after irradiation. The results are combined from a number of maps obtained across the pellet radius. Again, this shows that irradiation has had little effect on the shape of the distributions. This suggests that no significant thermal redistribution of plutonium has taken place during irradiation. This is consistent with the irradiation temperature (maximum ~1000C for this sample). It is notable that the area of the largest region observed corresponds to an equivalent diameter of approximately 30 μm.

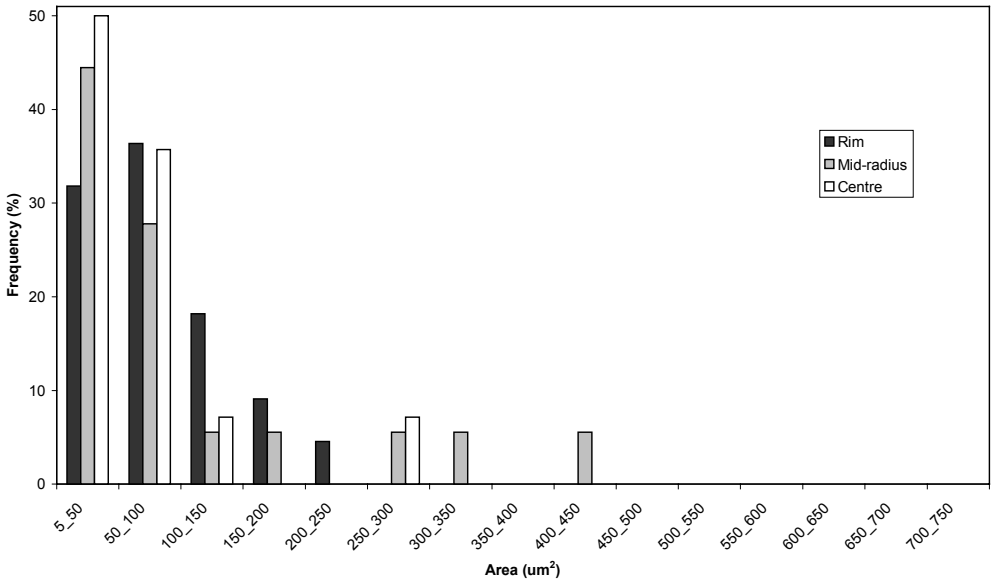

FIG. 8. Radial variation of size distribution for unirradiated M5 fuel.

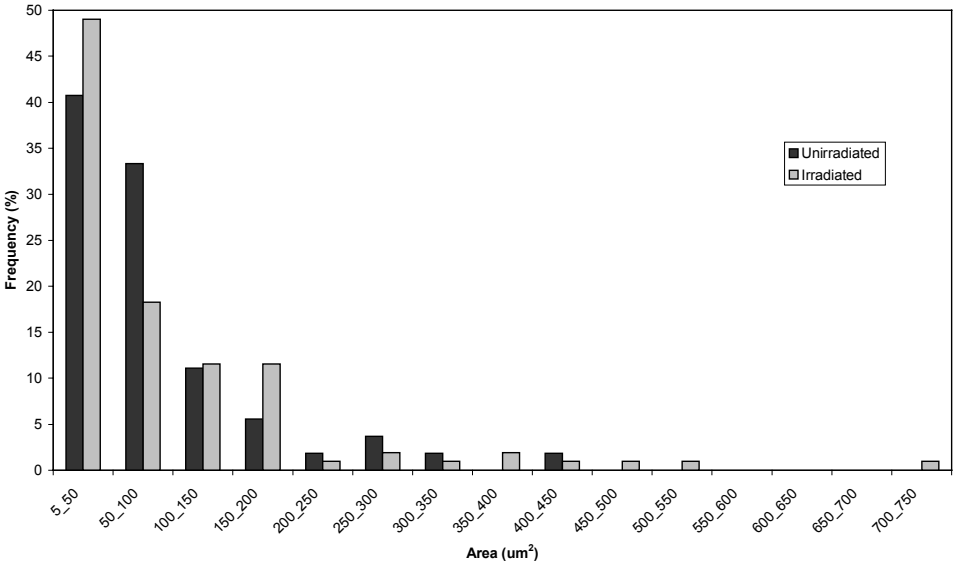

FIG. 9. Comparison of plutonium size distribution before and after irradiation.

4. SUMMARY AND CONCLUSIONS

X ray microanalysis methods have been used to obtain quantitative maps representing the plutonium distribution in SBR MOX fuel. Two techniques have been developed, both having specific advantages. Energy dispersive X ray analysis is applicable to semi-routine characterisation of unirradiated fuel and wavelength dispersive x ray analysis is suitable for detailed examination of irradiated fuel.

Plutonium distribution maps for both unirradiated and irradiated fuel show that SBR MOX is primarily a homogeneous mixture of UO_2 and PuO_2. High plutonium content regions are observed as small, discrete, spots distributed throughout the matrix. Quantitative image analysis techniques have been used to measure the volume and size distributions for these regions. In both cases, the shape of the distributions remains largely unchanged following irradiation. Less than 2% volume fraction of the fuel has a plutonium content greater than 20wt%. The largest high concentration region observed had an equivalent diameter of approximately 30 m.

This work demonstrates that these techniques are a useful and efficient way of characterising both unirradiated and irradiated MOX fuel.

REFERENCES

[1] GUERIN, Y., NOIROT, J., LESPIAUX, D., STRUZIK, C., GARCIA, P., BLANPAIN, P., CHAIGNE, G., 'Microstructure Evolution and In Reactor Behaviour of MOX Fuel', ANS International Topical Meeting on LWR Fuel Performance, Park City, Utah, USA (April 2000).

[2] COOK, P., STRATTON, R., WALKER, C.T., 'PIE of BNFL MOX Fuel', ANS International Topical Meeting on LWR Fuel Performance, Park City, Utah, USA (April 2000).

[3] WALKER, C.T., GOLL, W., MATSUMURA, T., 'Effect of Inhomogeneity on the Level of Fission Gas and Cesium Release from OCOM MOX Fuel During Irradiation', Journal of Nuclear Materials 228 (1996) pp.8 – 17.

[4] GARCIA, P., BOULORE, A., GUERIN, Y., TROTABAS, M., GOEURIOT, P., 'In-Pile Densification of MOX Fuels in Relation to their Initial Microstructure', ANS International Topical Meeting on LWR Fuel Performance, Park City, Utah, USA (April 2000).

[5] IVISON, P.K., FISHER, S.B., 'Quantitative Pu Mapping using Energy Dispersive X ray Analysis', Topfuel99, Avignon, France (September 1999).

[6] RUSS, J.C., 'Computer-Assisted Microscopy', Plenum Press, New York (1990).

MODELLING OF MOX FUEL′S THERMAL CONDUCTIVITY CONSIDERING ITS MICROSTRUCTURAL HETEROGENEITY

BYUNG-HO LEE, YANG-HYUN KOO, DONG-SEONG SOHN
Korea Atomic Energy Research Institute,
Daejeon, Republic of Korea

Abstract

This paper describes a new mechanistic thermal conductivity model considering the heterogeneous microstructure of MOX fuel. Even though the thermal conductivity of MOX has been investigated extensively by experimental measurements and theoretical analyses, they show wide scattering making the performance analysis of MOX fuel difficult. Therefore, a thermal conductivity model that considers the heterogeneous microstructure of MOX fuel has been developed by using a general two-phase thermal conductivity model. In order to apply this model to heterogeneous MOX fuel, the fuel is assumed to consist of Pu–rich particles and UO_2 matrix including PuO_2 in solid solution. Since little relevant data on Pu–rich particles is available, MOX data including Siemens–KWU results are only used to characterize the microstructure of un-irradiated and irradiated fuel. Philliponneau′s and HALDEN models are used for the local thermal conductivities for Pu–rich particles and the UO_2 matrix, respectively. By combining the two models, the overall thermal conductivity of MOX fuel is obtained. The new proposed model estimates the MOX thermal conductivity about 10% less than that of UO_2 fuel, which is in the range of the MOX thermal conductivity available in the open literature. The ratio of the thermal conductivity of MOX to UO_2 increases with temperature because the electronic conduction becomes dominant at high temperatures. The developed thermal conductivity model has been incorporated into KAERI′s fuel performance code, COSMOS, and then evaluated using the measured data of irradiated MOX fuel. A comparison of predicted centerline temperatures with the measured values shows reasonable agreement together with satisfactory results of the fission gas release and gap pressure when the amount of fission gas release is not enough to recover the irradiation damages. However, it indicates that the recovery of thermal conductivity is included to analyze more realistically after significant fission gas release.

1. INTRODUCTION

Since fuel temperature has an influence on most physical processes related to in-pile fuel behavior, it is one of the most important controllable operating parameters. The slight lower thermal conductivity of MOX fuel compared to UO_2 is leading to different central fuel temperatures and to different fission gas releases for the same linear heat generation ratings. Therefore, it is indispensable to develop a more accurate model for temperature prediction, which is determined from thermal conductivity [1].

Until now, several researchers have published results on the thermal conductivities of MOX fuels by experimental measurements and theoretical analyses. For example, Gibby [2] measured the thermal conductivity of MOX fuel up to a Pu content of 30% and fitted by linear regression to $1/(A + B \cdot T)$, which showed the decrease of thermal conductivity of MOX with increasing Pu contents. On the contrary, the analytical thermal conductivity of MOX fuel was analyzed by the available measured data by that time [3,4]. These models showed a sensitive dependence on the stoichiometry, while they were not influenced by Pu contents ranging from about 10 to 30%. Recently, CEA [5] measured the thermal conductivity of un-irradiated MOX fuel, which showed no significant dependence on Pu content from 3 to 15% and a decrease with O/M ratio. It is, however, generally accepted that the thermal conductivity of MOX is slightly less than that of UO_2, even though the content of Pu is less than 10% in the $(U,Pu)O_2$ fuel.

These relevant data on the thermal conductivity of MOX does not make the universal thermal conductivity available, especially in commercially used Pu contents owing to considerable scattering of thermal conductivities.

In the present paper, a new methodology was proposed to develop the thermal conductivity of MOX fuel considering its microstructural heterogeneity. The newly developed thermal conductivity model has been incorporated into a code, COSMOS [6] and then verified by using the MOX irradiation data.

2. METHODOLOGY FOR THE THERMAL CONDUCTIVITY OF MOX

2.1. Heterogeneity of MOX

It is recognized that MOX fuel has an in-reactor behavior almost identical to UO_2. MOX fuel, however, shows a fine dispersion of Pu across a pellet, with the presence of some microscopic Pu-rich zones with Pu contents larger than the pellet average one [7]. To develop a new mechanistic thermal conductivity model, it is assumed that the heterogeneity of MOX fuel causes a significant scattering of the thermal conductivity. Since sufficient data related to the heterogeneous MOX microstructure for un-irradiated and irradiated fuel are not available, only two experimental results are used to characterize the MOX microstructure.

Recently, the FIGARO program [7] studied the microstructure of unirradiated MOX fuel in PSI. The Pu contents in the Pu agglomerates have a distribution ranging from 1 to 20 wt% and the size of agglomerates has a log-normal type distribution as shown in Fig. 1.

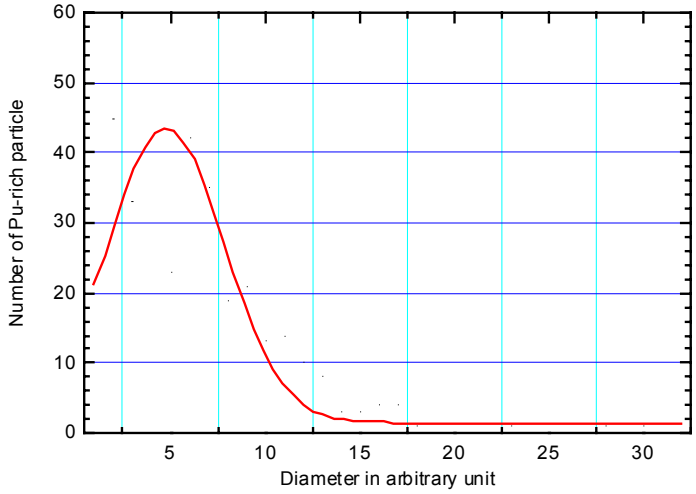

Fig. 1. Heterogeneous Pu-rich particle distribution.

For irradiated fuel, Siemens–KWU [8] published data on the microstructure of two MOX fuels produced by the Optimized Co–milling (OCOM) process. The OCOM 15 fuel contained 34 vol.% of MOX agglomerates with a nominal PuO_2 concentration of 15 wt.%, whereas the OCOM 30 fuel contained 17 vol.% of MOX agglomerates with a nominal PuO_2 concentration of 30 wt.%. They reported similarities between MOX agglomerates and the high burnup structure at the rim of conventional UO_2 fuel.

From these relevant data, the Pu agglomerates can be characterized by twice or 3 times higher burnup than the matrix and a porosity of about 20 ~ 30% in high burnup MOX fuel.

2.2. Thermal conductivity of MOX fuel

Thermal conductivity for UO_2 and MOX fuel that considers the burnup effect can be described as follows:

$$k = \frac{1}{\left(A + \beta \cdot BU + C \cdot T\right)} + D \cdot e^{E \cdot T}$$

where $\beta \cdot BU$ is the term that considers the thermal conductivity degradation with burnup. The hyperbolic term results from the lattice contribution through a phonon–defect and the phonon–phonon scattering processes. On the other hand, the exponential term is caused by the electronic conduction that becomes dominant for temperatures higher than 1900 K.

The burnup–induced degradation phenomenon results from the introduction of defects by irradiation to a previously almost perfect matrix. Furthermore, the thermal conductivity steeply decreases across the Pu–rich agglomerates because of their porous microstructure and higher local fissioning. Accordingly, the thermal conductivity of irradiated MOX fuel is dependent on porosity, volumetric fraction and burnup of Pu–rich spots.

The effect of the Pu–rich agglomerates on the thermal conductivity can be estimated by the assumption that MOX fuel consists of UO_2 matrix and Pu–rich agglomerates. The UO_2 matrix can contain Pu oxide in solid solution. The dependence of thermal conductivity on Pu–rich agglomerates is given as follows.

The generally applicable thermal conductivity for two-phase material is used to assess the thermal conductivity of MOX fuel containing the heterogeneity. The thermal conductivity of MOX fuel can be estimated by the following simple relation [9]:

$$k_{MOX} = k_{UO_2} \cdot \left\{ 1 - a \cdot P_{PuR}^{\frac{2}{3}} \cdot \left[1 - \frac{1}{1 + \frac{1}{a} \cdot P_{PuR}^{\frac{1}{3}} \cdot \left(\frac{k_{UO_2}}{k_{PuR}} - 1 \right)} \right] \right\}$$

where

k_{MOX} = thermal conductivity of heterogenous MOX fuel (W/m – K)

k_{UO_2} = thermal conductivity of UO_2 and PuO_2 in solid solution (W/m – K)

k_{PuR} = thermal conductivity of Pu rich particles (W/m – K)

P_{PuR} = volumetric fraction of Pu rich particles

a = anisotropy factor (a = 1 means isotropic pore distribution).

Philliponneau′s model [4] and the HALDEN model [10] are selected for the local thermal conductivities for Pu–rich particles and UO_2 matrix, respectively, which are expressed by

$$k_{UO_2} = \frac{1}{0.1149 + 4.015 \times 10^{-3} \cdot BU + \left(2.475 \times 10^{-4} - 6.982 \times 10^{-7} \cdot BU\right) \cdot TC} + 0.0132 \cdot e^{0.00188 \cdot TC}$$

$$k_{PuR} = \left(\frac{1}{1.528\sqrt{x + 0.00931} - 0.1055 + 0.44 \cdot BU + 2.885 \times 10^{-4} \cdot TK} + 76.38 \times 10^{-12} \cdot TK^3 \right) \cdot f(p)$$

where

$f(p)$ = correction factor for porosity
BU = burnup in MWd/kgHM not MWd/kgMOX
x = stoichiometry
TK = temperature in Kelvin
TC = temperature in Celsius

Since little relevant data on Pu–rich particles are available, FIGARO [7] and Siemens–KWU [8] results are used only to characterize the microstructure of un-irradiated and irradiated fuel. The present characteristics are adequate for MOX fuel for verification of the developed model although they are not sufficient to accommodate all features of MOX fuel.

Fig. 2 shows thermal conductivity variation as a function of temperature. The thermal conductivity of UO_2 from HALDEN is also plotted for comparison. The MOX thermal conductivity is slightly less than that of UO_2.

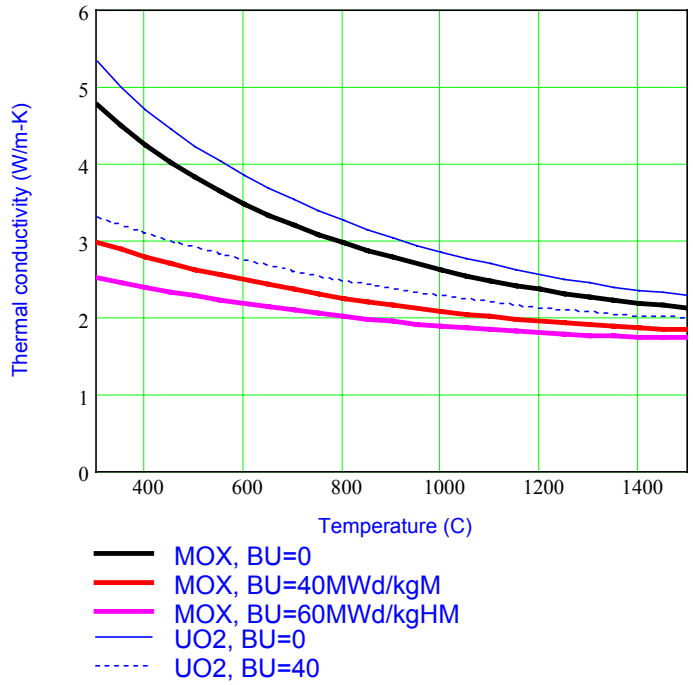

Fig. 2. Thermal conductivity of MOX fuel as a function of temperature.

To directly compare MOX and UO_2 thermal conductivity, the ratio of thermal conductivity of MOX to UO_2 is plotted in Fig. 3 as a function of burnup and temperature. The new proposed model indicates the reduction in MOX thermal conductivity ranging from 7 to 10% compared to UO_2 fuel up to a burnup of 60 MWd/kgHM. The difference between MOX and UO_2 thermal conductivity decreases with temperature because the electronic conduction becomes dominant at high temperatures.

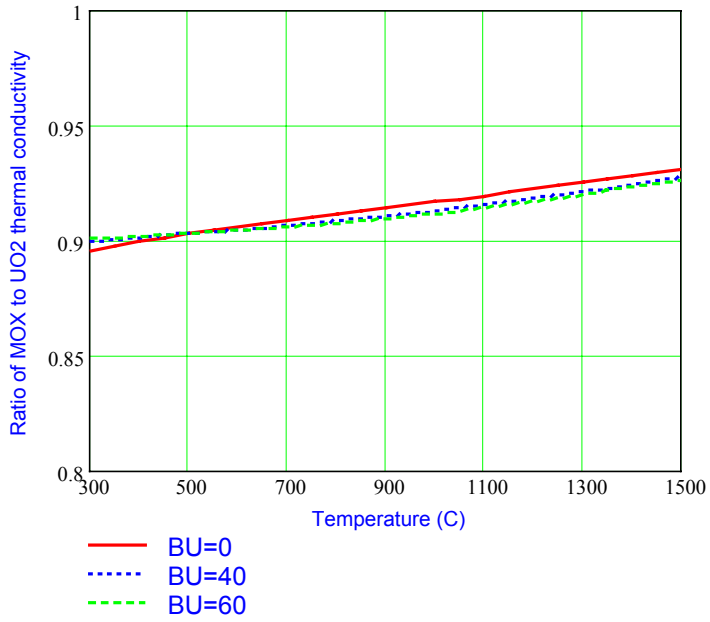

Fig. 3. Ratio of MOX to UO_2 thermal conductivity as a function of temperature.

This reduction is comparable to ENIGMA′s [11] and Siemen′s [12] MOX thermal conductivities, which indicate 8% less than that of standard UO_2 fuel and a relative decrease of 4~5%, respectively. However, it is slightly more conservative than BN′s results [13] which show the 4% reduction of thermal conductivity for 10% Pu/(Pu + U) fuel.

3. BENCHMARK CALCULATION AND DISCUSSION

3.1. COSMOS code

The developed thermal conductivity model has been incorporated into KAERI′s fuel performance code, COSMOS [6] and then verified using the results from the FIGARO program and recent Halden MOX data.

3.1.1. Power distribution

Since the accurate calculation of fuel temperature is a prerequisite for analyzing the overall in-pile behavior of a fuel, a subroutine that calculates the radial power distribution for MOX fuel rods has been developed as a function of burnup and radial position based on a neutron physics calculation. The subroutine gives the radial power density for each radial ring when a pellet is divided into an arbitrary number of radial rings with equal volume and it has been incorporated into a computer code, COSMOS, that is being developed and verified for the performance analysis of MOX fuel.

Fig. 4 shows the typical radial power density distributions across fuel pellet in a MOX rod as a function of pellet average burnup. Generally, the radial power distribution in a MOX pellet is different from that in a conventional PWR UO_2 pellet because of the following two factors. First, the neutron spectrum originated from Pu fission is harder than that for UO_2 fuel leading to the longer migration distance of thermal neutrons in the MOX pellet before they are mostly absorbed by Pu isotopes or U-238. Second, due to a rather high total Pu weight content of about 6 to 8%, the amount of U-238 contained in MOX fuel is obviously less than that of typical UO_2 fuel and thus creates a lesser amount of Pu-239 from U-238 resulting in a more even distribution of radial power generation in MOX fuel.

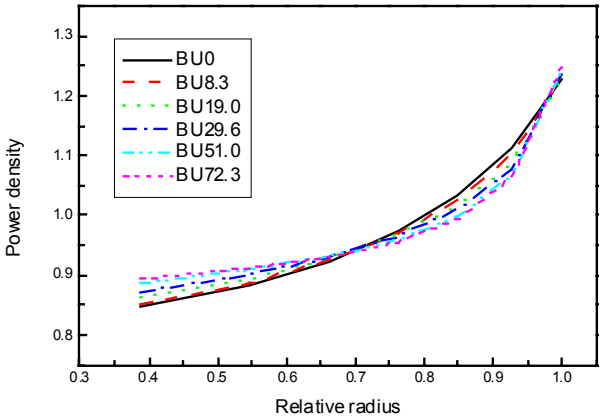

Fig. 4. Typical radial power density profile for 6 w/o Pu-fissile MOX.

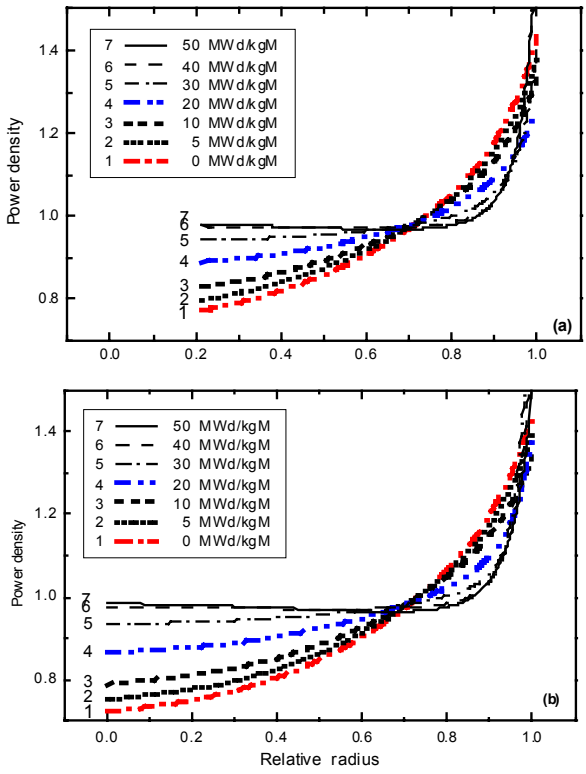

Fig. 5. Radial power density distributions versus pellet average burnup for (a) annular and (b) solid pellets in the HBWR..

Two more factors in the Halden reactor influence the radial power distribution in MOX fuel. To begin with, heavy water, which is used as a moderator in the Halden reactor in contrast with light water in PWRs, produces a different neutron spectrum due to the less effective moderation ability of heavy water. In addition, the fuel-to-moderator ratio that also determines the degree of fission neutron moderation is different from that used in typical commercial PWRs. The combination of these four factors yields the radial power distributions of Fig. 5 in the Halden reactor for MOX pellets [14].

3.1.2. Fission gas release model

A mechanistic fission gas release model for MOX fuel has been incorporated in the COSMOS code based on a model for UO_2 fuel. Using the concept of an equivalent cell [15], the model considerers the uneven distribution of Pu within the UO_2 matrix and a number of Pu-rich particles that could lead to a non-uniform fission rate and fission gas distribution across fuel pellet. The model was verified by the experimental data obtained from the FIGARO program, which consisted of the base irradiation of MOX fuels in the BEZNAU-1 PWR and the subsequent irradiation of four fabricated fuel segments in the Halden reactor. The calculated gas releases show good agreement with the measured ones. In addition, the developed analysis indicates that the microstructure of MOX fuel used in the FIGARO program is such that it has produced little difference in terms of gas release compared with UO_2 fuel [15].

3.2. Comparison with measured temperature

3.2.1. FIGARO program

The main objective of the FIGARO program [13,16] is to evaluate the thermal behavior of MOX fuel at a burnup of about 50 MWd/kgHM and to determine whether fission gas release threshold for MOX fuel was different from UO_2 fuel.

The pellets have been fabricated by the MIMAS process. A micronised master blend of UO_2 and PuO_2 powders had been mixed with depleted UO_2 powder to reach the necessary Pu concentration. Two types of pellets with different grain size were used. The two MOX rods were irradiated during five cycles at moderate power in Bezanu-1 PWR (Switzerland). Four segments, two from each rod, were cut at the same position for both rods and re-fabricated with a pressure transducer and fuel central thermocouple.

Figures 6 and 7 show the difference between the COSMOS calculated temperatures and the measured temperatures for MOX1 and MOX2, respectively. During the calculation, the integral in-pile performance, including fission gas release and gap pressure, is also compared with the measured values.

Figure 6 shows that COSMOS well predicted the measured temperature within ±50°C without a severe bias during irradiation time. However, COSMOS substantially over-predicted the MOX2 temperature as shown in Fig. 7. This over-estimation is considered to result from a larger estimation of thermal conductivity degradation than that of the irradiated fuel rods. That is, the irradiated pellets have the saturated thermal conductivity or recover their thermal conductivity at high burnup due to some recovery of irradiation damage. The saturation effect is not enough to explain MOX2′s over-prediction because MOX1 and MOX2 fuels have almost the same burnup from base-irradiation. The recovery of thermal conductivity seems to be more reasonable to give an explanation of the higher temperature prediction in MOX2, because the MOX2 showed a larger fission gas release than MOX1.

3.2.2. Recent HALDEN MOX data

The developed thermal conductivity model was verified by the recent data obtained from MOX fuel which has been irradiated in the Halden reactor to study the thermal fission gas release behavior of both solid and hollow MOX fuels.

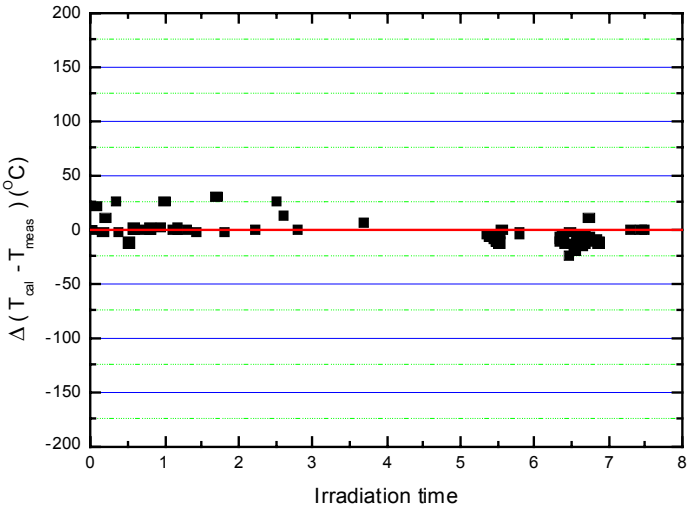

Fig. 6. Difference between the calculated and measured centerline fuel temperature for MOX1.

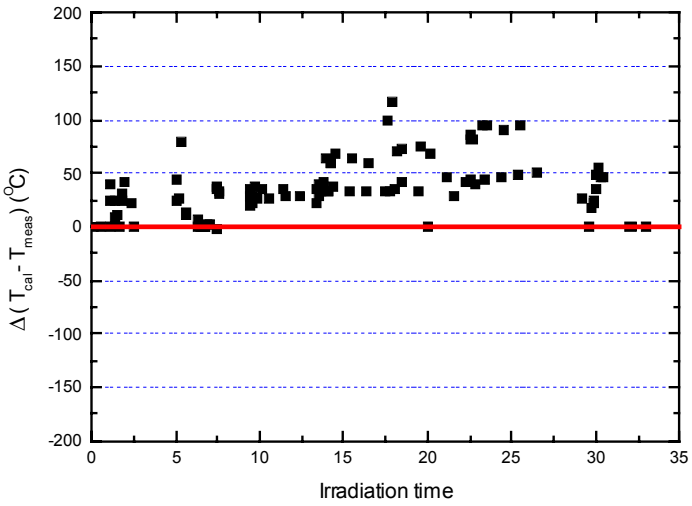

Fig. 7. Difference between the calculated and measured centerline fuel temperature for MOX2.

The calculated fuel centerline temperature for solid fuel is compared with the measured values as shown in Fig. 8. COSMOS well predicted in the beginning stage of irradiation. COSMOS however shows over-prediction after significant fission gas release. As mentioned in 3.2.1, this over-estimation seems to be caused by the recovery of thermal conductivity after a substantial fission gas release occurred.

Hence, it seems that the COSMOS code can more accurately analyze the in-pile fuel performance behavior including the recovery effect of thermal conductivity.

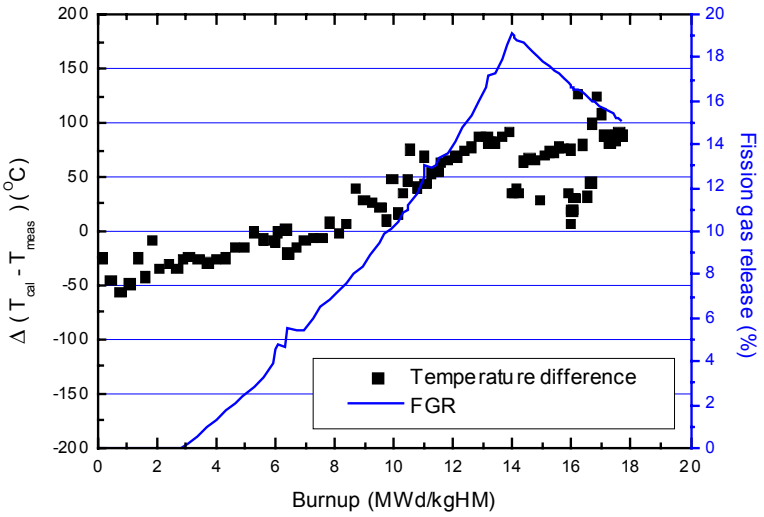

Fig. 8. Comparison of calculated fuel centerline temperature with the data from Halden.

4. CONCLUSION

A new mechanistic thermal conductivity model for MOX fuel was developed by considering its heterogeneous microstructure. The general thermal conductivity model applicable to two-phase materials such as porous nuclear fuel was used to take into account the Pu–rich particles in the UO_2 matrix including PuO_2 in solid solution. The Pu–rich particles were characterized by FIGARO and Siemens–KWU results. The proposed model estimates that the MOX thermal conductivity with the Pu content of commercial LWR fuel is about 10% less than that of UO_2, which is in the range of thermal conductivities available in the open literature. The developed thermal conductivity model was incorporated into a fuel performance code, COSMOS and then verified by the MOX in-pile database. A comparison of predicted centerline temperatures with the measured values shows reasonable agreement together with satisfactory results of the fission gas release and gap pressure when the amount of fission gas release is not enough to recover the irradiation damages. However, it indicates that the recovery of thermal conductivity is included to analyze more realistically after significant fission gas release.

ACKNOWLEDGEMENTS

The authors would like to express their appreciation to the Ministry of Science and Technology (MOST) of the Republic of Korea for the support of this work through the Mid– and Long–term Nuclear R&D Project.

REFERENCES

[1] B.H. LEE, Y.H. KOO, and D.S. SOHN, "Modeling of thermal conductivity for high burnup UO_2 fuel retaining rim region," Journal of Korean Nuclear Society, **29** (1997) 201.

[2] R.L. GIBBY, "The effect of plutonium content on the thermal conductivity of $(U,Pu)O_2$ solid solution," Journal of Nuclear Materials, **38** (1971) 163–177.

[3] D.G. MARTIN, "A re–appraisal of the thermal conductivity of UO_2 and mixed (U, Pu) oxide fuels," Journal of Nuclear Materials, **110** (1982) 73–94.
[4] Y. PHILIPPONNEAU, "Thermal conductivity of $(U,Pu)O_{2-x}$ mixed oxide fuel," Journal of Nuclear Materials, **188** (1992) 194–197.
[5] C. DURIEZ et al., "Thermal conductivity of HYPO stoichiometric low Pu content $(U,Pu)O_{2-x}$ mixed oxide," MOX Fuel Cycle Technologies for Medium and Long Term Deployment (Proc. Int. Symp. Vienna, Austria, May 17~21, 1999) IAEA, Vienna, 3/P (2000).
[6] Y.H. KOO, B.H. LEE, and D.S. SOHN, "COSMOS: A Computer Code for the analysis of LWR UO_2 and MOX Fuel Rod," Journal of Korean Nuclear Society, **30** (1998) 541.
[7] M. LIPPENS and the COMETHE team, "Comparative thermal behavior of MOX and UO_2 fuels," Proceedings of the Seminar on Thermal Performance of High Burnup LWR fuel, NEA, Cadarache, France, 3–6 March 1998.
[8] C.T. WALKER, W. GOLL, and T. MATSUMURA, "Further observation on OCOM MOX fuel: microstructure in the vicinity of the pellet rim and fuel–cladding interaction," Journal of Nuclear Materials, **245** (1997) 169–178.
[9] H. KAMPFf and G. KARSTEN, "Effects of different types of void volumes on the radial temperature distribution of fuel pins," Nuclear Technology, **9** (1970) 288.
[10] W. WIESENACK, "Assessment of UO_2 conductivity degradation based on in-pile temperature data," Proc. Int. Topl. Mtg. LWR fuel performance, Portland, Oregon, March 2-6, 1997, p.507, American Nuclear Society (1997).
[11] G.A. GATES, P.M.A. COOK, P. KLERK, P. MORRIS and I.D. Palmer, "Thermal performance modeling with the ENIGMA code," Proceedings of the seminar on thermal performance of high burnup LWR fuel, Cadarache, France, March 3~6, 1998.
[12] L. HEINS, H. LANDSKRON, "Fuel rod design by statistical methods for MOX fuel," IAEA-SM-358/21, Vienna, Austria, May 17~21, 1999.
[13] M. LIPPENS, and COMETHE team, "Comparative thermal behavior of MOX fuel and UO_2 fuels," Proceedings of the seminar on thermal performance of high burnup LWR fuel, Cadarache, France, March 3~6, 1998.
[14] Y.H. KOO, B.H. LEE, and D.S. SOHN, "Irradiation experiment with MOX fuels in the Halden Reactor and Preliminary analysis of their in-reactor behavior" Journal of Korean Nuclear Society (in press).
[15] Y.H. KOO, B.H. LEE, and D.S. SOHN, "A fission gas release model for MOX fuel and its verification," MOX Fuel Cycle Technologies for Medium and Long Term Deployment (Proc. Int. Symp. Vienna, Austria, May 17~21, 1999) IAEA, Vienna, 3/P (2000) 500.
[16] M. LIPPENS, Th. MALDAUE, J. BASSELIER, D. BOULANGER, L. MERTENS, "Highlights on R&D work related to the achievement of high burnup with MOX fuel in commercial reactors," MOX Fuel Cycle Technologies for Medium and Long Term Deployment (Proc. Int. Symp. Vienna, Austria, May 17~21, 1999) IAEA, Vienna, 3/P (2000) 220.

GAS FLOW MEASUREMENTS ON SBR MOX FUEL

G.A. GATES
MOX Research and Technology,
British Nuclear Fuels Ltd,
Sellafield, Cumbria, United Kingdom

Abstract

To obtain a better understanding of the release of both stable and unstable fission release from Short-Binderless Route (SBR) MOX fuel BNFL are conducting an in-pile fuel experiment in the Halden HBWR, Instrumented Fuel Assembly (IFA)-633. This experiment contains both SBR MOX and UO_2 fuel rods and was loaded into the test reactor in early 1999. The present paper gives a brief description of the overall rig design and concentrates on the unstable fission product release data obtained during the start-up of the experiment. This data shows that on the first rise to power there is an initial increase in the measured fuel surface-to-volume ratio, *S/V*, due to fuel cracking which is followed by a decrease in *S/V*. Overall the MOX and UO_2 unstable fission gas release behaviour is similar.

1. INTRODUCTION

One of the most important features of the BNFL gas-flow experiment, IFA-633, is the ability to use on-line gamma spectrometry to monitor the unstable fission gas release from both the MOX and UO_2 fuel within the assembly. Within a gas flow rig, the rod ends are connected to a gas transport system by fine capillary tubing. This allows the gas composition and pressure in a rod to be changed during irradiation and also permits operation under a gas flowing regime. By sweeping the gas past a gamma spectrometer short-lived fission products can be detected. This gives fission gas measurements of ^{85m}Kr, ^{87}Kr, ^{88}Kr, ^{98}Kr, ^{90}Kr, ^{135}Kr, ^{135}Xe, ^{135m}Xe, ^{137}Xe, ^{138}Xe, ^{139}Xe, ^{131}I, ^{133}I and ^{135}I. The gas can also be cold trapped to obtain data on longer-lived isotopes, ^{85}Kr, ^{131m}Xe and ^{133}Xe. By measuring the release of the short-lived unstable fission products it is possible to determine the fuel surface-to-volume ratio (S/V) during irradiation which in turn gives an indication of the change in the fuel microstructure as a function of burnup [1].

The gas-flow rig contains six rods of approximately 0.5 m in length, three MOX rods containing SBR MOX pellets manufactured in the MOX demonstration facility (MDF) at BNFL's Sellafield site [2] and three UO_2 rods containing pellets manufactured at BNFL's Springfields site. Each rod is connected to the gas-flow system via a gas line of 0.6 mm inner bore diameter allowing the fission products to be flushed out to the gamma spectrometer for fission product analysis (Fig. 1). The rods are also fitted with a combination of in-pile instrumentation including fuel centreline thermocouples, stack elongation detectors and pressure transducers which provides data on the thermal performance, fuel densification and swelling.

The gas-flow experiment was loaded into the Halden reactor in January 1999 and irradiation started in March 1999. During the first few days of operation a detailed start-up experiment was performed providing data on both unstable fission gas release and fuel thermal performance. The thermal performance data, covering both start-of-life fuel temperatures and an analysis of fuel-clad gap conductance, was presented as the recent ANS Fuel Performance meeting in Utah [3]. The present paper covers the unstable fission product release results obtained during this period.

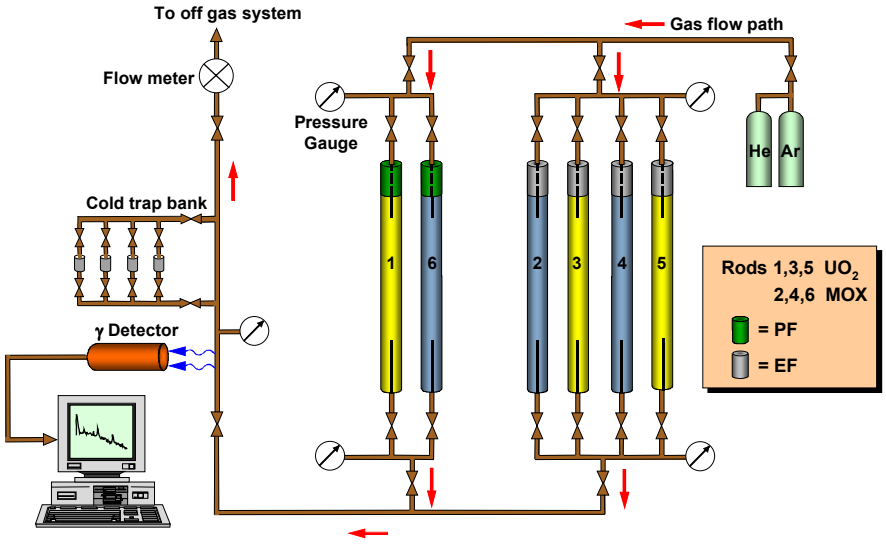

FIG. 1. Schematic diagram of gas flow system for the BNFL gas flow experiment, IFA-633. The rods are instrumented with centreline thermocouples, pressure transducers (PFs) and stack elongation detectors (EFs).

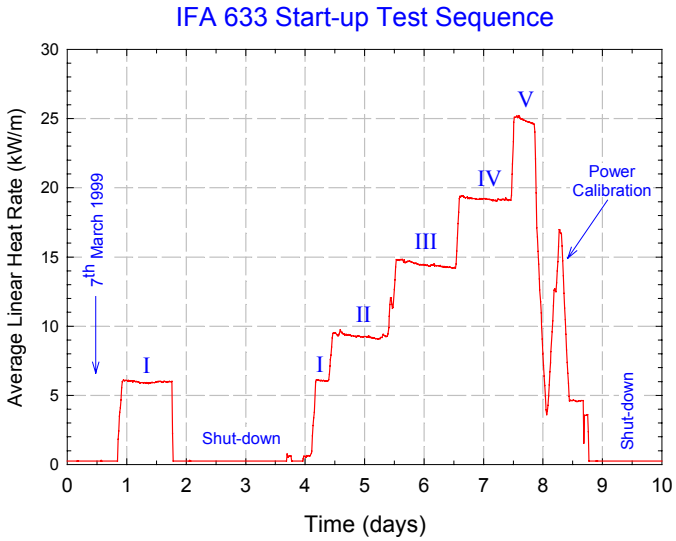

FIG. 2. Start-up test sequence.

2. MEASUREMENT SCHEDULE

The start-up of the gas flow experiment consisted of a stepwise rise to full power over a period of eight days (Fig. 2). At each of the five power levels a number of different measurements were made on rods 2–5, including on-line fission product release measurements using both a helium and argon sweep gas, fuel temperature measurements and gap conductance measurement. A detailed analysis of the fuel temperature and gap conductance data obtained during the start-up of the experiment can be found in reference [3].

The fission product release data collected during the start-up, which included 115 gamma spectra, are presented in Sections 4 and 5. Following the start-up tests in March 1999 the assembly has now been irradiated for three reactor cycles in the Halden Reactor with the assembly reaching an average burnup of 9 MWd/kgHM.

3. UNSTABLE FISSION PRODUCT RELEASE

3.1. Release-to-birth rate ratio

Unlike stable fission gas release, which is expressed as a fractional release, the release of unstable fission gas products cannot be expressed in this manner because the concentration of fission products saturates to a maximum within approximately 4-5 half-lives for a given isotope. Therefore the release of unstable fission products is described by the release rate to birth rate ratio, which is express as,

$$\frac{R}{B} = \frac{\text{Instantaneous Fission Product Release Rate}}{\text{Instantaneous Fission Product Generation Rate}} . \quad (1)$$

The release rate, R, is calculated from the gamma spectra [1]. The birth rate, B, for a given isotope, i, is expressed as follows,

$$B_i = 3.12 \times 10^{13} \cdot R \cdot L \cdot Y_i , \quad (2)$$

where R is the rod linear heat rate (kW/m), L is the length of the fuel stack (m) and Y_i is the fission yield of the isotope of interest. The fission product yield for a given isotope is dependent on the fissile elements within the fuel with the yield of Kr isotopes being less from ^{239}Pu and ^{241}Pu than for ^{235}U [1]. Therefore the fission yield is calculated to be the weighed sum of fissionable isotopes present in the fuel,

$$Y_i \quad (3) \quad \frac{W_{U-235} \cdot Y_i^{U-235} + W_{Pu-239} \cdot Y_i^{Pu-239} + W_{Pu-241} \cdot Y_i^{Pu-241}}{W_{U-235} + W_{Pu-239} + W_{Pu-241}} ,$$

where W_x is the weight of isotope x in the fuel and Y_i^x is the isotopic yield from x of isotope i.

Each gas flow measurement consists of a series of three gamma spectra, one flow plus two static spectra. The average release to birth rate ratio (R/B) for each unstable fission product is then calculated by averaging the results obtained from these three spectra based on the half-life of each fission product [4]. A total of 11 unstable fission isotopes are considered in the analysis of the on-line spectra, ranging from ^{133}Xe with a half-life of 5.25 days to ^{90}Kr with a half-life of 32 seconds.

3.2. Surface-to-volume ratio

The experience gained from previous UO_2 gas flow experiments has shown that the release to birth rate ratio can be described by two components, a component which is independent of isotopic half-life and a diffusion component dependent on the square root of the half-life [1], i.e.

$$\frac{R}{B} = \left.\frac{R}{B}\right|_{\lambda-indep} + \left.\frac{R}{B}\right|_{diff} . \quad (4)$$

The half-life independent term is due to direct recoil release from fission events occurring close to the free surface. The general form of the recoil release component is expressed as follows [1],

$$\left.\frac{R}{B}\right|_{\lambda-indep} = \left.\frac{R}{B}\right|_{recoil} = \frac{1}{4}\cdot\frac{S}{V}\cdot l_f\cdot\varepsilon_r\,, \tag{5}$$

where S/V is the surface to volume ratio of the fuel, l_f is the fission fragment range and ε_r is the recoil release efficiency. The half-life dependent term arises from the diffusion of single gas atoms to the free surface of the fuel, and following the work of Booth [5] and Friskney & Speight [6] can be expressed as follows,

$$\left.\frac{R}{B}\right|_{diff} = \frac{S}{V}\cdot\sqrt{\frac{\alpha\cdot D}{\lambda}}\,, \tag{6}$$

In the equation above λ is the fission product decay constant, D is the single gas atom diffusion coefficient [1] and α is the precursor enhancement factor [1], which arises because the release of a fission product can be enhanced by the prior release of its precursor, which may have a higher diffusion coefficient, e.g. the bromine precursors of the krypton isotopes.

Combining equations (4) & (6) yields the following expression for the release-to-birth rate ratio,

$$\frac{R}{B} = \left.\frac{R}{B}\right|_{recoil} + \frac{S}{V}\cdot\sqrt{\frac{\alpha\cdot D}{\lambda}}\,. \tag{7}$$

Therefore by plotting R/B as a function of $\sqrt{(\alpha/\lambda)}$ it is possible to determine both the recoil release component and the fuel surface-to-volume ratio, where the surface-to-volume ratio is a measure of the amount of open porosity within the fuel, with fresh fuel having a low S/V value of approximately 10-50 cm^{-1} and fully interlinked fuel that has released a significant amount of fission gas having a value of approximately 1000-1500 cm^{-1}.

4. UNSTABLE FISSION PRODUCT RELEASE DATA

At each of the five power levels during the start-up of the experiment fission product release data were obtained from rods 2-5 using a helium sweep gas. Due to the lower thermal conductivity of argon, the argon sweep gas-flow measurements were not performed at the highest power level (~25 kW/m), to limit the measured fuel temperatures.

An example of the data collected during the start-up period from a UO_2 rod is shown in Fig. 3. In this figure the R/B values have been plotted against the log of the decay constant, λ, for each measured isotope. For both the helium sweep gas data (top graph) and the argon sweep gas data (bottom graph) it is clearly seen that the data can be expressed as a linear combination of two components; a recoil (λ-independent) and a diffusion component ($\lambda^{0.5}$-dependence), as expected from equation (7).

With reference to the upper graph in Fig. 3, as the linear heat rating is increased, and hence the fuel temperatures, the diffusion component becomes more pronounced as the fission gas mobility within the fuel increases, whereas the recoil component is invariant to changes in the linear rating. For the shorter lived isotopes the fission product release rate is dominated by recoil release since a significant proportion of these isotopes would have decayed before they could reach the free surface of the fuel by the diffusion process. This is in contrast with the longer lived isotopes where the release is dominated by single gas atom diffusion.

Comparing the two sets of measurements in Fig. 3, with both the helium and argon sweep gas, it is seen that the results obtained with the argon sweep gas are broadly similar to those obtained with helium, however, the recoil release component is approximately four times larger when using argon. The reason for this difference is simply due to the more effective stopping power of argon compared to helium, i.e. the argon sweep gas is more efficient at collecting the highly energetic fission products that are ejected from the free surface of the fuel due to fission fragment collisions.

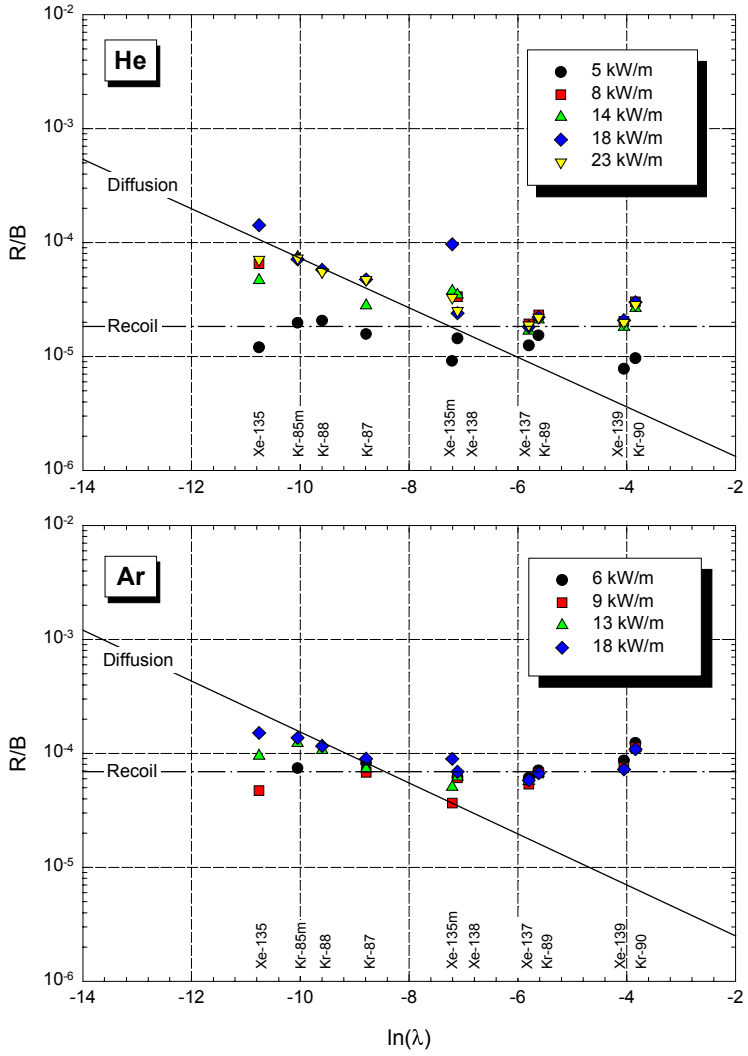

FIG. 3. Measured release-to-birth rate ratio for a UO_2 rod using both a helium and argon sweep gas during the start-up ramp. The diffusion component of the release becomes more pronounced at higher ratings.

It should be noted that it takes approximately four to five half-lives for an isotope to reach radioactive equilibrium therefore the two longest lived isotopes, ^{133}Xe ($\lambda \sim 5.25$ days) and ^{135}Xe ($\lambda \sim 9$ hrs), will not be in equilibrium during the start-up tests due to the changes in the experimental conditions every 12 hours. Therefore there is a large scatter in some of the ^{135}Xe results. In most cases it was not possible to get an R/B value for ^{133}Xe.

5. DATA ANALYSIS

As indicated in equation (7) it is possible to use the fission product release data to obtain a value for the *S/V* ratio of the fuel. An example of this is shown in **Fig. 4**, where the *R/B* data are plotted as a function of $(\alpha/\lambda)^{0.5}$ for one of the MOX rods during the start-up tests. Plotted in this way the data can be fitted to a straight line with the intercept giving the recoil release component and the slope giving the *S/V* ratio.

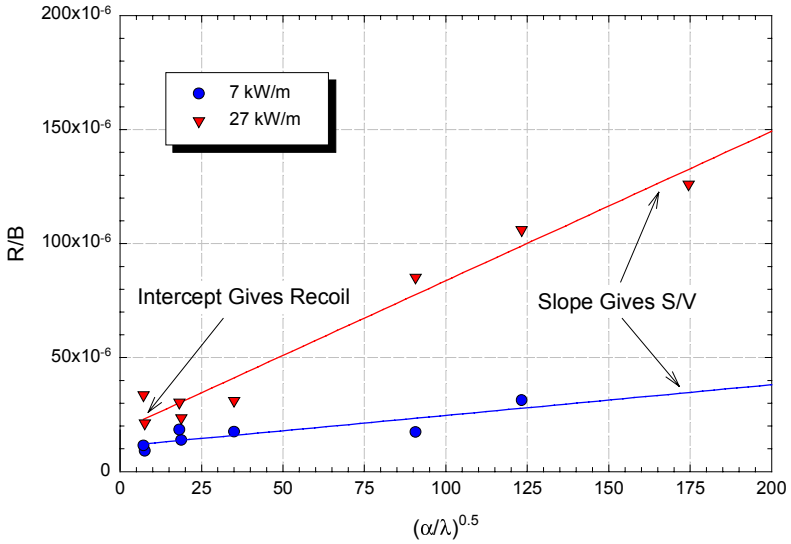

FIG. 4. An example of fitting the R/B data to a straight line as defined by equation (7). The example shown is for a MOX rod during the start-up tests when using a helium sweep gas.

The *S/V* values derived from the start-up measurements are plotted as a function of linear heat rating in Fig. 5 for both helium and argon sweep gases. The first point to note from these figures is that for a given sweep gas there appears to be no significant difference in the behaviour of the MOX and UO_2 fuels.

Examining the data in more detail, when using a helium sweep gas, Figure 5a, the *S/V* ratio has an initial value of ~35 to 70 cm^{-1} at approximately 5 kW/m, rising to a maximum value of ~190 cm^{-1} at ~10 kW/m, which then falls to ~35cm^{-1}. This peak in the value of *S/V* indicates that the fuel is undergoing a fundamental change in its structure as the linear heating is increased. A possible explanation for this behaviour is the axial and radial cracking caused by the differential thermal expansion of the cylindrical fuel pellet during the first rise to power, giving rise to the classical '*wheatsheaf*' shape. This process of pellet cracking and to a lesser extent relocation leads to an increase in the exposed free surface within the fuel, which results in an increase in *S/V* during the initial stages of irradiation.

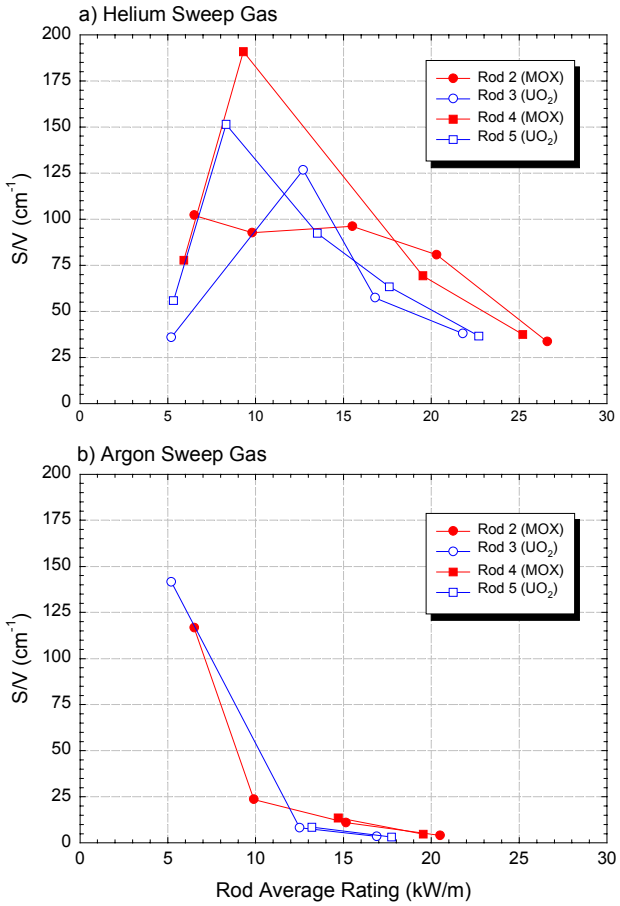

FIG. 5. Surface-to-volume ratio as a function of average linear heat rating measured during the start-up tests using both (a) Helium sweep gas and (b) Argon sweep gas.

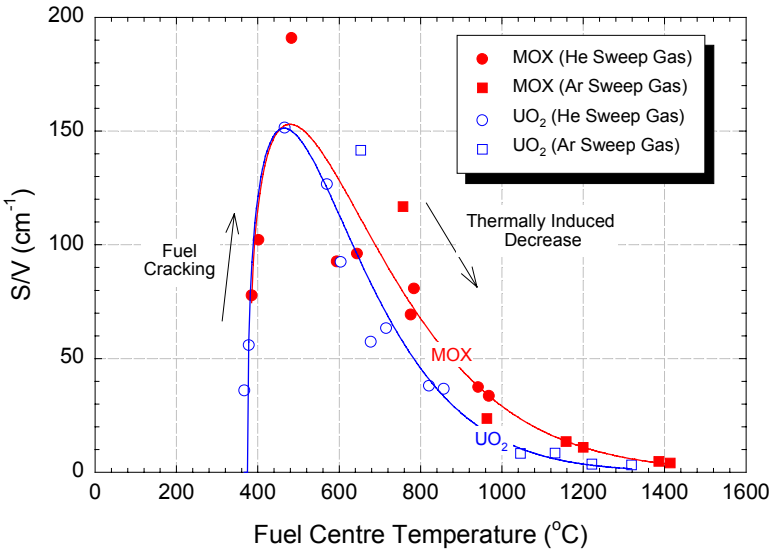

FIG. 6. Surface-to-volume ratio as a function of the measured fuel centre temperature. Note that the helium and argon data form one consistent data set for each fuel.

As the ratings, and hence, fuel temperatures are increased it could be expected that thermal processes, such as crack closure, could occur giving rise to a reduction in *S/V*. This appears to be the case from the helium data, however, in Fig. 5b when using the argon sweep gas no peak is evident in the data, with the *S/V* ratio starting at a high value of ~150 cm^{-1} at 5 kW/m and then decreasing steadily as a function of the linear heat rating to a value of ~5 cm^{-1}. Due to the lower thermal conductivity of the argon gas it is not possible to make a direct comparison of the argon and helium *S/V* values since for the same nominal rating the fuel temperatures will be much higher with an argon fill gas [3]. To reconcile the two data sets the argon and helium data are plotted as a function of the measured fuel centre temperature in Fig. 6. The argon and helium data now form one consistent data set with the *S/V* values initially increasing to a maximum at ~500˚C and then steadily decreasing to 5 cm^{-1} at the maximum measured temperature of 1400˚C.

From Fig. 6 it is seen that the initial increase in *S/V*, caused by pellet cracking, is the same for both in the MOX and UO_2 rods. However, after reaching the maximum value at ~ 500˚C there appears to be a slight departure in the behaviour of the two fuel types, with the *S/V* values decreasing more rapidly in the UO_2 than the MOX fuel.

In Fig. 7 the recoil component of the release is plotted as a function of the fuel centre temperature for both the measurements with the helium and argon gas sweep gases. The recoil component reaches a stable value following the first few measurements with the argon values being a factor of approximately four higher then those measured with a helium sweep gas. As explained in the previous section this difference is due to the more efficient stopping power of the argon sweep gas compared to helium.

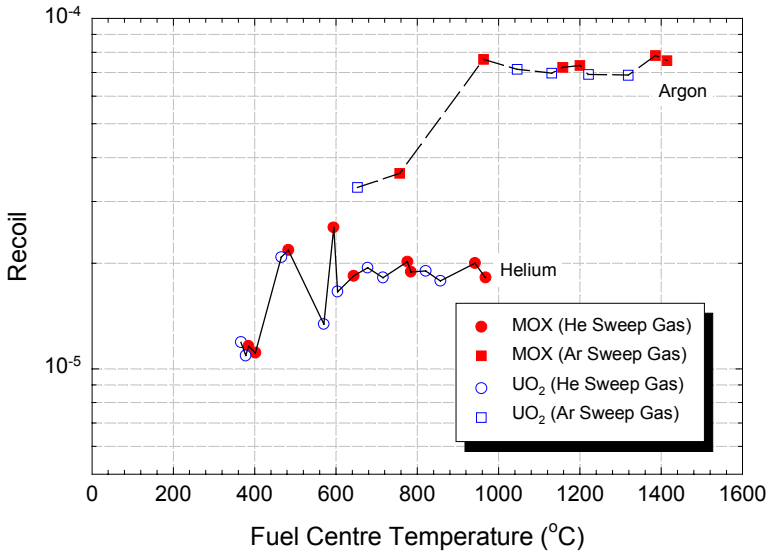

FIG. 7. Recoil component plotted as a function of the measured fuel centre temperature for the start-up tests.

6. CONCLUSIONS

Start-of-life gas flow measurements have been presented from the BNFL gas-flow experiment for both SBR MOX and UO_2 fuels. A detailed analysis of these data has shown that the experiment is producing a large amount of high quality unstable fission gas release data, which gives detailed information on both the changes in the fuel macro/microstructure, and the fission gas release behaviour of the MOX and UO_2 fuel.

From the analysis presented in this paper a number of key observations can be made:

- For both the MOX and UO_2 fuels the fission gas release process can be described by two components, a half-life independent component which is due to direct recoil release from fission events close to the free surface of the fuel and a diffusion component which is dependent on the square root of the half-life of the unstable fission products.
- The start-of-life data shows that on the first rise to power there is an initial increase in the measured fuel surface-to-volume ratio, *S/V*, due to fuel cracking which is followed by a decrease in *S/V* due to thermally activated processes, such as crack closure, leading to a reduction in the sweeping efficiency of the flow gas. Overall the MOX and UO_2 behaviour is similar.

The unstable fission gas measurements will continue during the irradiation and thus provide a comparison between the behaviour of the MOX and UO_2 fuels. A detailed interlinkage experiment will be performed between 15 to 20 MWd/kgHM when the fuel will be taken over the 1% empirical fission gas release threshold [7] to study the dynamics of the fission gas release process between the MOX and UO_2 fuels.

ACKNOWLEDGEMENTS

The author would like to thank the people who assisted in taking the start-of-life measurements, including Rod White, Knut Bråten, Henning Horn, Margaret McGrath, Johan Magnus Aasgaard and Arvid Rånes. An acknowledgement must also be made to Rod White for his useful discussions on the analysis and interpretation of the gas flow measurements.

REFERENCES

[1] WHITE R J AND TURNBULL J A, "The Measurement of Fission Product Release Using the Gas Flow Rigs: A Review of Experiments, Methodology and Results from 1980-1997", HWR-553, February 1998.

[2] EASTMAN R J AND TOD S, "The Microstucture of Unirradiated SBR MOX Fuel", IAEA MOX Fuels Symposium, Vienna, May 1999 IAEA-SM-358/9.

[3] GATES G A AND WHITE R J, "Start-of-life Gap Conductance Measurements on SBR Mixed Oxide Fuel", ANS International Topical Meeting on LWR Fuel Performance, 9-13th April 2000, Park City Utah USA.

[4] WHITE R J AND SKATTUM E, "Experimental Methods Used in the determination of Unstable Fission Product Release Rates in the Gas Flow Rigs", IDG-NOTE 3008 (Halden Report), May 1985.

[5] BOOTH A H, “A Method for Calculating the Diffusion of Radioactive Rare Gas Fission Products from UO_2 Fuel Elements”, AECL Chalk River Report DIC-27, 1957.
[6] FRISKNEY C A AND SPEIGHT M V, “A Calculation on the In-Pile Diffusional Release of Fission Products Forming a General Decay Chain”, Journal of Nuclear Materials, Vol. 62 89-94, 1976.
[7] VITANZA C, KOLSTAD E AND GRAZIANI V, ANS Topical Meeting on LWR Fuel Performance, Portland, Oregon, USA, May 1979.

DEVELOPMENT OF CODES AND METHODS
(Session 5)

Chairpersons

M. El SHANAWANY
United Kingdom

K. LASSMANN
Germany

CONSTITUTIVE EQUATIONS USING THE BACK STRESS INTERNAL VARIABLE TO MODEL CWSR ZIRCALOY PLASTIC DEFORMATION

V.I. ARIMESCU
Siemens Power Corporation,
Richland, Washington,
United States of America

Abstract

A variety of engineering correlations have been used to describe thermal creep deformation of Zr alloys. The primary creep, which occurs after the initial loading, is typically characterized by a decreasing creep strain rate and thus, formulations with time at a power close to 0.5 have been fitted to experimental data. By differentiating such an expression, a strain rate constitutive equation can be obtained for the plastic strain rate, ε, as dependent on σ, the applied stress and on T, the temperature. This equation is used in conjunction with a multi-axial anisotropy model whereby the equivalent plastic strain rate calculated by relation (1) is distributed along the three principal directions according to generalized Hill anisotropy model. This type of constitutive plastic strain rate equation was successfully applied in fuel rod behavior codes to model cladding plastic deformation by incorporating the effect of irradiation hardening. However, this type of relation is unable to model the steady-state creep regime and also it is difficult to account for the previous deformation history. A more mechanistically based model is needed to describe both the primary and the steady-state stages of the creep deformation and also to capture the effect of microstructural processes underlying the plastic deformation. A set of two coupled equations is proposed to describe the plastic deformation of Zircaloy tubes including both the tensile and creep regimes. It is the simplest form that uses the concept of internal variables to represent the microstructural processes occurring during plastic deformation. For the creep regime it provides a natural transition from primary to secondary creep and also allows for simulation of inverted primary creep. The "back stress," σ_b, is included in the model as a macroscopic variable representing the dislocation sub-structure resistance to deformation. The evolution of this back stress is the result of the competition between the opposing hardening and recovery processes. Hardening is created during deformation by the emerging dislocation sub-structure and by internal defects and impurities which act as obstacles to deformation. Recovery is due to thermal processes that enable dislocations to be released from the walls of the dislocation sub-structure by climbing and other mechanisms. The pool of data used to build the model consisted of both unirradiated and irradiated CWSR Zry4 cladding. Results from tensile and creep tests of both uniaxial or biaxial type have been used to obtain the fitting constants of the model and the effect of fast fluence on some of them. The paper presents the comparison of calculated and measured deformation to support the favorable conclusion of applicability of the back-stress constitutive equations to modeling Zry plastic deformation.

1. INTRODUCTION

The engineering thermal creep model, implemented in numerous fuel codes, models the plastic deformation through a constitutive plastic strain rate equation of the form [1]:

$$\frac{d\varepsilon}{dt} = \frac{[A\exp(\frac{-Q}{kT})\sinh(a\sigma)]^2}{2\varepsilon} \qquad (1)$$

which is used in conjunction with a multi-axial anisotropy model (the equivalent plastic strain rate calculated by relation (1) is distributed along the three principal directions according to generalized Hill anisotropy model).

This expression is a reformulation of the original parabolic time relation, which was developed by fitting the measured yield and creep data. The sinh law for the stress dependence follows the model proposed by Garofalo [2] which unifies the low stress domain, traditionally present in creep tests, and the high stress region, typically involved in the tensile tests. Thus, relation (1) is a unified inelastic deformation type of constitutive equation and it is easy to use in fuel codes.

However, Equation (1) models only the primary creep behavior. Also, it cannot reproduce inverted primary creep, which is sometimes observed at high stresses for a class of particle-strengthened materials, Zr alloys included [3]. A more sophisticated model is needed to capture the effect of microstructural processes underlying the plastic deformation. A model with one internal parameter, as the next level up in order of complexity, is presented below.

2. PROPOSED BACK-STRESS PLASTIC DEFORMATION MODEL

A set of two coupled equations is proposed to describe the plastic deformation of Zircaloy tubes including both the tensile and creep regimes. It is the simplest form that uses the concept of internal variables to represent the microstructural processes occurring during plastic deformation. This feature permits a more realistic modeling of complex loading histories which accounts for previous history. For the creep regime it provides a natural transition from primary to secondary creep and also allows for simulation of inverted primary creep.

The "back stress", σ_b, is included in the model [4] as a macroscopic variable representing the dislocation sub-structure resistance to deformation. Also, particle-strengthening processes [5] that oppose to the plastic deformation, are equally represented by a back stress. The evolution of this back stress is the result of the competition between the opposing strain hardening and recovery processes. Hardening is manifested by increased strength during deformation due to the emerging dislocation sub-structure and to internal defects and impurities, all of which act as obstacles to deformation. Recovery, on the other hand, softens the material during deformation and is due, among other things, to thermal processes that enable dislocations to be released from the walls of the dislocation sub-structure by climb and other mechanisms.

The net stress that dictates the plastic deformation rate is the difference between the applied stress, σ_a, and the back stress introduced before. The constitutive equation for the strain rate is based on the phenomenological plastic strain rate equation, as described in [6] and [7], and is formulated as follows:

$$\frac{d\varepsilon}{dt} = C\exp(-\frac{Q}{kT})\{\sinh[\frac{v_0}{skT}(\sigma_a - \sigma_b)]\}^s \qquad (2)$$

where T is the temperature in K, Q is the activation energy in cal, and k is the gas constant in cal/K (equal to 1.98). The sinh function unifies the low-stress with the high-stress domains of the plastic deformation which according to all previous experience are characterized by a power law and by an exponential law, respectively.

The constitutive equation for the back stress describes the competition between hardening and recovery. The following relation was used to describe the kinetics of these two competing processes:

$$\frac{d\sigma_b}{dt} = \frac{A\, d\varepsilon / dt}{\sigma_b^p} - \frac{B \exp(-\frac{Q_b}{kT})}{T} \sigma_b{}^m \qquad (3)$$

A static recovery term can be added to Equation (2) to represent the static recovery during annealing. Equation (3) is similar to the equation proposed for particle-strengthened materials in [5], where the equation is written in terms of the dislocation density, as:

$$\frac{d\rho}{d\varepsilon} = k - k_2 \rho \qquad (4)$$

However, the relation between the back stress and the dislocation density is not the traditional square root dependence as assumed in [5], but rather a power law with an exponent of 1/3 (the exponent is ½ in the square root expression). In this case, Equation (4) can be re-written as Equation (3). It is interesting to note that Equation (3) can be solved analytically for constant temperature and constant average strain rate. The result is a exponentially decreasing primary creep strain, similar to the Dorn proposed model [8], and which was used by Murty [9], to formulate a primary creep relation for Zr alloys.

3. MODEL PARAMETERS DERIVATION

Two coefficients can be determined from experimental data at steady-state deformation by regression analysis: Q by linear regression of the logarithm of the strain rate versus inverse temperature for the same stress, and v_0 by linear regression of the logarithm of the strain rate versus stress. The value of the s parameter was chosen to be consistent with the low-stress data which indicate a power law with exponent around 5 for dislocation creep. The remaining constants, C, A and B, as well as the initial back stress remain to be determined as fitting parameters of the model.

A pool of data available at SPC, characteristic of stress-relieved cladding, was used to build the model. Creep and tensile tests of either longitudinal or biaxial type were available for unirradiated material, and irradiated material at two fluences. The data was enough to determine the s parameter (see Fig. 1) but not Q. The value for Q was taken approximately equal to the self-diffusion activation energy, as indicated by the vast majority of experimental studies. The other model parameters were fit in order to obtain the best agreement possible with both the creep and tensile data. The following values were obtained for the model parameters and given in Table 1.

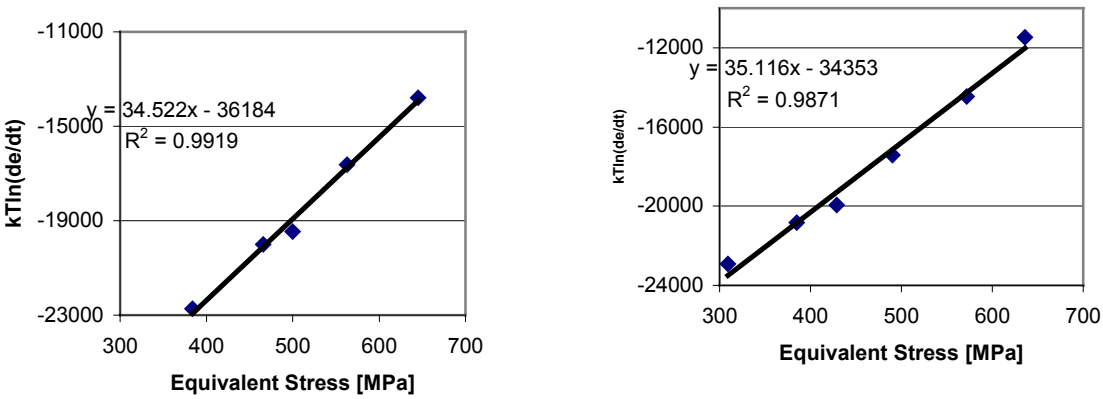

FIG. 1. Linear fit to derive v from the slope at 623 K (left) and 653 K (right).

TABLE 1. MODEL PARAMETERS FOR UNIRRADIATED AND IRRADIATED MATERIAL

	Unirradiated Zry		Irradiated Zry	
			Fluence after 1 irrad. cycle	Fluence after 3 irrad. cycles
C	1.E14		1.E14	1.E14
Q	62000		62000	62000
v_0	**40**		**37**	**34**
s	5	5	5	
A	**3.5E7**		**5.E7**	**4.E8**
B	**3.E21**		**8.E20**	**1.E19**
Q_b	68000		68000	68000
p	2		2	2
m	1		1	1

The bold face values are for the parameters that change with irradiation exposure, and reflect the effect of irradiation hardening on the creep strain rate through v_0 and on the internal dislocation dynamics through the coefficients A and B of the back stress evolution equation.

4. RESULTS

Examples of the good agreement of the calculated and measured creep strain time evolution for unirradiated material are presented in Fig. 2 for uniaxial creep conditions and in Fig. 3 for bi-axial creep conditions. The agreement for the two test conditions, characterized by the hoop stress to axial stress ratio of 0 and 1, respectively, shows that the anisotropy is well represented. The values of R = 2 and P = 1 have been used for the anisotropy coefficients, according to the information on similar Zircaloy-4 material presented in References [9] and [10]. Texture measurements on the irradiated material showed no discernable change from the unirradiated condition. The good agreement for the bi-axial creep tests on Zry-4 cladding irradiated for three cycles are presented in Fig. 4.

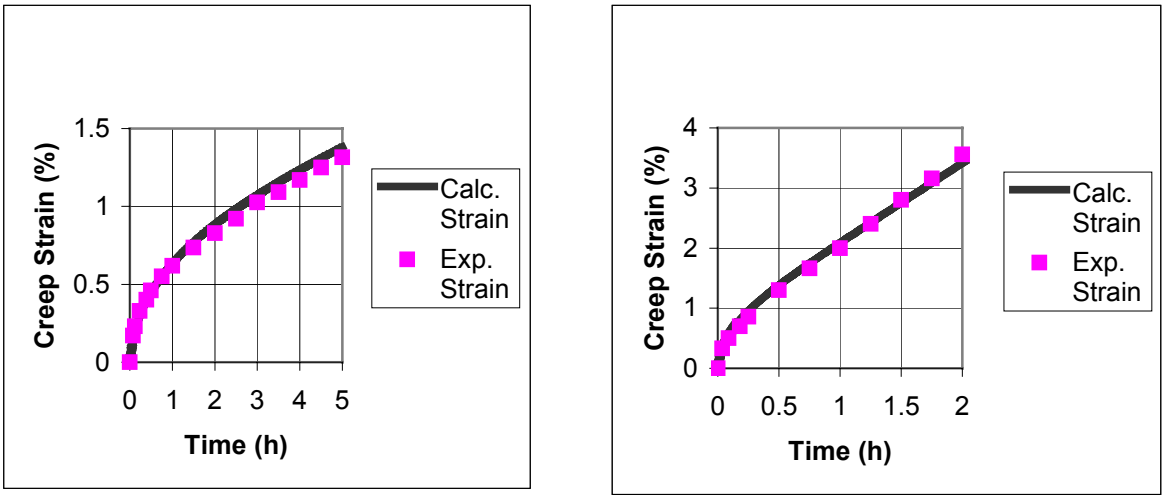

FIG. 2. Unirradiated CWSR Zry, axial creep at 350 °C & 353 MPa (left) and 380 °C & 364 Mpa (right).

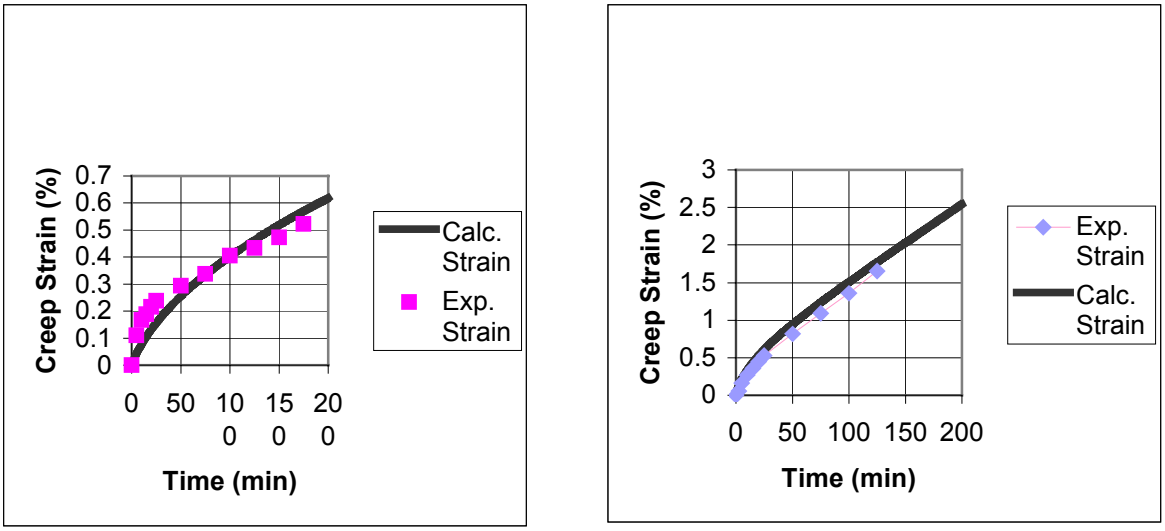

FIG. 3. Unirradiated CWSR Zry bi-axial creep at 350 °C & 324 Mpa (left) and 380 °C & 328 Mpa (right).

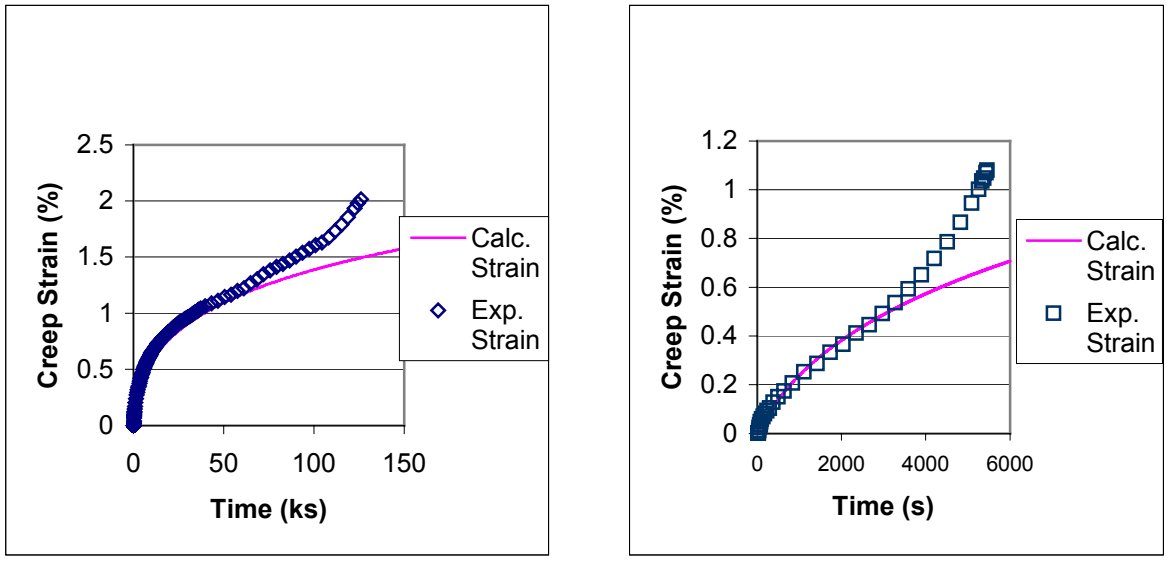

FIG. 4. Irradiated CWSR Zry creep at 350 oC & 514 Mpa (left) and 395 ^{O}C & 477 Mpa (right).

The simulation of the tensile test and its comparison with experimental data is presented in Fig. 5 for unirradiated material and in Figs 6 and 7 for irradiated material. The overall agreement obtained for both the creep and the tensile test conditions shows that the proposed constitutive equation can model the whole range of inelastic deformation.

Figure 8 shows the calculation-measurement comparison for a bi-axial creep test at 382^{0}C and 220 MPa The exposure of the fuel rods from which the sample was taken is lower than in the previous case. Accordingly, the model parameters affected by irradiation are different, as presented in Table 1. Also, it is remarked that the upward trend of the strain curve at large strains is reproduced by calculation. This is due to the inclusion of the geometric feedback on the stress calculation. This implies that larger stresses are generated with increasing strains even if the internal pressure remains constant.

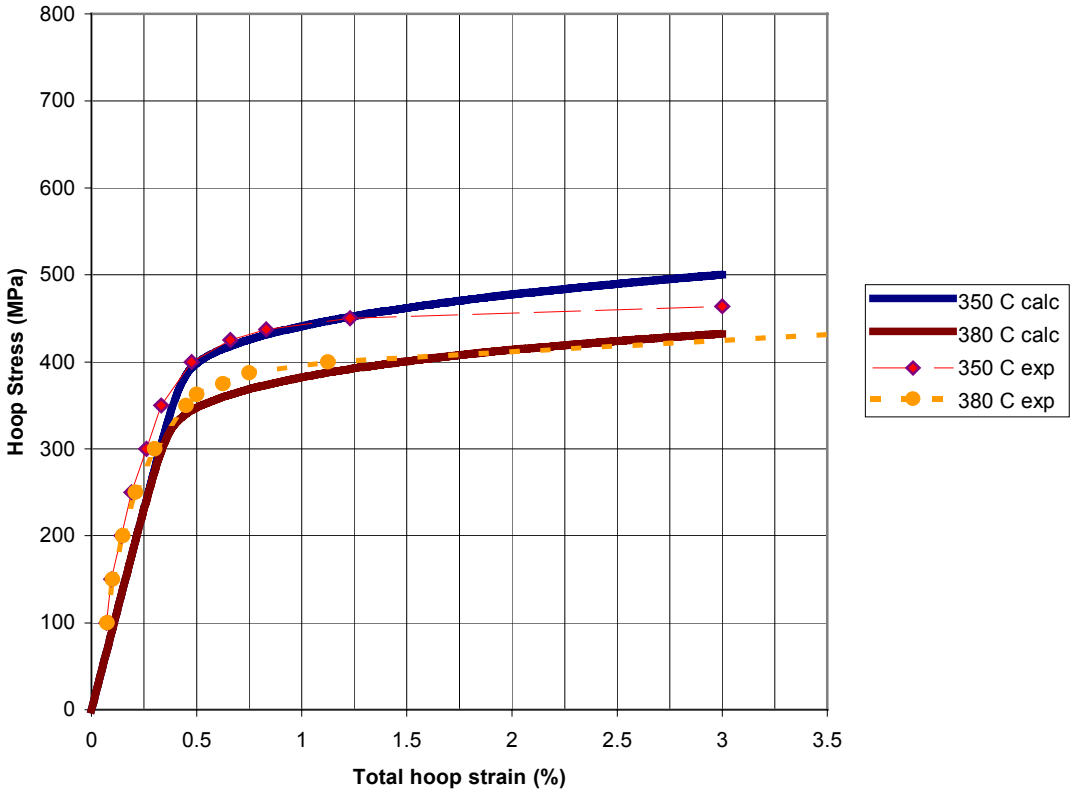

FIG. 5. Bi-axial tensile tests on unirradiated CWSR Zry at 350 °C,and 350 °C and 5 %/h.

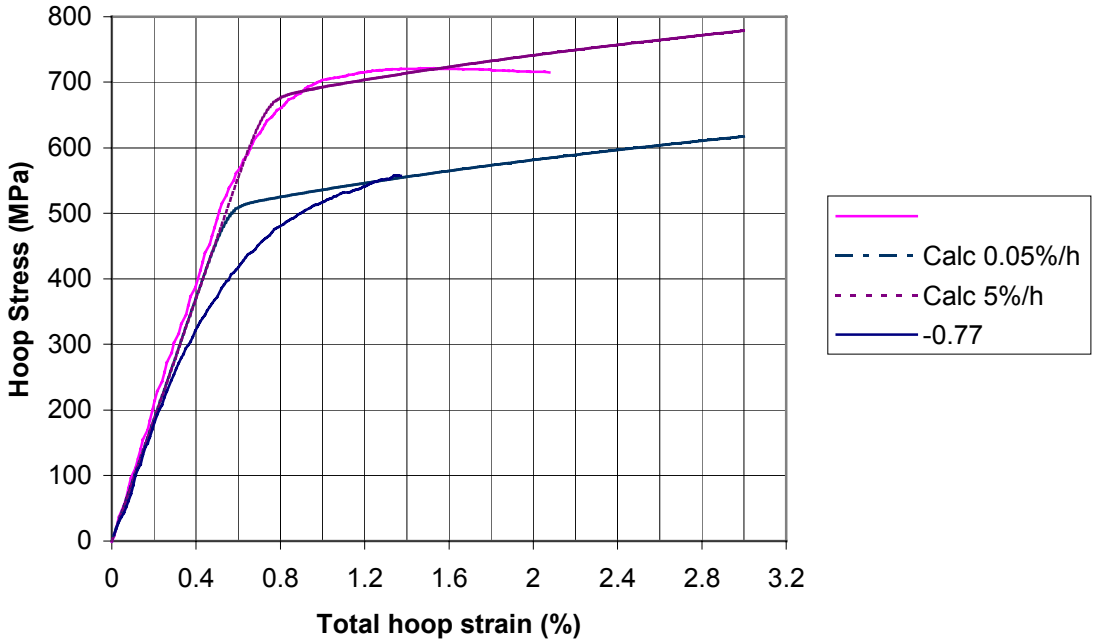

FIG. 6. Bi-axial tensile tests on irradiated CWSR Zry at 350°C.

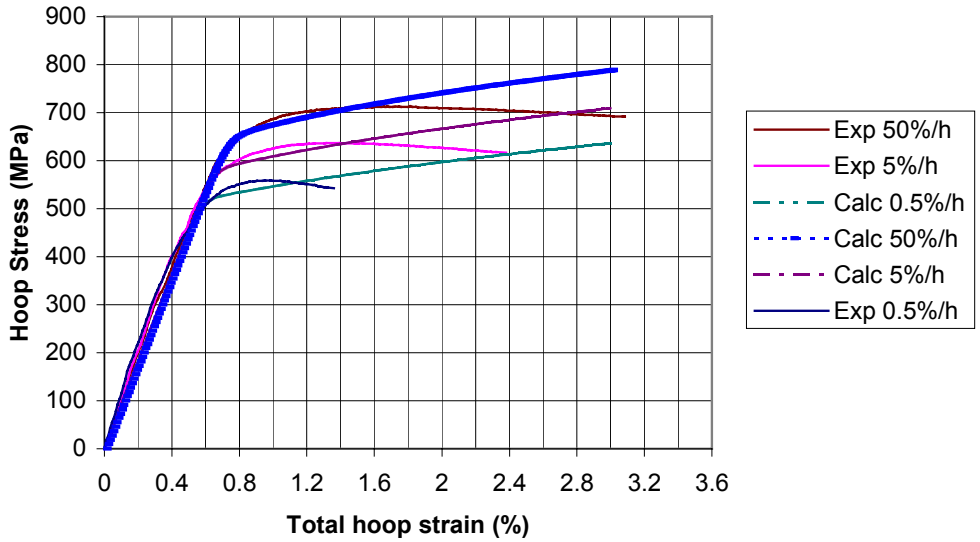

FIG. 7. Bi-axial tensile tests on irradiated CWSR Zry at 380 °C.

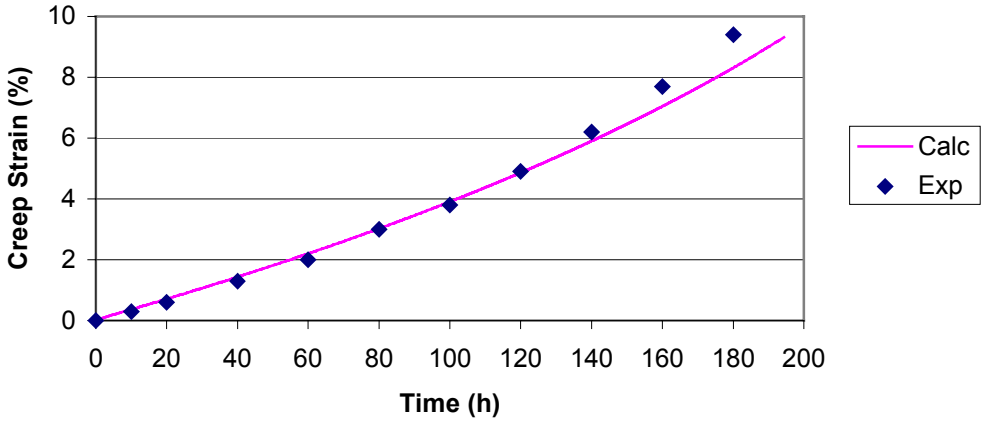

FIG. 8. Bi-axial creep tests on irradiated CWSR Zry at 382 °C and 220 MPa.

REFERENCES

[1] HOPPE, N. E., "Engineering Model for Zircaloy Creep and Growth," ANS/ENS International Topical Meeting on LWR Fuel Performance, Avignon, France, April 21-24 1991.

[2] GAROFALO, F., "Fundamentals of Creep and Creep-Rupture in Metals," MacMillan Co., New York, 1965.

[3] BURTON, B., "Inverse Primary Creep," Philosophical Magazine A, Vol. 48, No. 2, pp. 299-310, 1983.

[4] MILLER, A.K., "Unified Constitutive Equations for Creep and Plasticity," Elsevier Science Publishing Co., New York, 1987.

[5] ESTRIN, Y, MECKING H., "A Unified Phenomenological Description of Work Hardening and Creep Based on One-Parameter Models," Acta Metall., Vol. 32, No. 1, pp. 57-70, 1984.
[6] GIBBS, G.B., "The Thermodynamics of Creep Deformation," Phys. Stat. Sol. 5, 693, 1964
[7] JONAS, J.J., "The Back Stress in High Temperature Deformation," Acta Metall., Vol. 17, pp. 397-405, April 1969.
[8] AMIN, K.E., MUKHERJEE, A.K., and DORN, J.E., "A Universal Law for High_Temperature Diffusion Controlled Transient Creep," J. Mech. Phys. Solids, 18, 413, 1970
[9] MURTY K.L., CLEVINGER G.S., PAPAZOGLU T.P., "Thermal Creep of Zircaloy-4 Cladding," Paper C3/4, 4th SMIRT Int. Conference, San Francisco, Aug. 15-19, 1977.
[10] BATY, D.L., et. al., "Deformation Characteristics of Cold-Worked and Recrystallized Zircaloy-4 Cladding," 6th Int. Symposium "Zirconium in the Nuclear Industry", Vancouver, B.C., 1982
[11] BOUFFIOUX, P., RUPA, N., "Impact of Hydrogen on Plasticity and Creep of Unirradiated Zircaloy-4 Cladding Tubes," 12th Int. Symposium "Zirconium in the Nuclear Industry", Toronto, 1998.

IMPROVEMENT OF THE FPAC CODE

H. IKEDA, T. KIKUCHI, S. ONO
Nuclear Fuel Industries, Ltd,
Osaka, Japan

Abstract

FPAC (fuel performance analysis code) is a thermal and mechanical design code developed by Nuclear Fuel Industries, Ltd. (NFI). NFI has been utilizing FPAC to design the commercial PWR fuel rods, which are manufactured by NFI, or to analyze fuel rod's irradiation behavior. Japanese PWR utilities are planning to increase the discharged burnup limit of fuel assembly to 55GWd/t. Therefore, NFI has improved FPAC to enable to be used to more accurately estimate fuel rod behavior at high burnup. The integral assessment of improved FPAC has been verified from available data including measured centerline temperatures, PIE data and so on, and they cover burnup up to approximately 90GWd/t. The predicted results obtained from the improved FPAC show good agreement with measured data.

1. INTRODUCTION

FPAC (fuel performance analysis code) is a thermal and mechanical design code developed by Nuclear Fuel Industries, Ltd (NFI) [1]. Its integral assessment has been verified from available data, which includes measured fuel centerline temperatures irradiated up to 13 GWd/t and measured fission gas release (FGR) and so on irradiated up to 62 GWd/t [2]. NFI has been utilizing FPAC to design the commercial PWR fuel rods it manufactures, or to analyze fuel rod's irradiation behavior.

Japanese utilities are planning to increase the discharged burnup limit of fuel assembly to 55 GWd/t [3]. Therefore, NFI has improved FPAC to enable it to more accurately estimate the fuel rod behavior at high burnup. The improvements of FPAC are described as follows:

(i) Pellet thermal conductivity degradation with burnup has recently been reported [4]. This phenomenon affects fuel behavior, but it was not considered by FPAC. Furthermore, gap conductance estimation using the gap conductance model was conservative under pellet and cladding interaction (PCI) conditions. Therefore, pellet thermal conductivity degradation is now considered and the gap conductance model has been made more accurate. In addition, some models (including FGR model) that were affected by the introduced pellet thermal conductivity degradation and the modified gap conductance model have been modified.

(ii) Some models, for instance the Gd pellet thermal conductivity, cladding corrosion, and cladding yield strength models had too great a margin for design of fuel rods. These margins have been adjusted.

(iii) Fuel pellets crack due to thermal stress during the power increase at the beginning of irradiation. Then, pellet fragments move toward the gap between pellet and cladding (fuel relocation). The relocated pellet is less stiff than fabricated one [5]. When PCI occurs, fragments are compressed and the relocated diameter is recovered. As a result, pellet stiffness becomes large. The pellet relocation model considered the recovery of relocated diameter, but did not considered the variation of stiffness due to pellet relocation. Therefore, the relocation model has been improved to more accurately simulate the actual relocated pellet behavior. To analyze PCI behavior, the improvement FPAC utilizes the finite element method (FEM).

(iv) Some other models have been modified by PIE data obtained after the present FPAC development.

The integral assessment of improved FPAC has been verified from the available data including measured centerline temperatures, PIE data and so on, and they cover burnup up to approximately 80 GWd/t. The predicted results obtained from the improved FPAC show good agreement with measured data.

This paper describes the main improved models and their modeling way. It also confirms the integrity of the improved FPAC for high burnup data.

2. MODEL DESCRIPTION

Thermal models are mainly modified to more accurately estimate fuel behavior at high burnup. Improvements of main models are as follows:

Model	Improvement
Pellet thermal conductivity	• Ishimoto's model [6] is introduced to consider thermal conductivity degradation due to soluble elements (Gd, FP, Pu). • Consider thermal conductivity degradation with burnup. • The thermal conductivity of a Gd pellet is optimized from the conservative model.
Gap Conductance	• The gap conductance model is optimized from the conservative model under PCI conditions.
Relocation	• Simulate actual relocated pellet behavior such as recovery of relocated diameter and variation of stiffness due to relocation.
FGR	• The dependencies on temperature and burnup are modified.

Other models have also been modified to match PIE data. Modeling of pellet thermal conductivity, gap conductance, relocation and the FGR are summarized below.

2.1. Pellet thermal conductivity

(1) Unirradiated pellet

The thermal conductivity of a UO_2 pellet that dissolves Gd, Pu, and/or soluble FPs is lower than that of pure UO_2 [6,7]. Ishimoto's model is introduced into the improved FPAC to take into account thermal conductivity degradation due to soluble elements.

The model of thermal conductivity degradation due to soluble elements proposed by Ishimoto is expressed by the following equation.

$$k = \frac{kp}{x}\arctan(x) + ke \qquad (1)$$

$$x = \sum_i (Di \cdot yi^{1/2})k_0^{1/2} \qquad (2)$$

where, kp : phonon contribution term (pure UO_2)
ke : electronic contribution term (pure UO_2)
i : soluble element type (i=Gd, Pu, soluble fission products-FPs)
Di : term depending on temperature

(=Di0·exp(Di1·T)) (3)
Di0, Di1 : coefficients
T : temperature
yi : metallic fraction of element i
(Note : Pu is not considered in Ishimoto's report)

When yi approaches zero, eq. (2) agrees with the present models (k=kp+ke; unirradiated).

Di0 and Di1 in eq. (2) are determined from the thermal conductivity of unirradiated Gd pellets, MOX pellets, and SIMFUEL that simulates dissolution of FPs reported by Ishimoto [6] or Lucuta [8]. Figs 1 and 2 compare calculated and measured thermal conductivities for unirradiated Gd pellets and MOX pellets, respectively. They indicate good agreement.

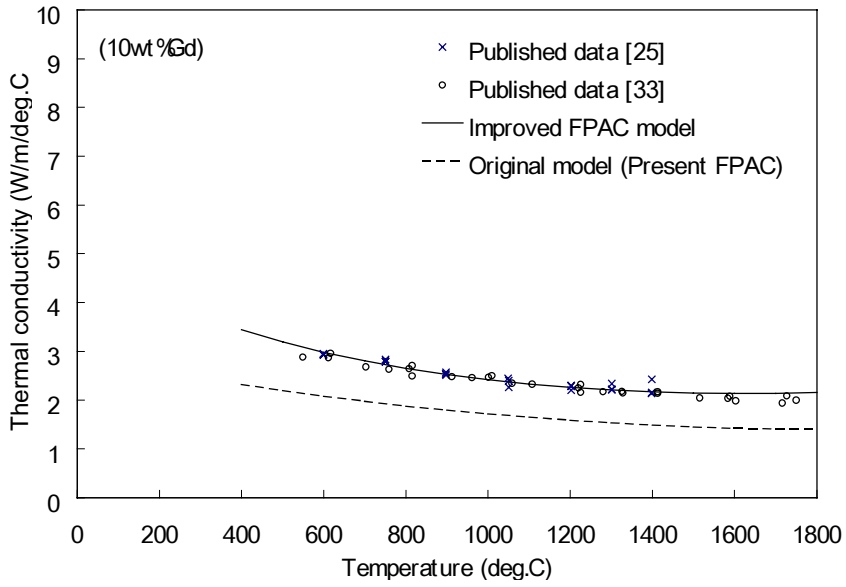

FIG.1. The thermal conductivity of unirradiated Gd pellets.

(2) Irradiated pellet

The thermal conductivity of an irradiated pellet is lower than that of SIMFUEL [4]. These phenomena are mainly due to irradiation induced defects, and recovery of thermal conductivity degradation was observed when the sample was heated to over 900°C [9].

Ishimoto's model proposed by reference 6 does not consider thermal conductivity degradation due to irradiation induced defects. Therefore, its effect is assumed to be similar to those for the soluble elements. Then, new coefficients Dirr0, Dirr1 and function yirr corresponding to the irradiation induced defect are incorporated in eq. (2) and eq. (3). The dependence of Dirr0 or Dirr1 on temperature or burnup does not depend on soluble elements (fuel type). Modified eq. (2) is expressed by the following equation:

$$x = \left(\sum_i Di \cdot yi^{1/2} + Dirr \cdot yirr^{1/2}\right) \cdot k_p^{1/2} \qquad (4)$$

where, Dirr : term depending on temperature
(=Dirr0·exp(Dirr1·T))
Dirr0, Dirr1 : coefficient
yi : function depending on burnup
(Note : yirr is corrected by soluble Gd fraction)

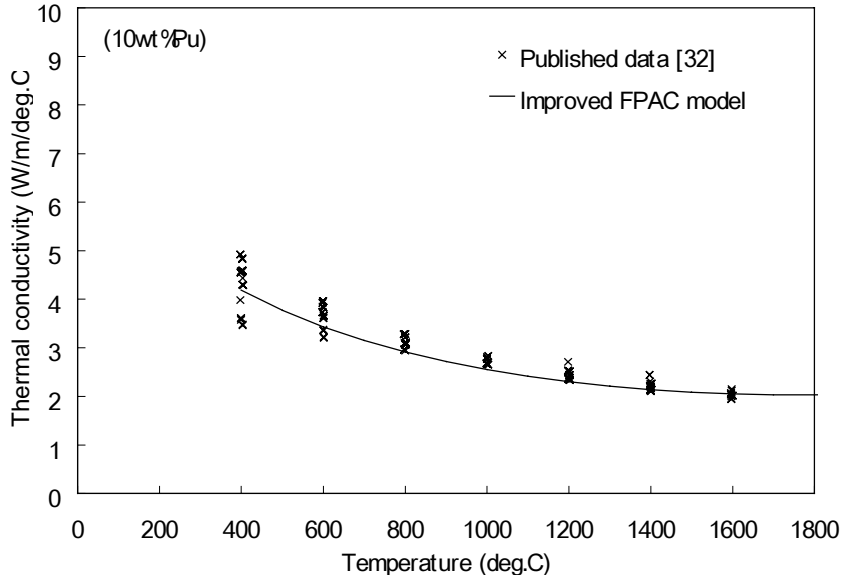

FIG. 2. The thermal conductivity of unirradiated MOX pellets.

Coefficients Dirr0 and Dirr1 are determined from the measured thermal conductivity of irradiated pellets. The databases of thermal conductivity of irradiated pellets are listed in Table1. These databases verify the integrity of the thermal conductivity model. Moreover, the thermal conductivity of more irradiated pellets than others will be measured by the High Burnup Rim Project (HBRP) [10].

TABLE 1. VERIFICATION DATA FOR THERMAL CONDUCTIVITY OF IRRADIATED PELLETS

Data	Burnup (GWd/t)
NFI [4]	61 (UO_2)
NFIR [20]	23 – 60 (UO_2), 21, 47 (Gd)
JAERI [9]	63 (UO_2)
Our experiment*	20, 40, 60 (UO_2), 20, 40, 60 (Gd)
NUPEC [21][22]	39 (UO_2), 28, 29 (Gd)
Our experiment*	10 - 19 (Gd)

Figs 3 and 4 compare the calculated and measured thermal conductivity of an irradiated UO_2 pellet (40 GWd/t) and a Gd pellet (40 GWd/t), respectively, which are obtained as a joint research with NFI and Japanese PWR utilities. Their results indicate good agreement between calculation and measurement.

They also verify that the thermal conductivity model can accurately estimate the thermal conductivity of unirradiated/irradiated pellets independently of pellet type up to high burnup.

* Joint research with NFI and Japanese PWR utilities.

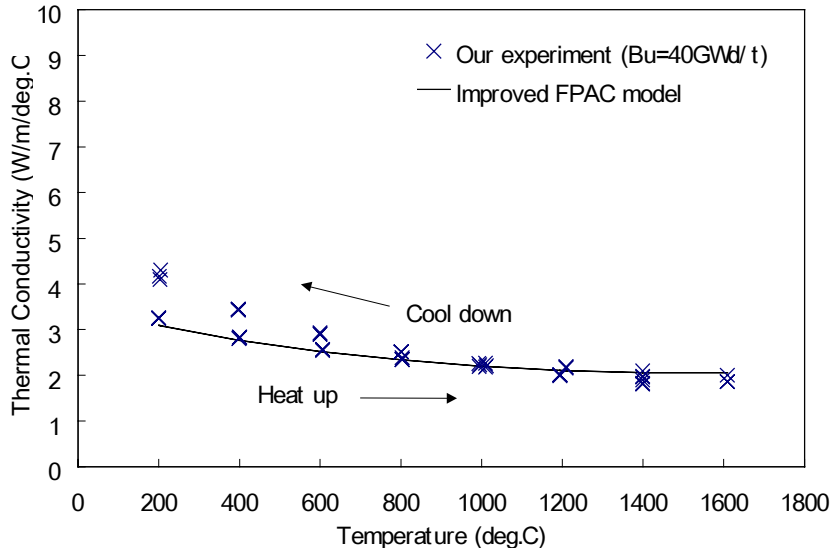

FIG. 3. The thermal conductivity of an irradiated UO_2 pellet.

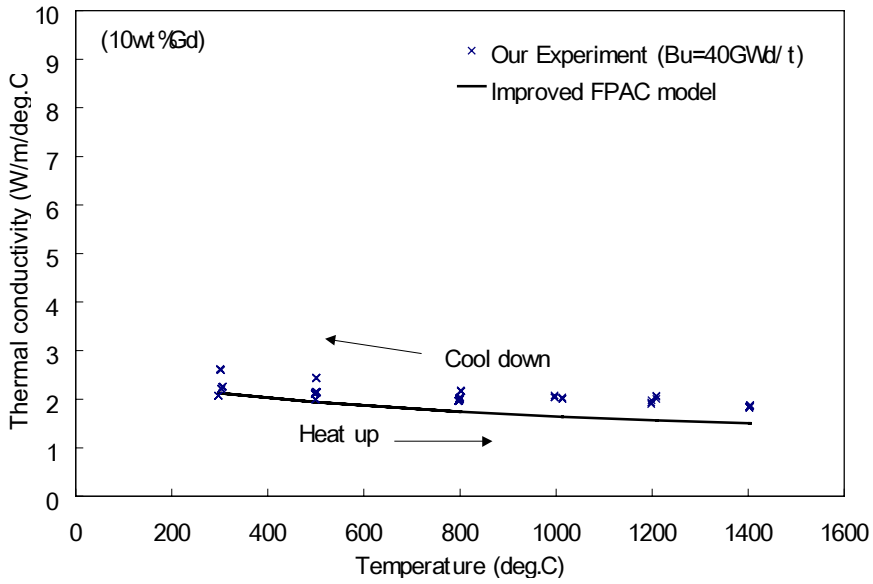

FIG .4. The thermal conductivity of an irradiated Gd pellet.

2.2. Gap conductance model

The simplified Ross & Staute's model [11] is used as the gap conductance model in the present FPAC. Predicted fuel centerline temperature from the present gap conductance model indicates that the predicted fuel centerline temperature becomes higher than the measured value as power density increase under PCI conditions. This tendency means that estimated gap conductance becomes smaller under PCI conditions. Therefore, a more accurate model based on Ross & Staute's model is introduced into the improved FPAC and some coefficients in the model are determined to agree with out-of-pile gap conductance measurement. This modification improves the accuracy of the calculated fuel centerline temperature.

2.3. Relocation model

Pellet fragments resulting from thermal stress at the beginning of irradiation move toward the gap between pellet and cladding (fuel relocation) as pellet diameter increases. The relocated pellet's stiffness is smaller than the fabricated one's. When PCI occurs continuously under steady state irradiation, parts of the fragments are compressed. As a result, pellet stiffness becomes large according to the recovered relocated diameter. The pellet relocation model in the present FPAC considers the recovery of relocated diameter, but it does not consider the variation of stiffness due to pellet relocation. Therefore, the relocation model is modified to simulate the variation of stiffness due to relocation. Furthermore, the recovery of relocated diameter is assumed to be accompanied by a partial recovery of compressed relocation strain.

Recovery of relocated diameter and the variation of stiffness are calculated below. The relocation strain is recovered by the compressive strain when PCI occurs. The compressive strain is expressed by the following equation.

$$\varepsilon^{i}_{comp} = \varepsilon^{i}_{r} - (\varepsilon^{i}_{th} + \varepsilon^{i}_{dens} + \varepsilon^{i}_{swel}) \text{ (r-direction)} \quad (5)$$

where, i : time step

ε^{i}_{r} : strain increment at i

ε^{i}_{comp} : compressive strain increment at i

ε_{th} : thermal strain increment at i

ε_{dens} : densification strain increment at i

ε_{swel} : swelling strain, which contributes to recovery of relocation at i.

Due to the compressive strain, it is assumed that partial relocated strains are recovered and remaining relocated strain acts to push the cladding out. The relocated strain at step i is expressed by the following equation.

$$\varepsilon^{i}_{rel} = \varepsilon^{i-1}_{rel} - \varepsilon^{i}_{comp} \times \alpha \text{ (r-direction)} \quad (6)$$

where, ε^{i}_{rel} : relocation strain

ε^{i}_{comp} : compressive strain

α : coefficient

The compressive strain calculation considers the variation of stiffness. The stress/strain relation that considers the variation of stiffness due to relocation is expressed by the following equation:

$$\{\varepsilon\}=[C]\{\alpha\} \quad (7)$$

When relocation strain exists, the C matrix is expressed by the following equation:

$$[C]=\begin{pmatrix} \frac{1}{E_r} & -\frac{\nu_{rz}}{E_0} & -\frac{\nu_{r\theta}}{E_\theta} & 0 \\ -\frac{\nu_{rz}}{E_0} & \frac{1}{E_0} & -\frac{\nu_{z\theta}}{E_\theta} & 0 \\ -\frac{\nu_{r\theta}}{E_\theta} & -\frac{\nu_{z\theta}}{E_\theta} & \frac{1}{E_\theta} & 0 \\ 0 & 0 & 0 & \frac{E_0}{2(1+\nu)} \end{pmatrix} \quad (8)$$

And, when relocation strain is completely recovered, C matrix is expressed by the next equation:

$$[C]=\begin{pmatrix} \frac{1}{E_0} & -\frac{\nu}{E_0} & -\frac{\nu}{E_0} & 0 \\ -\frac{\nu}{E_0} & \frac{1}{E_0} & -\frac{\nu}{E_z} & 0 \\ -\frac{\nu}{E_0} & -\frac{\nu}{E_0} & \frac{1}{E_0} & 0 \\ 0 & 0 & 0 & \frac{E_0}{2(1+\nu)} \end{pmatrix} \quad (9)$$

The elastic modulus and the Poisson ratio are expressed by the following equation.

$$E_r = E_0 \times \{a + (1 - a) \times \exp(b \times \varepsilon)\} \quad (10)$$

$$E_y = c \times E_r \quad (11)$$

$$\nu_{rz}, \nu_{z\theta}, \nu_{r\theta} << \nu \quad (12)$$

where, ε : relocation strain
E_0 : elastic modulus of solid pellet
E_r, E_θ : elastic modulus of relocated pellet
ν : Poisson ratio of solid pellet
$\nu_{rz}, \nu_{z\theta}, \nu_{r\theta}$: Poisson ratio of relocated pellet
a,b,c : coefficients

When the tensile stress acts against the pellet, the elastic modulus after relocation generated is assumed to be small.

2.4. FGR

KWU FGR model [12] is used in the improved FPAC in the same way as the present FPAC. The basic concept of the KWU model is to calculate the FP gas concentration at the grain boundary and the amounts of released FP gas from the grain boundary depends on temperature, burnup and open porosity. The KWU model is expressed by the following equation.

$$\frac{df(t)}{dt} = \alpha \cdot K1 \cdot K2 \cdot K3 \cdot g(t) \quad (13)$$

where, f(t) : amount of FP gas release from grain boundary
g(t) : FP gas concentration in grain boundary
t : time
K1 : function depending on temperature
K2 : function depending on temperature and burnup
K3 : function depending on porosity
α : coefficient (used for MOX fuel)

The improved FPAC considers the thermal conductivity degradation of the pellets and so on, as mentioned. Therefore, functions K1 and K2 are modified to agree with PIE data.

TABLE 2. SUMMARY OF THE VERIFICATION DATA (OBTAINED AFTER DEVELOPMENT OF THE PRESENT FPAC)

Reactor(Program)	Fuel type	Rod average burnup (GWd/t)	Measurements(*)				
			FT	FGR	RD	PD	OT
Ohi1 (H/B Demonstration) [23]	17	42～48		X	X	X	X
Ohi2 (Gd Demonstration) [23]	17(UO_2,Gd)	21～25(Gd),32～35(UO_2)		X	X	X	X
BR3 (TRIBULATION) [16]	17	20～56		X	X		
BR3 (HBEP) [20]	17	25～69		X	X	X	
BR3 (GAIN) [24]	17(Gd)	8～57(Gd)		X	X		
Oconee [25]	15(UO_2,Gd)	45～47(Gd),6(UO_2)		X		X	X
BR3 [26]	17(Gd)	13(Gd)		X	X	X	
DR3 [26]	17(Gd)	13(Gd)	X	X			
Gravelines [27]	17	46～58		X	X	X	X
Halden (IFA562) [15]	-	～87	X	X			
Halden (IFA559) [28]	17(UO_2,MOX)	～30(UO_2,MOX)	X	X			
Halden (IFA596) [18]	17(small diameter)	～60(UO_2,MOX)	X	X			
Halden (IFA515.10)	-	53～58(UO_2,Gd)	X				
Halden (IFA539)	17(Gd)	～7.3	X	X			
Siloe [29]	17(Gd)	2～5	X	X			
DR-3(RISO FGP3) [17]	17(Gd)	～41	X	X	X		
Ohi2 (High Performance) [23]	17	33～36		X	X	X	X
Takahama3 [30]	17(UO_2,Gd)	31～46(UO_2), 25～37(Gd)		X	X	X	X
U.S.commercial Reactor [31]	17	～42		X	X	X	X
BR3 (PRIMO1) [32]	17(MOX)	～46		X	X	X	X
St.Laurent B1 [32]	17(MOX)	～43		X	X	X	X
Gravelines4 [32]	17(MOX)	～52		X	X	X	X

(*) FT : Fuel centerline temperature.
FGR : Fission gas release rate, Rod internal pressure.
RD : Rod diameter.
PD : Pellet density; OT : Oxide thickness.

3. BENCHMARK RESULTS

The integrity of the fuel centerline temperature for present FPAC has been verified from available data, mainly from the irradiated Halden reactor (maximum burnup is 13 GWd/t [13]). The integrity of the FGR and so on applied to the present FPAC has also been verified from BR-3 (maximum burnup is 62 GWd/t) [14] and so on.

The integrity of the improved FPAC is also verified from available data above 30, including IFA562.2 (Halden Ultra high burnup UO_2 fuel, maximum burnup is 87 GWd/t) [15], TRIBULATION [16], domestic or foreign programs and so on. As a result, the integrity is verified for UO_2 fuel, Gd fuel and MOX fuel. Verified data obtained after development of the present FPAC are listed in Table 2. The integrity of fuel centerline temperature, FGR and rod diameter are verified as described below.

3.1. Fuel centerline temperature

The integrity of the fuel centerline temperature for high burnup fuel including IFA562.2, RISO-FGP3 [17] is also verified.

Fig. 5 compares predictions and measurements for IFA562.2_16 through its life. Predictions show good agreement with measurements. Fig. 7 shows the temperature difference between predictions and measurements for IFA562.2_16, IFA515.10 (Gd fuel) and IFA596 (UO_2 and MOX fuels) [18] through their lives. These results show that temperature differences and deviations are small.

Fig. 6 compares predictions and measurements for all verified data. Predictions show good agreement with measurement within small deviation.

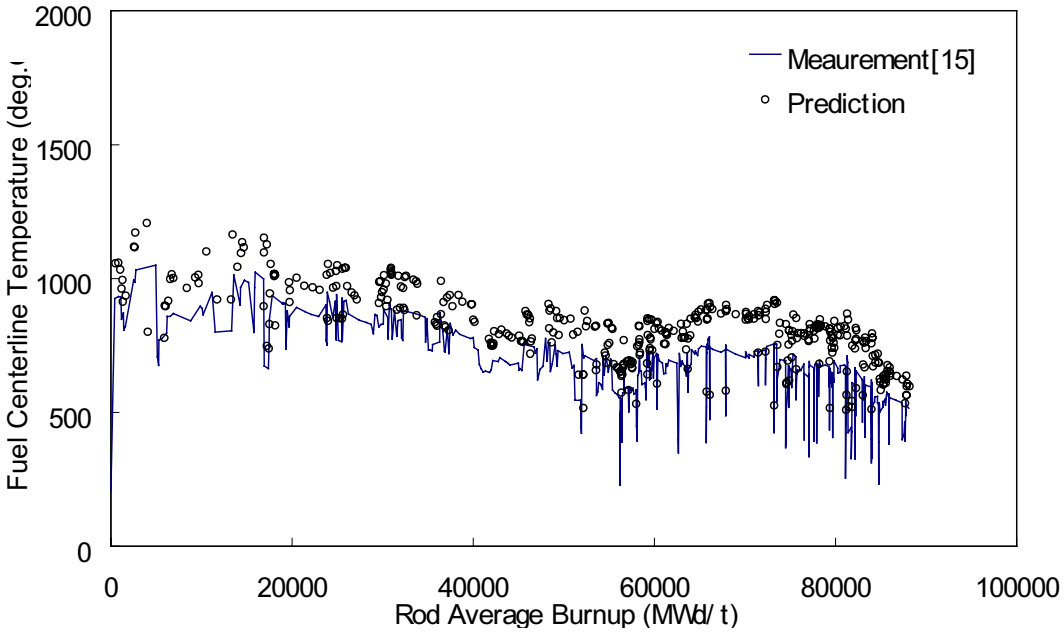

FIG .5. Predicted and measured fuel centerline temperature for IFA562.2_16 through the life.

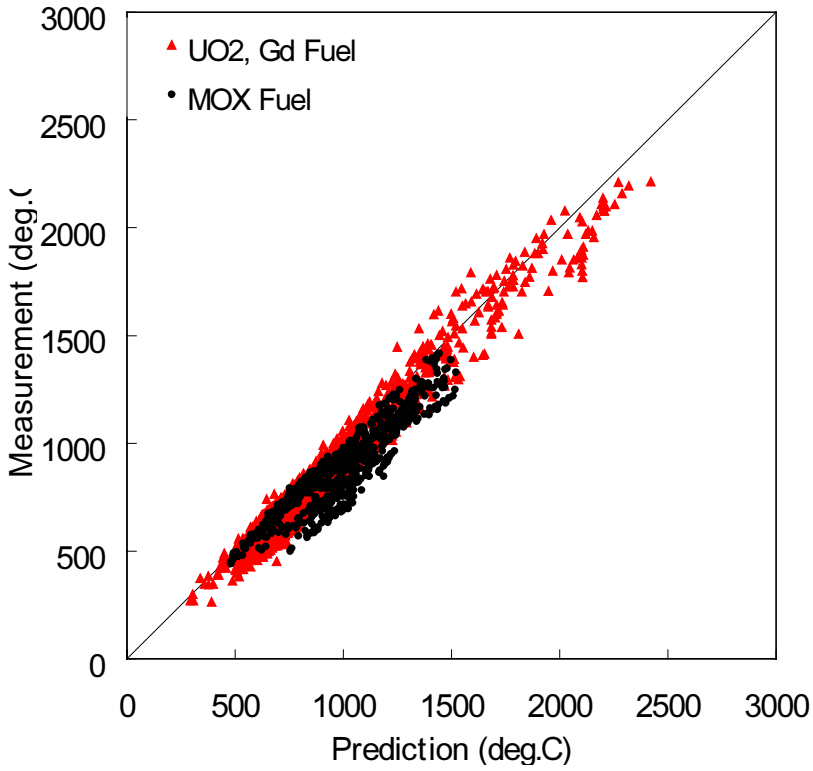

FIG .6 Predicted and mesured fuel centerline temperature for all verified data.

The RISO FGP3 project measured the fuel centerline temperature during bump irradiation. According to the improved FPAC analysis, PCI strength increases in proportion to power density increase. Fig. 8 shows two cases of temperature difference between predictions and measurements. One prediction is calculated from a present gap conductance model introduced in the improved FPAC, and the other is calculated from the modified gap conductance model. This result shows that the temperature difference calculated by the modified gap conductance model is small during bump irradiation. Conversely, the temperature difference calculated by the present gap conductance model increases in proportion to power density increase.

From the results, thermal models including the pellet thermal conductivity model and the gap conductance model are able to predict the fuel centerline temperature up to approximately 90 GWd/t.

3.2. Fission gas release

The integrity of FGR is verified from available data including TRIBULATION, HBEP TASK3 [19] and so on.

Fig. 9 compares predictions and measurements. Predictions show good agreement with measurements within small deviation. These results show that the modified FGR model is able to predict FGR for high burnup fuel.

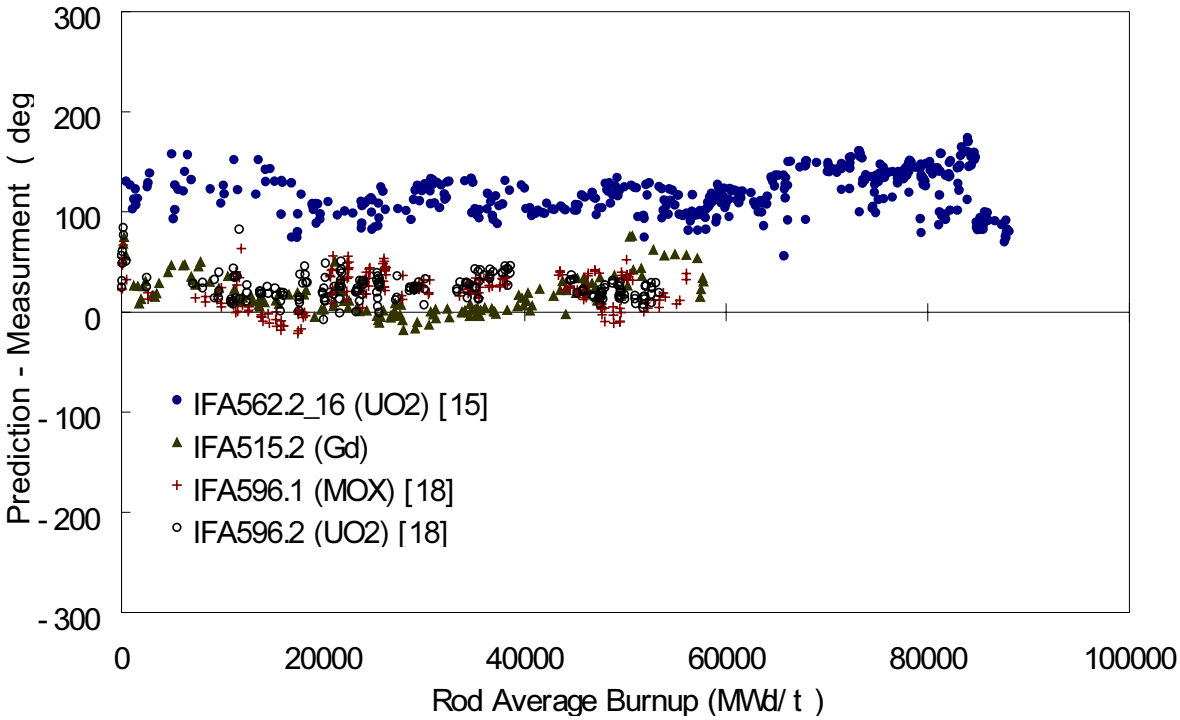

FIG .7. Fuel centerline temperature difference through the lives.

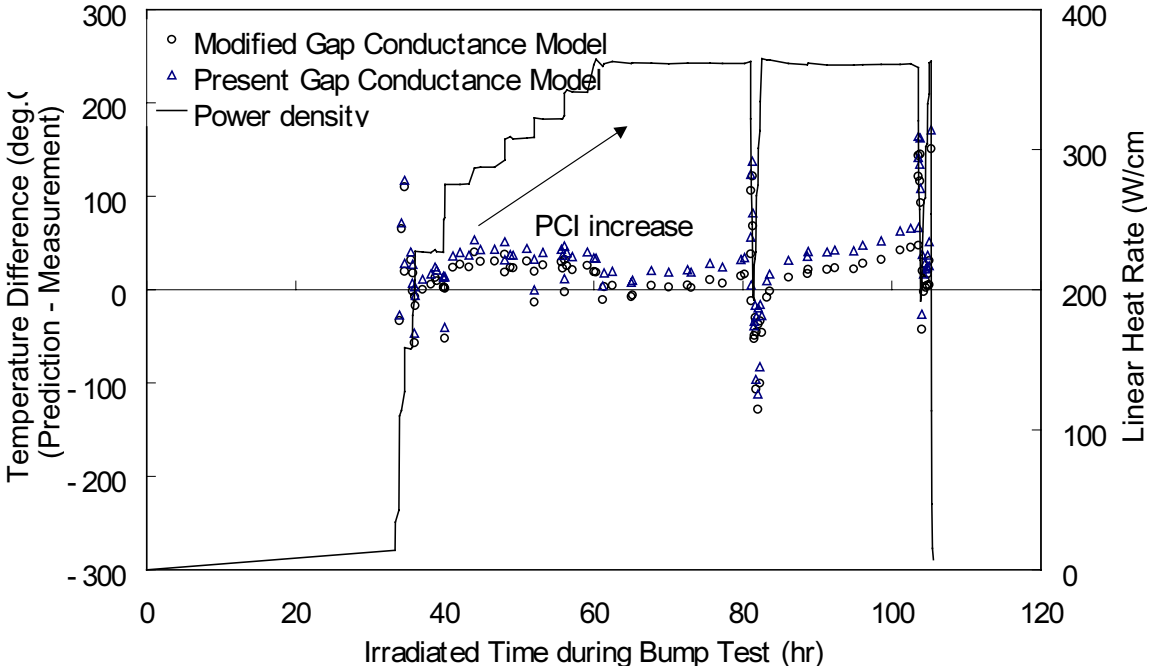

FIG .8. Fuel centerline temperature difference compared by the gap conductance model [17].

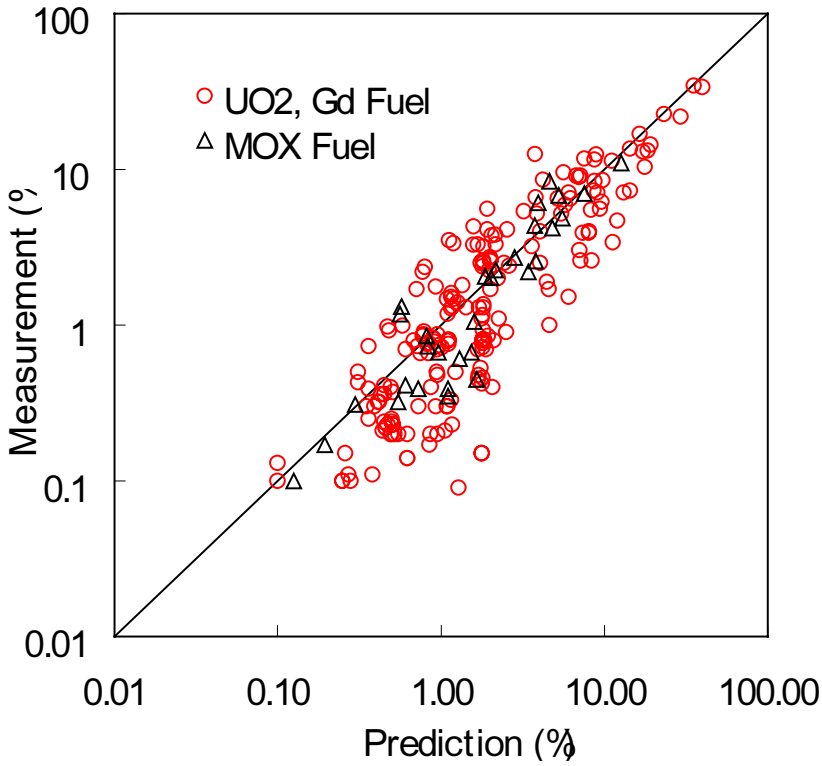

FIG .9. Predicted and measured FGR..

3.3. Rod diameter

Rod diameter is calculated from the result of interactions between models, for instance fuel temperature, internal pressure, relocation, cladding creep, swelling and so on.

The integrity of rod diameter prediction is verified from available data including TRIBULATION and so on .Fig. 10 shows the difference between predicted and measured creep down (rod diameter decrease) with burnup. Predictions show good agreement with measurements within small deviation for any burnup. These results verify the integrity of the models in assessing the interactions during the irradiation.

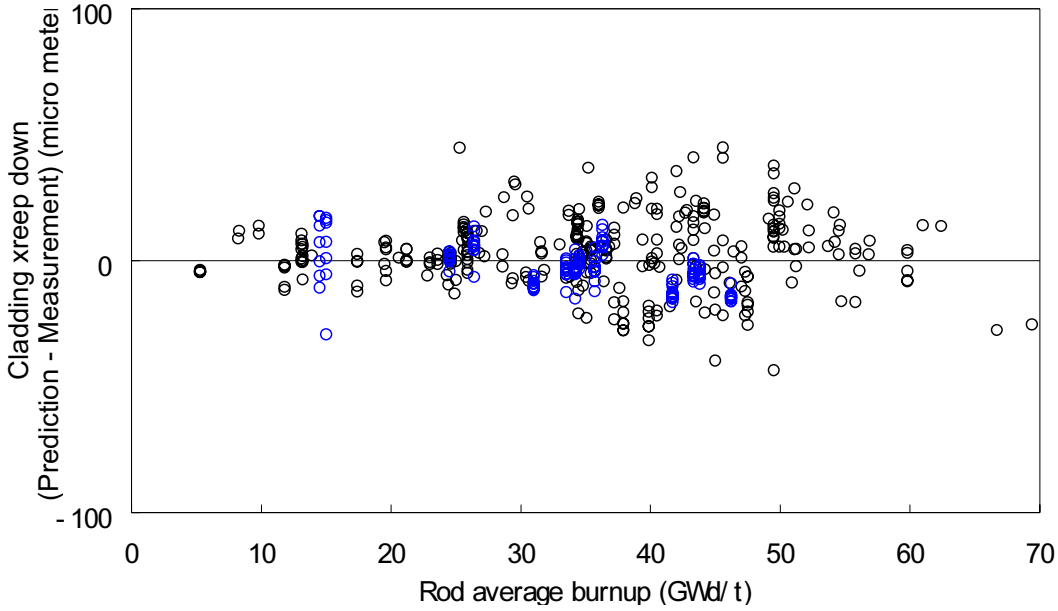

FIG .10. Predicted and measured cladding creep down.

4. CONCLUSION

NFI has improved the thermal and mechanical code (FPAC) for design of high burnup fuel. The improvements take into account the pellet thermal conductivity degradation with burnup and modify other models to increase their accuracy for high burnup fuel.

Ishimot's model is introduced into the improved FPAC to consider pellet thermal conductivity degradation due to soluble elements such as Gd, Pu, FPs. Moreover, the effect of pellet thermal conductivity degradation due to irradiation induced defects is added to Ishimoto's model. As a result, calculated pellet thermal conductivity for unirradiated/irradiated pellets shows good agreement with measured value independently of pellet type. Other models including the gap conductance model and the FGR model are also modified.

Integral assessment of the improved FPAC is verified from the available data covering burnup up to approximately 90GWd/t. Predictions using the improved FPAC shows good agreement with measurements.

ACKNOWLEDGEMENTS

Some irradiation experiments had been performed as a joint research with Japanese PWR utilities and authors would appreciate their grateful cooperation.
The Kansai Electric Power Co., Inc.
Hokkaido Electric Power Co., Inc.
Shikoku Electric Power Co., Inc.
Kyushu Electric Power Co., Inc.
Japan Atomic Power Co., Inc.

Authors would also appreciate N. Sugitomo and M.Chiyonobu of The Japan Research Institute, Ltd.

REFERENCES

[1] K.Mori et al., IAEA Technical Committee Meeting on Fission Gas Release and Fuel Rod Chemistry Related to Extended Burnup, Pembroke, Ontario, Canada
[2] Fuel performance analysis code (FPAC), NFK-8011 Rev.4, 1988 (Japanese)
[3] K.Yamate et al., International Topical Meeting on Light Water Reactor Fuel Performance, Portland, Oregon, 1997
[4] K.Ohira et al., International Topical Meeting on Light Water Reactor Fuel Performance, Portland, Oregon, 1997
[5] R.Williford et al., PNL-SA-8637, 1980
[6] S.ISHIMOTO et al., J.Nucl.Sci.Tech.31, 1994
[7] R.L.Gibby, J.Nucl.Mat.38, 1971
[8] P.G.Lucuta et al., J.Nucl.Mat.217, 1994
[9] J.Nakamura et al., IAEA-TECDOC-1036, 1998
[10] M.Kinoshita et al., International Topical Meeting on Light Water Reactor Fuel Performance, Park City, Utah, 2000
[11] A.M.Ross et al., AECL-1522, 1962
[12] W.Hering, J.Nucl.Mat.114, 1983
[13] G.H.Chalder, 'Long Term Fuel Temperature Behaviour in Pressurized Fuel Rods', 1975
[14] M.G.Balfour et al., WCAP-10238, 1982
[15] L.C.Bernard et al., International Topical Meeting on Light Water Reactor Fuel Performance, La Grange Park, Illinois, 2000
[16] M.Lippens et al., 'Final Report', TR89/79/, 1989
[17] 'The Third RISO Fission Gas Project Final Report: The Project', RISO-FGP3-FINAL, Pt.1, 1991
[18] JAERI-Tech 97-066, 1998 (Japanese)
[19] J.O.Barner, 'High Burnup Effects Program – Final Report', HBEP-61, 1990
[20] S.K.Yagnik, International Topical Meeting on Light Water Reactor Fuel Performance, La Grange Park, Illinois, 2000
[21] 'A Report regarding the Verification Tests of Improvement Technology (related to High Burnup Fuel) for LWR', 1996 (Japanese)
[22] 'A Report regarding the Verification Tests of Improvement Technology (related to High Burnup Fuel) for LWR', 1999 (Japanese)
[23] K.Mori et al., International Topical Meeting on Light Water Reactor Fuel Performance, West Palm Beach, Fl, 1994
[24] P.Blanpain et al., 'GAIN FINAL REPORT', GN89/48, 1982
[25] 'NFI Lead-Used Advanced PWR Fuel Assembly', NFK-8099, 1994 (Japanese)
[26] K.Kawanishi et al., 93EHPG, 1993

[27] M.MOREL et al., IAEA Technical Committee Meeting on Fuel Performance at High Burnup for Water Reactor, 1990
[28] H.Kuwahara et al., 91EHPG, 1991
[29] M.Bruet et al., ANS Topical Meeting on Light Water Reactor Fuel Performance, 1985
[30] 'A Report regarding the Verification Tests of Improvement Technology (related to High Burnup Fuel) for LWR', 1998 (Japanese)
[31] K.Goto et al., International Topical Meeting on Light Water Reactor Fuel Performance, Park City, Utah, 2000
[32] 'Mechanical and Thermal Design for MOX Fuel', NFK-8100 rev.3, 1988 (Japanese)
[33] M.Hirai, J.Nucl.Mat.173, 1990

OVERALL MODELS AND EXPERIMENTAL DATABASE FOR UO_2 AND MOX FUEL INCREASING PERFORMANCE

L.C. BERNARD, P. BLANPAIN
FRAMATOME, Lyon, France

Abstract

COPERNIC is an advanced fuel rod performance code developed by Framatome. It is based on the TRANSURANUS code that contains a clear and flexible architecture, and offers many modeling possibilities. The main objectives of COPERNIC are to accurately predict steady-state and transient fuel operations at high burnups and to incorporate advanced materials such as the Framatome M5-alloy cladding. An extensive development program was undertaken to benchmark the code to very high burnups and to new M5-alloy cladding data. New models were developed for the M5-alloy cladding and the COPERNIC thermal models were upgraded and improved to extend the predictions to burnups over 100 GWd/tM. Since key phenomena, like fission gas release, are strongly temperature dependent, many other models were upgraded also. The COPERNIC qualification range extends to 67, 55, 53 GWd/tM respectively for UO_2, UO_2-Gd_2O_3, and MOX fuels with Zircaloy-4 claddings. The range extends to 63 GWd/tM with UO_2 fuel and the advanced M5-alloy cladding. The paper focuses on thermal and fission gas release models, and on MOX fuel modeling. The COPERNIC thermal model consists of several sub-models: gap conductance, gap closure, fuel thermal conductivity, radial power profile, and fuel rim. The fuel thermal conductivity and the gap closure models, in particular, have been significantly improved. The model was benchmarked with 3400 fuel centerline temperature data from many French and International Programs. There are no measured to predicted statistical biases with respect to linear heat generation rate or burnup. The overall quality of the model is state-of-the-art as the model uncertainty is below 10 %. The fission gas release takes into account athermal and thermally activated mechanisms. The model was adapted to MOX and Gadolinia fuels. For the heterogeneous MOX MIMAS fuels, an effective burnup is used for the incubation threshold. For gadolinia fuels, a scaled temperature effect is used. The Framatome steady-state fission gas release database includes more than 290 fuel rods irradiated in commercial and experimental reactors with rod average burnups up to 67 GWd/tM. The transient database includes close to 60 fuel rods with burnups up to 62 GWd//tM. The hold time for these rods ranged from several minutes to many hours and the linear heat generation rates ranged from 30 kW/m to 50 kW/m. The quality of the fission gas release model is state-of-the-art as the uncertainty of the model is comparable to other code models. Framatome is also greatly concerned with the MOX fuel performance and modeling given that, since 1997, more than 1500 MOX fuel assemblies have been delivered to French and foreign PWRs. The paper focuses on the significant data acquired through surveillance and analytical programs used for the validation and the improvement of the MOX fuel modeling.

1. INTRODUCTION

COPERNIC [1] is the advanced Framatome fuel rod performance code, based on the TRANSURANUS [2] code. COPERNIC has been recently improved to take into account new data at high burnup, on mixed oxide fuels, and on the Framatome M5-alloy [3]. New or upgraded models have been developed. The focus of this paper is on thermal, fission gas release, and mixed oxide modeling.

Section 2 presents the new improvements that were needed for good temperature prediction on high burnup data for UO_2 [4], MOX [5], and gadolinia [6] fuels, and data at ultra-high burnup [7]. A new model is derived for fuel thermal conductivity in order to predict well all data. The rim model for temperature degradation inside the pellet rim at high burnup is upgraded. A simple

and efficient gap closure model is derived. The validation of the full thermal model on the Framatome database is then presented.

Section 3 presents the fission gas release model. This model needed to be upgraded as fission gas release greatly evolves with temperature. It includes key phenomena for fission gas release: athermal and thermal release, rim model for fission gas release, steady-state and transient regimes, diffusion and burst effect release, UO_2 and mixed oxide fuels. The COPERNIC fission gas release model have been described in part [1,8,9] and will be presented in detail elsewhere [10]. The model parameters are upgraded because of the new thermal model. Also, the rim model for fission gas release is upgraded to be consistent with the temperature rim model, and the modeling of the MOX fission gas release is refined to include differences in the MOX microstructures according to the MOX type.

2. THERMAL MODEL

2.1. Fuel thermal conductivity

The degradation of fuel conductivity with burnup is a key effect that must be addressed to accurately predict high burnup fuel. Many works have been undertaken to assess this effect, but here is still a need for further progress. Two fuel conductivity relationships have been widely used, namely, the Lucuta *et al.* [11] relationship and the HALDEN [7] relationship. The prediction of fuel conductivity degradation with burnup differs somewhat between these two relationships, as shown on Figure 1.

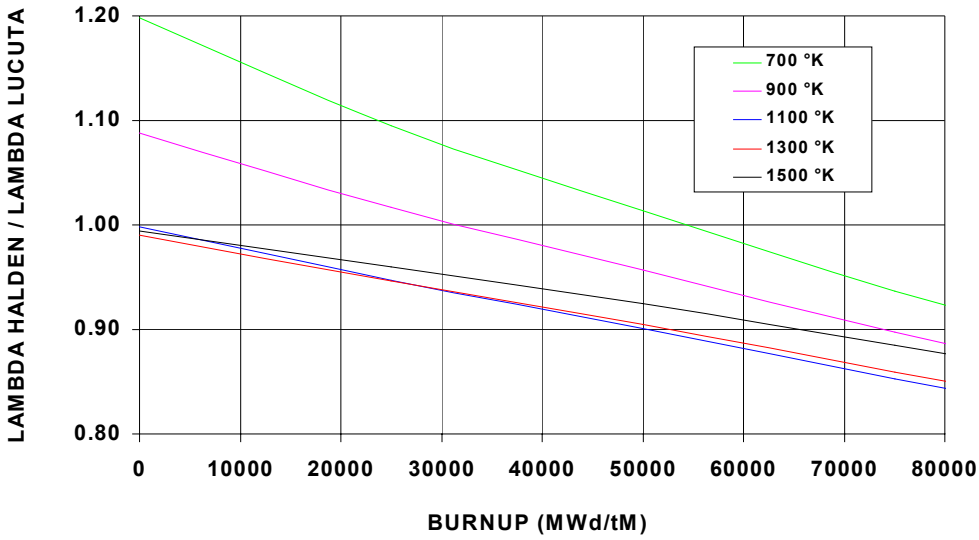

FIG. 1. Comparison between the UO_2 pellet thermal conductivities of HALDEN [7] and of Lucuta et al. [11].

This difference is reflected in the prediction of experiments at high burnup. Two most valuable sets of data were obtained from the French Commissariat à l'Energie Atomique (CEA) EXTRAFORT [4] experiment and from the Ultra-High-Burnup HALDEN IFA-562.2-16 experiment [7]. In the EXTRAFORT experiment, a rodlet with a burnup of 62 GWd/tM was re-fabricated from a rod that was irradiated for 5 cycles in a French PWR reactor and re-irradiated in the CEA OSIRIS test reactor at several power levels. The IFA-562.2-16 rod was

irradiated in the HALDEN reactor up to a very high burnup, greater than 100 GWd/tM. The EXTRAFORT centerline temperatures were well predicted with the Lucuta *et al.* relationship but were under-predicted [4] by up to 120°C with the HALDEN relationship. On the other hand, most HALDEN data are of course well predicted with the HALDEN relationship derived from HALDEN data.

A unique and simple relationship that matches both data sets well was developed for the COPERNIC code. This relationship has the form:

$$\lambda_{100\%} = \left(A + BT + C\beta + Df(T)\right)^{-1} + g(T)$$

where $\lambda_{100\%}$ is the 100% dense UO_2 fuel conductivity, β is burnup, and T is temperature. The porosity correction for the fuel conductivity is taken from the literature [12]. The function $f(T)$ is the radiation damage term derived by Lucuta *et al.* [11] that is important at low temperatures and $g(T)$ represents the electronic conductivity. The A and B coefficients are those of the Harding and Martin's [13] relationship for unirradiated UO_2. The C and D coefficients were obtained with centerline fuel temperature data where the pellet is in contact with the cladding, i.e. data that do not depend upon gap closure. Figure 2 shows that the COPERNIC and the Lucuta *et al.* relationships are quite close. Overall, the COPERNIC relationship predicts a slightly higher degradation with burnup.

2.2. Rim model

To achieve good agreement between model predictions and measurements, it was important to take into account specific features of the HALDEN heavy-water boiling reactor, such as specific radial power profiles [14]. HALDEN radial power profiles are typically flatter at high burnups than those in PWR's. As a result and from our understanding of the rim structure that develops in the rim region at high burnups (the so-called rim effect), the width of the rim must be higher in a fuel irradiated in HALDEN than in a fuel irradiated in a PWR. A simple fuel rim model has been implemented that has the form:

$$w = Max\left[0, C_1(\beta_S - 70), C_2(\beta_A - 45)\right]$$

where w is the width of the rim, and β_S and β_A are the pellet surface and pellet averaged burnups (in GWd/tM), respectively. Inside the rim, the porosity fraction, p, takes the form:

$$p = Max\left[0.15, p_0 + C_3(r - r_S + w)\right]$$

where p_0 is the porosity fraction in the absence of the rim, r is the radial distance to the pellet center, and r_S is the pellet surface radius. The coefficients C_1, C_2 and C_3 are based upon experimental data. The rim model is illustrated on Figure 3.

2.3. Gap closure model

A simple gap closure model has been developed and qualified with open-gap data. It is expressed in terms of the ratio, X, between the thermal and mechanical gaps. When a fraction, F, of the pellet is in contact with the cladding, the thermal conductivity of the gap is improved, i.e., X should be lower than 1. This is correlated with observation that if the thermal gap is set equal to the mechanical gap (i.e. X=1), large gap (where F~0) temperature

data are well predicted and small gap temperature data are over-predicted. X was estimated from the classical formulation:

$$h_{GAS} = Fh_{CONT} + (1-F)h_0$$

where h_{GAS} and h_0 are the heat transfer coefficients for the thermal and mechanical gaps respectively, and h_{CONT} is the contribution due to contact. The mechanical gap conductance model includes a description of gap conductance [15] and an adjustment on contact conductance data [16,17]. From the above expression:

$$X = \rho / \left[F + (1-F)\rho\right] - \rho$$

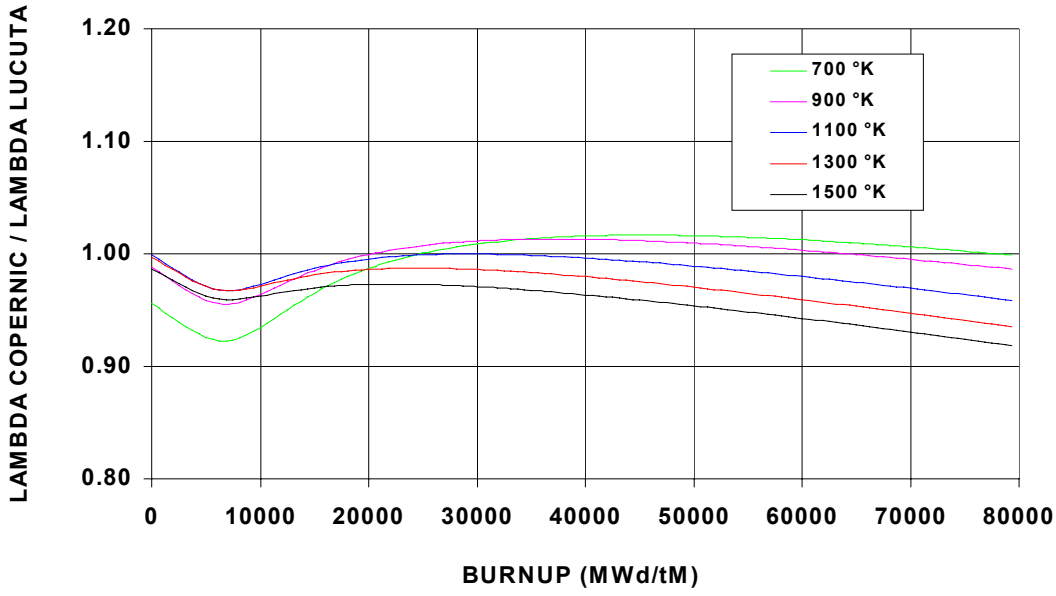

FIG. 2. Comparison between the UO_2 pellet thermal conductivities of COPERNIC [1] and of Lucuta et al. [11].

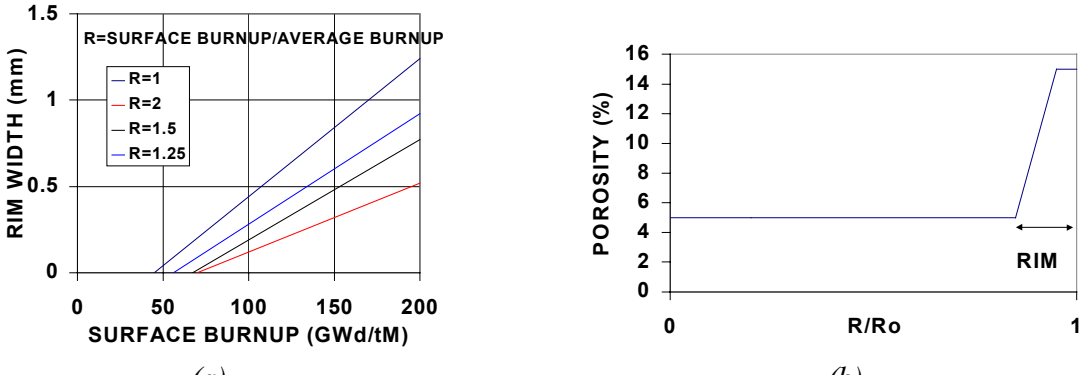

(a) *(b)*

FIG. 3. Illustration of the rim model: a) Evolution of the rim width with burnup and power radial profile. b) Evolution of the porosity inside the rim.

where ρ is the ratio of the combined pellet/cladding roughness to the diametral mechanical gap. A simple and good approximation is found for X, by using the above expression and the Charles and Bruet's [18] expression:

$$F = C_4 + C_5 \exp(-C_6 d_M)$$

where d_M is the mechanical diametral gap and C_4, C_5, and C_6 are constants. This simple expression reads:

$$X = 1 - \exp(-d_M / d_0)$$

where d_0 is a constant, based upon experimental data.

2.4. UO_2 fuel validation

The new thermal model was benchmarked with approximately 2000 fuel centerline temperature UO_2 data from many French and International Programs. As an illustration, Figures 4 and 5 show the measured and predicted centerline temperatures for the EXTRAFORT and the IFA-562.2-16 experiments, respectively. There are no measured to predicted temperature statistical biases with respect to linear heat generation rate or burnup. Furthermore, the upper bound uncertainty for the fuel temperature predictions is small as shown on Figure 6. This uncertainty is below 10%, a value that can be considered as state-of-the-art [19]. Two sets of data appear on Figure 6. The bigger set is well predicted. The smaller set is under-predicted and belongs to the HALDEN experiment IFA-432-3. This data set is older than many data from the bigger data set. We chose to put more weight on the newer data. Also, over-prediction is on the conservative side.

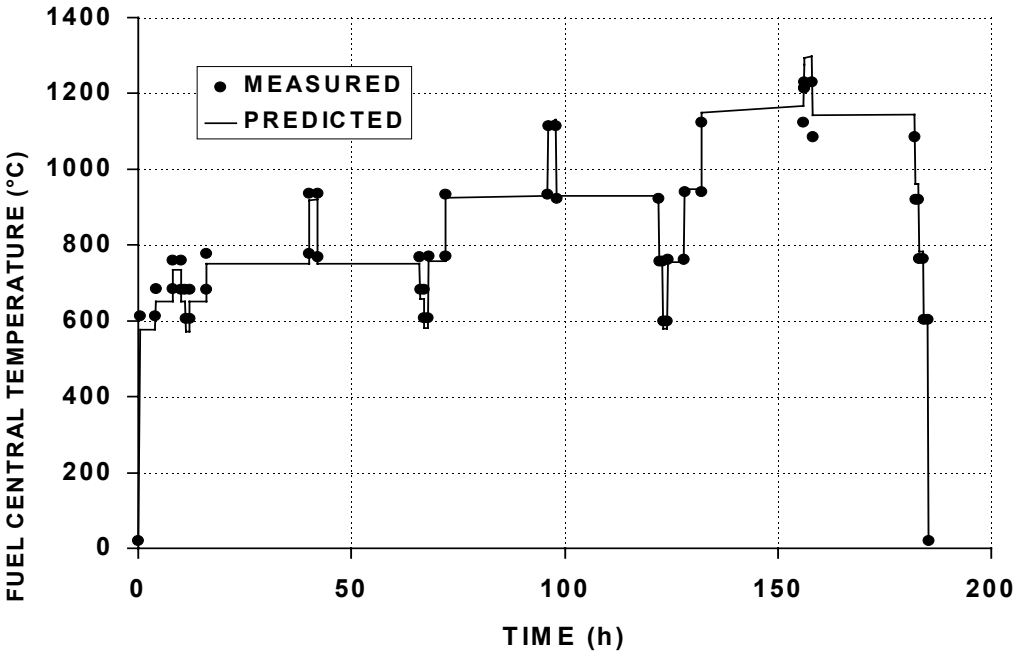

FIG. 4. EXTRAFORT experiment at the CEA OSIRIS test reactor: comparison between measurements and predictions of the fuel centerline temperatures.

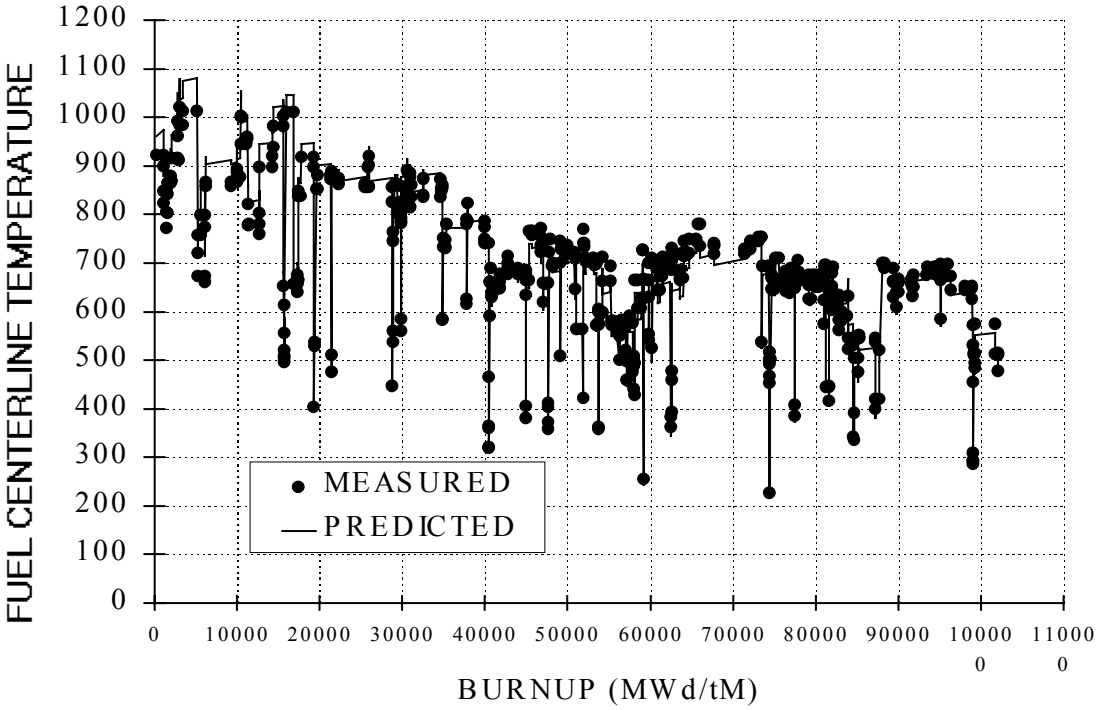

FIG. 5. IFA-562.2-16 experiment at the OECD HALDEN test reactor: measured and predicted fuel centerline temperatures.

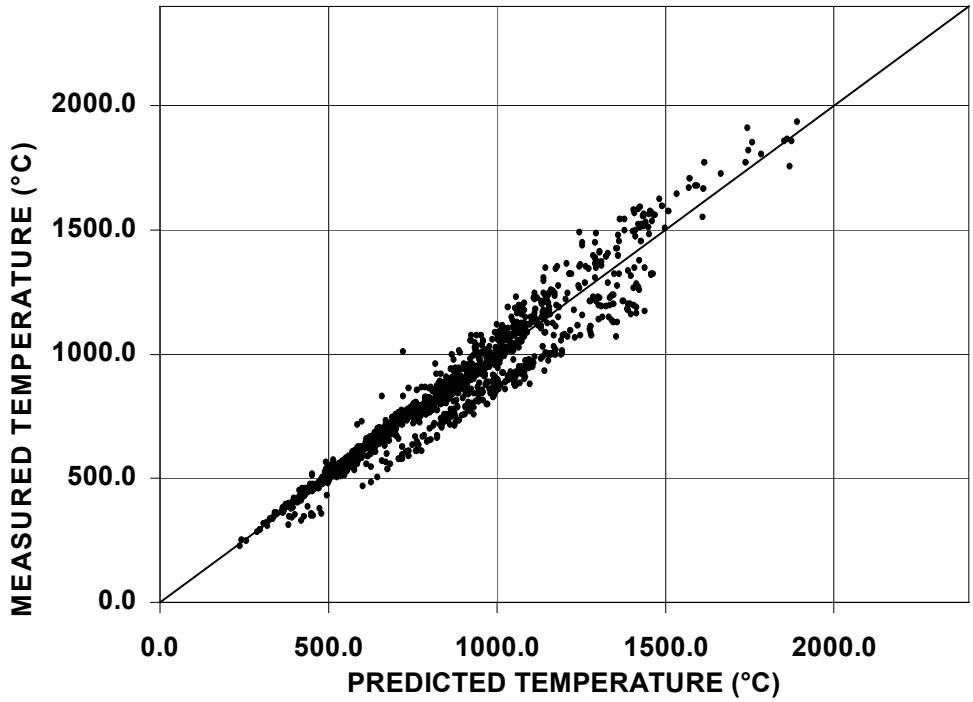

FIG. 6. Comparison between measured and predicted fuel centerline temperatures from the FRAMATOME database.

2.5. Mixed oxides

The same fuel thermal conductivity relationship was chosen for MOX and Gadolinia fuels with corrective factors that include Pu and Gd contents. The MOX factor was derived from the GRIMOX [20] experiment. In this experiment, a rodlet containing both UO_2 and MOX fresh fuel pellets was irradiated in the SILOE French CEA test reactor up to a burnup of 5 GWd/tM. A direct comparison between centerline temperature data was then possible. The MOX relationship was validated up to a burnup of 47 GWd/tM with the data from the FIGARO experimental program [5]. In this experiment, 4 rodlets were re-fabricated from 2 rods irradiated in the Beznau reactor for 5 cycles. These 4 rodlets were re-irradiated in the HALDEN reactor (IFA-606 experiment) with variable power steps up to a power level of 32 kW/m in order to obtain both centerline temperature and fission gas release data. Figure 7 compares measurements and predictions for rodlet number 2. The agreement is excellent. Figure 8 extends the comparison to all data (rodlets number 1, 2, and 4). Overall, there is a slight under-prediction but well within the 10% uncertainty limit.

The gadolinia factor was derived from FRAMATOME data and then validated with HALDEN IFA-515.10-2 data [6] up to a burnup in excess of 60 GWd/tM. Figure 9 shows that there is a good agreement between measurement and predictions.

3. FISSION GAS RELEASE

Athermal and thermally activated mechanisms are taken into account in the COPERNIC Fission Gas Release model (FGR). Athermal release, produced through recoil and knockout mechanisms, remains low. Neglecting the recoil contribution, the athermal FGR fraction is of the form [21] $C_7(S/V)\,\beta$ where $C_{\square}$ is a model parameter, S/V is the specific surface of the fuel and $\square$ is burnup. Contributions from fuel open porosity and from the rim are included in the specific surface. The rim models for fission gas release and temperature are similar. The rim width is common to both modes (see Figure 3a). The evolution of the specific surface inside the rim is similar to that of porosity (see Figure 3b). The athermal model parameters were adjusted on experimental data where no thermal release was observed (absence of a radius of intergranular bubble precipitation).

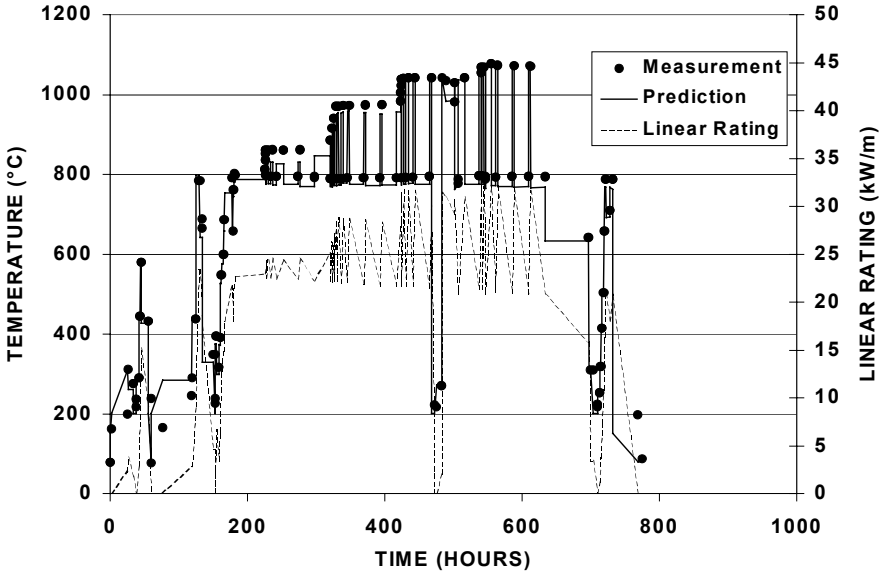

FIG. 7. IFA-606.2-2 experiment: comparison between measurements and predictions of fuel centerline temperatures of MOX fuel at 47 GWd/tM.

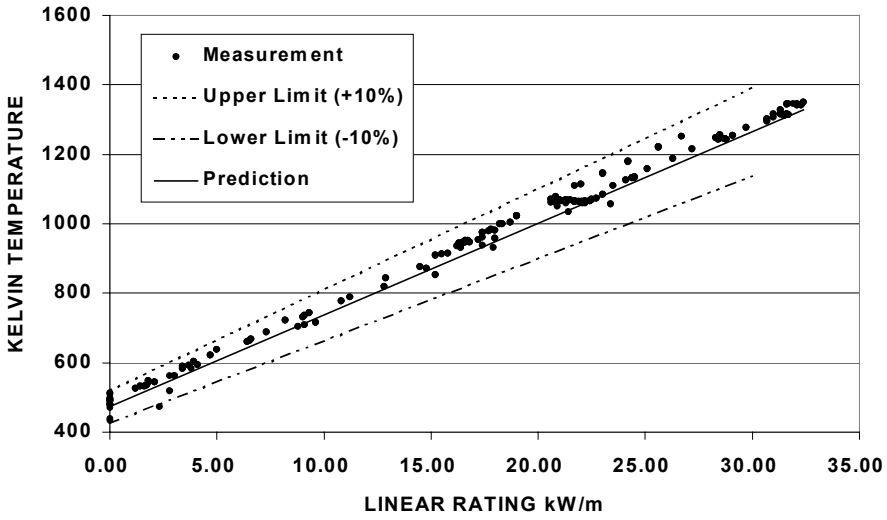

FIG. 8. IFA-606.2-2 experiment: comparison between measurements and predictions of fuel centerline temperatures of MOX fuel at 47 GWd/tM.

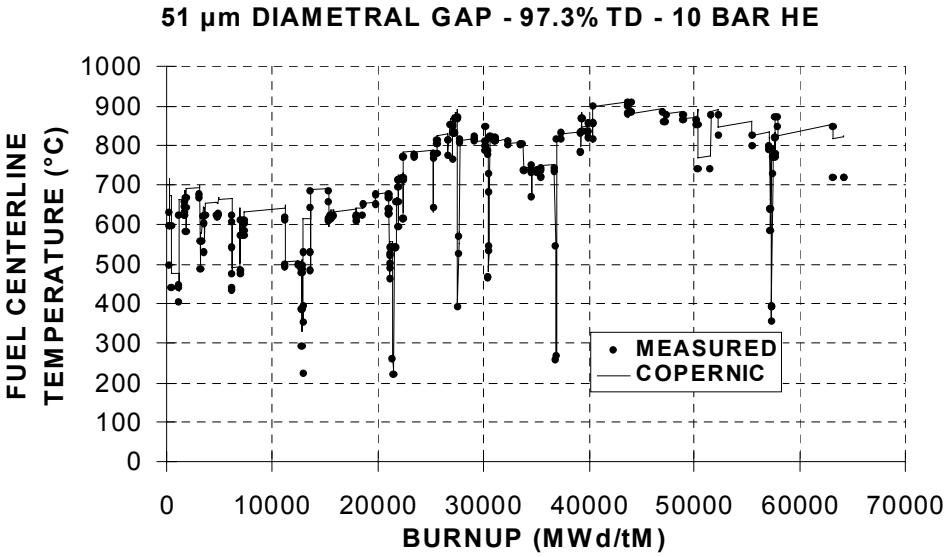

FIG. 9. IFA-515.10-2 experiment: comparison between measurements and predictions of fuel centerline temperatures of MOX fuel at 47 GWd/tM.

The thermal FGR model is based on previous closely related models [8,22,23]. Thermal FGR follows a two-stage diffusion process. First, the gas atoms diffuse from inside the grain to the grain boundaries where they accumulate until a saturation (incubation) threshold is reached. In a thin layer outside the grain, gas atoms are brought back into solution from the grain boundary by fission spikes. This irradiation-induced re-solution counteracts the diffusion flux and delays the onset of release.

The problem is then to solve a diffusion equation inside the grain with a time-varying condition at the grain boundary. The 3-term diffusion coefficient of Turnbull's *et al.* [24] is used. In order to solve the diffusion problem, simple approximations were found to be in excellent agreement with a more rigorous numerical treatment [8]. First, for standard irradiation conditions, the re-

solution flux almost balances the diffusion flux in the re-solution layer. It is then possible to derive an analytical form for the incubation threshold [8]:

$$\beta_I = \frac{B_1}{\exp\left(-\frac{T_1}{T_K}\right) + \frac{(T_K - T_2)}{T_3}} + B_2$$

where β_I is the incubation burnup at temperature T_K (in Kelvin) and B_1, B_2, T_1, T_2, and T_3 are model parameters adjusted on the FGR experimental database. The incubation expression threshold (given for the onset of thermal release) is illustrated on Figure 10 and can be viewed as a generalization of the engineering HALDEN threshold (given for 1% release). The COPERNIC incubation temperature is, on average, lower than the HALDEN temperature, as expected because their definition differs (0% versus 1% release).

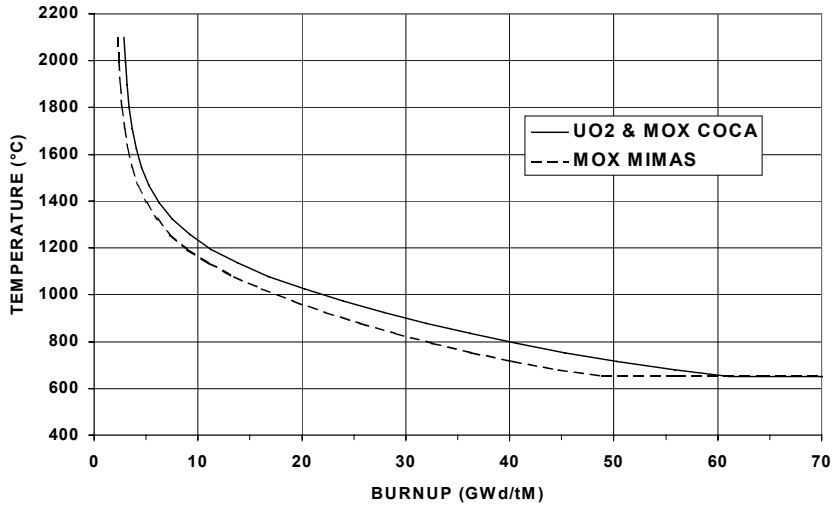

FIG. 10. COPERNIC fission gas release model: incubation threshold for thermal release.

Second, two classical analytical solutions, which correspond respectively to ideal steady-state and transient conditions, are used. The modeling of the general case with varying conditions is obtained with semi-analytical fast algorithms. The model also simulates the so-called burst effect that allows for a fast release from the grain boundary gas during a transient.

The model was extended to MOX and Gadolinia fuels. MOX MIMAS fuels have a heterogeneous structure with Pu-rich agglomerates where the local burnup is high. This effect is simply modeled by using an incubation burnup that is lower for MOX fuels than for UO_2 fuels, depending on the degree on homogeneity of the MOX fuel:

$$. \beta_I)_{MOX} = C_8 (\square_I)_{UO2}$$

where $(\beta_I)_{MOX}$ is the incubation burnup for MOX and C_8 is a model parameter less than one for MOX MIMAS fuel. For the homogeneous MOX COCA fuel, the incubation burnup is chosen to be the same as for UO_2 fuel ($C_8 = 1$). Figure 10 illustrates the incubation thresholds, obtained by fitting model parameters on experimental data for different microstructures.

The temperature of the gadolinia fuel is higher because the thermal conductivity is less than that of UO_2 fuels. However, the observed releases from these types of oxide are comparable. The

temperature effect is offset by a decrease in the diffusion coefficient with increasing quantities of gadolinium. This effect is simply modeled by decreasing the temperature used in the FGR model by an amount that is proportional to gadolinium content.

The FRAMATOME steady-state fission gas release database includes more than 290 fuel rods irradiated in commercial or experimental reactors with rod average burnups up to 67 GWd/tM. The transient database includes more than 60 fuel rods with burnups up to 62 GWd/tM. The transient hold times for these rods ranged from one minute up to many hours and the Linear Heat Generation Rates (LHGR) ranged from 30 kW/m to 50 kW/m. The comparison of the measured and predicted fission gas release for steady-state irradiation is shown in Figure 11. The quality of the transient fission gas release model is illustrated in Figure 12 where the predictions are compared with the measurements for the HATAC-C2 experiment [25] irradiated in the French CEA test reactor SILOE. In this experiment, a measurement device obtained on-line measurements of fission gas release from a 50 GWd/tM rodlet submitted to ten successive transients. Figure 13 details the validation of the MOX model according to fuel microstructure. Figure 14 compares predictions to the fission gas release fraction measured in the experiment IFA-606.2-3. There is a slight over-prediction but within uncertainty bounds at the 95% level.

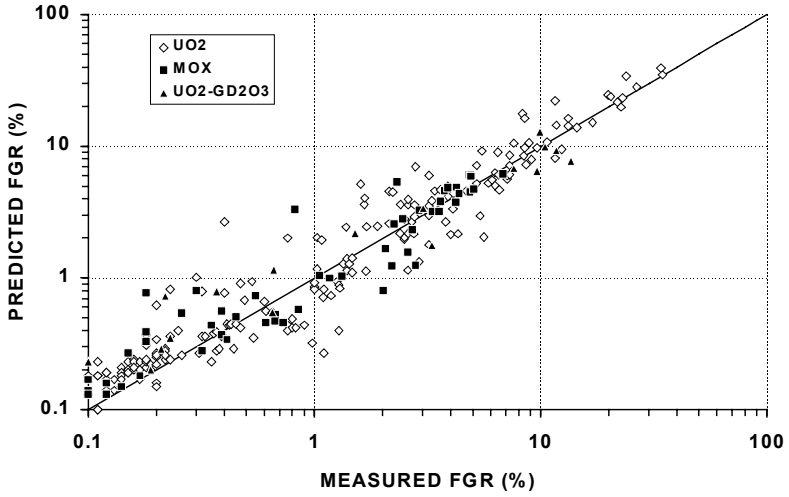

FIG. 11. COPERNIC fission gas release steady-state model: comparison between measurements and predictions.

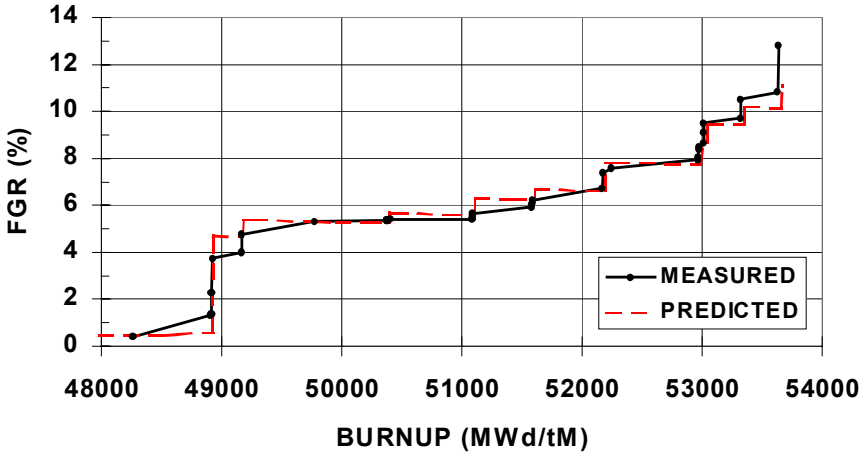

FIG. 12. HATAC-C2 experiment at the CEA SILOE test reactor: measured and predicted fission gas release.

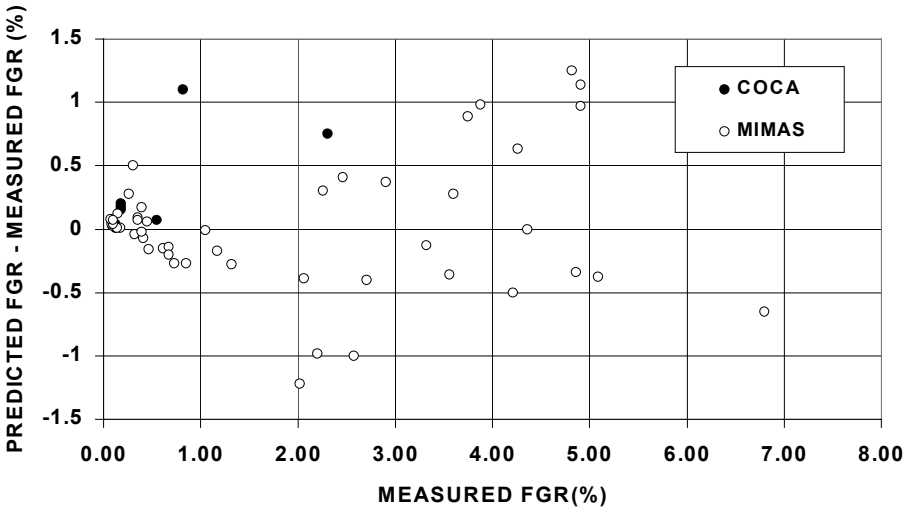

FIG. 13. Effect of MOX microstructure: measured and predicted fission gas release.

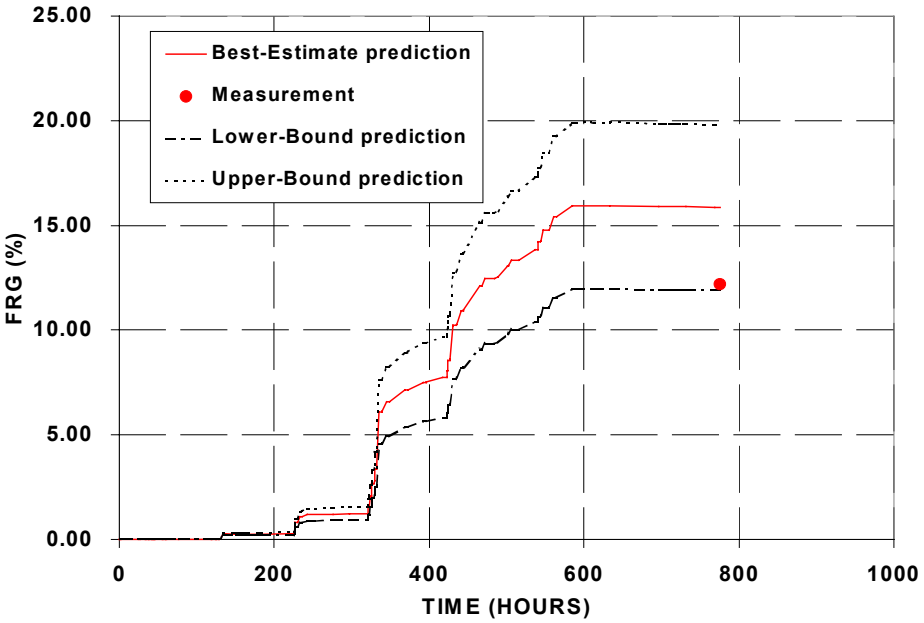

FIG. 14. IFA-606.2-3 - experiment on MOX fuel at HALDEN: measured and predicted fission gas release.

4. CONCLUSION

Many Framatome's fuel performance models have been improved or upgraded and included in the COPERNIC fuel performance code, as recent experimental data become available on high and ultra-high burnup and on mixed oxides. The thermal model is one of the key models that have been revised. A new model for fuel thermal conductivity has been developed in order to predict well the measured centerline temperatures of the whole Framatome database. This database includes over 3400 data (73% from the HALDEN project and 27% from the French CEA programs). The new thermal conductivity relationship is close to the Lucuta *et al.* [11] relationship (the COPERNIC temperature degradation is slightly enhanced). It is validated for mixed oxides at high burnup without changing the Plutonium or Gadolinium

influence that were derived at low burnup. The rim model for temperature degradation inside the rim and the gap closure model have also been improved for better temperature prediction.

The model for fission gas release that depends strongly on temperature was upgraded because the thermal model was modified. The model is simple but contains key phenomena: athermal and thermal effects, steady-state and transient regimes, gas accumulation on grain-boundaries, diffusion and burst effect release, rim model, and influence of mixed oxides. The fission gas release model for MOX has been refined to take into account the MOX microstructures, which vary with the fabrication route. Overall, the quality of the predictions of both thermal and fission gas release model is comparable to the state-of-the-art.

New mechanical models have also been implemented in the COPERNIC code to better assess the pellet-cladding mechanical interaction and to include new data on the Framatome M5-alloy. These models will be presented elsewhere.

REFERENCES

[1] L.C. BERNARD, E. VAN SCHEL, V. REBEYROLLE, C. FOISSAUD, D.A. Wesley, The Framatome copernic fuel rod performance code, recent high burnup and advanced cladding developments, Inter. Topical Meeiting on Light-Water-Reactor-Fuel-Performance, Vol. I, (2000) 155-162.

[2] K. LASSMANN, H. BLANK, Modelling of fuel rod behaviour and recent advances of the TRANSURANUS code, Nuclear Engineering and Design Vol. 106, (1988) 291-313.

[3] J.P. MARDON, A. FRICHET, D. CHARQUET, J. SENEVAT, P. BILLOT, T. FORGERON., The M5 fuel rod cladding, Proceedings of the Top Fuel Meeting, Avignon , France, (1999) 407-414.

[4] S. BOURREAU, B. KAPUSTA, P. COUFFIN, G.M. DECROIX, J.C. COUTY, E. VAN SCHEL, Temperature measurements in high burn-up fuel: EXTRAFORT experiment, Proceedings of the Seminar on Thermal performance of high burn-up LWR fuel, Cadarache, France, (1998) 211-222.

[5] L. MERTENS, M. LIPPENS, J. ALVIS, The FIGARO programme: the behaviour of irradiated MOX fuel tested in IFA-606 experiment, description of results and comparison with COMETHE calculations, HALDEN Report HPR-349 Vol. II (1998).

[6] M.T. ALVAREZ, M. HIRAI, W. WIESENACK, Analysis of the thermal behaviour of Gd-bearing fuel in IFA-515.10, Report HALDEN HWR-470.

[7] W. WIESENACK, Assessment of UO_2 conductivity degradation based on in-pile temperature data, Proceedings of the International topical meeting on light water reactor fuel performance, Portland, U.S.A., (1997) 507-511.

[8] L.C. BERNARD, E. BONNAUD, Finite volume method for fission gas release modeling, J. Nucl. Mater., Vol. 244, (1997) 75-84.

[9] L.C. BERNARD, P. BLANPAIN, E. BONNAUD, E. VAN SCHEL, Analyses of fuel rod thermal performance and correlations with fission gas release, Proceedings of the Seminar on Thermal Performance of High Burn-up LWR Fuel, Cadarache, France, (1998) 311-322.

[10] L.C. BERNARD, J.L. JACOUD, P. VESCO, Framatome analysis of fission gas release and related topics, presented at the Inter. Seminar on Fission Gas Behaviour in Water Reactor Fuels, Cadarache, France (2000).

[11] P.G. LUCUTA, HJ. MATZKE, I.J. HASTINGS, A pragmatic approach to modelling thermal conductivity of irradiated UO_2 fuel: review and recommendations, J. Nucl. Mater., Vol. 232, (1996) 166-180.

[12] M.J. NOTLEY, J.R. MCEWAN, Nucl. Appl. Technol., Vol. 2, (1966) 117.
[13] J.H. HARDING, D.G. MARTIN, A recommendation for the thermal conductivity of UO_2, J. Nucl. Mater., Vol. 166, (1989) 223-226.
[14] M. SUZUKI, H. SAITOU, Analysis of high bunrup fuel IFA-519.9 by exburn-I code, Report HALDEN HPR-349, Vol. II (1998).
[15] D.A. WESLEY, M. YOVANOVICH, A new gaseous gap conductance relationship, Nucl. Technol., Vol. 72 (1986)70-74.
[16] J.E. GARNIER, S.BEGEJ, Ex-reactor determination of thermal gap and contact conductance between Uranium dioxide-Zircaloy 4 interfaces. Stage I: Low gas pressure, NUREG/CR-0330, Vol. 1 (1979).
[17] J.E. GARNIER, S.BEGEJ, Ex-reactor determination of thermal gap and contact conductance between Uranium dioxide-Zircaloy 4 interfaces. Stage II: High gas pressure, NUREG/CR-0330, Vol. 2 (1980).
[18] M. CHARLES, M. BRUET, Gap conductance in a fuel rod: modelling of the FURET and CONTACT results, Proceedings of the IAEA specialists's meeting on water reactor fuel element performance computer modeling, Bowness-on-Windermere, England, (1984).
[19] J.A. TURNBULL, W. WIESENACK, How good id fuel modelling at extended burnup?, Nuclear Engineering International, Vol. 42, No. 518, (1997) 32-36.
[20] L. CAILLOT, A. CHOTARD, J.P. BERTON, Analytical studies of the behaviour of MOX fuel, Proceedings of the International topical meeting on light water reactor fuel performance, Portland, U.S.A., (1997) 62-69.
[21] D.R. OLANDER, Fundamental aspects of nuclear reactor fuel elements, ERDA, U.S.A. (1974).
[22] D.M. DOWLING, R.J. WHITE, M.O. TUCKER, The effect of irradiation-induced re-solution in fission gas release, J. Nucl. Mater., Vol. 110, (1982) 37-46.
[23] K. FORSBERG, A.R. MASSIH, Diffusion theory of fission gas migration in irradiated nuclear fuel UO_2, J. Nucl. Mater., Vol. 135, (1985) 140-148.
[24] J.A. Turnbull, R.J. White, C. Wise, The diffusion coefficient for fission gas atoms in Uranium dioxide, Proceedings of the IAEA technical committee meeting on water reactor fuel element computer modelling, Preston, UK, (1988).
[25] E. Porrot, M. Charles, J.P. Hairon, C. Lemaigan, C. Forat, M. Montagnon, Fission gas release during power transients at high burnup, *Proceedings of the International topical meeting on LWR fuel performance,* Vol. 2, Avignon, France, (1991) 558-566.

MODELLING OF PWR AND WWER FUEL BEHAVIOUR IN HALDEN: COMPARATIVE TESTS USING THE NEW CODE SPAN

B. VOLKOV, P. STRIZHOV, E. RYAZANTZEV, V. YAKOVLEV
Reactor Technology and Materials Research Institute of RRC "Kurchatov Institute",
Moscow, Russian Federation

E. KOLSTAD
IFE OECD Halden Reactor Project,
Norway

Abstract

Russian nuclear fuel has been used in WWER commercial reactors operating both in Russia and other countries. General tendency towards enhancement of the safety of NPPs required verification of reliability of the fuel produced with other nuclear technology. The main objective of the tests in IFA-503 (which have been carried out at Halden reactor since 1995) is to provide the comparative information of in-reactor behaviour of different WWER-440 fuel types (fabricated at MSZ Electrostal) and typical PWR fuel. Based on the in-pile measurements, data on common fuel characteristics, such as densification and swelling, fission gas release and degradation of fuel conductivity, have been obtained. The comparative data were generated for standard WWER-440 and PWR fuel types up to a burnup of 25 MWd/kg UO_2 in the first loading (IFA-503.1). Analysis of the results showed identical behaviour of these two fuel types with the exception of fuel densification. The results obtained in the first loading prompted a new test with state-of-the-art WWER fuel produced by MSZ Electrostal with improved technology. Currently, three modified WWER-440 fuel types are also being investigated together with the same PWR fuel type in the second loading (IFA-503.2). Preliminary results show much reduced in-reactor densification in all new WWER fuel types. The data on densification of the different fuel types tested in IFA-503 have been analyzed in detail and were used for development of the densification model presented in this paper. The model has been included into a new fuel performance computer code SPAN which is being developed for modelling LWR fuel rod behaviour under steady-state and operational transient conditions. Overall comparison between the SPAN predictions and data from IFA-503 has been carried out and sampled results are also presented in this paper.

1. INTRODUCTION

Joint program of the in-pile tests with Russian fuel in Halden reactor is carried out not only to compare behaviour of WWER and PWR fuel types but also to study fuel performance in support of modelling. The first comparative test (IFA-503.1) has generated a representative and comparative database of standard WWER-440 fuel fabricated by the MSZ Elektrostal (Russia), and typical PWR fuel [1]. The results showed that there were insignificant differences in these types of fuel behaviour with exception of somewhat larger densification revealed in the standard WWER-440 fuel as compared to PWR fuel. These results prompted a new test with different modified WWER-440 fuel types produced by MSZ Electrostal with improved technology. Three different types of WWER-440 and PWR fuel types were incorporated into 12 instrumented fuel rods for the second loading IFA-503.2. The results from the current test have indicated that the densification properties in all modified WWER fuel were improved [2].

In addition the results obtained from in-pile fuel monitoring in both IFA-503 loadings provided the information of UO_2 fuel behaviour with different initial microstructure. These data allow not only verifying models for WWER fuel behaviour but also improving or

developing new models for dioxide uranium fuel. In particularly, the information concerning fuel densification have been derived from the test results and was used for development of a tentative densification model. This model has been introduced into a new fuel performance code SPAN developing for simulation of LWR fuel behaviour under different operation conditions. All last innovations and modifications, having been introduced into the last version of well-known PIN99w code [3,4], prompted development the code SPAN which allows improving fuel behaviour modelling up to high burnup under steady state and transients. This code was used for analysis of the WWER and PWR fuel behaviour in IFA-503. Some results from this analysis are presented in this paper.

2. MAIN FEATURES OF THE SPAN CODE.

The fuel performance SPAN code is developing for thermal and mechanical LWR fuel behaviour simulation up to high burnup under steady state and operational transients. Multilevel structure of the code allows separately modelling each physical process, taking place in fuel rod during irradiation. Detail structuring of the code also allows modification of the modules and models without any serious changes in the code core. The SPAN is quite high-speed code and has unlimited number of time steps that allows modelling complicated power histories, which appropriate to research reactors, covering re-instrumented fuel rods pre-irradiated in commercial reactors. Brief description of the main models including in the code are given below:

A mechanistic FGR model has been developed to predict the fission gas release from UO_2 fuel during steady state and transient conditions. The model considers the following processes in fuel:

- diffusion of gas atoms to the grain boundary, trapping of gas atoms by intragranular and intergranular bubbles;
- resolution of gas atoms from these bubbles;
- sweeping of gas atoms due to grain growth;
- fission gas release due to the intergranular bubble interconnection and micro-cracking during ramps;
- FGR from the RIM-region at high burnup is calculated by an original model developed on the basis of the data derived from Electron Probe Micro Analysis (EPMA) and X ray Fluorescence (XRF) examinations in fuel which has been irradiated up to very high burnups in the High Burnup Effects Program (HBEP) [5];
- this model has been integrated with the general diffusion FGR model for prediction thermal and athermal FGR up to high burnup;
- FGR model was also extended for MOX (UO_2+PuO_2) fuel where some specific processes depend on the fuel microstructure and plutonium heterogeneity in the fuel matrix. As a consequence of these a non-uniform fission rate and fission product distribution across fuel pellet is produced. The model of spherical cells with Pu–rich agglomerates was developed for heterogeneous MOX fuel [3].

Power and burnup radial profiles are calculated by integral model developed for very high burnup fuel [6]. This module is based on special physic calculations carried out for different reactor types.

A high-speed steady state and transient modules were developed for computation of the temperature fields. Fuel thermal conductivity accounted for degradation effects with burnup is calculated with the correlation obtained from latest Halden data.

Local porosity in the RIM-layer is calculated as a function of the local burnup up to 200 MWd/kg U.

Tentative densification model, based on the IFA-503 data and presented below, has also been introduced into the mechanical module of the code. All predictions and comparative calculations also presented in this paper have been carried out with this model.

The comparative analysis between data from IFA-503 and calculations, presented in this paper, should be considered, as a first attempt for verification of the SPAN code, which is in progress now.

3. WWER/PWR COMPARATIVE TESTS IN HALDEN REACTOR

3.1. Experimental

The tests are carried out under HBWR conditions, which mean natural circulation of the coolant with saturation temperature of about 240 C and system pressure of 34 bars. Both tests in rig IFA-503 comprised two clusters incorporating 6 test rods in each. All fuel rods were equipped with in-pile detectors such as fuel expansion thermometers, fuel stack elongation detectors and pressure transducers.
The claddings in all test rods were made from Zr-1%Nb alloy used in WWER type reactor.

3.2. Fuel characterisation

First loading IFA-503 tested standard WWER-440 fuel pellets randomly selected from the batch produced by MSZ Electrostal in 1995. In the second loading are being tested modified WWER-440 fuel pellets selected from three experimental batches produced with improved technology. The PWR fuel pellets are supposed to be produce by IFE (Kjeller) with typical for PWR technology and they have the same characteristics in both tests. Fuel pre-characterisation data are given in Table I.

TABLE I. FUEL PRE-CHARACTERISATION DATA

PARAMETER / FUEL TYPE	PWR	WWER-1	WWER-2	WWER-0	WWER-st
Fuel density, % TD	95.1	96.1	96.1	96.4	97.1
Average grain size, μm	9	11	10	7	7
Average pore size, μm	0.6	-	-	-	0.5
Enrichment, % U-235	4.4	4.4	4.4	4.4	4.4
Sintering, ^{o}C/time, hr	1700/3	1700/3	1700/3	1650/1	1650/1
Re-sintering test, dD/D, %	-	-0.19	-0.27	-0.28	-0.53

3.3. Irradiation history

IFA-503.1 was irradiated in the HBWR for three years and the average burnup achieved about 25 and 20 MWd/kg UO_2 in the low and in the upper cluster rods, respectively. For two thirds of the irradiation time the assembly was irradiated under relatively low power which allowed the comparison of densification and swelling rates between standard WWER and PWR fuel types without any influence from fission gas release (FGR). After this a power up-rating was performed to study behaviour at higher power with emphasis on FGR.

IFA-503.2 with modified WWER fuel types currently being irradiated in HBWR has achieved a burnup of about 10-15 MWd/kg UO_2. The irradiation was started at a maximum average power of about 30 kW/m corresponding to maximum power rating in commercial WWER-440 fuel rods early in life. The data obtained so far allowed the comparison of fuel densification between different fuel types and data from the first loading as well.

3.4. Main results from the tests in IFA-503

Detail analysis of the results from the first loading and preliminary one for the modified WWER fuel types loaded later in IFA-503 has been presented both at EHPG meeting [1] and WWER fuel performance seminar held in Bulgaria [2]. Based on the in-pile measurements, data on common fuel characteristics, such as densification, swelling and fission gas release are collected in Table II. Some of these data have been re-evaluated and corrected a little in comparison with last publications. In particularly it was concerning fuel densification which was specified more carefully. FGR was also re-estimated a little for the test fuel rod in IFA-503.1. All these results are presented in this paper.

TABLE II. IFA-503: COMPARATIVE TEST DATA FOR DIFFERENT FUEL TYPES

PARAMETER / FUEL TYPE	PWR	WWER-1	WWER-2	WWER-0	WWER-st
Maximum fuel shortening at HSB, (dL/Lo), %	0.1-0.14	0.12-0.20	0.28	0.20	0.35
Relative fuel shortening at power, (dL/Lo), %	0.2-0.3	0.15-0.25	0.35	0.35	0.45
Maximum fuel proper densification, at HSB, (dV/Vo),%	0.45-0.55	0.5-0.7	1.0	0.8	1.5-1.6
Maximum fuel proper densification at power, (dV/Vo), %	0.7-1.2	0.8-1.1	1.4	1.3	1.7-1.8
Burnup at maximum densification, MWd/kg UO_2	3-4	3-4	4-5	4-5	5-6
Average fuel swelling, %/10 MWd/kg UO_2,	0.4-0.5	~0.5	~0.5	~0.5	0.5-0.6
FGR, % (IFA-503.1)	<1.0	-	-	-	<1.0

The results obtained in these tests are discussed together with a new fuel densification model presented in this paper as well as with the fuel performance SPAN code analysis and predictions. It should only be noted that there was not revealed substantial difference between WWER and PWR fuel behaviour in the test. It is believed that WWER fuel behaviour is consistent with general principles of UO_2 irradiation.

The causes of the differences revealed in the behaviour of the different fuel types under irradiation can be ascribed to the WWER hollow pellet design as well as to the fuel microstructure characteristics such as-fabricated grain and pore size. Results obtained from the first loading with standard WWER fuel provided the information allowed the improvement the WWER fuel characteristics. All types of the modified WWER fuel currently tested in the second loading have shown much reduced fuel densification. Other common fuel parameters such as swelling, thermal conductivity degradation, fission gas release is estimated to be similar for all fuel types. Despite this fact a quantitative comparative analysis of the different WWER and typical PWR fuels behaviour in IFA-503 should be done with model analysis using fuel performance code in order to understand and explain the causes of some differences.

4. TENTATIVE SEMI-EMPIRICAL FUEL DENSIFICATION MODEL.

There are several empirical, semi-empirical or theoretical models known for the quantitative description of UO_2 fuel densification [7-12]. These models are usually based on either out-of-pile and in-pile data or on not well-known estimations of fuel material properties. Theoretical models should also be provided by detail fuel pre-characterisation data (for instance, fractional pore distribution by classes) which are not always available for modelling.

Usually, fuel average grain size and density are available as pre-characterisation data which are also tempted to use for fuel densification models [7,8]. However, these temptations to develop such a kind of models either led to rough predictions or restricted utilisation. It has been experimentally established that detail knowledge of fuel microstructure is necessary to provide more reliable fuel behaviour modelling. In particular, this concerns fuel densification which strongly dependent on as-fabricated fuel microstructure. Fresh UO_2 fuel contains multifarious pores and grains in order of sizes and forms. In fact it is quite difficult not only obtain a full-ranged description of such a variety of pores and grains from microstructure analysis but also utilise it in fuel performance codes. Unification of these data for each fuel type could be useful for understanding the nature of fuel densification and other irradiation-induced effects as well as for verification of physical models.

This chapter presents a tentative densification model suggesting some unification of fuel microstructure data for quantitative description of fuel densification. The model based on both theoretical solutions, given by Assmann and Stehle [11] and verified on number of tests [14,15], and experimental data derived from the test IFA-503. According to this model the main fuel densification mechanisms are as follows:

(1) *generation of an excess vacancy concentration around the pores, and*

(2) *migration of vacancies to the grain boundaries by diffusion;*

(3) *annihilation of the vacancies on grain boundaries;*

(4) *acceleration of removal of irradiation-generated vacancies with fuel temperature increase.*

In contradiction from Assmann's model, which must be provided by pore size distribution by classes, the present one proposes to use a simplified fuel pre-characterisation data set:

$\boldsymbol{d_g}$ - average grain size; $\boldsymbol{d_{avp}}$ - average pore size;
$\boldsymbol{P_{dp}}$ - fraction of pores with sizes less than $\boldsymbol{d_{avp}}$; $\boldsymbol{\Pi_o}$ - fuel porosity; (1)

It is assumed that:

1) the average pore size is a boundary between two pore fractions - P_{dp} (densifiable pores) and P_{cp} ("coarse" pores), sum of which is equal unity, that is:

$$P_{dp}+P_{cp}=1; \tag{2}$$

2) the average pore size $\boldsymbol{d_{avp}}$ can be estimated from ceramography analysis of polished cross section of fuel pellet with assumption of round shape of the average pore on the plane of sample.

3) average size of "fine" pores $\boldsymbol{d_{fp}} < \boldsymbol{d_{avp}}$ and average size of "coarse" pores $\boldsymbol{d_{cp}} > \boldsymbol{d_{avp}}$ but their fractions may differ from each other.

On the basis the assumptions that density of all-size pores is a sum of densities of "fine" and "coarse" pores: $Z_{dp}=Z_{cp}+Z_{fp}$; the fraction of "densifiable" pores can be obtained from ceramography analysis in the following form:

$$P_{dp} = \frac{d_{fp}^2(d_{cp}^2 - d_{avp}^2)}{d_{avp}^2(d_{cp}^2 - d_{fp}^2)} \tag{3}$$

Common solution of the diffusion equation, describing re-solution controlled fuel densification, can be written in the form obtained for fuel volume change [13]:

$$\frac{\Delta V}{V_0} = -a \cdot P_0 \left\{1 - \exp(-b \cdot \eta \cdot \Omega_s Ft)\right\} \tag{4}$$

where the coefficients a and b given in form proposed by Assmann [11] but for an interpretation of some parameters which are suggested to be changed for the present model:

P_0 - fraction of "fine" porosity is changed with "densifiable" porosity (P_{dp}) in this model;

η - fraction of vacancies per encounter that can escape from the *average* pores (instead of fine pores);

other parameters are not changed:

F - fission rate; Ω_s - volume of fission spike; t - irradiation time.

The equation (4) expresses a law for the removal vacancies from the "densifiable" pores to grain boundary where their annihilation leads to the fuel densification. This equation can be transformed to relative volume porosity shrinkage by dividing on Π_0. Replacing burnup variable Ft in fission/cm^3 with Bu in MWd/kgUO$_2$, usually used in Halden tests, the Eq (4) can be re-written in following form:

$$\frac{\Delta v}{v_0} = -A \cdot \left\{1 - \exp(-B \cdot \eta^* Bu)\right\} \tag{5}$$

where:

$$A = \frac{P_{dp}}{1 + 1/5 \cdot \Pi_0 (1 - P_{dp}) \cdot (d_g / d_{cp})^2} \tag{6}$$

$$B \approx 2.962 \cdot (1 - \Pi_0) \left\{ 1 - \frac{P_{dp} \Pi_0}{15} (d_g / d_{fp})^2 \right\} \tag{7}$$

η^*- is a mantissa of value $(\eta \Omega_s) \approx 1 \cdot 10^{-19}$ [14].

All these transformations allow us to obtain the porosity shrinkage rate in the form suited for fitting to experimental data:

Coefficients ***A***, ***B,*** $\boldsymbol{\eta^*}$ can be derived from experimental data either to reconstruct some unknown pre-characterisation parameters or to verify model at all. Actually, coefficient ***A*** is a value of maximum porosity shrinkage while ***B*** and $\boldsymbol{\eta^*}$ are controlling densification rate with burnup. The value of $\boldsymbol{\eta^*}$ has been experimentally estimated from Halden data [14] within the range of 1.5-3.0 (order of this value is 10^{-4}) for very fine pores. However, the parameter $\boldsymbol{\eta^*}$ is assumed to be dependent on pore sizes since it has been defined as a fraction of vacancies escaped from pore penetrated by fission spike.

The equation (5) was used for reconstruction of unknown pre-characterisation parameters for 4 types of WWER fuel and typical PWR fuel tested in IFA-503. The fraction of densifiable pores can be found from Eq (7) as a function of "fine" pore size:

$$P_{dp} = \frac{15 \cdot d_{fp}^2 \cdot \left(1 - B / \left(2.962 \cdot \left(1 - \Pi_0\right)\right)\right)}{\Pi_0 \cdot d_g^2} \tag{8}$$

and from Eq(6) as a function of "coarse" pores size:

$$P_{dp} = \frac{1 + \Pi_0 / 5 \cdot \left(d_g / d_{cp}\right)^2}{1/A + \Pi_0 / 5 \cdot \left(d_g / d_{cp}\right)^2} \tag{9}$$

The joint solution of Eqs (3) and (6) as a function of "fine" pore sizes can be written:

$$P_{dp} = \frac{A \cdot \left(1 + \Pi_0 / 5 \cdot \left(d_g / d_{avp}\right)^2\right)}{1 + A \cdot \Pi_0 / 5 \cdot \left(d_g / d_{fp}\right)^2} \tag{10}$$

Fraction of the densifiable pores determined from Eqs (8), (9) and (10) for PWR and standard WWER fuel types as a function of pore sizes are shown in Fig. 1A and Fig 1B.

As can be seen the test data show that there are different fractions of the densifiable pores in PWR and standard WWER fuel for average pores sizes obtained from micro-structural analysis. However, it should be noted that the coefficient ***B*** being responsible for densification rate, was fitted to average pore size while the best estimation of the parameter $\boldsymbol{\eta^*}$ was evaluated within the range of 0.2-0.25 for standard WWER and PWR fuel types, respectively. Since the pre-characterisation data on pore sizes have not been available for other fuel types tested in IFA-503, their reconstruction was made on the test results with assumption that $\boldsymbol{d_{fp}}$ =

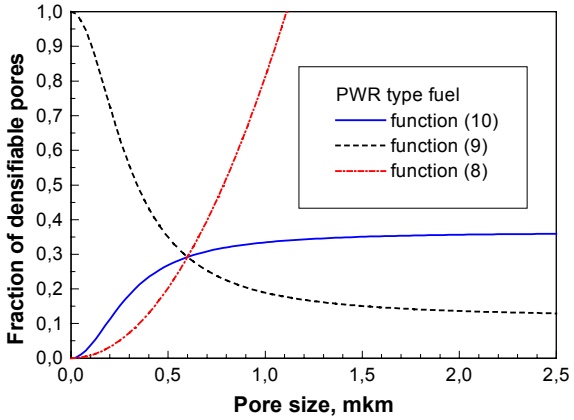

FIG. 1A. Solution of equations (8), (9) and (10) for PWR fuel tested in IFA-503.

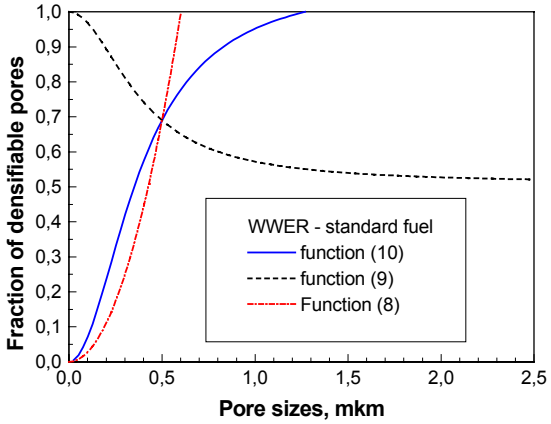

FIG. 1B. Solution of equations (8), (9) and (10) for standard WWER fuel tested in IFA-503.1.

TABLE III. DATA AND MODEL RECONSTRUCTION PARAMETERS FOR FUEL TYPES TESTED IN IFA-503

Type of fuel	**PWR**	**W-st**	**W-1**	**W-2**	**W-0**
Grain size, d_g, μm	9	7	11	10	7
Average pore size, d_{avp}, μm	0.6	0.5	*0.75***	*0.9***	*0.65***
Density from TD	0.953	0.971	0.961	0.961	0.964
Porosity, Πo	0.047	0.029	0.039	0.039	0.036
Re-sintering test, (porosity hrinkage)	-	0.53	0.15	0.21	0.23
A* - see Eqs (6)	**0.117**	**0.510**	**0.155**	**0.245**	**0.23**
B* - see Eqs (7)	**0.567**	**0.444**	**0.75**	**0.95**	**0.68**
η*	**0.255**	**0.213**	**0.319**	**0.383**	**0.276**
P_{dp} **	***0.280***	***0.690***	***0.330***	***0.390***	***0.350***

- - experimental data; ** - model evaluation.

$d_{avp} = d_{cp}$. In result both the available pre-characterisation data and parameters reconstructed for 5 fuel types tested in IFA-503 are given in Table III. Parameter η^* is a function of fuel porosity, grain size and average pore size. This function is strongly dependent on pore size.

According to Ref [11] shrinkage of porosity in the temperature range below 450°C is controlled by *athermal* generation of vacancies and their migration to grain boundaries i.e. by fissioning effects. In this case, Eq (5) is to be described an irradiation-induced fuel densification at the level of temperatures covering fuel surface in UO_2 fuel rods with ~9 mm pellet diameter and gap size about 0.20 mm. That is why the fuel stack elongation data at hot-stand by reactor conditions can be considered as a low-temperature fuel densification.

The analysis above suggested that fraction of pores less than average pore size and average pore size itself as well as fuel grain size and porosity may be used for description of fuel densification. Addition analysis allowed us to obtain some correlation for average pore as a function of average fuel grain size and porosity:

$$d_{avp} \geq d_g \cdot \sqrt{\Pi_0 / 15} \qquad (11)$$

Comparison between this correlation and data on the fuel types tested in IFA-503 is shown in Fig. 2.

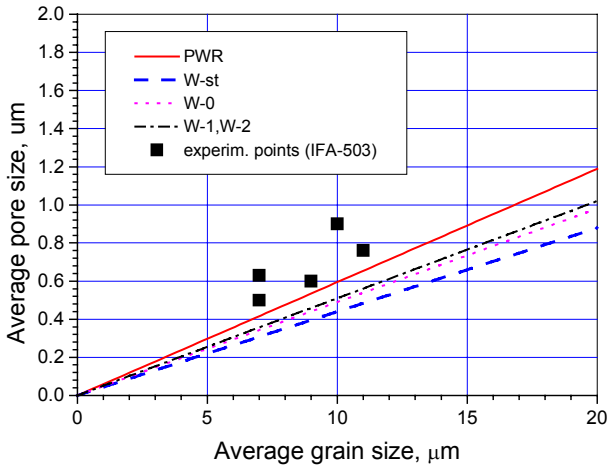

FIG. 2. Average pore sizes as a function of average grain sizes for different fuel types.

The data from IFA-503 also suggested that fuel densification was dependent on temperature. This dependence is estimated from both elongation measurements at hot-stand-by condition (zero power and coolant temperature about 240°C) and at power as a function of fuel temperatures measured in the centre of the identical rods or calculated at the fuel surface. The relative difference is clearly seen in Fig. 3 where is shown a deviation of the measured fuel stack elongation versus heat rating from thermal expansion calculated from the fuel centreline temperatures measured both at BOL and at the maximum densification. Such kind of data were possible to obtain due to flat-ended pellets utilised in all tested rods.

However, there are some problem with interpretation of this hot fuel shrinkage. It could be suspected that the main cause is thermal diffusion creep [13] under axial stresses arising in the contact hot points between pellets due to the spring force on the fuel column and inner gas pressure and/or PCMI. The relevant discussion has been done in Ref. [9] where a maximum

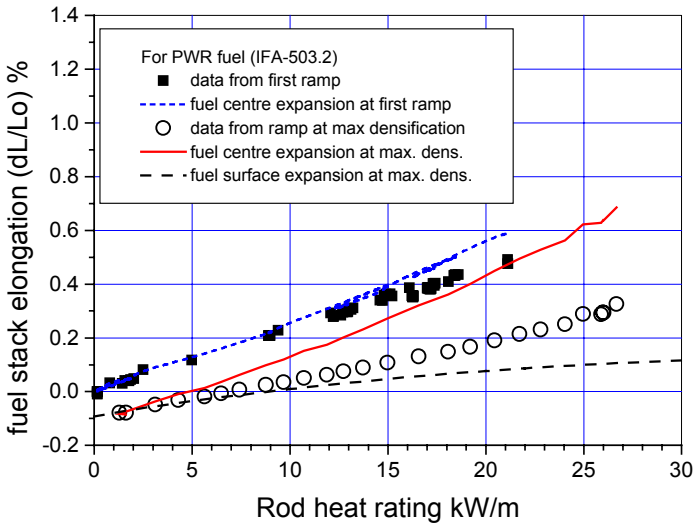

FIG.3. Fuel stack elongation data in comparison with fuel expansion calculated from fuel centreline temperature measured in identical PWR fuel rod from IFA-503.

relaxation rate of the fuel column was estimated in the range of 10^{-7}-10^{-5} /hr taking into account high enough PCMI forces. Some of the rods in IFA-503.1 have been irradiated under a relatively low power rating (~10-15 kW/m) which unlikely caused the high PCMI forces during the first irradiation period. However, the power uprating, which occurred thereafter, showed that so-called "in-pile dishing" is seemed to be somewhat deeper than that could be formed due to the thermal creep only. Moreover, the volume fuel shrinkage estimated from inner gas pressure measurements suggested that there was an additional fuel densification as compared to that derived from the elongation data at hot stand-by [1,2]. Perhaps, primary fuel creep may contribute to the "in-pile dishing" formation during the first ramps when a contact area between pellets is very small leading to high stresses. Then these stresses are likely decreasing very fast due to a flattening of the contact area. This effect has to be estimated separately via modelling but it has not been accounted for in the model proposed in this paper. It should be noted that a radial power profile across a standard designed PWR and WWER fuel pellets at BOL is not so steep enough to find any dependence on fission rate whereas a fuel temperature profile is strongly dependent on a heat generation rate under similar coolant conditions.

The maximum volume porosity shrinkage, evaluated for five fuel types tested in IFA-503 in dependent on fuel temperature averaged over the densification period, were fitted to the function in the following form (also graphically shown in Fig.4):

$$\Delta\varepsilon_{por} = \Delta\varepsilon_{\max} - \frac{(\Delta\varepsilon_{\max} - \Delta\varepsilon_{irr})}{1 + (\Psi(T, d_g))^3} \qquad (12)$$

where: $\Delta\varepsilon_{irr}$- the irradiation-induced volume porosity shrinkage defined by Eq (6) ($\Delta\varepsilon_{irr}$= A)

$\Delta\varepsilon_{\max}$ - a maximum porosity shrinkage which can be determined as a fraction of the densifiable porosity P_{dp}

$\Psi(T, d_g)$ - is a function of fuel temperature, which also included the inverse dependence on original grain size and can also cover the grain growth at higher temperatures;

This function influences fuel densification at temperatures higher than ~600 K and reflects a thermal migration of vacancies, generated by fission spikes, to the grain boundaries.

Moreover it should be noted that data from IFA-503 also confirmed that $\Delta\varepsilon_{irr}$ = A are correlated well with results from the resintering tests, which are also given in Table I. This correlation has been proposed by R. Meyer [10] and it was included in the MATPRO densification models [11]. In the present model the values coming from re-sintering test can also be used ($\Delta\varepsilon_{irr}$= A in Eq. (12)) if other relevant pre-characterisation data are not available.

The best fitting to the data for all fuel types from IFA-503 was done with the exponential function modification (Eq. (5)), proposed by R. White for prediction of "rapid" and "slow" densification rate [9]. The following assumptions was made:

- the "rapid" densification rate at higher temperature is due to the "densifiable" porosity P_{dp}, whereas the "slow" densification is dependent on fraction of "coarse" pores ($P_{cp}=1-P_{dp}$);
- the densification rate is dependent on temperature as it has been described in Eq. (12);
- parameter η^*, obtained above, is to be related to "slow" part of the densification rate in which the "coarse" pores are involved while a similar parameter η_{fp} for "rapid" densification was specified for "fine" pores (η_{fp} ~ 1.5-2.0).

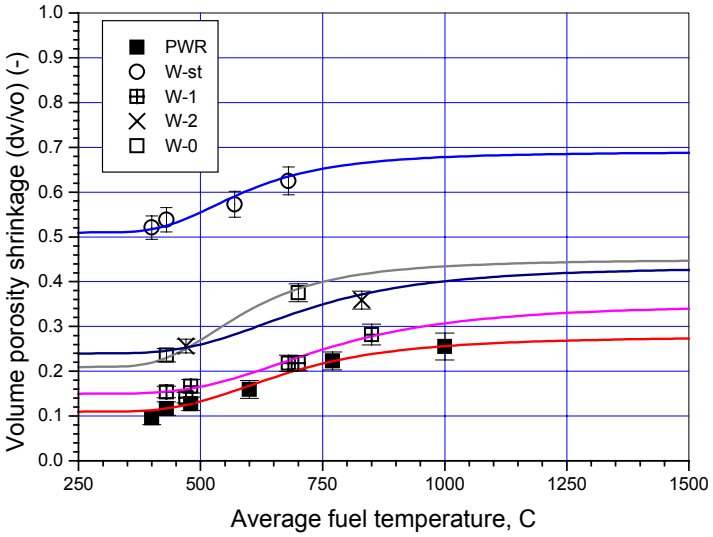

FIG. 4. Maximum volume porosity shrinkage as a function of local fuel temperatures estimated in fuel types tested in IFA-503.

Finally, the best estimation of the densification data obtained for different WWER fuel types as well as for PWR type tested in IFA-503 was made with function (16) modified as follows:

$$\frac{\Delta V}{V_0} = -\Pi_0 \left\{ \Delta\varepsilon_{\max} - \frac{(\Delta\varepsilon_{\max} - A)}{1+(\Psi(T,d_g))^3} \right\} \cdot \left[1 - C\exp(-B\cdot\eta_{fp}\cdot Bu) - (1-C)\exp(-B\cdot\eta^*\cdot Bu) \right] \qquad (17)$$

where:

$$C = P_{dp} \cdot \left(1 - \frac{1}{1 + (\Psi(T, d_g))^3} \right) \tag{18}$$

Coefficients A and B can be obtained from Eqs (6) and (7).

As can be seen this correlation is transformed to Eqs (5) for fuel pellet irradiated at temperature below 600 ^{o}K. Some examples of the comparison between data from IFA-503 and model calculations are given in Figs. 5-7 for a few fuel types.

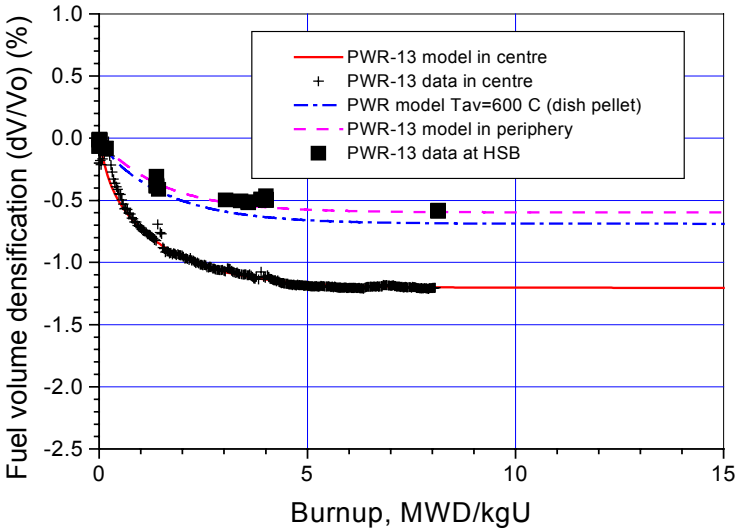

FIG. 5. Comparison between data and model calculations for PWR fuel.

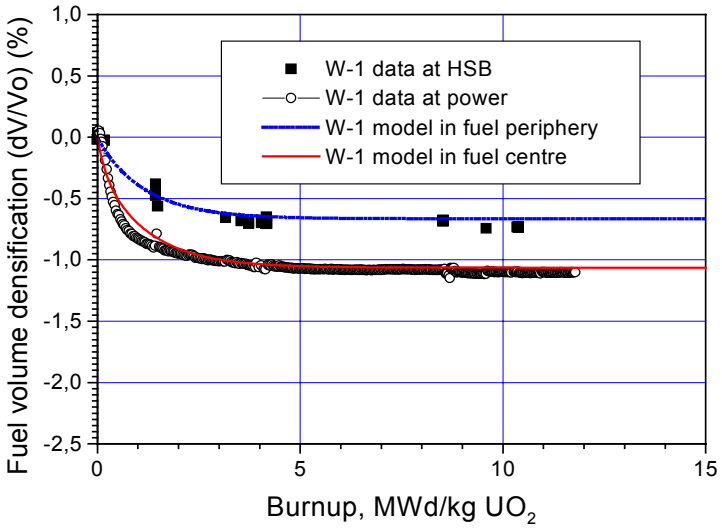

FIG. 6. Comparison between data and model calculations for WWER-1 fuel.

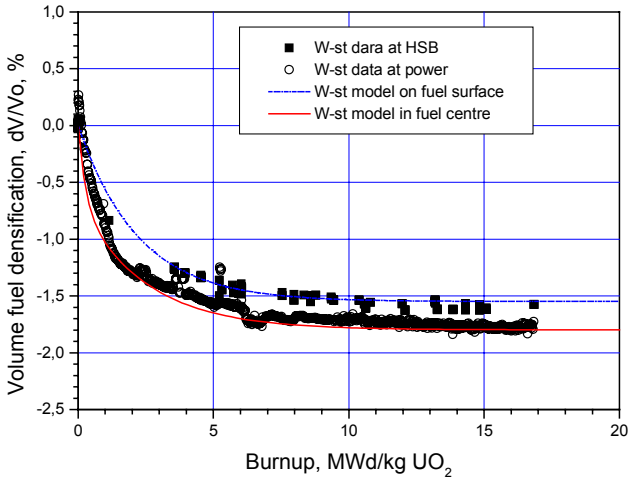

FIG. 7. Comparison between data and model calculations for standard WWER fuel.

5. MODELLING OF WWER AND PWR FUEL BEHAVIOUR USING THE SPAN CODE.

Validation and verification of fuel performance codes like the SPAN usually conducted on the basis of comparison between code predictions and common fuel characteristics such as cladding and fuel stack elongation, fuel centreline temperature, inner gas pressure and relative fission gas release derived from in-pile data. In some cases this comparison gives useful information of separate effects influence the integral fuel behaviour.

5.1. Fuel densification and swelling

Fuel stack elongation data provide the information of fuel densification and swelling which simultaneously affects fuel dimension changes at BOL. Provisional analysis of the data from IFA-503 and SPAN model predictions of fuel solid swelling has shown approximately identical results. It was found that the solid swelling evaluated from the data and predicted by the code were within 0.5-0.7 %/10 MWd/kg UO_2. This fact allowed implementation into the code the densification model presented above and analysing the behaviour of different fuel types in IFA-503. Figures 8 and 9 show comparison between the fuel stack elongation measured in WWER-standard and PWR fuel rods and predicted by the code. It should be noted that condensed power histories used for calculations could likely somewhat affect the fuel stack elongation predictions.

However, as can be seen from the figures the SPAN with new densification model predicts good enough the fuel stack elongation which reflects a higher densification in the standard WWER fuel than in the PWR fuel tested in IFA-503.1. Probably, somewhat underprediction of the fuel stack elongation at power can also be related to modelling of the “in-pile dishing” developed in the flat-ended pellets loaded into the fuel rods in the IFA-503. In order to estimate this effect on fuel stack elongation with power, a comparison between data and the code predictions during power ramps should be presented. Figs 10 and Fig. 11 show the fuel stack elongation measured and calculated in different WWER fuel types tested in IFA-503 as function of rod heat rating during several steady state power ramps. One of the ramps shown in these figures occurred when the fuel had achieved maximum densification. As can bee seen

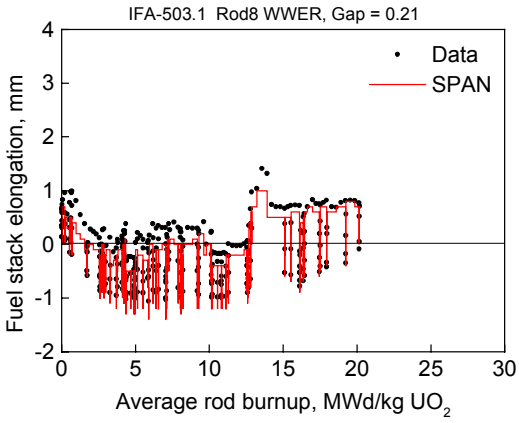

FIG. 8. Fuel stack elongation vs. burnup for standard WWER fuel in IFA-503.1.

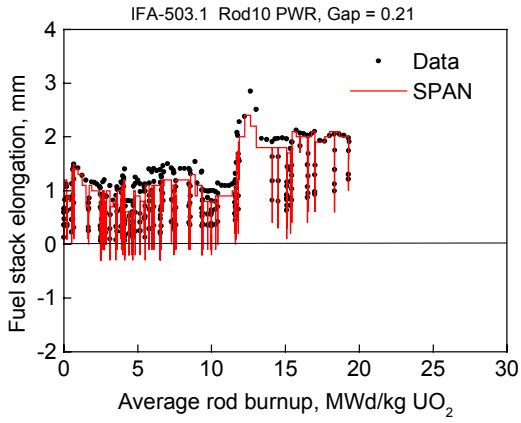

FIG. 9. Fuel stack elongation vs. burnup for PWR fuel in IFA-503.1.

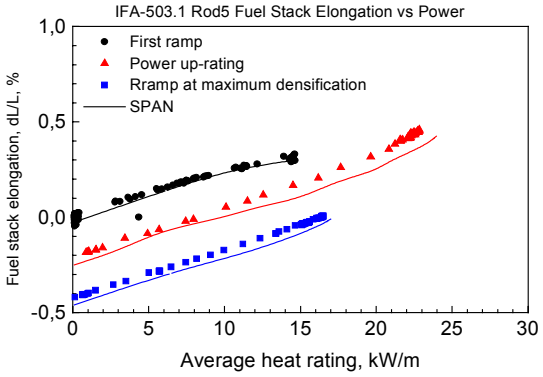

FIG. 10. Fuel stack elongation as a function rod heat rating for WWER fuel in IFA-503.1.

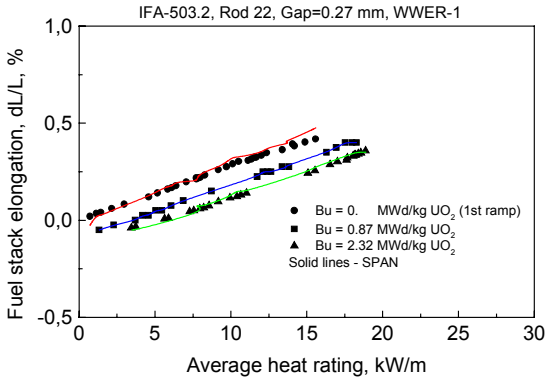

FIG. 11. Fuel stack elongation as a function rod heat rating for WWER fuel in IFA-503.1.

modified WWER fuel (denominated WWER-1) densified much less than the WWER fuel tested in the first loading in IFA-503.1. In all cases a slope of the calculated curves quite good fitted to the in-pile data on fuel stack elongation versus, that demonstrates correct simulation of fuel elongation at power ramps. It can be concluded that the SPAN code satisfactorily predicts fuel stack elongation for both standard and modified WWER fuel types tested in IFA-503.

5.2. Thermal fuel behaviour

The fuel centerline temperature is very important parameter for code verification. Fuel temperature responds to many effects, taking place during irradiation, such as fuel conductivity degradation, fuel densification, swelling, relocation as well as fission gas release affecting fuel-cladding gap conductance. Moreover, there is a temperature feed back effect, intensifying all mentioned processes in the fuel rods. Thus a comparison of measured and predicted fuel centerline temperature can be good indicator for code qualification. Figures 12 and 13 show such a kind of comparisons between fuel centerline temperatures predicted and measured in standard WWER fuel and in PWR in IFA-503.1.

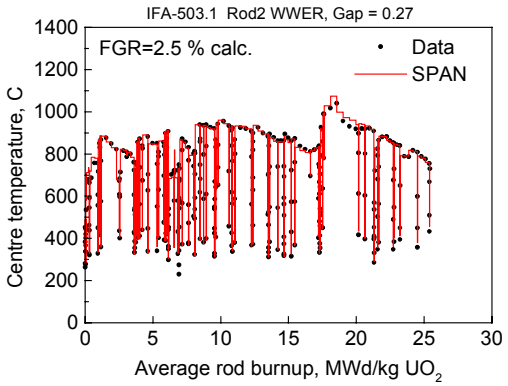

FIG. 12. Centerline temperature vs burnup, measured and predicted in standard WWER fuel tested in IFA-503.1.

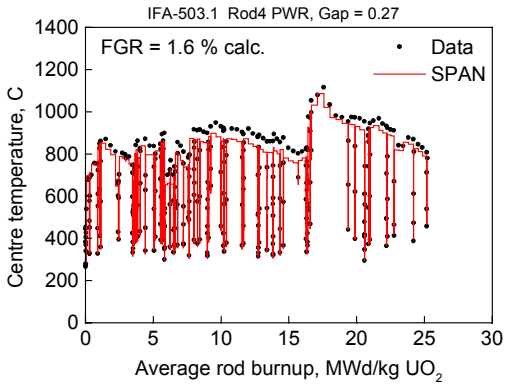

FIG. 13. Centerline temperature vs burnup, measured and predicted in PWR fuel tested in IFA-503.1.

5.3. Thermal fuel behaviour

The fuel centerline temperature is very important parameter for code verification. Fuel temperature responds to many effects, taking place during irradiation, such as fuel conductivity degradation, fuel densification, swelling, relocation as well as fission gas release affecting fuel-cladding gap conductance. Moreover, there is a temperature feed back effect, intensifying all mentioned processes in the fuel rods. Thus a comparison of measured and predicted fuel centerline temperature can be good indicator for code qualification. Figures 12 and 13 show such a kind of comparisons between fuel centerline temperatures predicted and measured in standard WWER fuel and in PWR in IFA-503.1.

Analysis of the temperature measurements show not only good enough predictions with code calculations but also practically identical fuel temperatures measured and calculated in the WWER and PWR fuel rods despite somewhat differences in the densification revealed in these fuel types. It should be noted that the calculations also predicted approximately the same temperatures in the WWER and PWR fuels during all irradiation time.

5.3. Fission gas release

Fission gas release is most important and quite complicated for prediction process. The SPAN FGR model based on White and Tacker's hypothesis [16] assumed that all fission gas, accumulated on grain boundaries, immediately releases in the free volume when its concentration exceeds a certain saturation level. FGR evolution derived from IFA-503.1 in-pile data and SPAN predictions are shown in Figs. 14 and 15 for standard WWER fuel tested in IFA-503.1. As can be seen the predicted FGR response to the power up-rating, occurred in IFA-503.1, showed an "explosive" behaviour in oppose to more or less its gradual increase derived from the data.

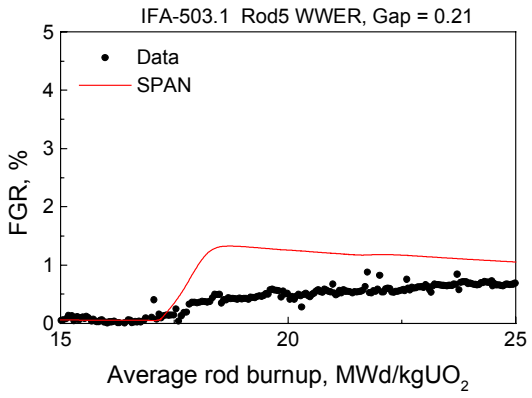

FIG. 14. FGR evaluated from data and predicted by the SPAN as a function of rod burnup

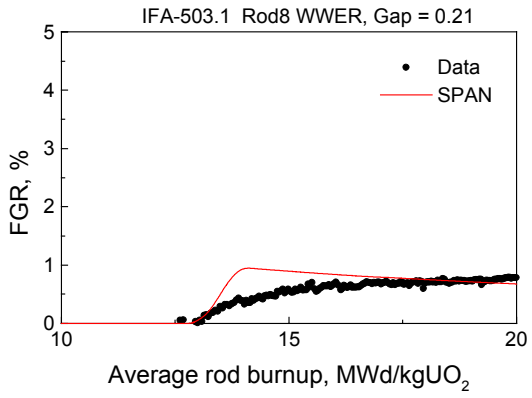

FIG. 15. FGR evaluated from data and predicted by the SPAN as a function of rod burnup

Nevertheless, the SPAN predictions are close the data despite the FGR revealed in the tests was very low and it was evaluated less than 1%. Note very important fact that SPAN code correctly predicted a commencement of FGR at the power uprating.

It should be noted that the SPAN code overpredicted the FGR from the PWR fuel. FGR response to a higher PWR fuel centre temperature due to solid fuel pellets loaded in the rod with pressure transducers was not clearly reflected in the gas pressure measurements. Relative FGR derived from the data showed approximately identical results for both fuel types. Overpredicted FGR calculated by the SPAN in the PWR fuel rods is not clear and will be estimated later.

6. CONCLUSION

The new SPAN code is developing for improved LWR fuel simulation at different burnups under steady state and operational transients. Some new models, related to high burnup fuel behavior, accounting for power and burnup radial distributions, athermal and thermal gas release from the RIM-region, as well as porosity development in the RIM, have been

incorporated into the SPAN. New tentative semi-empirical densification model is presented together with the data derived from the test IFA-503 in Halden reactor. Implementation of this model to the SPAN code allowed the carrying out model analysis of behaviour of the different fuel types tested in IFA-503. The code is in progress. Nevertheless, the good enough agreement with some data from IFA-503 gives a promise for successful applicability of the SPAN code to PWR and WWER fuel behavior simulations in future.

REFERENCES

[1] VOLKOV B., DEVOLD H., RYAZNTZEV E., YAKOVLEV V., “In-Pile Data Analysis of theComparative WWER/PWR Test IFA-503.”, Paper presented at EHPG Meeting, Loen, Norway, April 1999

[2] VOLKOV B., RYAZNTZEV E., YAKOVLEV V., DEVOLD H., “In-Pile WWER Fuel Investigation in the Halden Reactor.”, Third International Seminar "WWER Reactor Fuel Performance, Modeling and Experimental Support", Pamporovo, Bulgaria, October 1999

[3] STRIZHOV P., VOLKOV B., “Integral High Burnup Fuel Simulation Under Operational and Accident Conditions.”, An International Topical Meeting on LWR Fuel Performance, Park City, Utah, April 10-13, 2000.

[4] STRIZHOV P., VOLKOV B., “Integration of PIN and FRASM Codes Improved WWER Fuel Simulation under Operational and Accident Conditions”, Third International Seminar "WWER Reactor Fuel Performance, Modeling and Experimental Support", Pamporovo, Bulgaria, October 1999

[5] CUNNINGHAM M.E. et al., “Development and Characteristics of the Rim Region in High Burnup UO_2 Fuel Pellets.”, J.Nucl.Mater., 188 (1992) pp. 80-89.

[6] MATSUMURA T., KAMEYAMA T., “Burnup and Plutonium Distribution Near the Surface of High Burnup LWR Fuel”, IAEA Meeting “Water Reactor Fuel Element Computer Modelling in Steady State, Transient and Accident Conditions”, Preston, England, 1988.

[7] MEYER R.O., “The analysis of Fuel Densification”, NUREG-0085, July 1976.

[8] HAGRMAN D.T., “MATPRO- A library of Material Properties for Light-Water Reactor Accident Analysis”, INEL, NUREG/CR-6150, EGG-2720 Vol. 4. June 1995.

[9] WHITE R.J., “An Analysis of Halden Fuel Stack Length Changes and Comparison with UK Sintering Data” EHPG Meeting on Fuel Performance Experiments and Analysis and Computerised Man-Machine Communication, Bolkesjo, 1990.

[10] SMALL G.J., “Densification of Uranium Dioxide at Low Burnup”, Journal of Nuclear Materials, 148, 302, 1987.

[11] ASSMANN H., STEHLE H., “ Thermal and In-Reactor Densification of UO_2: Mechanisms and Experimental Results”, Nuclear Engineering and Design 48, 1978, 49-67.

[12] FRESHLEY M.D. et.al. Irradiation-induced densification of UO_2 pellet fuel, J. Nuclear Material,1976 vol. 62, 1976, 138.

[13] D.R.OLANDER D.R., “Fundamental Aspects of Nuclear Reactor Fuel Elements”, TID-26711-P1, 1976.

[14] CHALDER G.H., DEWES P, SCOTT D.B., “Measurements and Analysis of Fuel Densification
and Rod internal Gas Pressure in IFA-418 and IFA-419 Experiments.”, Paper presented at EHPG Meeting, Sanderstolen, Norway, March 1976.

[15] CALZA-BINI A. et.al., “Densification and Dimensional Instability of the Fuel under Irradiation.”, Paper presented at EHPG Meeting, Sanderstolen, Norway, March 1976.

[16] WHITE R.J. and TUCKER M.O., “A New Fission Gas Release Model.”, Journal of Nuclear Materials, 118, pp.1-38, 1983.

THE SPHERE-PAC FUEL CODE "SPHERE-3"

H. WALLIN, L.Å. NORDSTRÖM, C. HELLWIG
Paul Scherrer Institute,
Villigen, Switzerland

Abstract

Sphere-pac fuel is an advanced nuclear fuel, in which the cladding tube is filled with small fuel spheres instead of the more usual fuel pellets. At PSI, the irradiation behaviour of sphere-pac fuel is calculated using the computer code SPHERE-3. The paper describes the present status of the SPHERE-3 code, and some results of the qualification process against experimental data

1. INTRODUCTION

Sphere-pac fuel is one of the advanced nuclear-fuel technologies developed and investigated at PSI. In sphere-pac fuel pins, the cladding tube is filled with small fuel spheres instead of the more common fuel pellets. Compared to pellet fabrication, the inherent advantage of sphere fabrication is that it is a simple, dustless process, and one which can easily be remote controlled. The absence of dust has special importance in the re-cycling of alpha-active nuclides such as plutonium or certain "waste" nuclides, thereby reducing the amount of nuclear waste.

PSI has carried out several fuel tests in different research reactors to investigate the irradiation behaviour of sphere-pac fuel, and to compare its performance against ordinary pellet fuel. Experimental fuel testing is in close contact with the theoretical modelling of fuel. Modelling is needed, firstly, to support the fuel design; secondly, for optimal test planning; and thirdly, to ensure that operational limitations such as maximum fuel temperature and gas pressure are not exceeded. Equally, the most important feedback for further model development is the post-irradiation examination of the fuel.

Correct fuel temperature and fission gas pressure predictions require in-depth knowledge of the material properties and reliable modelling of sphere-pac fuel. At PSI, sphere-pac fuel has been modelled using the computer code SPHERE, which incorporates mechanistic models for sintering, fission gas behaviour, etc. Recently, numerous improvements have been made to the SPHERE program, including fundamental changes to the fission gas release model and addition of a fuel-restructuring (pore migration) model.

This paper describes the present status of the SPHERE-3 code, and highlights the new features which have been installed. Some results of the code qualification against experimental data are also presented.

2. SINTERING OF SPHERE-PAC FUEL

2.1. As-fabricated structure of sphere-pac fuel

The main reason why sphere-pac fuel cannot be modelled using existing codes for pellet fuel is the complicated heat transfer which occurs between the spheres, which increases considerably as the contact area grows as a result of sintering. Consequently, in order to

understand the structure and models in the SPHERE program, we must first examine these unique features of sphere-pac fuel, i.e. sintering behaviour and thermal conductivity.

Sphere-pac fuel consists of a coarse-sphere fraction (typically 500–1200 μm), and one or two fine-sphere fractions (from 40 to 250 μm) which are used to fill the empty spaces between the coarse spheres. The coarse and fine fractions can be packed at the same time, or the fine fraction can be infiltrated into the coarse fraction using a vibration technique.

2.2. Growth of the necks

The original, as-fabricated, sphere structure changes in the reactor as a result of sintering, in which spheres bind together via mass transport mechanisms. The bonds reduce free surface area, and minimise surface energy. Most materials sinter at temperatures exceeding approximately one half of the melting temperature.

During sintering, the contact area between two adjacent fuel spheres can grow from (initially) zero to total fusion of the spheres. The degree of sintering is usually described by the size of this contact area; i.e., the neck between the spheres. The neck size is given by the neck ratio x/r, where r is the fuel sphere radius and x is the radius of the spherical contact area.

2.3. Stresses as driving forces for sintering

Stresses in fuel spheres act as driving forces for different sintering mechanisms, and can be divided into an inherent sintering stress, caused by differences in surface curvature, and an external mechanical load.

2.3.1. Sintering stress

The non-uniform, disrupted atomic bonding on the surface is the source of surface energy, a form of potential energy. If the surface is curved, the surface energy causes a stress called the sintering stress [1]:

$$\sigma = \gamma \cdot \left(1/r_1 + 1/r_2\right) \qquad (1)$$

where σ = sintering stress,
γ = surface energy,
r_1, r_2 = radii of the principal surface curvatures.

The stress is positive (tensile stress) if the radius is inside the surface, and negative (compressive stress) if outside the surface. A flat surface has an infinite radius and no stress. According to Eqn. (1), the higher the surface energy, and the smaller the sphere radius, the higher is the stress. For a perfect sphere, of radius r, the stress on the surface is $2\gamma/r$.

In a single sphere, the stress is the same everywhere on the surface, and material transport is disabled. However, in the neck area, the radius of curvature is outside the surface, and the stress is negative, i.e. compressive. The sign of the stress changes over a small distance, causing a high stress gradient. This gradient is the driving force for several mechanisms which transport material from the sphere surface into the neck [1]. Stress differences can be

relatively high. For example, in the fine-sphere fraction, with small initial necks, a typical stress difference is 20 - 25 MPa. As mass transport increases, neck sizes and surface curvature differences are reduced, and sintering slows down.

In a similar way, the atomic bonding at the fuel grain boundary is disrupted, creating grain boundary energy. During sintering, grains grow and coalesce to minimise the grain boundary energy.

2.3.2. External mechanical load

Sintering stress is supplemented by an external mechanical load. Initially, the necks are small, and the external load is concentrated, and amplified, on the small contact areas. Theoretically, for a point contact, the stress would be infinite. As the neck grows, the stress in the contact area decreases, and gradually approaches the applied external stress.

2.4. Sintering mechanisms

The name of the sintering mechanism indicates by which route the mass flows into the neck area. The mechanisms are divided into two categories (Fig. 1):

- *Surface transport mechanisms*, which move mass from the sphere surface to the neck surface. As a result, spheres do not approach each other and, consequently, there is no shrinkage or densification of the fuel. The driving force is the difference in surface curvature between the neck and the surface far away from the neck. Curvature differences decrease as a consequence of mass flow, and the total surface energy is thereby minimised. External mechanical load has no effect on these mechanisms.

- *Bulk transport mechanisms*, which move mass from the sphere interior to the neck, causing the spheres to approach each other and the fuel to shrink. These mechanisms are affected by external mechanical load, and are more important at higher temperatures.

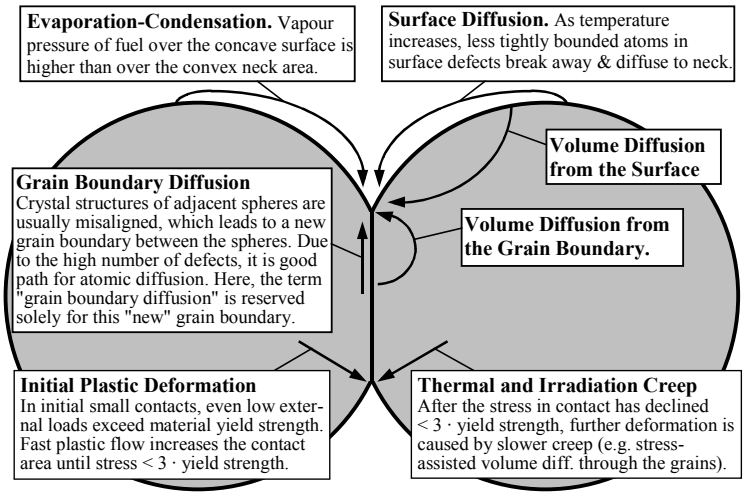

FIG. 1. Mass transport routes during sintering.

Models for the sintering mechanisms incorporated in the SPHERE code, and illustrated in Fig. 1, are [1]:

1) Plastic and elastic deformation (bulk deformation);
2) Surface diffusion (surface transport);
3) Grain boundary diffusion (bulk transport);
4) Volume diffusion (both bulk and surface transport);
5) Evaporation-condensation (surface transport);
6) Thermal creep (bulk deformation); and
7) Irradiation creep (bulk deformation).

With increasing temperature, the following mass transport mechanisms dominate successively: surface diffusion (low temperatures), grain boundary diffusion (intermediate temperatures), and volume diffusion (high temperatures). For each, a threshold exists below which the effect is negligible, each process then dominating till the next threshold occurs.

During sintering, free surface area and curvature gradients decrease and, at the same time, the new grain boundary between the spheres grows. As a consequence, surface diffusion progressively becomes less important in comparison to grain boundary diffusion.

Spheres can be sintered with or without shrinkage, and accompanying densification, depending on which mechanisms are exploiting the available driving forces. For example, if temperature increases slowly, necks can be formed by surface diffusion; i.e., without shrinkage. When higher temperatures are reached, curvature differences have already decreased, and the driving force for other sintering mechanisms causing shrinkage have already been exploited.

3. DESCRIPTION OF SPHERE-3

3.1. Main characteristics of SPHERE-3

In SPHERE-3, the fuel rod is divided into axial segments and radial rings, within which the material properties and the fuel behaviour are assumed uniform.

The code may be considered "1.5 dimensional" in that it involves a superposition of a 1-D radial and 1-D axial calculation. Any number of sphere size fractions can be considered, and the fuel data bank includes models for the most relevant properties for oxide, carbide and nitride type fuels, and for different clad materials such as zircaloy and stainless steel.

3.2. Calculation of thermal conductivity

Around neck ratio *x/r=45%* (neck-diameter/sphere-diameter), the thermal conductivity of sphere-pac fuel approaches that of pellet fuel of the same smear porosity. Thus, a neck ratio of 45% in the finest fraction has been chosen to indicate the transition from a sphere-like structure to one resembling porous pellet fuel. Therefore, to calculate the thermal conductivity of sphere-pac fuel, the fuel is divided into two zones:

- *The compact sintered body* in the inner, hotter part of the pin (Zone II in Fig. 7). Here, the original sphere structure has totally disappeared and the thermal conductivity can be calculated using the models for porous pellet fuel.

- *The cooler, outer area of the pin*, where the origi-nal sphere structure is still visible (Zones III and IV in Fig. 7). In this area, thermal conductivity is interpolated between the theoretical value for the porous pellet structure (*x/r = 45%)* and that for the totally unsintered spheres (*x/r= 0*). The latter is calculated using the model of Hall and Martin [2].

3.3. Calculation of sintering

SPHERE-3 calculates neck ratios until that of the smallest sphere fraction has reached 0.45. After this, the thermal conductivity models for a porous pellet are used. The shrinkage of the fuel due to sintering is also calculated by the code. However, at present, the information is not used further, and is needed only as input for a mechanical model, not yet implemented.

For every sintering mechanism, SPHERE-3 calculates the derivative of the neck size. Linear combination of the sintering mechanisms is assumed; i.e., the derivatives of different mechanisms are added together [1].

The high sensitivity of the sintering mechanisms to sphere and neck size can be seen if the derivatives are simplified to the form:

$$\frac{\partial}{\partial t}\left(\frac{x}{r}\right) = A \cdot \frac{1}{r^z} \cdot \frac{1}{(x/r)^y} \qquad (2)$$

where:

A = collection of different parameters like creep and diffusion coefficients, vapour pressure, surface energy, etc.
z =dependence on sphere size *(r)*:
4 for surface and grain boundary diffusion
3 for volume diffusion
2 for evaporation-condensation
0 for creep
y =dependence on neck size *(x/r)*:
5 for surface and grain boundary diffusion
3 for volume diffusion
1 for evaporation-condensation

Increasing the sphere size primarily slows down sur-face and grain boundary diffusion (*z = 4*). The latter is strongly affected, since the grain boundary energy decreases with sphere size. Sphere size has a much smaller effect in evaporation-condensation (*z = 2*), while creep is totally independent of sphere size.

Growing of necks principally slows down surface and grain boundary diffusion (*y = 5*). As the neck grows, curvature differences decrease, and the driving force for the mechanisms is reduced.

3.4. Iteration of temperature and sintering

Sintering has a strong effect on fuel temperatures, as the difference in thermal conductivity is large for neck ratios between 0 and 45%. Therefore, as sintering proceeds, the thermal conductivity increases rapidly, decreasing the fuel temperature, and further slowing down

sintering. Therefore, at every time step, the fuel temperature and sintering must be solved in an iteration loop consisting of the calculation of:

- the thermal conductivity of the fuel and cladding,
- the temperature in the fuel and cladding,
- the free gas pressure in the fuel rod, and
- the neck sizes and shrinkage of the fuel.

3.5. New features of SPHERE-3

The latest code version SPHERE-3 has several new features including:

A restart option, allowing the calculation of a separate base irradiation, followed by further irradiation after rod refabrication (including changes in gas composition, pressure, plenum volume and the addition of a central hole for a thermocouple), [3].

A pore migration (fuel re-structuring) model has also been added. In the pores, vapour pressure of the fuel is higher on the hotter pore surface compared with the colder side. Consequently, UO_2 molecules evaporate on the hotter, and condense on the colder side. As a result, the pores move towards the higher temperature region, i.e. towards the pin centre. As the pore moves, it leaves behind a new, elongated fuel grain (columnar grain). The model in SPHERE-3 takes into account the molecular diffusion of UO_2 molecules through the contained gas, the composition and state of the gas in the pore, and the reduction of pore velocity due to the combined effects of impurity accumulation on the hot face and condensation rate limitations on the cold face [3, 8].

A new fission gas model, based on work by Speight [4], Turnbull [5, 6], and White & Tucker [7]. Here, fuel is considered as a collection of spherical fuel grains, where fission gas exists as single, freely diffusing atoms. On their way out of the grain, gas atoms may become trapped at immobile intra-granular bubbles, or at as-fabricated pores. Bubbles grow by absorbing gas atoms before being destroyed by a fission fragment (intra-granular resolution). At grain boundary, atoms are absorbed into grain boundary bubbles. Interlinkage of the grain boundary bubbles initiates the gas release. Because of the resolution from the grain boundaries back to the grain, grain boundaries act as imperfect sinks for diffusing gas atoms (inter-granular resolution).

A model has been included to calculate the gas swept out by the moving grain boundaries during the growth of the equiaxed grains. Additionally, the pores which form columnar grains are assumed to sweep out and release 100% of the fission gas. The description of the fission gas model in SPHERE-3 is given in [3].

Numerous new physical models have been added, including the recent Lucuta model for degradation of thermal conductivity [9], and the code has an option to read large operation histories (power, coolant temperature) from a separate file [3], and an option to approximate the initial bed load during a startup ramp [10]. At input, the possibility exists to give the radial power profile as a function of time, and a new control structure allows for free selection of physical models and material properties from the material property library. Finally, there is an option for enhanced, time-dependent thermal creep rate immediately after introducing a stress which is higher than any which has existed in the material before [3].

4. OUT-OF-PILE SINTERING TEST

SPHERE has been validated by comparing code predictions against the following experimental data:

- an out-of-pile experiment with UO_2 spheres;
- the AC-3 irradiation test of mixed carbide, (U,Pu)C, fuel in the Fast Flux Test Facility (FFTF);
- the Halden-Gösgen experiment with UO_2 spheres.

In Sections 4, 5 and 6, some results of this validation programme are presented.
At PSI, an out-of-pile sintering test was performed in which UO_2 spheres were sintered in an Ar/8% H atmosphere at temperatures between 1350°C to 1650°C; the duration of sintering varied from 1 to 24 hours.

The sintering model of the former code version SPHERE-2 was compared against data from this test. The neck ratios calculated by SPHERE were between 9% and 58% higher than the measured values; i.e., the sintering calculated by SPHERE was faster than that measured. However, the differences between measured and calculated neck sizes were not large, and the sintering model was left unchanged.

5. AC-3 IRRADIATION TEST

5.1. Test description

The objective of the "Joint USA-Swiss Experiment AC-3" was to compare the irradiation performance of sphere-pac fuel pins fabricated here at PSI by the sol-gel process against pellet pins fabricated at the Los Alamos National Laboratory. Ninety-one mixed carbide $(U_{0.8}Pu_{0.2})C$ pins were irradiated in FFTF by the Westinghouse Hanford Company. Sixty-six of them contained pellet fuel and the remaining twenty-five pins had sphere-pac fuel. The smear density of sphere-pac pins ranged from 78.8% to 80.3% of the theoretical density. The irradiation of the AC-3 assembly began in 1986 and ended in 1988. The pins were irradiated for 620.3 effective full-power days to peak burnups of 8.4 at.% (% FIMA) at linear powers of up to 84 kW/m.

Before simulating the AC-3 test, the material properties and models in SPHERE-2 for (U,Pu)C were first reviewed. As a result, some of the models were first changed, either to meet the recommendations in the open literature, or to better suit the hyperstoichiometric $(U_{0.8}Pu_{0.2})C_{1.04\text{-}1.05}$ fuel. Unfortunately, the available material properties for (U,Pu)C fuels show large scatter. Consequently, the results of the SPHERE-2 calculation do not have the same confidence level as with oxide fuels.

5.2. Calculation versus PIE

In destructive post-irradiation examination (PIE), eight ceramographic sections were cut from four fuel pins. From these four pins, the pin 3L115, operating at the highest rating, was selected for comparison against a SPHERE-2 calculation. The comparison showed that:

- At the outer fuel area, close to the cladding, the neck sizes calculated by SPHERE-2 were consid-erable smaller than the measured values; 2.5% (SPHERE-2 calculation) vs. 9 - 26% (measured).

- Agreement was much better when comparing how much of the fuel had transformed into a compact sintered body; 52.5% (SPHERE-2 calculation) vs. 48% (measured); see Fig. 2.

- The SPHERE-2 calculation gave a similar overall fuel structure to that observed in PIE: the transition zone between the strongly sintered inner part and the less sintered outer region was narrow and distinct. In addition to this, the calculated transition zone was also in the correct radial position.

The seemingly good agreement between the calculated (5.2%) and measured (4.9%) fission gas release fractions should not be seen as a measure of the accuracy of the model, but as more or less coincidental since no precise data for fission gas behaviour in (U,Pu)C fuels were available.

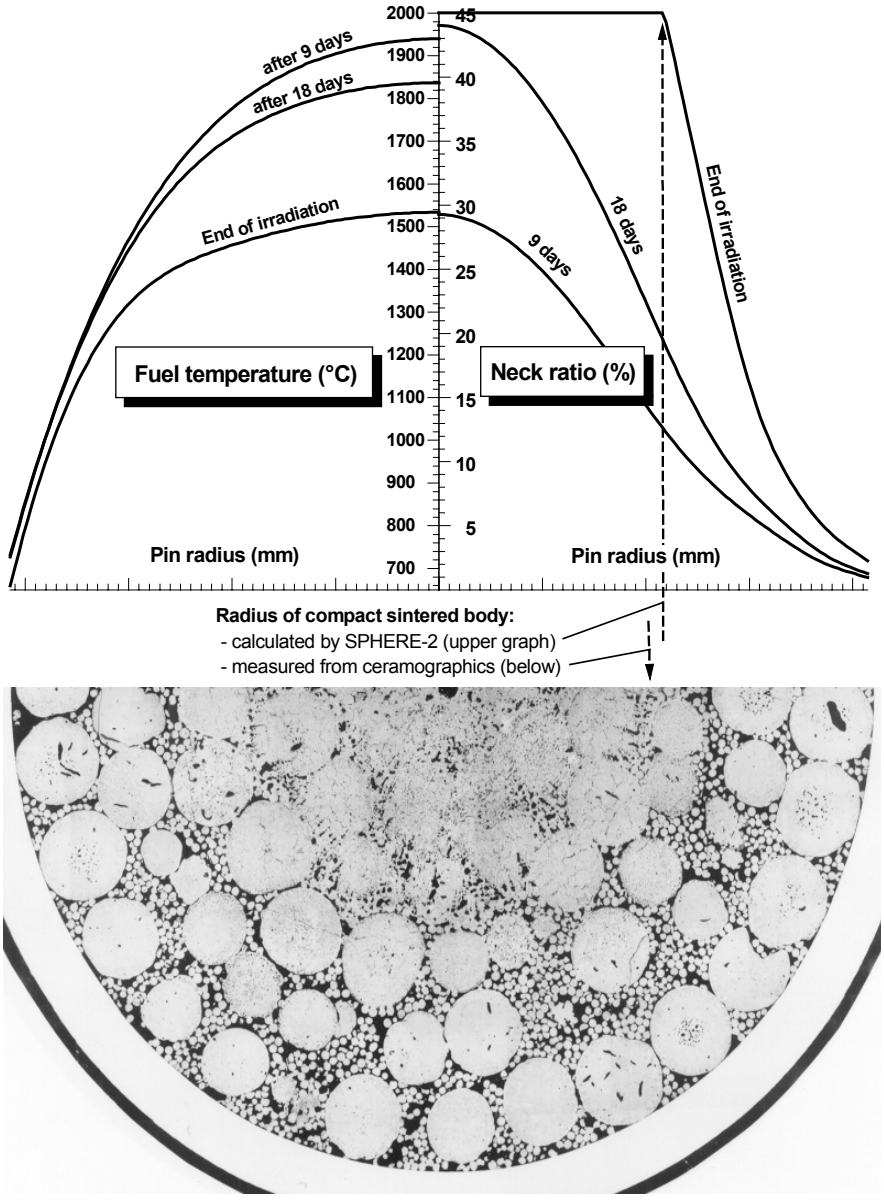

FIG. 2. Carbide test AC-3: calculated fuel temperatures and neck ratios (top), comparison of calculated (top) and measured (bottom) size of compact sintered body.

6. HALDEN-GÖSGEN IRRADIATION TEST

6.1. Test description

In 1986, twelve segments containing sphere-pac UO_2 fuel produced by the gelation method at PSI, and eight segments containing UO_2 pellets produced by Siemens AG, were loaded into the Swiss Gösgen PWR for a comparative irradiation test. The segments were grouped to make four full-length KKG fuel rods. One rod was to be withdrawn at each annual shutdown for post-irradiation examination in the PSI hot cells. The irradiation was completed in 1991, after which non-destructive and destructive post-irradiation examination was performed at PSI [13].

Sphere-pac segment S15 (Table 1) and pellet segment NO2 from the one-cycle rod were sent to Halden for a further ramp test (rapid power increase). After they were instrumented at the "Institutt for Energiteknikk" (IFE) in Norway, they were inserted into the Halden Boiling Water Reactor (Test IFA-550.9). After the ramp test, the two segments were examined at IFE, both non-destructively and destructively, and the results were compared against SPHERE-3 predictions.

TABLE 1. SPECIFICATION OF SEGMENT S15

DESCRIPTION	INPUT FOR SPHERE-3	UNIT
Fuel active length	39.33	cm
Clad inner / outer radius	0.4648 / 0.5377	cm
Fuel mass	252.24	g
Smear density	86.22	%
Initial He pressure	22.5 (at 20°C)	bar
	In fractions: 1 / 2 / 3	
Sphere diameter	1155 / 275 / 39	m
Mass fraction	0.6487 / 0.1996 / 0.1516	
As-fabric.porosity	0.0125 / 0.0135 / 0.0037	
Enrichment U-235	0.0431 / 0.0429 / 0.0425	
Grain diam. BOL	11.6 / 7.5 / 12.1	m

6.2. Modelling segment S15

To model segment S15, 9 axial slices were used, and 70 radial fuel rings. Due to the rod refabrication, after calculating the Gösgen base irradiation, the fill-gas pressure, composition and free volume were changed in SPHERE-3 before restarting for the Halden ramp test. Halden irradiation was calculated using the complete operation history; i.e., every 15 minutes, new operation history variables were read from the Halden data file. The entire irradiation history (Gösgen base irradiation + Halden ramp test) is shown in Fig. 3.

As SPHERE has no mechanical model, the mechanical bed load, created by the different thermal expansions of the fuel and clad, had to be estimated. The load was assumed to be constant at 0.01 bar, since the sintering and shrinkage of the "soft" centre zone relieves the load. However, it was shown that the results were not sensitive to bed load.

6.3. Results of the calculation

6.3.1. Calculated fuel temperature

The calculated fuel peak centre temperature during the entire irradiation is shown in Fig. 3. During the base irradiation, the fuel temperatures were low, most of the time under 1250°C. In Halden, the fast initial sintering led to better fuel thermal conductivity, this partly compensating for the higher power level. The power ramp at burnup 1.7% FIMA Metal Atom (FIMA) increased the centre temperature quickly to 2440°C. Because of continuous sintering and power decline, the fuel centre temperatures decreased steadily during the rest of the irradiation. Due to the absence of a fuel-clad gap, the fission-gas release increases temperatures in sphere-pac fuel much less than for pellet fuel.

6.3.2. Calculated average fission gas release

The rod-averaged fission gas release fraction is also shown in Fig. 3. At the end of the irradiation, the calculated fission gas release fraction was 36%. During the post-irradiation examination (PIE) of segment S15, a release fraction of around 45% was measured.

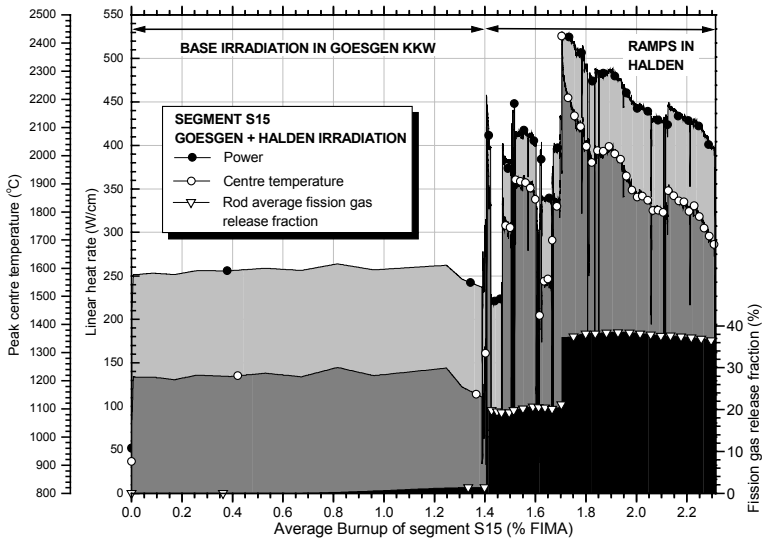

FIG. 3. Axial peak power, temperature and fission gas release fraction calculated by SPHERE-3.

6.3.3. Calculated local fission gas release

All the results which follow are shown as three-dimensional surfaces depicting parameter profiles (values along the fuel radius) as a function of burnup. Profiles are shown for axial elevation 327.8 mm, at which one of the samples for ceramography was taken (power at this elevation was 99% of the axial peak power).

Profiles in Fig. 4a (base irradiation) and Fig. 4b (Halden irradiation) show: i) local cumulative fission gas production; ii) local, cumulative fission gas release; and iii) local fission gas remaining in the grain boundary bubbles.

After the base irradiation, even in the fuel centre, most of the gas was not released, staying inside the fuel grains or at the grain boundaries (Fig. 4a). In SPHERE-3, lenticular pores, while moving towards the pin centre (creating columnar grains), are assumed to collect all

fission gas in the fuel and release it to the pin-free space. This is clearly seen in Fig. 4b as an enhanced release. After the power ramp, temperature decreased, pore movement ceased, and gas continued to collect in the fuel grains.

6.3.4. Calculated sintering

Base irradiation: Figure 5a shows the neck ratio profiles along the fuel radius in the fine fraction (39 μm) during the base irradiation. The symbol marks the dominant sintering mechanism at each time step. Through the entire base irradiation at low temperatures, grain boundary diffusion was the dominant sintering mechanism, and irradiation creep dominated only in the narrow, cooler area close to the cladding. At the end of the base irradiation, the maximum neck ratio at the centre was 27%, and at the area close to the cladding only 1%. Thus, the fuel had not lost its original sphere structure. This was confirmed in a PIE test performed for the sibling rod of S15 after the base irradiation.

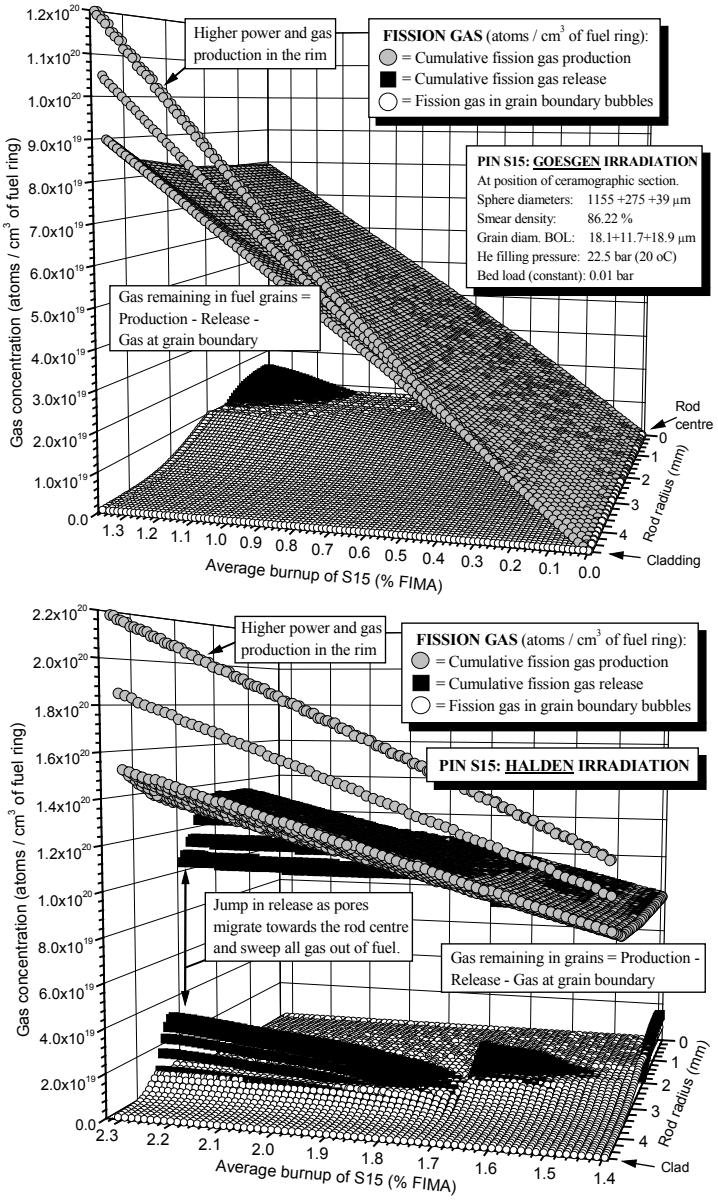

Fig. 4: Gas concentration profiles as function of time:
Top: Base irradiation in Gösgen (a)
Below: Ramp test in Halden (b).

Halden irradiation: In Halden, the temperatures were much higher, and the SPHERE-3 calculation showed rapid sintering. In the centre of the fuel pin, a compact, sintered body (*x/r = 45%*) was formed almost immediately at the beginning of the test (Fig. 5a). As the necks between the fuel spheres grew, thermal conductivity increased. As a result, temperatures decreased, and sintering slowed down.

The next, steep increase in sintered area was during the power ramp, at burnup 1.7% FIMA. After this, the growth of the compact sintered body towards the outer fuel zones nearly stopped, because:

- at the outer zones, temperatures were lower;
- sintering had decreased the fuel temperatures; and
- further temperature decrease occurred as a result of the steadily decreasing power.

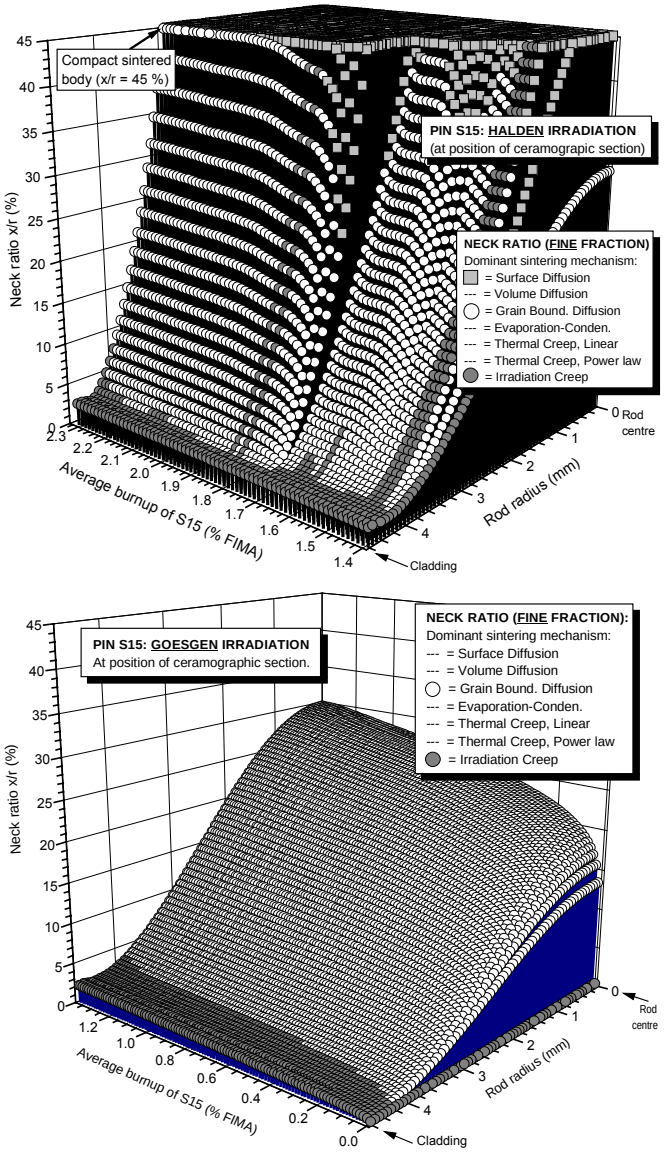

FIG. 5. Neck ratio profiles as a function of time: top: Ramp test in Halden (a); below: Base irradiation in Gösgen (b).

At the end of the irradiation, the sintered body consisted of 62.9% of the fuel outer radius. In the area close to the cladding, temperatures were still less than those needed to activate sintering mechanisms, and the neck ratio never exceeded 2 - 3%.

6.3.5. Calculated restructuring (central void)

Calculation showed no fuel restructuring during the base irradiation (confirmed with the sibling rod).
Figure 6 shows the calculated fuel density profiles along the pin radius during the Halden irradiation. During the power ramp, at burnup of 1.7% FIMA, first signs of an emerging central void were seen as the density in the pin centre decreased to 39%. However, the minimum density was not reached at the pin centre but slightly further out, where the calculation showed a nearly void zone, with a density 6%. This was formed because the pore movement slowed down near the centre as its driving force, i.e. the radial temperature gradient, decreased near the fuel centre. Further outwards still, the density increased to 91% as the pores moved from that area towards the centre.

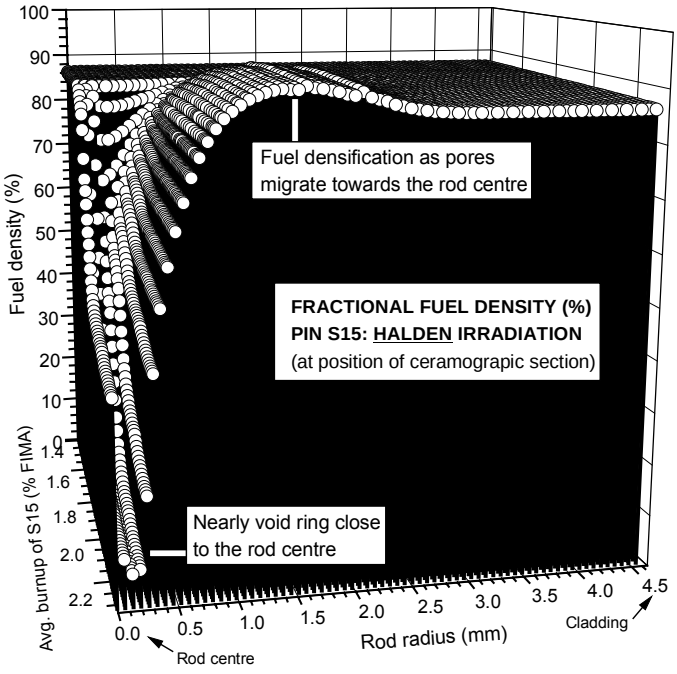

FIG. 6. Fuel density as a function of time (Halden).

6.4. SPHERE-3 calculation versus PIE

Results from the SPHERE-3 calculation are compared with the ceramographic section at the axial elevation of 327.8mm in Fig. 7. The section shows four distinct radial zones, typical for sphere-pac fuel. Starting from the pin centre:

Zone I: The central void, formed by pores migrating towards the pin centre. If the power is high enough (500-600 W/cm), a central void can appear in just a few hours. In Halden, ceramographics (Fig. 7) showed a nearly voided pin centre and another near-void ring at 0.6mm from the fuel centre. This structure is very similar to the calculated structure (Fig. 6).

Zone II: The strongly sintered zone (compact sintered body), where the original sphere structure is no longer visible, and the fuel structure is similar to porous pellet fuel. Early in the life of the fuel, this structure is found only at high temperatures (e.g. at 30 hours, at temperatures typically >1500°C). Later, it appears at lower temperatures (e.g. at 10000 hours, temperatures >1200°C). At these latter temperatures, fuel is mechanically "soft", and initial plastic deformation and thermal creep cause rapid sintering. The SPHERE-3 calculation gave the same radius of the compact sintered body as the ceramographics (62% vs. 62.9%).

Zone III: The transition zone between the slow- and the fast-sintering areas is relatively narrow, due to the small temperature difference needed to shift from slow to rapid sintering and the large temperature gradient in the fuel.

Zone IV: The weakly sintered outer zone is where the original sphere structure is visible. Temperatures are low (<800°C), and irradiation creep is the dominant sintering mechanism.

In Table 2, the sintering characteristics measured from the ceramographic section in Fig. 7 are compared with results from the SPHERE-3 calculation. The agreement is good in regard to the radius of the compact sintered body: 62% vs. calculated 62.9%. The calculation also showed similar overall fuel structure, with a narrow and distinct transition zone between the compact sintered body and the less sintered outer region.

Only in the outer area, close to the cladding, did SPHERE-3 underpredict the neck size compared with the PIE. The reason could be that, in SPHERE-3, the sintering mechanisms which dominate at lower temperatures are too slow. Another possibility is the radial transport of volatile fission products and fuel from the centre (by evaporation) to the cooler, outer zone (where it condenses). Neck growth by this mechanism has been observed recently in another experiment, and will be reported later.

TABLE. 2. SPHERE-3 CALCULATION VERSUS PIE

Position of neck (from pin centre):	**Neck Ratio x/r according to:**	
	PIE	**SPHERE-3**
62.4 %	34.3 - 44.6%	44.6 %
70.7 %	31.5 %	28.4 %
75.0 %	24.7 - 27.0 %	21.0 %

Compact sintered body (*% of fuel radius):*		
	PIE	**SPHERE-3**
Elevat. 327.8 mm	61.5 - 62.5 %	62.9 %

Fission Gas Release Fraction (Rod Average):		
	PIE	**SPHERE-3**
AFTER IRRADIATION:		
-IN GOSGEN	**0.8 %**	**1.36 %**
IN HALDEN	**45 %**	**36 %**

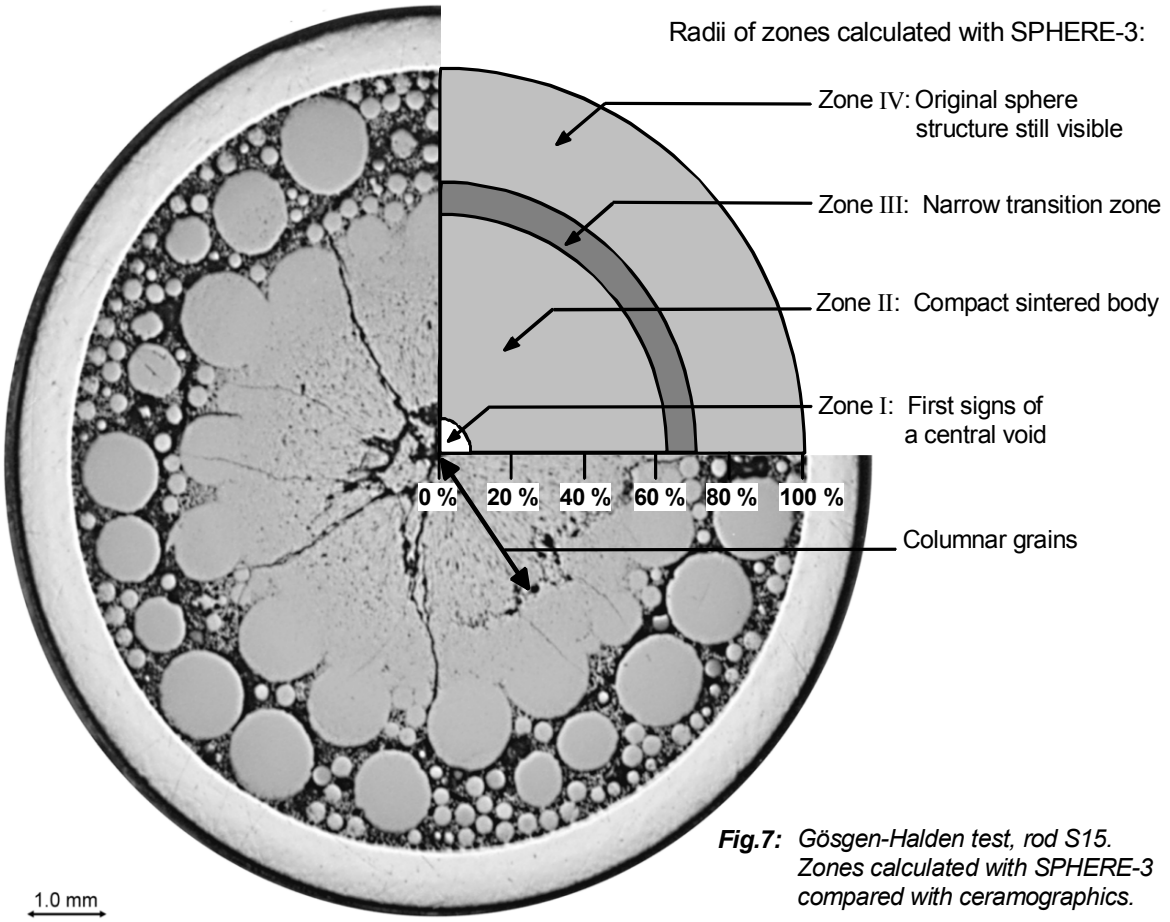

Fig.7: *Gösgen-Halden test, rod S15. Zones calculated with SPHERE-3 compared with ceramographics.*

7. CONCLUSIONS

The sphere-pac fuel code SPHERE-3 has been thoroughly reviewed, and old models have been up-dated or replaced. In addition, new features have been added, enabling experiments with higher temperatures and higher burnups to be simulated.

Modelling the irradiation of sphere-pac fuel has so far been very successful, as the comparison of the SPHERE-3 results with experimental data has demonstrated. Particular improvements have been noted in the following areas:

1. The fuel re-structuring (pore migration) model of SPHERE-3 could produce the same fuel structure observed in ceramographics.

2. The radius of the compact sintered body (where the original sphere structure has transformed into porous pellet structure) has been calculated correctly. However, in the outer fuel area, close to the cladding, the neck sizes calculated by SPHERE-3 have been generally smaller than the measured values.

3. The fission-gas release model in SPHERE-3 could predict about the same gas release as measured. However, two parameters need to be set: the temperature above which columnar grains are formed (set as 1600^{o}C), and a parameter for gas resolution from grain boundaries. In the next phase, SPHERE-3 will be used for the layout of a MOX sphere-pac irradiation test in the "High Flux Reactor" at Petten (NL).

ACKNOWLEDGEMENTS

The SPHERE-code was developed in the past fifteen years in the context of different PSI fuel research projects guided by R.W.Stratton and G.Ledergerber. The authors also like to thank the Swiss utilities for the financial support of the actinide and fuel research work in PSI. The last and very fruitful effort in establishing and validation was done in the framework of a co-operation with the Japan Nuclear Cycle Development Institute (JNC-PSI Sphere-Pac Fuel program).

REFERENCES

[1] J.R. MATTHEWS, "The Initial Stages of Sintering and Hot-Pressing in Vibro-Compacted Fuels", Journal of Nuclear Materials, **87,** p.356 (1979).

[2] R.O.A. HALL, D.G. MARTIN, "The Thermal Conductivity of Powder Beds, a Model, Some Measurements on UO_2 Vibro-Compacted Microspheres, and Their Correlation", Journal of Nuclear Materials, **101**, p.172 (1981).

[3] H. WALLIN, "SPHERE-3: A New Code Version. New Features Explained", PSI Internal Report, TM-43-99-39 (1999).

[4] M.V. SPEIGHT, "A Calculation on the Migration of Fission Gas in Material Exhibiting Precipitation and Re-solution of Gas Atoms under Irradiation", Nuclear Science and Engineering, **37**, p.180.(1969).

[5] J.A. TURNBULL, C. FRISKENEY, J. FINDLAY, F. JOHNSON, J. WALTER, *"The Diffusion Coefficients of Gaseous and Volatile Species during the Irradiation of Uranium Dioxide"*, Journal of Nucl. Mat. **107**, pp.168-184 (1982).

[6] J.A. TURNBULl, *"An Assessment of Fission Gas Release and the Effect of Microstructure at High Burn-up"*, OECD Halden Reactor Project, HWR-604 (1999).

[7] R.J. WHITE, M.O. TUCKER, *"A New Fission-Gas Release Model"*, Journal of Nuclear Materials **118**, pp.1-38 (1983).

[8] D.R. OLANDER, *"Fundamental Aspects of Nuclear Reactor Fuel Elements"*, published by Energy Research and Development Administration, ISBN 0-87079-031-5 (1976).

[9] P.G. LUCUTA, HJ. MATZKE, I.J. HASTINGS, *"A Pragmatic Approach to Modelling Thermal Conductivity of Irradiated UO_2 Fuel: Review and Recommendations"*, Journal of Nuclear Materials **232**, pp.166-180 (1996).

[10] Ch. HELLWIG, H. WALLIN, *"Shrinkage and bed load of sphere-pac fuel during irradiation"*, PSI Internal Report, TM-43-98-21 (1998).

[11] H. WALLIN, *"SPHERE-2: Comparison of Sintering Model with Out-of-Pile Measurements"*, TM-43-98-39, PSI Internal Report (1998).

[12] H. WALLIN, *"Irradiation of Mixed Carbide Fuel (AC-3 Test): Modelling of Pin 3L115 with the Fuel Code SPHERE-2"*, PSI Internal Report, TM-43-99-10 (1999).

[13] R.W. STRATTON, F. BOTTA, R. HOFER, G. LEDERGERBER, F. INGOLD, C. OTT, J. REINDL, H.U. ZWICKY, R. BODMER, F. SCHLEMMER: *"A Comparative Irradiation Test of UO_2 Sphere-pac and Pellet Fuel in the Goesgen PWR"*, Intern. Topical Meeting on LWR Fuel Perform., Avignon, France (1991).

THE PROBABILISTIC METHOD OF WWER FUEL ROD STRENGTH ESTIMATION USING THE START-3 CODE

Yu.K. BIBILASHVILI, A.V. MEDVEDEV, S.M. BOGATYR,
F.F. SOKOLOV, M.V. KHRAMTSOV
A.A. Bochvar Resarch Institute of Inorganic Materials,
Moscow, Russian Federation

Abstract

During the last years probability methods of studying were widely used to determine the influence exerted by the geometry, technology and performance parameters of a fuel rod on the characteristics of its condition. Despite the diversity of probability methods their basis is formed by the simplest schema of the Monte-Carlo method (MC). This schema assumes a great number of the realizations of a random value and the statistical assessment of its characteristics. To generate random values, use is usually made of a pseudo-random number generator. The application of the quasi- random sequence elements in place of the latter substantially reduces the machine time since it promotes a quicker convergence of the method. Probability methods used to study the characteristics of a fuel rod condition can be considered to be an auxiliary means of deterministic calculations that allows the assessment of the conservatism degree of design calculations.

1. DESCRIPTION OF PROBABILITY STUDY PROCEDURE

The stage of computations in the probability analysis of the fuel rod condition characteristics by the Monte-Carlo method is multiple calculations using the deterministic code START-3 [1,2,3] where as input parameters use is made of random values having characteristics similar to the probability characteristics of the geometry, technology and performance parameters of a fuel element.

The START-3 code is designed for the strength and thermophysics calculations with the aim of studying, validating and licensing fuel rods for nuclear power reactors on thermal and fast neutrons under normal and off-normal operating conditions. The code is commercially applied by the enterprise-the Lead designer-technologist of power reactor fuel rods – as an instrument for investigating, designing and licensing fuel rods.

1.1. General schematics of Quasi — Monte-Carlo method (QMCM)

The simplest schematics of QMCM assumes the acquisition of a large number of random value realizations and statistic assessment of its characteristics.

The standard procedure used to acquire random values consists in using a pseudo-random value generator. As it is known the rate of the convergence of the assessment acquired via the standard MC schematics is in proportion to $1/\sqrt{N}$ where N is the number of computations. There are other procedures promoting a higher rate of the MC method convergence as well as a reduced dispersion of an assessment which results in low machine time spent on calculations at the constant accuracy. Among those methods the most efficient procedure is the one that assumes the use of uniform sequences of points of integration formula with equal weights in the MC methods algorithm in place of random (pseudo-random) values.

Recently this method has been adequately applied to investigate the probability characteristics of fuel rods [4-5]. Mostly studied and qualitative are quasi-random sequences of Halton and Sobol; both the sequences in a 1-dimensional case coinciding.

In many instances the error order in QMCM is proportional $N^{-(1-\varepsilon)}$ ($\varepsilon>0$) for the above sequences which is much more than in MC method using random (pseudo-random) values.

To illustrate the advantage of using quasi-random sequences in place of pseudo-random ones two trial calculations using both the procedures were implemented.

Fig. 1 shows the assessed mean value for the integral of $\varphi = 5{,}818605\left(x_1 - 0{,}1\right)\sqrt{\left|x_2 - 1/9\right|\sqrt{\left|x_3 - 1/8\right|}}$ by $\iiint_{K^n} \varphi(P)dP \approx \frac{1}{N}\sum_{i=1}^{N}\varphi\left(P_i\right)$, (its exact value is unity) vs the number of points used in the calculation for the first 10 000 points. The figure illustrates the qualitatively more quicker convergence of the results acquired by QMCM compared to those acquired when standard random values are used in MC method.

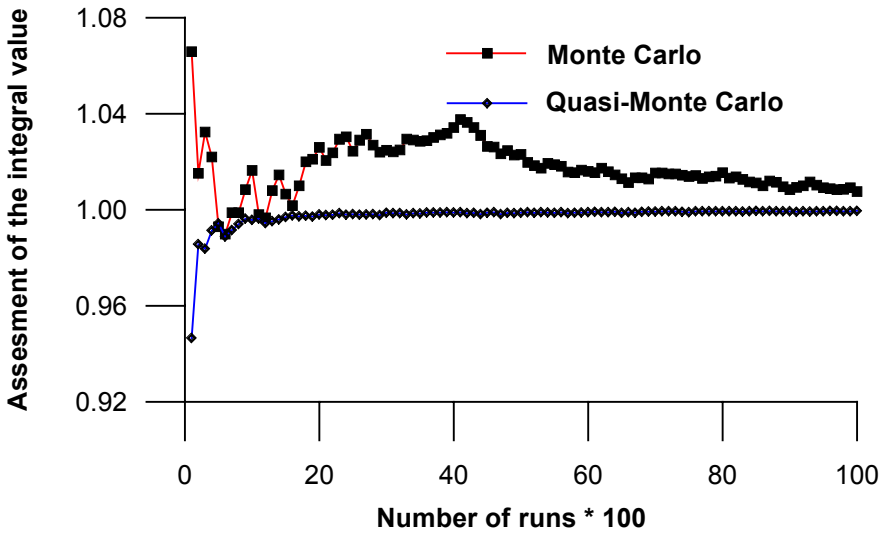

FIG. 1. The assessment of the integral value using the MC and QMC methods vs the number of points used in the calculation for the first 10 000 computations.

1.2. Construction of quasi-random sequences in order to calculate fuel rod statistic parameters

The problem investigating the probability characteristics of the fuel rod condition in a core has the following specific features:

(i) a nuclear reactor core contains some tens of thousands of fuel rods having different performance parameters
(ii) to assess the serviceability and, hence, the number of failures, all the probability characteristics of the fuel rod condition parameters have to be valid in the low probability range.

The main requirement placed on the sequences of the numbers used to investigate the effect of uncertainties in the input parameters influencing the fuel rod condition characteristics is the

requirement for the high degree of the sequence uniformity which ensures the quick convergence of the method and minimization of spent machine time. Sobol's quasi-random values conform to those requirements.

To construct the quasi-random values $Q_i^* = (q_{i,1}...q_{i,n})\, i = 1,2...$, that form a sequence which Sobol's sequence, a special algorithm was realized [6]. The quasi-random value sequence acquired via this algorithm was checked for the distribution uniformity of its elements in a multidimensional cube using the k-uniformity test [7]. Also, tests were carried out in which the numbers are categorized according to some attribute and the empiric frequencies are compared to their mathematical expectation using χ^2 test [8].

The frequency test implements the check-up of the frequency of appearance of numbers in a sequence intervals (the first decimal numbers are checked up).

The serial test: the frequency of various two-digit numbers among the independent pairs $\varepsilon_1\varepsilon_2, \varepsilon_3\varepsilon_4, \ldots, \varepsilon_{N-1}\varepsilon_N$ successively formed from the sequence of the random numbers $\varepsilon_1, \varepsilon_2, \ldots, \varepsilon_N$ is checked up. The run test: the number of various series of a length l ($\varepsilon_{k+1} = \varepsilon_{k+2} = ... = \varepsilon_{k+l}$) is checked up in the sequence of random values $\varepsilon_1, \varepsilon_2, \ldots, \varepsilon_N$. The total number of the series is $n = n_1 + ... + n_m + n'_{m+1}$.

Table I summarizes the results of checking-up quasi-random values acquired via the above described algorithm.

1.3. Procedure used to construct probability characteristics of the fuel rod condition

In the probability analysis of the characteristics of fuel rod conditions in a core consideration is given to a 60-degree sector of the symmetry. The WWER-1000 core sector contains 28 fuel assemblies with 312 fuel rods per each that are in operation for 3 or 4 years.

TABLE I. THE RESULTS OF CHECKING-UP QUASI-RANDOM VALUES ACQUIRED VIA THE GIVEN ALGORITHM USING THE SYSTEM OF TESTS

	Design value of the control $\chi 2$ test	Critical value of control $\chi 2$ test	Result of checking-up null hypothesis
Frequency test (9 degrees of freedom)	0.0003	16.9	Not rejected
Uniformitie test (99 degrees of freedom)	1609.5	10233.0	Not rejected
Serial test (99 degrees of freedom)	0.16	123.02	Not rejected
Run test (4 degrees of freedom)	1.3	9.5	Not rejected

The procedure of the probability calculations involves the following: the calculations consider all fuel assemblies in the symmetry sector, however, not all fuel rods within a fuel assembly are subjected to calculations but only a number of randomly taken ones.

To check up the results and refine the parameters of the design schematics at the preliminary stage, the probability calculation of all fuel rods within a fuel assembly is employed.

2. COMPARISON BETWEEN RESULTS OF PROBABILITY CALCULATIONS OF FUEL RODS IN FUEL ASSEMBLY E0325 AND RESULTS OF PIE

2.1. Description of calculations

WWER-1000 fuel assembly N^{o}E0325 has operated for four fuel cycles in Unit 1 of the Zaporozhie NPP to achieve the average burn-up of 48.9 MWd/kg U at the maximal linear heating up to 290 W/cm.

The following parameters were considered to be random:

(i) linear heat rating of fuel rods. Its distribution was assumed normal with the dispersion of 0.07.
(ii) fuel rod geometry and technology parameters are listed in Table 2
(iii) the distribution of all the parameters are considered to be normal which is corroborated by statistics studies at the production plant.

In total, 44 fuel rods were subjected to calculations for which PIEs of the gas composition and pressure under claddings were implemented.

TABLE 2. STATISTICS OF CHARACTERISTICS OF FUEL ROD GEOMETRY AND TECHNOLOGY PARAMETERS IN CALCULATIONS OF FUEL ASSEMBLIES 0325 [9]

	Mean	Standard deviation
Density g/mc3	10.6	0.0667
R clad Internal, mm	3.88	0.00667
R fuel External, mm	3.775	0.00333
Volume irradiation induced sintering,%	1.17	0.392
R fuel Internal, mm	1.2	0.00833
R clad External, mm	4.5575	0.0108
Open porosity, %	0.5	0.167
Gas plenum length, mm	241.5	4.17

2.2. Comparison between calculated results and PIE data

i. Gas release in fuel rods at the end of irradiation cycle

The values of the estimated mean value of gas releases at the end of the irradiation cycle in the calculated and PIE results are tabulated in Table 3.

TABLE 3. MEAN VALUE AND STANDARD DEVIATION IN GAS RELEASE BASED ON RESULTS OF CALCULATIONS AND POST-IRRADIATION MEASUREMENTS

	Mean value, %	Standard Deviation, %
Calculation	0.733	0.395
Measurement	0.780	0.623

Figs. 3-4 illustrate the frequency dependencies on gas releases at the end of irradiation cycle for the calculated results and the results of fuel rod PIE. For gas release samples the Wilcoxon test at the confidence level of 5% does not reject the hypotheses of the calculated and experimental samples belonging to the same general population.

2.2.2. Pressure in cold fuel rod at the end of its irradiation cycle

The values of the mean and standart deviation of the pressure (MPa) in a cold fuel rod at the end of its irradiation cycle are listed in Table 4. Figs.5-6 are histograms of pressure distribution based on the results of the calculations and the experimentally acquired data.

It is evident from the figures that there are some discrepancies in the values of the pressure distribution between the calculated results and the data acquired experimentally.

Based on the analysis of the PIE one can assume the availability of a procedure error in the results on the gas pressure measured under the fuel rod cladding at the end of the irradiation cycle. As is known, the value of the pressure is basically determined by the percentage of a gas release. The mutual accordance between the calculated pressure and gas release values is traceable; similar laws govern the distribution. As far as the results of PIE, no interrelation of this kind is observed and the modes of the distribution of both the parameters are quite different.

It is evident from the results given above that the probability methods may be useful not only at the stage of the design calculations of a fuel rod but also for investigations and analyses of the PIE results.

TABLE 4. MEAN VALUE AND STANDARD DEVIATION OF PRESSURE AND COLD FUEL ROD BASED ON CALCULATIONS AND PIE MEASUREMENTS

	Mean value, MPa	Standard Deviation, MPa
Calculation	2.651	0.041
Measurement	2.590	0.083

3. RESULTS OF DEMONSTRATIVE PROBABILITY CALCULATION OF WWER FUEL RODS UNDER TRANSIENT CONDITIONS

3.1. Calculation condition statistics characteristics of technology and geometry parameters of fuel rod

Consideration is given to a 60 degree sector of the core symmetry of the series WWER-1000 of a four year fuel cycle loaded with upgraded fuel assemblies and U-Gd fuel. The sector accommodates 28 fuel assemblies at a time. In actual fact, 3 four year cycle and 9 three year cycle fuel assemblies are to be calculated. Each fuel assembly contains 306 fuel rods and 6 U-Gd fuel rod.

The following parameters are considered to be random input ones:

(i) inner radius of cladding
(ii) outer radius of cladding
(iii) outer radius of pellet
(iv) inner radius of pellet
(v) fuel density
(vi) volume irradiation induced sintering of fuel.

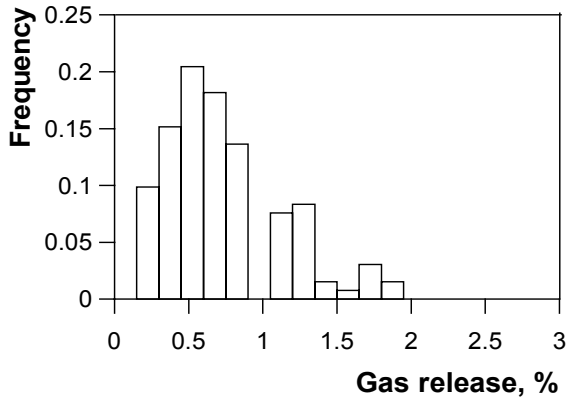

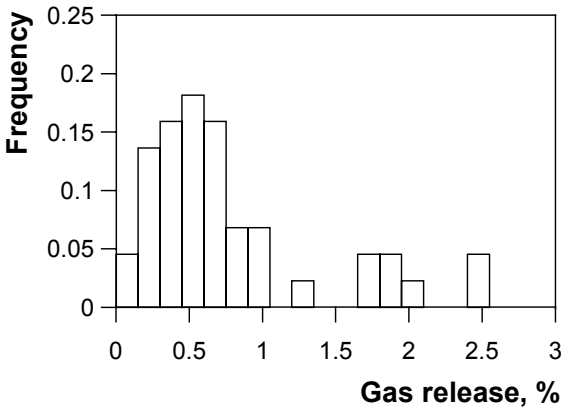

FIGs. 3 (left) and 4 (right). Gas release distribution in 44 fuel rods of fuel assembly E0325 according to calculation (3) and PIE (4).

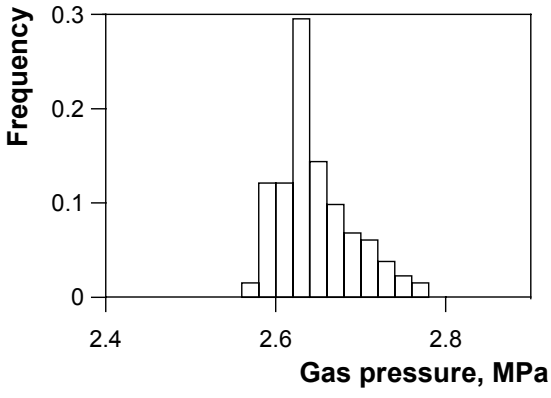

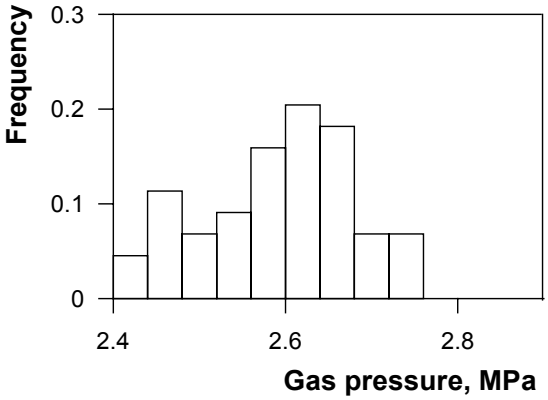

FIGs. 5 (left) and 6 (right). Gas pressure distribution in 44 fuel rods of fuel assembly E0325 according to calculation (5) and PIE (6).

The choice of the parameters is governed by the fact that they substantially affect the level of temperatures of a fuel rod, the gas pressure under the cladding as well as the stresses and strains of a fuel rod cladding.

Two series of the calculations were implemented with 100-50-100% realization of the transient conditions at the beginning (20 eff. days) and at the end (280 eff.days) of the operation cycle. To demonstrate the features of high level stress conditions in fuel claddings the special operational algorithm was involved into consideration. The main parameter to chose the algorithm was high level of power ramps in fuel rods and correspondingly high level of PCMI.

For the statistics analysis fuel assemblies in the 3-d and 4-th years of operation were taken since their burn-up levels are adequate for the PCI effect to show up in transients. The maximum hoop stress of a cladding in the irradiation cycle was assumed to be the fuel rod strength characteristic.

a. Results of probability calculations

i. Determination of design schema parameters

At the first stage fuel rods of a 3-year cycle fuel assembly were subjected to calculations; 13 times per each with different sets of random parameters. Based on the results of the calculation, the procedure was mastered to choose the minimally adequate quantity of calculations at which the distribution mode and the values of the distribution parameter estimations remain at an adequate level of accuracy.

It is found that depending on the needed accuracy of calculations, the design schema parameters can be chosen from the following range: calculation of 50-150 fuel rods; each fuel rod being calculated from 1 to 6 times.

ii. Results of probability calculations of power ramps by suggested procedure

75 fuel rods were subjected to calculations with each history being calculated 3 times. Altogether 12 fuel assemblies were calculated in 2 power ramp versions, namely, 20 and 280 days. The mode of the stress distribution for the 20 day version is shown in Fig. 7, for the 280 day version — in Fig. 8.

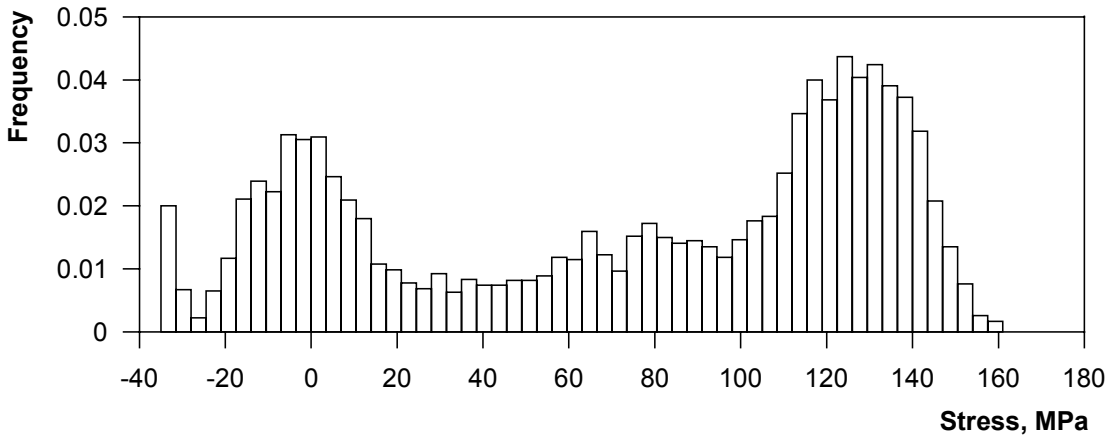

FIG 7. Maximum stress distributions in fuel rod cladding for a power ramp on the 20th effective day.

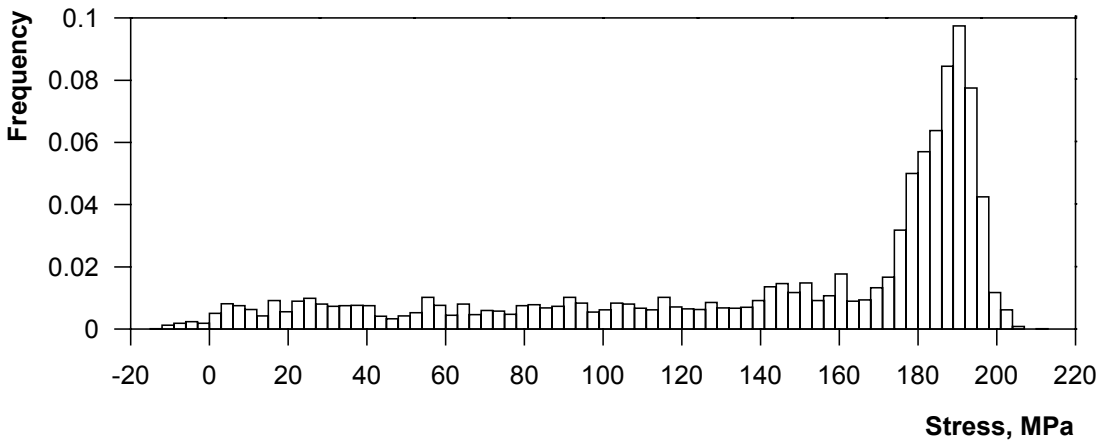

FIG. 8. Maximum stress distributions in fuel rod cladding for a power ramp on the 280th effective day.

It follows from the analysis of the stress value samples that:

(i) for a stress sample acquired from the calculation there is a significant symmetry in distribution (a ramp on the 280th day) or several distinct modes (a ramp on the 20th day)
(ii) mechanisms governing the behaviour of stress distributions in the range of low and mean stresses have a low influence on the stress behaviour in the high stress range.

Proceeding from the above to determine the behaviour of stresses in the high probability range (on the right hand "tail" of distribution), it is sufficient to consider random data under the condition of a ramp on the 280th day at high stress values.
Fig. 9 illustrates the randomly chosen values of stresses in excess of 200 MPa in fuel rods under power ramp conditions on the 280th day for 3-year fuel assemblies on the probability paper of Gnedenko-Gumbel distribution (dual exponential distribution). This particular distribution is one of the distributions of extreme values [10,11].

The approximation of the empirical function of distribution with the theoretical dependence allows the computation of the probability of rare events (involving in this case the exceeding of the standard value of the design parameters which is equivalent to a fuel rod failure on the strength acceptance criterion).

Using defined theoretical distributions of extreme stress values both the probability of ultimate value of 250 MPa (SCC criteria for Zr-1%Nb alloy) and the design limit of 210 MPa exceed were estimated:

The probability of ultimate value (250 MPa) exceed is up to $5{,}5*10^{-12}$.

The probability of design limit (210 MPa) exceed is up to $1{,}2*10^{-2}$.

The results of statistics calculations show that on the one hand probability of physical SCC limit exceed is negligible quantity. On the second hand, probability of design limit exceed of about 1% in comparison with SCC limit could be interpreted as overconservatism in design margin sizing. But design margin definition is more intricate problem that could be solved on the basis of probabilistic analysis of mechanical calculations. More other aspects both the operational and the design experience should be taken into consideration.

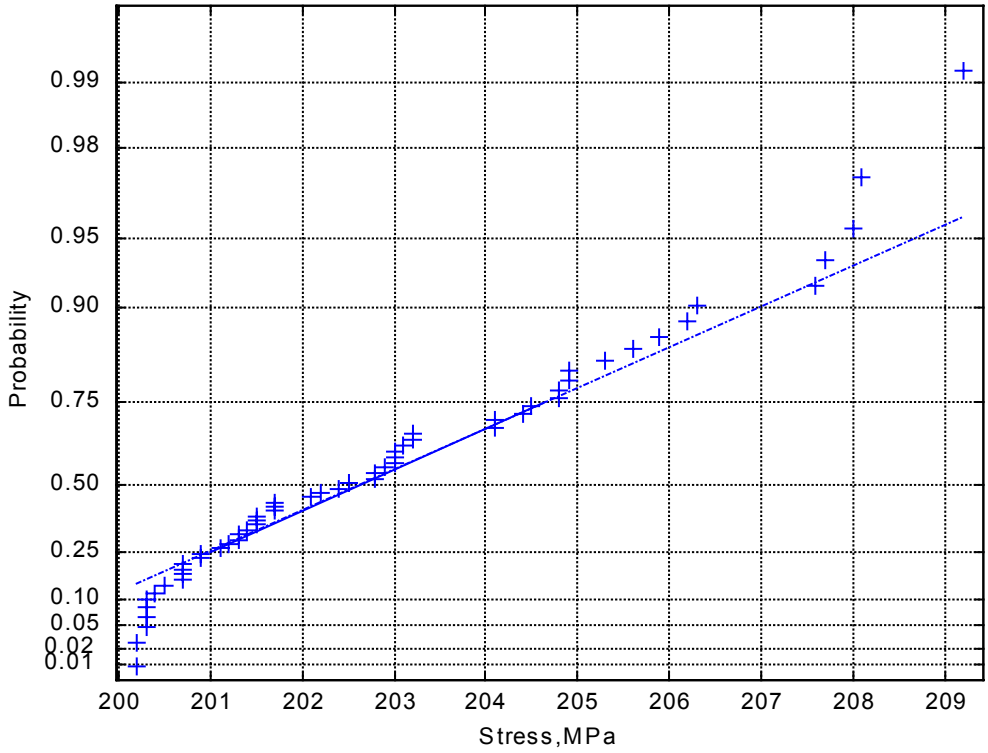

FIG. 9. Probability paper of Gnedenko-Gumbel distribution.

Carried out calculation enables to provide comparison of statistical estimation of mechanical FR parameters with deterministic one in investigated transients.

Conservative computation of the single maximum overrated in this transient fuel rod was carried out. It's necessary to note that selection of such kind of FR in huge file of neutron data is also probabilistic task. The calculations achieve the maximum cladding hoop stress of 225 MPa.

That could be interpreted as probability of realization of such stress level in core with value of $1/N_{pin}N_{FA} \approx 1.2 \cdot 10^{-4}$ as minimum ,

N_{FA} — number of FA in symmetry core sector, N_{pin} — number of pins in FA.

Statistical estimation of probability for that level of stress is not exceed $2 \cdot 10^{-5}$. Thus use of statistical computations in design of fuel permits to decrease limitation in operational conditions on power units.

4. CONCLUSIONS

The method for statistical analysis of mechanical and physical characteristics of fuel rods by START-3 code was developed.

Wide set of input both technological parameters and operational parameters are possible to be random in statistical analysis.

Special tests and verifications based on PIE of WWER fuel were carry out to provide the minimum adequate quantity of calculations at which the distribution mode and the values of the distribution parameter estimations remain at an adequate level of accuracy.

Two series of the statistical demonstrative calculations were implemented with 100-50-100% normal operation transient at the beginning (20 eff. days) and at the end (280 eff.days) of the WWER fuel cycle.

Analysis indicates that probability of SCC limits exceed in investigated transient acquired by statistical and deterministic methods differ more then tens.

Statistical methods provide on the one hand reliability estimations possibility on the other hand — estimations of conservatism of deterministic analysis

REFERENCES

[1] Program Code START-3. RF Licence # 76, 22.09.1997.

[2] MEDVEDEV A.V., BIBILASHVILI YU.K., et al., "Modelling at a WWER-1000 fuel, state and prospects", Seminar on WWER fuel modelling and experimental support, Varna, Bulgaria, 1994, INRNE Bulgarian Academy of Sciences Sofia, (1995) 163.

[3] MEDVEDEV A.V.,BOGATYR S.M.,KHVOSTOV G.A., 'Final Fumex Country Report. START-3', IAEA, Bombay,1996, see also: INTERNATIONAL ATOMIC ENERGY AGENCY, "Fuel modeling at extended burnup", IAEA-TECDOC-998, Vienna (1998).

[4] K. FORSBERG, NING HE, A.R.MASSIH, "Probabilistic analysis of nuclear fuel rod behavior using quasi-Monte Carlo method", Nucl.Sci.Eng. **122** (1996) 142-150.

[5] M. PIHLATIE, K. RANTA-PUSKA, "Probabilistic analysis of Loviisa nuclear fuel rod behavior", Seminar on WWER-reactor fuel performance modelling and experimental support, Sandanski, Bulgaria, 1997, INRNE Bulgarian Academy of Sciences Sofia, (1997) 135.

[6] I.M. SOBOL, "Mnogomernie kvadraturnie formuli i funkcii Haara", Moscow, Nauka, (1969) 288 (in Russian).

[7] S.M. ERMAKOV, G.A. MIHAJLOV, "Statisticheskoe modelirovanie", Moscow, Nauka (1982) 296 (in Russian).

[8] I.M. SOBOL, "Chislennie metodi Monte-Carlo", Moscow, Nauka (1973) 312.

[9] SHEGLOV A.S., PROSELKOV, V.N., ENIN A.A., in Atomnaja energija, **71**, 6 (1991) 23.

[10] E. GUMBEL, "Statistika extremalnih znachenij", Moscow, Mir (1965) (in Russian).

[11] "Nadezhnost i effektivnost v tehnike",v. 5, Ed. V.I. PATRUSHEV I A.I. REMBEZA, MOSCOW, Mashinostroenie (1988).

NON-PARAMETRIC ORDER STATISTICS METHOD APPLIED TO UNCERTAINTY PROPAGATION IN FUEL ROD CALCULATIONS

V.I. ARIMESCU
Siemens Power Corporation,
Richland, Washington, United States of America

L. HEINS
Siemens AG, Unternehmensbereich KWU,
Erlangen, Germany

Abstract

Advances in modeling fuel rod behavior and accumulations of adequate experimental data have made possible the introduction of quantitative methods to estimate the uncertainty of predictions made with best-estimate fuel rod codes. The uncertainty range of the input variables is characterized by a truncated distribution which is typically a normal, lognormal, or uniform distribution. While the distribution for fabrication parameters is defined to cover the design or fabrication tolerances, the distribution of modeling parameters is inferred from the experimental database consisting of separate-effects tests and global tests. The final step of the methodology uses a Monte Carlo type of random sampling of all relevant input variables and performs best-estimate code calculations to propagate these uncertainties in order to evaluate the uncertainty range of outputs of interest for design analysis, such as internal rod pressure and fuel centerline temperature. The statistical method underlying this Monte Carlo sampling is non-parametric order statistics, which is perfectly suited to evaluate quantiles of populations with unknown distribution. The application of this method is straightforward in the case of one single fuel rod, when a 95/95 statement is applicable: "with a probability of 95% and confidence level of 95% the values of output of interest are below a certain value." Therefore, the 0.95-quantile is estimated for the distribution of all possible values of one fuel rod with a statistical confidence of 95%. On the other hand, a more elaborate procedure is required if all the fuel rods in the core are being analyzed. In this case, the aim is to evaluate the following global statement: "with 95% confidence level, the expected number of fuel rods which are not exceeding a certain value is all the fuel rods in the core except only a few fuel rods." In both cases, the thresholds determined by the analysis should be below the safety acceptable design limit. An indirect method, which is computationally efficient, is presented for the evaluation of the global statement. It is proved that, r, the expected fraction of fuel rods exceeding a certain limit is equal to the (1-r)-quantile of the overall distribution of all possible values from all fuel rods. In this way, the problem is reduced to that of estimating a certain quantile of the overall distribution, and the same techniques used for a single rod distribution can be applied again. A simplified test case was devised to verify and validate the methodology. The fuel code was replaced by a transfer function dependent on two input parameters. The function was chosen so that analytic results could be obtained for the distribution of the output. This offers a direct validation for the statistical procedure. Also, a sensitivity study has been performed to analyze the effect on the final outcome of the sampling procedure, simple Monte Carlo and Latin Hypercube Sampling. Also, the effect on the accuracy and bias of the statistical results due to the size of the sample was studied and the conclusion was reached that the results of the statistical methodology are typically conservative. In the end, an example of applying these statistical techniques to a PWR reload is presented together with the improvements and new insights the statistical methodology brings to fuel rod design calculations.

1. INTRODUCTION

Statistical methods involving direct applications of the Monte Carlo sampling technique have been proposed in recent years as an alternative to the traditional conservative bounding calculations for fuel rod design and licensing analyses. They have been successfully applied

for licensing calculations of several utilities and accepted by licensing authorities in Germany, Sweden and Switzerland [1]. Probabilistic techniques are already accepted as legitimate ways of demonstrating that fuel behavior satisfies the imposed safety criteria [2]. Probabilistic techniques consist of a best-estimate code that is used in conjunction with an uncertainty evaluation to provide the assurance of not exceeding the applicable limits with a certain probability, nominally 95%.

The standard fuel rod mechanical analysis for normal operating conditions is based on conservative calculations with bias in the models and/or input values and power history to obtain the overall bounding output value to be compared with a pre-defined criterion. While these methodologies are overly conservative in some cases, they also have a certain procedure of defining limiting power histories which is difficult to prove as being all-covering, ab-initio. Therefore, more conservatism is introduced by uprating the power history and the operational margin is further reduced.

It is the purpose of the best-estimate methodology presented in this paper to offer an alternative analysis that provides a more realistic estimation of the operational margin and offers additional insight in the global characterization of a fuel reload.

2. METHODOLOGY OVERVIEW

The goal of the methodology can be stated as follows:

"Provide a methodology to analyze fuel rod performance during normal operating and anticipated abnormal occurrence conditions for given fuel reload and power plant. This goal will be achieved by using a best-estimate code and a method of analyzing the uncertainty propagation through the code of known statistical variances of input variables, including: manufacturing parameters such as gap, pellet and cladding dimensions, pellet density, etc; modeling parameters such as pellet thermal conductivity, fission gas diffusion coefficient, etc; environmental parameters of which the power history is the most important."

The performance judgement is based on pre-defined thresholds for the critical output parameters (such as gas pressure, cladding plastic hoop strain, etc.) that are evaluated by the code. The evaluation criteria will be adequately expressed in probabilistic terms. This means that the final statement must assure that the fuel rods subjected to the given power histories will not exceed the pre-established threshold or will exceed it by only a small probability. The location of different fuel rods in the core determines the power history that fuel rods will experience. Thus, when talking about a certain fuel rod it is implied that a certain power history is associated with it. From these requirements a suggested final statement was proposed and was explored in this study, as follows:

(a) The expected number of rods exceeding the threshold must be not greater than a pre-established value, typically 1 or a few fuel rods with 95% confidence level.

Alternatively or additionally, a second final statement can be considered:

(b) With 95% probability and 95% confidence level the extreme fuel rod, i.e. the fuel rod associated with the highest load, does not exceed the threshold"

The first part of the statement assures that there is no significant accumulation of fuel rods close to the threshold which could potentially lead to a higher than accepted probability of

having one of them exceeding the limit. The adequacy of this probabilistic statement is based on the extremely low probability that all the fuel rods belonging to the group of extreme fuel rods have their characteristics equal to the most unfavorable values. In the second part, the 95% probability level reflects that it is very unlikely to achieve in practice the particular combination of input parameters and power history that result in extreme output values. The 95% confidence level is required because of the statistical processing of uncertainties and adequately quantifies the level of conservatism of the analysis.

Whereas the first statement (a) can be treated in principle by direct Monte Carlo calculations with the full set of power histories, the second statement (b) needs a more sophisticated procedure, consisting of several steps. First, a sensitivity analysis (Response Surface Method and/or Monte-Carlo Sampling) is performed in order to define the combination of input variables which is appropriate to select the rods with the highest load. Next, the code is run for all the fuel rods (i.e. power histories) with the set of appropriate input values and the most limiting rods are identified. Finally, an uncertainty analysis is performed, based on Monte-Carlo sampling, to estimate for the extreme fuel rod the 95% percentile with 95% confidence level and verify that this is below the threshold.

The input variables considered in the uncertainty analysis can be categorized into dimensional as-fabricated data and material properties, modeling parameters, and power history.

The tolerance range for input variables is either given or obtained by truncating the given distribution at a percentile level, which is physically limiting or practically significant. Typically, the +/-3 times the standard deviation is the symmetrical uncertainty range used.

The internal rod pressure was selected as the output performance parameter to be evaluated in this study. Based on previous parametric sensitivity studies [3, 4] and on theoretical analysis, the most important fuel rod parameters affecting internal rod pressure are the fuel-to-clad gap and the initial fill gas pressure. Pellet densification and cladding creep are usually classified as modeling parameters and affect the internal rod pressure evolution through their controlling radial and axial gap evolution. The appropriate set of input variables that lead to the rod with the highest load contains variation of the following parameters: pellet-to-cladding radial gap, filling gas pressure, plenum and dishing volumes, densification, fuel swelling, cladding inward creep and fission gas release.

The modeling parameters are generally physical variables that are key to the physical models analyzed and present a material variability or are not accurately known. Gas atom diffusion coefficient and creep activation energy, are such examples. Also, constants of semi-empirical models which are obtained by calibrating against experimental data have an uncertainty range incorporating both the fitting and the experimental uncertainties. There are several ways of obtaining the uncertainty associated with modeling parameters. A more involved procedure [3] would be to perform an uncertainty analysis for the specific benchmarking databases and validate in this way several modeling parameters. A simplified and practical method [1] is based on selecting one modeling parameter for a specific benchmarking (i.e. the fission gas release database) and then varying it for each case in part until the experimental value is matched. The range of values obtained in this way for the respective modeling parameter defines its uncertainty range. This procedure incorporates in the modeling parameter uncertainty all other sources of uncertainty affecting the experimental data points. Care must be exercised when applying this modeling uncertainty in specific analyses not to double account some uncertainties which would introduce too much conservatism in the analysis.

The second method was used to derive the modeling uncertainties for the examples presented in this paper.

3. STATISTICAL ANALYSIS OF THE WHOLE CORE USING NON-PARAMETRIC ORDER STATISTICS

The statistical method used to evaluate the various distributions required by the final statement is the "non-parametric order statistics". This is particularly suited to estimate quantiles of populations with an unknown distribution function. Let the p-th population quantile be denoted by q_p. Then, q_p is defined in terms of the cumulative distribution function, $F_X(x)$,of the population as the real number which satisfies the equation:

$$F_X(q_p) = p$$

Then, irrespective of the distribution function, $F_X(x)$, the values of the sampled elements can be mapped into the range [0,1] of the cumulative distribution function, which is uniformly distributed regardless of what $F_X(x)$ is.

Thus, after drawing a random sample from the population, X_1, X_2, …, X_n an unique ordered arrangement exists, as follows: $X_{(1)} < X_{(2)} < \ldots < X_{(n)}$, where the bracketed indices indicate the order. This will provide different order statistics, one of which is a given quantile. It is proven theoretically that the r-th order statistics, $X_{(r)}$ is an un-biased and asymptotically exact estimator of the p = (r/n) quantile, q_p, of the population. Confidence bounds can be calculated and the upper 95% confidence bound is of special interest in our case. The distribution of the r-th order statistics is binomial since any sampled element can be classified as either being less than q_p , with probability $P(X < q_p) = p$, or greater than q_p with probability $P(X > q_p) = 1-p$. Thus the sampling process can be considered as a series of n repeated independent trials of a Bernoulli variable with parameter p. Then the upper α confidence bound can be calculated as follows. $X_{(s)}$ is the desired α confidence level estimate of q_p if the probability of having $X_{(s)}$ smaller than q_p is $(1-\alpha)$ (a small number). This happens for any combination where j of the largest sample values, with j greater or equal to s are smaller than q_p, and the following formula is obtained:

$$\sum_{j=s}^{n} C_n^j p^j (1-p)^{n-j} = I_p(s-1, n-s) = 1-\alpha$$

where I_p denotes the incomplete beta function. The solution of this equation, s, provides the required order statistics for the upper α-confidence level estimate of the q_p population quantile. This equation can be solved numerically, or an analytic approximation can be used for large (greater than 20) samples. Based on the normal distribution approximation to the binomial distribution [5], the result of which is:

$s = q_p n + z_\alpha [p(1-p)n]^{0.5}$ for $np(1-p) > 9$

where z_α is the normal distribution parameter corresponding to the one-sided α quantile and n is the number of sampled elements.

The application of the order statistics to the evaluation of the 95 percentile (quantile expressed in percentage) of the extreme fuel rod distribution is straightforward and follows the method just described. A random sample is obtained by directly Monte-Carlo sampling the multi-

variate input variable, consisting of fabrication parameters, modeling parameters and power history. The 95 percentile is then estimated according to the previous formula.

For the cumulative characteristic, the expected number of fuel rods exceeding the threshold, two approaches are possible. The direct way would be to sample a multi-variate input vector for all fuel rods prone to exceed the threshold and count how many fuel rods exceeded the threshold for each sample event. Then, the expected number can be estimated as the sample average. The second way is provided by the following link which exists between the distribution of all possible values from all fuel rods, called an overall distribution, and the distribution of the fraction of fuel rods exceeding the threshold:

"The expected fuel rod fraction, p, of all rods, that do not exceed the threshold q is equal to the p-quantile, q_p, of the overall pressure distribution."

This statement can be proved as follows. Let us assume that there are m fuel rods with probability, P(i) = p_i, of exceeding the limit q_p. Then, it can be shown (using mathematical induction), by constructing the discrete distribution of the number of fuel rods, that the expected number of fuel rods not exceeding the limit is equal to the sum of individual rod probabilities and then the expected rod fraction of fuel rods not exceeding the limit is obtained by dividing by m. There is an alternative simpler proof for the first part of the previous statement. Each fuel rod in part can have two possible outcomes: not exceeding the limit with probability p_i, or exceeding the limit with probability $(1-p_i)$, and thus it can be considered as a random variable:

$$\omega_i = \begin{cases} 1 & p_i \\ 0 & 1-p_i \end{cases}$$

The sum of all m random variables is also a random variable, $X = \sum_{j=1}^{m} \omega_j$, and its expected value is:

$$E(X) = E(\sum_{j=1}^{m} \omega_j) = \sum_{j=1}^{m} E(\omega_j) = \sum_{j=1}^{m} p_j$$ and then p = E(X)/m

On the other hand, the quantile, q_p, of the overall pressure distribution associated to p, can be calculated according to its definition: the quantile, q_p, associated to p is the probability that the output value, selected at random from all possible values of all fuel rods, is less than q_p. Since all fuel rods are equally probable, the probability of choosing any of the fuel rods is 1/m and for any fuel rod the probability of having the output value less than q_p is P(i) = p_i. Then the desired probability is the sum of individual rod failure probabilities weighted by 1/m, the equal probability factor. Thus the fraction associated to the q_p quantile is

$$\sum_{j=1}^{m} (\frac{1}{m}) p_j = E(X)/m = p$$

which obviously is the same as obtained before for the fraction of fuel rods exceeding the limit, and thus the statement is proved.

Therefore, the statement (a) can be re-formulated in terms of quantiles of the overall output distribution as:

"The overall output quantile equivalent to the pre-established number of expected fuel rods exceeding the limit should be less than the pre-defined threshold."

4. EXAMPLES OF APPLYING THE METHODOLOGY

The methodology presented before was implemented into a FORTRAN code which calls the selected fuel code as a subroutine. The front-end sampling part and the back-end statistical analysis part are code-independent. The modules to prepare specific fuel code input decks must be supplied by the user. The user can select the sampling method as either the Simple Monte-Carlo method (SMC) or Latin Hypercube Sampling (LHS). The distribution of different input variables can be specified as normal, log-normal, uniform, or tabulated form. The code can be run on either a PC or a UNIX-HP platform and a typical reload calculation can be done overnight.

Two PWR cases were considered to illustrate the methodology. Case 1 consisted of 60 fresh UO_2 17x17 fuel assemblies, to be inserted in the reactor in a typical reload for 3 cycles. The SIERRA-1 code [6], developed jointly by Siemens-SPC and Siemens-KWU was used as a best-estimate code in the first case. Case 2 comprised 10 fuel assemblies, 17x17 type, to be inserted in a PWR reload for 4 cycles. The best-estimate fuel code used for the second case was CARO-E [1], developed at Siemens-KWU. In both cases, design tolerance ranges have been used for fabrication values and the four-fold core symmetry was applied to reduce by 4 the number of fuel rods analyzed (3960 in the first case and 2640 in the second case). The output parameter considered was the maximum value the internal gas pressure attains during irradiation.

The calculations performed with SIERRA-1 considered variation according to a normal distribution of the following fabrication parameters: cladding outer and inner diameters, pellet diameter and initial filling gas pressure. Because no uncertainty range was available for modeling parameters, nominal values of calibrating factors for different models have been used with the exception of the densification model where the calibrating factor was set to the extreme value corresponding to the fastest and largest densification. This is consistent with the fission gas release model which was found during benchmarking calculations to slightly over-predict for the region of fission gas release expected during normal operation (a best-estimate agreement is achieved for the whole benchmarking domain). The linear power was assumed to be normally distributed around the nominal values with a +/-5% uncertainty range (covering a 2 σ band), which covers the calculational and measurement uncertainty associated with linear power estimation.

The SMC method was used in Case 1 as sampling technique after the initial selection step. This selection step consisted in running all power histories with the extreme combination of input variables, namely, maximum pellet-to-cladding radial gap and maximum initial filling gas. A total of 18 fuel rods, coming from two fuel assemblies, were found to have exceeded coolant pressure of 155 bar (taken as the threshold). The whole population can be divided into two groups with peak values around 120 bar and 140 bar, respectively. It is worth remembering that this is the equivalent of the conservative deterministic calculation since it assumes bounding tolerance range values for all rods, while in reality the fuel rods' characteristics cover only a part of the whole tolerance domain and they can not have simultaneously extreme values for all their characteristics. It is apparent that the selection process offers a clear advantage in saving computational time by focusing on only 18 fuel rods out of a total of 3960.

The next step implies the evaluation of the gas pressure value that corresponds to the 1-expected fuel rod exceeding the coolant pressure, taken as the criterion for Case 1. This amounts, according to the theory presented in Section 4, to obtaining the quantile of the overall distribution (all possible gas pressure values of all the 18 fuel rods) corresponding to the fraction of $\frac{1}{4 \times 18}$, which is equivalent 1-expected fuel rod exceeding the threshold in the whole core. A large number of runs, 60 × 18 = 1080, was possible in this case, owing to the reduced number of fuel rods with their maximum gas pressure exceeding the threshold. The results are presented in Figures 1 and 2, in terms of cumulative distribution and histogram. The 1-expected fuel rod over threshold equivalent quantile is 136.6 bar and thus, meets the criterion of being less than the coolant pressure of 155 bar, considered here as the threshold.

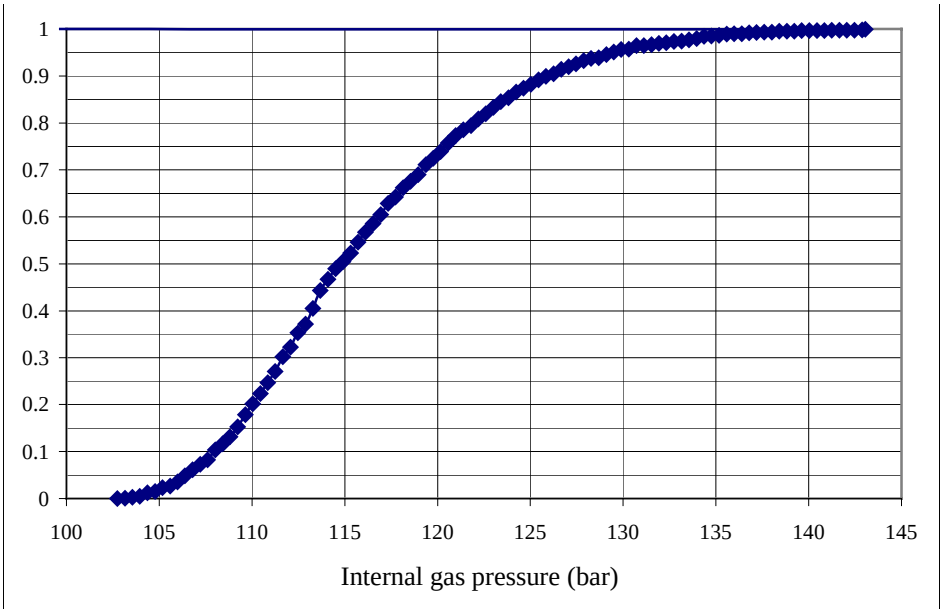

FIG.1. Gas pressure cumulative distribution for bounding fuel rods, Case 1.

Finally, the extreme fuel rod (which attains the largest maximum pressure for the set of extreme input values) is investigated statistically with the SMC sample of 300 to evaluate the 95 × 95 percentile. The results are presented in Figures 3 and 4 and the 95 × 95 percentile was estimated as 138.6 bar, again satisfying the criterion. It is noticed that larger fluctuations are present in the histogram, which is to be expected because of the smaller number of runs as compared to Figure 2. Nevertheless, the statistical accuracy of the 95x95 percentile is not impaired, on the contrary, it is actually over-estimated for the reduced number of runs.

The calculations performed with CARO-E for the second case considered variation according to a normal distribution of the following fabrication parameters: cladding outer and inner diameters, pellet diameter, initial filling gas pressure, plenum volume, pellet dishing volume and pellet density. Four modeling parameters have been considered for the following models: fission gas release and fuel densification-swelling with a normal distribution, and cladding creep and pellet radial relocation with a log-normal distribution. In addition, the power history was subject to a cycle-by-cycle variation of +/-10% (normal distribution with a 2 σ band), which represents a +/-5% variation of the average linear power during the irradiation lifetime. The LHS method was used as the sampling technique and no selection step was imposed.

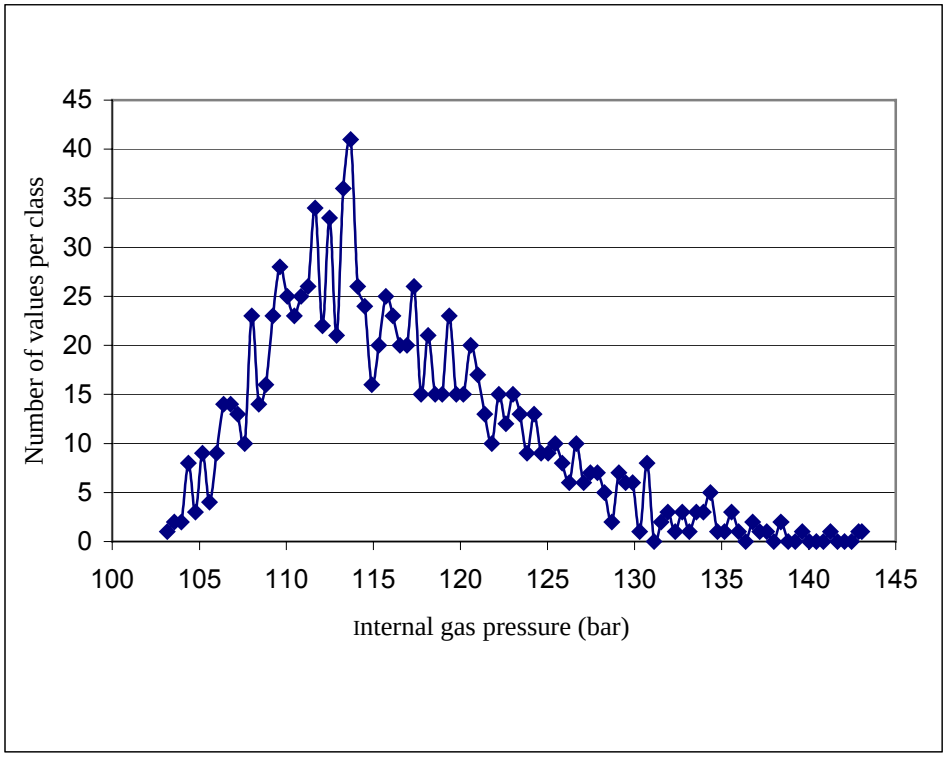

FIG. 2. Gas pressure histogram for bounding fuel rods, Case 1.

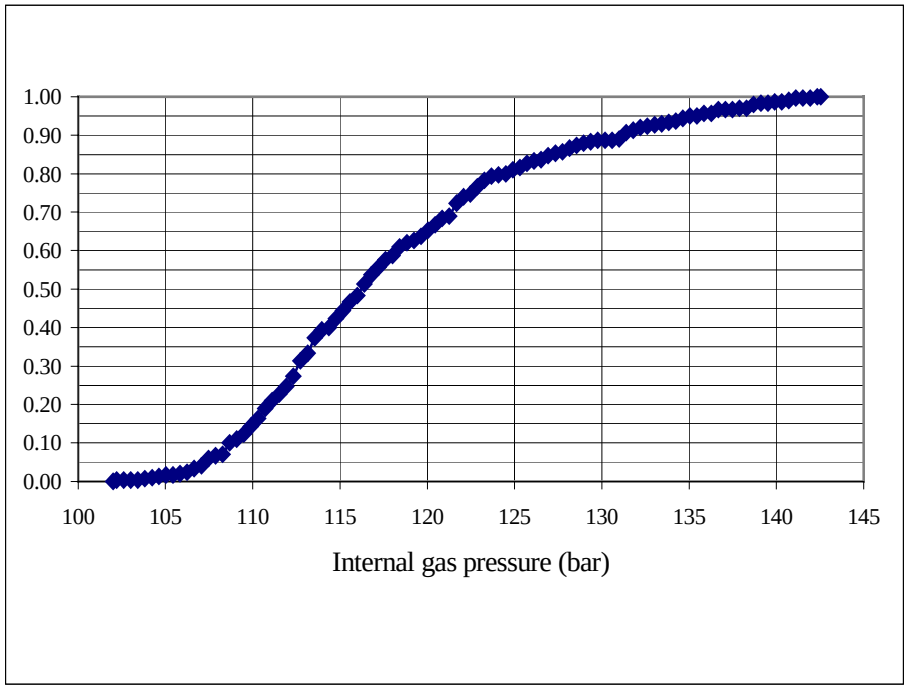

FIG.3. Cumulative distribution of the extreme fuel rod gas pressure, Case 1.

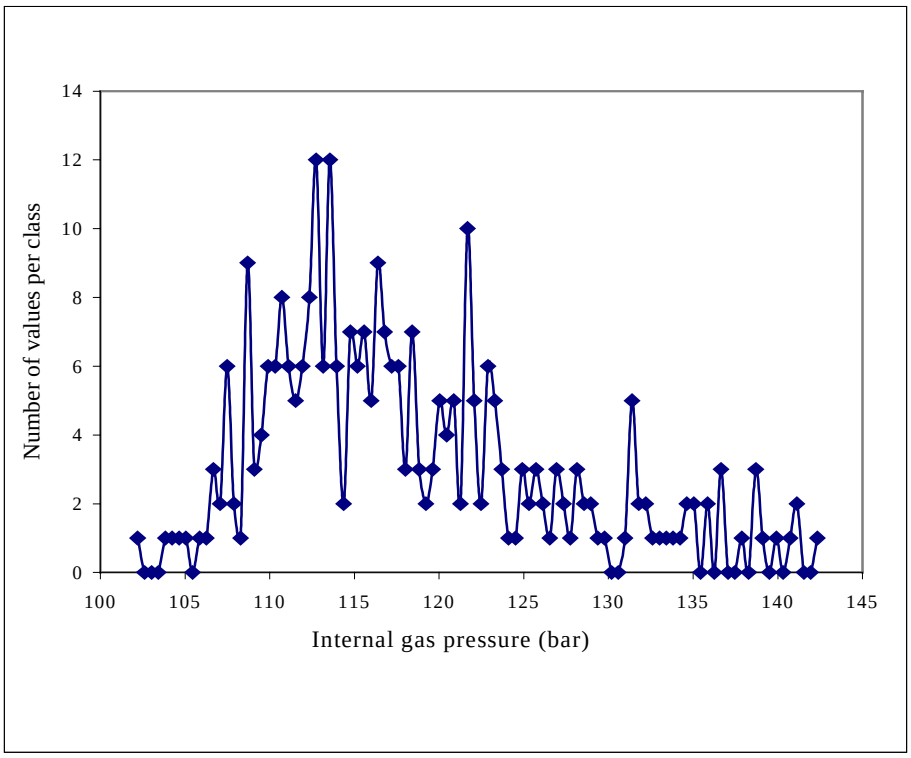

FIG. 4. Histogram of the extreme fuel rod gas pressure, Case 1.

In this example, the analysis of UO_2 fuel rods without lower plenum in 17 × 17 fuel assemblies is considered. The corresponding reload management scheme contains power histories, for which the design limit of maximum rod internal pressure (non lift-off criterion) is nearly reached by using deterministic methods. On the other hand, the statistical analysis shows a margin of about 30 bar, as shown in Figure 5. In this analysis each of the power histories has been taken into account 10 times in the Monte Carlo calculations. If the statistical variation of the power histories is performed as described above, one can demonstrate margins to cover variations of the given power histories for future reload management schemes, or increased enrichment etc., the result being also presented in Figure 5.

5. SIMPLIFIED EXAMPLE FOR ASSESSING STATISTICAL UNCERTAINTY METHODOLOGY

The simplified example case consists of 590 rods, two input variables subject to uncertainty and one output variable whose distribution is investigated both individually and in the global sense defined before in Section 2. This bivariate case is amenable to exact analytical calculations for individual rod output distributions and thus could be used as a validation case for any numerical statistical procedure.

The code is represented in this simplified example by a response (transfer) function, which is defined in such a way that the output values are the same order of magnitude as expected fission gas release values in a real fuel rod. The two input values are denoted as P, representing a combination of maximum linear power and UO_2 diffusion coefficient and B, representing the discharge burnup. The response function, Y, is given by:

$$Y = 1E\text{-}10 * P^2 * B^3$$

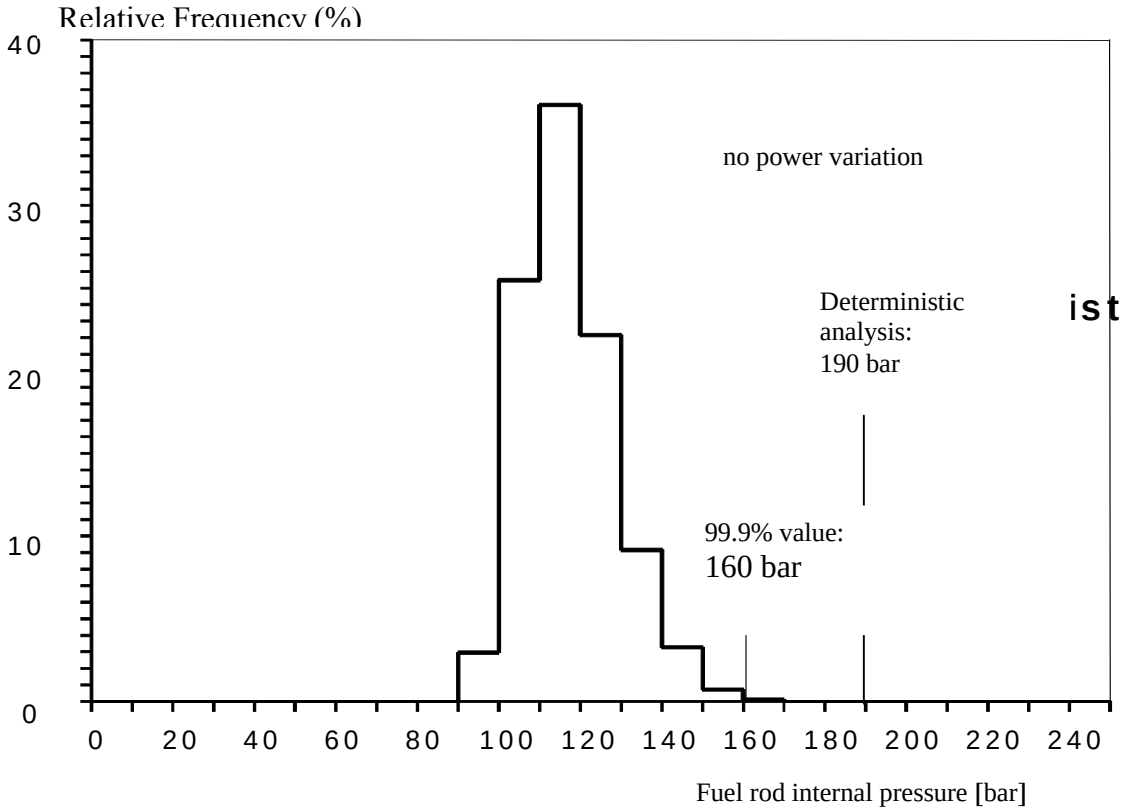

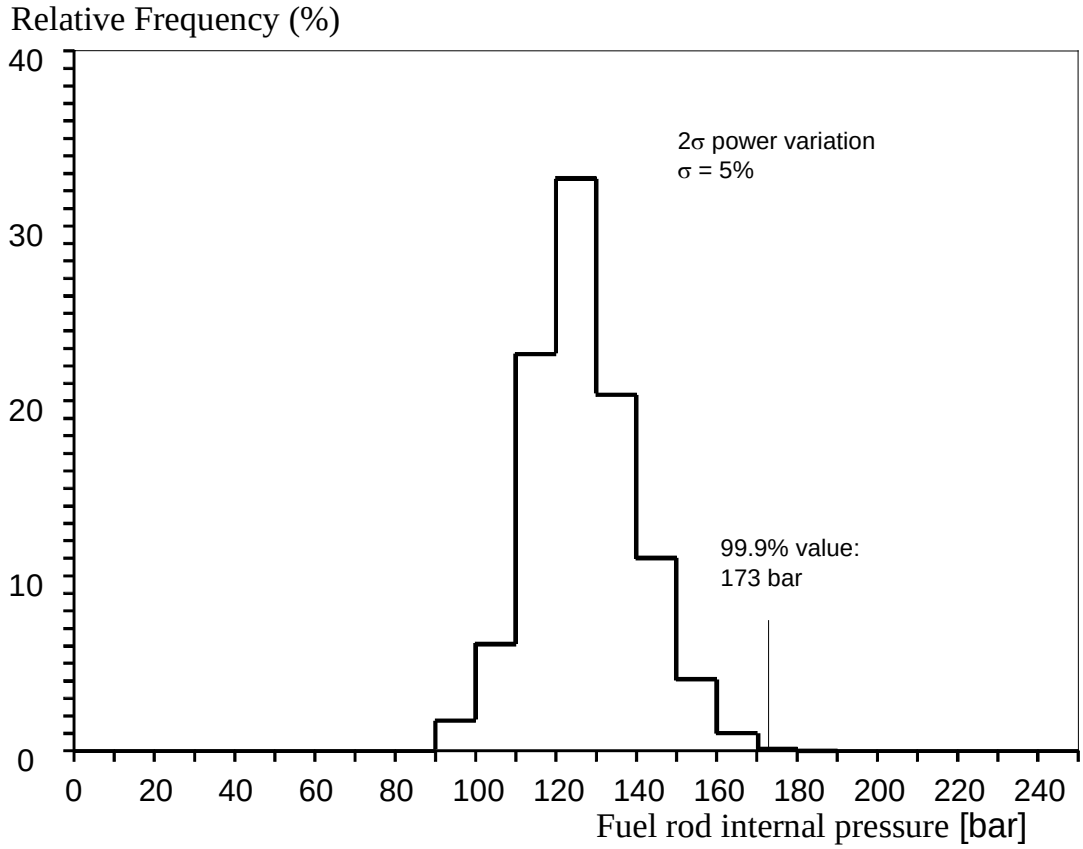

FIG. 5. Maximum rod internal pressure distribution without and with power variation.

The two input variables are assumed to be independent and therefore for each rod the problem is to evaluate the uncertainty propagation through the application of this transfer function. Both the input variables, P and B and the output variable Y are continuous random variables characterized by own probability distribution functions, pdf, and cumulative distribution functions, cdf, which are related by:

$$f_Y(y) = dF_Y(y)/dy$$

where lower case f is the pdf and the upper case F is the cdf, while upper case Y represents a random variable and lower case y represents the values of the random variable Y.

The cdf of the output random variable, Y, which is a bivariate function of P and B can be calculated from the following relation:

$$F_Y(y) = \iint_{D=\{(p,b),\ Y(p,b)\le y\}} f_P(p) f_B(b) dpdb$$

where use has been made of the independence of the two input variables in which case the joint pdf is simply the product of their two pdf's.

For this example the pdf for both input variables was considered to be either the uniform distribution over given finite intervals, or the truncated (cut-off at three standard deviations) normal distribution over the same finite intervals. With these assumptions the cdf and the pdf of the output variable can be calculated analytically

The input variable sets for the 590 rods have been selected as follows: a high FGR (Fission Gas Release) group of 160 rods starting with the highest FGR rod at p = 45 and b = 52 and then progressively lower values in decrements of 0.05% for the other rods; a low FGR group of 531 rods starting with the upper bound rod at p = 39 and b = 45 and then progressively lower values in decrements of 0.05% for the rest of the rods. The uncertainty range for all 590 values of both P and B was assumed to be +/-10% of their respective nominal values.

The parametric sensitivity analysis in this bivariate case is straightforward and the bounding input combination is easily determined as (maximum P, maximum B).

The shape and relative position of some pdf's revealed two aspects worth mentioning. First, the pdf becomes wider for high-output rods, similar to what would be expected for real fuel rods. Secondly, because of small differences between the input values for the rods in each of the two groups there is an overlapping in results which creates an apparent global output distribution. The overall output range for the 590 rods spans the interval [0.0148, 0.04568]

Although is possible in principle, an analytical evaluation of this amalgamation of the individual distributions from all rods, it is impractical because of computational complexity. A very good representation of the distribution can be derived by drawing a very large sample. To that end, two runs of 100 and respectively 500 random values for each rod have been processed with their comparison showing negligible differences, thus proving that the sample size is sufficient for obtaining a faithful image of the overall population distribution. The whole output range from all rods was divided into 100 classes of equal size and the relative histogram was obtained.

Then the cumulative distribution function was calculated by recursively adding the percentage value of a given class to the sum of percentages from all prior classes. By numerically differentiating this tabulated function, the probability distribution function can then be obtained. The resulting functions in the case of uniform distribution for the input variables are displayed in Figures 6 and 7. The quantile corresponding to the 1-rod expected to exceed the threshold for this population of 590 rods was obtained from the derived cumulative distribution and the corresponding percentile, p = 1-1/590 = 0.9983. For the uniform distribution q_p is 0.0395, while for the normal distribution q_p is 0.0367. These are the theoretical values against which numerical estimates have been evaluated. A study of the effect of sample size and sampling method was carried out. The sample was drawn from either the whole rod population, or the high FGR rod group, only. In each case the LHS and SMC methods were repeated 100 times each, to estimate the scatter of the calculated quantiles. The average and the standard deviation for the estimated quantiles are presented in the table below, where the number of rods tabulated for the LHS method indicates the whole rod population if it is equal to 590 and the group of highest FGR rods if it is equal to 59, respectively.

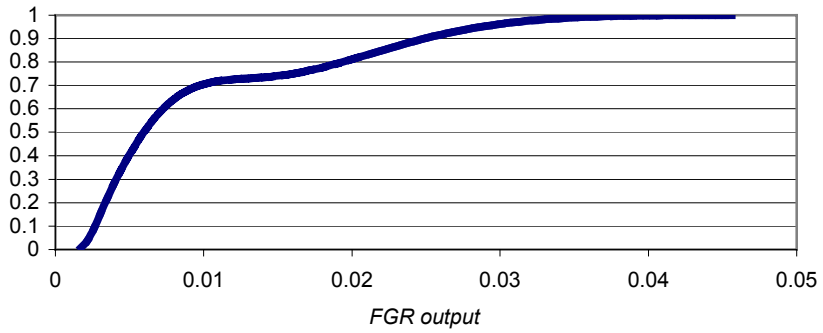

FIG. 6. Cumulative distribution function for all 590 rods.

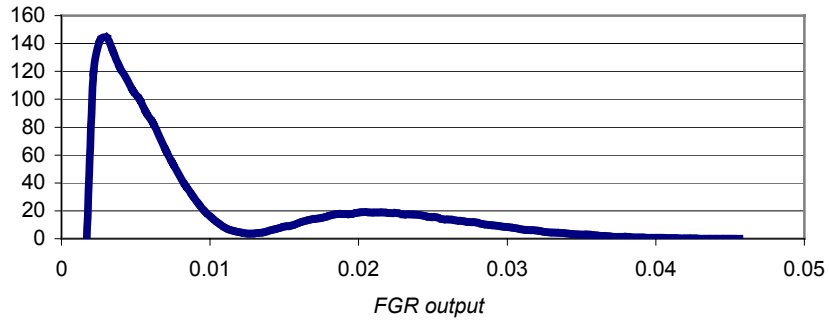

FIG. 7. Probability distribution function for all 590 rods.

It is apparent by inspecting the tabulated average quantiles and their corresponding standard deviations, that both methods are producing similar quantile values for the same sample size. This is to be expected since the statistical procedure evaluates the tail end of the distribution. The LHS method is more efficient than the SMC method when the overall cumulative distribution is estimated. Since the basis of the non-parametric order statistics procedure is a random sample, the increased uniformity of the LHS drawn sample has no clear advantage in this case.

Method type/Input Distribution	Number of rods/Sample size	Average Estimated q_p	Standard Deviation
LHS/Uniform	590/1770	4.211E-2	1.4E-3
SMC/Uniform	590/1770	4.217E-2	1.1E-3
LHS/Uniform	590/5900	4.1142E-2	7.2E-4
SMC/Uniform	590/5900	4.0962E-2	7.6E-4
LHS/Uniform	590/11800	4.0406E-2	4.6E-4
SMC/Uniform	590/11800	4.0524E-2	4.6E-4
LHS/Uniform	59/590	4.1107E-2	6.23E-4
SMC/Uniform	59/590	4.1126E-2	7.39E-4
LHS/Uniform	59/1180	4.0542E-2	4.55E-4
SMC/Uniform	59/1180	4.0519E-2	4.61E-4
SMC/Uniform	59/2360	4.0221E-2	2.68E-4
LHS/Normal	590/5900	3.8342E-2	8.2E-4
SMC/Normal	590/5900	3.8188E-2	8.7E-4
LHS/Normal	59/1180	3.7699E-2	4.82E-4
SMC/Normal	59/1180	3.7655E-2	4.29E-4
LHS/Normal	59/177	3.9741E-2	1.71E-3
SMC/Normal	59/177	3.9456E-2	1.67E-3

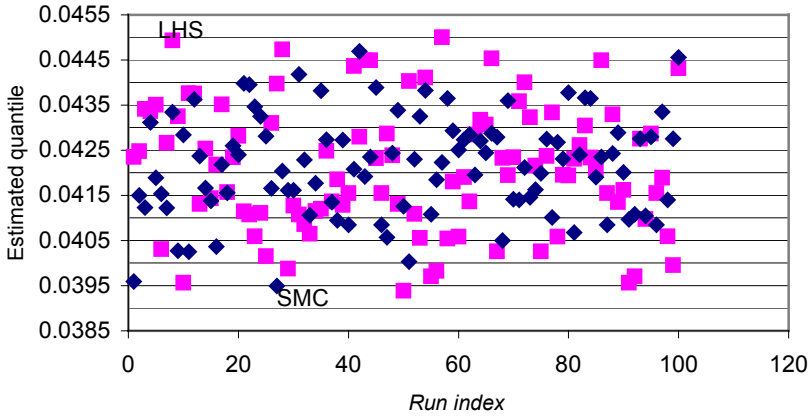

FIG. 8. Spread of calculated quantities.

It can be concluded, from the parametric study presented in the above table, that the statistical method produces conservative results. This means that the estimated quantiles are typically well above the exact theoretical quantile. The smaller the sample size, the larger the over prediction is. At the same time the scatter of possible outcomes for the quantile is larger when a reduced sample size is used. This is exemplified in Figure 8 for the case when all 590 rods were used to draw samples of 11 800 realizations.

The results also show the advantage of using only the rods (the high FGR rods in our case) that affect the upper tail end of the distribution where the sought after percentile is situated. The same result is obtained in the 59/590 case as in the 590/5900 case, but with 10 times fewer calculations. The results also show the impact of the distribution function of the input variables for otherwise the same total variation range and sampling method. The normal distribution case produces less spread and smaller estimated quantiles in both the theoretical

and numerical cases, in comparison with the uniform distribution case. This proves that using a uniform distribution is conservative when no information on the input variable distribution is available. Also, it reinforces the need for and advantage of working with real input variable distributions.

6. CONCLUSIONS

The best-estimate methodology presented in the paper is based on theoretically sound Monte-Carlo and non-parametric order statistics methods. It assumes the availability of a best-estimate fuel performance code and relies on good databases for fabrication and modeling parameters.

Two examples of applying the methodology have been presented. The internal gas pressure was considered as the output parameter of interest in connection with a coolant pressure threshold.

The statistical design methodology is potentially a powerful tool for assessing the behavior of the fuel rods in a reactor core. It has the capability of characterizing the degree of conservatism through the statistical evaluation of numbers of fuel rods coming close to a design limit or by making statements about the statistical certainty for the actual occurrence of extreme cases.

REFERENCES

[1] HEINS, L., 1999. Fuel Rod Design by Statistical Methods for more Demanding Conditions, Proc. TOPFUEL '99, Avignon, France.

[2] ANS, 1996. American National Standard for Light Water Reactors Fuel Assembly Mechanical Design and Evaluation ANSI/ANS-57.5-1996, Section 5.4.2

[3] ARIMESCU, V.I., WILLIAMS, A.F., 1998. Thermal Performance Modeling in CANDU-Type Fuel Codes and its Validation, Proc. Seminar Thermal Performance of High Burn-up LWR Fuel, Cadarache, France.

[4] HEINS, L, GROSS, H., NISSEN, K, WUNDERLICH, F., 1991. Statistical analysis of QC data and estimation of fuel rod behavior. J. of Nucl. Mat. **178**, 287-295.

[5] CONOVER, W.J., 1971. Practical Nonparametric Statistics, John Wiley & Sons, New York, pp. 99-105.

[6] BILLAUX, M.R., SHANN, S.-H., VAN SWAM, L.F., SONTHEIMER, F., 1997. SIERRA: A Fuel Performance Code to Predict the Mechanical Behavior of Fuel Rods up to High Burnup, Proc. International Topical Meeting on Light Water Reactor Fuel Performance, Portland, Oregon.

DEVELOPMENT OF IRRADIATED UO_2 THERMAL CONDUCTIVITY MODEL

CHAN BOCK LEE, JE-GEON BANG, DAE HO KIM, YOUN HO JUNG
Korea Atomic Energy Research Institute,
Taejon, Republic of Korea

Abstract

Thermal conductivity model of the irradiated UO_2 pellet was developed, based upon the thermal diffusivity data of the irradiated UO_2 pellet measured during thermal cycling. The model predicts the thermal conductivity by multiplying such separate correction factors as solid fission products, gaseous fission products, radiation damage and porosity. The developed model was validated by comparison with the variation of the measured thermal diffusivity data during thermal cycling and prediction of other UO_2 thermal conductivity models. Since the developed model considers the effect of gaseous fission products as a separate factor, it can predict variation of thermal conductivity in the rim region of high burnup UO_2 pellet where the fission gases in the matrix are precipitated into bubbles, indicating that decrease of thermal conductivity by bubble precipitation in rim region would be significantly compensated by the enhancing effect of fission gas depletion in the UO_2 matrix.

1. INTRODUCTION

Thermal conductivity of UO_2 pellet depends upon such variables as density, porosity, stoichiometry, temperature and impurities. In addition, under irradiation condition, it is affected by radiation damage and fission product buildup. Thermal conduction of UO_2 pellet occurs mainly via phonon transport at the temperature below 1500^{o}C, and at the temperature higher than 1500℃ thermal conduction by free electrons is added to the phonon transport. In UO_2 of ceramic lattice structure, thermal conduction by free electrons increases with temperature since mobility of free electrons increases with temperature. Thermal conduction by phonon transport is like hypothetical quantum particle transport through the solid lattice structure that also has the wave characteristics. Since vibration of atoms in the lattice increases with temperature, thermal resistance increases with temperature due to the interference with phonon wave. Lattice defects such as point defect, line defect and loop, and impurities also interfere with the phonon waves to decrease the thermal conductivity. Capability to scatter the phonon wave is known to be in the order of point defect, line defect and bubbles or large precipitates of fission product compound [1].

2. ANALYSIS OF UO_2 THERMAL CONDUCTIVITY MODELS

2.1. Variables

Porosity

Effect of porosity upon the thermal conductivity depends upon the shape and distribution of the pores. Porosity consists of the pores formed during the UO_2 pellet manufacturing and fission gas bubbles formed during the irradiation. Fission gas bubbles at the grain boundary have lenticular shape due to the surface effect of the grain boundary while the bubbles inside the grain and in the rim region of the high burnup UO_2 fuel are sphere. Pores formed during UO_2 manufacturing have irregular shape and surfaces. There are various porosity correction correlations available as shown below [2]. Thermal conductivity of the inner gases of the

bubbles and the pores is too small compared with that of the UO_2 matrix, so that thermal conduction through the pores can be neglected.

- Loeb correlation: $f_p = 1- \alpha p$
- Maxwell correlation: $f_p = (1-p)^{1.5}$
- Maxwell-Eucken correlation: $f_p = (1-p)/(1 + \beta p)$
- Schulz correlation: $f_p = (1-1.5p)$
- Bakker correlation: $fp = (1-p)^{1.7 \pm 0.7}$.

Values of α and β factors in Loeb and Maxwell-Eucken correlations is theoretically 1 and 0.5, respectively when the pore is sphere and uniformly distributed. However, fitting of the measured thermal conductivity of the unirradiated UO_2 showed that α is 2.5 $\pm$ 1.5, which means that reduction of the thermal conductivity is more enhanced due to the irregular shape and non-uniform distribution of the pores. Schulz correlation was analytically derived for the case of the sphere pores and uniform pore distribution. Bakker correlation was derived by finite element analysis of the actual pore and bubble distribution of 25 MWD/kgU irradiated fuel [3]. Fig. 1 compares different porosity correction correlations. It can be seen that decrease of thermal conductivity by porosity is enhanced in proportion to deviation from sphere in pore shape and deviation from uniformity in pore distribution.

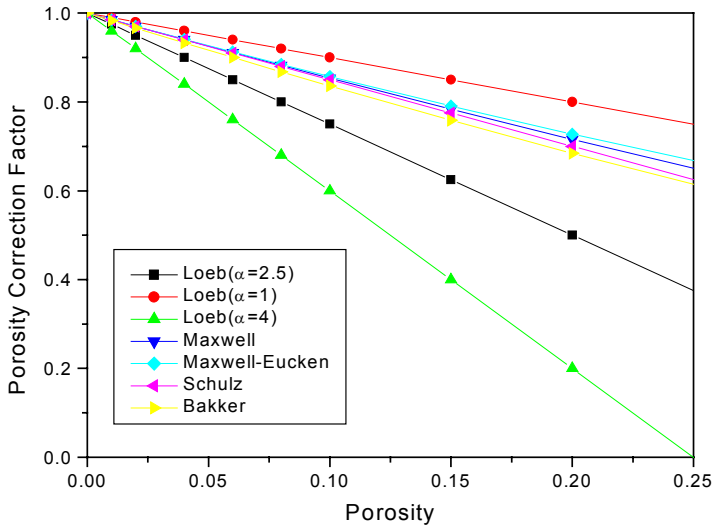

Fig. 1. Porosity Correction Factor.

Fission Products

Fission products exist mostly as four different states in UO_2 as follows [4].

- Dissolved in the matrix as an oxide: Sr, Zr, Nb, Y, La, Ce, Pr, Nd, Pm, Sm
- Metallic precipitate:: Mo, Tc, Ru, Rh, Pd, Ag, Cd, In, Sb, Te
- Oxide precipitate: Ba, Zr, Nb, Mo, (Rb, Cs, Te)
- Gas and volatile elements: Kr, Xe, Br, I, (Rb, Cs, Te).

Effect of fission products upon the UO_2 thermal conductivity were studied extensively by using SIMFUEL which simulates the irradiated fuel by mixing the non-radioactive fission

product elements [5]. Thermal conductivity measurement of SIMFUEL showed that metallic precipitates (0.05 ~ 1 μm) increase the thermal conductivity of UO_2 due to higher thermal conductivity of metallic precipitates than UO_2 matrix while other fission products decreases UO_2 thermal conductivity [6].

Impurities and Additives

Impurities or additives in UO_2 decrease thermal conductivity like fission products. Thermal conductivity of UO_2/Gd_2O_3 decreases with the content of Gd_2O_3. Gd_2O_3 is body centered cubic structure so that it may deform lattice structure of UO_2 and enhance the defect formation in UO_2 of face-center cubic structure. In addition, Gd_2O_3 changes the phonon-phonon scattering characteristic due to the mass difference between Gd_2O_3 and UO_2 [7].

Stoichiometry

Measured thermal conductivity of $UO_{2\pm x}$ showed that thermal conductivity would be decreased for hyper-stoichiometry($x > 0$) while it is slightly increased for hypo-stoichiometry($x < 0$). However, for the irradiated UO_2, effect of stoichiometry can not be simply separated from the fission product buildup due to fission of uranium element so that it should be taken into account along with the effect of the fission products or burnup. Therefore, thermal conductivity model for the irradiated UO_2 mostly does not consider the effect of stoichiometry as an independent factor.

Radiation Damage

Under the irradiation condition, radiation damage such as point defects, dislocation and loops are formed in UO_2. Those defects decrease thermal conductivity by interference with the phonon wave. As temperature increases, level of radiation damage decreases due to annealing of the radiation defects. Point and line defects are known to be annealed by recombination below 1000 K [10]. Radiation damage becomes saturated at lower burnup so that amount of radiation damage does not increase linearly with the burnup.

2.2. Analysis of UO_2 Thermal Conductivity Models

Lucuta Model [6]

Lucuta model for the irradiated UO_2 published in 1996 is as follows.

$$\lambda = K_{1d} K_{1p} K_{2p} K_{3x} K_{4r} \lambda_0$$

$$\lambda_0 = \frac{1}{(0.0375 + 2.165\times10^{-4}\cdot T)} + \frac{4.715\times10^{9}}{T^2}\exp(-\frac{16361}{T})$$

where,

λ = thermal conductivity of irradiated UO_2
λ_0 = thermal conductivity of unirradiated 100% dense UO_2
K_{1d} = factor for fission products
K_{1p} = factor for precipitated metal fission products
K_{2p} = factor for porosity
K_{3x} = factor for stoichiometry
K_{4r} = factor for radiation damage.

Effect of fission products is based upon the test results of SIMFUEL. Daniel and Cohen's data [11] were used for the effect of radiation damage. Maxwell-Eucken correlation was used for porosity correction and Harding and Martin data [12] are used for thermal conductivity of 100% UO_2 .

2.2.1. Halden Model [8]

Halden model is based upon the in-pile measured data of fuel centerline temperature in relation to power level. It has been continuously improved by adjusting the model constants as the new measured data are generated. Halden model published in 1997 is as follows.

$$\lambda_{95} = \frac{1}{0.1148 + 0.0035BU + 2.475\times10^{-4}(1-0.00333BU)T} + 0.0132\exp(0.00188T)$$

where λ_{95} is thermal conductivity of unirradiated 95% UO_2 (w/m.K), BU is burnup(MWD/kgU) and T is temperature (^oC). Halden model is considered to directly represent the in-pile thermal conductivity of UO_2 since it is based upon in-pile measured temperature data. However, since the temperature was measured only at the fuel center, it may not fully represent the wide range of radial temperature variation in the fuel and there may be somewhat uncertainties in the fuel gap conductance.

2.2.2. NFI Model [9]

NFI model was developed based upon the thermal diffusivity data of 61 MWD/kgU UO_2 fuel measured by laser flash technique. Thermal conductivity of UO_2 can be deduced from its relation with thermal diffusivity, density and heat capacity. NFI model is as follows.

$$\lambda_{95} = \frac{1}{4.52\times10^{-2} + 2.46\times10^{-4}T + 1.87\times10^{-3}BU + 0.038BU^{0.28}\cdot h(T)} - 5.47\times10^{-9}T^2 + 2.29\times10^{-14}T^4$$

$$h(T) = \frac{1}{1+396\exp(-6380/T)}$$

where λ_{95} is thermal conductivity of unirradiated 95% TD UO_2 (w/m.K), BU is burnup (MWD/kgU), T is temperature (K), and h (T) represents the effect of radiation damage.

3. DEVELOPMENT OF UO_2 THERMAL CONDUCTIVITY MODEL

3.1. Model Development

In NFIR (Nuclear Fuel Industry Research) Program managed by EPRI, thermal diffusivity of irradiated UO_2 fuel was measured by laser flash technique by changing temperature [13,14]. There were three different irradiated fuel specimens with the burnup of 24.9 MWD/kgU (U2), 36.23 MWD/kgU (U4) and 59.93 MWD/kgU (U6), respectively. Table 1 shows the temperature histories during thermal diffusivity measurement.

Thermal diffusivity was measured at every 100^{o}C from 300^{o}C to 1600^{o}C. Measured data during cycle 1 may represent the thermal diffusivity of the specimen with all the effects accumulated during irradiation. After cycle 1 of maximum temperature of 800^{o}C and cycle 2 of maximum temperature of 1100^{o}C, it may be assumed that all the radiation damage was

TABLE 1. HISTORY OF THERMAL CYCLING OF THE SPECIMENS

Cycle	Temperature (°C)			Duration of Cycle of Specimen (min)		
	Initial	Peak	Final	U2	U4	U6
1	300	800	300	269	330	332
2	300	1100	500	240	375	485
3	500	1500	300	422	412	485
4	300	1600	300	469	542	611

annealed out. Therefore, the data measured during cycle 3 may represent thermal diffusivity of irradiated fuel with the effect of fission products except radiation damage. After cycle 3 of maximum temperature of 1500°C, it may be assumed that fission gas atoms in the matrix would be released out of fuel or precipitated into fission gas bubble so that there may be no fission gas atoms left in the matrix. Therefore, measured data during cycle 4 may represent the thermal diffusivity of irradiated fuel with only the effect of solid fission products. The fact that there is not much difference between thermal diffusivity data measured during cycles 3 and 4 [13, 14] indicates that fission gas atoms in the matrix may have been mostly depleted during cycle 3.

Examination of the microstructure of the specimens after thermal cycling [14] showed that there were bubbles of micron size at the grain boundary for U4 specimen. For the high burnup specimen of U6, micron size bubble were found both at the grain boundary and inside the grain, and size of the bubbles increased near the periphery of the specimen due to the higher burnup in that region.

Separate effects of such variables as solid fission product, fission gas and radiation damage can be deduced from the variation of the thermal diffusivity during thermal cycling. Therefore, thermal conductivity model was derived from the measured thermal diffusivity data by considering the effects of solid fission product, fission gas and radiation damage as a separate factor, which is similar to Lucuta model. Those factors were derived by fitting the measured thermal diffusivity data. Since the porosity data of the irradiated UO_2 fuel specimens before and after the thermal cycling were not available, porosity variation during thermal cycling could not be considered.

$$\lambda = f_{sfp} f_{fg} f_{rd} f_p \lambda_0$$

$$f_{sfp} = \frac{10.152 + 0.0762T}{10.152 - 4.8054BU^{0.5} + 1.563BU + (0.0762 + 4.724\times10^{-3}BU^{0.5} - 8.624\times10^{-4}BU)\cdot T}$$

$$f_{fg} = \frac{10.152 - 4.8054BU^{0.5} + 1.563BU + (0.0762 + 4.724\times10^{-3}BU^{0.5} - 8.624\times10^{-4}BU)\cdot T}{10.152 - 1.423BU^{0.5} + 1.6072BU + (0.0762 + 3.043\times10^{-3}BU^{0.5} - 8.066\times10^{-4}BU)\cdot T}$$

$$f_{rd} = \frac{1}{4.0413\exp(31.598/T) - 3.1186}$$

$$\lambda_0 = \frac{1}{(0.0375 + 2.165\times10^{-4}\cdot T)} + \frac{4.715\times10^{9}}{T^2}\exp(-\frac{16361}{T})$$

where,

λ = thermal conductivity of irradiated UO_2
λ_0 = thermal conductivity of unirradiated 100% dense UO_2
f_{sfp} = factor for solid fission products
f_{fg} = factor for gaseous fission products
f_{rd} = factor for radiation damage
f_p = factor for porosity
T = temperature (K)
B = burnup (MWD/kgU).

Figs 2-4 compare the prediction results of solid fission product factor, gaseous fission product factor and radiation damage factor with the results derived from the measured thermal diffusivity data during thermal cycling, respectively. It can be seen that there is somewhat scattering in the fission gas factor. Dependency of fission gas factor upon the burnup seems to be smaller than that of the solid fission products factor. Radiation damage factor seems to be independent of the burnup since its effect may be saturated at low burnup. It can be seen that radiation damage is annealed at temperature above 1100^{oC}. Fig. 5 compares prediction of the burnup factor which is defined as multiplication of solid fission product, gaseous fission product and radiation damage, with the measured data. Except the scattering of the measured data above $1300^{o}C$, the model reproduced the measured thermal conductivity quite well.

Figs 6-9 compare the developed model prediction with prediction of Lucuta, Halden and NFI models. Developed model is closer to NFI model since both models were derived from the measured thermal diffusivity data of the irradiated UO_2 fuel. Halden model over-estimates the thermal conductivity at low temperature, which indicates that Halden model may not fully consider the effect of radiation damage at low temperature since the measure in-pile centerline temperature and fuel average temperature is somewhat higher [1]. Lucuta model has a separate factor for the metallic fission product precipitates which increases thermal conductivity, so that it generally over-estimates the thermal conductivity and, compared with other models, decrease rate of thermal conductivity with temperature is low between 500^{oC} and 800^{oC}.

3.2. Application to UO_2 rim region

Since the developed model takes into account the effect of fission gas as a separate factor, it can be directly applied to the prediction of thermal conductivity in high burnup UO_2 rim region where fission gas atoms in the matrix are depleted to be precipitated into fission gas bubbles with the porosity of 15–17% [15, 16]. Thermal conductivity in UO_2 rim region can be obtained by

$$\lambda_{rim} = f_{sfp}^{rim} f_{rd} f_p^{rim} \lambda_0.$$

Fission gas bubbles in rim region are sphere shape and uniformly distributed, so that Schulz correlation can be used for porosity correction. As an example, it was applied to thermal conductivity in the UO_2 rim region where bubble porosity is 15% and local burnup of 80 MWD/kgU at 600^{oC}, in comparison with that of normal UO_2 where fission gases are still in the matrix without fission gas bubble. In rim region, thermal conductivity is increased by 18% due to the depletion of fission gases from the matrix while it is reduced by 23% due to the porosity of 15% according to Schulz correlation. Therefore, compared with normal UO_2 at same burnup, net decrease of thermal conductivity in the UO_2 rim region due to fission gas bubble precipitation may be only about 9% for this case. It indicates that decrease of thermal conductivity by fission gas bubble precipitation in the UO_2 rim region would be significantly compensated by the enhancing effect of fission gas depletion in the UO_2 matrix.

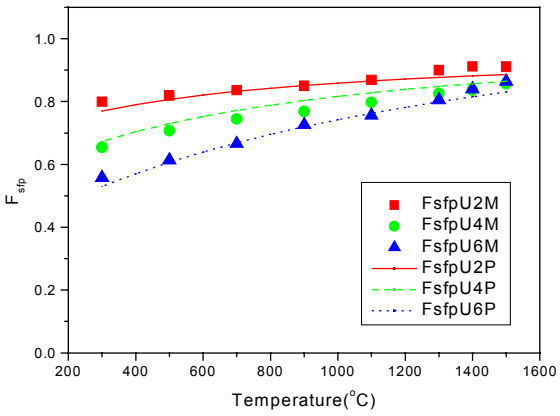

*Fig. 2. Solid fission product factor (*M: Measured, *P: Prediction).*

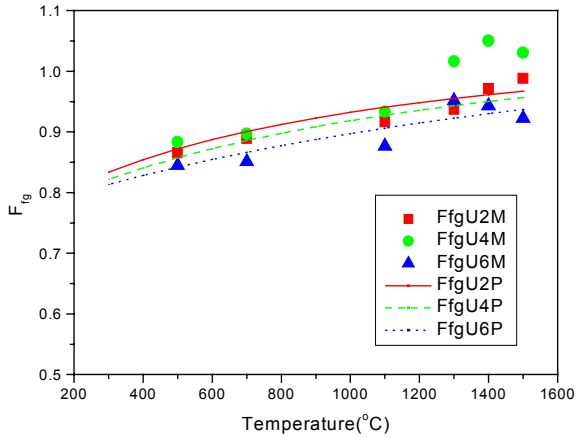

*Fig. 3. Gaseous fission product factor (*M: Measured, *P: Prediction).*

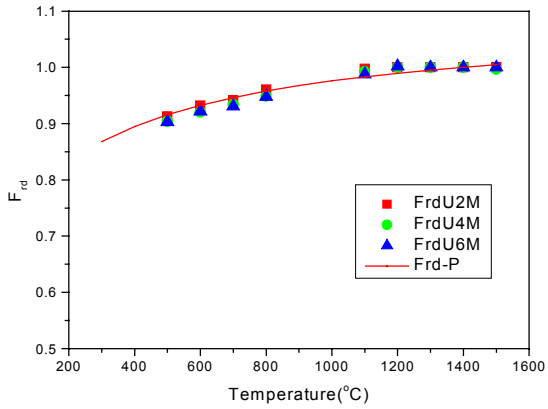

*Fig. 4. Radiation damage factor (*M: Measured, *P: Prediction).*

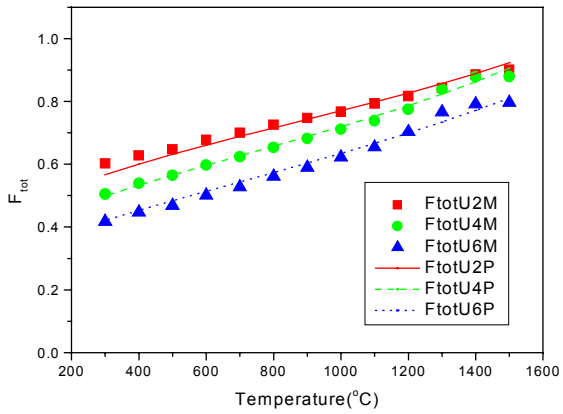

*Fig. 5. Burnup factor (*M: Measured, *P: Prediction).*

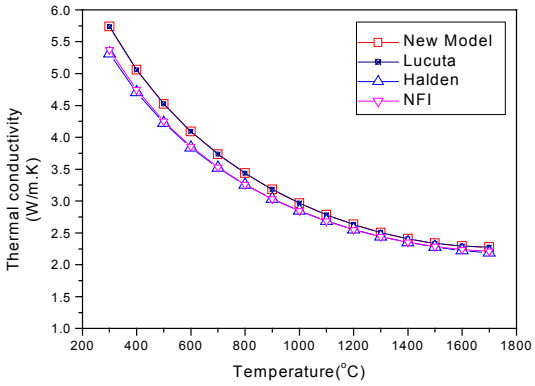

Fig. 6. Thermal conductivity of unirradiated (95% TD)% UO_2.

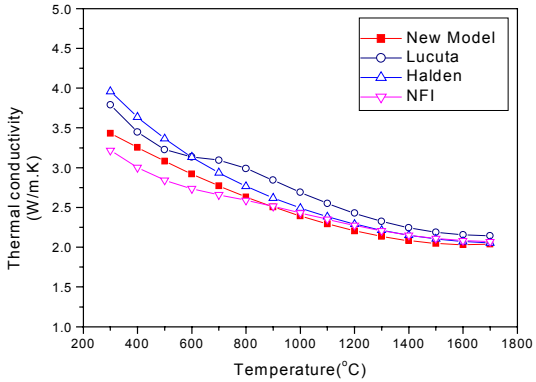

Fig. 7. Thermal conductivity of 20 MWD/kgU.

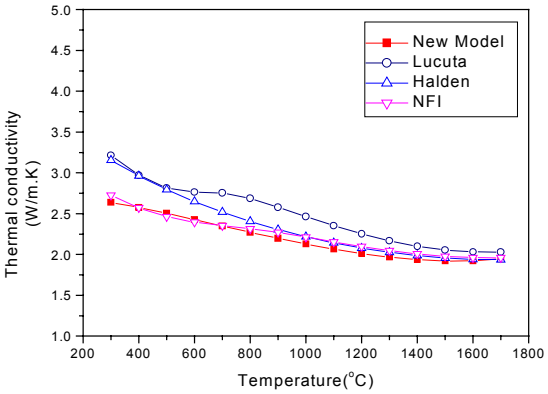

Fig. 8. Thermal conductivity of 40 MWD/kgU.

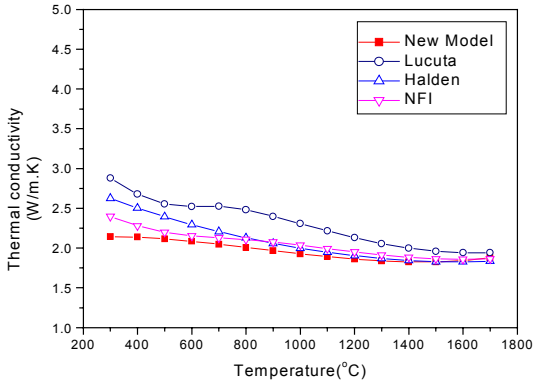

Fig. 9. Thermal conductivity of 60 MWD/kg UO_2.

4. CONCLUSION

Thermal conductivity model of the irradiated UO_2 pellet was developed, based upon the thermal diffusivity data of the irradiated UO_2 pellet measured during thermal cycling. The model predicts the thermal conductivity by multiplying such separate factors as solid fission products, gaseous fission products, radiation damage and porosity.

The developed model was validated by comparison with both the variation of the measured thermal diffusivity data during thermal cycling and the prediction of other UO_2 thermal conductivity models.

Since the developed model considers the effect of gaseous fission products as a separate factor, it can predict variation of thermal conductivity in the rim region of high burnup UO_2 pellet where the fission gases in the matrix are precipitated into the bubbles, indicating that decrease of thermal conductivity by bubble precipitation in rim region would be significantly compensated by enhancing effect of fission gas depletion in the UO_2 matrix.

ACKNOWLEDGEMENT

This work has been carried out under the Nuclear R&D Program supported by Ministry of Science and Technology in Korea. Thermal diffusivity data of the irradiated UO_2 fuel were generated in NFIR (Nuclear Fuel Industry Research) Program managed by EPRI. The authors would like to thank Dr. S. K. Yagnik for review of manuscript and helpful comments.

REFERENCES

[1] C. BEYER and D. LANNING, “Review of fuel thermal conductivity data and model”, Seminar on Thermal Performance of high burnup LWR Fuel, Cadarache, France, 2-6 March, 1998.

[2] D.G. MARTIN, “A Re-appraisal of the thermal conductivity of UO_2 and mixed (U,Pu) oxide fuel”, J. Nucl. Mater. 110 (1982) 73.

[3] K. BAKKER, et al., “Determination of a porosity correction factor for the thermal conductivity of irradiated UO_2 fuel by means of the finite element method”, J. Nucl. Mater. 226 (1995) 128.
[4] H. KLEYKAMP, “The chemical state of the fission products in oxide fuels”, J. Nucl. Mater. 131 (1985) 221.
[5] P.G. LUCUTA, et al., “Modelling of UO_2-based SIMFUEL thermal conductivity: The effect of the burnup”, J. Nucl. Mater. 217 (1994) 279.
[6] P.G. LUCUTA, et al., “A pragmatic approach to modeling thermal conductivity of irradiated UO2 fuel: review and recommendations”, J. Nucl. Mater. 232 (1996) 166.
[7] D. BARON and J.C. COUTY, “A proposal for a unified fuel thermal conductivity model available for UO_2, (U-Pu)O_2 and UO_2-Gd_2O_3 PWR fuel”, IAEA-TECDOC-957, 1997.
[8] W. WIESENACK, “Assessment of UO_2 conductivity degradation based upon in-pile temperature data”, Proc. of Int. Top. Mtg. on LWR Fuel Performance, Portland, Oregon, 1997.
[9] K. OHIRA and N. ITAKI, “Thermal conductivity measurements of high burnup UO_2 pellet and a benchmark calculation of fuel temperature”, Proc. of Int. Top. Mtg. on LWR Fuel Performance, Portland, Oregon, 1997.
[10] M. AMAYA and M. HIRAI, “Recovery behavior of thermal conductivity in irradiated UO_2 pellets”, J. Nucl. Mater. 247 (1997) 76.
[11] R.C. DANIEL and I. COHEN, “In-pile effective thermal conductivity of oxide fuel elements to high burnup depletion”, WAPD-246, 1964.
[12] J.H. HARDING and D.G. MARTIN, “Recommendation for the thermal conductivity of UO_2”, J. Nucl. Mater. 166 (1989) 166.
[13] S. YAGNIK, “Thermal conductivity recovery phenomenon in irradiated UO_2 and (U,Gd)O_2”, Proc. of Int. Top. Mtg. on LWR Fuel Performance, Parkcity, Utah, 2000.
[14] M. LIPPENS and L. MERTENS, “High burnup UO_2 and (U,Gd)O_2 thermal diffusivity measurements and post-irradiation characterizations”, EPRI Report TR-106501, 1996.
[15] J. SPINPO, et al., “Detailed characterization of the rim microstructure in PWR fuels in the burnup range 40-67 GWd/tM”, J. Nucl. Mater. 231 (1996) 179.
[16] J. SPINO, et al., “High burnup rim structure: evidences that xenon-depletion, pore formation and grain subdivision strat at different local burnups”, J. Nucl. Mater. 256 (1998) 189.

HIGH BURNUP FUEL MODELLING
(Session 6)

Chairpersons

F. SOKOLOV
Russian Federation

F. SONTHEIMER
Germany

DEVELOPMENT OF A FUEL ROD THERMAL–MECHANICAL ANALYSIS CODE FOR HIGH BURNUP FUEL

M. OWAKI, N. IKATSU, K. OHIRA, N. ITAGAKI
Nuclear Fuel Industries, Ltd,
Tokai-mura, Naka-gun, Ibaraki, Japan

Abstract

The thermal–mechanical analysis code for high burnup BWR fuel rod has been developed by NFI. The irradiation data accumulated up to the assembly burnup of 55 GWd/t in commercial BWRs were adopted for the modeling. In the code, pellet thermal conductivity degradation with burnup progress was considered. Effects of the soluble FPs, irradiation defects and porosity increase due to RIM effect were taken into the model. In addition to the pellet thermal conductivity degradation, the pellet swelling due to the RIM porosity was studied. The modeling for the high burnup effects was also carried out for (U, Gd)O_2 and MOX fuel. The thermal conductivities of all pellet types, UO_2, (U, Gd)O_2 and (U, Pu)O_2 pellets, are expressed by the same form of equation with individual coefficient γ in the code. The pellet center temperature was calculated using this modeling code, and compared with measured values for the code verification. The pellet center temperature calculated using the thermal conductivity degradation model agreed well with the measured values within $\pm 150\ ^{o}C$. The influence of rim porosity on pellet center temperature is small, and the temperature increase in only $30^{o}C$ at 75 GWd/t and 200 W/cm. The pellet center temperature of MOX fuel was also calculated, and it was found that the pellet center temperature of MOX fuel with 10wt% PuO_2 is about $60^{o}C$ higher than UO_2 fuel at 75 GWd/t and 200 W/cm.

1. INTRODUCTION

In recent years the thermal conductivity degradation with burnup progress and the porosity increase due to RIM effect have been reported. It is pointed out that the pellet property change with these high burnup effects influences the fuel rod behavior of high burnup fuels. In order to develop the thermal・ mechanical analysis code for high burnup BWR fuel rod, the irradiation data accumulated up to the assembly burnup of 55 GWd/t in commercial BWRs were used for the modeling.

In the code, a model of the pellet thermal conductivity degradation with burnup progress was incorporated. The model consists of two parts: (1) effects of the soluble FPs and irradiation defects; (2) porosity increase due to RIM effect. The former effects, soluble FPs and irradiation defects, were determined by measuring the thermal diffusivity in a temperature cycle of 700-1700-700 K [1]. The latter effect, RIM porosity, was evaluated by a FEM analysis using the SEM image of pellet RIM structure [2]. In addition to the pellet thermal conductivity degradation, the pellet swelling due to the RIM porosity was studied.

In discussion, the pellet center temperature was calculated using this modeling code, and compared with measured values for the code verification. In addition, temperature increase caused by each effect of the model, i.e. thermal conductivity degradation due to soluble FPs, irradiation defects, and rim effect, was evaluated in this paper. The pellet center temperature of MOX fuel was also calculated, and compared with that of UO_2 fuel.

2. GENERAL DESCRIPTION OF THE CODE

The fuel rod analysis code which predicts the thermal and mechanical behaviors of the fuels during irradiation has been used in NFI for the design of BWR fuel rods. Input data of the code are:

- geometrical parameters of the rod,
- initial pellet properties,
- time-dependent irradiation power and external pressure.

For the calculation, the pellet is divided into several rings at each axial level. The fuel rod behaviors during irradiation about fuel temperature, FP gas release, rod pressure, deformation of pellet and cladding, and gap conductance are obtained. In this work, several parts of the code were modified based on the irradiation data since the pellet properties of the unirradiated pellet are used by the original code to calculate the fuel rod behaviors at high burnup. Several pellet property models for (U, Gd)O_2 and MOX fuel were also reevaluated in this work.

3. MODELING OF THE CODE FOR HIGH BURNUP FUEL

3.1. Thermal conductivity degradation model with high burnup effects of soluble FPs and irradiation defects

It is known that the thermal conductivity of UO_2 pellet decreases with burnup increase due to the dissolution of solid FPs and irradiation defects. The effects of the soluble FPs and irradiation defects on thermal conductivity were modeled based on the measured thermal diffusivity of a high burnup UO_2 pellet irradiated to pellet local burnup of ca. 61 GWd/t in a commercial BWR [1]. The thermal diffusivity of the specimen was measured by the laser flash technique on a temperature cycle of 700-1700-700 K. The thermal conductivity was then calculated from the measured thermal diffusivity. Using this result, thermal conductivity model for the irradiated pellet was determined.

The thermal conductivity of the irradiated pellet is shown by the following equation, where f(Bu) denotes the effect of soluble FPs and G(Bu)·h(T) the irradiation defect.

$$\lambda = \frac{1}{\mathrm{A} + \mathrm{BT} + \mathrm{f(Bu)} + \mathrm{g(Bu)} \cdot \mathrm{h(T)}} + CT^2 + DT^4 \qquad \text{(W/mAK)} \qquad (1)$$

The quantity Bu is the pellet average burnup (GWd/t), T the pellet temperature (K), and A, B, C, D are the constants for the temperature dependent thermal conductivity at BOL (A = 4.52 × 10^{-2} (mAK/W), B = 2.46 × 10^{-4} (mAK/W/K), C = -5.47 × 10^{-9} (W/(mAK)/K^2), D = 2.29 × 10^{-14} (W/(mAK)/K^4)).

From Equation (1), the phonon contribution term of the thermal conductivity is obtained by subtracting the term [CT^2 + DT^4] from the measured data. The thermal resistivity is then obtained by the following equation:

$$1/\lambda^* = \mathrm{A+BAT+f(Bu)+g(Bu)Ah(T)} \qquad \text{(mAK/W)} \qquad (2)$$

As the irradiation defects are recovered by annealing, the term of soluble FPs, f(Bu) is obtained by subtracting the thermal resistivity of unirradiated pellet from that of annealed specimen.

Assuming that the function f(Bu) is linearly increased with burnup, the f(Bu) was determined as below:

$$f(Bu)=1.87 \times 10^{-3}\,Bu \qquad (mAK/W). \qquad (3)$$

The term g(Bu)Ah(T) was determined by using the thermal conductivity measurement results of an unannealed sample (heat-up period). The function g(Bu) is the term which shows the induced defects increase with irradiation. The function h(T) is the term of the defect recovered ratio with temperature increase. g(Bu) was determined by the benchmark calculation of the fuel center temperature measured in a wide burnup range. Function h(T) was determined by fitting a straight line to the data plotted as (1-h)/h vs. 1/T. The functions g(Bu) and h(T) were determined as below.

$$g(Bu)=0.038\,Bu^{0.28} \qquad (m \cdot K/W) \qquad (4)$$

$$h(T)=\frac{1}{1+396\cdot\exp(-6380/T)} \qquad (5)$$

The thermal conductivity degradation with burnup at 600°C and 1400°C are shown in FIG. 1 [1,3-5]. The calculated values (line) agree well with measured values (points) at each temperature. The results indicate that at low temperatute (600°C), thermal conductivity rapidly decrease in low burnup region. On the other hand, as most of irradiation defects are recovered, the thermal conductivity decreases almost linearly with burnup at high temperature (1400°C)

3.2. Thermal conductivity of (U, Gd)O_2 and (U, Pu)O_2 pellets

Thermal conductivity model of (U, Gd)O_2 fuel was reevaluated by using the experimental data reported by Hirai [6] and Sontheimer [7]. In the code, thermal conductivity degradation caused by the dopants, Gd or Pu, are shown by the common form of equation below:

$$\lambda=\frac{1}{A+BT+\varepsilon_M x_M}+CT^2+DT^4 \qquad (W/mAK) \qquad (6)$$

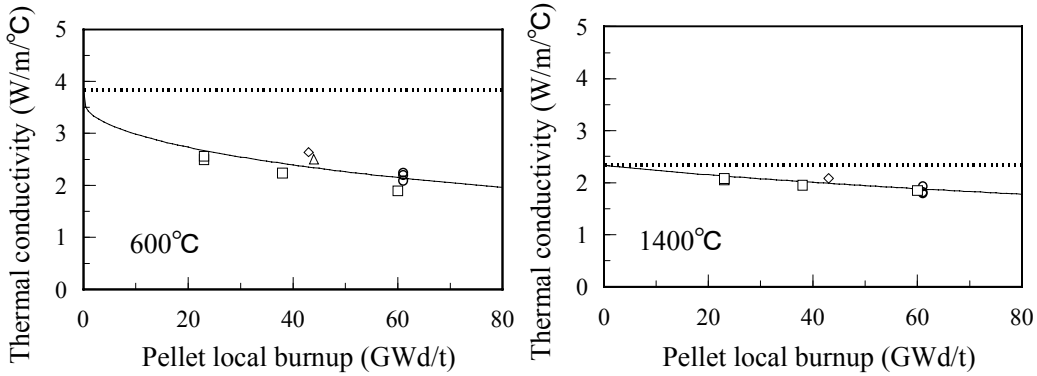

FIG.1. Thermal conductivity (W/m/°C) of UO2 pellet at 600°C (left) and 1400°C (right) as a function of burnup (95 % TD) [1].

where ε_M is the coefficient for (U, M)O_2 pellet and x_M the wt% of doped metal M (M: Gd, Pu). The coefficient for (U, Gd)O_2 pellet, ε_{Gd}, was determined as 8.12×10^{-3} by fitting the calculation values with measured values reported by Hirai [6] and Sontheimer [7] within the

Gd_2O_3 concentration range of 3-10 wt %. In FIG. 2, the calculated thermal conductivity of 7 wt% Gd_2O_3 is compared with measured values as an example. The good agreements between calculated values (line) and measured values (points) are seen in the figure. In the same manner, the coefficient $_{Pu}$ for (U, Pu)O_2 pellet was determined using the measured values of Hetzler [8], Gibby [9], and Goldsmith [10] for Pu concentration of 20, 25, and 30 wt% PuO_2. The value of 1.24×10^{-3} was obtained for ε_{Pu}. The calculated thermal conductivity of 30 wt% PuO_2 is compared with those of measured values in FIG. 3. Figure shows that the calculated values agree well with the measured values. From FIG. 2 and FIG. 3, the thermal conductivities of (U, Gd)O_2 and (U, Pu)O_2 pellets can be expressed by the same equation form using ε_{Gd} and ε_{Pu} described above.

The effect of soluble FPs, term f(Bu) in Equation (3), can be also expressed by a function of FP concentration as below:

$$f(Bu) = 1.87 \times 10^{-3} Bu = \gamma_{FP}\gamma_{FP} \qquad (7)$$

where γ_{FP} is the coefficient for (U, FP)O_2, γ_{FP} the atomic percent (at%) of FPs. The thermal conductivity of UO_2 pellet with soluble FPs is compared with that of 7 wt% Gd_2O_3 (=10.1 at% Gd). From Equation (3) and (6), it is calculated that the thermal conductivity with 10.1 at% Gd is comparable to that with soluble FPs at 30 GWd/t burnup. As the concentration of soluble FPs in a 30 GWd/t burnup fuel is calculated as 4.8 at% FPs by the ORIGEN2 code [11], the thermal conductivity with 10.1 at% Gd is comparable to that with 4.8 at% FPs as shown in FIG. 4.

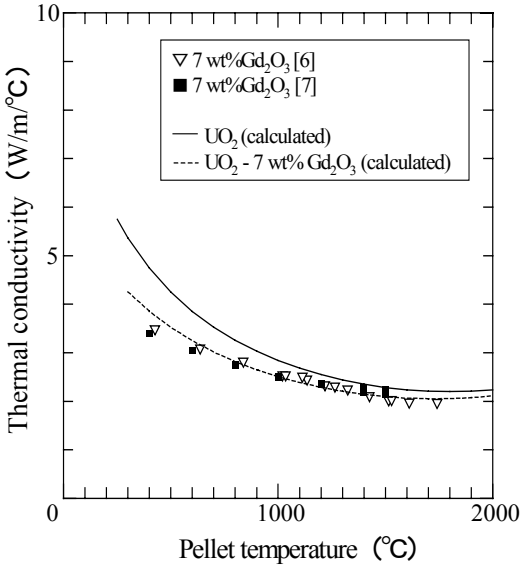

FIG. 2. Calculated temperature (°C) dependence of thermal conductivity (W/m/°C) of (U,Gd)O_2 compared with measured values:▽-7 wt% Gd_2O_3 of 95% TD[6];■-[7]

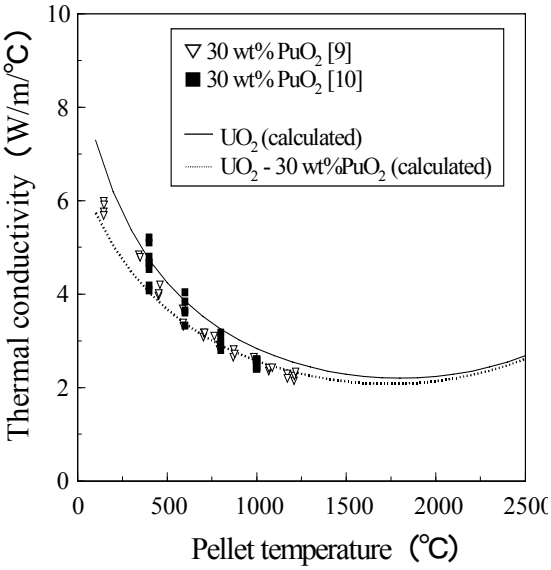

FIG. 3. Calculated temperature (°C) dependence of thermal conductivity (W/m/°C) of (U,Pu)O_2 compared with measured values: ▽-30 wt% PuO_2 [9]; ■-[10]

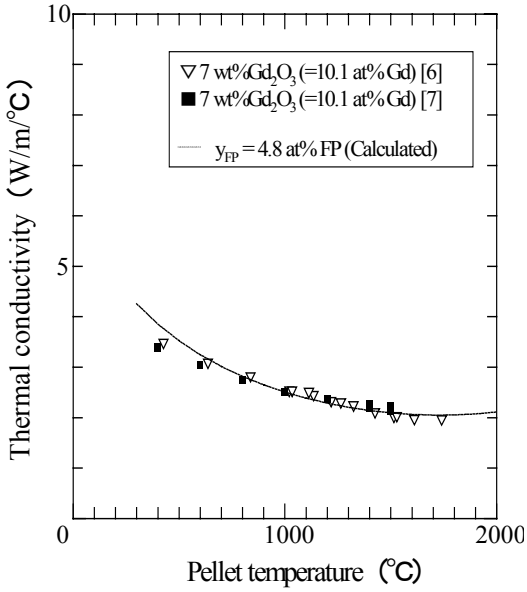

FIG. 4. Effect of soluble FPs on thermal conductivity (W/m/°C) compared with measured values of (U,Gd)O_2 pellet (95 % TD).

Finally, combination of Equations (1), (6), and (7) gives the thermal conductivities of UO_2, (U, Gd)O_2, and (U, Pu)O_2 pellets as the following equation:

$$\lambda = \frac{1}{A + BT + g(Bu)\cdot h(T) + \Sigma \gamma_M y_M} + CT^2 + DT^4 \quad \text{(W/mAK)} \qquad (8)$$

where γ_M is the coefficient for (U, M)O_2 and y_M the at% of the metal M (M: FPs, Gd, Pu), γ_{FP} 1.17 × 10^{-2} (30 GWd/t, y_{FP} = 4.8 at%), γ_{Gd} = 5.63 × 10^{-3}, γ_{Pu} = 1.24 × 10^{-3}, respectively.

3.3. Porosity increase by RIM effect

The porosity of the pellet in peripheral region increases by the RIM effect in high burnup fuel. As the thermal conductivity of the pellet decreases with porosity increase, the porosity distribution of the pellet in the radial direction was modeled. In the previous work, influence of the porosity on the thermal conductivity was evaluated by the FEM analysis using the pellet SEM images which samples were irradiated up to pellet burnup of 61 GWd/t in a commercial BWR reactor [2]. The following equation was obtained for the thermal conductivity correction in RIM region.

$$\lambda = \lambda_0 (1\text{-}P)^{1.6} \qquad (9)$$

where λ is the corrected thermal conductivity, λ_0 the thermal conductivity without porosity, P the porosity.

The porosity distributions of pellet in the radial direction were determined by the following step:
(1) Determine the width of RIM region as a function of pellet average burnup.
(2) Determine the porosity at pellet edge as a function of pellet local burnup.
(3) Using the relations (1) and (2), determine the porosity distribution of the pellet in radial direction.

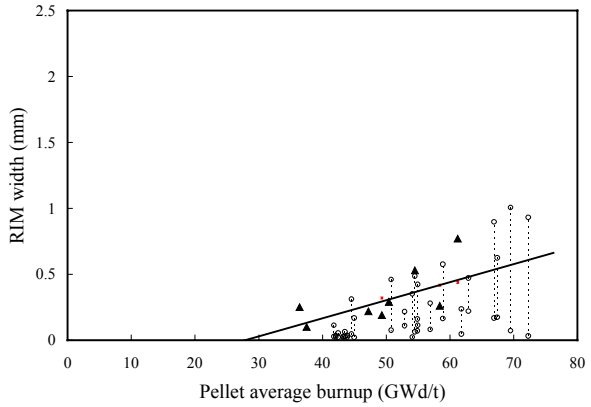

FIG. 5. RIM width vs. pellet average burnup [2].

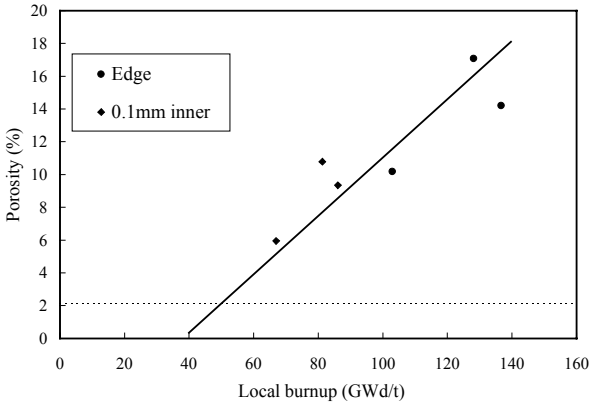

FIG. 6. Porosity vs. local burnup [2].

The observed RIM widths vs. pellet average burnup are plotted with the reported data up to 75 GWd/t in FIG. 5 [2]. From the figure, starting pellet average burnup of RIM formation was determined as ca. 30 GWd/t. The relation between the RIM width and pellet average burnup is expressed by the following equation for the burnup less than 75 GWd/t:

$$w = 1.37 \times 10^{-2} (PBu) - 0.384 \quad (mm) \qquad (10)$$

where W is the RIM width and PBu the pellet average burnup.

The measured porosities at the pellet edge and 0.1 mm inner from the pellet edge are plotted against pellet local burnup in FIG. 6. The relation between the porosity and pellet local burnup was determined as follows by the least square method:

$$P_x = 1.78 \times 10^{-1} (LBu) - 6.77 \quad (\%) \qquad (11)$$

where P_x is the porosity near pellet edge, LBu is the pellet local burnup. As RIM width and pellet edge porosity are obtained from Equations (10) and (11), the porosity distribution of the pellet in radial direction can be expressed by following equation:

$$\Delta P = \frac{\Delta P_0}{w^2}(r - r_0 + w)^2 \quad (\%) \qquad (12)$$

where ΔP is porosity increase at radial position of pellet r, ΔP_0 the porosity increase at pellet edge, and r_0 the radius of pellet. The distribution of porosity extends with burnup increase as shown in FIG. 7. The result shows that the porosity increases at pellet edge are about 10 % at 50 GWd/t and 20 % at 75 GWd/t, respectively.

The FP gas release rate and Xe/Kr ratio were measured of the fuel rods irradiated up to 50 GWd/t as reported in the previous work [2]. The FP gas release rate of this high burnup fuel was about a few percent, not a remarkable increase of FP gas release rate. From the result of Xe/Kr ratio measurement, it was found that the FP gas release from the pellet rim, where Pu burn ratio is larger, is negligible if compared with the total FP gas release. Based on these facts from PIE data, the FP gas release acceleration due to the rim formation was not included in the code in this work.

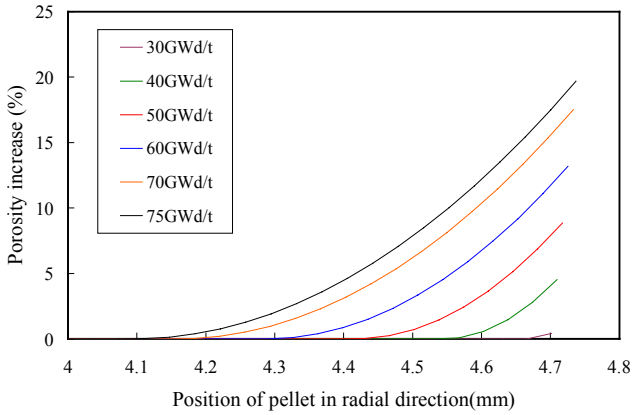

FIG. 7. Distributions of porosity increase vs. pellet position in radial direction.

3.4. (U, Gd)O_2 and MOX pellet properties reevaluated in this work

The modeling for the high burnup effects was also carried out for (U, Gd)O_2 and MOX fuel. In addition to the high burnup modeling, several pellet property models were reevaluated. As mentioned above, the parameters for the thermal conductivity models of (U, Gd)O_2 and MOX fuels were determined based on the experimental data [6-10]. The melting temperature [12], thermal expansion coefficient [13-15], Young's modulus [13,16], creep rate [17], and He gas release [18] of MOX fuels were reevaluated using the data from literature. Radial power distributions of MOX fuels were also reevaluated based on the detail nuclear calculation of MOX fuels. The calculated radial power distributions agreed well with the values obtained by chemical analysis measurement.

4. DISCUSSION

Using the thermal conductivity degradation model (Equation (8)), the pellet center temperature was calculated in order to verify the model. For this purpose, the pellet center temperatures calculated using the input data of the project RISO III [19] were compared with the pellet center temperatures measured in the project. In the RISO III project, total of 15 PWR and BWR rods were subjected to a power transient test after base irradiation. 9 fuel rods were then refabricated, and instrumented with thermocouples and pressure transducers to measure the fuel center temperatures and the fuel rod inner pressures during the power transient test. In order to calculate the fuel center temperatures, the fuel dimensions, oxide thickness before the test, the power history, the inner pressure, and the gas composition during the test were used as input data.

A comparison between the measured and calculated temperatures is shown in FIG. 8. The calculated values agree with the measured values within $\pm 150^{o}$C. The difference between the measured and the calculated temperatures against the burnup is shown in FIG. 9. The burnup range of the verification is 15-50 GWd/t in the figure. The figure shows that the calculated values agree with measured values with a small deviation in the burnup range of 15-50 GWd/t. FIG. 8 and 9 indicate that the thermal conductivity model described in this paper is well applicable to the fuel temperature evaluation over a wide burnup range of the fuel. The pellet temperature was calculated using porosity distribution described by Equation (12) up to pellet

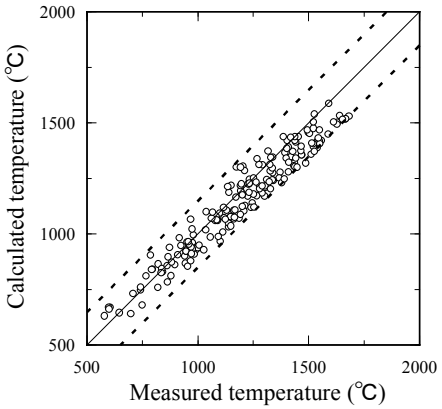

FIG. 8. Comparison of measured and calculated Temperatures (°C) for RISO III program [1].

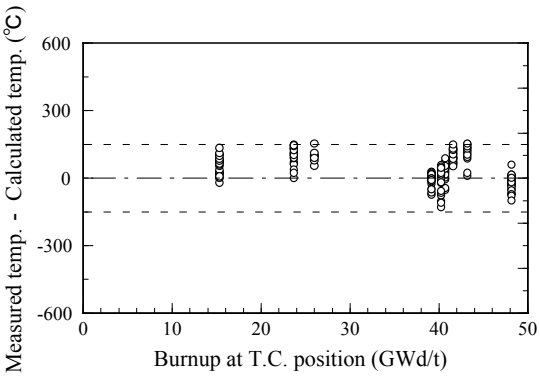

FIG. 9. Variation of measured and calculated temperatures (°C) with burnup for RISO III program [1].

average burnup of 75 GWd/t with linear heat rate of 200 W/cm. Except porosity distribution, the calculation conditions are same as that for the calculation without RIM effect. The pellet surface temperature was fixed at 380°C, that is the temperature obtained by using the original model (without RIM effect). The influence of RIM effect on pellet center temperature is shown in FIG. 10. The increase of pellet center temperature by RIM effect is about 15°C at 60 GWd/t, and 30°C at 75 GWd/t with linear heat rate of 200 W/cm.

The pellet temperature distribution against the radial position of pellet at 75 GWd/t and 200 W/cm is shown in FIG. 11 compared with distributions calculated by the original model and thermal conductivity degradation model considering only the effect of soluble FPs. The result indicates that the influence of the RIM porosity on the pellet temperature is small if compared with the effect of soluble FPs and irradiation defects. The increase of pellet center temperature due to soluble FPs and the effect of irradiation defects is about 220°C and 125°C, respectively. In other words, the increase of pellet center temperature caused by RIM porosity, soluble FPs, and irradiation defects are 7 %, 59 %, and 34 % in total increase of pellet center temperature, respectively. The pellet temperature distribution considering RIM porosity, shown by solid line in FIG. 11, was also compared with the distribution calculated without pellet burnup distribution in radial direction. These two temperature distributions are shown in FIG. 12. The figure shows that the influence of pellet burnup distribution in the radial direction on pellet center temperature is small, less than 10°C at 75 GWd/t and 200 W/cm.

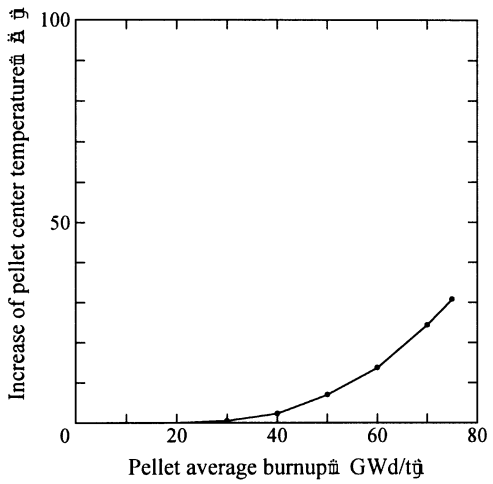

FIG. 10 *Increase of pellet center temperature due to RIM porosity in a function of pellet average burnup (200 W/cm).*

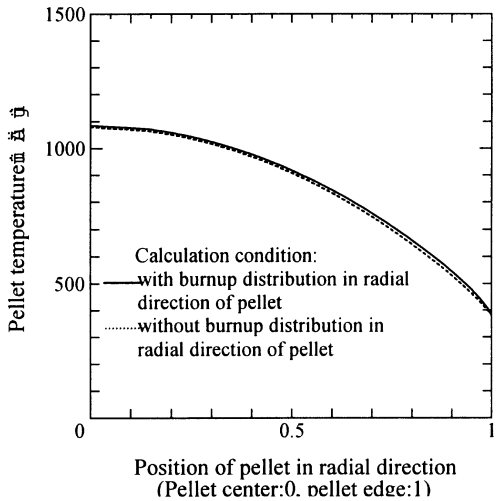

FIG. 12 *Pellet temperature distribution vs. radial position of pellet at 75 GWd/t, 200 W/cm. Thermal conductivity degradation by soluble FPs, irradiation defects, and RIM porosity.*

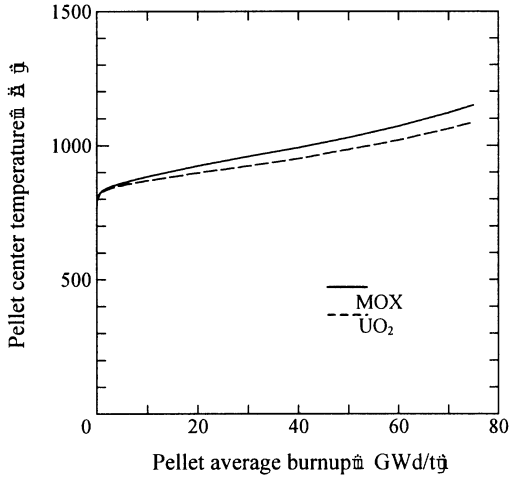

FIG. 14 *Pellet center temperature of 10 wt% MOX fuel compared with UO_2 fuel. (200 W/cm)*

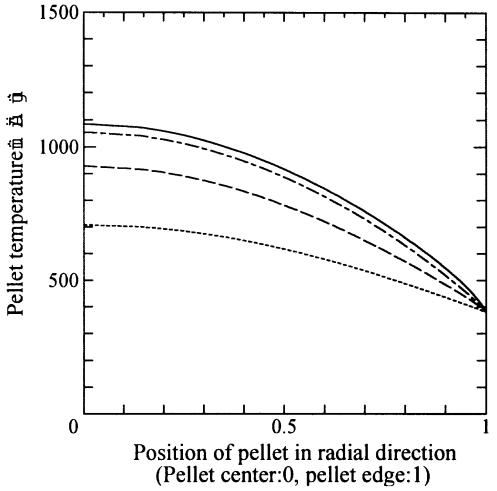

FIG. 11 *Pellet temperature distribution vs. radial position of pellet at 75 GWd/t, 200 W/cm. ·····: original model, – – : Thermal conductivity degradation by soluble FPs, —·—: Thermal conductivity degradation by soluble FPs and irradiation defects, ——: Thermal conductivity degradation by soluble FPs, irradiation defects and RIM porosity.*

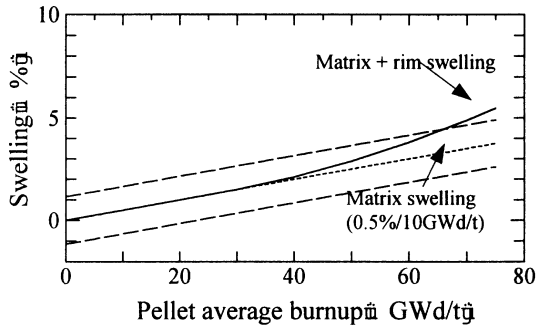

FIG. 13 *Pellet swelling caused by RIM effect.*

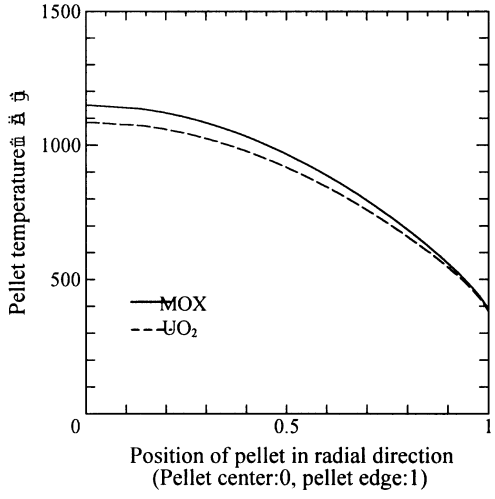

FIG. 15 *Pellet temperature of 10 wt% MOX fuel compared with UO_2 fuel. (75 GWd/t, 200 W/cm)*

In addition to the pellet thermal conductivity degradation, the pellet swelling due to the RIM porosity was evaluated. From the porosity distributions described by Equation (12), pellet swelling caused by the RIM effect is shown in. FIG. 13. The pellet swelling increase due to the RIM porosity is ca. 2 % at 75 GWd/t. The figure shows that the swelling by RIM porosity is not remarkable if deviation of the measured values (dashed lines) are considered.

The pellet center temperature of MOX fuel with 10wt% PuO_2 was also calculated, and compared with that of UO_2 fuel in FIG. 14. Although the thermal conductivity of MOX pellet is low if compared with UO_2 pellet, the pellet center temperature of MOX fuel at BOL is almost same as UO_2 fuel since the power distribution of pellet in radial direction differs between two fuels, that is, the power depression of MOX fuel across pellet radial direction is larger than UO_2 fuel. However, since the power depression of UO_2 fuel becomes larger with burnup progress, the pellet center temperature of MOX fuel becomes higher than UO_2 fuel with pellet burnup increase. The pellet temperature distribution of 10 wt% PuO_2 MOX fuel is compared with UO_2 fuel in FIG. 15. The pellet center temperature of MOX fuel with 10wt% PuO_2 is about 60℃ higher than UO_2 fuel at 75 GWd/t, 200 W/cm.

5. CONCLUSION

The thermal・mechanical analysis code for high burnup BWR fuel rod has been developed. In the code, pellet thermal conductivity degradation with burnup progress was modeled. Effects of the soluble FPs, irradiation defects, and porosity increase due to RIM effect were considered in the modeling. The modeling for the high burnup effects was also carried out for (U, Gd)O_2 and MOX fuel. Thermal conductivity of (U, Gd)O_2 and MOX fuels were reevaluated, and in the code, the thermal conductivities of all pellet types, UO_2, (U, Gd)O_2 and (U, Pu)O_2 pellets, are expressed by the same form of equation.

The pellet center temperature was calculated using the modeling code, and compared with measured values for the code verification. The pellet center temperature calculated using the thermal conductivity degradation model agreed well with the measured values within ±150°C. The influence of rim porosity on pellet center temperature is small, and the temperature increase is only 30 °C at 75 GWd/t and 200 W/cm. The pellet center temperature of MOX fuel was also calculated, and it was found that the pellet center temperature of MOX fuel with 10wt% PuO_2 is about 60 °C higher than UO_2 fuel at 75 GWd/t and 200 W/cm.

REFERENCES

[1] OHIRA, K., ITAGAKI, N., “Thermal Conductivity Measurement of High Burnup UO_2 Pellet and a Benchmark Calculation of Fuel Center Temperature”, ANS Topical Meeting on LWR Fuel, Portland, USA, 1997.

[2] IKATSU, N., ITAGAKI, N., OHIRA, K.,BAKKER, K., “Influence of RIM Effect on Fuel Center Temperature”, IAEA TCM on Fuel Chemistry and Pellet-Clad Interaction Related to High Burnup Fuel”, Nyköping, Sweden, 1998.

[3] YAGNIK, S., “Thermal Conductivity Recovery Phenomenon in Irradiated UO_2 and (U, Gd)O_2”, ANS Topical Meeting on LWR Fuel Performance, Park City, USA, 2000.

[4] AMAYA, M. et al, "Thermal Conductivity Measurements on Power-ramped Irradiated UO_2 Pellets", Top Fuel'97, London, 1997.

[5] WIESENACK W., "Experimental Techniques and Results Related to High Burnup Investigations at the OECD HALDEN REACTOR PROJECT," IAEA TCM Pembroke Ontario Canada, 1992, IAEA-TECDOC- 697, p.118, 1993.
[6] HIRAI, M., ISHIMOTO S., “Thermal Diffusivities and Thermal Conductivities of UO_2-Gd_2O_3” J. Nucl. Sci. Technol., 28, 995, 1991.
[7] SONTHEIMER, F., LANDSKRON, H., BILLAUX, M. R., “A Fuel Thermal Conductivity Correlation Based on Latest Experimental Results”, IAEA TCM on Fuel Chemistry and Pellet-Clad Interaction Related to High Burnup Fuel”, Nyköping, Sweden, 1998.
[8] HETZLER, F.J., LANNIN, T.E., PERRY, K.J., ZEBROSKI, E.L., "The Thermal Conductivity of Uranium and Uranium-Plutonium Oxides", GEAP-4879, 1967.
[9] GIBBY, R.L., "The Effect of Plutonium Content on The Thermal Conductivity of (U,Pu)O2 Solid Solution", J. Nucl. Mater. 38, p.163-177, 1971.
[10] 10. GOLDSMITH, L.A., DOUGLAS, J.A.M., "The Thermal Conductivity of Plutonium-Uranium Dioxide at Temperatures up to 1273K", J. Nucl. Mater. 43, p.225-233, 1972.
[11] 11. CROFF, A.G., ORIGEN-2 code, Oak Ridge National Laboratories Report ORNL-TM7175, 1980.
[12] 12. ADAMSON, M.G., AITKEN, E.A., CAPUTI, R.W., "Experimental and Thermodynamic Evaluation of the Melting Behaviour of Irradiated Oxide Fuels", J. Nucl. Mater. 130, p.349-365, 1985.
[13] 13. Matpro-v.11 Rev.2, NUREG/CR-0497, Tree-1280 Rev.2, 1981.
[14] 14. MARTIN, D.G., "The Thermal Expansion of Solid UO2 and (U,Pu) Mixed Oxides - A review and Recommendation", J. Nucl. Mater. 152, p.94-101, 1988.
[15] 15. RUBIN, B.F., "Summary of (U,Pu)O2 Properties and Fabrication Methods", GEAP-13582, 1970.
[16] 16. De NOVIN, C.H., et al., "Mechanical Properties of Uranium-and Plutonium-Based Ceramics", Nucl. Metallurgy, vol.17, p.508-517, 1970.
[17] 17. EVANS, S.K., BOHABOY, P.E., LASKIEWICZ, R.A., "Compressive Creep of Urania-Plutonia Fuels", GEAP-13732, 1971.
[18] 18. BILLAUX, M., LIPPENS, M., BOULANGER, D., NIDIFI, H., "Production of Helium in UO2-PuO_2 Mixed Oxide Fuel", IWFGPT-32, p.182-186, 1989.
[19] KNUDSEN, P., BAGGER, C., MOGENSEN, M, TOFTEGAARD, H., "Fission Gas Release and Fuel Temperature during Power Transients in Water Reactor Fuel at Extended Burnup," IAEA TCM Pembroke Ontario Canada, Apr. 28-May. 1, 1992, IAEA-TECDOC-697, p.25, 1993.

RECENT DEVELOPMENTS OF THE TRANSURANUS CODE WITH EMPHASIS ON HIGH BURNUP PHENOMENA

K. LASSMANN, A. SCHUBERT, J. VAN DE LAAR
Institute for Transuranium Elements
European Commission,
Karlsruhe

C.W.H.M. VENNIX
Statistics Netherlands,
Heerlen, Netherlands

Abstract

TRANSURANUS is a computer program for the thermal and mechanical analysis of fuel rods in nuclear reactors, which is developed at the Institute for Transuranium Elements. The code is in use in several European organisations, both in research and industry. In the paper the recent developments are summarised: the burnup degradation of the fuel's thermal conductivity as well as the effects of gadolinium on the radial power distribution and thermal conductivity. Fission gas release from the High Burnup Structure is discussed. Finally, a new numerical method is outlined that is able to treat the highly non-linear mechanical equations in transients (RIAs and LOCAs).

1. INTRODUCTION

TRANSURANUS is a computer program for the thermal and mechanical analysis of fuel rods in nuclear reactors, which is developed at the European Institute for Transuranium Elements [1]. The code is in use in several European organisations, both in research and industry and is under continuous development. In the following paper recent developments are outlined with emphasis on high burnup models.

2. THERMAL CONDUCTIVITY OF LWR FUEL AT HIGH BURNUP

In view of its relevance an extensive review of the degradation of the thermal conductivity with burnup was performed. In order to compare the various correlations in the literature, a conversion to the simplest form of the phonon term

$$\lambda \quad \frac{1}{a_0 \quad a_1 bu \quad bT} \tag{1}$$

was made, where λ is the thermal conductivity, T is the temperature and a_0, a_1 and b are parameters. Figure 1 shows that there is a very consistent picture of the coefficient a_1 from References [2-9]. In addition, it can be seen that the results from Simfuel measurements [10-12] gave a significantly lower value, due to the fact that radiation effects such as the formation of gas bubbles are not accounted for.

Traditionally, the thermal conductivity is formulated as a term related to a specified density multiplied by a function of the local porosity. Thus the enhanced porosity in the high burnup structure (HBS) needs to be considered, resulting from the formation of a new bubble population. The level of the increase in porosity is still a matter of discussion. No real

progress has been made for several years. Density measurements indicate that the measured porosity in highly irradiated samples may be affected by grain pull out leading to an overprediction of the porosity. Based on the data of one of the authors, Vennix [13], it was possible already in the years 1995-1996 to establish a clear trend by converting the porosity as a function of the radius to porosity as a function of the local burnup. Similar measurements have been made by other authors, for instance by Spino [14, 15]). The original data of Vennix are given in Figure 2. Using the TRANSURANUS burnup model, the local burnup can be calculated for each data point and the data can be correlated with the local burnup. The results are shown in Figure 3. Magnifications between 500× and 1600× were used, which give very consistent results. Above approximately 50000 MWd/tU the porosity increases linearly with the local burnup. We observe the same trend for the pore density which clearly saturates at about 100000 MWd/tU. Figure 3 a) is the basis for the correlation

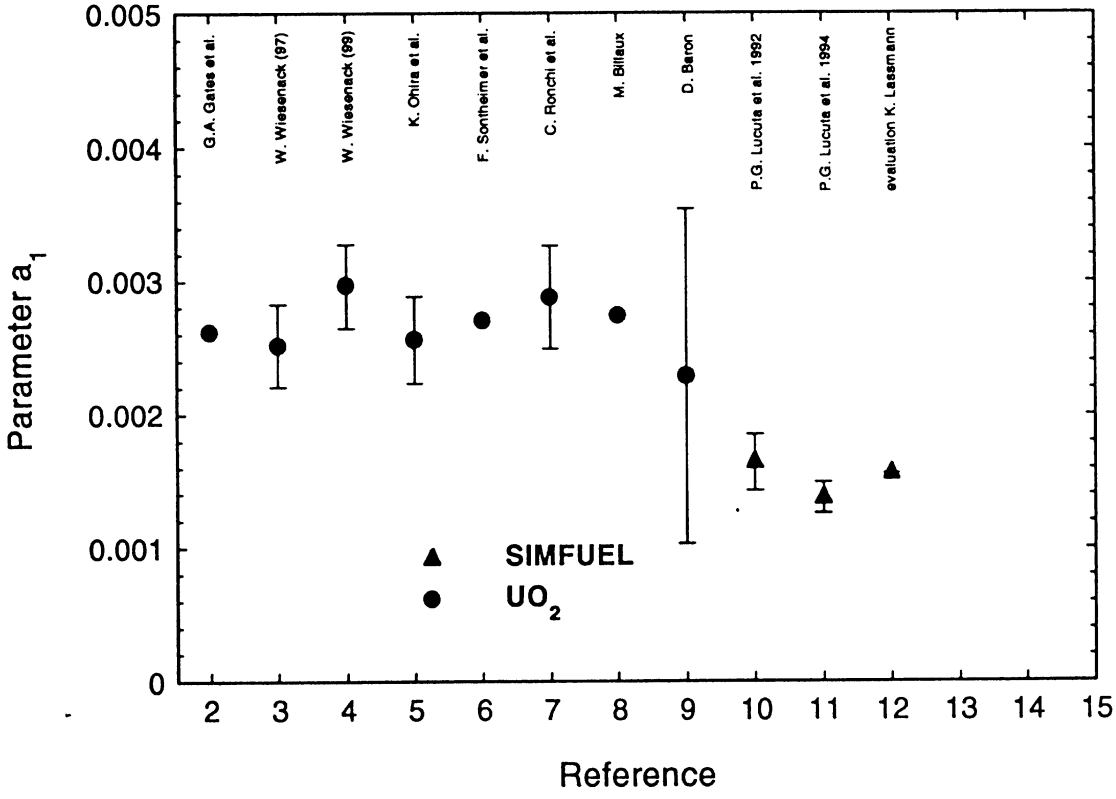

Figure 1. Value of the coefficient a1 , which describes the degradation of the thermal conductivity with burnup, according to various references. Simfuel gives a significantly lower value than irradiated UO_2.

$$\Delta P^{HBS} = 1.25 \cdot 10^{-6} \Delta bu \qquad \text{if } bu > 60000 \frac{MWd}{tU} \tag{2}$$

incorporated in the TRANSURANUS code. ΔP^{HBS} is the increase of the additionally formed porosity in the High Burnup Structure during the burnup increment Δbu. The maximum increase of this type of porosity is limited to 13%. Equation (2) has been included in Figure 3a. Also included are some first estimations derived from density measurements. Although there seems to be a good agreement, further clarification is needed.

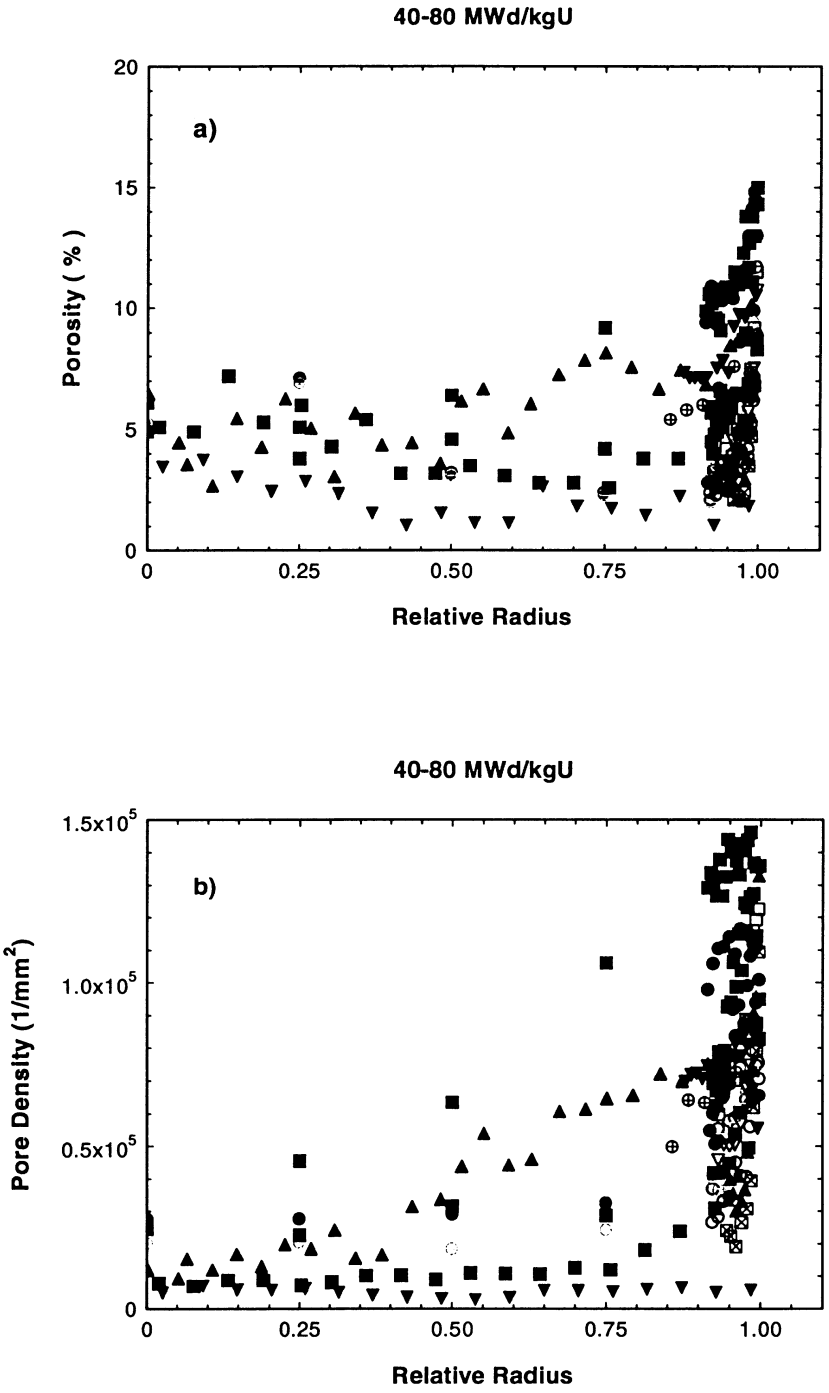

Figure 2 a). Porosity and b) pore density as a function of the radius for highly irradiated fuel according to the data of Vennix [13]. Note that these diagrams are used to investigate trends only (see Figure 3).

The trend of the porosity shown in Figure 3a was questioned by Sontheimer [16] and has not been confirmed by other authors. We consider that the reason lies in the high experimental uncertainties caused by difficulties in specimen preparation resulting in strong variations of measured porosities by different groups (and even individuals). It is interesting to note that a similar trend (although with higher porosities) as in Figure 3a results when the data of Spino are evaluated in the same way.

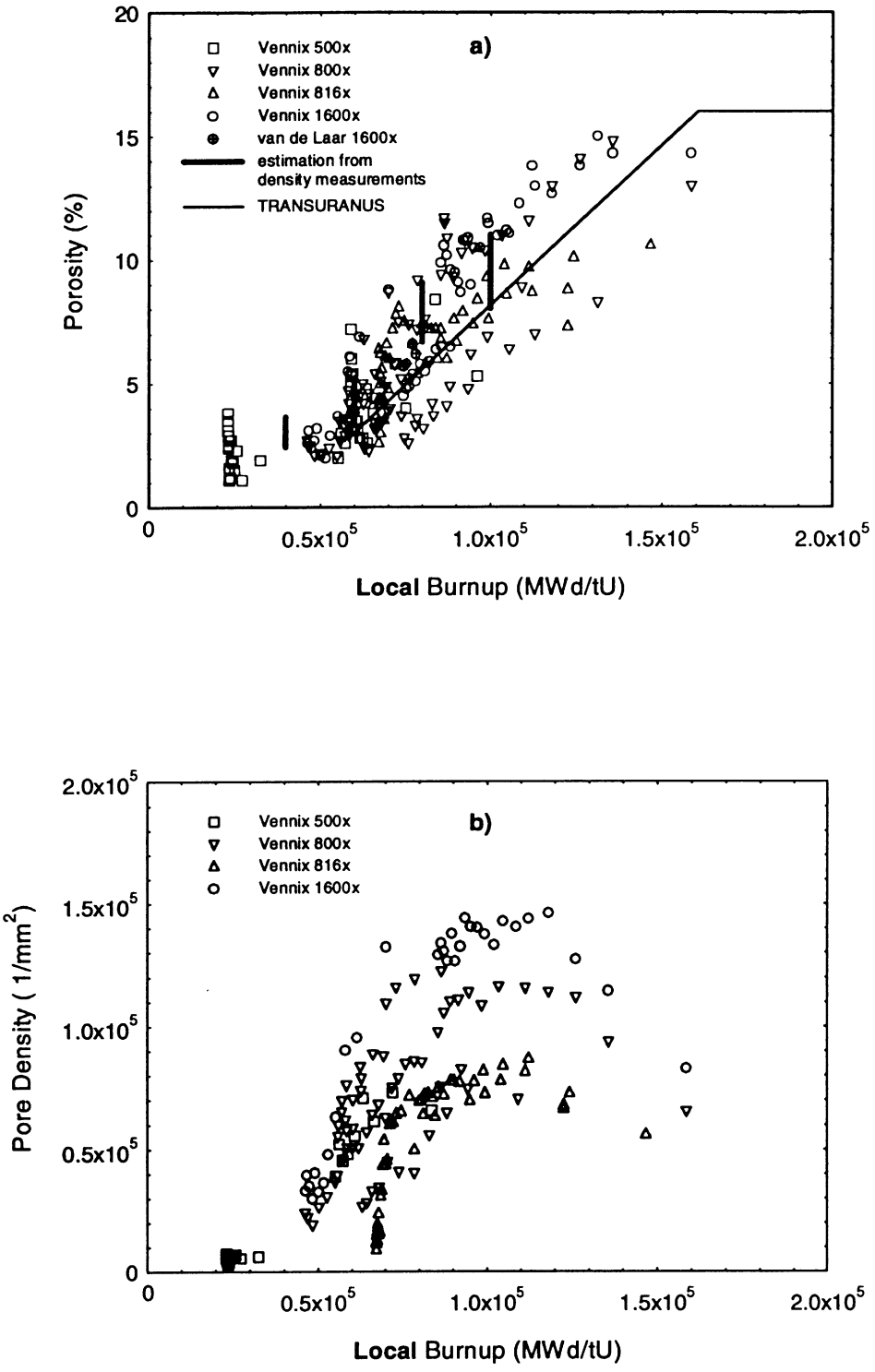

Figure 3. a) Porosity and b) pore density as a function of the local burnup for highly irradiated fuel. The data are the same as in Figure 2. Note that these diagrams are used to investigate trends only.

It is evident that the clarification of the porosity in the high burnup structure is of extreme importance since the expansion of the fuel due to the formation of porosity as well as the decrease of the thermal conductivity influence the thermal and mechanical behaviour. In spite of this importance, in none of the papers on the thermal conductivity of UO_2 at high burnup this question is addressed sufficiently.

Most correlations for the thermal conductivity from the open literature are incorporated into the TRANSURANUS code. An own correlation, developed from ITU measurements of Ronchi and Sheindlin [7], summarises our present-day knowledge. This correlation includes the porosity correlation (2) and the effect of gadolinium. Figure 4 shows the good agreement between this correlation and measured data for a wide range of conditions: UO_2 with $0 \le burnup \le 100000\ MWd/tU$ and Gd_3O_2 contents up to 19 wt% (References 7, 17, 18, 19).

3. TREATMENT OF BURNABLE ABSORBERS

The need to improve reactor performance through longer cycle lengths or improved fuel utilisation has been apparent since the beginning of commercial nuclear power generation. The fuel initial enrichment has been increased, with the consequence that the additional amount of fissile material in the core has had to be compensated for by the introduction of additional absorber material in the core [20]. This additional absorber can be introduced in the form of

- control rods
- soluble absorber (boric acid) in the coolant
- burnable absorbers inside the fuel (integral burnable absorbers).

For all BWRs integral burnable absorbers in the fuel are chosen, for PWRs the use of soluble absorber in the coolant was for many years standard. However, the increase of initial fuel enrichment cannot be indefinitely compensated for by increasing the boric acid concentration and therefore integral burnable absorbers are now considered in PWR designs also.

Two concepts of integral burnable absorbers are treated in the TRANSURANUS code:

- Gadolinia (Gd_2O_3)
- Zirconium diboride (ZrB_2).

These are discussed below.

3.1. Gadolinia (GD_2O_3)

A gadolinium content in the fuel is considered to have several significant effects on fuel performance

- It degrades the thermal conductivity of the fuel.
- It reduces the melting point.
- It produces a distorted, rapidly changing radial power profile.

Natural gadolinium consists of seven isotopes with mass numbers 152, 154, 155, 156, 157, 158 and 160. The natural percent abundances are 0.2, 2.1, 14.8, 20.6, 15.7, 24.8 and 21.8, respectively. This burnable absorber works by neutron capture of the two isotopes, ^{155}Gd and ^{157}Gd, with extremely high absorption cross-sections. The isotopes produced by this reaction, ^{156}Gd and ^{158}Gd have a small absorption cross-section and need not to be further considered.

The methodology to describe the neutron absorption of ^{155}Gd and ^{157}Gd is similar as for the standard TRANSURANUS burnup equations (for details, see Ref. [21], Eq. 3).

The difficulty in this simplified treatment is the definition of the effective absorption cross-section σ_a since the absorption cross-section is extremely high for neutron energies below 1 eV. The consequence is

- a local shift of the neutron spectrum of the thermal flux (hardening) and
- a significant spatial selfshielding of the fuel.

We have tried to fit the effective absorption cross-section in a reasonable way, i.e., the local change of the neutron spectrum is approximately taken into account. The selfshielding is treated by solving the diffusion equation

$$\nabla^2 f - \kappa^2(r) f = 0 \tag{3}$$

numerically. κ is the inverse diffusion length which depends on the radius.

This gadolinium model was fitted to the average concentrations of ^{155}Gd and ^{157}Gd of Fuji et al. [22]. Figure 5 shows a reasonable agreement with the data.

Having fitted the two parameter of the TRANSURANUS Gd burnup model, the model can be applied to predict the radial ^{155}Gd and ^{157}Gd profiles at different burnups. Reference [22] reports such data, which are compared to the model predictions in Figure 6 and Figure 7. As can be seen, the results are acceptable.

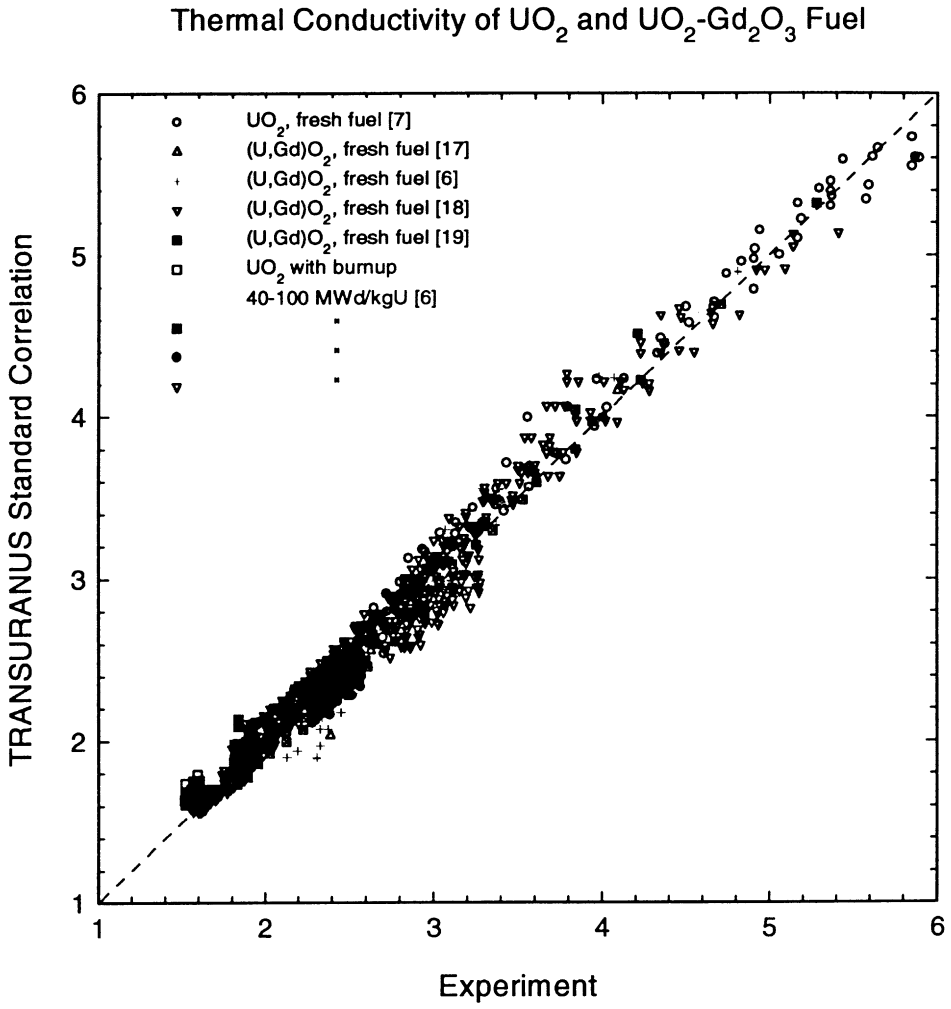

Figure 4. Comparison between measured and evaluated thermal conductivities.

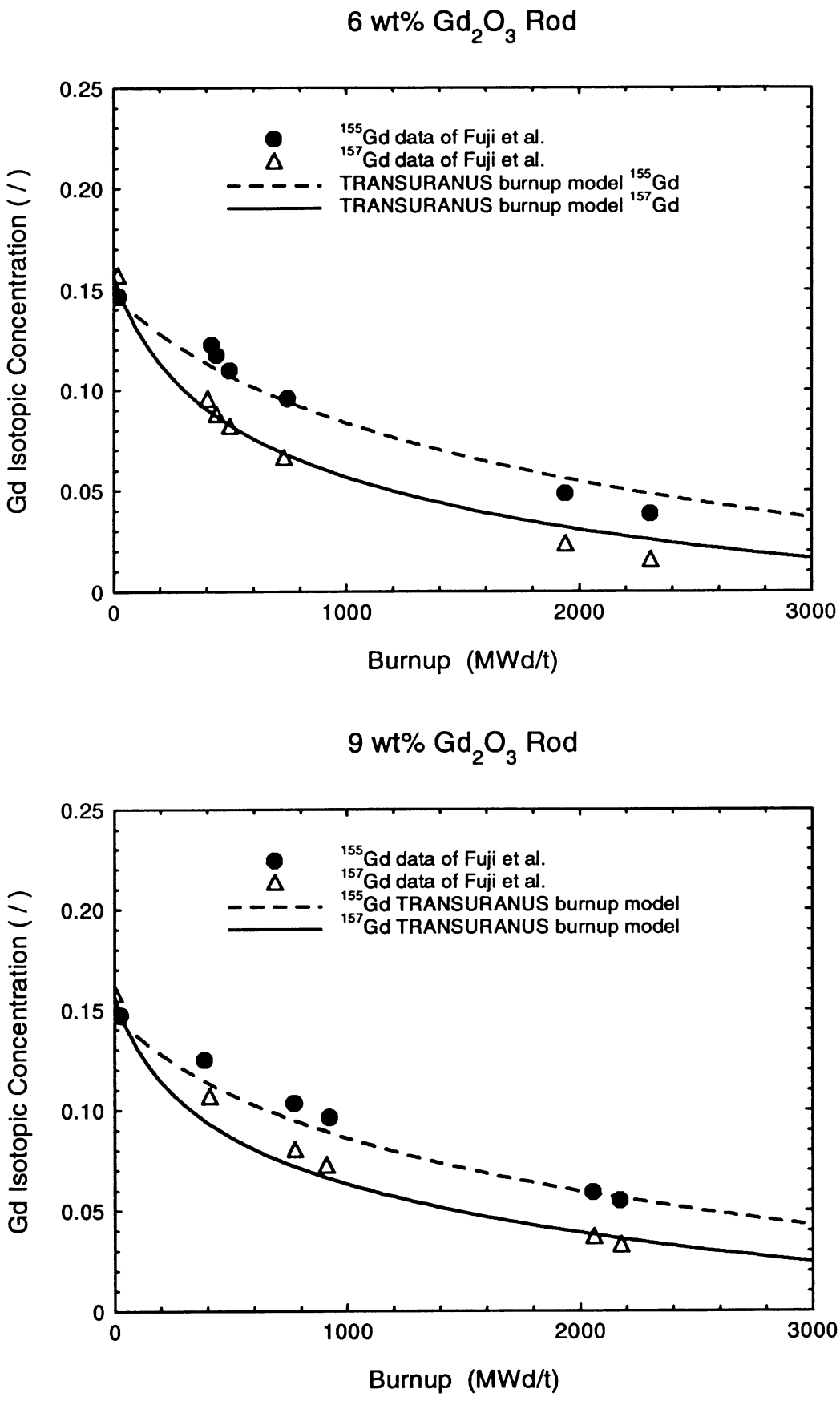

Figure 5. Average isotopic concentration of ^{155}Gd and ^{157}Gd in UO_2 fuels with 6 and 9 wt% Gd_2O_3 as a function of burnup. Comparison between the data of Fuji et al. [22] and the TRANSURANUS burnup model.

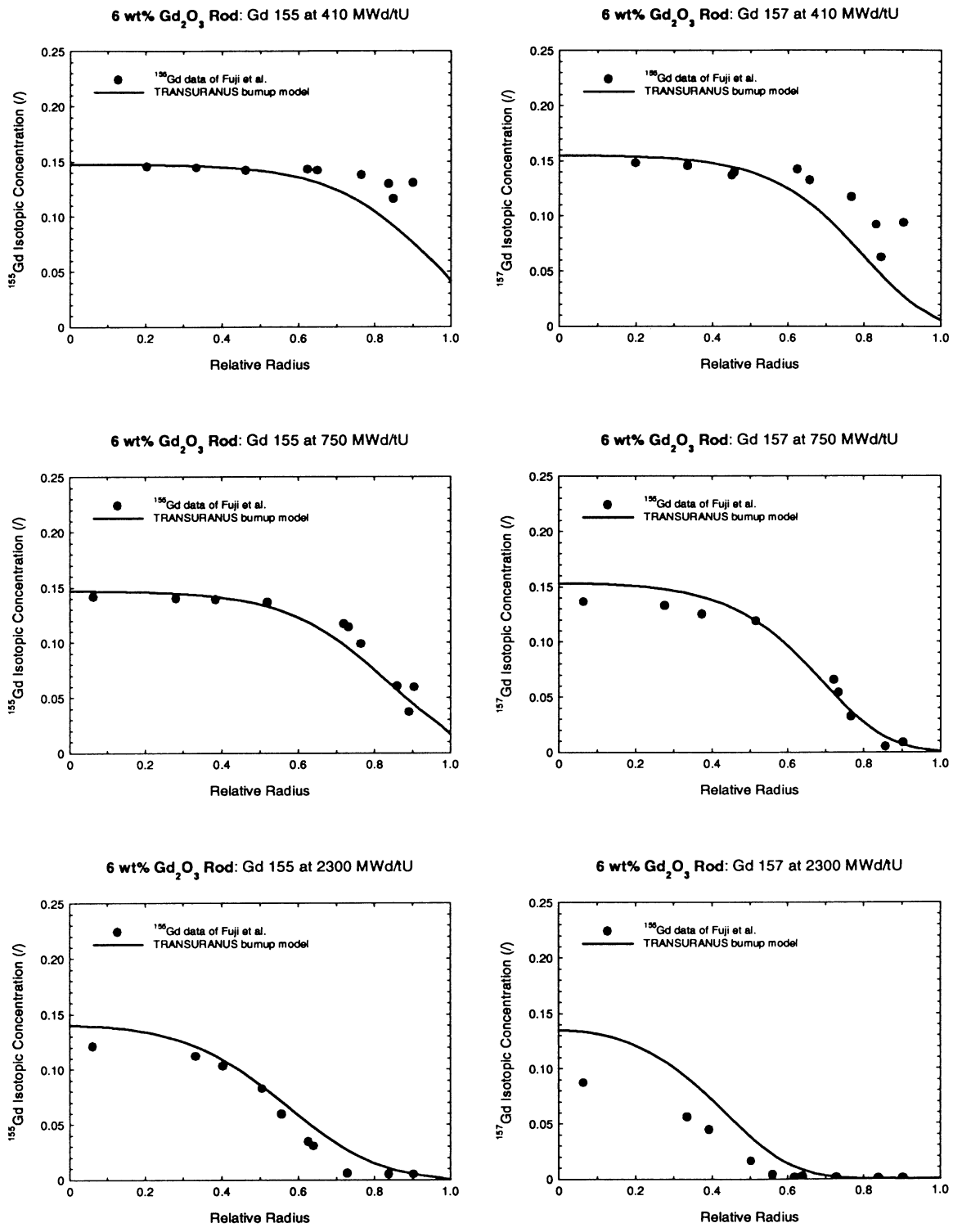

Figure 6. Radial distribution of ^{155}Gd and ^{157}Gd for different burnups; comparison between the data of Fuji et al. [22] and the TRANSURANUS burnup model. The initial concentration was 6 wt% of natural Gd.

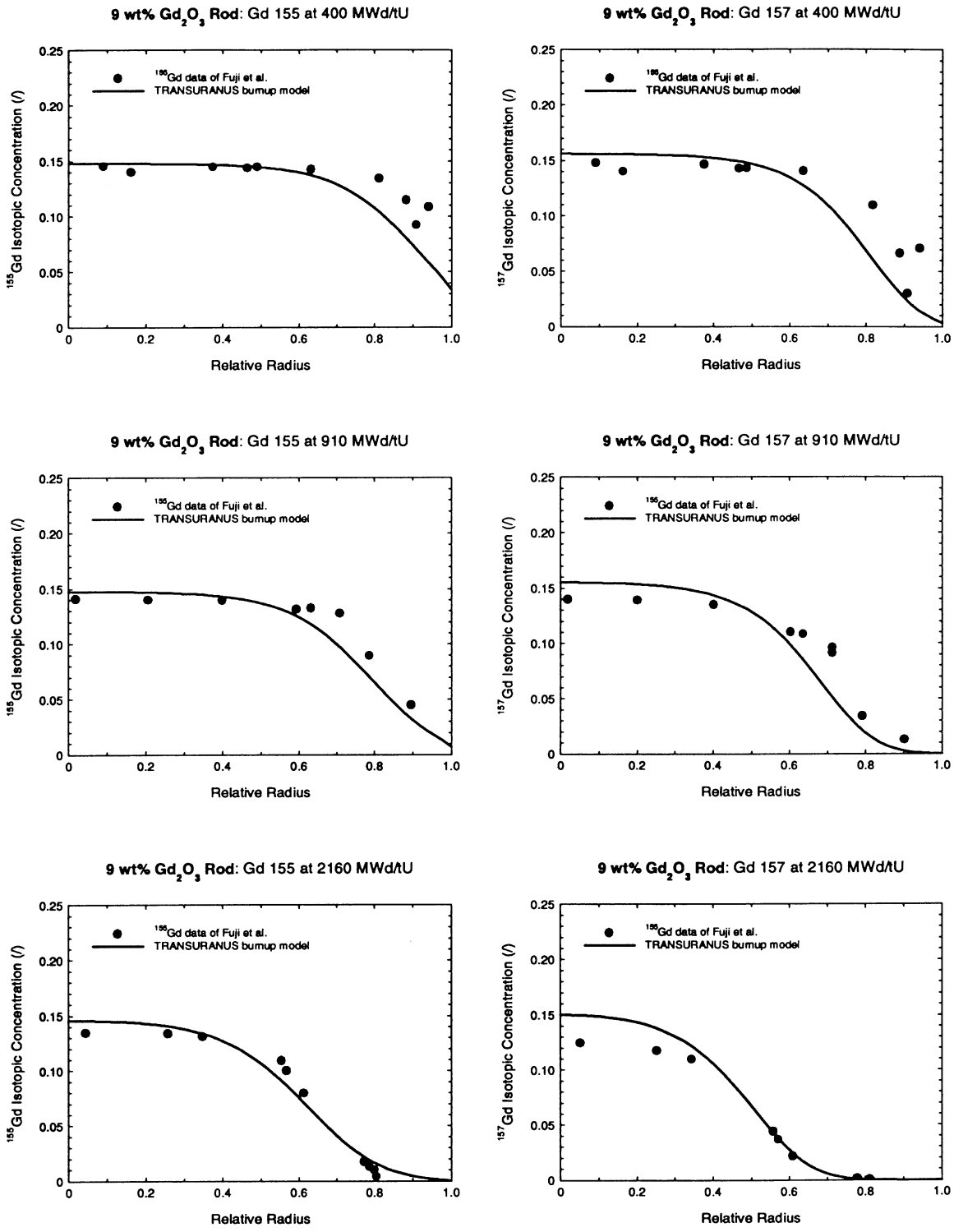

Figure 7: Radial distribution of ^{155}Gd and ^{157}Gd for different burnups; comparison between the data of Fuji et al. [22] and the TRANSURANUS burnup model. The initial concentration was 9 wt% of natural Gd.

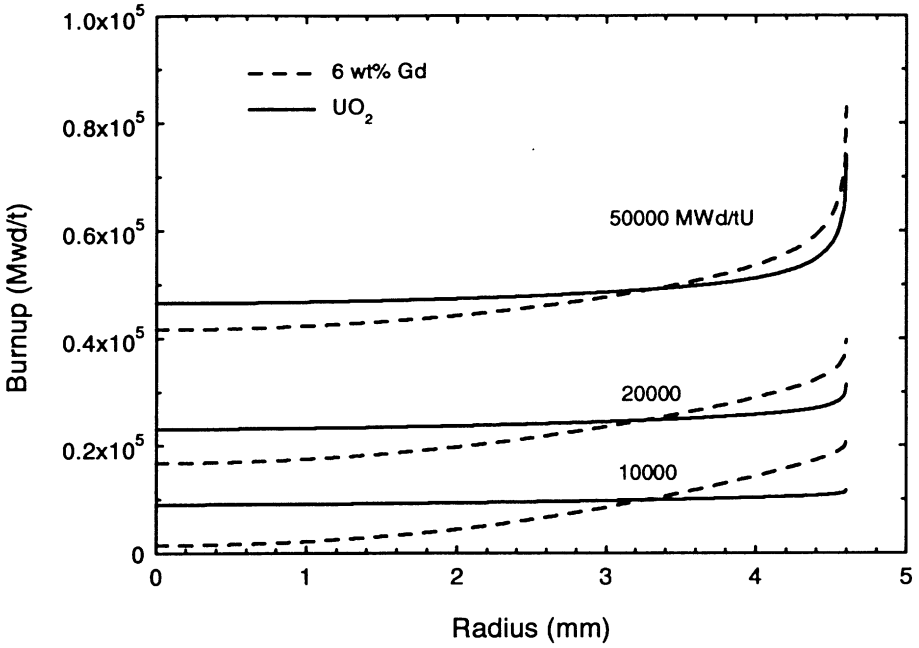

Figure 8. Comparison between the radial burnup profiles of a UO_2 and a $(U,Gd)O_2$ fuel (typical LWR fuel irradiated in the Halden reactor).

Differences between radial burnup profiles of standard UO_2 and Gd fuel are shown by way of example in Figure 8. As expected, the differences are pronounced at low burnup but even at a burnup of 50000 MWd/tU still visible.

3.2. Zirconium diboride (ZrB_2)

Developed by Westinghouse under the name IFBA (Integral Fuel Burnable Absorber), this fuel consists of a thin layer ZrB_2 ($\approx$ 5 μm) deposited by sputtering on the surface of the UO_2 pellets. The resulting ^{10}B loading is 1.7 mg ^{10}B per cm and the layer adheres perfectly to the UO_2 substrate [20, page 12]. This burnable absorber in the form of a thin layer works through the (n, α) reaction, e.g. He is produced. As a result there is a need to reduce the pre-pressurization level of the fuel rod.

The methodology to describe the neutron absorption of ^{10}B is the same as in the case of Gadolinia.

4. FISSION GAS RELEASE

It is commonly observed that fuel operated at "normal" rating shows very little fission gas release even up to high levels of burnup. Above 40 000 MWd/tU an enhancement takes place that could limit the lifetime of a fuel rod. In the following we take as an example Russian irradiation data of the KOLA-3 plant from the IFPE Database [23]. The data suggest that fission gas release below 40 000 MWd/tU is around 0.5% and rises linearly from 0.5% at 40000 MWd/tU to 1-2% at 50000 MWd/tU and $\approx$ 3% at 55000 MWd/tU.

Most theoretical fission gas release models are based on the assumptions that fission gas atoms diffuse inside the grain or precipitate into intra- and intergranular bubbles. Finally, they may reach the free pin volume basically by interlinkage of intergranular bubbles and subsequent venting of the grain boundary inventory. As a consequence, fission gas is released after an incubation time depending on the temperature. This is the physical understanding

behind the so-called Vitanza threshold, which states that as long as the temperature remains below this threshold temperature, fission gas release does not occur or is insignificant.

The general problem is that these mechanisms do not always explain the enhancement of fission gas release above 40 000 MWd/tU. In most irradiations the rating and hence the temperature decrease with burnup. Diffusion processes may be insufficient to account for the enhancement of fission gas release and therefore the question is:

"Where does the enhanced fission gas release that is observed at extended burnup in all reactor irradiations come from"?

- From the inner hot regions by thermal processes or
- By an athermal process from the outer cold region that exhibits the high burnup structure?

The KOLA-3 data offers a unique opportunity to investigate this question further because

- The rating (and therefore the fuel temperature) is rather low and decreases with burnup.
- The use of annular UO_2 pellets further decreases the maximum fuel temperature compared with solid pellets.

The analyses confirmed that the maximum temperatures stay well below 1000°C. As expected, for all KOLA-3 rods analysed a small fission gas release of 0.3-0.4% at EOL is predicted [24]. The standard TRANSURANUS models cannot predict the enhancement of fission gas release above 40 000 MWd/tU for the KOLA-3 rods. In order to understand why this is the case, the calculated temperatures in different fuel sections have been compared with the Vitanza threshold. As can be seen in Figure 9 throughout the irradiation, the fuel temperatures remained well below the Vitanza threshold. This means, that either the calculated temperatures are too low, or the diffusion coefficient is too low, or a yet unknown fission gas release mechanism exists.

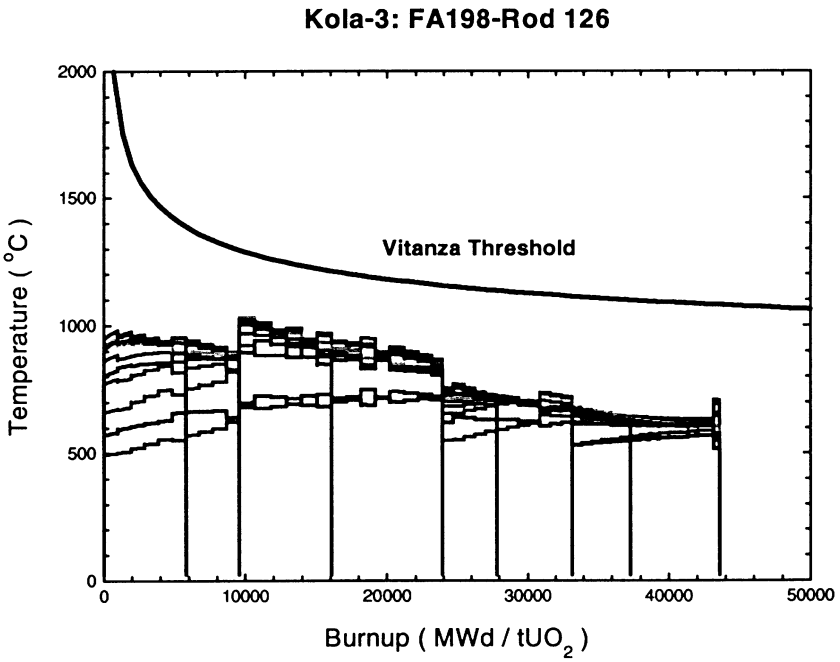

Figure 9. Comparison between the maximum fuel temperatures in different sections of rod 126 (fuel assembly 198) as calculated by the TRANSURANUS code with the Vitanza threshold. Note that the burnup is given in MWd/tUO₂.

This problem is not new and has also been found in Western fuel rods. We have analysed 2 hypotheses:

- During the formation of the High Burnup Structure, where a Xe-depletion of the matrix is observed, only part of the fission gas is released to pores inside the fuel, whereas the rest is released to the free volume. Glatz and Sätmark [25] have tried to answer this question by dissolving pellets of different shape in a sealed capsule. Fuel rod sections were cut from a UO_2 fuel rod irradiated in a power reactor to a burnup of 80000 MWd/tU. The fuel rod sections analysed were of different geometry: (a) a solid fuel pellet and b) two hollow sections with radii of $0.54 \le r/r_o \le 1$ and $0.91 \le r/r_o \le 1$, respectively. The conclusion is that in regions exhibiting the High Burnup Structure some of the fission gas is released. Since such experiments are extremely difficult, it is planned to repeat them with a slightly modified capsule to confirm the finding. A similar conclusion, however, is drawn by Walker from XRF analyses [26].
- From the many ITU EPMA data on high burnup fuels (for instance [27]) a constant Xe concentration of 0.2 to 0.3 wt% was found in the High Burnup Structure. This suggests that equilibrium exists between the created and the released Xe atoms given by

$$\bar{c}_1 \quad \frac{b}{15\,\frac{D_{Xe}}{a^2}} \approx 0.2 - 0.3 \quad wt\% \tag{4}$$

where b is the creation rate, D_{Xe} the effective (apparent) diffusion coefficient and a is the grain radius [28]. Equation (4) allows to estimate D_{Xe} in the High Burnup Structure to be of the order of $10^{-22}\ m^2/s$, which is an estimation for the athermal diffusion coefficient. Thus the second hypothesis for the enhanced fission gas release at high burnup is a simple irradiation enhanced (athermal) diffusion process. In order to investigate this effect, we have varied D_{Xe}.

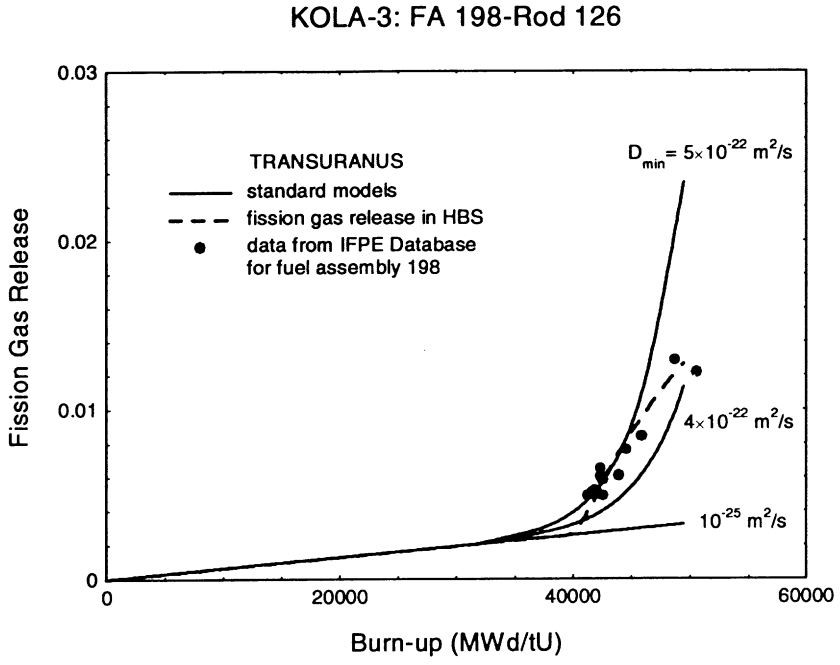

Figure 10. Fission gas release as a function of the rod average burnup for rod 126 of fuel assembly 198 (KOLA-3 irradiation) as calculated by the TRANSURANUS code by a) standard models with varying D_{Xe} and b) the assumption of a fission gas release from the High Burnup Structure.

Figure *10* shows that both hypotheses are in principle able to predict the measured fission gas release data in the KOLA-3 rods. The second hypothesis is also able to predict the Xe degradation in the High Burnup Stucture after grain subdivision (Figure 11). However, it is interesting to cross-check both hypotheses with measurements of the Xe to Kr ratio in the plenum. This ratio allows the origin of the fission gas released to be determined. Based on the assumption that the diffusion of Xe and Kr are identical, a relatively low ratio would indicate a release from the inner parts (more fissions of U than Pu) whereas a high ratio would indicate a release from the outer parts (more fissions of Pu than U). Unfortunately, no Xe to Kr data are available for the KOLA-3 data and we have compared the calculations with measurements performed by Toscano [31] at ITU on Western fuels. These experimental results indicate a rather low Xe to Kr ratio even at very high burnup which would indicate that the released fission gas does not originate from the outer parts. Figure 12 compares the data with the TRANSURANUS hypothesis that most of the released fission gas originates from the (outer) High Burnup Structure. For this mechanism the formation of a High Burnup Structure is essential, but once it has formed, the Xe to Kr ratio would increase significantly, clearly in contrast to the measured Xe to Kr ratios.

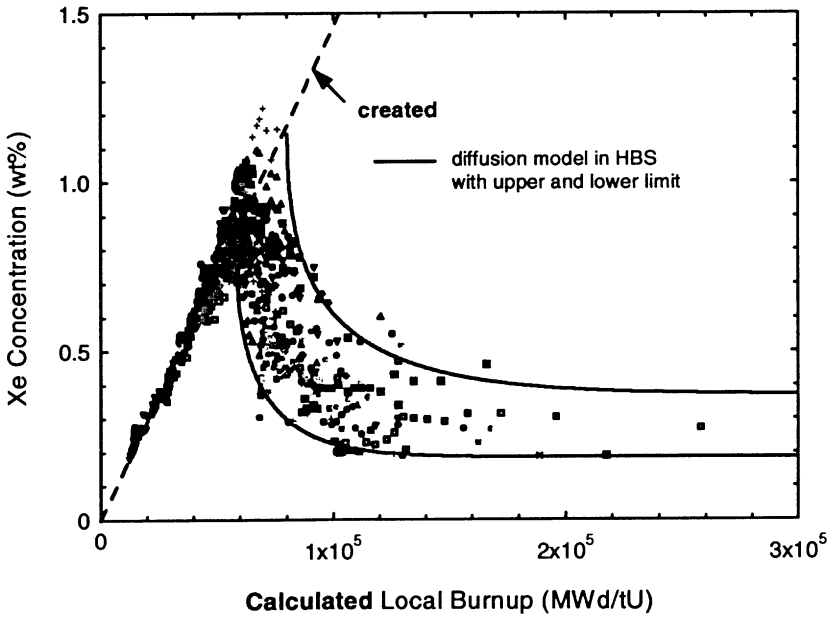

Figure 11. Comparison between measured EPMA data of C.T. Walker [29, 30] and predicted Xe concentraion in UO_2 fuel. The predictions are based on a diffusion process in the High Burnup Structure after grain subdivision.

Alternatively, the TRANSURANUS standard models are in good agreement with the measurements which would indicate that fission gas release originates more or less from the whole fuel (Figure 13).

The conclusion is evident: The standard TRANSURANUS fission gas release model can only explain the enhanced fission gas release above 40000 MWd/tU with a minimum (athermal) diffusion coefficient of the order of $10^{-11}\ m^2/s$. The assumption that most of the fission gas release stems from the High Burnup Structure must be questioned. Further research is needed to better understand the enhanced fission gas release at high burnup. This statement is valid for fuel rods of Western design as well as for WWER fuel rods.

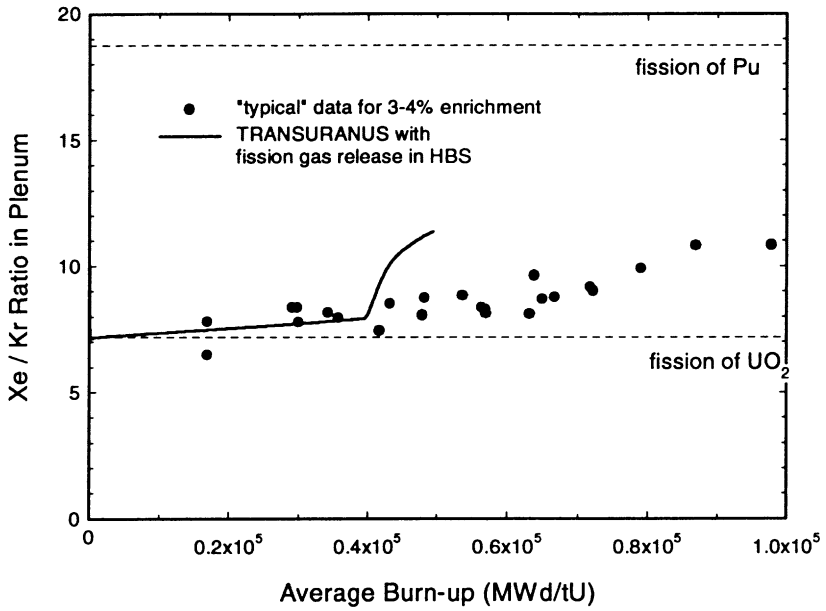

Figure 12. Xe/Kr ratio as a function of the rod average burnup for rod 126 of fuel assembly 198 (KOLA-3 irradiation) as calculated by the TRANSURANUS code on the assumption of a fission gas release from the High Burnup Structure. The data of Toscano [31] are included for the purpose of comparison.

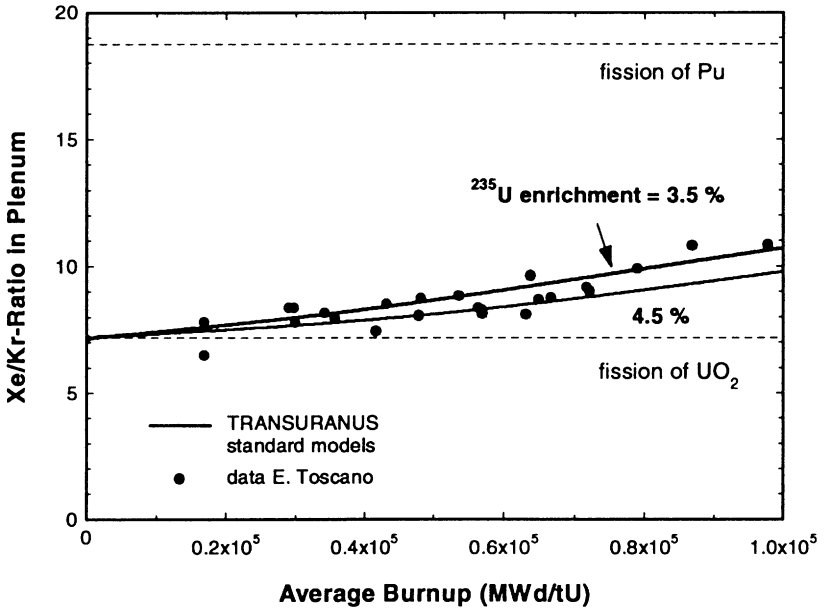

Figure 13. Xe/Kr ratio as a function of the rod average burnup for a "typical" rod as calculated by the TRANSURANUS code employing standard models. The predicted trends are in good agreement with the data of Toscano [31].

5. CONCLUSIONS

Two conclusions are drawn:

- The porosity in the High Burnup Structure needs clarification since the expansion of the fuel due to the formation of porosity as well as the decrease of the thermal conductivity are relevant for the thermal and mechanical behaviour.
- It seems that the standard TRANSURANUS fission gas release model can explain the enhanced fission gas release above 40 000 MWd/tU if a minimum (athermal) diffusion coefficient of the order of 10^{-22} m^2/s is applied. The assumption that most of the fission gas release stems from the High Burnup Structure must be questioned. Further research is needed to better understand the enhanced fission gas release at high burnup.

ACKNOWLEDGEMENTS

The authors would like to thank J. Spino, E.H. Toscano and C.T. Walker for many valuable contributions to the development of the TRANSURANUS high burnup models.

Appendix

FURTHER TRANSURANUS DEVELOPMENTS

MONTE CARLO STATISTIC

The Monte Carlo statistics was extended to include several different probability density functions and several further stochastic variables. In addition to the normal (Gaussian) distribution it is now possible to apply log-normal, uniform (rectangle) as well as Cauchy distributions. Each individual distribution can be cutoff, i.e. a minimum and a maximum value can be considered. The new program "DISTRIB" in which the different distributions are programmed can easily be extended to include more types of distributions in the future.

INCORPORATION OF BROYDEN'S METHOD

General methods for the solution of the highly non-linear equations for creep and plasticity in fuel and cladding have been analysed [32]. The standard Newton's multidimensional method solves the set of equations

$$\begin{vmatrix} F_1(x_1, x_2, \ldots, x_n) \\ F_2(x_1, x_2, \ldots, x_n) \\ \ldots \\ \ldots \\ F_n(x_1, x_2, \ldots, x_n) \end{vmatrix} \quad \mathbf{F}(\mathbf{x}) \quad \mathbf{0}$$

by an iteration process

$$\mathbf{x}_{new} \quad \mathbf{x}_{old} \quad d\mathbf{x}$$

where

$$\mathbf{J}\, d\mathbf{x} \quad \mathbf{F}$$

Here $\mathbf{J}$ is the Jacobian matrix.

Unfortunately, it is impossible to derive the Jacobian matrix for the mechanical equations used in the TRANSURANUS code [33] either analytically or approximately. Therefore, our research concentrated on the Broyden's method which is a multidimensional secant method. The Jacobian matrix $\mathbf{J}$ is approximated by the Broyden's matrix $\mathbf{B}$:

$$\mathbf{B}\, d\mathbf{x} \quad \mathbf{F}$$

The interesting feature of Broyden's method is that the Broyden's matrix is updated during the iteration process:

$$\mathbf{B}_{i+1} \quad \mathbf{B}_i \quad \frac{(d\mathbf{F}_i \quad \mathbf{B}_i \quad d\mathbf{x}_i) \otimes d\mathbf{x}_i}{d\mathbf{x}_i \quad d\mathbf{x}_i}$$

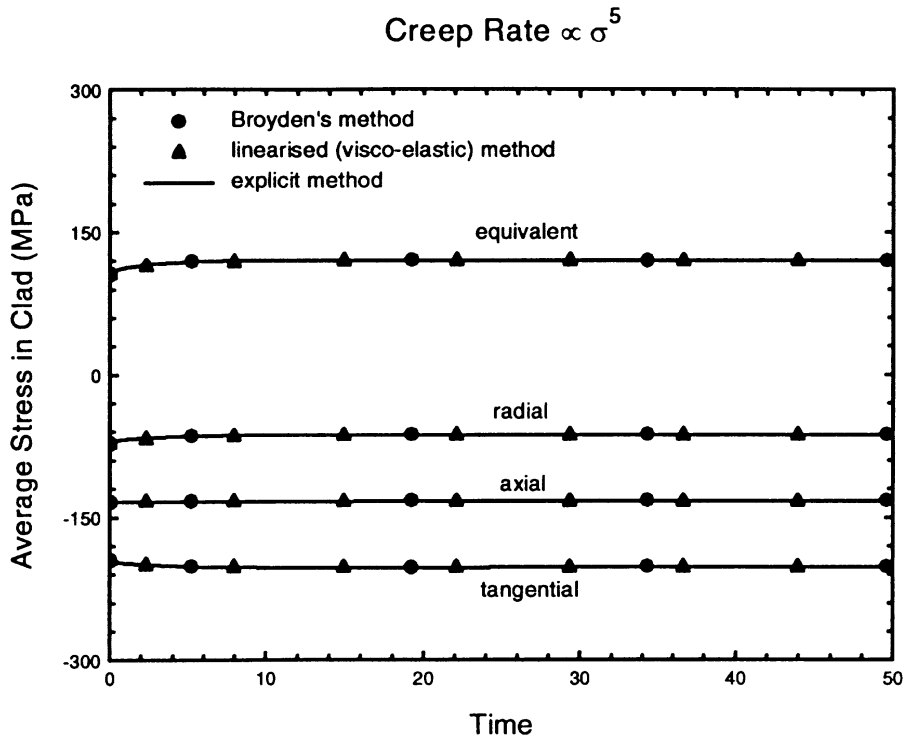

*Figure 14. Average stresses in a cladding under outer pressure as a function of time for a highly non-linear creep law (**creep rate** ‖ s^5_{eff}). Shown is the comparison between different methods.*

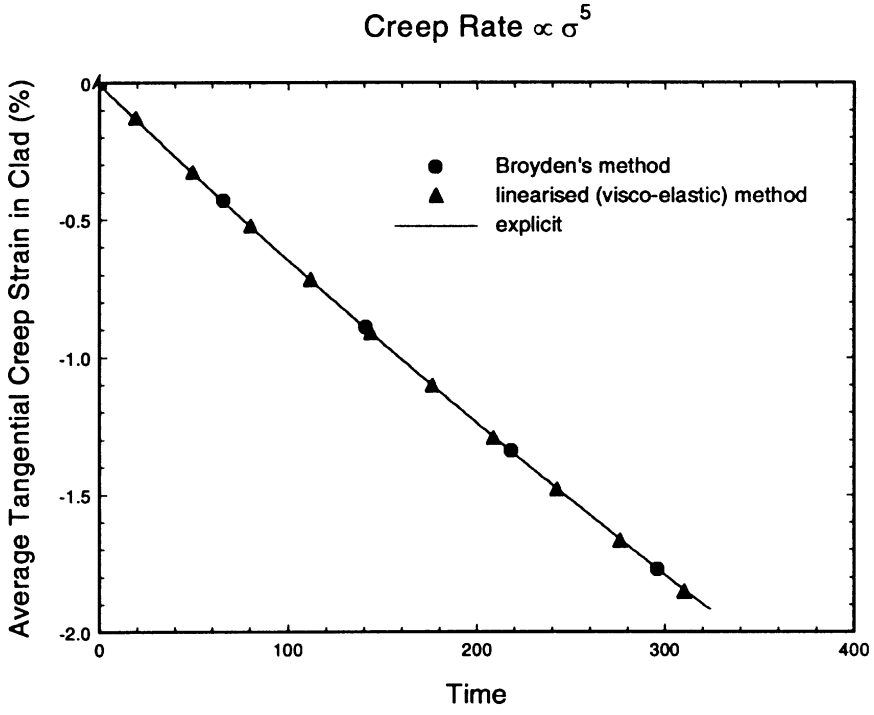

*Figure 15. Average tangential creep strain in a cladding under outer pressure as a function of time for a highly non-linear creep law (**creep rate** ‖ s^5_{eff}). Shown is the comparison between different methods.*

where $d\mathbf{F}_i = \mathbf{F}_{i+1} - \mathbf{F}_i$, $d\mathbf{x} = \mathbf{x}_{i+1} - \mathbf{x}_i$ and the symbols "$\cdot$" and "$\times$" denote the scalar and vector product, respectively. Various variants of Broyden's method have been studied and the most promising has been incorporated into the TRANSURANUS code. First tests confirmed excellent agreement with the existing explicit and linearised (visco-elastic) treatments. Two examples are given in Figure 14 and Figure 15. Note that in Figure 14 the average stresses need to be approximately constant due to the equilibrium condition. This is not the case for local stresses not shown here. Further tests will be necessary to study time step control (convergence) and efficiency.

REFERENCES

[1] K. LASSMANN, TRANSURANUS: a fuel rod analysis code ready for use, J. Nucl. Mater., 188 (1992) 295

[2] G.A. GATES, P.M.A. COOK, P. DE KLERK, P. MORRIS, I.D. PALMER, Thermal performance modelling with the ENIGMA code, Thermal Performance of High Burn-up LWR Fuel, Seminar Proceedings, Cadarache, 3-6 March 1998, France, Nuclear Science, OECD/AEN-NEA 1998, p. 301-310

[3] W. WIESENACK, Assessment of UO_2 Conductivity Degradation Based on In-pile Temperature Data, Proceedings of the 1997 International Topical Meeting on LWR Fuel Performance, Portland, Oregon, March 2-6 (1997), p. 507

[4] W. WIESENACK, personal communication (Nov. 1999)

[5] K. OHIRA and N. ITAGAKI, Thermal conductivity measurements of high burnup UO_2 pellet and benchmark calculation of fuel center temperature, Proceedings of the 1997 International Topical Meeting on LWR Fuel Performance, Portland, Oregon, March 2-6 (1997), p. 541

[6] F. SONTHEIMER, H. LANDSKRON, M.R. BILLAUX, A fuel thermal conductivity correlation based on the latest experimental results, Thermal Performance of High Burn-up LWR Fuel, Seminar Proceedings, Cadarache, 3-6 March 1998, France, Nuclear Science, OECD/AEN-NEA 1998, p. 119-127

[7] C. RONCHI AND M. SHEINDLIN, personal communication (1999)

[8] M.R. BILLAUX, S.-H. SHANN, L.V. VAN SWAM, F. SONTHEIMER, Proceedings of the 1997 International Topical Meeting on LWR Fuel Performance, Portland, Oregon, March 2-6 (1997), p. 576-585

[9] D. BARON, Fuel thermal conductivity: A review of the modelling available for UO_2, $(U\text{-}Gd)O_2$ and MOX fuel, Thermal Performance of High Burn-up LWR Fuel, Seminar Proceedings, Cadarache, 3-6 March 1998, France, Nuclear Science, OECD/AEN-NEA 1998, p. 99-118, evaluation of the Lokken and Courtright model on page 104

[10] P.G. LUCUTA, HJ. MATZKE, R.A. VERALL, H.A. TASMAN, Thermal conductivity of SIMFUEL, J. Nucl. Mater. 188 (1992) 198

[11] P.G. LUCUTA, HJ. MATZKE, R.A. Verall., Modelling of UO_2-based SIMFUEL thermal conductivity: the effect of burnup, J. Nucl. Mater. 217 (1994) 297

[12] K. LASSMANN, own evaluation of the data of Lucuta et al., Refs. [10,11] (Feb. 1996)

[13] C.W.H.M. VENNIX, work performed during 1995 and 1996 at ITU, several internal notes 1995-1996

[14] J. SPINO, K. VENNIX, M. Coquerelle, J. Nucl. Mater. 231 (1996) 179

[15] J. SPINO, D. BARON, M. Coquerelle, A.D. Stalios, J. Nucl. Mater. 256 (1998) 189

[16] F. SONTHEIMER, personal communication (1997)

[17] NFIR Part 2 data quoted by D. Baron in Ref [9]

[18] S. FUKUSHIMA, T. OHMICHI, A. MAEDA, H. WATANABE, J. Nucl. Mater. 105 (1982) 201

[19] Data of L.W. Newman et al., quoted by A. R. Massih, S. Persson, Z. Weiss, J. Nucl. Mater. 188 (1992) 323
[20] Characteristics and use of urania-gadolinia fuels, IAEA-TECDOC-844 (1995), ISSN 1011-4289
[21] K. LASSMANN, C. O'CARROLL, J. VAN DE LAAR and C.T. WALKER, The radial distribution of Plutonium in high burn-up UO_2, J. Nucl. Mater. 208 (1994) 223.
[22] A. FUJI, A. TOBA, T. IWAI, S. IZUTSU, K. KATO, T. ISHIDA, H. NOZAKI, T. SEINO, T. TANZAWA, K. SAKURADA, Bench mark experiments on poisoned fuel rods with high concentration gadolinia in BWR-type assembly, Topical meeting on advances in fuel management, American Nuclear Society, March 2-5 (1986) Pinehurst, North Carolina
[23] P.M. CHANTOIN, E. SARTORI, J.A. TURNBULL, The Compilation of a Public Domain Database on Nuclear Fuel Performance for the Purpose of Code Development and Validation, Thermal Performance of High Burn-up LWR Fuel, Seminar Proceedings, Cadarache, 3-6 March 1998, France, Nuclear Science, OECD/AEN-NEA 1998: KOLA-3 Corrected Data Set, March 1999
[24] M. MANOLOVA, D. ELENKOV, M. GEORGIEVA, S. BONEVA, V. SIMEONOVA, N. DJOURELOV, S. GEORGIEV, K. LASSMANN, J. VAN DE LAAR, Validation of the TRANSURANUS code-WWER version by the updated KOLA-3 data set, Proceedings of the Third International Seminar "WWER Fuel Performance, Modelling and Experimental Support", 4-8 October 1999, Pamporovo, Bulgaria, ISBN 954-9820-03-3
[25] J.P. GLATZ and B. SÄTMARK, Institute for Transuranium Elements, Annual Report 1996 (EUR 17296), p. 91
[26] M. MOGENSEN, J.H. PEARCE, C.T. WALKER, Behaviour of fission gas in the rim region of high burnup UO_2 pellets with particular reference to results from an XRF investigation, J. Nucl. Mater. 264 (1999) 99
[27] C.T. WALKER, Assessment of the radial extent and completion of recrystallisation in high burnup UO_2 nuclear fuel by EPMA, J. Nucl. Mater. 275 (1999) 56
[28] S. BRÉMIER and C.T. WALKER, Irradiation Enhanced Diffusion Controls Fission gas Release from Recrystallised UO_2 Grains in High Burnup Water Reactor Fuel, submitted paper (2000)
[29] K. LASSMANN, C.T. WALKER, J. VAN DE LAAR, F. LINDSTRÖM, Modelling the high burnup UO_2 structure in LWR fuel, J. Nucl. Mater. 226 (1995) 1
[30] R. MANZEL, C.T. WALKER, High burnup fuel microstructure and its effect on fuel rod performance, International Topical Meeting on Light Water Reactor Fuel Performance, Park City, Utah (USA), 10-13 April 2000
[31] E. TOSCANO, ITU Annual Report 1997 (EUR 17746), p. 70, Fig. 2.7
[32] W.H. PRESS, S.A. TEUKOLSKY, W.T. VETTERLING, B.P. FLANNERY, Numerical Recipes in FORTRAN, The Art of Scientific Computing, Second Edition, Cambridge University Press (1992)
[33] K. LASSMANN, URANUS- A Computer Programme for the Thermal and Mechanical Analysis of the Fuel Rods in a Nuclear Reactor, Nucl. Eng. Design, Vol. 45, No.2 (Feb. 1978) 325.
[32] W.H. Press, S.A. Teukolsky, W.T. Vetterling, B.P. Flannery, Numerical Recipes in FORTRAN, The Art of Scientific Computing, Second Edition, Cambridge University Press (1992)
[33] K. Lassmann, URANUS- A Computer Programme for the Thermal and Mechanical Analysis of the Fuel Rods in a Nuclear Reactor, Nucl. Eng. Design, Vol. 45, No.2 (Feb. 1978) 325

MODELLING OF ZIRCALOY-4 CLADDING BEHAVIOUR AT HIGH BURNUP

JE-GEON BANG, CHAN BOCK LEE, DAE HO KIM, YOUN HO JUNG
Korea Atomic Energy Research Institute,
Taejon, Republic of Korea

Abstract

Models of Zircaloy-4 cladding behavior at high burnup in the area such as creep-out and corrosion were developed. At high burnup, fuel rod internal pressure may exceed the external coolant pressure by fission gas release, which might result in cladding lift-off. Therefore, it is necessary to estimate the cladding creep-out rate precisely. Comparison of the cladding creep-out prediction of the fuel performance analysis codes which were based upon the cladding creep-down data with the Halden test data showed that the codes under-estimate the cladding creep-out rate. Therefore, based upon the existing creep model, new cladding creep-out model was developed by changing the dependence of the creep rate upon the fast neutron flux and stress, which then predicted the test results reasonably well. Corrosion model was developed by analyzing the corrosion mechanisms and other corrosion models. The parameters influencing the fuel cladding corrosion are the material and manufacturing characteristics of the cladding, coolant chemistry, hydride formation in the cladding and fast neutron flux. The model was derived by considering the effect of those parameters on the Zircaloy corrosion. The derived model was validated by both the sensitivity analyses of the parameters and prediction capability of such phenomena as the axial distribution of corrosion, effect of water chemistry and acceleration of corrosion at high burnup.

1. INTRODUCTION

Development of PWR fuel has been focused upon increase of the burnup to improve the economy. Introduction of high burnup fuel has resulted in the new phenomena at high burnup which were not considered enough at lower burnup. In the cladding behavior at high burnup, cladding creep-out, corrosion, irradiation growth and reduction of cladding ductility are among them.

At high burnup, rod internal pressure may exceed system coolant pressure due to fission gas release, so that clad creep-out can occur. The study on the creep-out behavior has been performed in Halden Reactor Project, by increasing the rod internal pressure higher than the system coolant pressure.[1-5] Therefore, the cladding creep-out model was developed based upon those data.

Corrosion of PWR fuel cladding has been a key performance parameter determining the limit of burnup. As the burnup increases, new cladding with high corrosion resistance have been developed. The study on the corrosion mechanisms was carried out with development of new cladding alloys. Therefore, various phenomena and parameters on corrosion mechanism of Zircaloy cladding were identified. Therefore, based upon newly identified corrosion mechanisms, corrosion model of Zircaloy-4 was developed.

2. DEVELOPMENT OF CREEP-OUT MODEL

The creep model in the current fuel performance codes was developed based upon the creep-down data. Creep-out data were obtained from Halden reactor project. Fuel characteristics and operation conditions of the Experiments are summarized in Table 1 [3,5]. Figures 1 and 2 show that the current codes under-estimate the creep-out rates. CARO-D code predicts better the primary and the secondary creep reasonably than FRAPCON-3 code. Comparing the

CARO-D predictions and measured data show that code predictions are about 20-30% lower than the measured data at the same stress.

Figure 2 shows that the secondary creep has barely occurred at lower hoop stress in the Experiment B-1, where the hoop stress is 30 MPa.

In this study, the creep-out model was developed by using the creep model in CARO-D code. Cladding creep rate consists of the thermal creep and the irradiation creep, and each creep is divided into primary and secondary creep. Total creep rate is given by,

$$\varepsilon_r = \varepsilon_{1,th} + \varepsilon_{2,th} + \varepsilon_{1,irr} + \varepsilon_{2,irr} \quad (1.1)$$

And primary and secondary creep rate are described by,

$$\varepsilon_1 = C\,\varepsilon\,(1 - e^{-k\sqrt{t}}) \quad (1.2)$$

$$\varepsilon_2 = \varepsilon \quad t \quad (1.3)$$

where creep rate, ε, represents the thermal creep rate or the irradiation creep rate and is expressed as follows, respectively,

$$\varepsilon_{th} = ½\, A_{th} \exp(-26116\ K/T_c)\, \sigma_{eff}^{m}\, \mathrm{sign}(\sigma_{eq}) \quad (1.4)$$

$$\varepsilon_{irr} = ½\, A_{irr}\, \varphi^{n}\, \sigma_{eff}\, \mathrm{sign}(\sigma_{eq}) \quad (1.5)$$

where C is strain-hardening constant of the cladding material; t: irradiation period, k: 5.5 exp(-1460.2/Tc), A_{th}: thermal creep rate factor, T_c: cladding average temperature (K), A_{irr}: irradiation creep rate factor, φ fast neutron flux (E > 0.821MeV), and thermal creep rate factor, A_{th}, and irradiation creep factor A_{irr} varied with the yield strength.

Figures 1 and 2 show that predictions in the primary creep region are higher than the measured data and predictions in the secondary creep region are lower than the measured data. Also the slope of predictions in the secondary creep region is smaller than that of the measured data. Therefore, through the sensitivity study the slope of prediction was made to be consistent with that of the measured data when the secondary creep rate constant is in the range of $1.7–1.75 \times 10^{-20}$. After determining the secondary creep constant, a value of primary creep rate constant was determined by sensitivity study. However, the results from the change of primary and secondary creep rate constant did not predict the creep-out rates well. Comparing the operating parameters of each experiment in the Table 1, the sensitivity study was performed by decreasing exponent of stress and increasing exponent of fast neutron flux in equations 1.4 and 1.5. Through the sensitivity study creep-out equation was determined as followings.

$$\varepsilon_{th} = ½\, A_{th} \exp(-26116\ /T_c)\, \sigma_{eff}^{1.57}\, \mathrm{sign}(\sigma_{eq}) \quad (1.6)$$

$$\varepsilon_{irr} = ½\, A_{irr}\, \phi^{0.86}\, \sigma_{eff}\, \mathrm{sign}(\sigma_{eq}) \quad (1.7)$$

while primary creep rate constant was determined to be 2800 h^{-1} and secondary creep rate constant 1.7×10^{-20} $(n/cm^2\text{-}s)^{-0.85}$ $(N/mm^2)^{-1}$ h^{-1}.

Figures 3 and 4 show the predictions calculated by using the derived creep-out equations. Predictions were in good agreement with measured data.

TABLE 1. FUEL CHARACTERISTICS AND OPERATION CONDITIONS OF EXPERIMENTS A AND B

	Experiment A	Experiment B-1	Experiment B-2
O Cladding			
- Outer Diameter (mm)	10.75	10.75	10.75
- Thickness (mm)	0.73	0.725	0.725
- Oxide Layer Thickness	-	26	26
- Cold work	76	76	76
O Pellet			
- Outer Diameter (mm)	8.9	9.0	9.0
- Inner diameter (mm)	-	3	-
- Enrichment (wt.%)	8.0	9.0	8.0
O Fuel-Clad Gap Width (μm)	300	300	300
O Neutron Flux (10^{17} n/m^2-s) (E>1MeV)	5	3.2	2.5
O Cladding Avg. Temperature (K)	370-380	375	380
O Hoop Stress (MPa)	50	85	30
O Rod Internal Pressure (bar)	-	100	100
O Coolant Pressure (bar)	162	157	157
O Irradiation Time (fph)	4000	3100	3100
O Pressure Difference (MPa)	10	15.5	9

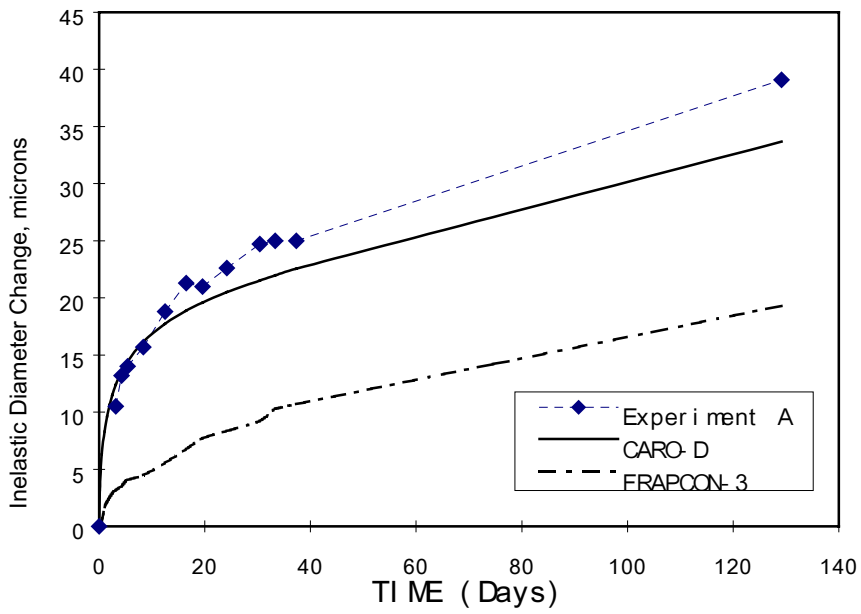

FIG 1. Comparison of code prediction for inelastic diameter change with measured data of experiment A.

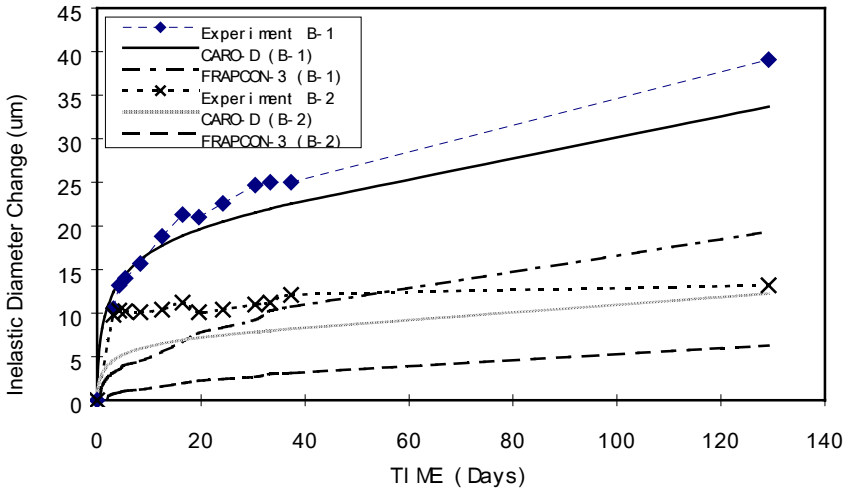

FIG. 2. Comparison of code predictions with measured data of experiment B.

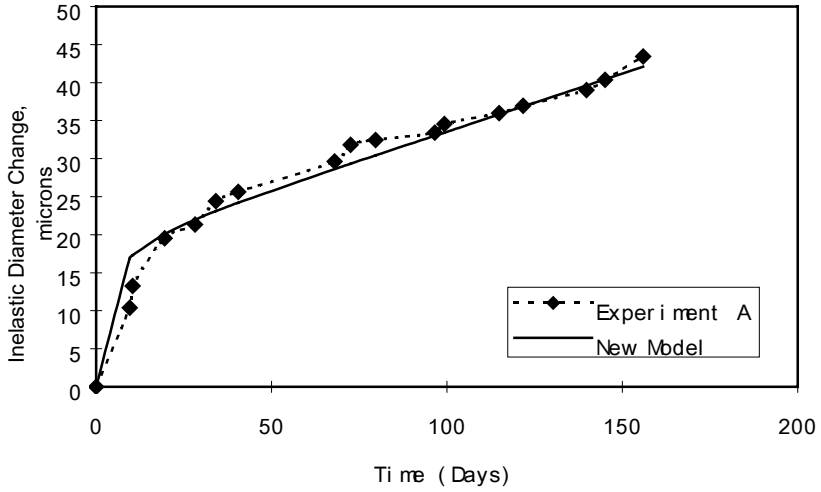

FIG. 3. Comparison of new model prediction with measured data of experiment A.

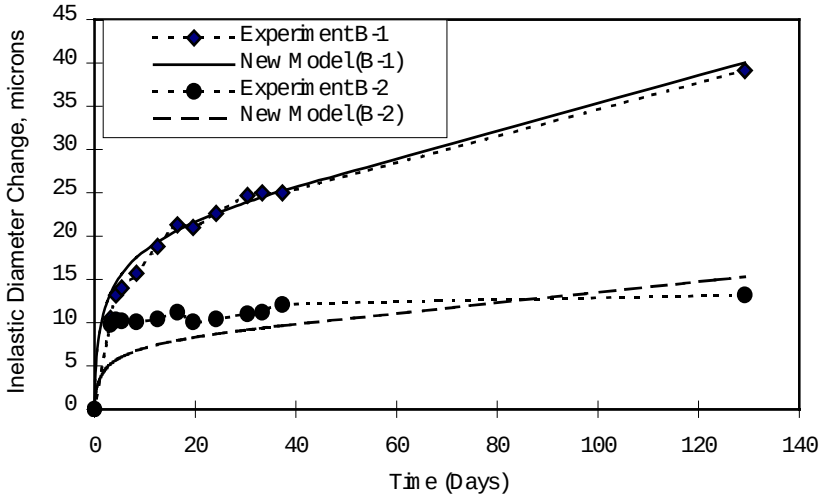

FIG. 4. Comparison of new model predictions with measured data of experiment B.

3. DEVELOPMENT OF CORROSION MODEL

3.1. Analysis of corrosion mechanisms and corrosion models

When Zircaloy-4 cladding reacts with high temperature coolant in the reactor, the corrosion rate increases by a cubic law until the oxide layer thickness reaches the pre-transition region of about 2 μ m. After pre-transition, the corrosion rate increase linearly with the time, which is called post-transition region. It is known that corrosion in the post-transition region occurs at the interface between the base Zircaloy metal and the oxide by the reaction of Zircaloy base metal with the oxygen which diffuse through the oxide layer from the coolant [6]. The oxide layer of several microns at the interface between the base metal and oxide is known to play the major protective role, regardless of the overall oxide thickness.

In order to improve the corrosion resistance of Zircaloy cladding the chemical composition of cladding and cladding manufacturing process such as heat treatments and cold work, were optimized. As tin content is reduced, the corrosion resistance increases. It is reported that corrosion of low tin Zircaloy is reduced by 20-30% at high burnup. New zirconium alloy has introduced by reducing tin content less than 1.2% or by adding the Nb out of the existing Zircaloy-4 specification. It is known that mechanical properties of these alloys are similar to Zircaloy, but the corrosion resistance is improved considerably. Also optimizing the micro-structure of the cladding through the heat treatment such as annealing and cold work may decrease the corrosion of cladding. However, mechanistic understanding of the effects of such variables as chemical composition, heat treatment and cold work have not been fully understood, so that it would be more realistic to consider the combined effect of those variables upon the corrosion.

Other factors influencing on corrosion of Zircaloy-4 cladding during the irradiation are the ionic radicals produced by radiolysis, lithium and boron. Lithium dissolved in the coolant may be incorporated into the oxide layer to enhance the diffusion of oxygen through the oxide layer and subsequently the corrosion rate. Hydrogen produced during the corrosion could be pickup by the cladding to form hydride. Volume expansion of the cladding due to the hydride may cause the tensile stress on the protective oxide layer to be weakened so that the corrosion rate may be increased due to the massive hydride [7-9]. In-reactor corrosion of Zircaloy-4 cladding involves an exponential thermal feedback, but each model has the different activation energy [10]. However, Billot [11] proposed the activation energy varying with Li concentration instead of fixed value. And at high burnup fuel after fuel-clad gap closure, tensile stress due to pellet swelling may also weaken the protective oxide layer and enhance the corrosion. Irradiation induced fast neutron flux may affect the structure of the oxide films and the chemistry within pores in the oxide [6].

Earlier corrosion models, such as KWU, EPRI and ESCORE model, took into account only the effect of fast neutron flux on corrosion rate in the post-transition region. COCHISE-94B model presented in 1994 by Billot et al [12] included the enhancement factor considering the effects of lithium concentration and presence of boron in coolant on corrosion rate. The frequency factors and activation energies were employed as a function of the lithium concentration. And the effect of the cladding surface heat flux was considered as the frequency factor in the post-transition region. NDC model developed by Kido [13] considered the effect of hydride in the cladding on the corrosion rate when the hydrogen content is higher than 400 ppm. Enigma model [14] took account of the effect of hydrogen content of cladding, lithium concentration and cladding final annealing on the corrosion rate. EPRI PFCC model

[15] developed in 1995 considered the effects of lithium concentration, hydrogen radial distribution, tin content and heat flux as the corrosion enhancement factors.

3.2. Corrosion model development

The oxide layer thickness in the pre-transition region is only about 2 μm, so that its effect on the overall cladding corrosion is not significant. Pre-transition corrosion model (Eq. 2.1) proposed by Garzarolli et al [6] was used here. The corrosion rate in the post-transition region is described as:

$$ds^3/dt = C_1 \exp(-Q_1/RT) \quad (2.1)$$

$$ds/dt = C_2 F_{Mat} F_{Flux} F_H \exp(Q^*(C_{Li})/RT) \quad (2.2)$$

where C_1 and C_2 are the corrosion constant; Q_1 is the activation energy in the pre-transition region; R is gas constant; T is the cladding metal-oxide interface temperature; F_i is the enhancement factor, and subscripts, i, means the factors influencing corrosion; $Q^*(C_{Li})$ is the activation energy in the post-transition region.

Manufacturing characteristics such as tin content, heat treatment and cold work may depend upon the manufacturer of the cladding. Effect of those parameter upon the corrosion may not be independent. Therefore material factor, F_{Mat}, was defined as follows:

.

$$F_{Mat} = f(Sn, Rx, etc.) \quad (2.3)$$

The effect of cladding hydride on the corrosion rate was considered by the enhancement factor, F_H, as follows:

$$F_H = 1 \quad \text{for } C_H \le 400 \text{ ppm} \quad (2.4)$$
$$F_H = 1 + 0.699 \log(C_H/400) \quad \text{for } C_H > 400 \text{ ppm}$$

where concentration of hydrogen, C_H, is calculated by:

$$C_H = C_{Ho} + 27100 P_H \delta_{ox}/(Wall_o - \delta_{ox}/\lambda) \quad (2.5)$$

where C_H is the average local hydrogen content; C_{Ho} is the initial hydrogen content; P_H is the hydrogen pickup fraction; δ_{ox} is the oxide thickness, $Wall_o$ is the initial cladding wall thickness; and λ is the Pilling-Bedworth ratio, 1.56.

Based upon the mechanism that Li in the coolant is incorporated into the oxide layer of the cladding and diffusion coefficient of the oxygen is increased, the effect of Li on corrosion is expressed by changing the activation energy such that

$$Q^*(C_{Li}) = 28200 - A (C_{Li} - 0.5) \quad (2.6)$$

where C_{Li} represents the Li concentration and A is the constant.

One of the major parameters determining the corrosion rate is the metal-oxide interface temperature. Temperature at the metal-oxide layer interface is dependent on the thermal conductivity of the oxide layer. The value of thermal conductivity in the new corrosion model is set to 1.2 W/m-K. And the effect of fast neutron flux, F_{Flux}, was considered according to

Garzarolli model as follows:

$$F_{Flux} = c\ \Phi^{0.24} \qquad (2.7)$$

where c is the fitting factor.

Figures 5 and 6 show the variation of oxide thickness at the cladding axial position with various Li concentration in coolant. The values of Li concentration were 0.5, 2.2 and 3.5 ppm, and the oxide layer thickness of cladding was increased by about 30%. The increase of the corrosion rate at peak oxide location in Figure 6 results from the accelerated corrosion due to temperature feed back. Figures 7 and 8 show the increase of the oxide layer thickness due to the effect of cladding hydrogen content.

Figures 9 and 10 show the measured and predicted oxide layer thickness as a function of axial position for two PWR fuel rods. The measured data in Figure 9 were with the Li effect. The derived corrosion model seems to predict the measured data reasonably well.

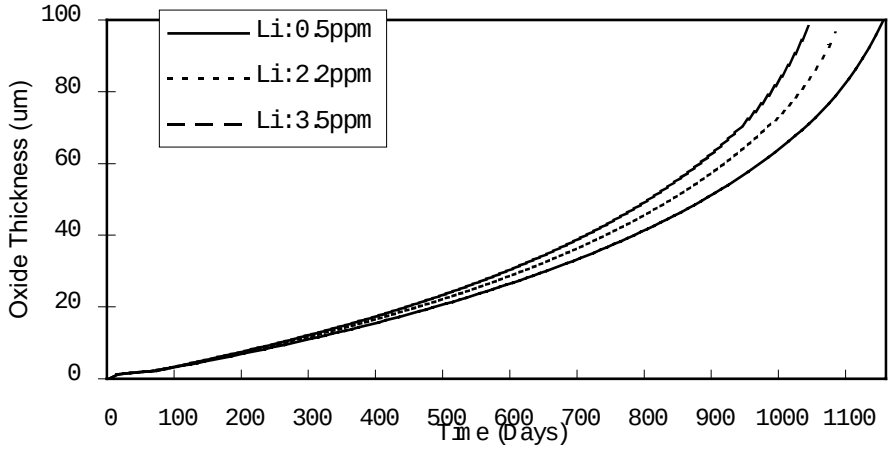

FIG. 5. Oxide thickness variation with Li concentration.

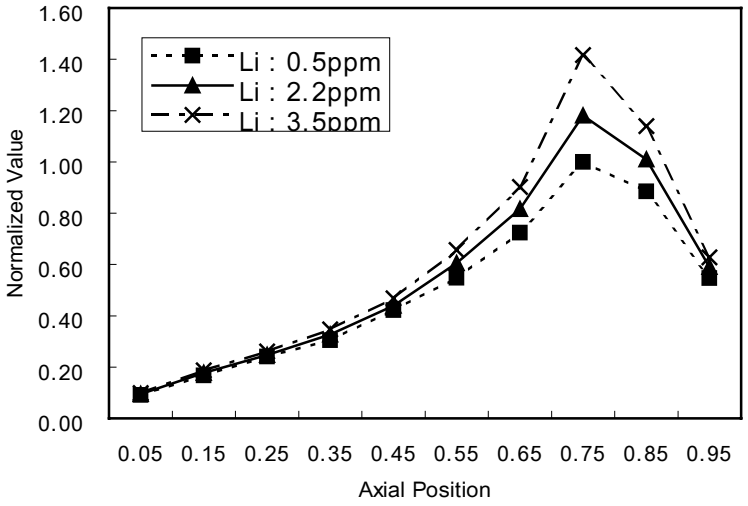

FIG. 6. Oxide thickness variation at axial position with various Li concentration.

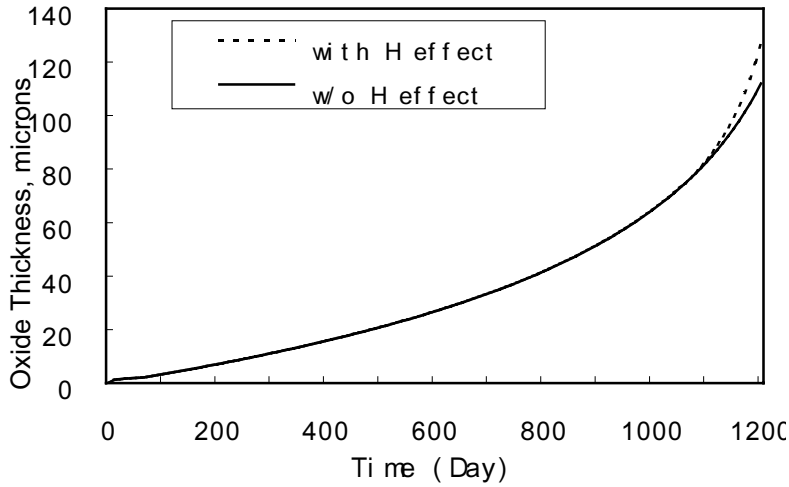

FIG. 7. Oxide thickness variation due to H_2 concentration.

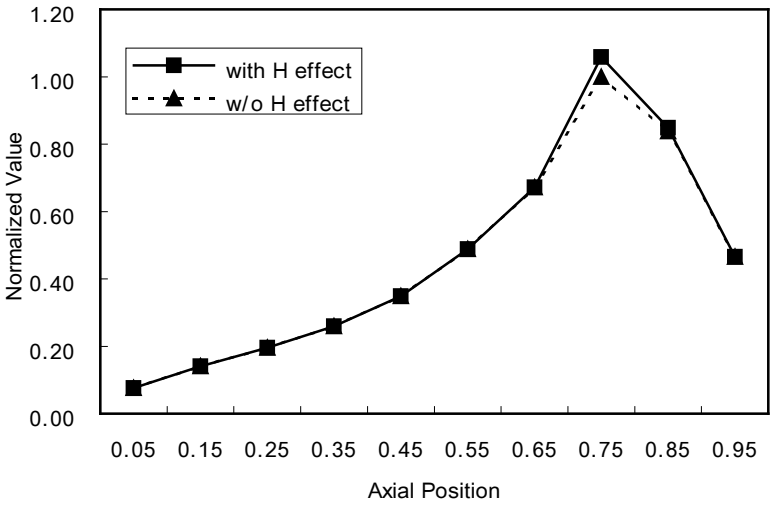

FIG. 8. Oxide thickness variation due to H_2 concentration.

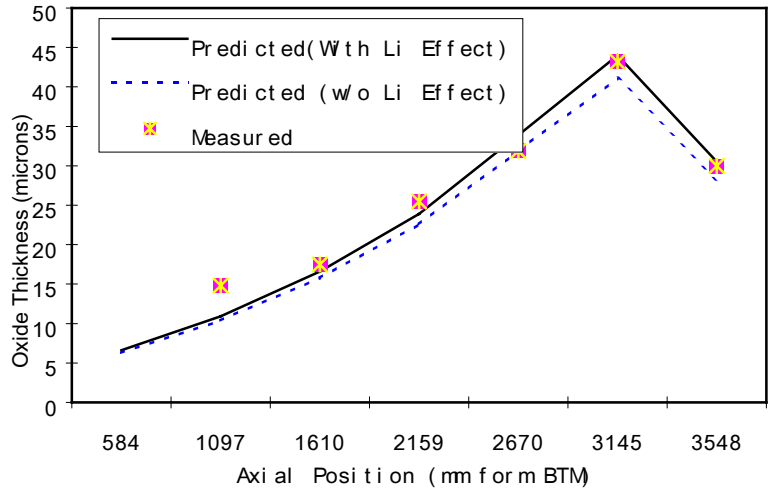

FIG. 9. Prediction and measured oxide layer thickness depending upon Li.

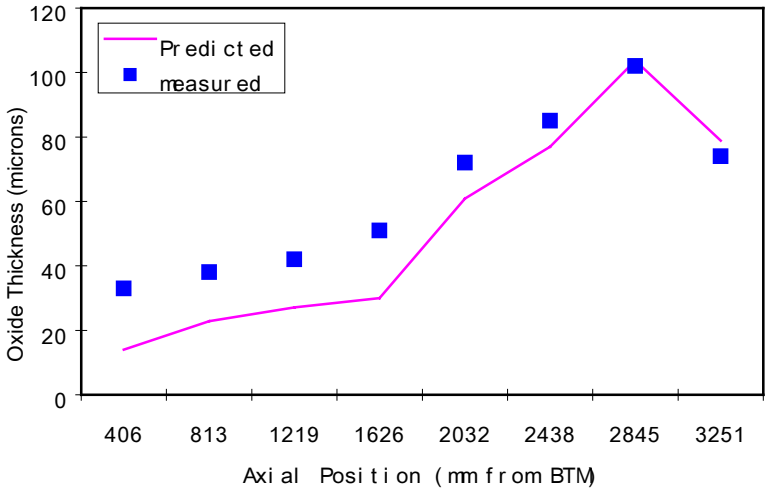

FIG. 10. Prediction and measured oxide thickness on plant A, rod C.

4. CONCLUSIONS

Creep-out model and corrosion model of Zircaloy cladding were developed for the application to the high burnup fuel behavior. Creep-out model was developed by changing the creep constants and the exponents for fast neutron flux and stress in the creep-down model based on Halden creep-out test data. Then, the derived creep-out model predicted the in-pie test results reasonably well.

Corrosion model of Zircaloy cladding was developed by analyzing the corrosion mechanisms and the existing corrosion models. Parameters affecting the cladding corrosion are the chemical composition and manufacturing characteristics of the cladding, coolant chemistry, hydride formation in the cladding, and fast neutron flux. Corrosion model was validated by both the sensitivity analyses of the parameters and prediction capability of such phenomena as the axial distribution of corrosion, the effect of water chemistry and acceleration of corrosion at high burnup.

ACKNOWLEDGEMENT

This work has been carried out under the Nuclear R&D Program supported by Ministry of Science and Technology in Korea.

REFERENCES

[1] D. SCHRIRE, F. SONTHEIMER, G.LYSELL, "ROPE-I: The Studsvik BWR Rod Overpressure Experiment", Int'l Topical Meeting on LWR Fuel Performance, West Palm Beach, Florida, April 16-19, 1994.

[2] F. SONTHEIMER, M.R. BILLAUX, "Mechanical Analysis for the Siemens Rods During ROPE-II Start-up with a New Advanced Siemens Fuel Rod Code", HPR-347 Volume I, Loen, 1996.

[3] K.L. NISSEN, A.T. DONALDSON, "Measurements of Zirclaoy In-Reactor Creep Behavior under Variable Loading Conditions in IFA-585", HWR-358, March 1993.

[4] A.T. DONALDSON' "In-Reactor Creep Behaviour of Zircaloy Under Variable Loading Conditionss In IFA-585", HWR-413, October, 1994.
[5] M.A. McGRATH, "In-Reactor Creep Behaviour of Pre-Irradiated Zircaloy-4 Under Tensile Hoop Stresses (IFA-585.4)", HWR-532, Jan. 1998.
[6] F. GARZAROLLI, W. JUNG, H. SHOENFELD, et al., "Waterside Corrosion of Zircaloy Fuel Rods," EPRI NP-2789, Research Project 1250-1, Kraftwerk Union, AG and Combustion engineering, Inc., Electric Power Research Institute, Palo, CA, Dec. 1982.
[7] A.M. GARDE, "Enhancement of Aqueous Corrosion of Zircaloy-4 Due to Hydride Precipitation at the Metal-Oxide Interface," Zirconium in the Nuclear Industry : Ninth International Symposium, ASTM STP 1132, C. M. Eucken and A. M. Garde, Eds., American Society for Testing Materials, West Conshohocken, PA, 1991, pp. 566-594.
[8] Y.S. KIM, K.S. RHEEM, and D.K. MIN, "Phenomenological Study of In-Reactor Corrosion of Zircaloy-4 in Pressurized Water Reactors," Zirconium in the Nuclear Industry : Tenth International Symposium, ASTM STP 1245, A. M. Garde and E. R. Bradley, Eds., American Society for Testing Materials, West Conshohocken, PA, 1994, pp. 745-759.
[9] S.J. KIM, K.H. KIM, J.H. PAIK, et al., “The Effect of LiOH and Hydride on Zircaloy-4 Alloy Corrosion”, Proceedings of the Korean Nuclear Society Autumn Meeting, Vol II, 1997, pp. 75-80.
[10] B. CHENG, P.M. GILMORE, and H.H. KLEPFER, "PWR Zircaloy fuel Cladding Corrosion Performance, Mechanics, and Modeling," Zirconium in the Nuclear Industry : Eleventh International Symposium, ASTM STP 1295, E. R. Bradley and G.P. Sabol, Eds., American Society for Testing Materials, Garmisch- Partenkirchen, Germanym 1995, pp. 137-160.
[11] P. BILLOT and A. GIORDANO, "Comparison of Zircaloy Corrosion Models from the Evaluation of In-Reactor and Out-of-Pile Loop Performance," Zirconium in the Nuclear Industry : Ninth International Symposium, ASTM STP 1132, American Society for Testing Materials, West Conshohocken, PA, 1991, pp. 539-565.
[12] P. BILLOT, J. ROBIN, A. GIORDANO and J. PEY, et al., "Experimental and Theoretical Studies of Parameters that Influenc Corrosion of Zircaloy-4”, Zirconium in the Nuclear Industry : Tenth International Symposium, ASTM STP 1245, American Society for Testing Materials, West Conshohocken, PA, 1994.
[13] T. KIDO, "A Study on Enhanced Uniform Corrosion of Zircaloy-4 Cladding during High Burnup Operation in PWRs”, Proceedings of the Sixth International Symposium on Environmental Degradation of Materials in Nuclear Power Systems – Water Reactors, San Diego, California, August 1-5, 1993, The Minerals, Metals & Materials Society, 1993.
[14] T.J. ABRAM, "Modelling the Waterside Corrosion of PWR Fuel," Proceedings of a Technical Committee Meeting, Windermere, United Kingdom, 19-23 September, 1994.
[15] P.M. GILMORE, H.H. KLEPFER and J.M. SORENSEN, "EPRI PWR Fuel Cladding Corrosion Model (PFCC) Model”, Vol. 1 Theory and user’s Manual, TR-105387-V1, December, 1995.

WWER FUEL BEHAVIOUR AND CHARACTERISTICS AT HIGH BURNUP

V.N. GOLOVANOV, V.I. KUZMIN, S.V. KUZMIN, G.I. MAYORSHINA
State Scientific Center of Russian Federation Research Institute of Atomic Reactors,
Dimitrovgrad, Ulyanovsk Region, Russian Federation

Abstract

The increase of fuel burnup in fuel rods is a task that provides a considerable cost reduction of WWER fuel cycle in case of its solution. Investigations on fuel and cladding behaviour and change in fuel characteristics under irradiation are carried out in the Russian Federation for standard and as well as for experimental fuel rods to validate the reliable and safe operation of the fuel rods at high burnups. The paper presents the results of examinations on cracking, dimensional, structural and density changes of fuel pellets as well as the results of examination on corrosion and mechanical properties of WWER-440 and WWER-1000 fuel rod claddings.

1. CHARACTERISTIC AND OPERATIONAL CONDITIONS FOR WWER FUEL RODS

Fuel pellets of uranium dioxide have a central hole of 1.6 and 2.4 mm for WWER-440 and WWER-1000, correspondingly. The outer diameter and density of fuel pellets incorporated into the fuel rod are 7.55 mm and 10.4-10.8g/cm^3. Fuel rod claddings are made of Zr-1% Nb alloy. The main operation parameters of the fuel rods are given in Table I.

TABLE I. OPERATIONAL CONDITIONS FOR WWER FUEL RODS

Parameter	WWER-440	WWER-1000
Coolant inlet temperature, °C	270	290
Coolant outlet temperature, °C	300	320
Coolant pressure, MPa	12,2	15,7
Maximum linear rating, W/cm	260	320
Operation period, years	3-5	3-4
Maximum burnup, MWd/kg U	64	58

2. CRACKING, DIMENSIONAL CHANGES OF PELLETS

It is well known that cracking is caused by thermal stresses. They are brought about by temperature gradient along the radius and fuel pellet height. Linear rating specifies the cracking rate. One of the possible parameters that characterize the cracking rate is the number of fragments appearing in the cross and longitudinal sections of the pellets.

The minimum cracking of pellets was noticed at a linear rating of 50W/cm when two fragments were formed. The number of fragments in the cross section increased up to 6-11 (FIG.1) together with the linear rating increase up to 300-320W/cm. All pellets had 2 ÷ 4 cross cracks at a linear rating of ~300W/cm.

The maximum cracking of pellets takes place when the maximum linear rating is achieved and in the course of further operation the fragmentation rate doesn't change.

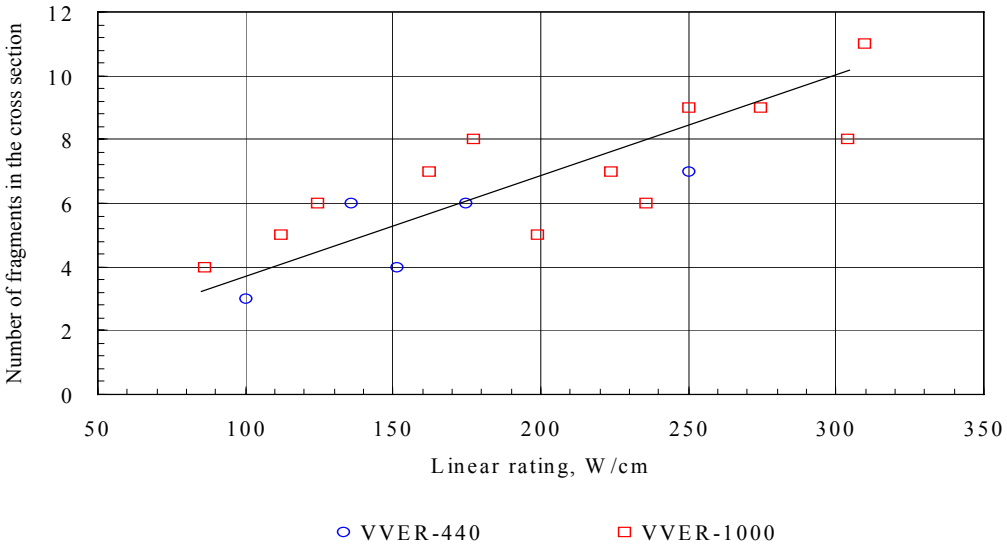

FIG. 1. WWER pellet fragmentation versus maximum linear rating.

The increase of free surface of pellets is a consequence of fragmentation. The calculated estimation demonstrated that free surface of the pellets increased from 100cm^2/cm^3 [1] to 120-130cm^2/cm^3 when the density is 95% of theoretical one. The results of fragmentation can be used for calculated models of gas release.

Basically, changes in the pellet size result from swelling. The results of the inner diameter measurements of pellets (Table II) at different burnups point to its stability in the whole studied range of mean burnup over the pellet section. As the diameter of the hole doesn't change essentially with a burnup increase all increases of volume caused by swelling result from the outer diameter and height increase.

TABLE II. INNER HOLE DIAMETER

Reactor	Burnup, MWd/kg U	Diameter after irradiation, mm
WWER-440	30,0	1.62
	34.9	1.56
	38.5	1.65
	42.0	1.60
	52.9	1.64
	58.3	1.54
	63.8	1.67
	68.2	1.65
WWER-1000	34.6	2.3
	36.0	2.5
	40.4	2.4
	42.0	2.4
	43.4	2.3
	44.8	2.5
	58.1	2.3

3. CHANGE OF DENSITY AND FUEL SWELLING

Density of pellets incorporated into the fuel rods was in the range 10.5-10.6 g/cm^3. Fig. 2 shows the relationship between the pellet density and burnup. Further radiation sintering of pellets that accompanied by the density increase by 0.2 ÷ 0.5% takes place at a burnup up to 15 MWd/kgU. The density swelling relationship is of the linear character at a burnup of more than 20MWd/kgU. It indicates that a 100% increase of the pellet volume depends upon "stable" swelling. Swelling of WWER-440 and WWER-1000 pellets is practically the same. The fuel volume increases from 15 to 68MWd/kgU with a mean rate of 0.8%/10MWd/kgU. The relationship between the pellet density change ($\Delta\rho/\rho$,%) and the burnup (B, MWd/kgU) is expressed as:

$$\Delta\rho/\rho = 3\cdot10^{-5}B^3 - 0{,}0041B^2 + 0{,}0747B.$$

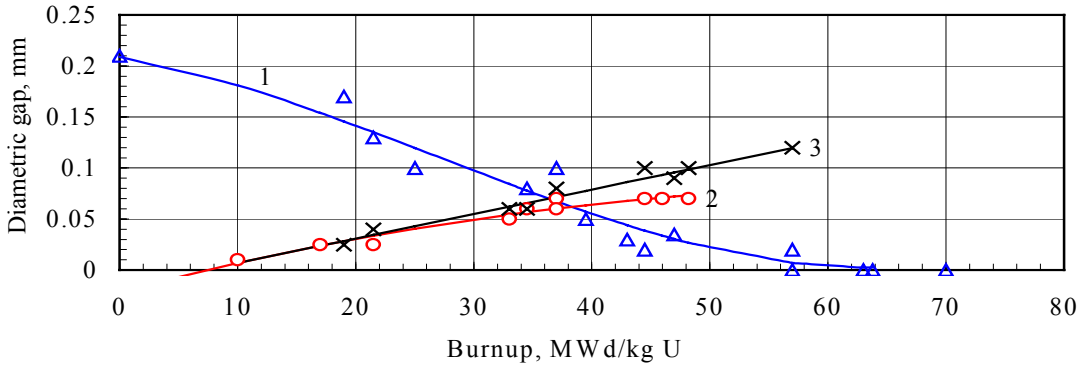

FIG. 2. Change of "cold" fuel to cladding diametric gap (1), contributions of cladding diameter decrease (2) and fuel pellet swelling (3) to gap changing.

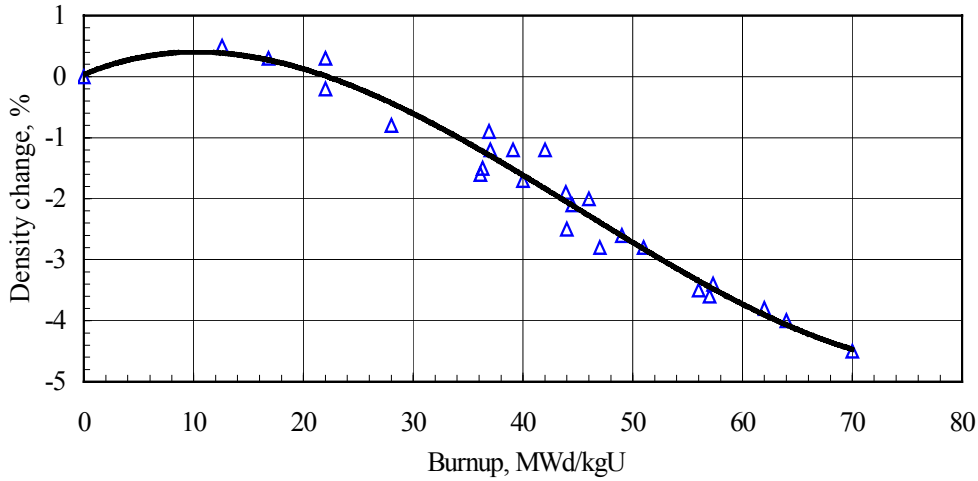

FIG. 3. Change of fuel density versus burnup.

4. CHANGE OF PELLET TO CLADDING DIAMETRIC GAP

Change of pellet to cladding diametric gap is caused by the change of the outer diameter of pellets and inner diameter of cladding. FIG. 3 demonstrates the dependence of "cold" diametric gap on the burnup. The gap goes down from the reference value of 0.21 mm up to 0.03mm at a burnup of 40-45 MWd/kgU. The gap values are in the range 0-0.03 mm at a higher burnup. Contributions of the cladding diameter decrease due to its deformation under

the coolant pressure and fuel swelling to diametric gap decrease are presented as curve 2 and curve 3, respectively.

It is evident form the FIG. 3 that:

i. the mechanical pellet- cladding interaction begins from the burnup of 40-45MWd/kgU with due regard for the difference in the thermal expansion of the cladding and fuel;
ii. the reverse deformation and increase of the outer diameter of the cladding are possible after diametric gap disappearance owing to the pressure of swelling solid fuel on the cladding;
iii. contributions of fuel swelling and cladding deformation caused by the coolant pressure to the diametric gap decrease are commensurable quantities.

5. FUEL STRUCTURE

The principal changes in the fuel structure are determined by the rim-layer formation where the shattering of grain into subgrains of 0.1-1μm and formation of small-size pores (up to 2μm) [3,4] have been observed. According to the studies performed with the help of optical microscope an increase of porosity in the WWER rim-layer begins at a burnup of 35-40 MWd/kgU. The rim-layer porosity achieved 10-15% at a burnup of 50 MWd/kgU. According to the data of optical microscopy the rim-layer thickness, where the porosity was over 10% reached the value of ~100 μm in case of the mean burnup of 60 ÷ 68MWd/kgU over the pellet section. The data obtained with the help of EPMA x-ray microanalyzer showed that the rim-layer thickness was 200 ÷ 300μm. The grain growth wasn't observed in the fuel pellets of the studied WWER fuel after its operation in the steady-state conditions. This fact is explained by the low maximum temperature (<1500°).

The crystal structure of fuel was studied at burnups of 45 MWd/kgU and 49 MWd/kgU [5]. It is known that the accumulation of radiation damages in the rim-layer leads to breaking of the ideal arrangement of uranium and oxygen atoms in the crystal lattice. As a consequence of it the intensity of the diffraction maximums reduces by 12-50 times in comparison with the central part of the pellet and their width increases by 2-3 times. Such great distortions of the structure indicate that the state of fuel in the rim-layer is close to roentgenoamorphous state.

6. STUCTURE AND MECHANICAL PROPERTIES OF CLADDINGS

Structural changes of WWER fuel rod claddings are related to oxidation and hydriding. Oxidation causes the formation of oxide layers on the outer and inner surfaces of claddings. The thickness of the uniform and dense oxide film formed on the outer surface grows together with the burnup increase (FIG. 4a.) and reaches the value of 8μm at a burnup 45-65 MWd/kgU. Locally the thickness of the oxide film run into 20 μm.
The broken oxide film forms on the inner surface of the cladding at a burnup of 30-40 MWd/kgU. At higher burnup when the regular fuel- to -cladding contact is established the film becomes continuous along the whole cladding perimeter but its thickness doesn't exceed 15-17μm (FIG. 4b.).

Hydriding of fuel rod claddings was insignificant during 3-5 years of operation. Hydrogen content in claddings increased up to $1 \cdot 10^{-2}$mass% but no more.

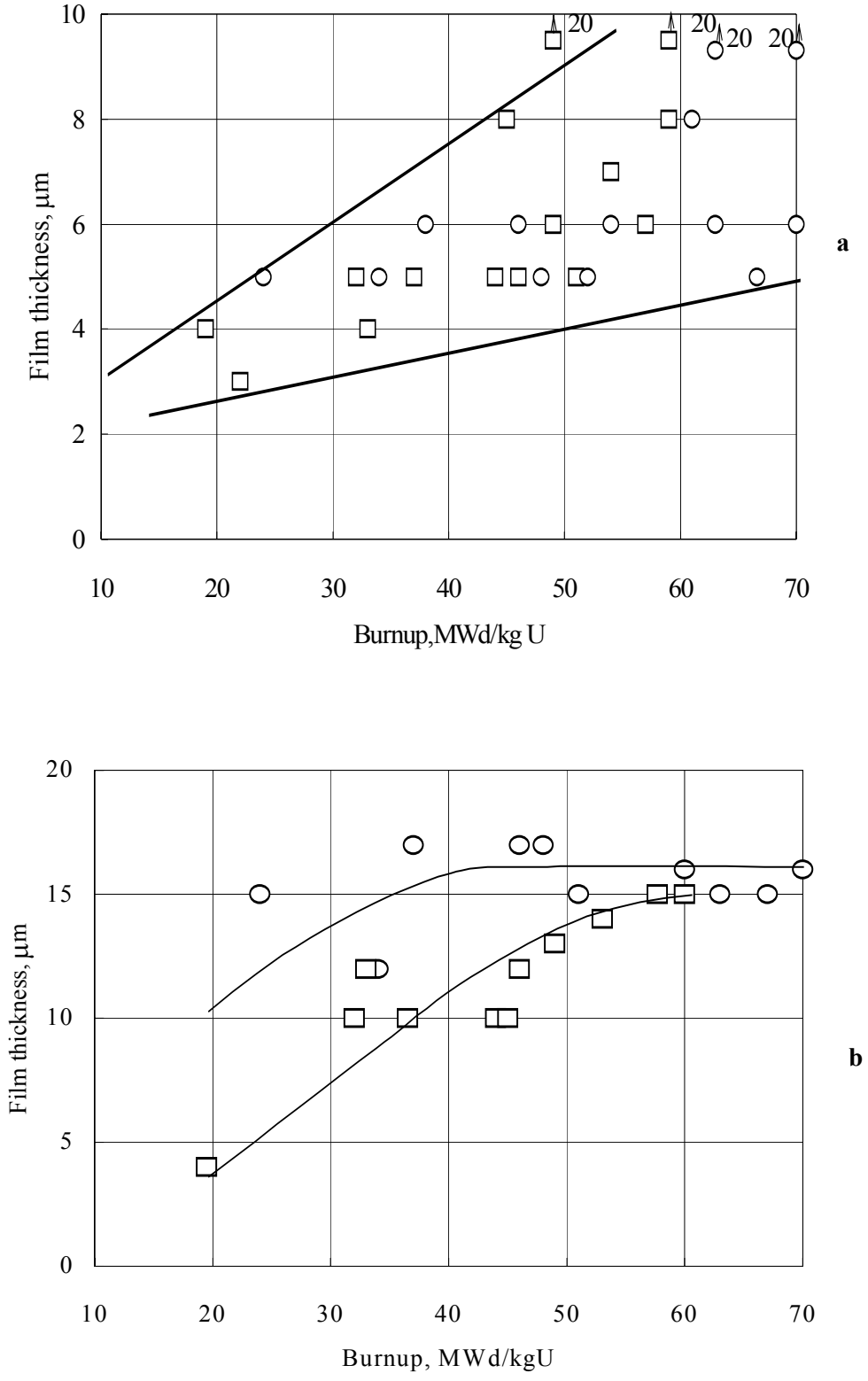

FIG.4. Oxide film thickness versus burnup on outer (a) and inner (b) surfaces of WWER-440 (o) and WWER-1000 (□) fuel rod cladding

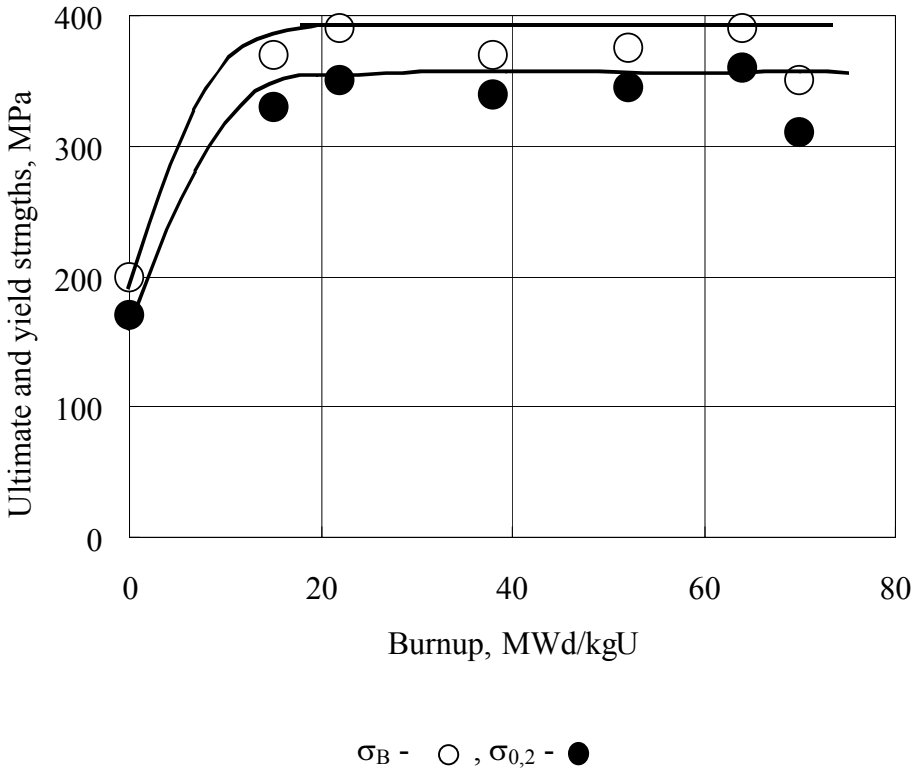

FIG.5. Strength properties of WWER-440 fuel rod cladding at a temperature of 350℃

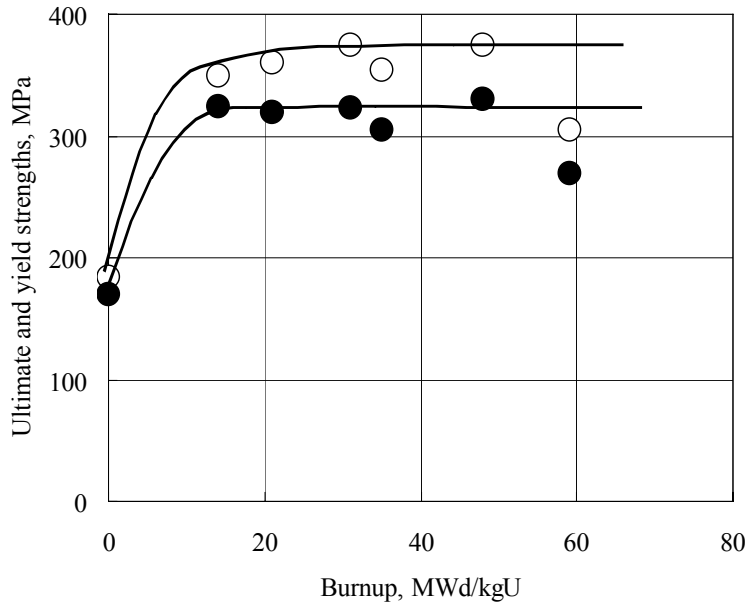

FIG. 6. Strength properties of WWER-1000 fuel rod claddings at a temperature of 380°C.

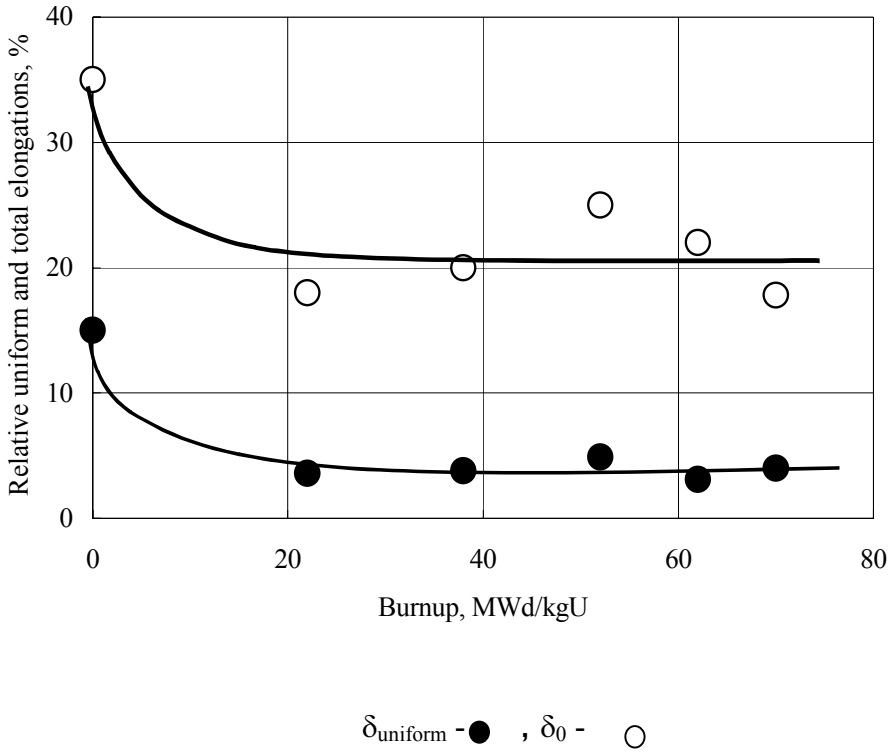

FIG.7. Relative elongation of WWER-440 fuel rod claddings at a temperature of 350℃.

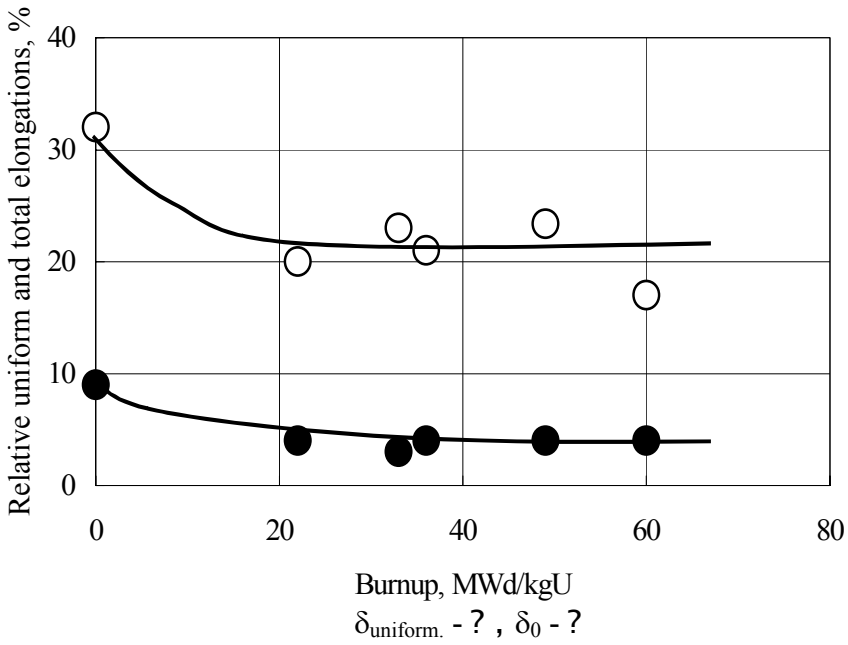

FIG.8. Relative elongation of WWER-1000 fuel rod claddings at a temperature of 380℃.

Such high corrosion and radiation damage resistance assures high mechanical properties of claddings. Conventional yield strength and ultimate strength at test temperatures of 350 and 380°C complying with the maximum operation values were not depend on the burnup in the range of 15-68MWd/kgU (Figs 5, 6.). The minimum value of the ultimate strength was 310MPa. Dependencies of total and uniform elongation versus burnup were identical except the burnup range from 0 to 20MWd/kgU. The uniform relative elongation was more than 3% in all cases and the total relative elongation – no less than 17% (Figs 7, 8.).

7. CONCLUSION

State, structural and property changes of the WWER fuel and claddings are within the permissible limits at a burnup up to ~70MWd/kgU.

Extrapolation of the obtained relationships in the fuel and cladding characteristic change allows us to predict the possibility of achievement of higher burnup.

The obtained results are used for improvement of models for fuel and cladding behaviour and calculation codes for the validation of the WWER fuel rod serviceability.

REFERENCES

[1] B. LASTMAN, Radiation Phenomena in Uranium Dioxide. Atomizdat, M., 1964.

[2] A.V. SMIRNOV, V.P. SMIRNOV, A.A. PETUCHOV, B.A. KONASHOV, V.S. POLENOK, V.I. KUZMIN, "Experimental Justification of the WWER Standard Fuel Reliability under Base-load Operation". Collection of Papers of the 5th Interindustry Conference on Reactor Material Science, V.1, P.1, Dimitrovgrad, SSC RF RIAR, page 33.

[3] V.V. VOTINOVA, V.I. GROMOV, V.I. KUZMIN, I.G. LEBEDEV, "Electron-microscopical Study of Porosity in the UO_2, PuO_2, $(0.2Pu - 0.8Pu)O_2$". Radiation Physics of Solid Body, Atomizdat, M, 1970, page 158.

[4] A. SMIRNOV, V. TSIBULJA, B. KANASHOV, "Examination of WWER-440 fuel microstructure and composition in a burup interval of 42-63 MWd/kg U". Report №6/1 IAEA Technical Committee Meeting on Advances in Pellet Technology for Improved Performance at High Burnup, Tokyo, Oktober 28 – November 1, 1996.

[5] V.I. KUZMIN, V.N. GOLOVANOV, G.I. MAYOERSHINA, et al, "Change of Fuel in WWER Fuel Rods at a Burnup of 40-60MWd/kgU". Collection of Papers of the 5th Interindustry Conference on Reactor Material Science, V.1, P.1, Dimitrovgrad, SSC RF RIAR, page59.

INVESTIGATION OF THE SEU43 ADVANCED CANDU TYPE FUEL BEHAVIOUR UNDER LOCA CONDITIONS

G. HORHOIANU, G. OLTEANU, A. PISICA, D.V. IONESCU
Institute for Nuclear Research,
Pitesti, Romania

Abstract

Presently, INR Pitesti developing an advanced CANDU fuel, SEU43 (Slightly Enriched Uranium fuel bundle with 43 elements). Compared with the current design, SEU43 will have higher power capability and higher burn-up potential. Fuel burn-up with 1.2 percent SEU is about 22 MWd/kg U, which is three times the burn-up usually achieved in CANDU-6 reactors fuelled with natural uranium. SEU 43 fuel bundles have reduced outer element linear powers, providing an opportunity to increase the power output of the CANDU 6 reactor. In this study, consequences of a postulated large loss of coolant accident (LOCA) were used as an indicator to determine the power increase. The power-uprating potential was determined by increasing the power in a SEU43 fuelled channel to the point where the predicted consequence in terms of fuel behaviour are the same as the consequences for a 37 -element fuelled channel operating at current nominal powers.

1. INTRODUCTION

Presently, INR Pitesti developing an advanced CANDU fuel, SEU43 (Slightly Enriched Uranium fuel bundle with 43 elements) [1,2]. The SEU43 bundle has some design improvements over the 37-element standard CANDU-6 bundle while maintaining capability with the existing CANDU reactor fuel handling systems and all other fuel performance characteristics. The SEU43 bundle contains 43 elements of two different diameters, thereby flattening bundle element ring power distribution and reducing peak linear element power by 20% (see Figure 1).

Compared with the current design, SEU43 will have higher power capability and higher burn-up potential. Fuel burn-up with 1.2 percent SEU is about 22 MWd/kg U, which is three times the burn-up usually achieved in CANDU-6 reactors fuelled with natural uranium. The resulting threefold reduction in the volume of spent fuel which must be disposed of is potentially of great significance given the concern over waste management.

The SEU43 Development Programme has been under way at INR Pitesti since 1990. It covers manufacturing, performance testing, thermal hydraulics confirmation and reactor physics. In order to demonstrate the performance of the SEU43 fuel element design and to prove the adequacy of the manufacturing teghnologies, experimental fuel elements have been introduced in the irradiation devices of TRIGA, INR Pitesti, research reactor. One of the current objective of these fuel behaviour studies are to investigate and to reliably predict the performance during power cycling conditions. The power cycling experiment has been performed in a special designed irradiation device, capsule C9 [3]. The specified variation of fuel element linear power was obtained by mechanical movement of the device into the TRIGA reactor core. During the power cycling test the experimental fuel element has successfully experienced up to 367 power cycles, mostly between 50% and 100% of the specified linear power, pointing out the role of graphite coating in preventing SCC defects. PIE results indicate a maximum cladding strain at ridge of 0.7% in the region with the highest linear power. There are also indications of strong axial interaction between pellet column and end cap.

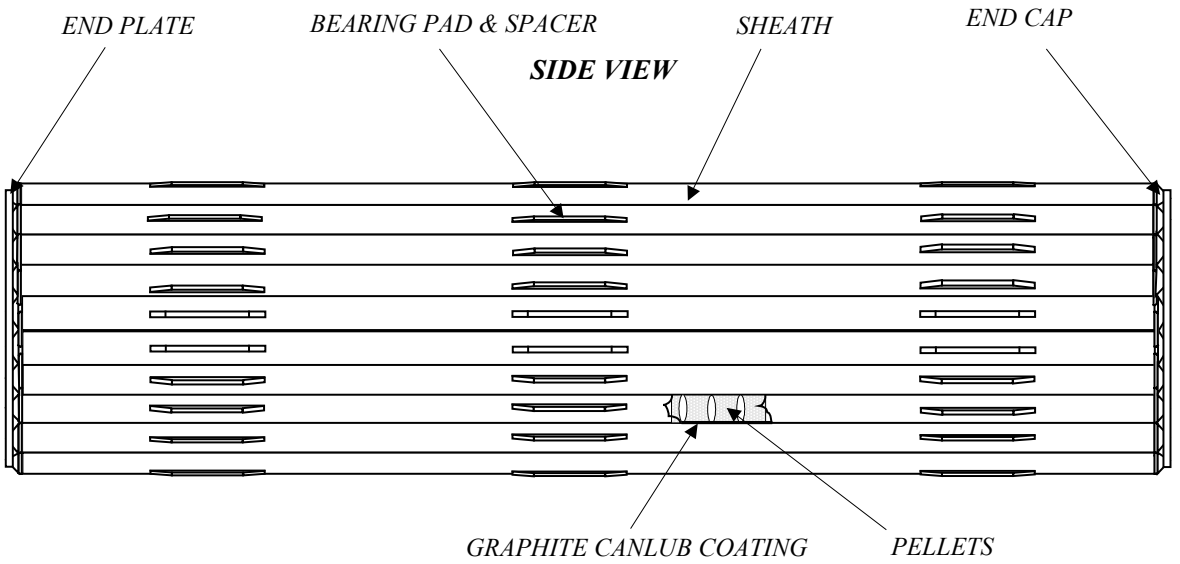

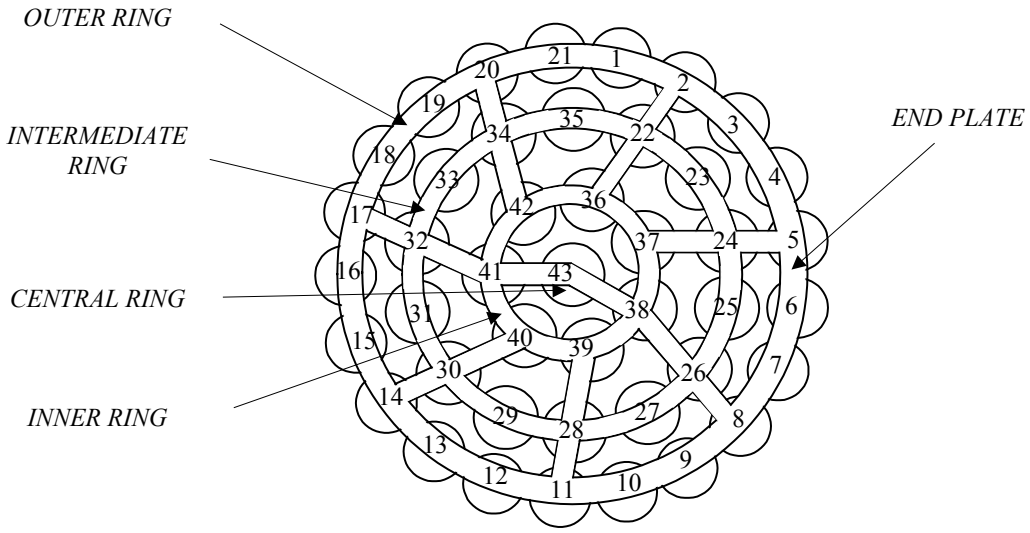

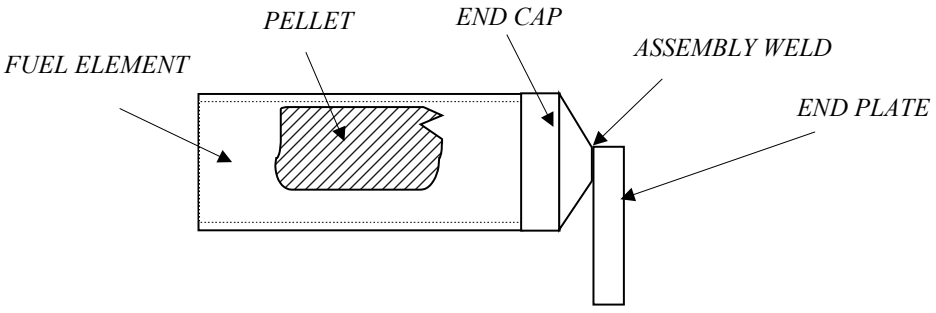

FIG. 1. SEU 43 fuel bundle.

This paper describes effect of the design changes of SEU43 bundle on CANDU-6 reactor safety and the analysis performed to determine the increase in nominal reactor power for a full core of SEU43 fuel so that consequences of postulated large break loss of coolant accidents (LOCA) are not increased relative to a 37-element bundle fuelled core. An analysis of the consequences of a large break LOCA will provide a limit on the reactor power increase from the current nominal power. Because of the lower outer element linear power ratings of SEU43 fuel, as compared with those of 37-element fuel, there is a potential for an increase in reactor power without a decrease in safety margins. The hydraulic properties of SEU43 fuel are essentially equivalent to the hydraulic properties of 37-element fuel [1].

To determine the approximate magnitude of the power increase, thermalhydraulic analyses were performed for two large break LOCA scenarios with shut down systems and emergency core cooling (ECC) available; these scenarios were a 20% reactor inlet header (RIH) break and a 80% reactor outlet header (ROH) break. The 80% ROH break was chosen because this break size leads to a great number of predicted fuel failures in a 37-element fuelled core. The 20% RIH break was chosen because it leads to a great amount of pressure tube ballooning contacts with the calandria tube in a 37-element fuelled core.

The power of the SEU43 channel was increased until the point where one of the following primary criteria was met:

a) The fission product release from the fuel to sheath gap of SEU43 fuel equals the gap release from 37-element fuel.
b) The internal gas pressure of SEU43 fuel element equals the internal gas pressure of 37-element fuel.
c) The sheath strain of SEU43 fuel element equals the sheath strain of 37-element fuel.

2. SIGNIFICANT ASPECTS REGARDING SEU43 FUEL ELEMENT DESIGN EVALUATION

The activity of defining feature of the SEU43 fuel bundle and of the fuel element design has started with the review of the intended design objectives including the specific extended burnup design objectives. In order to reduce the detrimental effects of the life limiting factors at extended burnup a set of solution have been adopted for SEU43 fuel element design (see Table 1).

Table 1. DESIGN SOLUTIONS FOR EXTENDED BURNUP FUEL ELEMENT

Design solution	Specific extended burnup design objectives
-Decreasing of sheath diameter	Decreasing of fuel element linear power and average fuel temperature
-Increasing of initial pellet grain size	Ensuring that fission gas release is within acceptable limits
-Increasing of pellet dish volume -Increasing of pellet land width -Increasing of pellet chamfer	Minimization of the local strain in the sheath ridges and reduction of SCC failure susceptibility in power ramps
-Increasing of axial gap	Accommodation of axial fuel stack expansion
-Increasing of graphite layer thickness	Reduction of SCC failure susceptibility

After the initial stages of the design process in which were established the new bundle operational conditions (maximum power, average burnup, typical envelope power histories and coolant parameters), these conditions have been prepared as input data for the design codes. For assessing the influence of the selected design solutions on the fuel element performance, we have primarily used a conservative approach coupled with a comparison with the performance of the standard design in similar conditions. In the cases where the results of the conservative calculations exceeded the design limit, we have used the probabilistic alternative. We have performed detailed analyses for each fuel element performance parameter. The most significant results have been selected and are presented in [1,2].

3. ANALYSIS METODOLOGY

In order to assess the fuel behaviour during the transient, the dynamic response of the fuel element must be considered. That is, phenomena such as sheath deformation, fuel-to-sheath heat transfer coefficient and internal gas pressure should be recognized in the analysis. The ROFEM code [4] and CAREB code [5,6] were used to simulate the fuel behaviour for the 20% reactor inlet header (RIH) and 80% reactor outlet header (ROH) break cases. ROFEM calculations are performed to estimate steady-state fuel-element conditions at the onset of the accident. Then, after the onset of the accident, the fuel and fuel-sheath behaviour of the outer fuel elements residing in the core pass downstream of the break (i.e. critical core pass) are evaluated by the CAREB code. The CAREB code requires information regarding the fuel-element state during normal operating conditions, which is obtained from ROFEM. It also requires the power transient, coolant temperature, coolant pressure and sheath-to-coolant heat transfer coefficients (obtained from FIREBIRD code) as transient boundary conditions [7]. The current version of FIREBIRD [7] contains improvements over the original.

The sequence of events that occur after a large break LOCA such as reactor trip, loop isolation, ECC initiation, pump trips, etc. will not vary significantly for a full core of SEU43 fuel. The channel and system thermal hydraulics for a full core of SEU43 fuel will not differ significantly from the thermal hydraulics for a full core of 37-element fuel. The reason for this similarity is that the channel flows as a function of pressure drop for SEU43 fuel are within approximately 1% of the value for a channel with 37-element bundles.

The ROFEM computer code was used to determine the initial fuel conditions for both the 37-element fuel and SEU43 fuel. The SEU43 fuel elements as well as the 37-element fuel elements, are assumed to follow the CANDU 600 reference high power curve scaled accordingly to each ring of fuel elements. The reference high power curve is a hypothetical power/burnup history that is higher than any power history experienced by fuel bundle in the core. As such, no fuel bundle will follow the entire reference over power curve to discharge.

4. EVOLUTION OF THE ROFEM CODE FOR APPLICATIONS TO EXTENDED BURNUPS

ROFEM is a computer code able to predict in-pile thermal and mechanical behaviour of fuel rods as a function of the reactor operating history [2,4]. The code has been developed based on the FEMAXI III code [8]. The first attempt to use the FEMAXI III code for CANDU type fuel rod behaviour modeling was unsuccessful due to the inadequate models included in the thermal part. Step by step, the models of this part of code have been firstly revised and then modified or changed, so the predictions of the code have been progressively improved. The most important changes in the thermal part of the code were [2,9]:

- microstructure dependent fission gas release;
- temperature dependent grain growth and pellet restructuring;
- temperature, porosity and burnup dependence of thermal conductivity;
- burnup dependence of the radial power profile in the fuel pellet;
- pellet to clad heat transfer via solid-solid, gas and radiative components.

The burnup dependent correlation for the thermal conductivity, deduced from the experimental data [10], has the following expression:

$$\lambda' = \lambda \frac{\arctan(\lambda \cdot bu)}{a\sqrt{\lambda \cdot bu}}$$

where λ' is the thermal conductivity of irradiated UO_2 (W/K·m), λ is the thermal conductivity of unirradiated UO_2 (W/K·m), bu is the burnup (at %) and a is a model constant (=0.241).

Related to the particular algorithm used for temperature calculation, is the necessity of evaluating the values of the local burnup, which is radially distributed in the pellet. Usually, the ROFEM code evaluates the radial power rate profile dependence on plutonium build-up using an approach similar to the RADAR model [11]. Starting from the information available after radial power profile calculation, an expression for evaluating radial profile of the burnup has been derived [10]. In the case of a solid cylindrical pellet the expression has the following form:

$$\Delta B(r) = I_0(k \cdot r) \frac{k \cdot R \cdot \left(\overline{\sigma}_{235} \cdot U(r) + \overline{\sigma}_{239} \cdot Pu(r)\right)}{2 \cdot I_1(k \cdot R) \cdot \left(\overline{\sigma}_{235} \cdot \overline{U} + \overline{\sigma}_{239} \cdot \overline{Pu}\right)} \Delta\overline{B}$$

where ΔB represent the local burnup increase (%) and $\Delta\overline{B}$ is the pellet average burnup increment (%), I_o and I_1 are Bessel functions, k is the neutron inverse diffusion length (m^{-1}), r is the local radius (m) and R the pellet radius (m). With U, Pu we noted the local concentration of U_{235} and Pu_{239} (at %) and $\sigma_{235}, \sigma_{239}$ are microscopic weighted cross sections for U_{235} and Pu_{239} (barn).

Using recent developments and experimental data, by calculating the effect of introducing the burnup dependent conductivity in the ROFEM fuel modelling code it was possible to obtain a quantitative understanding of the role of this phenomenon on CANDU type fuel performance [10]. There is significant evidence to suggest that reduction in thermal conductivity of the fuel is primarily responsible for the elevated fuel temperatures and fission gas release at extended burnup in this type of fuel.

ROFEM can analyze the integral behaviour of a whole fuel rod throughout its life as well as the local mechanical behaviour of a small part of fuel rod. The code consists of two major analysis parts, the thermal analysis part and the mechanical analysis part. In the thermal analysis part, the integral behaviour of the whole fuel rod is analyzed in one-dimensional axisymetric approach. The calculations are performed for one axial segment, dividing the fuel in 100 concentric rings. After the temperature distribution determination, the thermal expansion, densification, restructuring and fission gas release is evaluated for each ring. The

associated inner gas pressure and gas composition are then evaluated. After updating the gap conductance, the calculations are repeated until the given convergence criterion is reached.

The detailed local mechanical analysis is performed separately in the mechanical part of the code by means of two- dimensional axisymetric finite element method (FEM). The region of a half pellet height is analyzed in detail assuming axisymetry and a plane symmetry at the mid-plane of a pellet. Both fuel and cladding are divided in quadratic isoparametric ring elements which are linked by continuity lows of force and displacements. Elasto-plasticity, creep, thermal expansion, fuel cracking and crack healing, relocation, densification, swelling and fuel-clad mechanical interaction are modeled. The FEM analyses allow the prediction of stresses and strains in the cladding as well as the local deformation of the cladding like ridges.

The successive revisions of the ROFEM code have been permanently verified using the results of the instrumented experiments on CANDU type fuel performed in TRIGA reactor of INR Pitesti and the open literature experimental data [2,9].

5. CAREB CODE DESCRIPTION AND VERIFICATION

CAREB code [5,6] treats a simple Zircaloy-sheathed UO_2 fuel element and assumes axisymmetrical properties. Physical effects considered in the code are as follows: thermal, elastic and plastic sheath deformation; variation of internal gas pressure during the transient; variation of the fuel-to-sheath heat transfer coefficient and fuel-to-sheath radial gap during the transient; fuel expansion, cracking and melting; beryllium-assisted crack penetration of the sheath; and sheath oxidation.

The CAREB analysis is used to evaluate the fuel performance against the fuel-sheath integrity requirements. The newer version of CAREB has been compared against ELOCA code results. The predictions continue to show reasonable agreement with ELOCA results [6]. Sheath failures are assumed to occur if the CAREB results indicate that any of the following failure criteria are satisfied:

(i) 2% sheath hoop strain and sheath temperatures greater than 1273 K,
(ii) 5% sheath hoop strain and any sheath temperature,
(iii) fuel center-line melting (greater than 3113 K),
(iv) oxygen concentration in the sheath greater than 0.7 weight% over at least half of the cladding thickness, and
(v) probability of beryllium-braze assisted cracking greater than 1%.

6. ANALYSIS RESULTS

Analysis results associated with 20% RIH case and 80% ROH case are presented.

6.1. Fuel-element initial conditions (ROFEM simulations)

The power-burnup histories, which are based on the CANDU 6 reactor 660-FPD physics simulation, used in ROFEM code are shown in Figure 2(a). Figure 2(b) shows the pellet centerline temperature during irradiation. Pellet temperatures are dependent on power, and, to a lesser extent, on burnup. The maximum pellet temperature (about 1846 K for SEU43

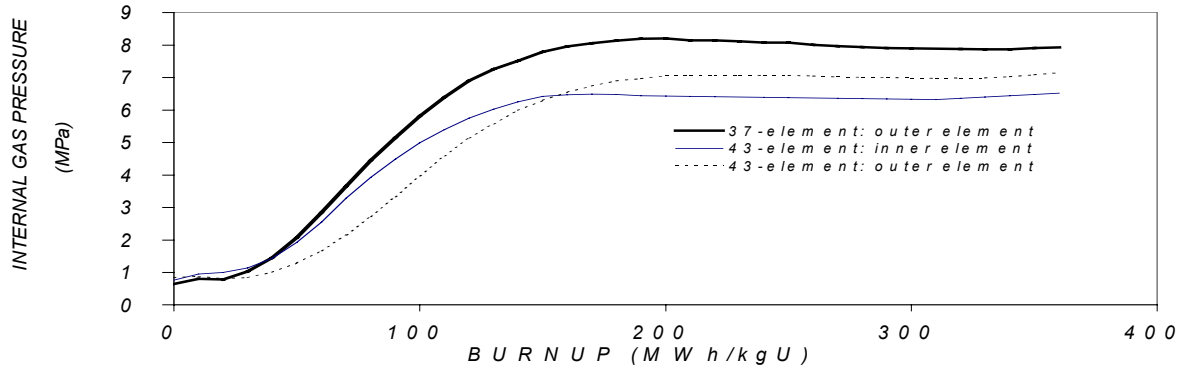

(d)

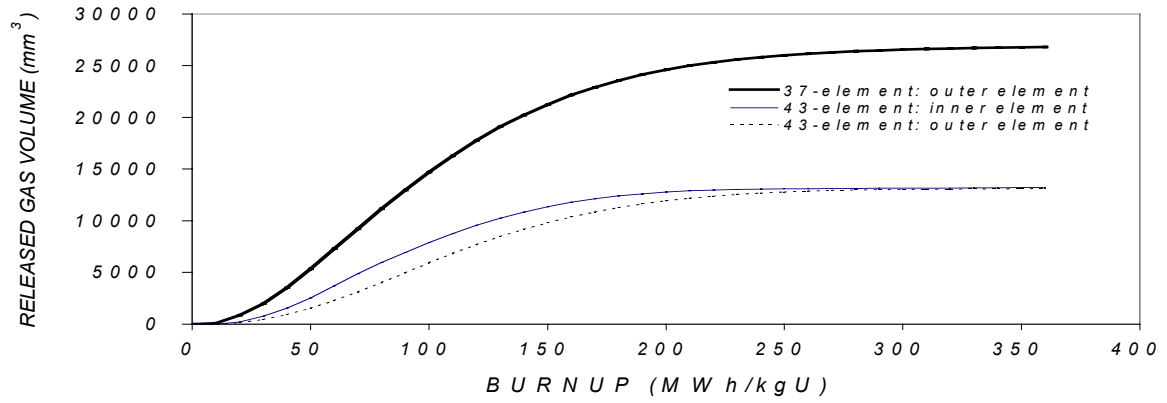

(c)

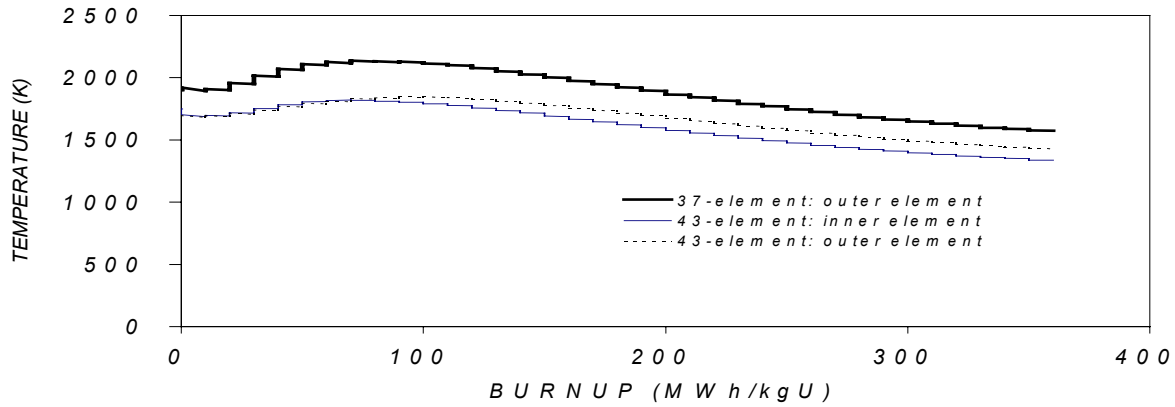

(b)

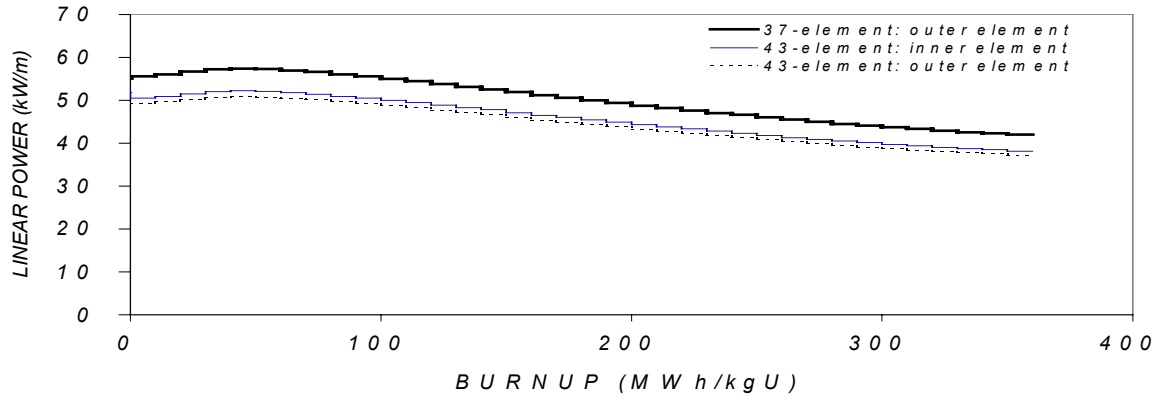

(a)

FIG. 2. Steady-state power history, fuel-centerline temperature, released gas volume and internal gas pressure versus burnup.

outer element) occurred at a burnup of 70 MWh/kg U. This is well below the UO_2 melting temperature of 3113 K. Figures 2(c) and 2(d) show the variation of fission gas volume and internal gas pressure respectively with burnup. For the power histories, the predicted gas pressures is below the coolant pressure of 10.4 MPa, thus the fuel element sheath will not be strained by the internal gas pressure. The maximum internal gas pressure was predicted to be about 7.1 MPa for SEU43 outer element. The end-of-life plastic strain was predicted to be less than 0.5%.

6.2. Fuel-element transient behaviour (CAREB simulations)

The CAREB simulations used the predicted ROFEM fuel-element initial conditions and FIREBIRD output for coolant pressure, coolant temperature and sheath-to-coolant heat transfer coefficient during transient. The LOCA is assumed to occur at the time of highest fuel element internal pressure during steady-state operation. Therefore, the fuel-element initial conditions associated with this time and predicted by ROFEM are applied in the CAREB simulations. The input boundary conditions (channel pressure, coolant temperature, fuel-to-sheath heat transfer coefficient and overpower transient) are shown in Figures 3(a) through 3(d) respectively.

The acceptance criterions were applied to the 20% RIH and 80% ROH accidents analysis. The outer element power history of SEU43 outer element and SEU43 inner element was increased until one of the acceptance criterions for transient behaviour was met. At about 110% of initial high power history the internal gas pressure of SEU43 outer element is little lower than the internal gas pressure of 37-element operating at 100% of initial high power history. The element internal gas pressure predicted by CAREB are provided in Figure 4. Figures 5 and 6 present results of the CAREB calculated fuel center-line temperature and sheath temperature. The maximum fuel centerline temperatures for the SEU43 fuel an standard fuel are well below melting and occur both at 1.8s. The maximum sheath temperature for the SEU43 fuel and standard fuel are 1086.7 K and 1095.5 K respectively and occur both at about 4s. Figure 7 shows the prediction of CAREB, for sheath hoop strain. During the transient the elevated temperatures in the pellet increase the sheath hoop strain. The sheath strains predicted by CAREB are significantly below the 5% failure criterion; therefore sheath failure caused by excessive straining is precluded.

Fuel-element behaviour were also assessed using 80% ROH accident scenario. Figures 8,9,10 and 11 have been plotted for 37-outer element case at 100% of initial high power history and for the SEU43 fuel operating at 110% of high power history. The internal gas pressure of SEU43 outer element is little lower than the internal gas pressure of 37 element fuel. Comparatively with 20% RIH break leater in the transient (~15 s) the sheath experience a second heat-up period resulting from near stagnation conditions (Figure 11). The sheath strains predicted are significantly higher than in the case of 20% RIH break but below the 5% failure criterion. From these figures it can be seen that even at the elevated power of 110% of initial, the center-line temperature, internal gas pressure and sheath-strain are lower for SEU43 fuel than those of 37-element fuel. The results indicate that SEU43 fuelled channel would have an up-rating potential of 10% when compared to the 37-element fuelled channel.

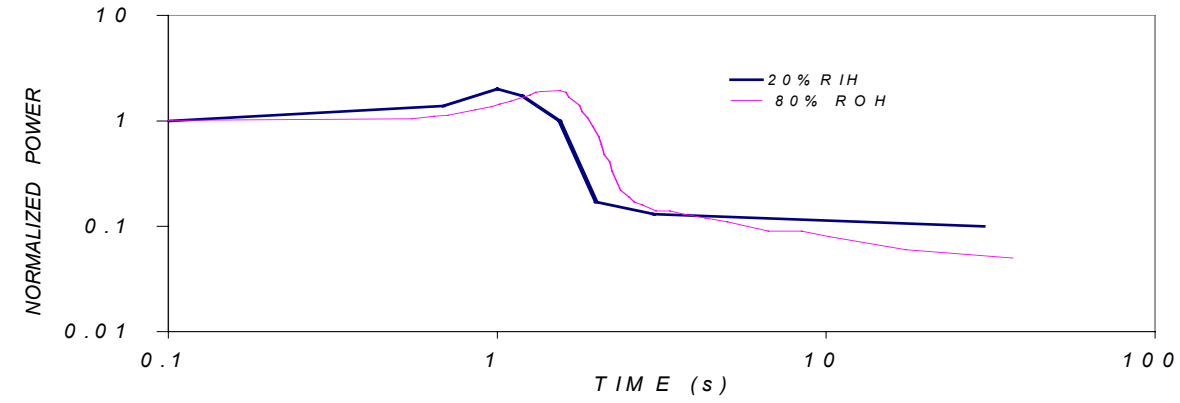

(d)

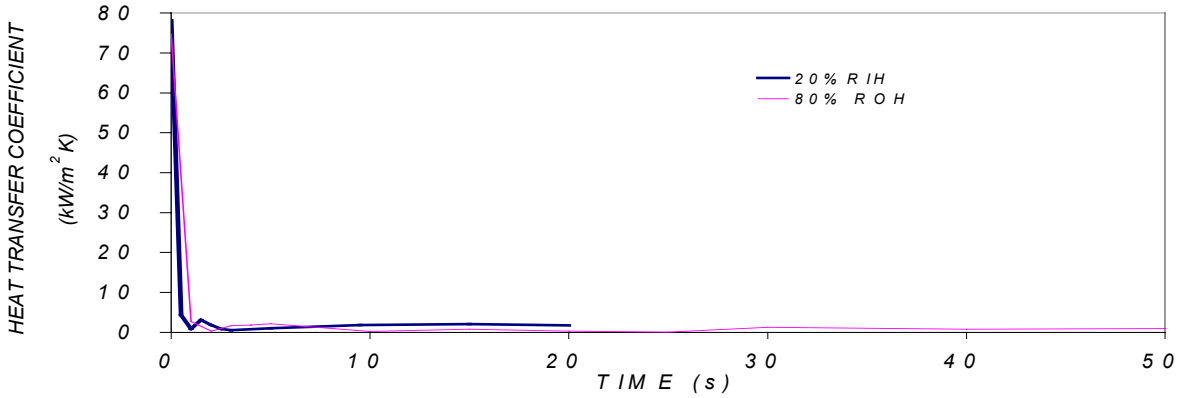

(c)

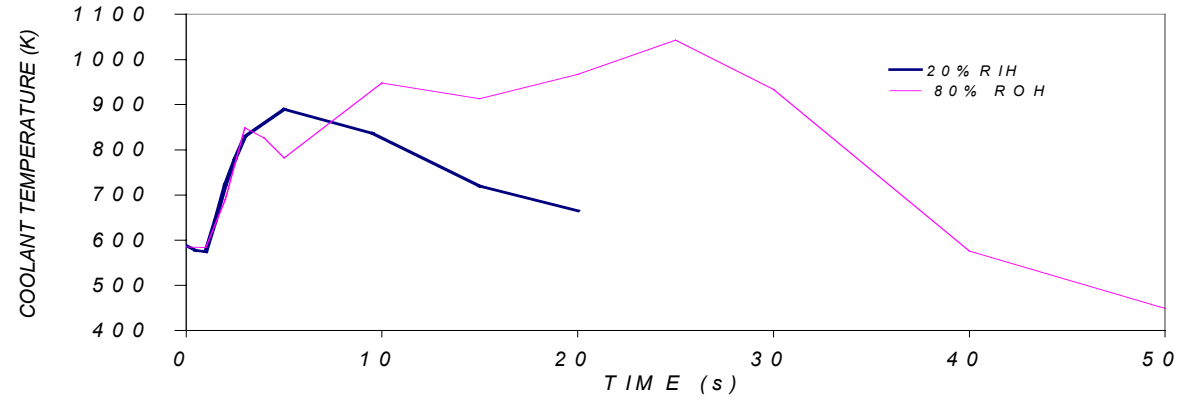

(b)

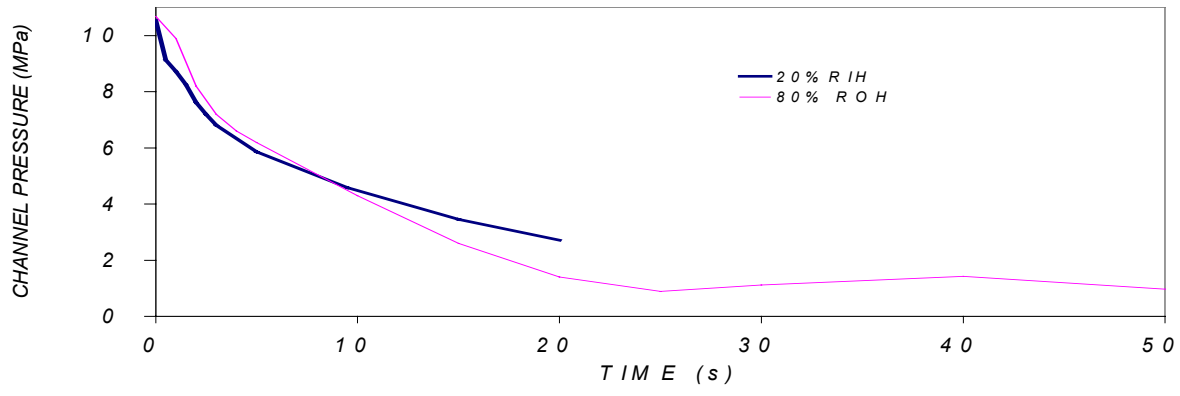

(a)

FIG. 3. 20 %RIH AND 80%ROH transient boundary conditions.

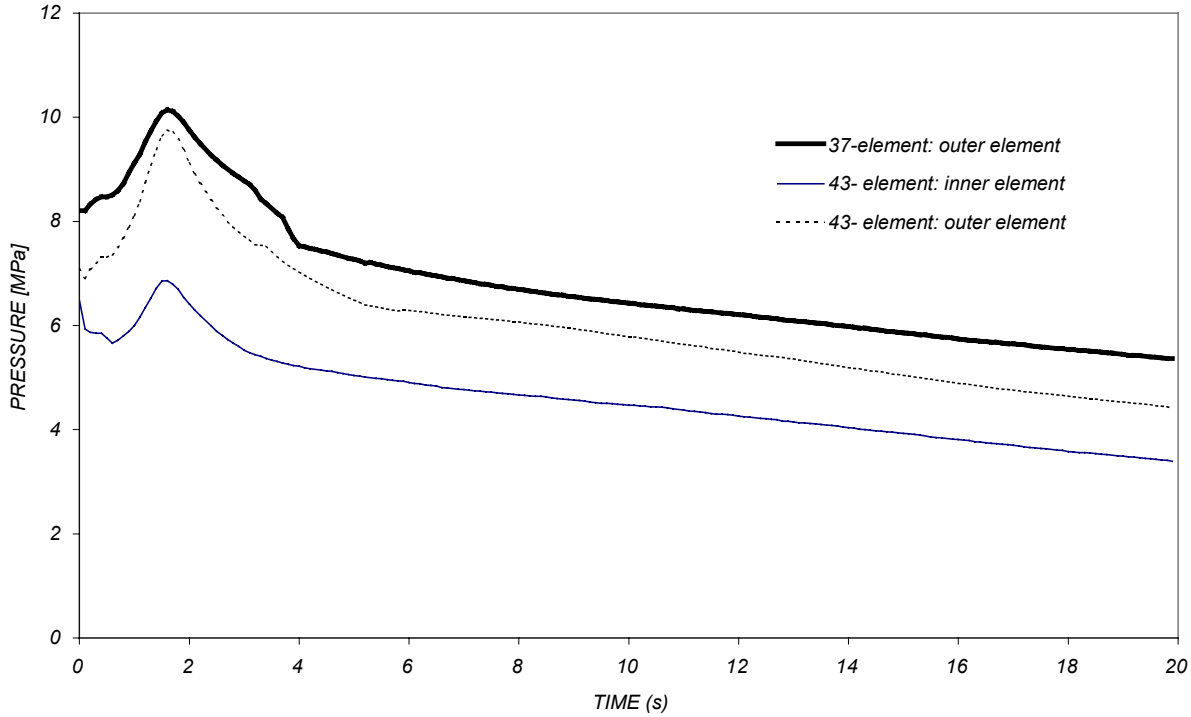

FIG. 4. 20% RIH internal gas pressure.

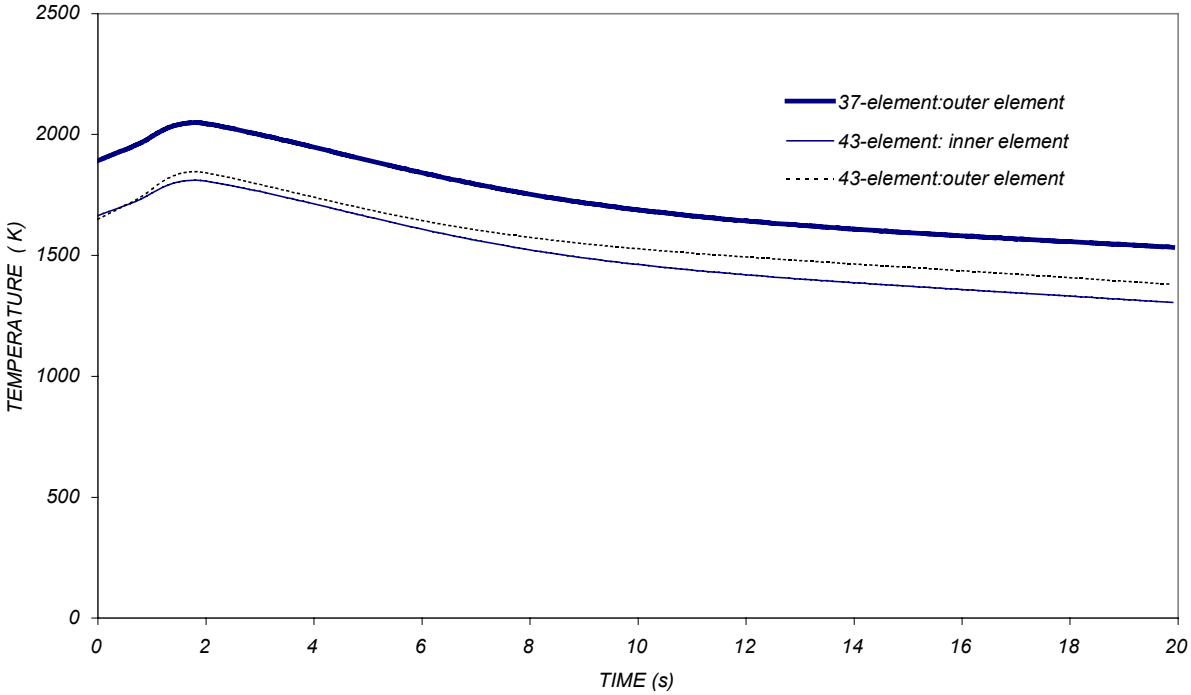

FIG. 5. 20% RIH fuel centerline temperature.

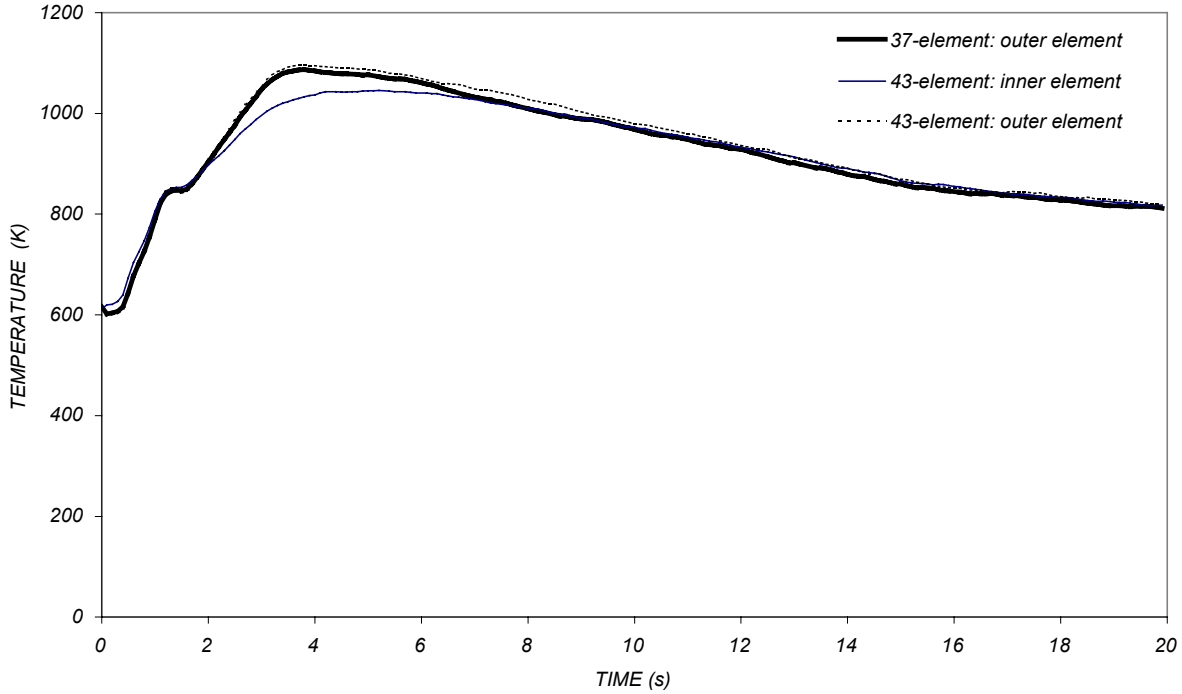

FIG. 6. 20% RIH fuel sheath temperature

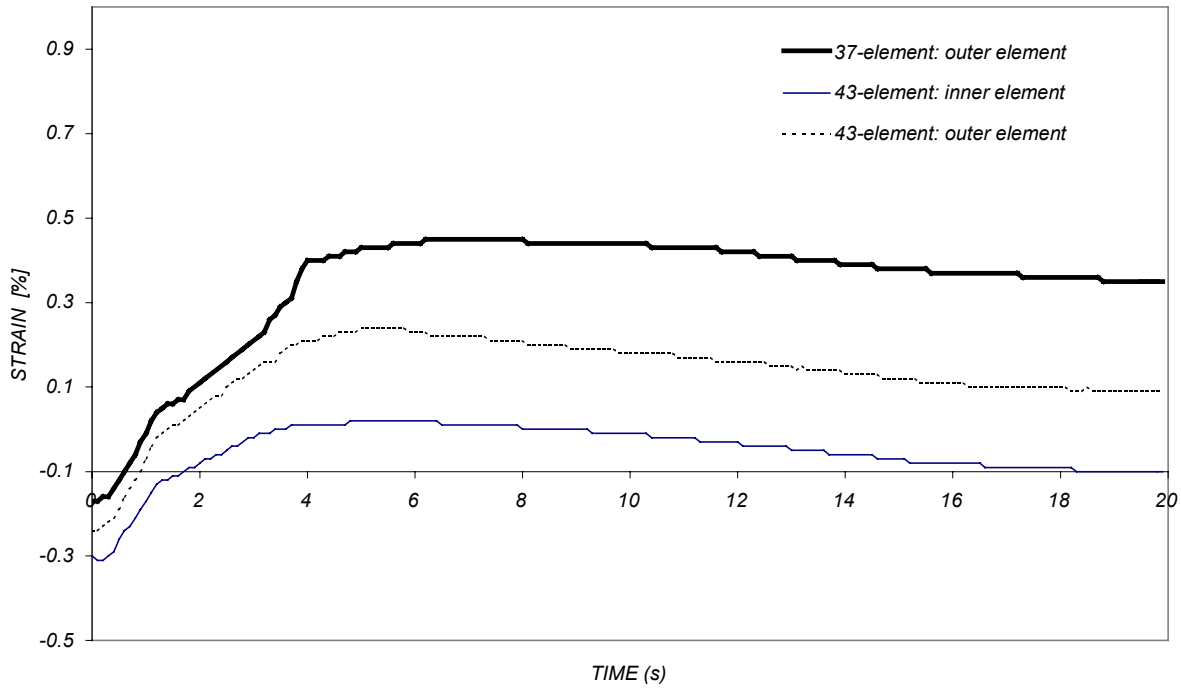

FIG. 7. 20% RIH total sheath strain.

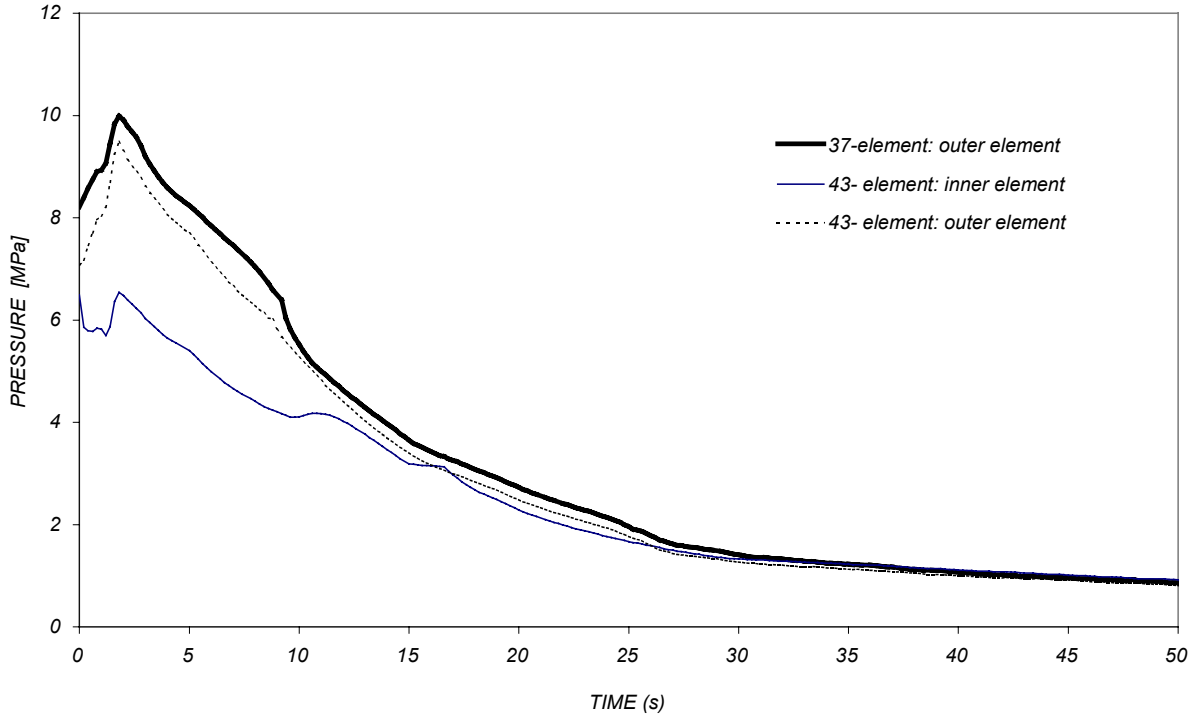

FIG. 8. 80% ROH internal gas pressure.

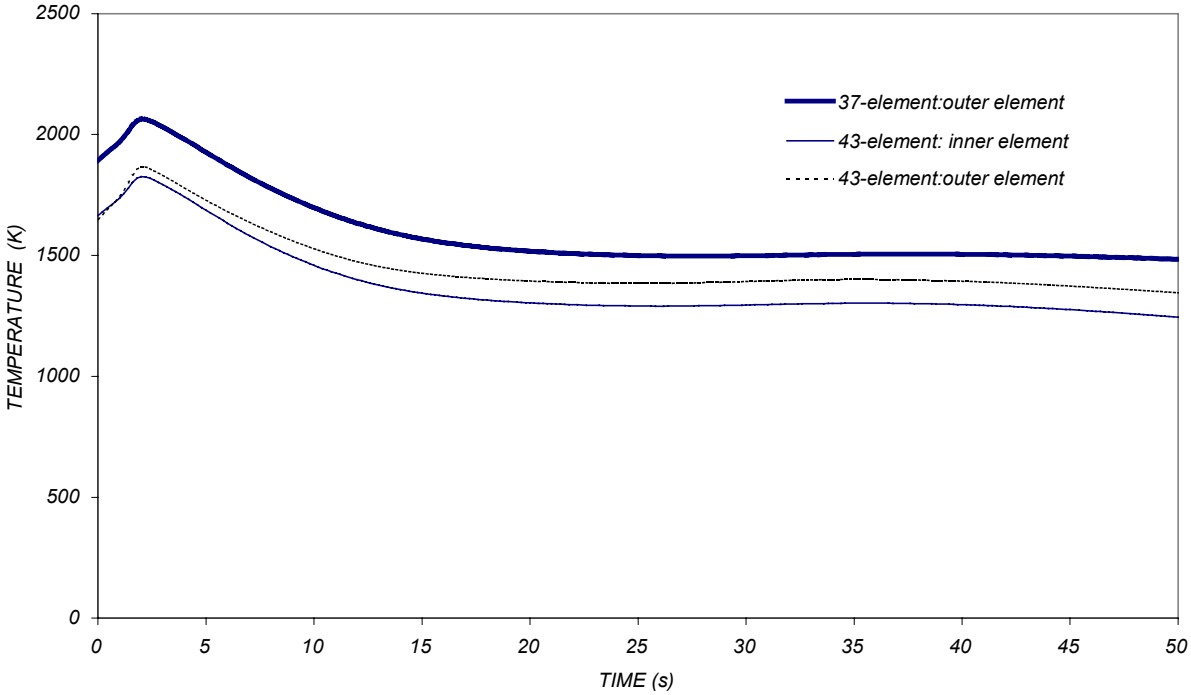

FIG. 9. 80% ROH fuel centerline temperature.

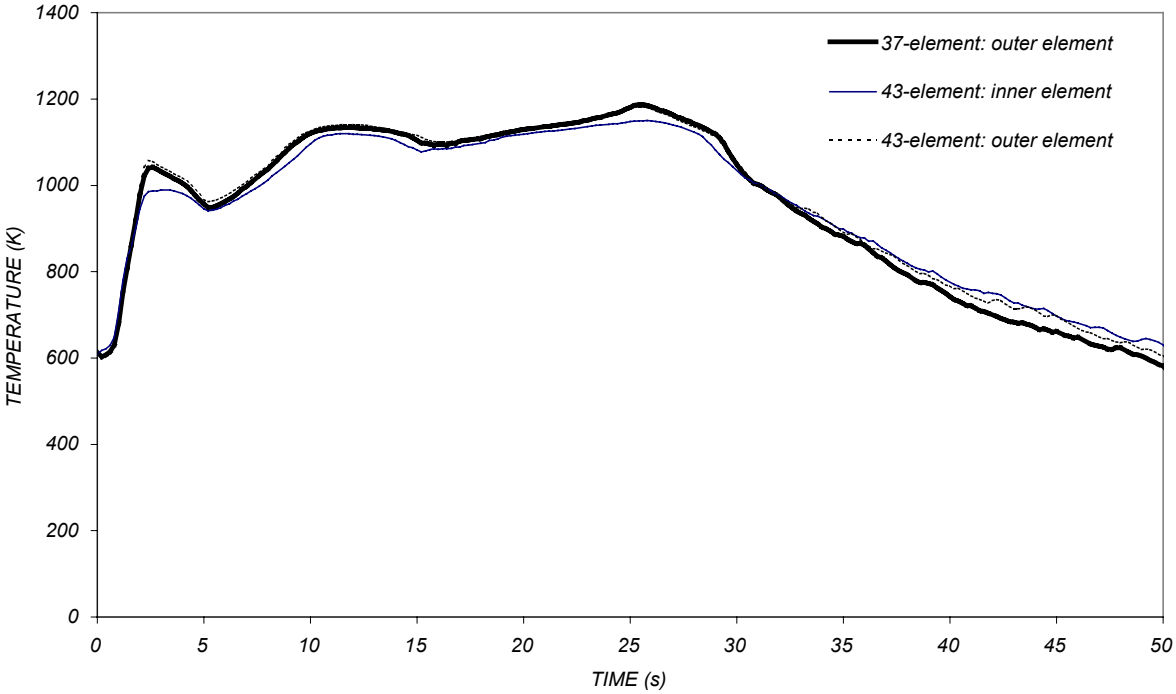

FIG. 10. 80% ROH fuel sheath temperature.

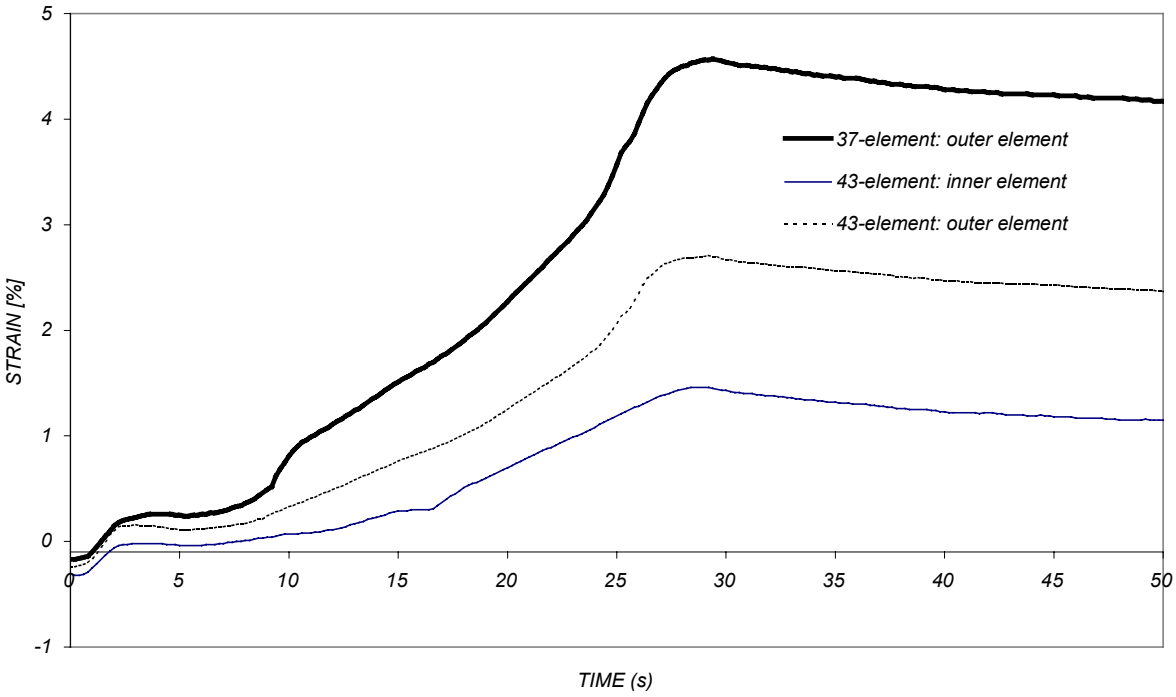

FIG. 11. 80% ROH total sheath strain.

7. DISCUSSION

Early in the transient, the flow in the channel approaches stagnation and the sheath-to-coolant heat transfer is significantly reduced resulting in an increase in the net heat flow into the sheath. The heat content within the fuel is rapidly redistributed (i.e. a decrease in the fuel centerline temperature with an increase in the fuel surface temperature) and therefore the sheath experience a significant temperature rise. The coolant flow moves away from the stagnation point and a reverse flow rate is established. The reverse flow results in an increase in heat removal from the sheath and the sheath temperature decreases. In the case of 80% ROH later in the transient (~15s), the sheath experiences a second heat-up period resulting from near stagnation conditions. However, at this time the heat content within the fuel has been significantly reduced by the heat removal associated with the previous off-stagnation periods. At this point, the relatively slow heat-up indicates that the decay heat generated is slightly greater than the heat removed by convection and radiation. For the range of break size considered, the stagnation period is insufficient to increase the sheath temperature beyond the 1473 K threshold.

The sheath strains failure due to internal gas pressure is one of the mechanisms, which is of concern with respect to fuel integrity during the postulated accident. The sheath strains predicted by CAREB are significantly below the 5% failure criterion; therefore, sheath failure caused by excessive straining is precluded. The total sheath strain is composed of three components: elastic straining, thermal expansion straining, and plastic/creep straining. The stresses and temperatures occurring during a LOCA transient may result in significant changes in the Zircaloy microstructure (grain size, dislocation density and phase changes alpha-to-beta). The creep behaviour of the Zircaloy sheath during a LOCA is dependent on these microstructural changes. The pre-transient analysis predicts that the sheath is in contact with the fuel pellet at the onset of the accident; however, a radial gap develops during the LOCA transient. The stress in the sheath becomes tensile (as the coolant pressure falls below the element internal gas pressure) and eventualy reaches a peak stress (between 10-12 MPa at about 20 s). During the time when most of the strain takes place, the sheath temperature is steady due to the superheated steam conditions in the channel. For all the reactor header breaks analyzed the maximum sheath strain is less than ~5%.

8. CONCLUSIONS

A recently developed advanced CANDU fuel bundle has major design improvements over the 37-elements standard bundle.

Although the maximum element-burnup of the SEU43 design is extended beyond the CANDU 6 burnup, the maximum linear power of SEU43 (47.2 KW/m) is significantly lower than the maximum linear power of a CANDU 6 reactor (57.5 KW/m). The reduced element-power level in conjunction with internal design modification for the SEU43 design resulted in significantly lower internal gas pressure under steady state and transient conditions, as compared with CANDU 6 design.

The computer codes ROFEM and CAREB were used to predict the SEU43 fuel performance during a LOCA. The conceptual feasibility of the SEU43 design was evaluated against specific criterions. The maximum sheath temperature for the cases analyzed is less than 1473 K. The maximum sheath strain is less than 5%.

From the analysis of a 20% RIH break and 80% ROH break the power in a channel within a full core of SEU43 fuel can be increased to 110% of initial power at which the internal gas pressure in outer element is approximately equal or little lower than the internal gas pressure of the 37-element fuelled channel.

There is uprating potential available with a SEU43 fuelled core, and the consequences of a large break LOCA for the uprated SEU43 core would be no worse than the consequences after a large break LOCA for a 37-elemente fuelled core at nominal power.

REFERENCES

[1] HORHOIANU, G. et al, Development of SEU43 Fuel Bundle for CANDU Type Reactor, Ann. Nucl. Energy, vol 25, No.16, pp.1363-1372, 1998.

[2] HORHOIANU, G. et al, Improvement of the CANDU Type Fuel Element Performance in Order to Increase the Ability to Operate at High Powers and to Meet High Burnup, Final Report to IAEA research contract 6197/RB, INR Pitesti, Romania, 1992.

[3] HORHOIANU, G. et al, Experimental Aspects of Load Cycling Capability of CANDU Type Nuclear ` Fuel, Annual Meeting on Nuclear Technology'96, Mannheim, Germany, Procedings, pp.442-445, 1996.

[4] HORHOIANU, G. et al, Investigation of Fuel rod Behaviour under Extended Burnup Conditions with ROFEM Fuel Performance Code, Ann. Nucl. Energy, Vol 25, No.10, pp.695-708, 1998.

[5] ARIMESCU, I., CAREB a Computer Code to Predict Fuel Element Behavior during High-Temperature Transients, Internal Report No. 1336, INR Pitesti, Romania, 1983.

[6] STEFAN, I., PAPADOPOL, G., Recent Validation of the CAREB code, Internal Report No.4806, INR Pitesti, Romania, 1996.

[7] PANDELE, A.et al, FIREBIRD III Mod1-77 A Thermalhydraulic and Neutron Kinetics Code for CANDU Analysis, Internal Report No. 5230, INR Pitesti, Romania, 1998.

[8] NAKAJAMA, T., ICHIKAWA, M., IWANA, Y., FEMAXI III, A Computer Code for the Analysis of Thermal and Mechanical Behavior of Fuel Rods, Report JAERI 1298, 1985.

[9] MOSCALU, D.R., TITA, M., GHEORGHIU, E., The Validation of CANDU Type Fuel Performance Codes, Internal Report No. 4381, INR Pitesti, Romania, 1994.

[10] MOSCALU, D.R., "On the Role of the OU_2 Thermal Conductivity Degradation at Extended Burnup in PHWR Type Fuels", Paper presented to TOPical Meeting on Nuclear Fuel, Wurzburg, Germany, March 12-15, Transactions TOPFUEL'95 volume II, pp 96 – 100, 1995

[11] PALMER, I.D. et al, A Model for Predicting the Radial Power Profile in a Fuel Pin, in Proc. IAEA Tech. Comm. Meeting of Fuel Behaviour Modelling, Preston,1984.

LIST OF PARTICIPANTS

Amaya, M.	Japan Nuclear Fuel Co Ltd, 2163 Narita-cho, Oarai-Machi, Higashi-Ibaraki-gun, 311-1313, Japan
Arimescu, I.	Siemens Power Corporation, 2101 Horn Rapids Road, Richland, Washington 99352, United States of America
Bang, J.G.	Korea Atomic Energy Research, P.O. Box 105, Yusung, Taejon 305-600, Repuplic of Korea
Bairiot, H.	FEX, 24 Lysterdreef, MOL, B-2400, Belgium
Bentejac, F.	Commissariat à l'Energie Atomique, Centre De Saclay, DRN/DMT/SEMI/LEMO, F-91191Gif-sur-Yvette, France
Bernard, L.C.	Framatome Nuclear Fuel, 10 Rue Juliette Récamier, F-69456, Lyon Cedex 06, France
Bogatyr, S.	Bochvar Institute, Rogova Str 5, Moscow 123060, Box 369, Russian Federation
Bowsher, B.R.	AEA Technology Nuclear Science, A50 Winfrith, Dorchester, Dorset, DT2 8DH, United Kingdom
Bremier, S.	Institute for Transuranium Elements, Postfach 2340, D-76125 Karlsruhe, Germany
Brown, C.	British Nuclear Fuels plc, B582/3S Sellafield, Seascale, Cumbria, CA20 1PG, United Kingdom
Cook, P.	British Nuclear Fuels plc, B582/3N Sellafield, Seascale, Cumbria, CA20 1PG, United Kingdom
Denis, A.	Comisión Nacional de Energía Atómica, Av. del Libertador 8250, 1429 Buenos Aires, Argentina
Eastman, R	British Nuclear Fuels plc, B33 Sellafield, Seascale, Cumbria, CA20 1PG, United Kingdom
Elenkov, D.	Institute of Nuclear Research and Nuclear Energy, 72 Tsarigradsko shoes, 1784-Sofia, Bulgaria

Ellis, B.	AEA Technology plc, Windscale, Seascale, Cumbria, CA20 1PF, United Kingdom
El Shanawany, M.	NSD, Health & Safety Executive, Room 311, St Peter's House, Bootle, Merseyside, L20 3LZ, United Kingdom
Enine, A.	The Novosibirsk Chemical Concentrates Plant, 94 B Khmelnitsky St, Novosibirsk, 630110, Russian Federation
Esteves, R.G.	Indústrias Nucleares do Brasil S/A, 161 R Mena Barreto, Rio de Janeiro 22271-100, Brazil
Fandeur, O.	Commissariat à l'énergie atomique, Centre de Saclay, DRN/DMT/SEMI/LEMO, F-91191Gif-sur-Yvette, France
Fisher, S.	British Nuclear Fuels plc, B582/N Sellafield, Seascale, Cumbria, CA20 1PG, United Kingdom
Gates, G.A.	British Nuclear Fuels plc, B582/N Sellafield, Seascale, Cumbria, CA20 1PG, United Kingdom
Gomme, R.A.	AEA Technology plc, Windscale, Seascale, Cumbria, CA20 1PF, United Kingdom
Goethals, S.H.	Tractebel Energy Engineering, avenue Ariane 7, B-1200 Brussels, Belgium
Green, R.	British Nuclear Fuels plc, B582/N Sellafield, Seascale, Cumbria, CA20 1PG, United Kingdom
Hede, G.	Westinghouse Atom AB, Finnslätten, Bränslegatan, Västerãs 72163, Sweden
Horhoianu, G.	Institute for Nuclear Research, PO Box 78, 0300 Pitesti, Romania
Ivison, P.K.	British Nuclear Fuels plc, B582/N Sellafield, Seascale, Cumbria, CA20 1PG, United Kingdom
Kamimura, K.	Nuclear Power Engineering Corporation, Fujita Kanko Toranomon Building 6F, 3-17-1, Minato-ku, Tokyo, 105-000, Japan

Kikuchi, T.	Nuclear Fuel Industries, 950 Ohaza-Noda Kumatori-Cho, Sennan-Gun, Osaka, Japan
Kouzmine, V.	Research Institute of Atomic Reactors, 433510, Dimitrovgrad-10, Uljanovsk Regionru, Russian Federation
Kromar, M.	Jozef Stefan Institute, Jamova 39, Ljubljana 1000, Slovenia
Lansiart, S.	Commissariat à l'énergie atomique, CEN-Cadarache, F13108 St Paul-Lez-Durance Cedex, France
Lassmann, K.	Institute for Transuranium Elements, Postfach 2340, D-76125 Karslruhe, Germany
Lee, B.H.	Korea Atomic Energy Research Institute, P.O. Box 105, Yusung, Taejon 305-600, Republic of Korea
Leigh, G**.**	British Nuclear Fuels plc, B582/N Sellafield, Seascale, Cumbria, CA20 1PG, United Kingdom
Lemoine, F.	IPSN, Bât 702, CEA-Cadarache, F-13108 St Paul Lez Durance Cedex, France
Medvedev, A.V.	Bochvar Institute (VNIINM), Rogova Str 5, Moscow 123060, Box 369, Russian Federation
Mertens, L.	Belgonucléaire, 4 Avenue Ariane, B-1200 Brussels, Belgium
Onoufriev, V.	International Atomic Energy Agency, Wagramer Strasse 5, PO Box 100, A-1400 Vienna, Austria
Owaki, M.	Nuclear Fuel Industries, 3135-41, Muramatsu, Tokai-mura, Naka-gun, Ibaraki, 319-1196, Japan
Palmer, I.	British Nuclear Fuels plc, B709 Springfields, Preston, Lancashire, PR4 OXJ, United Kingdom
Quecedo, M.	ENUSA, Santiago Rusiñol 12, Madrid 28040, Spain
Ranta-Puska, K.	Technical Research Centre of Finland, Tekniikantie 4C, 1604 Espoo, Finland

Rashid, J.	Anatech, 5435 Oberlin Drive, San Diego, California 92121, United States of America
Schubert, A.	Institute for Transuranium Elements, Postfach 2340, D-76125 Karslruhe, Germany
Serna, J.J.	ENUSA, Santiago Rusiñol 12, Madrid 28040, Spain
Sharpe, M.	British Nuclear Fuels plc, B582/N Sellafield, Seascale, Cumbria, CA20 1PG, United Kingdom
Shaw, T.	AEA Technology plc, Windscale, Seascale, Cumbria, CA20 1PF, United Kingdom
Shea, J.	British Energy Generation Ltd, Barnett Way, Gloucester, GL4 3RS, United Kingdom
Sokolov, F.F.	Bochvar Institute (VNIINM), Rogova Str 5, Moscow 123060, Box 369, Russian Federation
Sontheimer, F.	Siemens AG, Unternehmensbereich KWU, NBTM, Bunsenstraβe 43, Erlangen, Germany
Stephen, R.	British Nuclear Fuels plc, B33 Sellafield, Seascale, Cumbria, CA20 1PG, United Kingdom
Stephenson, K.	British Nuclear Fuels plc, B582/3S Sellafield, Seascale, Cumbria, CA20 1PG, United Kingdom
Strizhov, P.	Kurchatov Institute, 3-238 Leningradskoe shosse, Moscow 125080, Russian Federation
Szuta, M.	Institute of Atomic Energy, Otwock, Swierk 05-400, Poland
Tverberg, T.	OECD Halden Reactor Project, P.O. Box 173, N-1751 Halden, Norway
Volkov, S.	Joint-Stock Company TVEL, 24/26 B Ordynka St, Moscow 101000, Russian Federation
Wallin, H.T.	Paul Scherrer Institut, OFLA, CH-5232 Villigen PSI, Switzerland

Weiner, R.A.	K W Consulting Inc., P.O. Box 101567, Pittsburgh, Pennsylvania 15237 United States of America
Weston, R.	British Nuclear Fuels plc, B582/3N Sellafield, Seascale, Cumbria, CA20 1PG, United Kingdom
White, R.	18 Green Close, Uley, Gloucestershire GL11 5TH, United Kingdom
Wright, J.	British Nuclear Fuels plc, B33 Sellafield, Seascale, Cumbria CA20 1PG, United Kingdom